A spectroscopic study of water vapor on Mars

Elise Wright Knutsen

▶ **To cite this version:**

Elise Wright Knutsen. A spectroscopic study of water vapor on Mars. Earth and Planetary Astrophysics [astro-ph.EP]. Université Paris-Saclay, 2023. English. NNT : 2023UPASP136 . tel-04306633

HAL Id: tel-04306633
https://theses.hal.science/tel-04306633

Submitted on 25 Nov 2023

HAL is a multi-disciplinary open access archive for the deposit and dissemination of scientific research documents, whether they are published or not. The documents may come from teaching and research institutions in France or abroad, or from public or private research centers.

L'archive ouverte pluridisciplinaire **HAL**, est destinée au dépôt et à la diffusion de documents scientifiques de niveau recherche, publiés ou non, émanant des établissements d'enseignement et de recherche français ou étrangers, des laboratoires publics ou privés.

université PARIS-SACLAY

A spectroscopic study of water vapor on Mars

Une étude spectroscopique de la vapeur d'eau sur Mars

Thèse de doctorat de l'université Paris-Saclay

École doctorale n◦ 127 : astronomie et astrophysique d'Ile-de-France (AAIF)
Spécialité de doctorat: Astronomie et Astrophysique
Graduate School : Géosciences, climat, environnement et planètes. Référent: Université de Versailles Saint-Quentin-en-Yvelines

Thèse préparée dans les unités de recherche **LATMOS/IPSL (Université Paris-Saclay, UVSQ CNRS),** souss la direction de **Franck MONTMESSIN**, Directeur de Recherche

Thèse soutenue à Guyancourt, le 25 octobre 2023, par

Elise Wright KNUTSEN

Composition du Jury

Membres du jury avec voix délibérative

Valérie CIARLETTI Directrice de Recherche CNRS à l'Université Paris-Saclay	Présidente
Agustin SANCHEZ-LAVEGA Professeur à l'Universidad del País Vasco, UPV/EHU, Espagne	Rapporteur & Examinateur
Colin WILSON Project Scientist, European Space Agency aux Pays-Bas	Rapporteur & Examinateur
Ann Carine VANDAELE Senior Researcher, Institut d'Aéronomie Spatiale de Belgique	Examinatrice
Mike WOLFF Senior Researcher, Space Science Institute, États-Unis	Examinateur

THESE DE DOCTORAT
NNT : 2023UPASP136

université PARIS-SACLAY
ÉCOLE DOCTORALE
Astronomie
et Astrophysique
d'Île-de-France (AAIF)

Titre : Une étude spectroscopique de la vapeur d'eau sur Mars

Mots clés : Spectroscopie, Mars Express, SPICAM, PFS, Perseverance rover, SuperCam

Résumé : La vapeur d'eau est un composant mineur dans l'atmosphère de Mars, mais elle joue un rôle significatif dans la formation du climat actuel de la planète. L'eau était autrefois beaucoup plus abondante, ce qui se traduit ajourd'hui par des caractéristiques telles que des lits de rivières asséchées, des canaux d'écoulement et des minéraux hydratés, suscitant ainsi des recherches approfondies sur sa disparition. La vapeur d'eau atmosphérique a été largement surveillée et étudiée au cours des dernières décennies, et la plupart de ses caractéristiques chimiques et dynamiques sont désormais connues. Cependant, l'une des rares difficultés restantes concerne sa distribution verticale. Des missions telles que Mars Express, MAVEN et ExoMars Trace gas Orbiter ont ouvert une nouvelle ère dans les études de profils verticaux de l'eau, fournissant des informations précieuses. Cependant, l'accès à la partie la plus basse de l'atmosphère est resté limité. La vapeur d'eau est généralement supposée avoir une distribution uniforme en dessous de la couche de condensation des nuages, mais certaines mesures remettent en question cette hypothèse, suggérant un profil plus complexe près de la surface où les échanges entre le régolithe et l'atmosphère pourraient jouer un rôle. Le principal travail de cette thèse est lié à la vapeur d'eau, avec pour objectif l'étude de la teneur en eau près de la surface dans un contexte saisonnier et géographique. Pour cela, nous avons exploré deux techniques non conventionnelles : une méthode de synergie spectrale appliquée aux observations au nadir, et des observations spectroscopiques infrarouges de surface. Cette thèse contient également un chapitre sur la météo spatiale martienne, qui présente des travaux secondaires menés tout au long de cette thèse.

La synergie spectrale utilise des spectres infrarouges proches et thermiques provenant respectivement du SPICAM et du PFS sur Mars Express. La vapeur d'eau est récupérée simultanément à partir des deux bandes spectrales, et comme ces deux intervalles de longueurs d'onde ont sensibles à des régions altitudinales atmosphériques distinctes, le degré de liberté accru qui en résulte permet d'obtenir des informations sur la distribution verticale. La synergie a été appliquée à près de 200 000 observations co-localisées, échantillonnées sur environ huit années martiennes. Des climatologies composites d'abondances de colonne très précises et de profils verticaux ont été rassemblées. Les abondances de colonne s'accordaient avec les études précédentes, mais les résultats présentaient des différences significatives avec la base de données climatiques de Mars, autant pour les abondances de colonne que la distribution verticale. Le pic de sublimation printanier a été observé comme moins extrême et son apparition était plus tardive par rapport au modèle. Le confinement vertical est observé comme étant plus fort par rapport au modèle dans presque toutes les saisons et latitudes, et la distribution est rarement uniforme. Le confinement en fonction de la saison et de la latitude a été étudié en détail, et un comportement de type ondulation latitudinale a été découvert.

Pour les observations de surface, nous utilisons le spectromètre infrarouge de SuperCam sur le rover Perseverance, et réalisons des mesures dites "passives du ciel". À ce jour, nous avons effectué 64 observations régulières sur une année martienne. Dans la technique du ciel passif, des spectres infrarouges sont acquis à deux angles d'élévation puis rationnés afin d'éliminer les effets continus et instrumentaux. Le spectre résultant est principalement sensible à l'atmosphère en dessous de 15 km et peut donc sonder directement des altitudes peu accessibles depuis l'orbite. Nous présentons ici les progrès réalisés en matière de traitement des données et de développement d'un outil de récupération. Un modèle direct et une routine de minimisation ont été composés et sont en cours de test et de d'amélioration.

université PARIS-SACLAY
ÉCOLE DOCTORALE
Astronomie
et Astrophysique
d'Île-de-France (AAIF)

Title : A spectroscopic study of water vapor on Mars

Keywords : Spectroscopy, Mars Express, SPICAM, PFS, Perseverance rover, SuperCam

Abstract : Water vapor is a minor species in the atmosphere of Mars, yet it has played and still plays a significant role in shaping the climate of the planet. Water was once much more abundant, evident today from features such as dry riverbeds, outflow channels and hydrated minerals, prompting extensive research into its disappearance. Atmospheric water vapor has been monitored and studied extensively in the past decades, and most of its chemical and dynamical behaviors are now known. One of the few remaining challenges is related to its vertical distribution. Missions like Mars Express, MAVEN, and the ExoMars Trace gas Orbiter ushered in a new era in water vertical profile studies and have all provided valuable insights, but access to the lowest part of the atmosphere has remained limited. Water vapor is commonly assumed to have a uniform distribution below the cloud condensation layer, but some measurements are challenging this view, suggesting a more complex profile near the surface, where regolith-atmosphere exchanges might be present.

The main work of this thesis is related to water vapor, with the objective of investigating the near-surface water content in both a seasonal and geographical context. To do this, we have explored two unconventional infrared spectroscopic techniques; a spectral synergy method applied to nadir observations, and surface observations. This thesis also contains one chapter about Martian space weather, which contains a collection of smaller projects conducted throughout the duration of this PhD.

The spectral synergy uses near- and thermal-infrared spectra from SPICAM and PFS respectively on Mars Express. Water vapor is retrieved simultaneously from both spectral bands, and since these two wavelength intervals are sensitive to separate altitude regions, the resulting increased degree of freedom allows information on the vertical distribution to be gained. The synergy was applied to almost 200 000 co-located observations, sampled across roughly eight Mars year. Composite climatologies of very accurate column abundances and vertical profiles were assembled. The column abundances were in good agreement with previous studies, but the results exhibited some significant differences from the Mars Climate Database, both with respect to the column abundances and the vertical distribution. The spring sublimation peak was observed to be less extreme, and the sublimation onset occurred later than the model. The vertical confinement is observed to be stronger compared to the model at almost all seasons and latitudes, and the distribution is rarely uniform. The confinement as a function of season and latitude was studied in details, and a latitudinal wave-like behavior was discovered in both hemispheres, as well as a prevailing double-layer structure in the northern hemisphere.

For the surface observations, we make use of the infrared spectrometer part of SuperCam on the Perseverance rover, and conduct so-called passive sky measurements. To date, we have 64 observations taken regularly across one Martian year. In the passive sky technique, infrared spectra are acquired at two elevation angles and then ratioed in order to remove continuum and instrumental effects. The resulting spectrum is mainly sensitive to the atmosphere below 15km, and can therefore directly probe altitudes rarely accessible from orbit. Here we outline the progress made so far regarding data processing and the development of a retrieval pipeline. A forward model and minimization routine has been developed, and is currently undergoing testing and further maturing.

Contents

Acknowledgements **9**

Introduction **13**

1 Mars and its atmosphere **15**
1.1 Mars exploration . . . 17
1.1.1 Historic overview of past Mars missions . . . 18
1.2 The surface of Mars . . . 21
1.2.1 Geological evolution . . . 21
1.2.2 Hemispheric dichotomy . . . 22
1.2.3 Mineralogy . . . 24
1.2.4 Regolith . . . 24
1.3 The Martian atmosphere . . . 25
1.3.1 Composition . . . 26
1.3.2 The CO_2 cycle . . . 28
1.3.3 Vertical structure . . . 29
1.3.4 Aerosols . . . 33
1.3.5 Dynamics and circulation . . . 38
1.4 Water vapor . . . 39
1.4.1 Role of the polar caps . . . 40
1.4.2 Annual cycle of water vapor column abundance . . . 41
1.4.3 Water vertical profile . . . 42
1.5 Carbon monoxide . . . 48
1.6 Outstanding questions and purpose of this thesis . . . 49

2 Instruments used in this thesis **53**
2.1 The basis of spectroscopy . . . 53
2.2 The Mars Express mission . . . 54
2.2.1 PFS . . . 56
2.2.2 SPICAM . . . 57
2.2.3 SPICAM and PFS water vertical sensitivity . . . 59
2.3 The Mars2020 Perseverance rover . . . 62
2.3.1 SuperCam . . . 63
2.3.2 SuperCam IRS studying water vapor . . . 67

3 Data processing **69**
3.1 SPICAM and PFS in spectral synergy . . . 69
3.1.1 Synergistic retrieval . . . 69
3.2 SuperCam IRS observations . . . 72
3.2.1 Passive sky pre-processing . . . 73
3.2.2 Passive sky post-processing . . . 76

4 Water vapor from spectral synergy **79**
4.1 Data selection . . . 79
4.2 Water vapor column abundance climatology . . . 80
4.2.1 Column abundance comparison, Synergy vs MCD . . . 84
4.3 Near-surface water vapor content . . . 84
4.4 A closer look at the North Pole sublimation season . . . 86
4.5 Vertical distribution climatology . . . 88
4.6 Summary . . . 89

5 SuperCam investigations **93**
5.1 The forward model . . . 93
5.1.1 Incorporating gases using the correlated-k method . . . 93
5.1.2 Implementing dust . . . 97
5.1.3 H_2O and CO modeling . . . 98
5.1.4 Final synthetic spectrum . . . 99
5.2 Minimization scheme . . . 102
5.3 Discussion and summary . . . 105
5.3.1 Data handling . . . 105
5.3.2 Retrieval routine . . . 105
5.3.3 Summary . . . 105

6 Space weather and Mars' magnetic environment **107**
6.1 Introduction to space weather . . . 107
6.1.1 Galactic background radiation . . . 108
6.1.2 Transient solar particle events . . . 109
6.1.3 Influence of particle radiation on the Mars local environment . . . 110
6.2 Space weather as sensed by EDAC counters . . . 114
6.2.1 EDAC data set and processing . . . 116
6.2.2 Heliospheric Galactic Cosmic Ray behaviour . . . 118
6.2.3 Solar particle events at Mars . . . 121
6.3 Martian aurora with SuperCam . . . 124
6.3.1 Auroral campaign preparations . . . 125
6.3.2 SuperCam VIS nighttime observations . . . 130
6.4 Space weather summary . . . 131
6.4.1 EDAC projects . . . 131
6.4.2 Aurora with SuperCam . . . 133

Conclusions and perspectives **135**

List of publications **139**

List of public speaking events **141**

Appendices **143**

A Article: Water Vapor on Mars: A Refined Climatology and Constraints on the Near-Surface Concentration Enabled by Synergistic Retrievals **145**

B Conference proceedings: A spectral synergy method applied to PFS and SPICAM nadir observations to constrain near-surface water content in the Martian atmosphere **173**

C Article: Galactic cosmic ray modulation at Mars and beyond measured with EDACs on Mars Express and Rosetta **181**

References **190**

Acknowledgements

Completing this PhD has been the greatest journey of my professional life, and rounding it all off with this thesis, I feel is a worthy conclusion. I want to sincerely express my gratitude to everyone who has helped me along the way, to achieve this milestone.

First and foremost, many thanks to my excellent supervisor Dr. Franck Montmessin, for proposing this subject, for all his insights, advice, support and encouragements along the way. Thank you for letting me explore side-projects, and for providing me with the means to pursue any opportunity that came my way. Thanks to you, I have had the amazing experience of being included in several instrument teams, and so I also want to thank all the contributors to the SPICAM, PFS, ACS and SuperCam teams, who considerably widened my understanding of the international space community. My appreciation also goes out to LATMOS, where I spent most of my time, and to CNRS, for providing funding so that I had to chance to undertake this study.

My deepest gratitude also goes out to all the members of the jury; chair Dr. Valérie Ciarletti, examiners Dr. Mike Wolff and Dr. Ann Carine Vandaele and reviewers Dr. Colin Wilson and Dr. Agustin Sanchez-Lavega. It takes much effort to read and provide feedback on a doctoral thesis, and I thank you all for your time and insightful comments. I also wish to thank my thesis committee; Aymeric Spiga and Alice Le Gall, for being very accommodating (starting a thesis during a pandemic has its own set of challenges), and for providing guidance and support, both scientifically and career-wise.

I also want to give a special thanks to Dr. Loïc Verdier for his endless patience, skills with technical difficulties, for always taking the time to walk me through any struggle I encountered. Without your support and guidance this thesis would never have seen the light of day. And to Dr. Cyrine Nehmé, thank you for creating a space where we shared laughter, tears and liters of Bloody Mary.

I am forever grateful to Dr. Anni Määttänen, for lending me her Le Petit Prince, and many mind-opening conversations, and most of all for her valuable mentorship. Thanks to Drs Ashwin Braude, Margaux Vals, Loïc Rossi, Lucio Baggio and Aurélien Stcherbinine for your support and personal motivation. I am endlessly grateful to you all for your good humor, wisdom and generosity, for plenty of coffee breaks and entertaining lunches. There are so many others who contributed to my time at LATMOS being a wonderful experience, the list is endless, and I appreciate you all.

To Dr. Tim McConnochie, thanks for your enormously generous use of video calls, facilitating so many inspiring scientific conversations and an infinite number of tangents. I hope we will continue our projects going forward. My gratitude also goes out to Dr. Tanguy Bertrand who kindly introduced me to DISORT and generously shared his code so I did not have to start from scratch.

I am so lucky to have a network also outside my immediate local sphere in France. Thanks to my friends, mentors and former colleagues Drs Geronimo Villanueva, Sara Faggi, Giuliano Liuzzi and Vincent Kofman for their support, career advice, and good times. Cheers to many more reunions in the future.

I would also like to extend a word of gratitude to Dr. Olivier Witasse, for your continued support and for bringing my attention to Franck's team here in France in the first place. And for introducing me to Dr. Beatriz Sanchez-Cano, for your encouragement, enthusiasm and for being an awesome role model. I am looking forward to carry on our collaborations in the future.

To my friends, especially (soon-to-be) Dr. Marie Henriksen, for all the good times, yoga and shared moments of despair and clarity. To Jack, for being my eternal sounding board and occasional emotional punching bag. To Greta De Marco, my Italian disaster and soulmate in space. To everyone who visited and shared my time in France and made it a such wonderful adventure.

Thanks also to my family, my brother and my parents, for their encouragements and assistance. You know an infinite amount more about how to be a grown-up in the real world and how to navigate it than I do.

A final thanks to Michael Mach, who for the longest time has requested his name in writing in any of my works. Mike was my first ever mentor, at the Alpbach summer school in 2017 where I interacted with astronomers for the first time, and the experience left me with an unwavering desire to pursue a career in planetary science. Thank you for showing me this path.

"Now let us step out into the night and
pursue that flighty temptress, adventure."
- J.K. Rowling, Harry Potter and the Half-Blood Prince

Introduction

Mars has incited a special kind of excitement in me for as long as I can remember. The initial thrill probably came from it being *right there*, easily recognizable in the night sky, seemingly almost close enough to touch. It is truthfully closer than most planetary objects, which obviously makes it easier to explore than more distant ones, resulting in me hearing of it more frequently when growing up. I was 10 years old when Mars Express was inserted into orbit, and when Spirit and Opportunity landed on Mars. I grew up watching documentaries about them on TV, and it was more fascinating than anything I'd ever seen. As an air-breathing human vulnerable to radiation, I am inherently curious about atmospheres and their interactions with the space environment. This curiosity has guided all my educational choices, and before I knew it my dream of Mars was within reach.

I am of course far from unique; Mars has captured humanity's fascination for centuries, inspiring legends and myths in dozens of cultures across the world since ancient times. It continues to be the source of inspiration for great science fiction, and is currently the object of focus for the next step in human space exploration.

The detailed study of Mars and its atmosphere started in the 1960s with the Soviet Union and the USA both launching spacecraft towards the red planet. The effort was reinvigorated in the 1990s, and since then Mars has had a continuous presence of operational orbiters, landers and rovers. A plethora of evidence suggests Mars was once a very different planet than today, with a much denser atmosphere and liquid water flowing on the surface. The work to unravel what processes governed this dramatic change is still an ongoing effort. Discrepancies between various models and measurements reveal that our overall picture of the atmospheric composition, dynamics and evolution is understood well, yet gaps in our knowledge remain, and new questions arise with every discovery.

Atmospheric water vapor is in particular an intriguing trace species considering Mars' significantly wetter past. It was first discovered in 1963 from a ground-based observatory here on Earth (Spinrad et al., 1963), and has since been measured extensively from both Martian orbit and surface (e.g. Jakosky and Farmer (1982); Smith (2002); Tamppari et al. (2010). Along with the annual cycles of CO_2 and dust, the water cycle is one of the three main cycles that define the current Mars climate. At present, the annual cycle of water vapor column density is fairly well understood; countless observations of water vapor from orbit in nadir viewing geometry has provided a wealth of column density measurements. A few data points from the Martian surface provide constraints about the near-surface environment, yet the vertical distribution of water vapor eluded the scientific community for a long time.

When Mars Express arrived in December 2003, the capability of performing solar and stellar occultations were present at Mars for the first time. With this technique, the vertical profiles of atmospheric species could finally be resolved, and profiles of water vapor were measured between roughly $15\text{-}50\,\mathrm{km}$ (Fedorova et al., 2009). This new capability helped revolutionize the view of supersaturation in the Martian atmosphere, yet one piece of the puzzle was still missing; the very near-surface water vapor distribution. This region has remained unreachable even with more advanced solar occultation instrumentation from the more recent ExoMars Trace Gas Orbiter satellite.

In an effort to shed light on lowest part of the atmosphere, two methods were explored; firstly, a spectral synergy method developed for Earth observation was applied to Mars. We used infrared spectrometers on Mars Express (now one of the oldest spacecraft that are still operational) to obtain

novel insights into the near-surface vertical distribution of water vapor. Using such a veteran of a spacecraft also provided us with a data set covering almost two decades, corresponding to approximately 10 Martian years. Secondly, we developed a water vapor retrieval scheme for the SuperCam infrared spectrometer on the M2020 Perseverance rover, providing a unique perspective on the water column from ground, with high sensitivity to the bottom layers. Secondly, we use the infrared spectrometer SuperCam on the M2020 Perseverance rover to probe water vapor from the Martian surface. This provides a new perspective on the water column, and the viewing geometry enables particular sensitivity to the lowest part of the atmosphere. Perseverance has now been on the surface of Mars for roughly 2.5 years, and have collected a set of about 60 atmospheric measurements.

Questions also remain regarding the photochemical balance of the atmosphere, and studying carbon monoxide and oxygen in tandem is providing hints as to how CO_2 is recycled in Mars's atmosphere. CO has been monitored from orbit for quite some time, but again the near-surface environment eludes observation. The Mars2020 Perseverance rover has for the first time the capability to observe both CO and O_2 at the same time, and here the efforts to retrieve gaseous abundances from infrared spectroscopic measurements are described in detail. The rover also provides another golden opportunity; to observe aurora from the surface of another planetary body for the first time. Several types of auroral phenomena have been detected from orbit, but so far only in the ultraviolet. Perseverance gives us a chance to capture what aurora looks like to human eyes from the surface of Mars, with the opportunity to learn more about how common these events are, what conditions are necessary to facilitate them and if they pose any dangers to surface exploration.

The work in this thesis encompasses studies of the Martian atmosphere from top to bottom from two perspectives; from orbit and the Martian surface. To unravel the secrets of Mars we require a variety of techniques and approaches, and I have been lucky enough to explore several.

The thesis is organized in 6 Chapters:

Chapter 1 introduces Mars, the history of humanity's exploration of it, and presents an overview of our current knowledge about the planet, with emphasis on its atmosphere and the trace gases water vapor and carbon monoxide.

Chapter 2 describes the instruments used and the observation techniques that were performed by the different observatories.

Chapter 3 presents the data processing methods, including a description of the exploration of the data provided by the SuperCam instrument.

Chapter 4 is devoted to the published results of the near-surface water vapor study, and some further work performed later.

Chapter 5 describes the atmospheric investigations performed with the SuperCam instrument and our preliminary retrieval attempts.

Chapter 6 includes several projects related to space weather, and Martian space weather specifically. It considers the EDAC housekeeping parameter and the results from my energetic particle detection projects, as well as Martian aurora detection attempts with SuperCam.

Chapter 1

Mars and its atmosphere

Figure 1.1: Image of Mars taken by OSIRIS camera during the voyage of ESA's Rosetta spacecraft in February 2007. Credit: ESA.

The oldest known records of Mars observations are from Babylonian astronomers during the second millennium BC (Sachs, 1974). Through history Mars has been known by many names, common to them all is a reference to its striking color. The Babylonians themselves named it Nergal, the great hero, or king of conflict, similar to the Greek and Romans who named it after their god of war (Ares and Mars respectively), while ancient Egyptian and Chinese names translate to "The red one" and "The fire star".

At 1.5 astronomical units from the Sun, Mars is the fourth and last rocky planet in our Solar System, and the second smallest planet, being larger only than Mercury. It has two small moons, which were both discovered in 1877 by the American Asaph Hall. He named them Phobos and Deimos, the mythological twin sons of Ares. Both moons are still of uncertain origin, and while Phobos is so close to Mars that it is expected to either crash into or break apart and form a ring of debris around the planet within 50 million years, Deimos, which is much smaller and at a greater distance from Mars, will eventually be cast out into space and become a wandering moon.

Currently Mars has a rotational axis tilt very similar to that of Earth ($25°$ to our $23°$), but with no large moon to stabilize the precession of its obliquity, Mars experiences a highly varying and chaotic

tilt to its rotational axis. Combined with a more eccentric orbit, Mars has undergone a wide range of climates throughout its evolution (Laskar et al., 2004; Jakosky and Phillips, 2001).

Mars is a small rocky planet with a radius roughly half that of Earth, yet is a planet of striking surface features, hosting the tallest mountain and the longest, deepest valley in the entire Solar System: the Olympus Mons volcano and the canyon system of Valles Marineris. Olympus Mons stands $25\,\mathrm{km}$ tall and is $624\,\mathrm{km}$ wide at its base, covering a surface area roughly equivalent to the size of Italy, while Valles Marineris, shown in Figure 1.2, stretches more than $4000\,\mathrm{km}$ across the surface, and plummets down around $7\,\mathrm{km}$ at its deepest. This canyon, among several other several features, gave rise to the misconception that Mars is home to an intelligent species with technological abilities far beyond our own. The misunderstanding arose from the mistranslated word "canali", which the Italian astronomer Giovanni Virginio Schiaparelli used to describe the surface features he observed on Mars in 1877. In 1894, the American astronomer Percival Lowel observed the same structures, and concluded that these were indeed artificial canals. He mapped hundreds of them, and went on to author several books about the highly intelligent Martians, thus launching the golden era of Martian science fiction. The observed canals turned out to be Valles Marineris, and even though it is real enough, the complex canal structures recorded by Lowel were never confirmed by the scientific community, and were later proven to be only a product of the confusion with large-scale atmospheric dust phenomena as well as the human tendency to recognize patterns even where none exist. Nevertheless, this misunderstanding sparked a global interest in the search for life on Mars, and certainly inspired generations of students to pursue a career in astronomy.

There might not have been any intelligently made canals on Mars, but the planet's surface has clearly been shaped by dynamic processes. There are ample evidence of water-carved geomorphic features, such as outflow channels, valley networks and lake structures, all of which making H_2O a hugely important species in terms of planetary evolution. Yet liquid water does not exist (at least not much) on the surface of Mars today, and for water to have flowed freely before, a vastly different climate mush have persevered at least for some time. A wetter, warmer and denser planet leaves us with multiple open questions: Where did all the water go? What were the escape mechanisms, and did life ever exist on Mars? And if so, could we detect traces of it today? These questions drive the underlying motivation of this thesis; in this work we will focus on atmospheric water vapor and carbon monoxide.

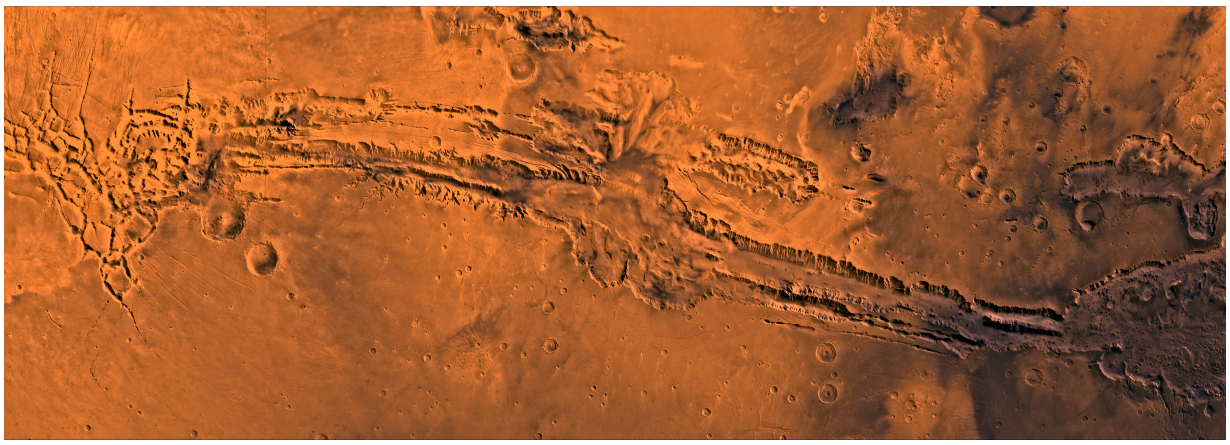

Figure 1.2: Image mosaic from the Viking orbiter showing the canyon system of Valles Marineris. The image extends from 0 to 20 degrees latitude south, and from 45 to 102.5 degrees longitude, with north towards the top. Credit: NASA/JPL/USGS.

1.1 Mars exploration

For centuries our knowledge of Mars was limited to what was discernible with telescopic observations from Earth. Galileo was first to observe Mars with a telescope in 1610, and for 350 years ground-based observations of varying quality dominated the scientific debate, and on occasion spurred extraordinary speculation.

The study of Mars's atmosphere specifically has only been an ongoing effort for about a century. Mars's atmosphere is a tenuous one, and was only confirmed to exist in 1926 (Wright, 1925; Menzel, 1926), before this, it was debated whether or not Mars had any atmosphere at all. Its main constituent CO_2 was detected for the first time in 1947 (Kuiper, 1950), water vapor followed two decades later (Spinrad et al., 1963), and CO shortly thereafter (Kaplan et al., 1969).

As Mars exploration gained momentum, efforts were made to put measurements into seasonal context. Martian dates are given in terms of solar longitude (Ls), which describes the orbital position of Mars with respect to the Sun, see Figure1.3. Ls=0° is defined as Northern Hemisphere (NH) spring equinox (and Southern Hemisphere (SH) fall equinox), such that Ls=90°, 180°, and 270°, becomes NH summer solstice, fall equinox, and winter solstice, respectively (Piqueux et al., 2015a). A Martian day is is denoted "sol", lasts for 24 hours and 39 minutes, and one Martian year consists of 668.6 sols. Martian months are defined as spanning 30° Ls, and due to the eccentricity of Mars' orbit, they range from 46 to 67 sols, with the shortest months near southern summer and perihelion, and consequently the longest months in northern summer. This system arose in the community early on in the Mars space probe era, and consensus has remained since.

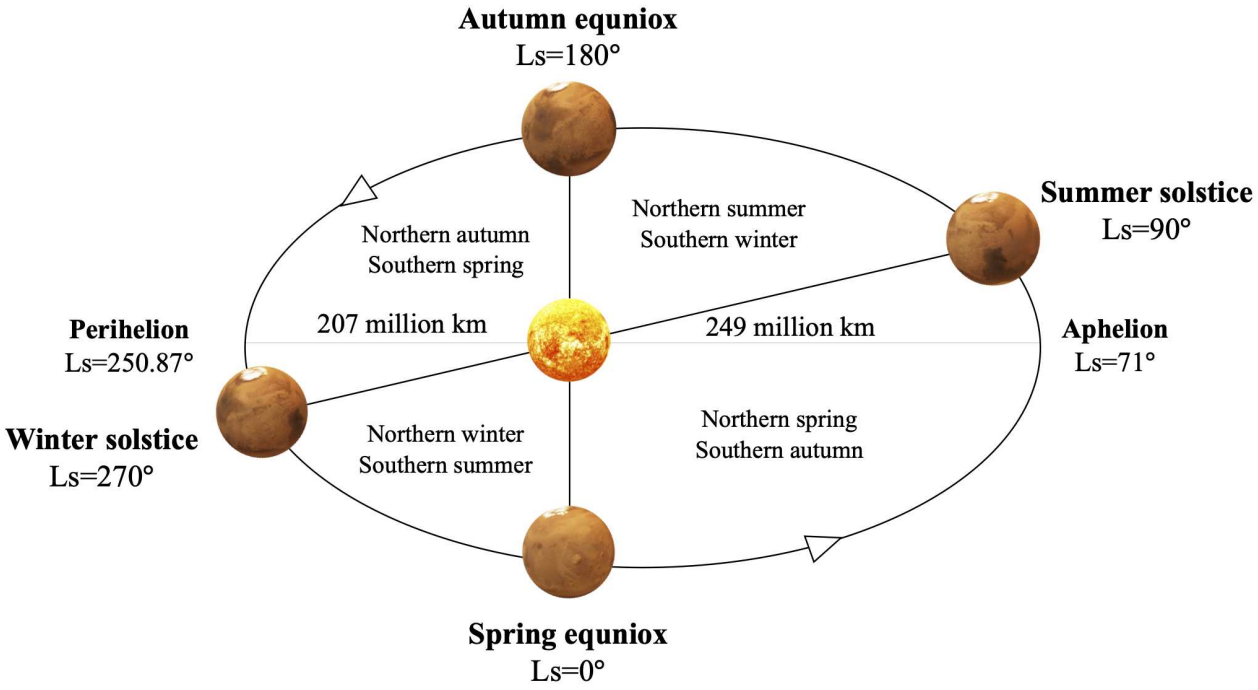

Figure 1.3: Overview of the Martian year. The equinoxes and solstices are given for the northern hemisphere. Orbital direction is indicated as counter clockwise, viewed from the Suns north pole. Eccentricity of ellipse is not to scale.

Timekeeping in terms of years was only put into system in 2000, when scientists decided to log Mars years to simplify orbital interannual data comparisons. The beginning of year one was defined rather arbitrarily by Clancy et al. (2000) as April 11, 1955. This starting point provided a convenient marker as the great dust storm of 1956 fell in Mars Year 1 (MY 1). The system was later expanded to include a MY 0 (defined from May 24, 1953), and so allowing for negative year numbers. Upon completion of this thesis we are roughly halfway through MY 37.

1.1.1 Historic overview of past Mars missions

The study of Mars and its atmosphere has come in two waves; the first starting in the 1960s with both the Soviet Union and the USA launching spacecraft, and ending after the Viking landers. The interest picked up again in the late 1990s with the arrival of Pathfinder, and since then Mars has had a continuous presence of operational orbiters and rovers. At the time of writing, 48 attempts to reach Mars have been made, only 23 of which were partially or fully successful. Figure 1.4 outlines some of the most important milestones in Mars exploration through history.

The first successful mission was the American Mariner 4 spacecraft which made a flyby of the planet in 1965, followed by Mariner 6 and 7 conducting more flyby's, all contributing to improving our understanding of cratering history (Chapman, 1974). In addition to geological surveys, the Mariner missions also made significant atmospheric discoveries, for example; Mariner 4 made the first pressure measurements, which were later confirmed with Mariner 9 (Kliore et al., 1965), and Mariner 7 made the first detection of ozone (Barth et al., 1971). After this, a series of unsuccessful attempts from both the Soviet and the USA followed.

In 1971, Mariner 9 and the Soviet Mars 2 were inserted into orbit. Well-known features such as volcanoes and the Valles Marineris were discovered with these orbiters, (Masursky, 1973), and Mars 2 measured dust grain distributions and the downward extent of the ionosphere (Marov and Petrov, 1973) for the first time. Weeks after the arrival of Mariner 9 and Mars 2, Mars 3 made the first soft landing, but contact with the spacecraft was lost shortly after touchdown. In 1974 Mars 5 reached orbit and later returned more than 60 images.

Next came the Viking missions in 1976, two identical orbiter and lander pairs, two hugely successful missions that both returned images from the surface for the first time. All four spacecraft operated far beyond the expected mission lifetime; the last transmission was made by the Viking 1 lander, sent to Earth on November 11, 1982. Large expectations were tied to the potential discovery of microbial life, yet none of the landers could prove the presence of micro-organisms (Klein, 1979) despite a very intense debate among scientists. After this Mars was more or less declared desolate which effectively halted any new Mars missions for almost two decades, while Venus exploration was put into focus with successful missions such as Pioneer and Magellan.

1997 turned out to be a busy year for Mars with the arrival of the Mars Global Surveyor (MGS) (Albee et al., 1998) and Pathfinder accompanied by the Sojourner, the first moving vehicle on Mars (Golombek et al., 1997). MGS performed extensive mapping from pole to pole for almost a decade (Fishbaugh, 2001). Mars Odyssey arrived in 2001, and is at the time of writing still operational, making it the longest running Mars mission to date (Saunders et al., 2004). It has mapped the amount and distribution of various surface elements, and served for two decades as data relay.

Europe's first Mars mission, the Mars Express satellite (MEX), arrived in 2003, and is still operational and performing science. Its accompanying lander, Beagle 2, landed successfully but was unable to communicate with MEX and was soon declared lost. MEX has delivered many discoveries; the detection of hydrated minerals, the presence of which are indicative of a wetter, and warmer climate in Mars' early youth (Bibring et al., 2006), the first detection of aurora on Mars (Bertaux et al., 2005), a highly localized phenomenon closely linked to the remnant crustal magnetic field, the first detection of methane from Mars orbit (Formisano et al., 2004), and found evidence indicating the existence of a subsurface water deposit under the south pole (Orosei et al., 2018), and the first unambiguous observation of CO_2 ice clouds (Montmessin et al., 2007). In addition to science results, MEX has relayed data for seven different Mars surface missions – a new record.

During the summer of 2003, the Mars Exploration Rovers Spirit and Opportunity touched down on Mars. These were twin spacecraft and ended up operating on the Martian surface far beyond expected mission duration. Some of their most important findings were the discovery of hematite, an iron-bearing mineral, associated with flowing water (Hurowitz et al., 2006). NASAs Mars Reconnaissance Orbiter reached Mars in 2006, and is still operational at the time of writing. MRO has delivered higher resolution measurements than previously available when it reached orbit, providing a wealth

of science results, among these are high resolution surface imaging(Kirk et al., 2008) and observations of polar night airglow (Clancy et al., 2012), to mention some. In addition to its scientific work, the orbiter has been invaluable as a data relay station for later missions.

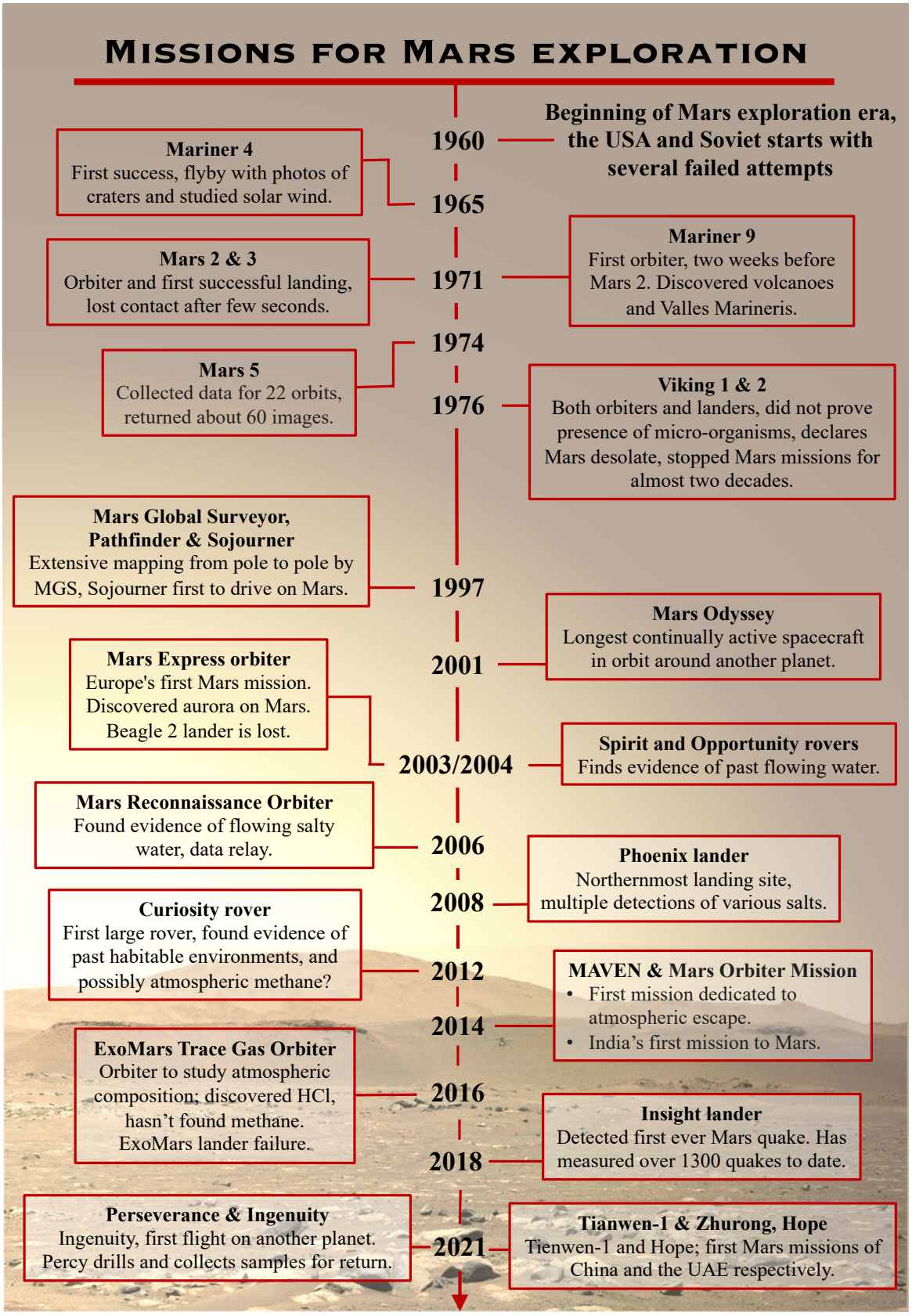

Figure 1.4: Historic overview of some of the most noteworthy missions to Mars.

In 2012, the Mars Science Laboratory rover named Curiosity arrived on Mars. Curiosity has made many significant findings; shortly after landing it observed smoothed, rounded pebbles indicative of the persistent presence and flow of liquid water (Williams et al., 2013). By drilling into bedrock and analyzing the powder, the rover detected sulfur, nitrogen, oxygen, phosphorus and carbon, highlighting the biological viability habitable environments in the early history of Mars (Grotzinger et al., 2014). In-situ measurements of atmospheric methane has also been made, where a seasonal varying background level of 0.41 ppbv on average is measured, in addition to occasional large spikes more than an order of magnitude stronger (Webster et al., 2018).

India's first interplanetary mission, made India's space agency the fourth to reach Mars, when Mangalyaan was successfully inserted into Mars orbit in 2014, the mission was meant as a technology demonstrator and communications with the orbiter was lost (as expected) in October 2022 (Sundararajan, 2013). NASA's MAVEN arrived shortly after, designed to explore the interactions of solar wind with the Mars magnetosphere and upper atmosphere and to study atmospheric escape processes (Jakosky et al., 2015b). The rate of loss has been measured (Jakosky et al., 2018), and MAVEN discovered a new type of aurora, global in nature and connected to the precipitation of solar energetic particles (Schneider et al., 2015).

The joint ESA-Roscosmos ExoMars project originally consisted of an orbiter, lander and rover (Vago et al., 2015). The orbiter Trace Gas Orbiter (TGO), and lander Schiaparelli arrived at Mars in 2016 with TGO successfully inserted into orbit, however Schiaparelli failed during descent. As its name suggests, TGO is optimized for atmospheric studies, specifically to detect trace gases with two spectrometers dedicated to this task (Vandaele et al., 2018; Korablev et al., 2018). Multiple attempts have been made to detect methane, but at the time of writing no statistically measurements have been made (Korablev et al., 2019; Knutsen et al., 2021a; Montmessin et al., 2021). Another gas, hydrogen chloride, has been detected for the first time however, and represents a new chemical cycle not previously thought to be present on Mars (Korablev et al., 2021).

The Insight lander arrived in 2018 with the objective to detect movements within the Martian core, and only after 128 days was the first ever seismic event on Mars recorded. In 2022 the tremors from an meteoroid impact was also measured, teaching us more about the planetary interior (Garcia et al., 2022).

2021 was also a very busy year at Mars. First, The United Arabic Emirates' first interplanetary mission HOPE arrived, with a unique orbit and the purpose of studying the Martian atmosphere (Sharaf et al., 2020). A new type of discrete, but extremely large aurora was detected (Lillis et al., 2022). Almost simultaneously, China successfully inserted their satellite Tianwen-1 in orbit and soon after landed their first Mars rover Zhurong (Zou et al., 2021). A week later, on the 18th of February, NASAs Mars2020 Perseverance rover touched down, with an international suite of instruments and the helicopter Ingenuity, a technology demonstration to test powered, controlled flight on another planet for the first time (Farley et al., 2020).

Current missions

In 2022 there are eight orbiters (Mars Odyssey, MEX, MRO, Mangalyaan, MAVEN, ExoMars TGO, HOPE and Tianwen-1), three rovers (Curiosity, Perseverance and Zhurong), one lander (Insight) and one helicopter (Ingenuity) operational at Mars. Their main targets are the search for ancient life, with continuously more efficient robotics designed for this purpose, and technology demonstrators such as MOXIE (Mars Oxygen In-Situ Resource Utilization Experiment) on Perseverance which produces oxygen in view of astronaut usage and fuel production, and Ingenuity which demonstrated our ability for flight for the first time on another planetary body. The exploration of Mars has never been more intense, and in preparation for sample return and human exploration, it is not likely to decrease significantly in the coming years.

The future of Mars exploration

Perseverance is currently performing regolith and atmospheric sampling which are to be collected and sent back to Earth, by the Mars Sample Return mission (Muirhead et al., 2020). Perseverance will bring the samples to a sample retrieval lander, where also three small helicopters will serve as redundancy if needed, to collect the sample tubes. A robotic arm of the retrieval lander will transfer the sample tubes to the ascent vehicle, which will rendezvous in low Mars orbit with the Capture, Containment, and Return System aboard the Earth Return Orbiter. The Earth return orbiter will capture the Orbiting Sample container and transfer it into a clean zone for return to Earth. The Earth Return Orbiter will ferry the Earth Entry System, which contains the orbiting sample inside a disk-shaped vehicle, with a heat shield for safe entry through the Earth's atmosphere. The estimated return is set to early 2030s.

Coming up, there are seven already confirmed missions through 2024, and at least a dozen more through the mid-2040s, with many more in the development stage. The joint ESA-Roscosmos ExoMars Rosalind rover was delayed yet again in 2022 due to Russia's tragic invasion of Ukraine, subsequently losing the Russian counterpart. The spacecraft is built and ready for launch, with the prime objective of searching of traces for life. Japan is planning to send a micro-satellite with an accompanying lander TEREX, carrying a terra hertz sensor to measure oxygen isotopes. India is planning a Mangalyaan 2 expected to launch in 2024 to study the interactions of solar wind with the upper atmosphere, and the Japanese space agency (JAXA) is sending the Martian Moon Explorer (MMX) in 2025, which will travel to Phobos, Mars' largest moon. It will land on Phobos, collect samples, and return to Earth, while also observing Deimos and the Martian climate. In a collaborative effort, NASA, JAXA, the Canadian and Italian space agencies are preparing the Mars Ice Mapper, expected to launch in 2026, with the objective of mapping water ice resources on the Martian surface.

On the human exploration front, NASAs stated goal is to put humans on the surface during the 2030s. While ESA is planning on having the first European astronaut on Mars by 2040, Russia plans to send humans in the 2040–2045 time-frame. One thing is certain, the future of Mars exploration will be busy.

1.2 The surface of Mars

The study of Mars' surface evolved from telescopic to remote-sensing techniques and then to in-situ measurements, bringing ever-improving resolution and instrument capabilities to the Martian surface with rovers and landers. Any classical image of Mars is dominated by reddish, brighter and darker areas, and it was these differences in albedo that astronomers first observed through Earth-based telescopes before the age of space probes. The origins of the albedo contrasts were a mystery, yet it was known that they rarely correlated with topography. The lighter patches at the poles were correctly believed to be either frozen water or carbon dioxide, but the nature of the darker patches contrasted against the reddish tint of Mars was uncertain for centuries. Some of the suggested hypothesis were wetlands such as seas, lakes, swamps, and later it was put forth that it could be signs of vegetation. Now these areas are known to be the exposed surface of darker basaltic rock, where the wind has swept away the paler dust (Singer et al., 1979).

1.2.1 Geological evolution

The age of a planet is most commonly defined from after it finished forming, which was roughly 4.5 billion years ago in the case of Mars (Carr and Head, 2010). The geological history of Mars can divided into three main epochs, each named after a type of surface area based on the number of superimposed impact craters; the Nochian, Hesperian and the Amazonian periods, though the exact duration and start/end times of each is not known exactly (Tanaka, 1986; Ivanov, 2001) as illustrated in Figure1.6.

A fourth pre-Nochian time period defined as having lasted from 4.5-4.1 billion years ago characterized by Mars having its global and intrinsic magnetic field, and large impacts which likely caused the global dichotomy, is also often included when considering Mars' evolution. The Nochian period is characterized by heavy bombardment, and shows signs of erosion from large amounts of liquid water, and is thought to have ended around 3.7 billion years ago (Hartmann and Neukum, 2001). During this period the Martian atmosphere was likely much thicker, in order to support the existence of liquid water. Model estimates of the effects of the heavy bombardment indicate that much of the atmosphere could have been lost by the end of the Late Heavy Bombardement (Melosh and Vickery, 1989). The Hesperian period ended between 3.3 and 2.9 billion years ago, and is identified by the formation of extensive lava plains, likely also Olympus Mons, and many water outflow channels (Carr and Head, 2010). Though outgassing from volcanoes probably contributed to the atmosphere, it had likely thinned to its current density by the end of the Hesperian period (Pepin, 1994). The boundary between the Hesperian–Amazonian periods could incorporate significant errors, since Amazonian areas are quite varied; they are marked by few impact craters, include lava flows, glacial activity, and there are signs that liquid water continued to flow during this period (Salese et al., 2016).

1.2.2 Hemispheric dichotomy

The northern and southern hemispheres of Mars exhibit significant differences in terms of elevation and albedo, clearly depicted in Figure1.5. The NH is considerably lower compared to the SH, with an altitude difference of $1\text{-}3\,\mathrm{km}$ due to a change in crustal thickness that manifests as an irregular boundary encircling the planet (Zuber et al., 2000). The NH is of relatively recent volcanic origin (dominated by Amazonian areas), while the SH mostly consists of a raised, ancient, primordial crust with a much higher crater count (Smith et al., 1999), primarily from the Nochian epoch (see Figure 1.6 for geological timeline). Hesperian areas are most commonly found in the equatorial region and at low latitudes (Tanaka, 1986). Intense crustal magnetization is also confined mostly to the ancient southern highlands, consistent with an internal magnetic dynamo that halted early in Mars' evolution (Connerney et al., 2001). Mitchell et al. (2007) found that the magnetic field amplitude at the Tharsis rise is around the detection threshold of a few nT at MGS altitude (roughly 170 km). Strong magnetic locations are present in the southernmost regions of Tharsis, while weaker sources are found along its western and eastern borders. This implies that the creation of Tharsis thermally demagnetized a large region of the planet. The reasons for the hemispheric dichotomy is still very much a topic of debate, with the two most supported explanations being mantle convection or a giant impact. There exists little evidence to distinguish between the theories, but recent studies lend favor to the giant impact hypothesis (Marinova et al., 2008; Andrews-Hanna et al., 2008).

Most of Mars's large volcanoes lie in the northern hemisphere, with the major volcanic regions of Tharsis and Elysium located around 10°N and 30°N (see 1.5. Tharsis contains 12 large volcanoes, the four largest of which are the shield volcanoes named Ascraeus Mons, Pavonis Mons, Arsia Mons, and Olympus Mons. Olympus Mons is the largest volcano in our solar system, and was formed by thousands of individual slow eruptions of fluid lava. It is one of the youngest large volcanoes on Mars, and was one of the last volcanoes to be active. Some evidence suggests that the most recent activity of the Tharsis volcanoes could have happened only 100–200 million years ago, coinciding with radiometric ages of several Martian meteorites found on Earth, and that Olympus Mons erupted as little as four million years ago, suggesting that eruptions in the future can't be excluded (Neukum et al., 2004). The forging of Valles Marineris to the east of Tharsis is suggested to have been caused by a significant tectonic crack, due to the rise of Tharsis from volcanic activity and the interior cooling following the planet formation (Yin, 2012). Subsequent erosion widened the channel over time, resulting in the canyon we know today, the largest in the solar system.

In addition to enormous volcanoes and great valley systems, the Martian surface bears countless scars from asteroid and meteoric impacts. The craters vary in size and age, and today most are found

in the older SH as shown in Figure1.5, as many ancient impacts in the NH have had their craters covered over by more recent volcanic resurfacing. Some ancient crates hint at a sustained presence of liquid and flowing water, making them high priority targets for robotic exploration. Currently the Curiosity and Perseverance rovers are investigating such craters, Gale and Jezero respectively, and each has found evidence of flowing water and rocks altered by liquid water (Fairén et al., 2014; Farley et al., 2022).

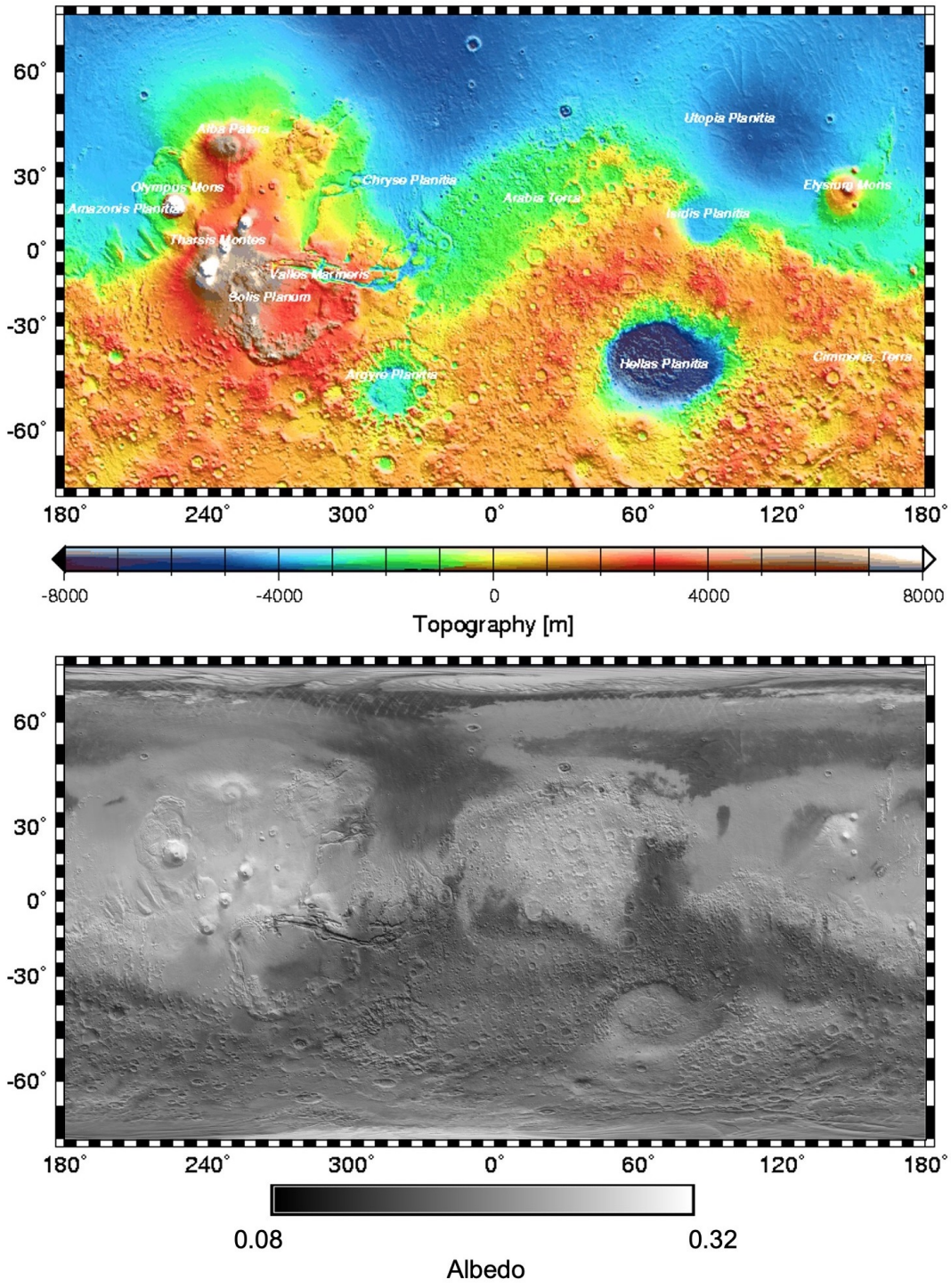

Figure 1.5: Global maps showing the topography and albedo variations of Mars as a function of latitude and eastern longitude. The measurements were made with the MOLA (topography) and TES (albedo) instruments on MGS. Major surface features, such as large craters and volcanic regions, are labeled in the top panel. Albedo map from Christensen et al. (2001), and credit to the MOLA Science Team for the topography map.

1.2.3 Mineralogy

From Martian meteorites, data from Pathfinder and spacecraft observations, a general picture of the Martian surface has been composed; the northern hemispheric low lying plains are mostly felsic in composition, while the ancient highlands in the SH are mainly mafic. Before the Pathfinder mission, it was believed that the Martian surface was primarily mafic and made from volcanic lava as indicated by Martian meteorites found on Earth. Data from Pathfinder suggested instead that the rocks are felsic and more like the Earth's continental crust, containing the whitish mineral feldspar (Greeley et al., 1999). Typical for felsic rocks is they are rich in silicates, potassium and sulphur and low in magnesium. They are thought to be derived from masses that have undergone significant processing following the planetary formation (Wray et al., 2013).

Several spacecraft with a multitude of instruments have provided detailed spectroscopic analysis of the entire Martian surface for the past decades (e.g. Christensen et al. (2000, 2005); Murchie et al. (2009)). Three main periods of geological alteration processes were identified by Bibring et al. (2006), with phyllosilicates formed first by nonacidic aqueous alteration, followed by acidic aqueous alteration traced by sulfates, then lastly the formation of anhydrous ferric oxides by atmospheric aqueous-free alteration, visualized in Figure1.6. The transition between the Phyllosian and the Theiikien periods happened during a time when Mars underwent critical climate change, moving from an alkaline and possible moist environment to a more acidic environment. This drastic change was driven by volcanic activity along with substantial volatile outgassing (Bibring et al., 2006).

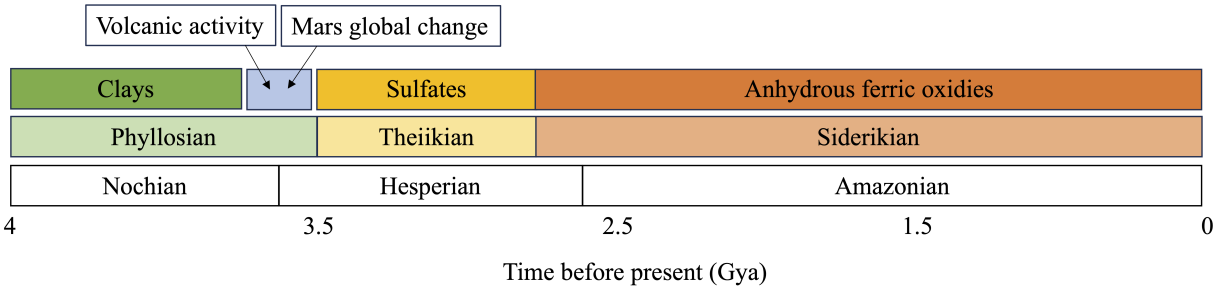

Figure 1.6: Simplified overview of the geological time periods on Mars, along with the proposed periods based on chemical weathering derived from OMEGA data. The limits for each period is highly uncertain. Adapted from Bibring et al. (2006) and Carr and Head (2010).

1.2.4 Regolith

Fine grained dust is a dominant feature of Mars. The planet is covered in it (as can be seen in Figure1.7, which shows an image made from the Perseverance rover in 2021), a result of billions of years of erosion from persistent Martian winds. Spectral analyses of Martian soil and dust show that it is made from a mixture of small grains of felsic and mafic rock, roughly in proportion to their presence in the surface. Martian dust has a globally uniform composition, and is slightly enriched in silicone, chlorine and iron compared to typical soils (Berger et al., 2016). Aeolian processes suspend the finest fraction of surface dust (around 2 microns), which is mixed in the atmosphere by local dust devils and seasonal, regional dust storms (Clancy, 2003). The dust is then distributed globally, and eventually re-settles on the ground and rocks, and once again becomes a component of the soil. With very little available atmospheric water vapor, the arid Martian climate enhances dust availability, causing dust distribution and aeolian processes to be important factors in the cycling processes of S and Cl, and is probably closely linked to the recent discovery of HCl in the atmosphere (Korablev et al., 2021).

Mars has no global magnetic field, a thin atmosphere and no persistent ozone layer to absorb photons in the ultraviolet, thus the Martian regolith is highly radiated. As a result, Mars' surface is

Figure 1.7: Image from the surface of Mars taken on April 29 2021. In the photo a hill named *Santa Cruz* is visible about 2.4 km away. The image was captured with the MastCam-Z camera on board the Perseverance rover. Credit: ASU/MSSS/JPL-Caltech/NASA.

inhospitable to life as we know it. Any exposed organic compounds, current biological life or future astronauts will require some kinds of shielding to sustain life, leading to the hypothesis of ancient underground lava tubes being locations of interest both in the search for Martian life (Schulze-Makuch et al., 2005) and also for potential habitats for future human exploration (Blamont, 2014).

1.3 The Martian atmosphere

The Martian atmosphere has been and is studied in a variety of ways. Atmospheric quantities has been measured from orbit, where the primary techniques have been thermal infrared sounding, infrared spectroscopy, visible imaging of clouds and dust, radio, ultraviolet and infrared occultations. Measurements from the surface have complemented orbital data. Again, thermal infrared sounding has been useful, and imaging of the sky and Sun, along with meteorological instrumentation including near-surface temperature sensors, atmospheric pressure and wind velocity. Data on atmospheric temperatures and densities has also been collected during aerobraking passes, and during entry, descent, and landing.

The atmosphere of Mars is an extremely tenuous one, with less than 1% of Earth's atmospheric volume. Being in an elliptical orbit around the Sun, Mars's average temperature varies greatly between summer and winter, but has a global annual average near the surface of about 210 K. The average surface pressure is roughly $6.5\,\mathrm{mbar}$, though as the seasonal temperature varies, much of the atmosphere cycles in and out of a gaseous state, causing the atmospheric surface pressure to also vary with season. Every winter when the temperature falls below $-123\,^{\circ}\mathrm{C}$, the atmospheric pressure drops by up to 30% as CO_2 condenses and deposits at the winter pole.

The following subsections will present the Martian atmosphere as a whole to give the reader an overview of the complete Martian system, and establish the framework for the later pieces of work, especially in the context of atmospheric water vapor (see Section 1.4) and carbon monoxide (Section (see Section 1.5), which are some of the main atmospheric target species of Mars Express and Perseverance.

1.3.1 Composition

The atmosphere of Mars is heavily oxidized and primarily composed of CO_2 (95.1%), N_2 (2.59%) and Ar (1.94%), with modest amounts of O_2 and water vapor (Trainer et al., 2019). Trace amounts of other noble gases are present (Ne, Kr, Xe) (Owen et al., 1977), as well as molecular species such as CO, O_3, NO and H_2O_2 (see Table 1.1), which are produced photochemically from the primary volatiles (Haberle et al., 2017). N_2, O_2, Ar and CO are the four most abundant noncondensable gases on Mars, this means that low/high atmospheric temperatures and pressures are not expected to deposit/sublime these gases from the polar caps, as happens with CO_2. Thus, total atmospheric content of these species remain unchanged through the Martian seasons, though they are sensitive to the changes in global pressure, leading to seasonal variation in their mixing ratio. In this way, they can function as tracers for atmospheric circulation and dynamics, as has been done for argon and carbon monoxide (Sprague et al., 2007; Sindoni et al., 2011).

Compared to most other planetary bodies in our solar system with atmospheres, Mars lacks complex organic chemistry, and no sulfur chemistry like the one on Earth or Venus has been detected so far. But despite its apparent simplicity, the Martian photochemistry is complex, and still not completely understood. Mars' trace species exist largely because of the dissociation of CO_2 and H_2O initiated by solar UV.

Ozone is a minor constituent in the atmosphere of Mars, but it is the most chemically active. The local abundance of ozone is controlled by the amount of odd hydrogen species (H, OH, HO_2, called the HOx family), which are produced by the photolysis of water vapor. With only (hundred of ppbv) trace amounts of ozone, no persistent ozone layer exists on Mars as it does on Earth. Without an ozone layer, ultraviolet radiation from the Sun and other astronomical sources reaches the surface unhindered, resulting in a monotonously colder atmosphere with no distinct warm layer corresponding to Earth's stratosphere.

The composition of the Martian atmosphere has likely changed over the course of billions of years. A denser, warmer and more moist atmosphere is required to explain several geological and mineralogical features such as the apparent previous existence of liquid water, and measurements of isotopic composition of various species shed light on the long-term changes of the atmosphere (Conrad et al., 2016; Villanueva et al., 2022). Mars's atmosphere is depleted in lighter stable isotopes, suggesting the composition has changed through loss processes to space over its history (Jakosky et al., 2018).

Mars is a very dry planet, yet water vapor plays a major role in shaping the climate along with the CO_2 and dust cycles. Water controls the stability of the atmosphere in terms of radiative equilibrium through cloud formation (Madeleine et al., 2012), and photolysis which supplies HOx radicals, the main oxidant of the Martian photochemical cycle (McElroy and Donahue, 1972). It was for a time debated how Mars retains its CO_2 atmosphere when photochemical models indicated that the photolysis of CO_2 should over time lead to a build-up of the dissociation products O_2 and CO, with twice the amount of CO compared to oxygen (Nair et al., 1994). If not for the presence of water vapor, this would indeed be the case; the oxidizing photodissociation products of H_2O catalytically convert carbon monoxide back into CO_2 (McElroy and Donahue, 1972), maintaining the stability of CO_2 content. The global annual average of water vapor is about 15 precipitable-microns (Knutsen et al., 2021a; Trokhimovskiy et al., 2015), with strong enhancements over the poles in early summer (more details in Section 1.4).

To this day Mars continues to lose atmosphere to space, mainly through atomic hydrogen and oxygen escape, yet the exact processes were long uncertain. The escape is facilitated by interconnected physical processes with nonlinear relationships that are spatially and temporally varying, and is thus considered by many a notoriously challenging problem (Lillis et al., 2015). Monitoring the deuterium-to-hydrogen ratio in water vapor is valuable to constrain volatile escape and to trace the transport of water between reservoirs such as the seasonal transport between the polar caps (Villanueva et al., 2015, 2021; Rossi et al., 2022). The discovery of high-altitude water vapor (Maltagliati

Gas species	Abundance	Upper limit	Source
CO_2	95.1%	-	Trainer et al. (2019)
N_2	2.59%	-	Trainer et al. (2019)
Ar	1.94%	-	Trainer et al. (2019)
O_2	0.16%	-	Trainer et al. (2019)
CO	0.058%	-	Trainer et al. (2019)
H_2O	0.016%	-	Knutsen et al. (2022b)
Ne	2.5 ppmv	-	Owen et al. (1977)
Kr	0.3 ppmv	-	Owen et al. (1977)
Xe	0.08 ppmv	-	Owen et al. (1977)
O_3	0.05-0.5 ppmv	-	Clancy et al. (2016)
H_2O_2	0.032 ppmv	-	Encrenaz et al. (2004)
HCl	1-4 ppbv	-	Korablev et al. (2021)
CH_4	0.41 ppbv	<0.02 ppbv	Webster et al. (2018), Montmessin et al. (2021)
H_2C_4	-	<0.7 ppbv	Knutsen et al. (2021a)
H_2C_6	-	<0.1 ppbv	Knutsen et al. (2021a)
CH_3OH	-	<3.9 ppbv	Villanueva et al. (2013)
H_2CO	-	<0.1 ppbv	Villanueva et al. (2013)
H_2C_6	-	<0.1 ppbv	Knutsen et al. (2021a)
SO_2	-	<1.1 ppbv	Khayat et al. (2015)
H_2S	-	<1.3 ppbv	Khayat et al. (2015)
SO	-	<0.7 ppbv	Khayat et al. (2015)
HCS	-	<0.4 ppbv	Braude et al. (2022)
NO	-	<1.7 ppbv	Krasnopolsky (2006)
HCN	-	<0.1 ppbv	Villanueva et al. (2013)
NH_3	-	<8 ppbv	Villanueva et al. (2013)

Table 1.1: Table listing the main constituents of the Martian atmosphere, along with a selection of molecules where only upper limits have been found. All the abundances from CO_2 until H_2O are given as annual averages. From ozone and onward, the gases are transient and highly variable, and thus the listed abundances are the detected concentrations. This table does not contain an extensive list of upper limits of non-detected gases.

et al., 2013) has driven the field forward, and dust storms as a source for elevated water is now considered a possible dominant pathway for atmospheric escape (Holmes et al., 2021; Chaffin et al., 2017).

Minor atmospheric constituents can have a significant impact on the climate of Mars, and some could potentially point to processes beyond atmospheric physics. It is an old idea that life on Mars could be detected by measurements of purely physical and atmospherical properties, as any planetary biota that interacts with its atmosphere will drive that atmosphere to a state of disequilibrium (Hitchcock and Lovelock, 1967). Methane has been considered a possible biomarker since the Viking era (e.g. Oyama et al. (1976)), but could also point to a more geologically active planet than first assumed (Oehler and Etiope, 2017). Consequently, the hunt for methane began, but all attempts to detect a statistically significant signal were for a long time consistent with no observed methane (Maguire, 1977; Krasnopolsky et al., 1997; Lellouch et al., 2000). After 2004, things changed drastically; positive methane detections have been reported by five independent teams: Mumma et al. (2003, 2009), Krasnopolsky et al. (2004), Formisano et al. (2004), Giuranna et al. (2019) and Webster et al. (2015). During the same time period, more attempts were made that still provided negative detections (yielding upper limits below 15 ppbv): Krasnopolsky (2007); Villanueva et al. (2013); Aoki et al. (2018);

Korablev et al. (2018); Knutsen et al. (2021a); Montmessin et al. (2021). Only a few studies survived the scrutiny of the community, namely the Mumma et al. (2009), Formisano et al. (2004) and Webster et al. (2015) detections. Webster et al. (2018) even claims to discern a seasonal cycle (although this has been contested in Gillen et al. (2020)) and occasional large plumes.

In 2016 ESA and Roscosmos launched the ExoMars TGO orbiter, its main goal is to discover and constrain the abundance of trace gases in the Martian atmosphere, methane being one of the main target species. As of yet, no methane has been detected by any instrument onboard, but new and more stringent upper limits have been set (Knutsen et al., 2021a; Montmessin et al., 2021), keeping the methane mystery alive. The community is now exerting great efforts to reconcile the orbital non-detections with surface detections (e.g. Zhang et al. (2022b); Webster et al. (2021)).

TGO did however discover hydrogen chloride (HCl) (Korablev et al., 2021), which was a target species due to its relation to volcanic activity on Earth. At the time of writing, no other gases connected to volcanism have been detected simultaneously, thus HCl is not likely indicative of active volcanism or subsurface magmatic outgassing. A seasonal behaviour of HCl is however clear, and its close correlated to the dust cycle and water vapor was recently revealed (Olsen et al., 2021). The appearance of HCl appears to be synchronous with the perihelion dust activity, suggesting a partial explanation of dust-driven atmospheric dynamics, where chloride is sourced from salts observed at the surface (Ojha et al., 2015; Simon et al., 2023) are lifted along with the dust (Olsen et al., 2021).

1.3.2 The CO_2 cycle

As established in the previous section, CO_2 is by far the most abundant species in the Martian atmosphere, and a major feature of the Martian climate is the cycling of a considerable fraction of the atmospheric mass from gas to solid phase through the seasonal polar caps.

CO_2 was detected for the first time in 1947 in the atmosphere of Mars (Kuiper, 1952), but was not confirmed to be the most abundant species until about 20 years later (Kliore et al., 1965). The question of the composition of the polar ice caps remained unanswered until years later. The most supported candidates were water ice, CO_2 ice and ice of nitric oxides, but model studies in the early 1960s strongly suggested that a rather simple thermal model could explain the observed growth and shrinking of the polar caps with season, if CO_2 is the main constituent of the ice (Leighton and Murray, 1966). In this scenario, atmospheric CO_2 condenses into CO_2 ice in the winter pole, along with a much smaller amount of water ice. It was also pointed out in the same study that even though the quantity of H_2O ice is much smaller, it will remain at the winter pole until all the CO_2 ice has sublimed. This hypothesized mechanism forms the basis of our current understanding of the Martian CO_2 cycle.

That CO_2 ice is indeed the major constituent of the seasonal polar caps was later confirmed by surface temperature measurements from Mariner 7, which were indicative of CO_2 ice equilibrium temperatures (Neugebauer et al., 1971). Shortly after, the composition of the residual north polar cap was also confirmed to be water ice (Kieffer et al., 1976), while the conditions at the residual south polar cap turned out to be very different. With temperatures permanently close to the freezing point of carbon dioxide, it indicated that a small residual CO_2 ice cap could exist (Kieffer, 1979).

After almost one Martian year on the surface, the Viking landers reported significant seasonal variations in surface pressure (Ryan et al., 1978) as visualized in Figure 1.8. It became clear from such pressure monitoring that roughly 30% of the atmosphere takes part in this cycling of CO_2 between gaseous and solid states. Pressure change over seasonal timescales is then a tracer of CO_2 phase changes at the poles (James and North, 1982). Further modelling efforts found that the large difference in minima depths can be explained by the formation of polar hood clouds exclusively in the NH (James and North, 1982). These clouds are radiatively active water ice clouds, and can affect the atmospheric temperature. More on water clouds and their impacts in Chapter 1.3.4.

The polar caps on Mars are the solid state of the major atmospheric species, and is thus always

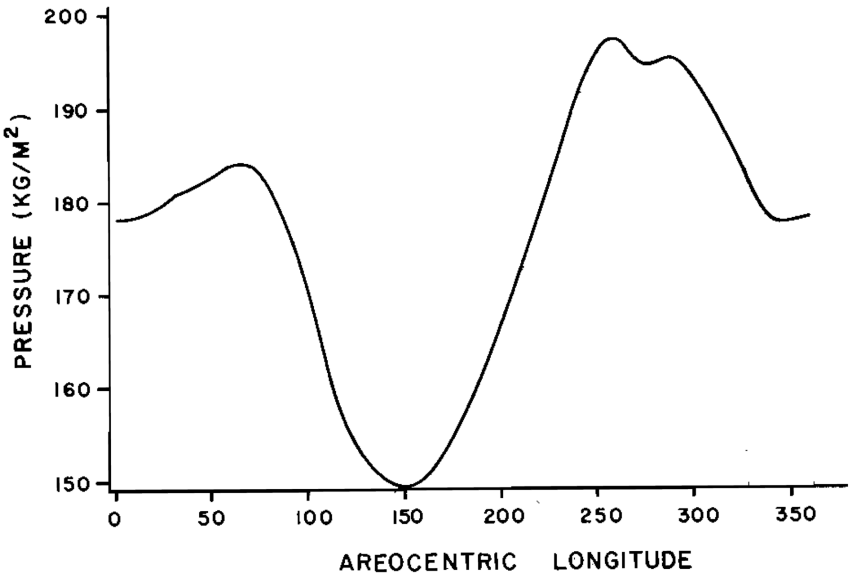

Figure 1.8: Average, smoothed daily surface pressure as measured by Viking lander 1 during first year of operations. As the lander is located 2 km below the mean level, the values have been corrected to the assuming a scale height of 10 km. Figure from James and North (1982).

in equilibrium with the atmosphere. This equilibrium changes seasonally due to variations in temperature, but it also varies on much longer time scales as the planetary obliquity (and other orbital parameters) changes (e.g. Mischna et al. (2013)). CO_2 frost formation is initiated when the local CO_2 pressure exceeds saturation, which at the surface equates to temperatures lower than $\sim$145 K. Similar conditions can also be found in the Martian mesosphere (45-100 km), and so the presence of CO_2 ice clouds were expected for years before a spectroscopic unambiguous observation was first made by Montmessin et al. (2007). The clouds appear seasonally before and after aphelion, and only in a latitude band around the equator (Määttänen et al., 2010).

Piqueux et al. (2015b) analysed eight Mars years of data of the polar cap extents from the Thermal Emission Spectrometer on MGS, and found that the growth season of the north polar cap is highly repeatable, that the effect of dust storms is variable in the north, and that the south polar cap overall is much more variable than the north polar cap. Figure 1.9 from Calvin et al. (2017) shows the recession of the seasonal CO_2 South Polar Cap in MY 29 during an eight month period covering the southern spring and summer from Ls=195° to Ls=327°. The multi-year monitoring of the spatial extent of the polar caps, our understanding of the relationship between the surface and atmospheric CO_2 reservoirs is increasing. Determining seasonal rates of cap growth and recession is important as they strongly influence the global energy budget and are indicators of the regional and global environment.

1.3.3 Vertical structure

The vertical structure of any atmosphere is largely governed by the balance between how energy from the Sun is introduced into the atmosphere and simultaneously lost through reflection of solar energy and thermal emission to space. Being relatively thin, Mars' atmosphere is almost transparent to sunlight, and solar energy is essentially deposited at the surface with only a part of the visible wavelengths being absorbed by dust particles. CO_2 is an efficient thermal emitter, so at night the Martian atmosphere is able to rapidly lose the energy received from the Sun during the day, leading to large day-night fluctuations. Another factor in the energy balance is absorption by lofted dust, which is abundant in the lower atmosphere. Dust plays a significant role in atmospheric heating (more about this in Section 1.3.4, as elevated dust absorbs large quantities of incoming solar radiation, effectively

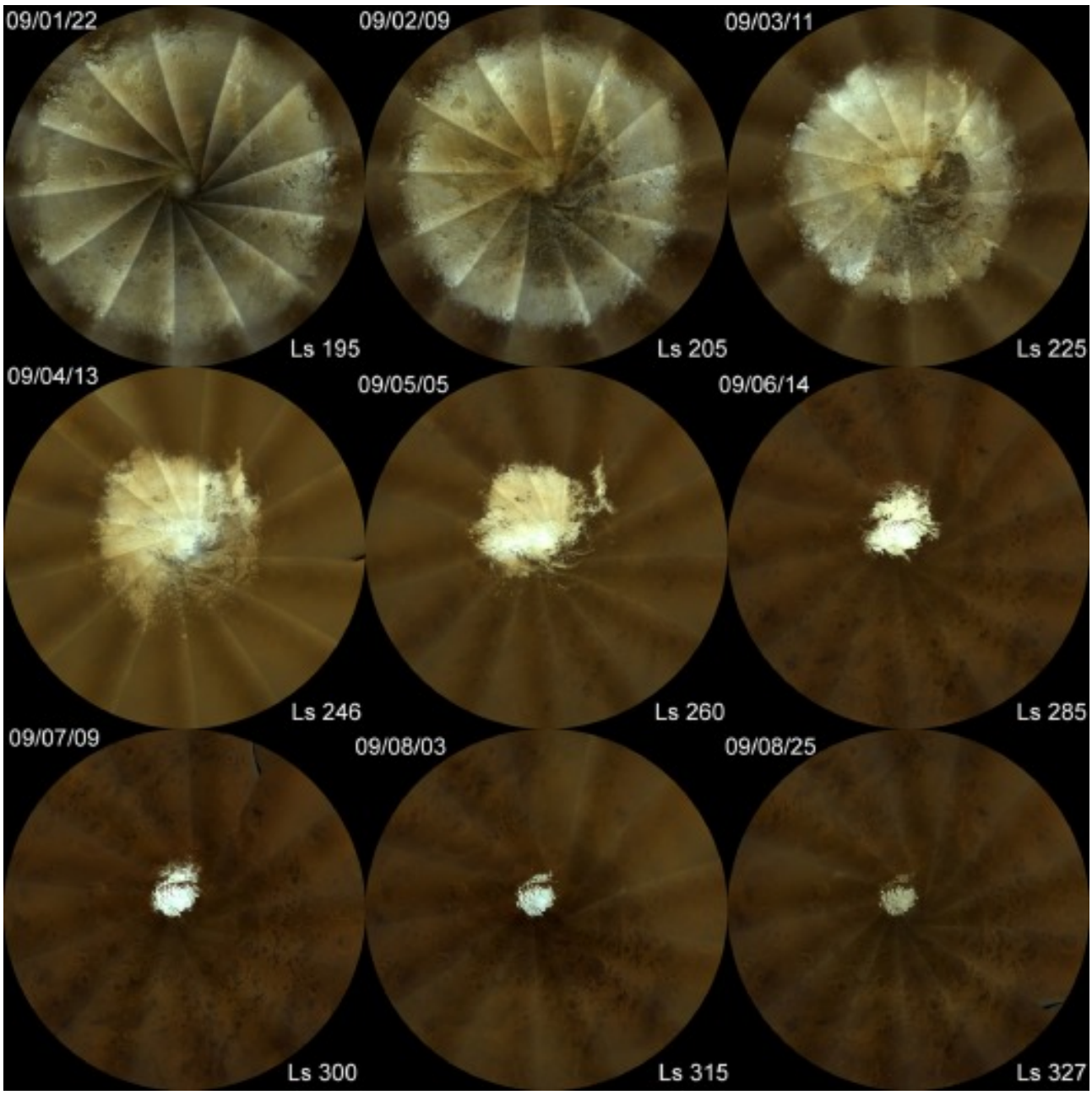

Figure 1.9: The recession of the South Polar Cap in MY 29, as imaged by MARCI on MRO. The CO_2 ice cap is at it largest at Ls=195°, and rapidly sublimates as Mars approaches southern summer solstice. Figure from Calvin et al. (2017).

distributing heat throughout the lower atmosphere. These temperature (and pressure) oscillations, or tides, are regular and diurnal as they are synchronized with the Sun, and give the Martian atmosphere a rather complex vertical structure.

The most common technique to infer atmospheric temperatures is through sounding the thermal infrared 15-micron CO_2 band. Temperature profiles have been extensively measured this way by e.g. IRIS on Mariner 9 (Hanel et al., 1972), with MGS/TES (Conrath et al., 2000), the Planetary Fourier Spectrometer (PFS) on Mars Express (Grassi et al., 2005), and the Mars Climate Sounder (MCS) on MRO (Kleinböhl et al., 2009). An example spectra from PFS covering this region is shown in Figure 1.11.

Figure 1.11 shows typical temperature variations as a function of latitude, season and altitude. Panels a) to d) show latitudinal cross sections measured by TES covering altitudes approximately from the surface to $60\,\mathrm{km}$, and panel e) demonstrates that different instruments and techniques (MGS/TES,

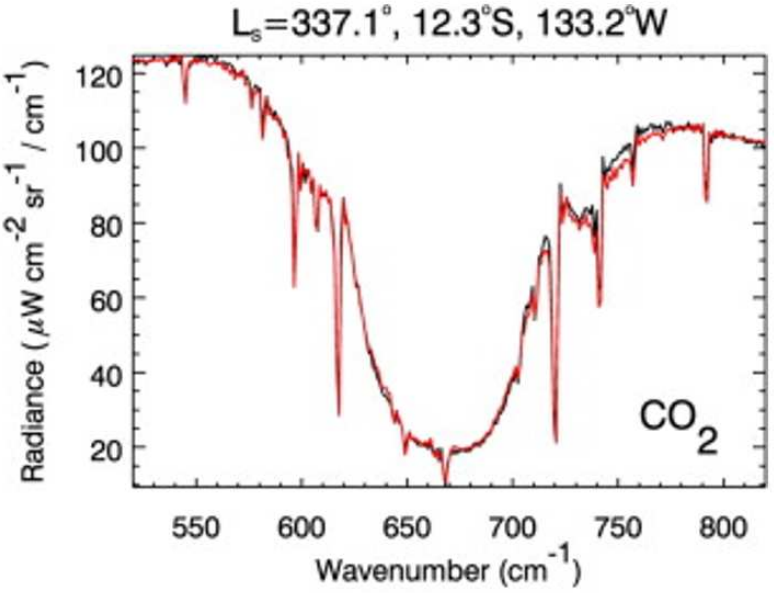

Figure 1.10: Example of thermal infrared spectrum from PFS (black) and best fit (red) in the region of the CO_2 15 µm ($666.67\,\mathrm{cm}^{-1}$) band. Figure from Fouchet et al. (2007).

MRO/MCS and the radio science experiment also on MGS) are in good agreement in the range 0-50 km. Panel f) compares nighttime and daytime vertical profiles, all obtained by MGS radio occultations at mid-latitudes during southern summer.

Subplots a)-d) outline the seasonal evolution of the atmospheric thermal behavior, with clear near-surface maxima during summer and winter solstice in the northern and southern polar region respectively (panels b) and d)). The southern summer reaches warmer temperatures due to it nearly coinciding with perihelion (which, given the current eccentricity of Mars, imposes 25% more sunlight than at aphelion), as visualized in Figure 1.3. In the winter hemisphere a polar front is created at mid-latitudes between the warmer adiabatically heated downwelling air and the cold air found within the polar night. This cold air is then advected equatorward at low altitudes. This polar front has a vertical tilt, particularly prominent in the south, leading to temperature inversion at altitudes below about 1 mbar. The warm air in the south is transported more efficiently to higher altitudes compared to the northern hemisphere, indicating the presence of strong dynamical processes.

During the equinox periods in panels a) and c), the thermal behaviours are almost identical both in magnitude and structure, with a maximum near the surface at equator and a symmetrically decreasing trend towards the poles. The vertical temperature gradient at equator sees a minimum at roughly 30 km (0.3 mbar), with local maxima above each pole somewhat higher. These large scale temperature variations are mainly caused by traversing planetary waves, the Martian topography, and diurnal tides caused by solar heating, but atmospheric dust loading also affects the planetary heat budget.

The variation of temperature with height produces a troposphere, mesosphere, and thermosphere. As Mars does not have a dense enough ozone layer (or any other abundant short-wave absorbing species) no substantial stratosphere exists as on Earth. With an average scale height of about 11 km, the atmospheric lapse rate is $\sim 2.5\,\mathrm{K/km}$, much lower than the dry adiabatic lapse rate ($4.5\,\mathrm{K/km}$ on Mars). Absorption of solar radiation by suspended dust particles does contribute to heating the atmosphere, and on Mars as on Earth, the temperature is further stabilized by vertical heat fluxes associated with large-scale circulation systems (see Section 1.3.5).

The Martian troposphere is very deep, reaching up to ~ 60 km in altitude. The lower part of the troposphere is called the boundary layer (planetary boundary layer, PBL), and is subject to direct surface-atmosphere interactions. It responds to forcings such as frictional drag and surface heating. The extent of the PBL depends on surface heating and convection and thus inflates during the day,

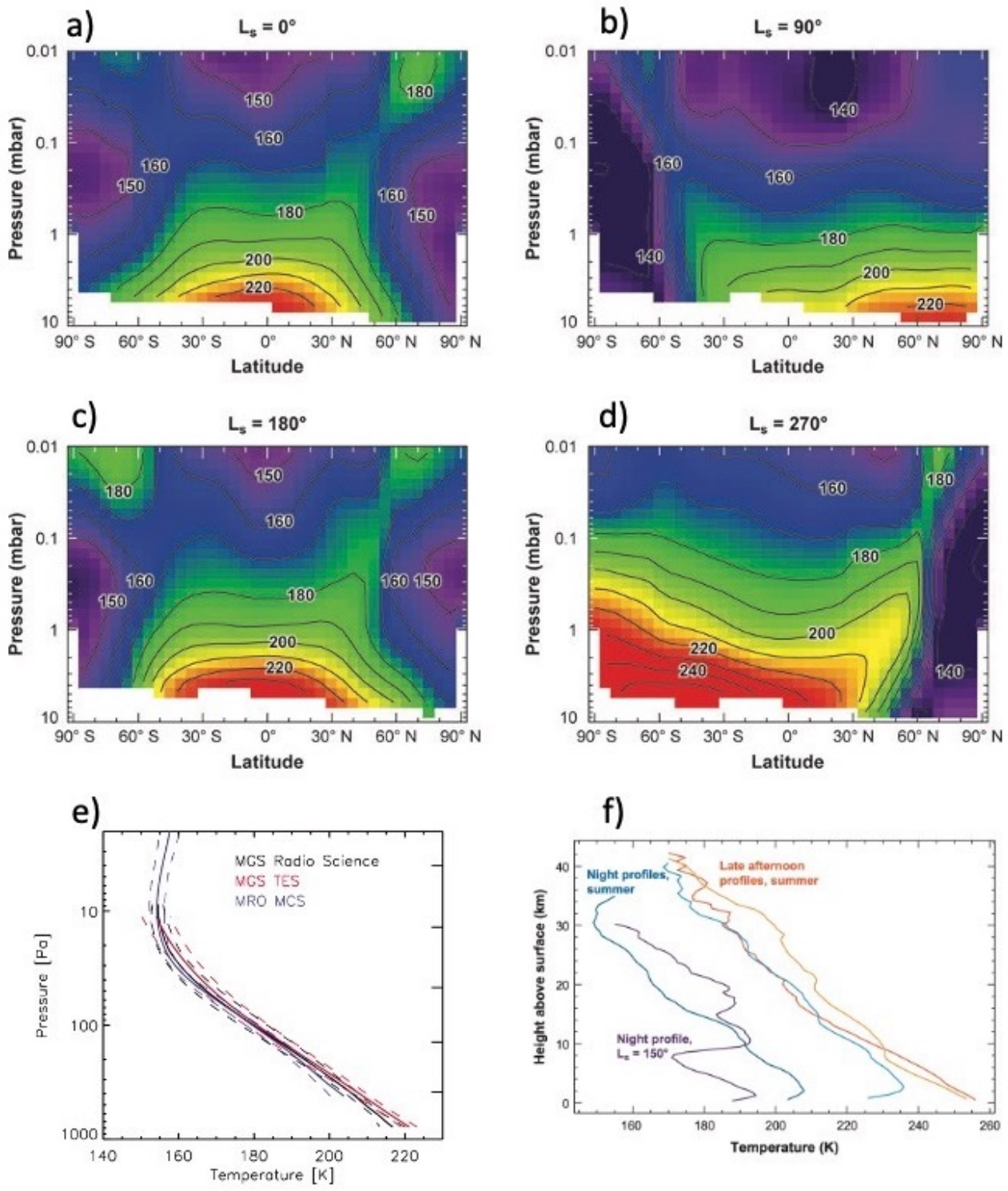

Figure 1.11: Typical temperature variations by altitude and location. a)-d) from Smith (2008), TES daytime (around 2:00 pm local time) temperatures as a function of latitude and pressure for different seasons (top boundary of 0.01 mbar is approximately 65 km above the surface). e) from Kleinböhl et al. (2009), temperature profile comparison between average temperature profiles by MGS radio science (black), MGS TES (red), and MRO MCS (blue). All measurements for MGS were made in 2001 during Ls=110°-120°, and in 2006 for MRO. The dashed lines give the standard deviation of the measurement. f) from Smith (2008), temperature profiles derived from MGS radio occultation data at mid-latitudes during southern summer. A nighttime profile taken near the Tharsis volcanoes shows large waves.

making the turbulent layer reaching altitudes of up to $10\,\mathrm{km}$. The PBL height also depends on topography and contains about 63% of the total atmospheric mass (Hinson et al., 2008). In the afternoon when the cooling surface becomes colder than the near-surface atmosphere, convection shuts down. The near-surface temperature gradient becomes inverted, the inversion layer grows through the night and reaches a depth >$1\,\mathrm{km}$ before suddenly reversing again at sunrise. In the mesosphere (the base of which varies from $\sim$40-60 km), the temperatures show no gradient and are instead oscillating due to vertically propagating planetary waves. In the thermosphere above approximately $100\,\mathrm{km}$, the temperatures increase with altitude because of heating from absorption by CO_2 of solar radiation in the far and extreme UV.

Knowledge of the behaviour of the atmospheric temperatures on Mars is essential to obtain a complete understanding of the water cycle. Atmospheric and polar surface temperatures control the large fluctuations in the water cycle, allowing it to condense from vapor to ice over the poles each winter, and causing it to sublime once more each spring. The sublimation temperature of water at standard Martian pressure is $\sim 180\,\mathrm{K}$, compared to CO_2 which does not sublime until $\sim$245K, explaining why water ice frost does not disappear before CO_2 ice frost. The temperature profile also controls the water vapor saturation altitude, which varies with season. During northern spring close to aphelion the average atmospheric temperature reaches its annual minimum in the tropics. As a result, the saturation altitude is lowered and water vapor seems to remain below $10\,\mathrm{km}$ until the atmosphere starts heating up. On the other hand, during southern spring around perihelion, the saturation altitude in the tropics increases to 40-$60\,\mathrm{km}$ (Clancy et al., 1996).

1.3.4 Aerosols

Martian aerosols include lofted mineral dust particles and water ice clouds. Together they influence atmospheric density, temperatures and wind patterns. The dust cycle is a crucial component in shaping the daily, seasonal and interannual climate variability. The atmospheric thermal and dynamical structures, and the transport of atmospheric species all strongly depend on the dust spatial and temporal distribution.

Dust in the Martian atmosphere has been extensively studied since the late 1960s, and during the 1970s dust was recognized to play a significant part in the heating budget by absorbing incoming solar radiation in the visible wavelength range while emitting in the infrared (e.g. Gierasch and Goody (1972); Barth (1974); Leovy et al. (1973)). As it was soon after recognized that dust can provide both positive and negative radiative feedbacks into dynamical processes (Pollack et al., 1979), a large-scale community effort was initiated to further understand the fundamental radiative and microphysical properties of the dust particles. Higher atmospheric dust loading has been found to be strongly connected to a deepened and intensified circulation (e.g. Haberle et al. (1982); Newman et al. (2002)), more intense thermal tides (Leovy and Zurek, 1979), and enhanced polar warming (Wilson, 1997). There are many aspects of aerosols being studied, especially their microphysical properties are of great interest to constrain models of the Martian atmosphere, but for the purposes of this work the particle size distribution and dust cycle behaviour are the primary focus.

Atmospheric dust particles are typically around 1.5 micron in size, ranging from approximately 0.8-$2\,\mu\mathrm{m}$ (e.g. Clancy (2003); Lemmon et al. (2004)). Smaller particles can be found in the north around spring and summer, while larger particle sizes are more common in the south and particularly during dust storm periods (Clancy, 2003). The size distribution of the particles have a large impact on the shape of the atmospheric continuum in infrared spectroscopic measurements, so a good understanding of the dust properties at any given time is crucial for the production of accurate synthetic spectra for atmospheric retrievals of gaseous abundances (more on this in Section 5.1).

The amount of dust in the atmosphere is most commonly estimated indirectly by measuring the total opacity of the atmosphere at a reference wavelength (often $0.69\,\mu\mathrm{m}$, $9\,\mu\mathrm{m}$ or $12\,\mu\mathrm{m}$). This total opacity is a good proxy to account for the radiative heating and cooling effects of the dust.

The total opacity has been monitored closely for two decades now with various instruments such as Mars Odyssey/THEMIS (Smith, 2009), the PanCam cameras on board the Mars Exploration Rovers (Lemmon et al., 2004) and MEX/PFS (Wolkenberg et al., 2020) to mention some, but one of the most widely used dust climatologies was provided by MGS/TES nadir infrared spectra (Smith et al., 2001; Smith, 2004, 2008).

The dust cycle

The column integrated opacity displays a strong seasonal behaviour, as shown in Figure 1.12 from Forget and Montabone (2017). The Figure shows the column integrated optical depth for nine consecutive Martian years, as a function of Ls and latitude. Like clockwork, every year starts with a period between Ls=$\sim$0°-140° where the atmosphere is weakly opaque almost globally, the exception is near the polar cap edges where lifting still occurs. This season is marked by its low dust loading in both hemispheres, but rather suddenly around Ls=140° dust storms start to occur at low latitudes. There are differences from year to year, both in magnitude, commencement time and duration, but generally the time between Ls=140°-360° is considered as a period of high dust loading. This period includes the perihelion, when greater forcings in the atmosphere induces lifting events. The low elevation Hellas and Argyre basins (see Figure 1.5) are known as the dustiest places on Mars, along with both polar regions. The least dusty places are the northern lowland plains at mid- and high latitudes between 45° and 75°N.

Dust storms on Mars are recurrent phenomena, particularly in the southern hemisphere. Sometimes regional dust storms grow to engulf the entire planet, though the exact mechanisms for this process remains elusive (Forget and Montabone, 2017). During such global dust storms (GDS), dust becomes so abundant in the atmosphere that surface features are no longer distinguishable from space. This is clearly demonstrated in Figure1.13, where a regional storm can be seen in the left image of Mars close to the south polar cap as a brighter spot. One month later most of the planet is obscured by lofted dust. Global dust storms have been monitored and studied for some time, and as our presence at Mars continues, we are capable of comparing dust storm events. Wolkenberg et al. (2020) compared the global dust storms of MY 25 (shown in Figure 1.13, 28 and 34, and found that the three storms had similar duration of the expansion phase, yet there are differences in decay phases, onset timing and location of the precursor local dust storms.

The vertical distribution, and the vertical size distribution, has a significant impact on the thermal response. To describe the vertical distribution of dust mass mixing ratio, Conrath (1975) created a model for an idealized vertical profile by including the competing effects of mixing and sedimentation during a decaying global dust storm, according to equation 1.1,

$$q = q_0 \cdot e^{\nu(1-\sigma^{-1})} \tag{1.1}$$

where q_0 is the surface mass mixing ratio, ν is the ratio between the rates of sedimentation and vertical atmospheric diffusion (known as the Conrath parameter), σ is exp(-z/H), where z is the height above the surface and H is the atmospheric scale height. The Conrath parameter is typically in the range of 0.001 to 1, where higher values indicate that dust is more strongly confined to low altitudes. The Conrath parameter is widely used to model the vertical distribution of dust on Mars (e.g. Montmessin et al. (2006); Neary et al. (2020)), and is also used in the work presented later in this thesis related to the creation of a synthetic spectrum for SuperCam retrievals (see Chapters 5 and 5.1. The Conrath model, was derived to describe the vertical distribution during a global dust storm, and might not reproduce the vertical variations during non-GDS time periods. It is also not capable of capturing detached layers in the vertical profile, only a monotonically decreasing profile (or increasing if the Conrath parameter is set to a negative value). If additional dust removal processes occur, the Conrath model will not properly take into account the increased sedimentation by the condensation of volatiles on dust particles, and it is not sensitive to the dust particle size varying with altitude.

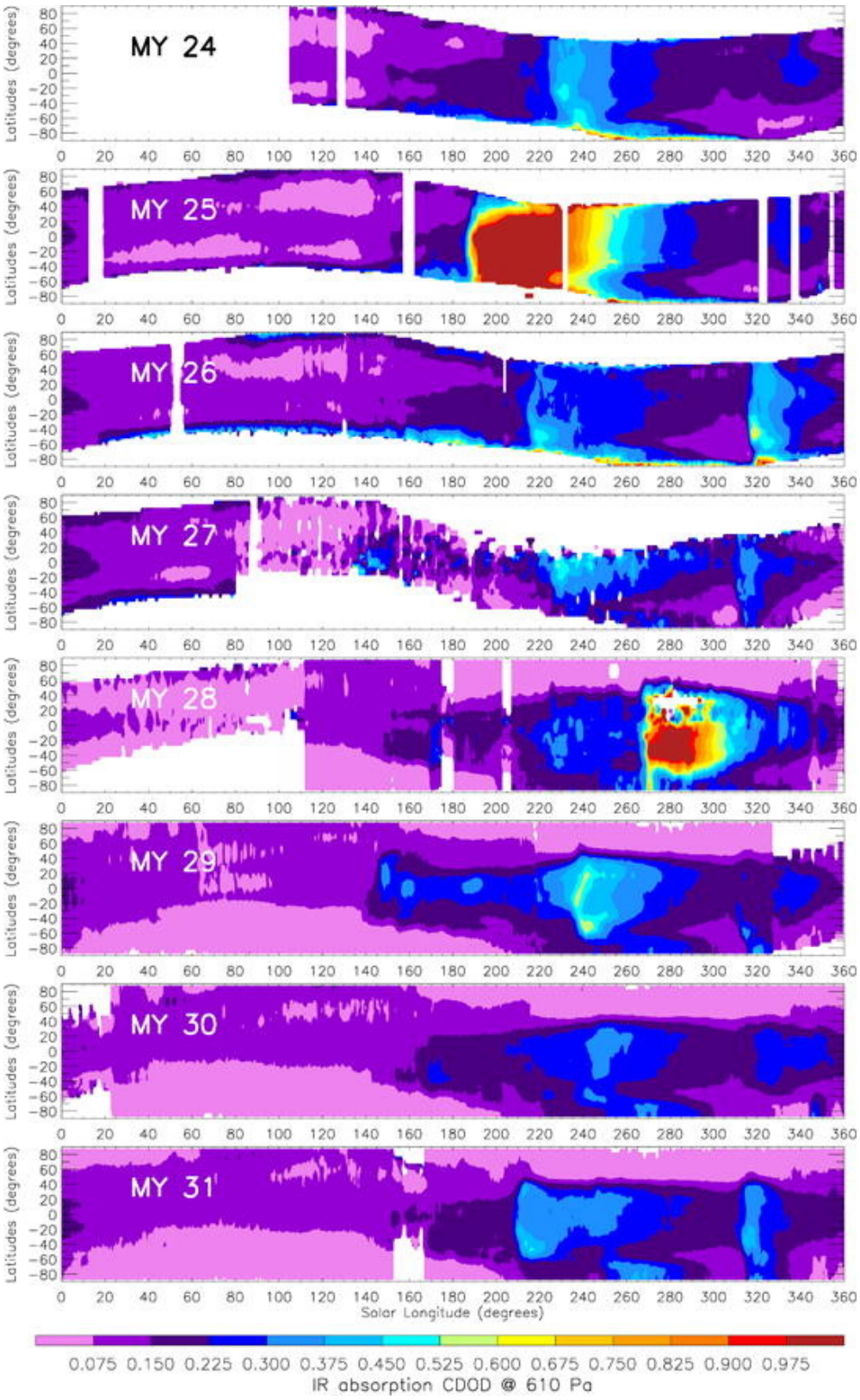

Figure 1.12: Zonal means of equivalent-visible extinction column dust optical depth normalized to the reference 610 Pa pressure level for 9 Martian Years (MY 24 through MY 32). The column dust optical depth averages are plotted as a function of Ls and latitude. White spaces indicate times and places of missing data. Figure from Forget and Montabone (2017) with data from Montabone et al. (2015).

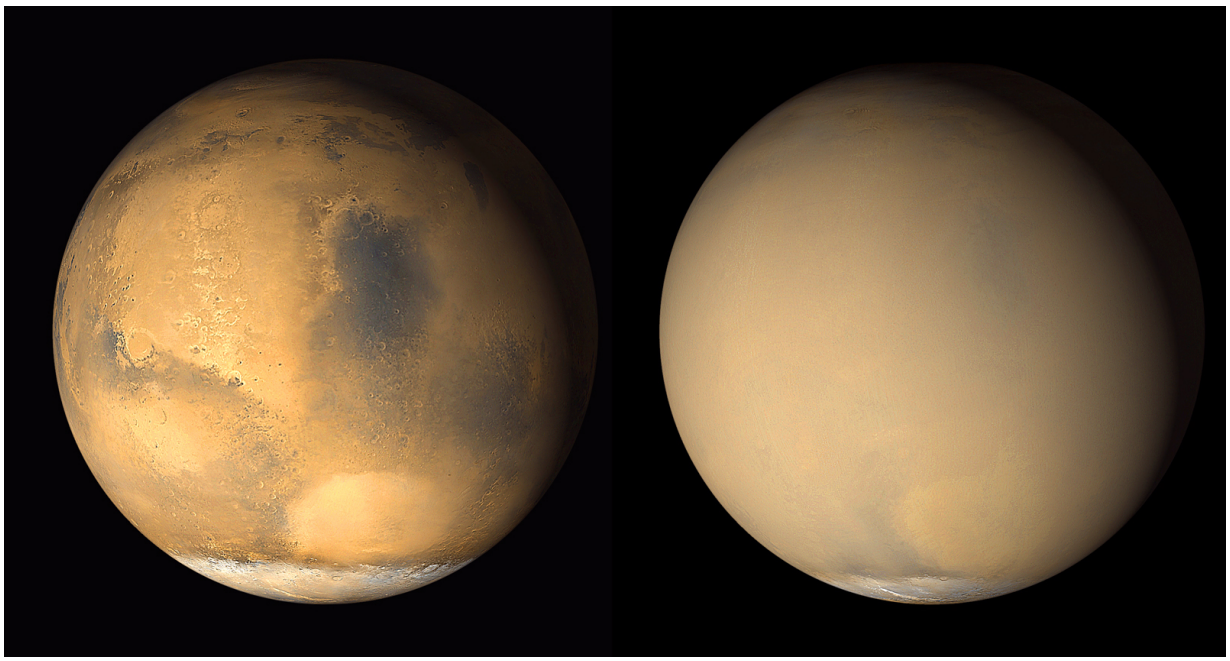

Figure 1.13: Images taken by the Mars Orbiter Camera on Mars Global Surveyor in 2001. Left: image from late June showing clear conditions across most of the planet, except for a regional dust-storm over Hellas basin visible as a bright and smooth oval feature near the edge of the south polar cap. Right: image from July with the same perspective showing the planet almost completely enveloped by dust as the regional dust storm in the south extends across to globe and to altitudes of more than 60 kilometers. Credit: NASA/JPL/MSSS.

Shortly after the arrival of MRO at Mars with its Mars Climate Sounder (MCS) infrared limb radiometer, the MCS profiles became the most used observational database on Mars climate, forming the basis for a significant number of studies on atmospheric structure, dynamics, and aerosols (e.g. McCleese et al. (2010); Heavens et al. (2011); Kleinböhl et al. (2009)). By studying high vertical resolution limb scans, McCleese et al. (2010) revealed a more complex vertical dust distribution than previously assumed, with a nightside maxima around $20\,\mathrm{km}$ in the spring and summer. Heavens et al. (2011) showed that the Conrath model is incompatible with dust profiles observed by MCS, which contained a high-altitude local maxima in the tropics. Instead an empirical alternative was presented which is able to produce detached layers and to describe seasonal variability (Heavens et al., 2011).

Using limb scans with TES Guzewich et al. (2013) observed a two-layer structure of the dust profile, with a maxima at around $25\,\mathrm{km}$ and another at $\sim 55\,\mathrm{km}$, and also measured the dust size distribution. The size distribution with altitude was found to be rather constant below $40\,\mathrm{km}$, with an effective radius of $1\,\mu\mathrm{m}$ throughout the Martian year, including the detached tropical dust layer mentioned above (Guzewich et al., 2014).

Water ice clouds

Suspended dust is essential for the creation of water ice clouds as a source of cloud condensation nuclei (Gooding, 1986). White clouds on Mars were speculated to be water ice before spectroscopic evidence was available (Smith and Smith, 1972), but with Mariner 9, final confirmation of the existence of water ice clouds on Mars was obtained (Curran et al., 1973). Water ice clouds play an important role together with dust in shaping the Martian atmospheric temperature structure (although in a more restricted manner as clouds are way more concentrated in space and time), and has since their discovery been an active field of study (e.g. Clancy et al. (1996); Wang (2002); Smith (2004)). Recent combinations of modelling and observations indicate that these clouds affect the atmosphere

both directly by direct extinction of visible and infrared radiation, and indirectly in other regions of the planet by modifying the whole atmospheric circulation (Hinson, 2004). There also seems to be a diurnal dependence where the clouds heat the atmosphere in the daytime and cool the atmosphere during night Madeleine et al. (2012).

Martian water ice clouds are similar to terrestrial cirrus clouds in that they both form onto foreign substrates, assuming that Martian dust particles are the cloud condensation nuclei. Michelangeli et al. (1993) developed the first microphysical model representing the interactions between water ice clouds and dust on Mars. The optical depth of water ice clouds is often anti-correlated with that of dust, as water ice aerosols nucleating on dust particles seem to cleanse the atmosphere of dust, and at the same time deposits water ice and dust to the surface in the polar regions (Navarro et al., 2014). Water ice clouds have been observed to form through various processes and take many forms such as topographically induced clouds, ground fogs, extended polar hoods, and a low-latitude aphelion season cloud belt (ACB) (Clancy et al., 1996; Pearl et al., 2001), and in general their location is often indicative of regions of upward-moving air. Several cloud types are present in the pictures in Figure 1.14. With respect to the water cycle, the ACB and the polar hoods are the most significant large-scale manifestation of clouds. Both are triggered by seasonal processes are thus themselves seasonal in nature, though the ACB displays with very little interannual variability.

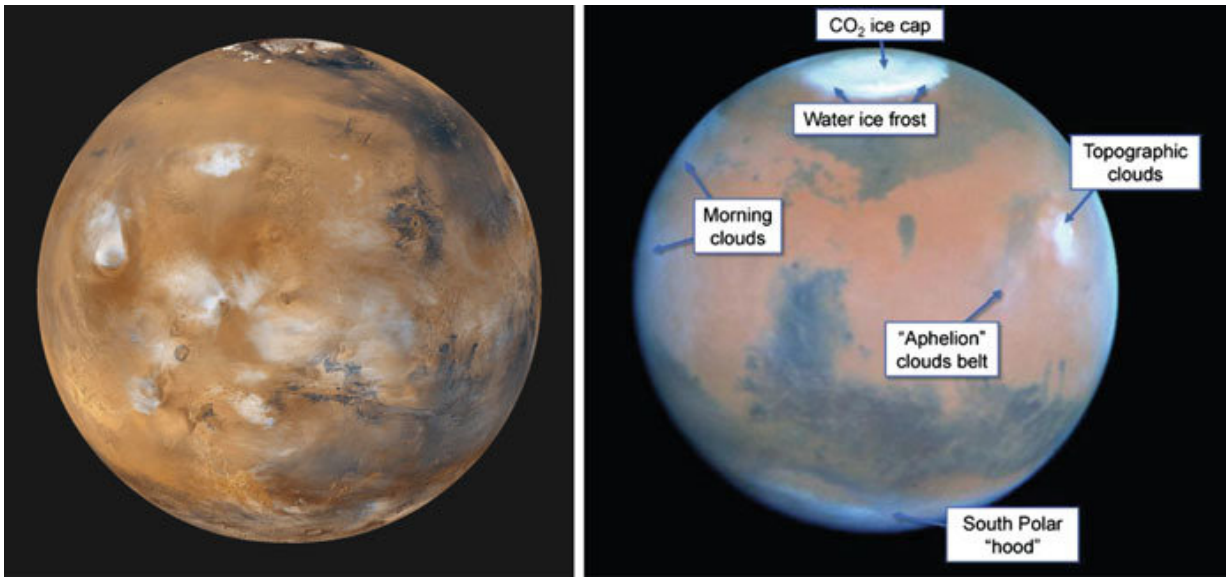

Figure 1.14: Images of Mars showing water ice clouds forming the aphelion cloud belt near the topographic features of the Tharsis plateau in the close to the equator. The elongated shape of the cloud is indicative of the prevailing orientation of the regional atmospheric flow. Figure from Montmessin and Määttänen (2018). Credit: NASA/JPL-Caltech-MSSS.

The recurring ACB was first identified by Clancy et al. (1996) using ground based observations. The aphelion cloud belt appears around Ls=30° and remains until ∼140°, at latitudes between 10°S-30°N (e.g. Clancy (2003); Madeleine et al. (2012); Clancy et al. (2017a); Montmessin and Määttänen (2018)), as a result of adiabatic cooling of water vapor recently released as the north polar cap sublimates. Water ice clouds, and particularly the ACB, play a vital role in governing the water vapor vertical profile, and thus impacts the water transport and potential exchange with ground reservoirs. In the tropics, a significant cold bias was found during the aphelion season between models and observations before radiative active clouds were included (Madeleine et al., 2011). A strong interconnection between waves and clouds was found by Hinson (2004) using global models in combination with radio occultations. Clouds were found to form in response to wave-induced adiabatic cooling, and the tides in turn were intensified by radiative forcing from the clouds. This tide-cloud coupling results in for instance strong diurnal modulation of the cloud properties in the tropics.

The polar hoods appear over both polar caps in the early summer, around Ls 20°, and last until early fall, induced by atmospheric radiative cooling in mid- to high-latitudes. They are much more prominent in the north, likely due to the much drier SH polar summer, and a clear wave number two wave structure is observable in the north but much less so in the south (Wang, 2002). Models indicate that the presence of clouds over the poles in summer is vital for the vertical redistribution of water vapor, and thereby affecting the rate of sublimation. During the sublimation season of the polar cap, the presence of these low clouds balance the upward transport of the sublimed. At higher altitudes the southward advection is more effective, thus clouds significantly influence the amount of water that is extracted from the cap in spring and summer and transported equatorward (Montmessin et al., 2004).

Water ice particles are typically larger than dust particles, varying between 1 and 4 microns, an expected result considering that water ice crystals form onto dust. It has been suggested that these can be divided into two distinct cloud populations (Clancy, 2003), and a third class was proposed with particles in the sub-micron size range (Montmessin et al., 2006). The smallest ice particles are more prominent in the SH during Ls=0°–140° and in general over the largest volcanoes for any season. Larger particles are commonly found within the ACB (Clancy, 2003). The aphelion cloud belt exhibits a strong sorting of size with height with the larger particles (>3 microns) mostly below $20\,\mathrm{km}$, and smaller particles($\sim$1 microns) up to $40\,\mathrm{km}$. Interestingly, the polar hood clouds display an almost uniform particle size throughout the atmospheric column, averaging at $1.5\,\mu\mathrm{m}$ (Guzewich et al., 2014).

1.3.5 Dynamics and circulation

The circulation of the Martian atmosphere consists of several interacting wind systems including the mean meridional circulation, stationary and transient eddies, thermal tides, and mass condensation flow. Dynamics and circulation patterns could be considered on at least three different scales; global scales (hundreds to thousands of kilometers, such as the Hadley cells), mesoscales (one to hundreds of kilometers, such as gravity waves), and microscale (tens of meters to one kilometer, such as dust devils), although these definitions are somewhat arbitrary. Figure 1.15 illustrates some of these circulation systems for the NH winter season.

The largest circulation structure on Mars is the Hadley cell. Hadley circulation is a thermally driven circulation, with air rising at warm latitudes and descending at colder ones. It is highly dependent on solar forcing, and is present on, and dominates, the meridional circulation of terrestrial atmospheres such as Venus, Earth, Mars and Titan. On Earth the Hadley cells maintain a stable configuration due to the oceans acting as a buffer, dampening temperature variations. On Mars no ocean equivalent exists, resulting in the Hadley cell exhibiting a seasonal cycle, transitioning from two hemispherically symmetric cells at equinox, to one tilted cell at solstice. The Hadley cell is a powerful cross-equatorial circulation, effectively transporting species and aerosols up in the summer hemisphere and down in the winter hemisphere just equatorward of the polar vortex. The return circulation remains near the surface in the opposite direction in each hemisphere (Guendelman and Kaspi, 2018). Typical surface wind speeds are around $10\,\mathrm{m/s}$ (Viúdez-Moreiras et al., 2019).

A prominent feature of the winter hemisphere is the polar vortex, a cold region located above the pole surrounded by strong westerly winds. Around solstice (Ls=$\sim$90/270°, see Figure 1.3), the large latitudinal gradient in temperature between the warm mid-latitudes and the cold winter polar night (see Figure 1.11 b) and d)) produces a strong eastward jet, referred to as the polar vortex. The wind speeds in this vortex can reach well beyond $100\,\mathrm{m/s}$ (Mitchell et al., 2015) around the north pole, and is significantly stronger than its southern counterpart.

Those are the main circulation patterns on Mars, but the dynamics of the planet is complicated by other effects than temperature gradients. Gravity waves are produced when air flows over a surface with varying elevation. In the PBL, the gravity waves propagate upwards without much change in mean velocity and amplitude, but since the amplitude is inversely proportional to density, they grow

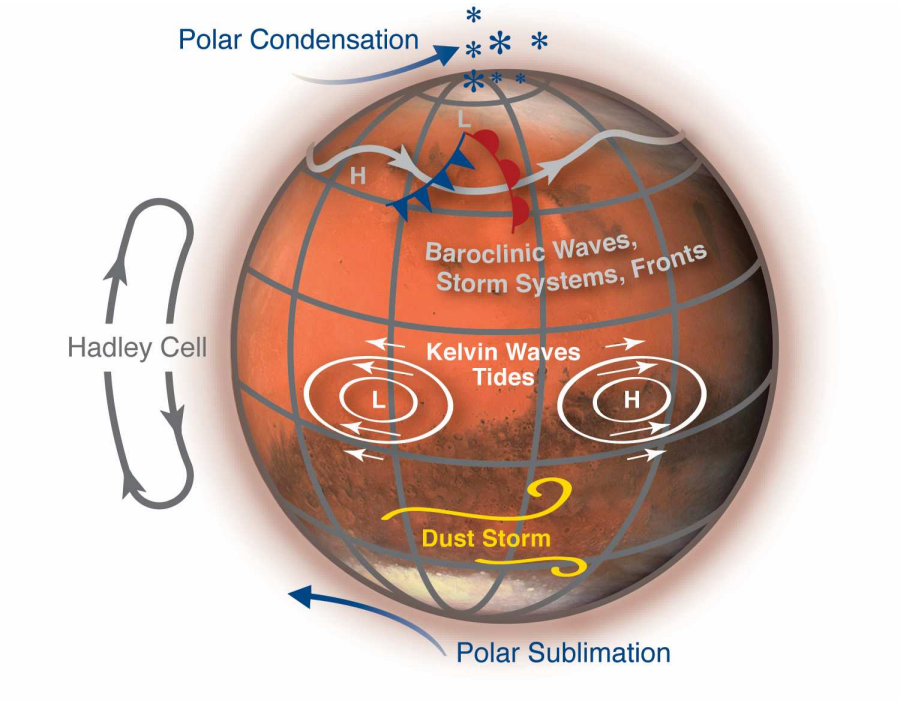

Figure 1.15: Examples of circulation patterns during northern winter. The polar vortex is illustrated in grey around the north pole, and the blue arrows indicate water vapor transportation towards the north pole where it condenses. Credit: NASA/Mars Climate Modeling Center.

larger as they reach higher altitudes. Eventually the waves break, transferring momentum high up in the mesosphere. Gravity waves were hypothesized to exist and modeled in the Martian atmosphere (e.g. Forget et al. (1999); Théodore et al. (1993)) for years before they were inferred by observational evidence by Creasey et al. (2006) using radio occultation on MGS to measure variations in the temperature profile. The gravity waves were found to exhibit strong seasonal variations, with the wave energy in the northern summer tropics being enhanced. As they break, gravity waves play an integral part in vertical mixing of the atmosphere, and it has also been suggested that they induce heating and cooling at different altitudes (Parish et al., 2009).

1.4 Water vapor

The presence of water on a planet has significant consequences for the chemistry and physics of both the surface and atmosphere. On the surface, liquid water causes physical and chemical alterations, affecting both topography and climate. Moreover, liquid water is a vital component for life as we know it, motivating our search for water in our solar system and beyond. In Earth's atmosphere, water has a major effect on heat transport and thus overall climate due to its high heat capacity and the ability to form clouds. In addition, photolysis of water produces reactive hydrogen and oxygen species, which are strong oxidants and creates more photo-by-products and hence complexifies chemistry.

Water vapor was first detected on Mars from Earth-based telescopes in 1963, by the observation of eleven near-infrared absorption lines (Spinrad et al., 1963). Numerous missions have observed this volatile trace gas to understand its climatology, transport processes, and influence on Martian climate. Photolysis of H_2O produces hydroxyl radicals which are the main oxidants of the Martian photochemical cycle (e.g. McElroy and Donahue (1972)), and impacts the climate through altering the radiative equilibrium through cloud formation (Madeleine et al., 2012). For this reason, water vapor controls the long-term stability of the CO_2-dominated atmosphere, by allowing CO_2 to quickly recycle after being decomposed.

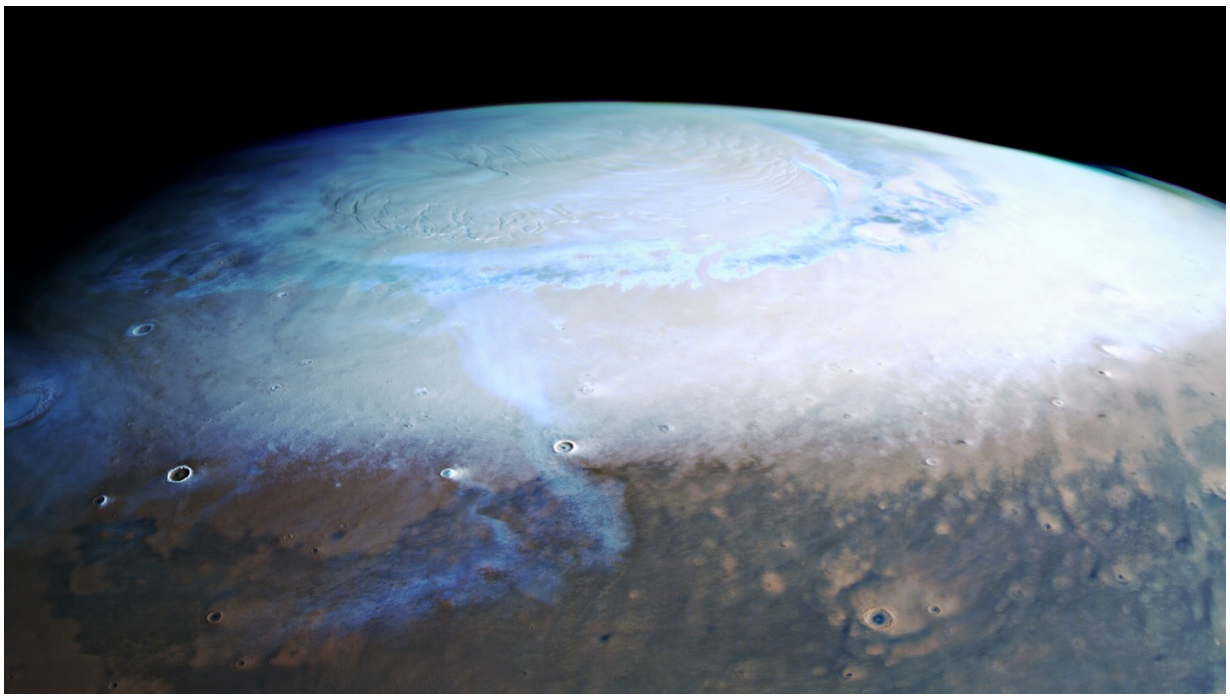

Figure 1.16: Mosaic image of the North polar cap taken by MEX/HRSC on June 17th 2019, corresponding to Ls=40°, northern spring. Credit: ESA/DLR/FU Berlin.

1.4.1 Role of the polar caps

The North polar cap (NPC) is by far the largest reservoir of water on Mars, playing the role of the main seasonal source and sink for the atmosphere (Montmessin et al., 2017). The NPC is at it largest in extent around Ls=270°, when it consists of seasonal CO_2 ice and water ice (Piqueux et al., 2015b). It gradually decreases through the winter and spring, and the CO_2 ice is completely sublimed by Ls=80°. Figure 1.16 shows the north polar cap deposits at Ls=40°, when both CO_2 and water ice is present. When the water ice is gradually exposed to sunlight, it starts subliming, and by summer the amount of water vapor present in the atmosphere globally has roughly doubled (Smith, 2002).

Using OMEGA observations Appéré et al. (2011) observed a water ice annulus forming around the edge of the CO_2 ice cap in winter, appearing at its broadest at ∼6° latitude at Ls=320°, before shrinking towards Ls=350°. During the first half of NH spring, the annulus increases somewhat again and water spectral signatures dominates the ice deposits. This is interpreted as a very active surface ice and atmosphere vapor cycle in northern spring, where water forms an optically thick layer on top of the CO_2 ice, shielding its spectral signatures from orbit. This water ice is hypothesized to come from water ice grains previously embedded in the CO_2 ice, and by cold trapping of water vapor from the sublimating water ice annulus. The dynamic processes responsible for transporting sublimed water away from the NPC and across the equator, in some works referred to as the Houben effect, are described in the previous section (Section 1.3.5), and will not be discussed further here.

The south polar cap undergoes much more extreme conditions as southern summer is short and hot during perihelion, and southern winter is long and cold during aphelion. During NH winter solstice, Ls=270°, the southern cap is almost free of water ice, in stark contrast to the situation in the NH at the corresponding season (Langevin et al., 2007). Yet, even during southern summer Bibring et al. (2004) and Langevin et al. (2007) both reported finding areas of water ice. The existence of a residual southern polar ice cap, indicates the south polar cap might be a permanent water vapor sink.

1.4.2 Annual cycle of water vapor column abundance

The Viking orbiters 1 and 2 were both equipped with the Mars Atmospheric Water Detector (MAWD), and each provided evidence that the NPC is the primary source of atmospheric water, while also indicating a strong north–south asymmetry in the atmospheric water abundance (Farmer et al., 1976; Jakosky and Farmer, 1982). The first comprehensive climatology was provided by the Mars Global Surveyor mission (MGS) and its Thermal Emission Spectrometer (TES) (Smith, 2002, 2004), and it is from this data set that most modern Martian water climatologies are based. Figure 1.17 depicts what has become the basis for our understanding of the seasonal variations of water vapor. There are now several multi-year water vapor climatologies available; the TES data set was later revisited using an updated retrieval scheme Pankine et al. (2010), Trokhimovskiy et al. (2015) provided a 5 MY of SPICAM observations, from CRISM another 5 MY year climatology exists (Smith et al., 2018), and a combined climatology covering MY 24–27 (TES) and MY 28–30 (CRISM) can be found in Montmessin et al. (2017).

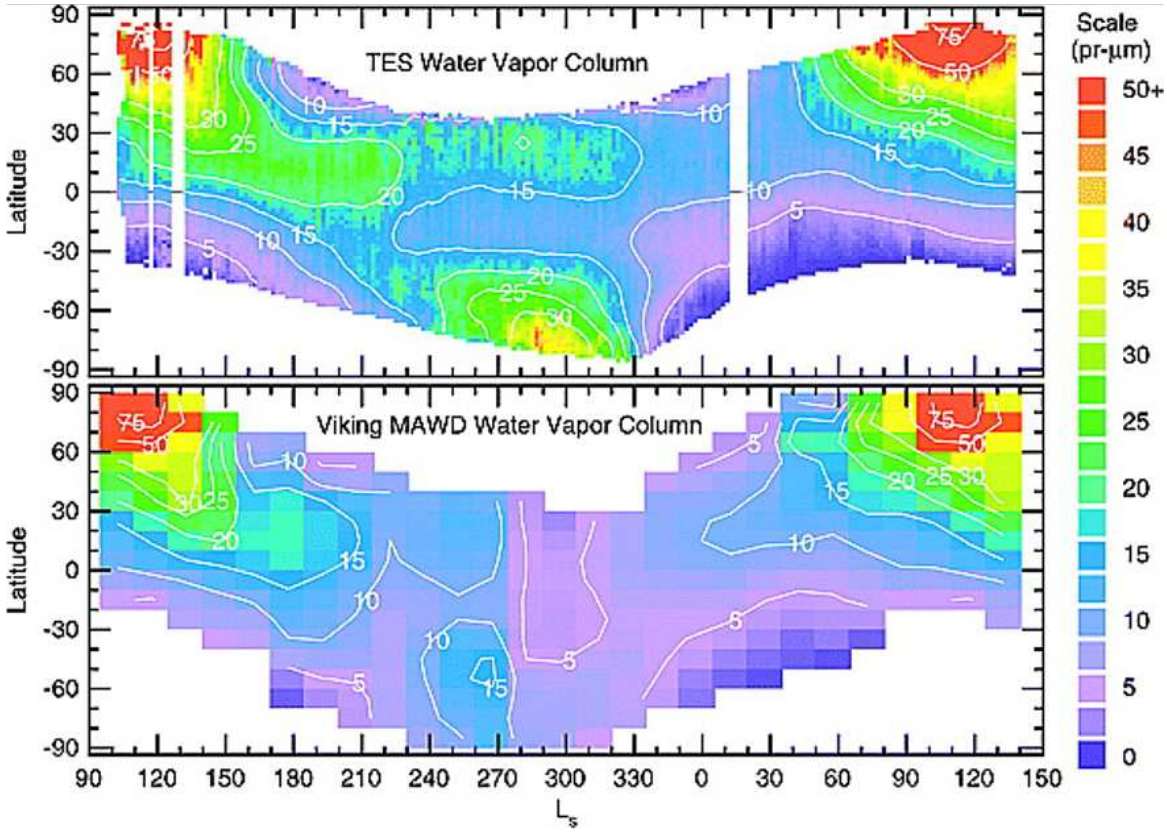

Figure 1.17: The annual cycle of water vapor on Mars as observed by the Thermal Emission Spectrometer (Smith, 2002) (top panel) and by the Viking MAWD instrument (Jakosky and Farmer, 1982). The column abundance of water vapor is shown as a function of Ls and latitude for both panels. Contours show a smoothed representation of the results. Note that the data has not been adjusted for topography or scaled to an equivalent pressure surface.

The results from these works revealed an annual pattern where water vapor is effectively cycled from pole to pole, subliming as spring turns to summer when it is transported equatorward and across, before eventually freezing back out of the atmosphere at the other pole. The mechanisms by which Mars' water cycle can evolve in a steady state (minus some net annual transfer from the North cap to the south) has amongst others been described in Richardson (2002); Montmessin et al. (2004).

This climatology outlines a column abundance maximum at high latitudes during midsummer in both hemispheres, reaching a peak of $\sim$60 pr-μm on average in the north, and $\sim$25 pr-μm in the south. Low water abundances are observed during fall and winter at middle and high latitudes of both

hemispheres. General circulation models along with TES observations indicate that water from the southern summer maximum is transported to the NH more efficiently than the reverse process (e.g. Montmessin et al. (2004); Steele et al. (2014)).

Water vapor transport

The cross-equatorial water transport is facilitated by the Hadley circulation, but for some time it was not understood how sublimed water from the NPC could escape the polar region. A sea-breeze circulation at the edge of the north residual cap was identified in a 2D model and found to be capable of transporting water equatorward, but too weakly to reproduce the observed summer vapor increase over the mid and low latitudes (Haberle and Jakosky, 1990). What was recognized later, is that the NH mid-latitude circulation is dominated by waves produced by the combination of areas with similarly alternating thermal inertia [1] and topography (the Aecadia, Acidalia and Utopia Planitiae at low elevations). These effects force the development of a zonally asymmetric summertime circulation taking the shape of a zone-3 wave, spreading across the 45°-70°N latitude band. Sublimated water coming off the NPC is thus locked into a wave-3 pattern, in large part concentrating southward transport via advection to three longitudinal corridors located around 90°E, 230°E and 340°E (see Figure 1.5) (Montmessin et al., 2017).

From late summer until early the next spring, the climate from the mid- to high-latitudes and polewards is driven by the latitudinal and seasonal wandering of the polar vortex. The shrinking of the polar vortex during winter and spring is associated with a strong horizontal mixing across the vortex boundaries (Houben et al., 1997). During this time the polar vortex turns dynamically porous, and allows poleward invasion of moist air where water condenses. Models indicate that the frost that sublimed from the surface of the seasonal cap edge moves up and poleward, and eventually precipitates at higher latitudes (Richardson, 2002). The seasonal cap edge consequently experiences a notable increase of water ice frost thickness during the shrinking phase. As a consequence, the south polar region exhibits a summer maximum even when no extensive reservoir of water ice exists there.

1.4.3 Water vertical profile

Attempts at determining the vertical location of water vapor were made for the first time with Viking Orbiter 1 (Davies, 1979). It was found that he H_2O vertical distribution was indistinguishable from the dust distribution and was well mixed up to about $10\,\mathrm{km}$. The first ever direct measurements of the water vertical distribution were accomplished by solar occultation observations from Phobos 2, which produced very few profiles over a time span of two months. The results show a sharp decrease above $25\,\mathrm{km}$, and a close to constant mixing ratio below it Rodin et al. (1997). These results suggested an altitude for the Martian hygropause, the level above which the atmosphere is cold enough for water ice cloud formation due to a lower vapor pressure.

From these early observations and the assumption that condensation would not allow water vapor to supersaturate, the distribution of water vapor with altitude was for a long time assumed to be rather uniform and well-mixed with CO_2, up to the hygropause where the atmosphere reaches saturation. Above this point water vapor was thought to quickly diminish. With the arrival of MEX in 2004, and later MAVEN and the ExoMars Trace gas Orbiter (TGO) with its infrared spectrometers NOMAD and ACS, a new era in water vertical profile began.

The vertical distribution of water vapor can be tentatively inferred from nadir measurements, but such observations are not optimal for this task (as will be detailed later in Section 1.6). Solar occultations are in many ways more suitable, but SPICAM occultation campaigns are not the primary focus of MEX and therefore these observations are not regularly executed. TGO on the other hand

[1] Physical property that controls the diurnal and seasonal cycles in surface temperature. It is defined as a function of the thermal conductivity, heat capacity, and density.

was designed to primarily operate in solar occultation and thus flies in an orbit adapted for solar occultation measurements, and obtains a nearly global coverage with good vertical and temporal resolution. This mode of observation has allowed for several ground-breaking discoveries such as the existence of supersaturation above the hygropause by Maltagliati et al. (2011b) using SPICAM, and the occurrence of high altitude water during dust storms (e.g. Aoki et al. (2019); Fedorova et al. (2020); Belyaev et al. (2021)). The main limitation of solar occultations is caused by dust which obscures the line-of-sight and eventually prevents accessing the lowest and thus densest levels where dust and water are present in higher absolute abundances. A floor in altitude ranging between 2-30 km is usually found, depending on location and season.

Climatologies of vertical distribution now exist (e.g. Fedorova et al. (2021); Aoki et al. (2022), as shown in Figure 1.18. In these studies, the seasonal variations of the water profiles are clearly visible, with strong contrasts between perihelion and aphelion for both hemispheres. In general, a vertically deep Hadley cell carries water equatorward from the NPC, but it remains confined near the surface in the mid- to low-latitudes as it is hindered by the aphelion cloud belt (Montmessin et al., 2004; Kahre et al., 2020). In the southern hemisphere on the other hand, perihelion leads to a warmer atmosphere and intensified circulation, causing the subliming water to rapidly reach very high altitudes.

The sudden increase of water vapor at mid-altitudes observed around Ls=190° of MY 34 in Figure 1.18 was driven by the global dust storm that occurred at that time (Wolkenberg et al., 2020). The increased dust load warmed the atmosphere which prevented water from condensing (Neary et al., 2020). As a result, water vapor reached altitudes greater than 100 km (Aoki et al., 2019). The other increases in the NH at around Ls=330° of both MY 34 and 35 can be attributed to the seasonally repeatable occurrences of regional dust storms.

In the SH increases of water vapor can be linked to dust storm activities, but are also due to the increased solar forcings at perihelion close to southern summer. The strong increases around Ls=270° in both MY 34 and MY 35, (the trend was first observed during the dust storm of MY 28 (Fedorova et al., 2018; Heavens et al., 2018), and more recently by Fedorova et al. (2020) and Villanueva et al. (2021) amongst others) and can be explained by a combination of concurrent events; water ice subliming off the south polar cap, a strong Hadley cell causing meridional circulation from the south to the north, and warmer atmospheric temperatures leading to little to no sequestration of the water vapor by the formation of water ice clouds. Modelling effort have shown that water vapor can indeed be transported to around 80 km by such processes (Holmes et al., 2021; Shaposhnikov et al., 2019; Vals et al., 2022).

Supersaturation and escape

The notion that Mars previously had a much warmer and wetter climate is also substantiated from atmospheric research. Owen et al. (1988) first observed HDO on Mars from ground-based high-resolution spectra, and found D/H value of 6±3VSMOW, much enriched compared to Earth's oceans. Assuming Mars and the Earth accreted water from similar sources, this implies that hydrogen escaped more rapidly from Mars in the past than it does now, consistent with an ancient dense and warm atmosphere. The question of where Mars' water has gone is a mystery that has occupied scientists for decades. TGO has also revolutionized the study of D/H by providing simultaneous observations of H_2O, HDO and water ice (e.g. Villanueva et al. (2021); Alday et al. (2021); Villanueva et al. (2022)).

That Mars has lost a substantial part of its atmosphere is widely acknowledged, but the specific processes have yet to be determined with certainty. The rate of water loss to space depends on hydrogen, and the former commonly held hypothesis was that water beneath the hygropause was broken down by HOx chemistry and photodissociation to produce H_2, which would steadily diffuse to higher altitudes, where photodissociation again destroys it and produces H which can escape to space (Haberle et al., 2017). This process should be fairly stable with no large variations due to the long lifetime of H_2, yet strong variability in the high-altitude H abundance has been observed (e.g.

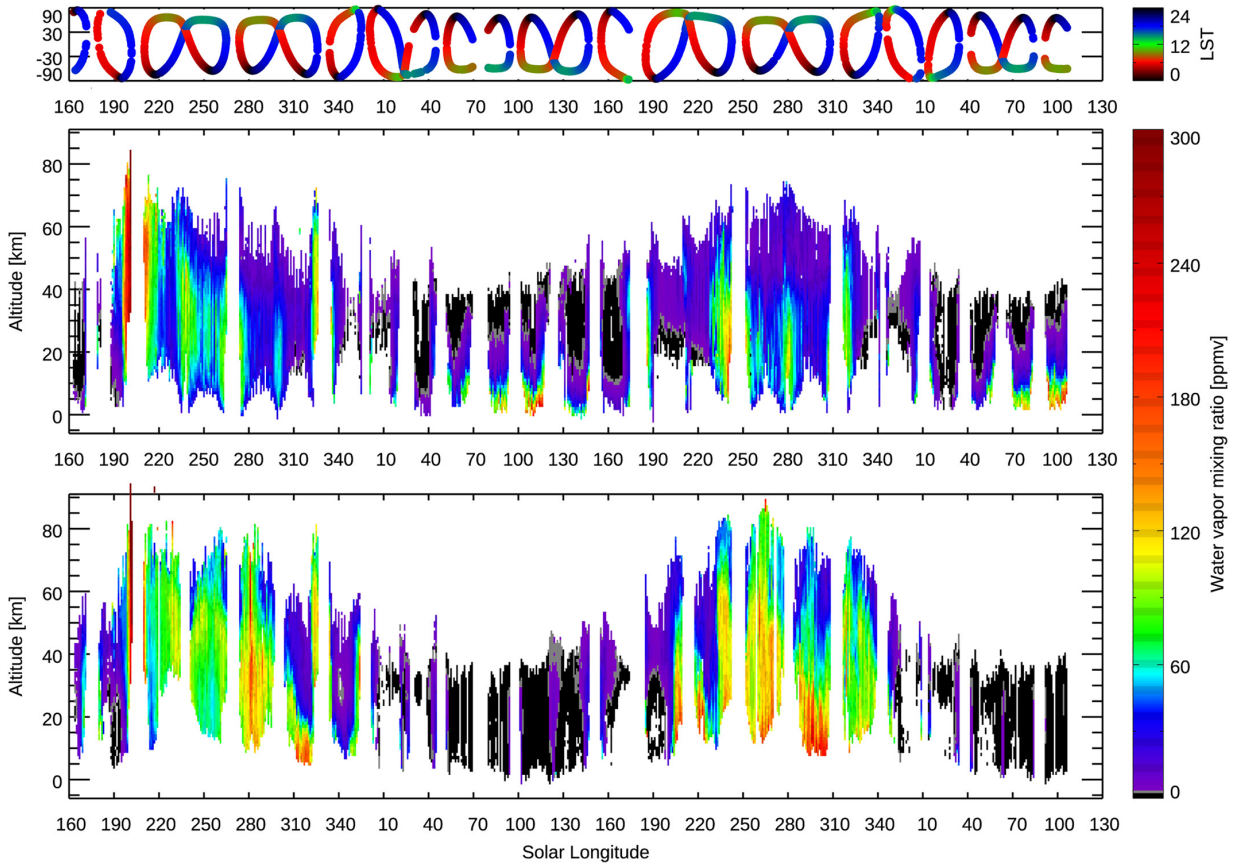

Figure 1.18: Seasonal variations of water vapor vertical profiles from MY 34 Ls=160° to MY 36 Ls=130°. Data was retrieved from NOMAD solar occultation measurements. The top panel shows the latitudes and local solar time of the measurements, the middle and bottom panel show water vapor profiles in the northern and southern hemisphere respectively. The white areas represent either no water detection or no measurements. Figure from Aoki et al. (2022).

Chaffin et al. (2014); Bhattacharyya et al. (2015)). Chaffin et al. (2014, 2017) posed an explanation for this by suggesting water vapor could be transported directly to higher altitudes, connecting it to the occurrence of dust storms.

Condensation and saturation are central in controlling the vertical distribution of water vapor on Mars. For water to condense, cloud condensation nuclei are required along with a combination of pressure and temperature which allows water to change phase from gas to ice. As temperature is one of main parameters controlling the saturation of water, which governs cloud formation, and subsequently the vertical distribution of water, one needs to measure water vapor abundance and temperature concomitantly in order to determine if water vapor exceeds saturation. Maltagliati et al. (2011a) achieved this with MEX/SPICAM measurements and co-located MGS temperature data, and found for the first time evidence of water existing in a supersaturated state in the atmosphere of Mars. The occurrence of supersaturation has been explained by a lack of dust nuclei due to scavenging, where already condensed water formed and later sedimenting ice, or by dust being present but the particles being too small (Fedorova et al., 2014).

With TGO, concomitant measurements of water abundance and temperature is possible, and using TGO/ACS, Fedorova et al. (2023) assembled a 2.5 Martian year data set, displaying an overview of temperature, water vapor profiles and saturation profiles as a function of Martian season, as shown in Figure 1.19. It was found that supersaturation is common on Mars, occurring both in the aphelion and perihelion seasons above the cloud layer, and in the lower polar atmosphere.

During the aphelion season, water mixing ratio above $40\,\mathrm{km}$ in the mid-to-high latitudes was very low (>3 ppmv) and still supersaturated. During the dusty perihelion season, water was also found to

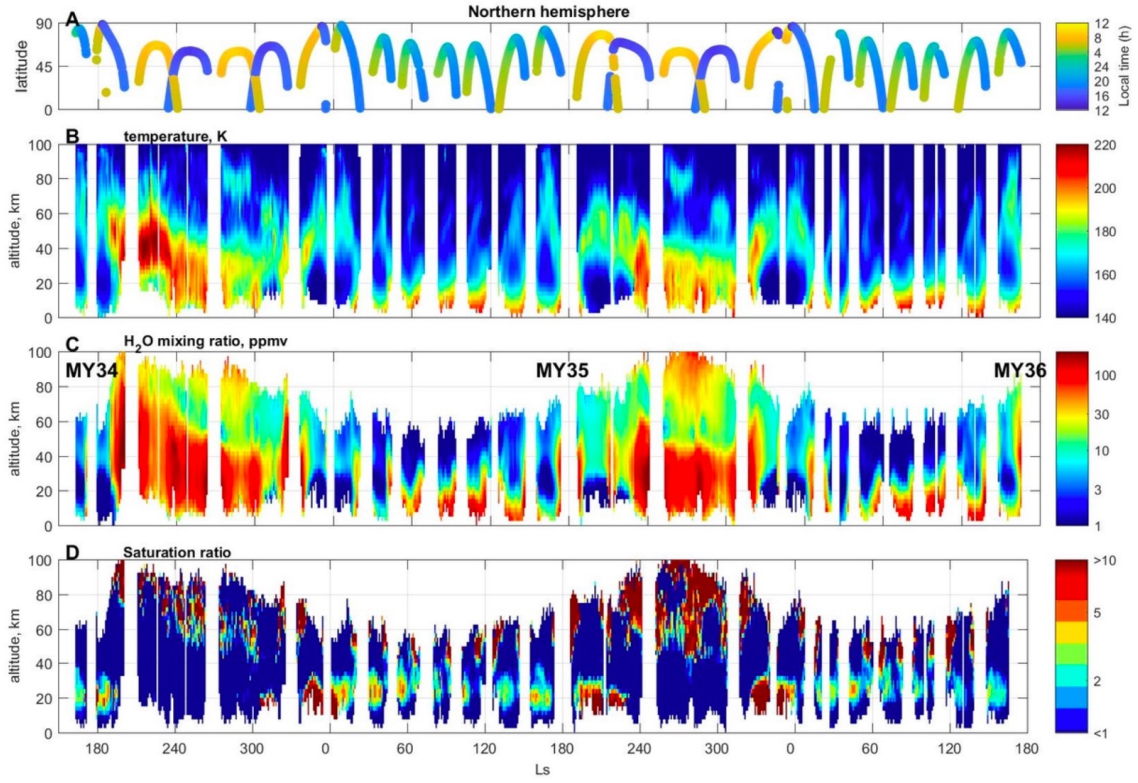

(a)

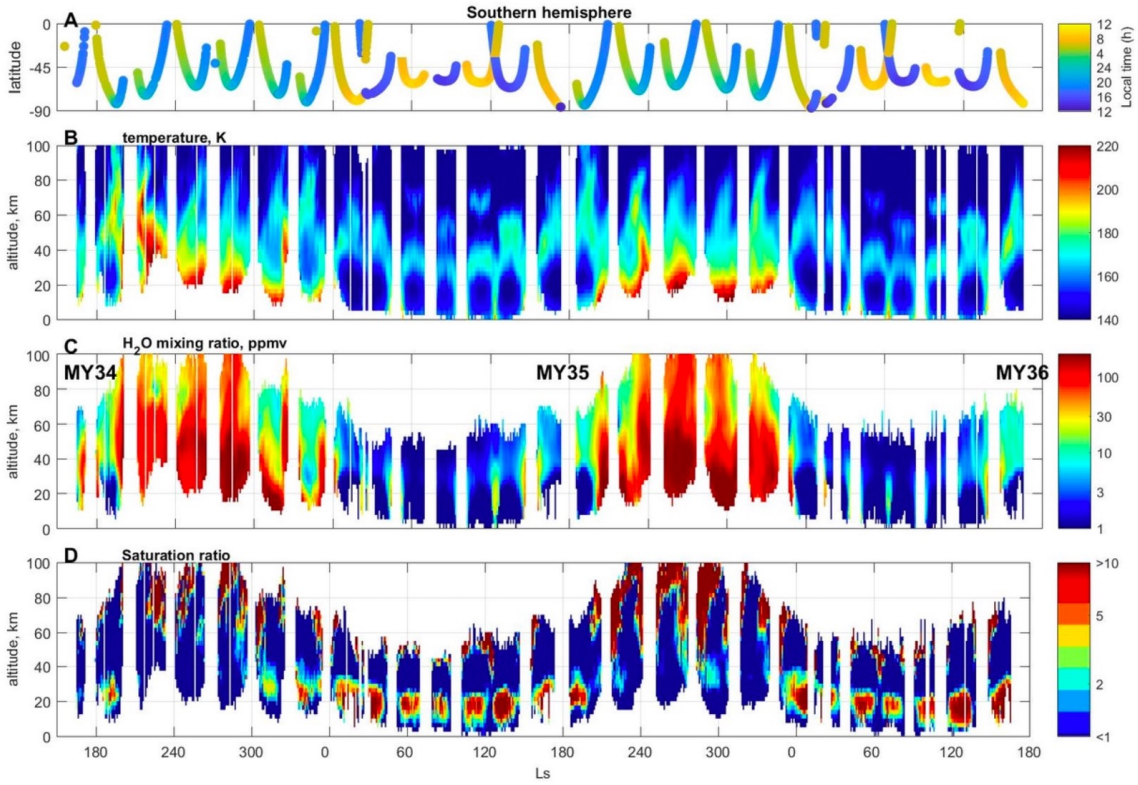

(b)

Figure 1.19: Seasonal variation of profiles of temperature B), water vapor C) and saturation ratio D) during Ls=163° of MY 34 to Ls=170° of MY 36 as retrieved from TGO/ACS-NIR data for each hemisphere. The three top panels show the northern hemisphere, while the three bottom panels show the south hemisphere. The top panel shows the latitudes and local time of the measurements. Figures from Fedorova et al. (2023).

be supersaturated above $60\,\mathrm{km}$ with a much higher mixing ratio of 30-50 ppmv. In the polar regions near the equinoxes, water is found to be supersaturated even below $20\,\mathrm{km}$ for both hemispheres. When comparing the new TGO results with those from MEX/SPICAM, supersaturation appears to follow an annually repeatable trend, revealing that supersaturation clearly promotes water escape, particularly during the dust season.

This new paradigm for water vapor on Mars has significant implications on our understanding of atmospheric escape, and particularly the water loss that Mars has undergone through history (Jakosky and Phillips, 2001). If water vapor is indeed the source of hydrogen in the upper atmosphere, chemical intermediate states, such as water ions, should exist in this region and should exhibit a seasonal trend. This hypothesis was tested, and verified, by Stone et al. (2020), as summarized in Figure 1.20. Panel A) shows variations in water ions normalized by the total electron content near MAVEN's periapsis during more than two Martian years. Three types of variable behaviour are visible here; first, a diurnal variation across two orders of magnitude, clearly visible from the changing of colors from red to blue, secondly, H_2^+ displays a seasonal cycle with maxima near Ls=270° and minima around Ls=40°, where the dayside relative abundance varies by more than an order of magnitude, and thirdly a significant and rapid increase in water ion abundance coinciding with dust storms, indicated by the black boxes. Panels B) and C) in Figure 1.20 corresponds to the regional dust storm of MY 32 and the global dust storm in MY 34, both of which caused substantial perturbations to the background seasonal trend, particularly the global dust storm which increased the water ion abundance by more than an order of magnitude, and increases by a factor of about 3 over the course of only two days (Stone et al., 2020).

Recent modelling work however also suggests that atomic hydrogen may be produced in significant quanta already below $60\,\mathrm{km}$, before being directly advected up to the exosphere (Montmessin et al., 2022). The study suggests that a dominant fraction of the atomic hydrogen is formed between 60-$80\,\mathrm{km}$, and, in agreement with Stone et al. (2020), found that the perihelion season plays a key role in the hydrogen transfer to the upper atmosphere overall. All this indicates that lofted supersaturated water vapor acts as a direct source of atomic hydrogen to the upper atmosphere, and could likely have played a substantial role in the evolution of the Martian climate from its warm and wet state billions of years ago to the cold and dry planet we observe today.

Near-surface water content and role of the regolith

Just as the high-altitude part of the water vertical profile controlled by saturation/supersaturation is interesting due to its implications for atmospheric escape, near-surface water content is interesting as it has implications for the amount of water vapor that could possibly be exchanging between the atmosphere and the regolith.

The region below $\sim 10\,\mathrm{km}$ is of particular interest, it is here surface-atmosphere interactions are believed to dominate, and unfortunately solar occultations cannot easily access this region due to significant signal degradation from aerosol loading. Convection, frost sublimation and deposition are expected to be the main forcers on the vertical distribution in this region, along with adsorption and desorption. This makes it markedly different from the mid-to-high altitude region where water ice clouds are thought to be the governing factor (Montmessin et al., 2004; Richardson, 2002)). Below the saturation level, controversy still exists about whether water vapor is well mixed with CO_2, or dispersed in a more complex fashion.

Regolith adsorption was first suggested by Davis (1969), involving the adhesion of CO_2 to surface dust grains. The hypothesis was later expanded to include water vapor (Fanale and Cannon, 1971), where a porous regolith actively adsorbs water vapor at night, and releases it when the Sun heats the surface. A nocturnal depletion of atmospheric water vapor was later inferred by Ryan et al. (1982) using Viking Lander air temperature measurements, which were suggesting by Jakosky et al. (1997) by model comparisons to be due to a diurnal exchange cycle between the porous regolith and the atmosphere. Similar results were also found with the thermal and electrical conductivity probe on

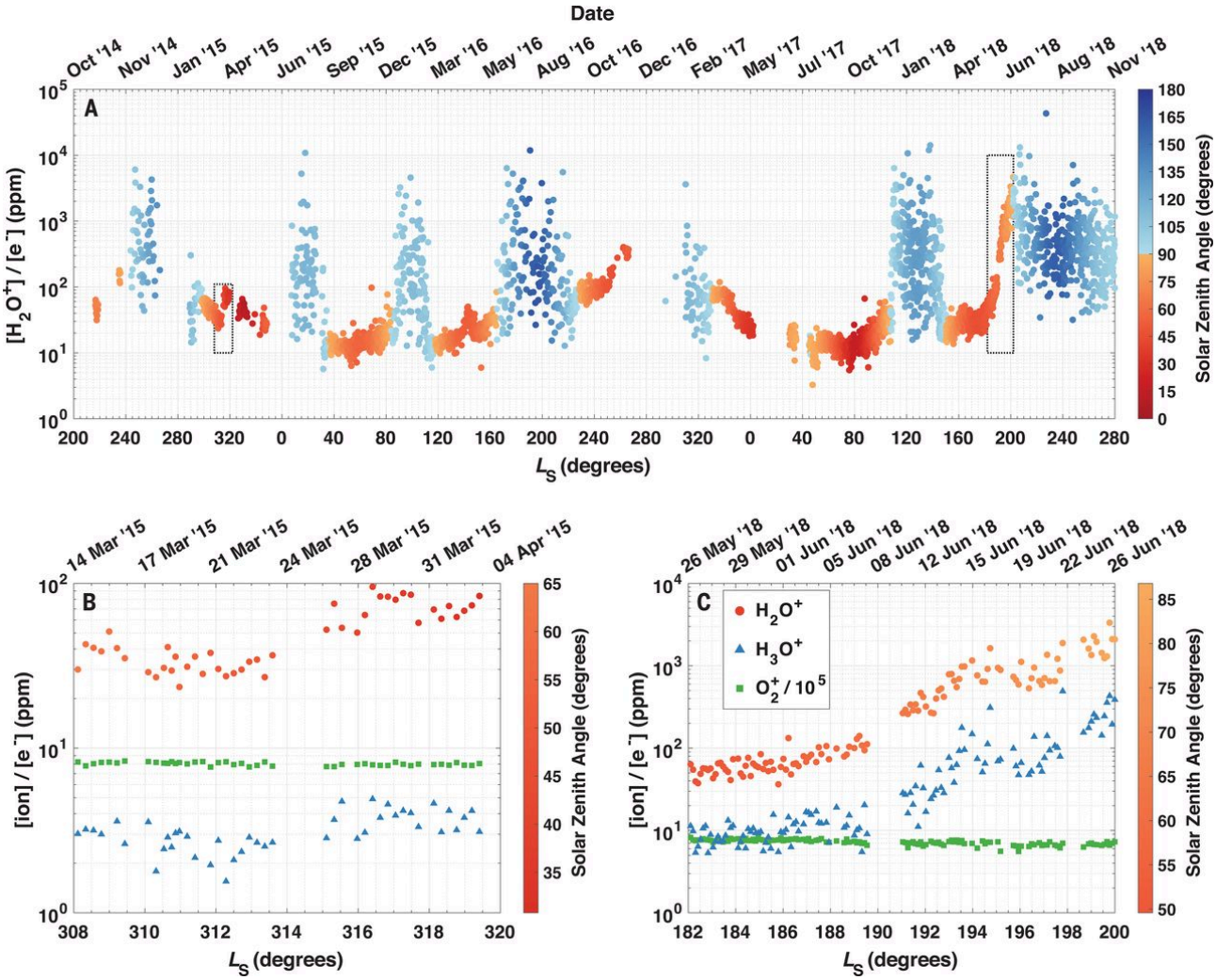

Figure 1.20: Ion variations during MY 32-34 as measured by MAVEN/NGIMS for each orbit. A) Mean H_2 ion abundance between October 2014 and November 2018. B) Ion abundances during a regional dust storm in MY 32. C) Ian abundances during the global dust storm in MY 34. The boxes in A) indicate the periods focused on in B) and C). Each data point is the mean at MAVEN's nominal periapsis for a single orbit. The value of the solar zenith angle is indicated by the color of the circle, as indicated by the colorbar. The transition from red to blue in A) corresponds to the shift from day to night. Figure from Stone et al. (2020).

the Phoenix lander (Zent et al., 2010; Fischer et al., 2019). The data indicate that a vapor layer of 0.5-1 km depth experiences diurnal exchange with the surface (Tamppari et al., 2010).

The commonly assumed uniform mixing below the saturation level was challenged further in Tamppari and Lemmon (2020) when analysis of data from the Surface Stereo Imager on the Phoenix lander indicated that water is strongly confined to a near-surface layer of 2.5 km. By investigating the correlation of water columns and pressure, Fouchet et al. (2007) inferred a situation where the vertical distribution is controlled by atmospheric saturation on one hand, and confined to a surface layer on the other. Similar results were found with OMEGA Melchiorri et al. (2009), hinting at potentially significant regolith-atmosphere exchange processes that have yet to be observed directly.

Adsorption is not the only possible mechanism however. In addition to the polar caps, evidence exists of shallow sub-surface water ice from observational campaigns of the Martian surface (e.g. Feldman et al. (2011) and Audouard et al. (2014)) at non-polar latitudes on Mars. Such water ice could potentially diffuse through the above regolith and contribute to atmospheric water vapor on diurnal and seasonal scales. However, Audouard et al. (2014) also suggested that any surface water is

likely either strongly bound to minerals and amorphous components in the regolith, or the dehydration and re-hydration is a very slow process due to Mars' low temperatures, concluding that the observed subsurface water is not easily exchangeable with the atmosphere.

A diurnal cycle was hinted at again when water vapor volume mixing ratios obtained with the REMS-H device on the Curiosity rover showed a distinct variation with local time (Harri et al., 2014; Martínez et al., 2017). The most compelling evidence supporting a diurnal cycle came with measurements from the Thermal and Electrical Conductivity Probe (TECP) on the Phoenix lander, where Savijärvi and Harri (2021) found a clear diurnal trend with water being depleted at night and a maxima around midday, as shown in Figure 1.21. The results also indicated that regolith exchange is mostly indifferent to surface properties, and that diurnal adsorption/desorption generates approximately 1% variation in the total column abundance, which is very similar to Earth analogue measurements.

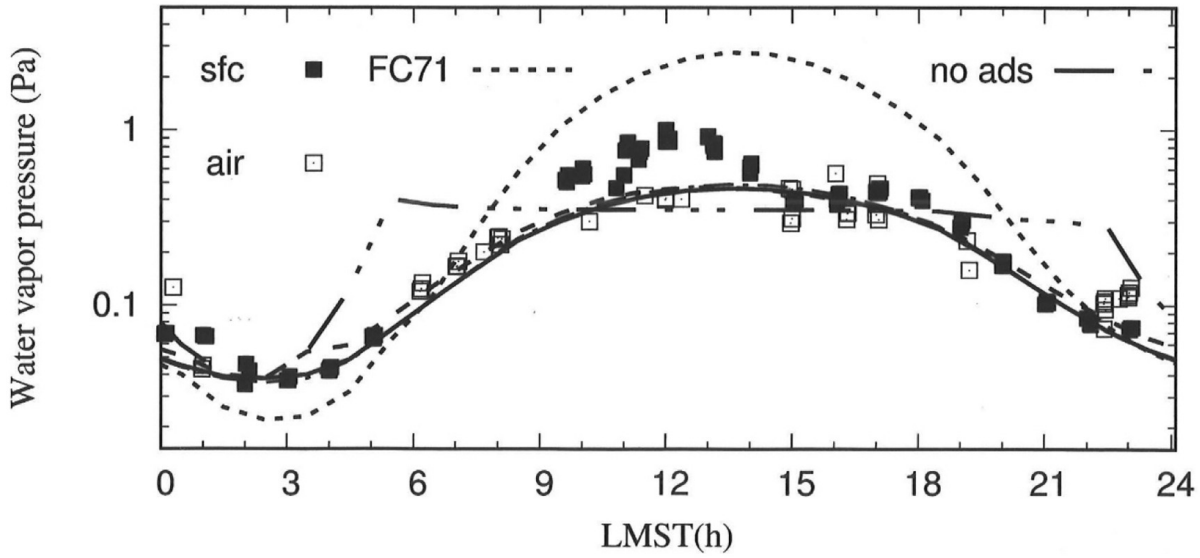

Figure 1.21: Modelled and Phoenix/TECP water vapor pressures during Phoenix sols 48–60. Data points 3 cm above the surface are shown as filled squares, while data taken at ∼0.5-1 m are indicated as open squares (Fischer et al., 2019). Five models with different adsorption isotherms are shown. The total precipitable water content is equal to roughly 30 microns. Figure from Savijärvi and Harri (2021).

Other studies, using OMEGA (Maltagliati et al., 2011b) and SPICAM Trokhimovskiy et al. (2015) on MEX also attempted to discern a diurnal exchange process between atmosphere and regolith, but found no statistically significant evidence of local time variation in H_2O abundances. The role of the regolith in modulating the near-surface water vapor content has thus not been conclusively determined by observations, and remains a highly elusive component of the water cycle. In order to shed more light on the near-surface distribution of water vapor, and possibly disentangle atmosphere-regolith exchange from seasonal variations, more observations are needed. Specifically, observations that are capable of differentiating the very first few kilometers from the rest of the column are required.

1.5 Carbon monoxide

Noncondensable gases are of interest as their seasonal and spatial variations hint at atmospheric transport and dynamics. Photochemical modelling of the observed carbon monoxide abundances have turned out to be a bigger challenge than anticipated. The main end products of the photolysis of CO_2 are O_2 and CO, both remaining well-mixed due to their long photochemical lifetimes and them being noncondensable gases in the Martian environment. From this, it follows that over time the CO_2 content would diminish and a build-up of O_2 and CO would occur with twice the amount of

CO compared to oxygen (Nair et al., 1994). This is far from the observed reality however. It was discovered that water vapor photo-dissociation products (H, OH, HO_2, known as HOx) help catalytically convert CO back into CO_2 (Parkinson and Hunten, 1972; McElroy and Donahue, 1972). Since water is the main source of HOx species, the oxidation rate and consequent reformation rate of CO_2 is subject to considerable temporal and spatial variations. The calculated reformation rate was so fast that photochemical 1D models struggled with the opposite problem of underestimating CO relative to observations (e.g. Clancy and Nair (1996)). Full 3D GCMs are best suited to solve this issue, but due to the long lifetime of CO, significant computational power is required to integrate a full GCM for sufficiently long periods to investigate the long-term equilibrium of slowly evolving species such as CO. Therefore, the significant underestimation of CO predicted by 1D models remains an outstanding problem, and the classical problem of Mars' photochemical stability cannot therefore be considered fully understood (Lefèvre and Krasnopolsky, 2017). 3D GCMs are however successfully reproducing the dynamical patterns of CO quite well, as shown in for example Smith et al. (2018), where the seasonal and spatial behaviour is represented, apart from that mixing is observed to be happening slower than in the simulations. Regardless, CO remains a species of particular interest for photochemical experts as it reveals the balance of chemical reactions that destroy and form CO_2 and ensures its long term stability on Mars.

Krasnopolsky (2003) was the first to identify the seasonal variations of CO and couple it to the condensation/sublimation cycle of CO_2. Since then, measurements of CO have been obtained by several studies (e.g. Smith et al. (2018); Encrenaz et al. (2006); Bouche et al. (2021), and good agreement about the seasonal and latitudinal trends are found, with maxima being observed when the condensation of CO_2 occurs in the polar regions for each hemispheric winter as shown in Figure 1.22, where data sets from MEX/PFS and MRO/CRISM are compared along with model simulations.

With PFS, Bouche et al. (2021) found a global mean volume mixing ratio of 820 ppm, with large temporal and spatial variability. The most extreme values were retrieved in the polar regions, with the abundances changing rapidly, creating maxima and minima near the poles during local spring and fall, respectively (see Figure 1.22 panels b) and i)). The retrieved Southern minimum was $\sim$400 ppm compared to $\sim$600 ppm in the North, where this North/South dichotomy is due to the difference in the CO_2 ice mass condensed at the poles during fall and winter. The times correspond to periods of rapid CO_2 sublimation, diluting the CO concentration. At polar latitudes, PFS tends to retrieve larger values than those obtained with CRISM, but agree well with models. At lower latitudes the CO column abundance is less susceptible to seasonal variations, there is however a local maxima in the middle of the Martian year (around Ls=180°) for all latitude bands between 50°N and 50°S (panels c)-g)). Overall, PFS, CRISM and simulations all show very similar values and seasonal trends.

A first long-term climatology of the vertical distribution of CO was compiled by Fedorova et al. (2022) using solar occultation measurements with TGO-ACS. There a global mean mixing ratio of 960 ppm was found between 0-$35\,\mathrm{km}$ and 45°S-45°N. A previously unobserved layer of significant CO enhancement (at 3000 ppm at least) is detected around 10-$20\,\mathrm{km}$ at high southern latitudes during local fall (Ls=100°-200°), and another enhancement above $50\,\mathrm{km}$ at the equinoxes near both poles.

1.6 Outstanding questions and purpose of this thesis

Much of the Martian water cycle is now known and the most important processes are understood as described in the previous section. One of the few missing pieces encompass the vertical distribution of water vapor, particularly below the cloud condensation level, and its behaviour with respect to location, season and local time. The following section will give a brief overview of the two most common observing modes used in atmospheric studies on Mars (nadir and solar occultation), describing their benefits and limitations, with emphasis on the implications for sensing the vertical distribution of water.

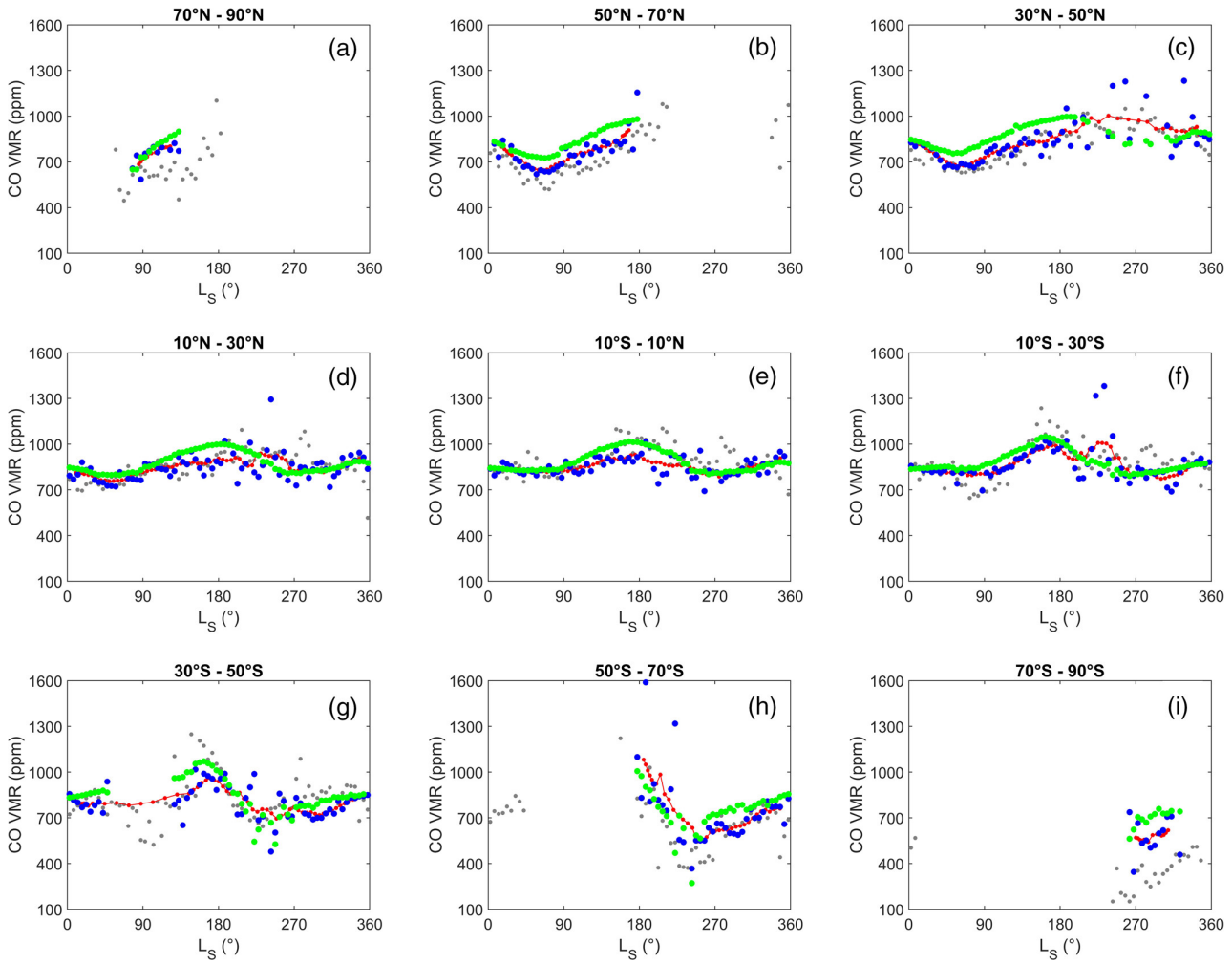

Figure 1.22: Column-averaged volume mixing ratios of CO retrieved from MEX/PFS (blue dots). Data are plotted as a function of Ls for different latitude bands, in boxes of 5°Ls. The red line is a running-average of the PFS data points, the green dots represent simulated column-averaged CO volume mixing ratios from Daerden et al. (2019), and gray points are retrieved column-averaged CO volume mixing ratios from CRISM by Smith et al. (2018). Figure from Bouche et al. (2021).

Traditionally the water vapor content on Mars has been probed using nadir observing instruments (e.g. Trokhimovskiy et al. (2015); Fouchet et al. (2007); Maltagliati et al. (2011b)). When observing an atmosphere in nadir viewing geometry, the retrieved quantity is normally the column abundance of the target species, since the geometry of observation implies the signal is an integrated absorption/emission along the line of sight, as indicated in Figure 1.23. Thus, any nadir-looking spectrometer covering a wavelength interval where water vapor has absorption bands is capable of measuring the total integrated column abundance of water vapor. This approach often yields excellent spatial coverage (and relatively high spatial resolution) and is able to probe a wide range of local times (depending on the orbit), but can be limited when aerosol loading in the atmosphere is significant. High dust loads can effectively shield the lower part of the atmosphere from being sensed by causing part of the incoming solar flux to be reflected back to space without having reached all the way to the surface. As the atmosphere on Mars is rarely dust free, especially at lower latitudes, this may lead to biased retrievals.

It is also theoretically possible to obtain the vertical distribution of a gas by nadir observation. In the thermal infrared, the water vertical profile is directly accessible by spectrally resolving the individual water lines and thereby discretizing the information in several altitude regions, as is commonly

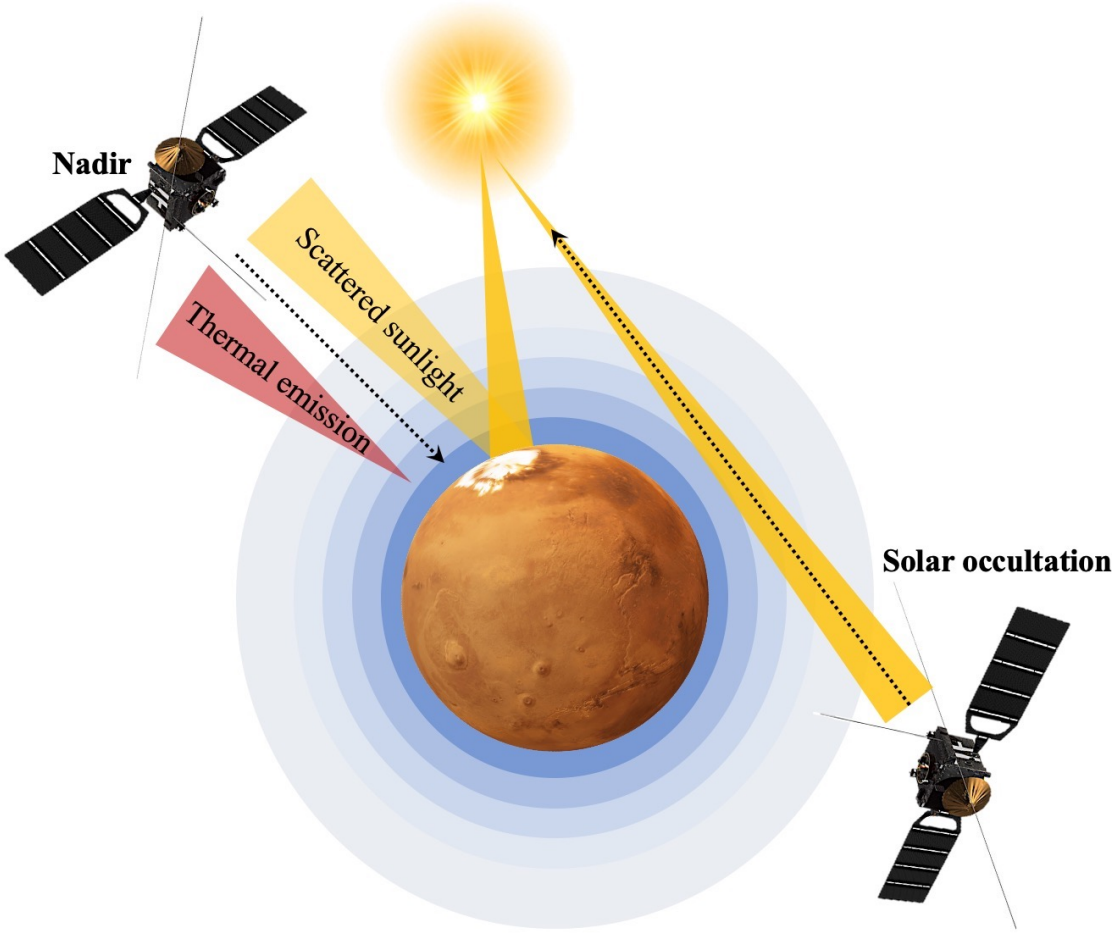

Figure 1.23: Graphic showing the viewing geometry of nadir and solar occultation observations. Radiation is shown reaching the spacecraft in the near- and thermal-infrared, the former depicted as being scattered and reflected from the surface, while the latter thermal radiation is shown to originate somewhere in the near-to-mid atmosphere.

done for for example CO_2 on Mars, whose $15\,\mu m$ band is shaped by the separate contributions of a variety of regions extending up to $40\,km$. Unfortunately, trace species like water vapor do not produce deep and wide enough bands to exploit the same effect.

Another strategy to obtain information on the water vertical profile from nadir observation is by observing multiple wavelength bands simultaneously. This approach is referred to as *spectral synergy*, and was developed for Earth observation by Pan et al. (1995, 1998), who predicted higher sensitivity to near-surface layers of CO if near and thermal infrared spectral bands were combined. This was later confirmed by Edwards et al. (2009), who demonstrated that combining near-infrared (NIR) and thermal-infrared (TIR) measurements in a common retrieval pipeline allowed for significantly higher sensitivity in the troposphere. The method has also been used to increase near-surface sensitivity to other gasses such as CO_2 (Christi and Stephens, 2004), O_3 (Landgraf and Hasekamp, 2007), and CH_4 (Razavi et al., 2009).

For the spectral synergy to work, concomitant acquisition of spectra containing diagnostic features of water vapor originating mainly from separate regions of the atmosphere are required, as illustrated in Figure 1.23. The design of MEX/PFS offers this capability (see chapter 2 and Section 2.2.1 for a detailed description of the instrument). Using PFS, Formisano et al. (2002) expected that the combination of measurements of rotational lines in addition to the 2.56 and 1.38 micron bands would provide information of the water vertical profile. However, this turned out to not be achievable due to several reasons, among them the SNR was too low for accurate determination of water vapor at

1.38 microns, except in very large averages (Fouchet et al., 2007). As a result, the water vertical distribution could not be obtained with any single nadir observing instrument currently in orbit around Mars. While a single instrument could not, a combination of instruments could, and MEX is the only payload platform capable having this multi-instrument combination option.

The spectral synergy technique was first applied to Mars by Montmessin and Ferron (2019) on a small selection of co-located observations between SPICAM and PFS on MEX. It was found that the synergy did indeed bring new information in addition to robustness to the retrieval of the water vapor concentration, compared to standard single-interval retrieval approaches (more on this in sections 2.2.3 and 2.2.3). Although the spectral synergy cannot resolve a detailed vertical profile of water vapor, it sets constraints on the partitioning of the water column, distinguishing between a near-surface layer and the rest of the column.

Another technique of sensing atmospheric abundances is by solar occultation observations, which are performed with SPICAM, but have become even more intensively used since the arrival of TGO (e.g. Fedorova et al. (2009); Aoki et al. (2022)). Solar occultation provide excellent vertical resolution, at the expense of poor horizontal resolution, sensing all the atmosphere along the line-of-sight between the spacecraft and the Sun. As the observation technique relies on a specific spacecraft-Sun geometry (see Figure 1.23), measurements are only possible at dawn and dusk local times, and this configuration happens more frequently at higher latitudes, significantly limiting the temporal and geographical coverage of the planet. In addition, solar occultation measurements in the near-infrared are impacted by dust, so that despite fine vertical resolution, the very near-surface region remains essentially unavailable. The lower limit for observation is typically around 5-$10\,\mathrm{km}$ for dust-free conditions, and as high as 20-$30\,\mathrm{km}$ during the dusty perihelion season (e.g. Aoki et al. (2019)). Only under very clear conditions will solar occultation observations be able to probe below $10\,\mathrm{km}$. Such conditions rarely occur at low-to-mid latitudes, consequently observing in solar occultation mode is a powerful tool for sensing water vapor above $10\,\mathrm{km}$, but to gain insight into the lowest part of the atmosphere, it is not a reliable option.

A fourth option to learn about the near-surface water content is to perform observations from the Martian surface. This can be done in-situ with for example humidity sensors such as MSL Curiosity's REMS-H or MEDA on M2020 Perseverance, or with spectroscopy, with ChemCam or SuperCam on Curiosity and Perseverance respectively. SuperCam is essentially very similar to SPICAM, and by pointing it to the sky, one can observe the scattered near-infrared radiation and retrieve water vapor abundances, integrated along the line-of-sight, much as in nadir viewing geometry. When observing from the surface, one circumvents the issue of dust obscuring the lower atmosphere, but high dust loads can still diminish the signal.

From the inherent limitations of single-domain nadir and occultation observations, two alternative approaches to obtain information of the water vapor content in the very lowest part of the atmosphere have been explored in this thesis; a spectral synergy approach between SPICAM and PFS (detailed in chapter 4), and by probing the atmospheric water content from the surface of Mars, where the sensitivity is highest close to the ground (detailed in Chapter 5).

Chapter 2

Instruments used in this thesis

To increase our understanding of any planetary body, a variety of instruments and techniques are required. Identifying and quantifying atmospheric species requires spectrometers. Spectrometers observing in different wavelength regimes and viewing geometries complement each other, as their combined power is greater than the sum of their parts. At Earth, a plethora of orbiting and ground-based observatories are continuously monitoring the planet and its surroundings, and on Mars we are now also reaching a level of monitoring providing a nearly complete view. The studies included in this thesis utilize a variety of spectrometers, two on the ESA satellite Mars Express (MEX), and one on the NASA rover M2020 Perseverance.

2.1 The basis of spectroscopy

Spectroscopy is a technique used to study the amount of light emitted or absorbed by matter at different wavelengths, in order to determine the atomic or molecular abundance of a substance within the aforementioned matter. The interaction between electromagnetic radiation and matter result in a spectrum when the received light is spread as a function of wavelength or frequency, and the relative amount of light within each wavelength interval provides information about the source matter. Investigating the dispersion of light as a function of wavelength has been conducted for centuries. The Romans were familiar with the uses of prisms and how it could be used to spread solar light into a rainbow of colors, yet Newton is commonly regarded the father of spectroscopy, but he was far from the first to have studied and reported the solar spectrum.

Fraunhofer significantly improved on the experimental setup used by most up until this point when he replaced the prism by a diffraction grating as the dispersive element. This improved the spectral resolution, but more importantly it provided a quantification of the wavelength scale, allowing accurate comparisons to be made between instruments, light sources and laboratories. The dark bands that had been previously observed in the solar spectrum (and a common belief was that these bands were natural limits between colors), were now systematically measured by Fraunhofer. Although not yet recognised as being indicative of the absorption from elements in the solar atmosphere, Fraunhofers work was so disruptive that these solar absorption lines are now known as Fraunhofer lines. The connection between chemical elements and their unique spectral patterns was developed by Bunsen and Kirchoff starting in the 1860s, and shortly after Beer found the relationship between light absorption and elemental abundance (Thomas, 1991).

The first infrared spectrometer was developed during World War 2 by companies contracted by the American government. It was soon recognised that many molecular signatures are found in the infrared part of the spectrum, and scientists all over the world started using the now commercially available infrared spectrometers for their studies (Rabkin, 1987). By the early 1970s the Fourier Transform infrared spectrometers were available, which could collect spectra in a matter of seconds of very high quality (by signal averaging) (Thomas, 1991). Today, infrared spectroscopy is used in a

wide variety of fields, such as atmospheric physics, astronomy, chemical threat detection and disease detection, among others.

In general remote sensing spectrometers consists of an entrance slit, a collimator, a dispersive element such as a diffraction grating or prism, focusing optics, and a detector. Light enters the spectrometer through the slit, and the slit width affects both the spectral resolution and the ability to sense in low-light conditions. These characteristics must undergo a trade-off, as one will come at the expense of the other. As needed a system of mirrors and collimating lenses will guide the light onto the prism or grating, and the prism or grating will split the light into its constituent wavelengths, the intensity of which are then recorded by the detector as a function of wavelength. The specific optical layout of the instruments used in this work is detailed in the following subsections.

2.2 The Mars Express mission

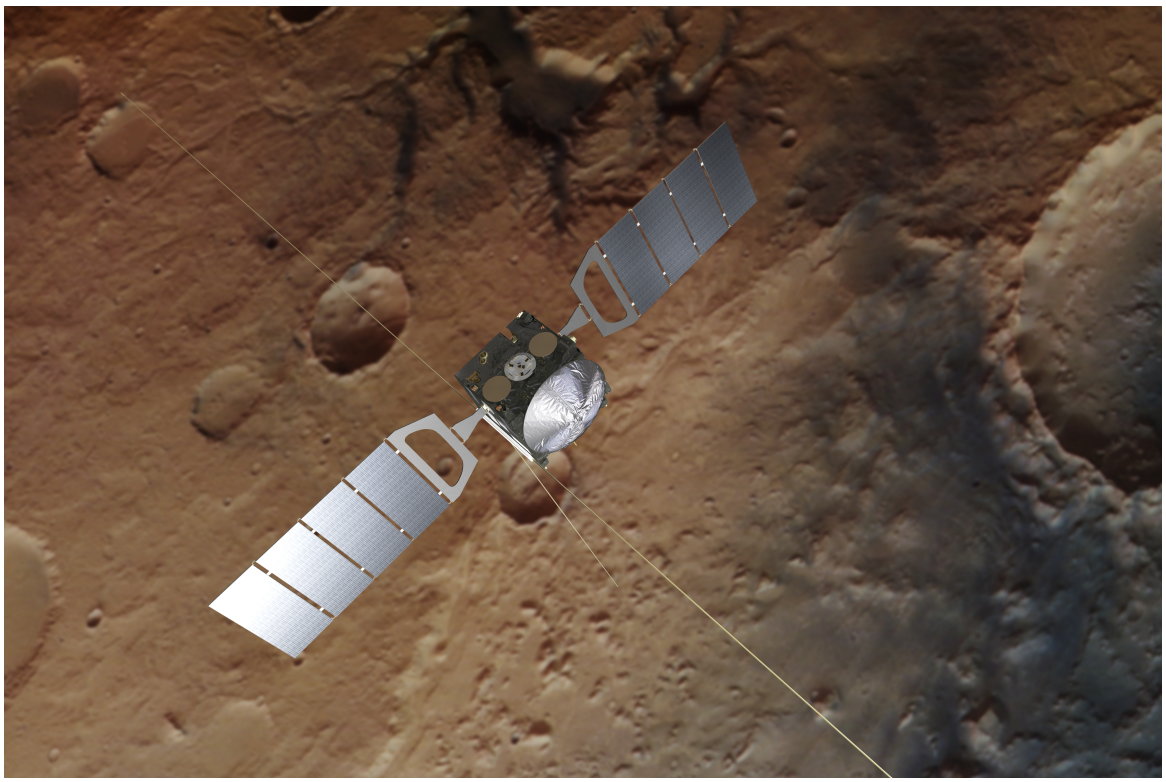

Figure 2.1: Artist's impression of the Mars Express satellite orbiting Mars. The background surface image is based on an image taken by the spacecraft's high resolution stereo camera (HRSC), credit: ESA/DLR/FU Berlin. Spacecraft image credit: ESA/ATG medialab.

The Mars Express satellite (MEX) is a European Space Agency (ESA) space mission, launched from the Baikonur launch pad in Kazakhstan on a Soyuz-Fregat launcher on 2 June 2003. MEX successfully entered orbit around Mars on 25 December 2003, and began nominal science operations in mid-January 2004 (Chicarro et al., 2004), corresponding to the very end of MY 26. MEX carries seven scientific instruments (High Resolution Stereo Camera (HRSC), Observatoire pour la Minéralogie, l'Eau, les Glaces et l'Activité (OMEGA), Mars Advanced Radar for Subsurface and Ionospheric Sounding (MARSIS), Planetary Fourier Spectrometer (PFS), SPectroscopy for the Investigation of the Characteristics of the Atmosphere of Mars (SPICAM), Analyzer of Space Plasmas and EneRgetic Atoms (ASPERA), Mars Radio Science Experiment (MaRS)), and an additional engineering camera that has been repurposed for atmospheric and outreach (Visual Monitoring Camera (VMC)), as detailed in Table 2.1.

MEX also deployed the lander Beagle 2, which unfortunately was lost after landing. At the time of writing, MEX is still operational and returning data from the Red Planet. Mars Express got its name since it was built and launched in record time and for a much lower cost than similar missions at the time. Some equipment was reused from Rosetta, and the nadir-pointing instruments HRSC, OMEGA, PFS and SPICAM have heritage from the Russian Mars 96 mission. In turn, the experience with MEX led to the very similar Venus Express mission.

Acronym	**Purpose**	**Technique**
HRSC	Image and study the surface	Push-broom scanning camera
OMEGA	Study the surface and atmosphere	Visible- and near-infrared spectrometer
MARSIS	Study the subsurface and ionosphere	Subsurface radar and altimeter
PFS	Atmospheric studies	Infrared spectrometer
SPICAM	Atmospheric and plasma studies	UV and infrared spectrometer
ASPERA	Plasma studies	Neutral- and charged- particle sensors
MaRS	Atmospheric and ionospheric studies	Radio-wave propagation
VMC	Atmospheric studies and outreach	Basic optical monitoring camera

Table 2.1: Table listing the eight instruments carried by MEX, and their main scientific purpose.

The main science objectives of the mission are to study the Martian atmosphere and climate, the planet's structure, mineralogy and geology, and to search for indicators of water. This would be done by determining the sub-surface structure down to a depth of a few kilometres, imaging the entire surface at high resolution including a mineralogical map, determining the effect of the atmosphere on the surface, studying the atmospheric composition and its global circulation patterns and lastly by investigating atmosphere-solar wind interactions.

Mars Express has proven to be an extremely productive mission. It has, and continues to, provide scientists with data to make discoveries such as finding minerals that form only in the presence of water (Bibring et al., 2006), the detection of water-ice deposits underground (Orosei et al., 2018), finding evidence to suggest volcanism on Mars may have persisted until recent times (Neukum et al., 2004), and detecting aurora for the first time on Mars (Bertaux et al., 2005). Furthermore, MEX has mapped how key gases such as water and ozone vary throughout the atmosphere (e.g. Maltagliati et al. (2011a); Fedorova et al. (2018); Määttänen et al. (2022), and tracked how dust gets lifted from the surface and distributed through the atmosphere (e.g. Maltagliati et al. (2013); Fedorova et al. (2009)), and studied Mars' moons in unprecedented detail (Witasse et al., 2014). In addition to scientific purposes, MEX is also providing relay communication services between the Earth and other Mars missions.

From a quasi-polar and highly elliptical orbit with a periapsis of $\sim$300 km and a period of 7.5 h, MEX has a particularly detailed view of the polar caps. With three instruments able to measure the atmospheric water vapor content (OMEGA, PFS, and SPICAM), either in the solar reflected or in the thermal component, MEX has delivered a vast amount of valuable data with complete global and seasonal coverage. The PFS and SPICAM instruments cover the thermal and near-infrared domains, respectively, within which water vapor possesses diagnostic signatures.

The measurements used in the following analysis were retrieved from nadir observations, and were selected according to a number of criteria to ensure satisfactory quality of every individual measurement, sufficient geographical and seasonal coverages, and a minimum error of radiative transfer modeling due to surface inhomogeneity (Montmessin and Ferron, 2019). For a detailed description on the selection and averaging processes used for the creation of a data set compatible with a synergistic extraction of water vapor, the reader is referred to Montmessin and Ferron (2019).

2.2.1 PFS

The Planetary Fourier Spectrometer (PFS) is an infrared double pendulum interferometer with two wavelength channels optimized for atmospheric sensing, and is shown in Figure 2.2. PFS performs Mars observations in nadir viewing geometry, in two wavelength channels. The short wavelength channel (SWC) covers the range 1700-8200 cm^{-1} ($\sim$1.22-5.88 µm) with a full width at half maximum (FWHM) of the instantaneous field of view (FOV) of 1.6°, while the long wavelength channel (LWC) spans the 250-1700 cm^{-1} (5.88-40 µm) with a FWHM FOV of 2.8°, which at the pericenter corresponds to a 440 km^2 surface footprint. Only the long wavelength channel was utilized for this work. Both channels have a spectral resolution of 1.3 cm^{-1}. For further details, see Formisano et al. (2005); Giuranna et al. (2005). PFS was unable to produce scientific data from around May 2005 until November. First the problem was related to the switching on of MARSIS which led to several instruments being switched off, then PFS suffered a fault in the pendulum motor. A full recovery was made possible by switching to the more powerful back-up motor, and science operations resumed as normal from early November 2005 (Fouchet et al., 2007).

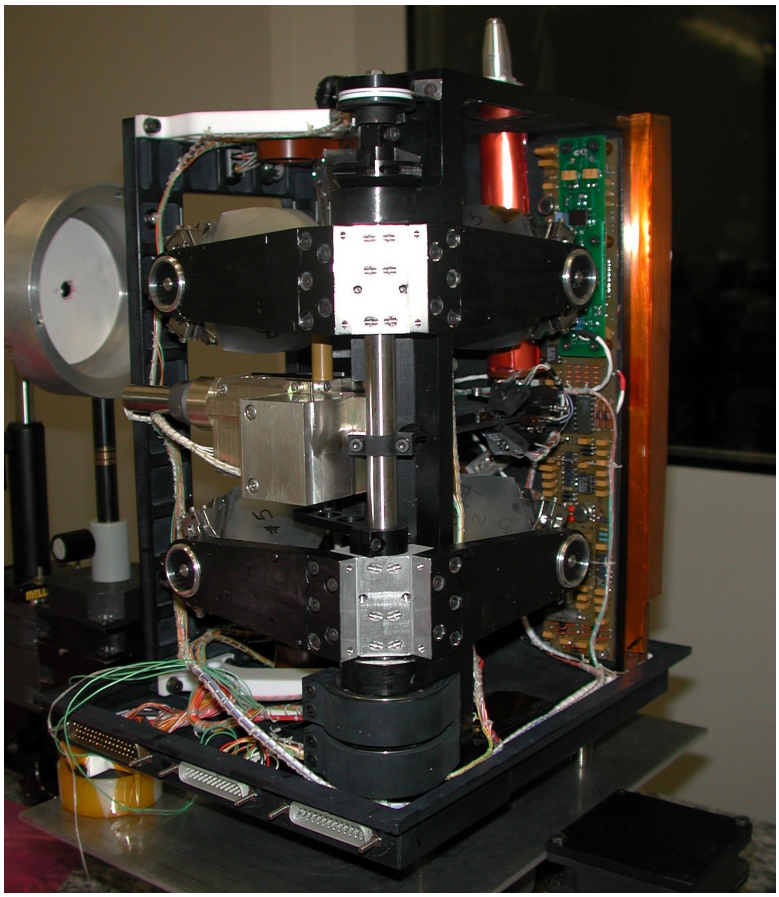

Figure 2.2: Close-up image of the interferometer at the center of the PFS instrument. Credit: ESA/ASI/INAF.

The main science objectives of PFS are to improve our knowledge of atmospheric properties and the surface mineralogical composition as well as surface-atmosphere interactions. PFS is capable of observing at any local time, and can provide data to retrieve surface and atmospheric temperatures during both day and night. (Formisano et al., 2005). PFS became the first instrument at Mars to infer the presence of methane in the Martian atmosphere in 2004 (Formisano et al., 2004), and has since, most notably, detected the elusive gas just a day after the Curiosity rover measured a significant methane spike (Giuranna et al., 2019). Other trace gases are also monitored, such as carbon monoxide and water vapor (Sindoni et al., 2011). PFS also provides data to study the atmospheric dust content,

and the observational coverage is designed so as to achieve complete global coverage of the planet in each season in order to study seasonal variations in the global circulation. Thus PFS is in an excellent position to shed light on phenomena such as the global dust storms (Wolkenberg et al., 2020).

PFS is a double pendulum interferometer, the optical schematics of which is shown in Figure 2.3. The two wavelength channels are placed one on top of the other, such that one motor can move both pendulums simultaneously and in this way sample both wavelength ranges independently at the same time. Mars radiation enters through element 1, the entrance aperture, and is guided by the pointing mirror (element 2) to the dichroic filter (element 3) which separates the radiation into the SWC and LWC. The dichroic filter reflects all the wavelengths shorter than $5.5\,\mathrm{mm}$ and transmits longer wavelengths. For the SWC, a silicon cut-off filter (element 4) is placed in the optical inlet, ensuring that radiation with wavelengths shorter than $1.2\,\mathrm{mm}$ do not enter. A folding mirror (element 5) guides the light into the SWC interferometer, which lies on another plane on top of the LWC. A beamsplitter in each channel (elements 6 and 7) then splits the light onto the retroreflectors (element 8). All four retroreflectors are attached to an axle that is rotated by a torque motor which forms a double pendulum. The optical path length is changed by rotating the shaft of the double pendulum along its axis. The detectors (elements 9 and 10) are placed in the center of the parabolic mirrors (element 11).

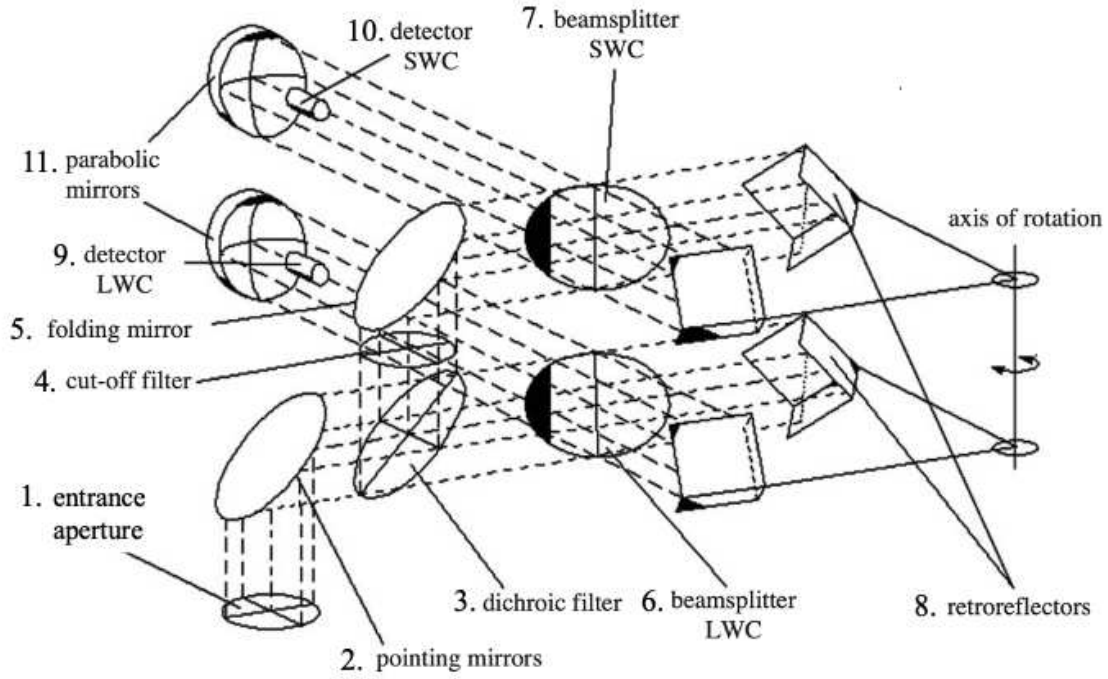

Figure 2.3: Optical scheme of the double pendulum interferometer of PFS. The two wavelength channels correspond to two planes, shown here with the short wavelength channel on top of the long wavelength channel. Illustration from Formisano et al. (2005).

2.2.2 SPICAM

The Spectroscopy for the Investigation of the Characteristics of the Atmosphere of Mars (SPICAM) instrument is a dual-channel spectrometer designed to study the Martian atmosphere from top to bottom in both the ultra violet and infrared wavelength domains (Bertaux et al., 2006; Korablev et al., 2006). SPICAM consists of two main blocks; a sensor unit and a processing unit, the first of which is depicted in Figure 2.4. The total mass of both units is just below $5\,\mathrm{kg}$, where about $3.8\,\mathrm{kg}$ is from the sensor unit. Technically SPICAM can observe in nadir, solar and stellar occultation modes in both

UV and IR, though the UV channel is primarily dedicated to stellar occultation. A description of the UV part of SPICAM can be found in Bertaux et al. (2006). Monitoring of UV-derived species such as ozone was concluded at the end of 2014/MY 30 due to the failure of the UV channel.

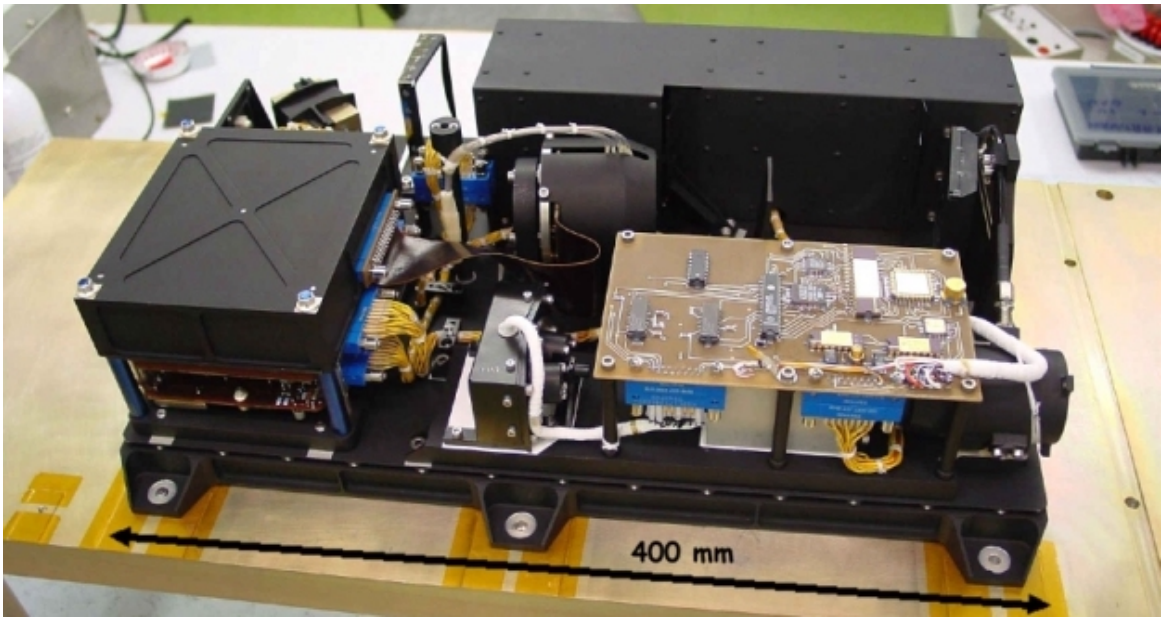

Figure 2.4: The SPICAM sensor unit, including the UV and the IR channels. Credit: CNES.

In this study, only the IR channel was utilized, working in the spectral range of 1-1.7 µm with a spectral resolution of 3.5-4 cm^{-1}, a complete description of which can be found in (Korablev et al., 2006). The principal observation configuration for SPICAM IR is nadir orientation, but it can also provide limb observations and solar occultations. SPICAM IR was built for the primary purpose of measuring the water vapor column abundance on Mars, but is also being extensively used for studying CO_2 and H_2O ice clouds and surface ice, as well as airglow detections (see for example Maltagliati et al. (2011b); Fedorova et al. (2012)).

The IR channel uses an Acousto-optic tunable filter (AOTF), providing sequential scanning of the spectrum, (element 10 in Figure 2.5), representing the first time an AOTF was used in deep space. An AOTF is an electronically tunable optical filter, where a variable radio frequency signal (typically below few watts) is applied to a piezoelectric transducer bonded to the crystal. As there are no moving parts, an AOTF spectrometer can be built as a compact, lightweight, long lived and reliable device. The design of the infrared channel of SuperCam on Perseverance was duplicated from SPICAM-IR.

For the IR channel in nadir configuration, upwelling radiation from Mars is collected by a three-lens telescope (element 7 in Figure 2.5) with a diameter of 30 mm, before passing through a circular diaphragm (element 8) forming a field of view (FOV) of 1° corresponding to surface footprint of about 230 km^2 (4.5 km radius) when MEX is at pericenter (roughly 250 km altitude). Before and after the AOTF the light passes through collimating lenses (elements 9 and 11). When the RF signal is applied to the AOTF (element 10), the radiation is split into two diffracted, monochromatic beams (the wavelength of which are dependant on the applied RF signal). The beams are deflected each to one side at 7.5°, while the bright undiffracted orders continue straight and are captured in a central light trap (element 12). Each diffracted beam eventually reaches the "ordinary" and "extraordinary" (elements 14 and 15) detectors and are analyzed simultaneously. The telescope, the FOV diaphragm and the collimator are assembled in a tube-like structure attached to the AOTF unit. The dimensions of the AOTF with its electronics and the telescope are 104×60×40 mm with a mass of 330 g.

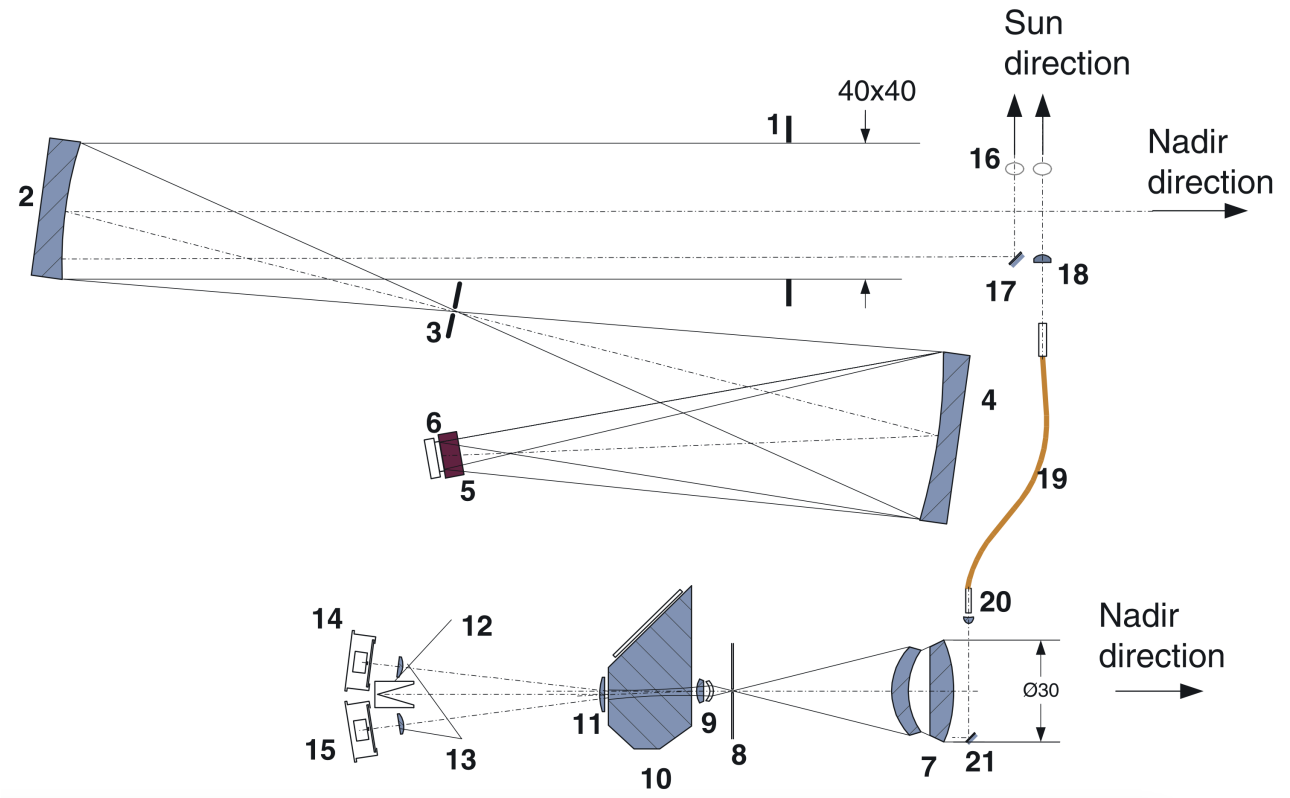

Figure 2.5: Optical scheme of SPICAM on Mars Express. Elements 7-21 apply to the IR channel. The elements are as follows; 1, aperture blend of the UV channel; 2, off-axis parabolic mirror; 3, changeable slit (mechanical actuator can change between wide and narrow openings); 4, concave UV grating; 5, intensifier; 6, CCD; 7, IR channel objective; 8, IR FOV diaphragm; 9 and 11, collimating lenses; 10, AOTF crystal; 12, light trap for undiffracted light; 13, detector proximity lenses; 14, "extraordinary" beam detector; 15, "ordinary" beam detector; 16, solar opening (closed by a shutter when not looking to the Sun); 17 and 21, flat mirror; 18, IR solar entry; 19, optical fiber; 20, fiber collimator. Figure from Bertaux et al. (2006).

2.2.3 SPICAM and PFS water vertical sensitivity

As discussed in Section 1.6, no single nadir-viewing instrument is capable of resolving a water vertical profile. But depending on the observed wavelength band, the received radiance might carry information from different altitude regions, thus placing stronger constraints on how to adjust the vertical distribution of water vapor to fit observations.

TIR measurements are mostly sensitive to the low and middle atmosphere. Atmospheric brightness is observed against that of the surface, so for spectroscopic features of the atmosphere to emerge, the two must be contrasted in temperature. NIR measurements on the other hand are sensitive to any molecule present in the column as the technique relies on solar photons traversing the atmosphere twice, as illustrated in Figure 1.23. Although Trokhimovskiy et al. (2015) indicate that the NIR technique is mostly sensitive to the atmosphere below 30 km (see Figure 2.6), it is only true from a mixing ratio perspective, which favors the denser layers of the atmosphere. In other words, any given change in H_2O mixing ratio will be easier sensed at the bottom of the atmosphere as pressure and number density are assumed to be continuously increasing toward the surface. If seen from a number of molecules perspective, the NIR inversion technique has no preference to a particular position of the column, unless this portion concentrates more water molecules at a specific location. One must note, however, that dust modulates this assertion. At high dust opacity, part of the incoming flux does not reach the surface and is sent back to space without sampling the entire column, which is evident in the right panel of Figure 2.6. Only in such cases will the NIR technique become altitude dependent.

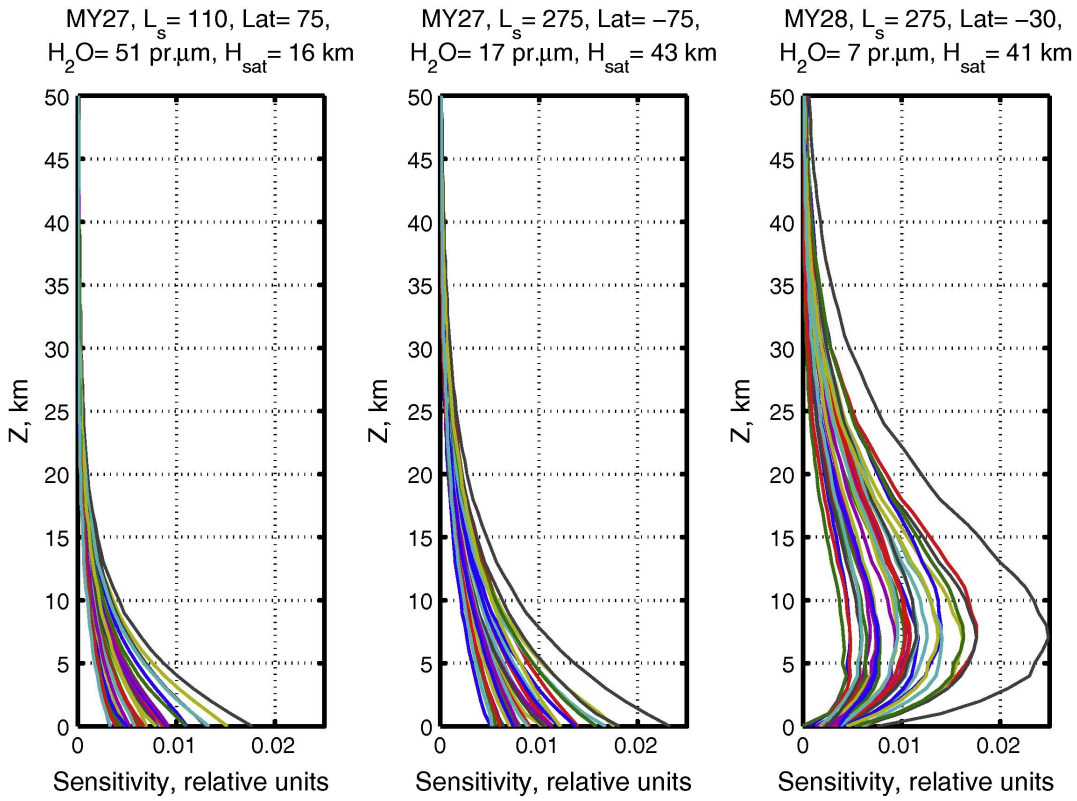

Figure 2.6: Sensitivity kernels in the 1.38 µm band. The x-axis is the difference between a reference spectrum and spectra with added water, where the different colors correspond to different wavelengths within the band. Left panel: MY 27 northern summer. Middle panel: MY 27 southern summer. Right panel: MY 28 dust storm. Figure from Trokhimovskiy et al. (2015).

This difference in sensitivity of NIR and TIR can be viewed as a difference in the shape and peak altitude of the weighting function of water vapor retrieval in a particular wavelength domain, and has been advocated to explain the dispersion of H_2O column abundance values retrieved by the various instruments of MEX (Tschimmel et al., 2008). On the other hand, the difference in sensitivity can also be considered a way to offer simultaneous access to different regions of the atmosphere, leading to the derivation of more than a single parameter representative of the whole column, as is usually the case with instruments that study water vapor using nadir observations. In fact, combining two spectral domains increases the degree of freedom (DOF) of the signal. The DOF gives an estimate of the number of independent bits of information in an atmospheric measurement (Rodgers, 2000), and a DOF higher than 1 indicates the presence of some amount of profile shape information.

Montmessin and Ferron (2019) compared the averaging kernels of different widths for NIR and TIR separately against the synergistic case (NIR+TIR) for two different environmental cases; a dry and extended ($\sim$6 pr-microns at Ls=20° and at $\sim$11° latitude) or a wet and confined ($\sim$40 pr-microns at Ls=120° and 60° latitude) atmosphere. The diagonal of the averaging kernel matrix, as shown in Figure 2.7 as a function of altitude, gives a measure of the sensitivity along the line of sight. The values differ between the NIR and TIR cases as a result of the different information brought by the solar scattered and the thermally emitted fluxes. The trace of the averaging kernel matrix equates to the DOF, which corresponds to the number of independent parameters possible to constrain by the data. For nadir measurements of an atmospheric species it also corresponds to a sort of vertical resolution. The synergy increase the DOF by 30% compared to NIR and 50% with respect to TIR in the dry case. For the wet case, the synergy does 40% and 50% better respectively, demonstrating the significant complimentary effect of performing the water vapor inversion simultaneously from the two spectral domains.

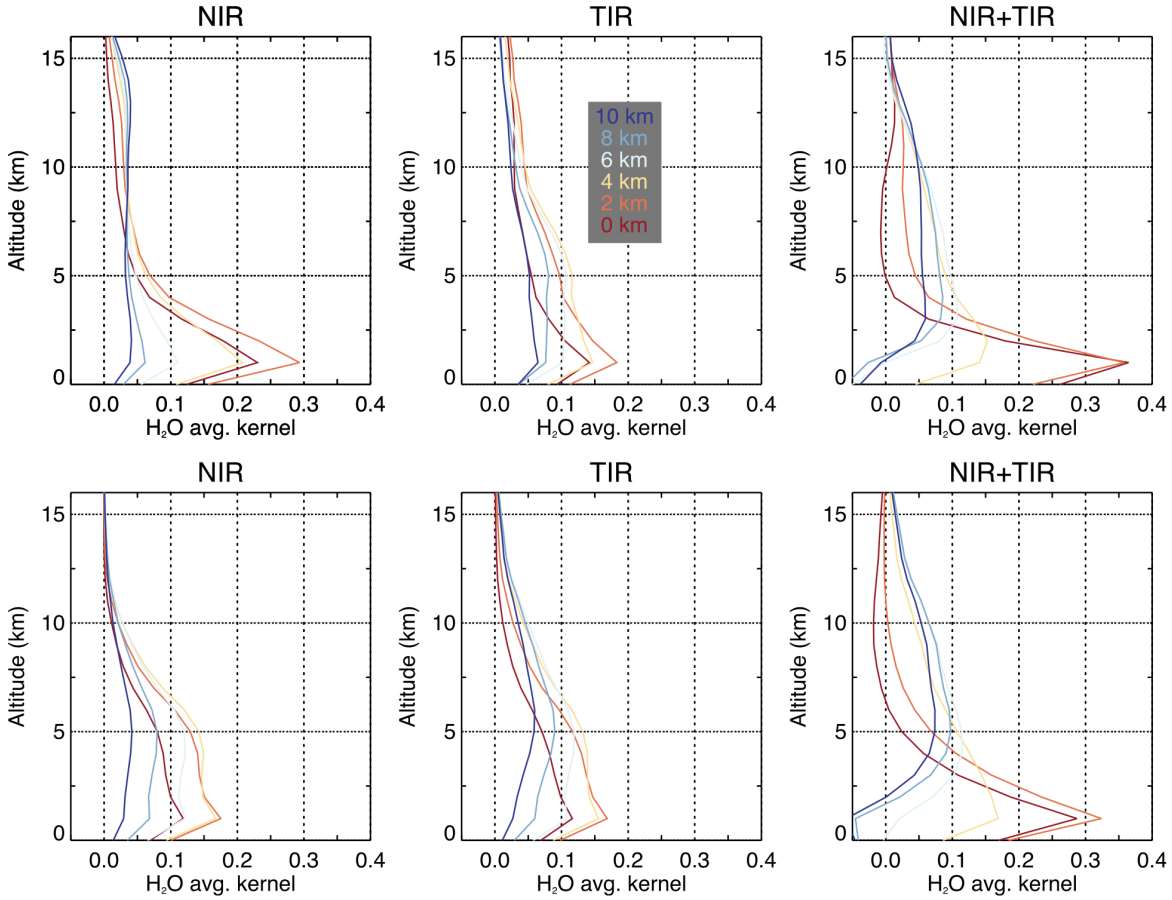

Figure 2.7: Averaging kernels for NIR, TIR and synergy (NIR+TIR) obtained in a dry (upper line of plots) and a wet (lower line of plots) configuration. The line color indicates the width of the kernels. Figure from Montmessin and Ferron (2019).

SPICAM and PFS in spectral synergy

To shed light on the vertical distribution of water on Mars, and particularly the distribution near the surface, MEX with SPICAM and PFS is in a unique position, as outlined in Section 1.6. On their own, neither PFS nor SPICAM can contribute much towards this goal, but by operating concomitantly, one can use complimentary wavelength intervals and design a retrieval scheme where the spectral inversion is done simultaneously on both regions, thus obtaining information on the vertical profile. By employing the spectral synergy with SPICAM and PFS, sensitivity to the fraction of water contained in the first few kilometers of the column is increased while significantly reducing the uncertainty in the total column abundance, as demonstrated in Figure 2.7.

For the synergistic approach used in this thesis, several windows in the long wavelength channel of PFS were selected (as in Montmessin and Ferron (2019)). The windows from $8\,\mu m$ to $10\,\mu m$ and $19\,\mu m$ to $25\,\mu m$ were used to obtain surface temperature and dust model properties, the range 12-19 μm is dominated by the absorption of the $15\,\mu m$ CO_2 vibrational transition which was used to retrieve atmospheric temperature profiles, while the 20-35 μm thermal emission band was used to retrieve the water vapor abundance, henceforth referred to as TIR. Because PFS was used to retrieve several parameters, a high signal-to-noise ratio (SNR) is required. One individual spectrum does not yield a sufficiently low noise level, therefore, the retrievals were performed on the average of nine consecutive spectra. The total time passed between the acquisition of the first spectrum to the last of the nine to be averaged is $108\,sec$, as it takes $4.5\,sec$ to acquire a single PFS interferogram and the repetition time is $8.5\,sec$ (Fouchet et al., 2007). This corresponds to a cumulative surface footprint at

the pericenter of $3900\,\mathrm{km}^2$, roughly $12\,\mathrm{km}$ wide and $325\,\mathrm{km}$ long along the satellite track. However, note that as the orbit is elliptical, this area will vary depending on spacecraft altitude.

For SPICAM, the wavelength interval 1.34-$1.43\,\mu\mathrm{m}$ is defined as the NIR range for the synergy, as it covers the strong water absorption band at $1.38\,\mu\mathrm{m}$. Averages of ten SPICAM-IR spectra are demonstrated to have a SNR sufficient for reliable retrievals of water vapor column abundances (Fedorova et al., 2006; Trokhimovskiy et al., 2015), but for the sake of the synergy, a SPICAM cumulative footprint similar to that of PFS is desirable. Therefore, the SPICAM observation closest in time to the center PFS spectrum is selected, and averaged together with the seven previous and the seven following spectra. The 15 spectrum cumulative surface footprint area at pericenter corresponds roughly to $3700\,\mathrm{km}^2$, roughly $9\,\mathrm{km}$ wide and $411\,\mathrm{km}$ long along the satellite track, close to that of the nine PFS spectrum average. Together, the SPICAM and PFS average spectra constitute a co-located observation.

2.3 The Mars2020 Perseverance rover

The M2020 Perseverance rover is the successor to the hugely successful Mars Science Laboratory Curiosity rover. They are share much of the rover body design, Perseverance even uses some of Curiosity's spare parts, but has significantly upgraded the wheels, the robotic arm and instruments, to mentioned some. The rover was launched on July 30, 2020 from Cape Canaveral on top of an Atlas V rocket. Aided first by parachute, then by powered descent and finally a spectacular sky crane rover separation, Perseverance, depicted in Figure 2.8, touched down safely in Jezero Crater on February 18, 2021. Perseverance also carried with it the first ever helicopter to Mars, Ingenuity, which has proven a hugely successful technology demonstrator. From landing until the end of July 2023, the rover has driven $19.7\,\mathrm{km}$, sealed 23 sample tubes (17 rock, 2 regolith, 1 atmosphere and 3 witness tubes), 10 of which have been dropped at the Three Forks sample depot for potential pick-up in a sample-return mission, and the small helicopter it carried with it (Ingenuity) has completed 52 successful flights.

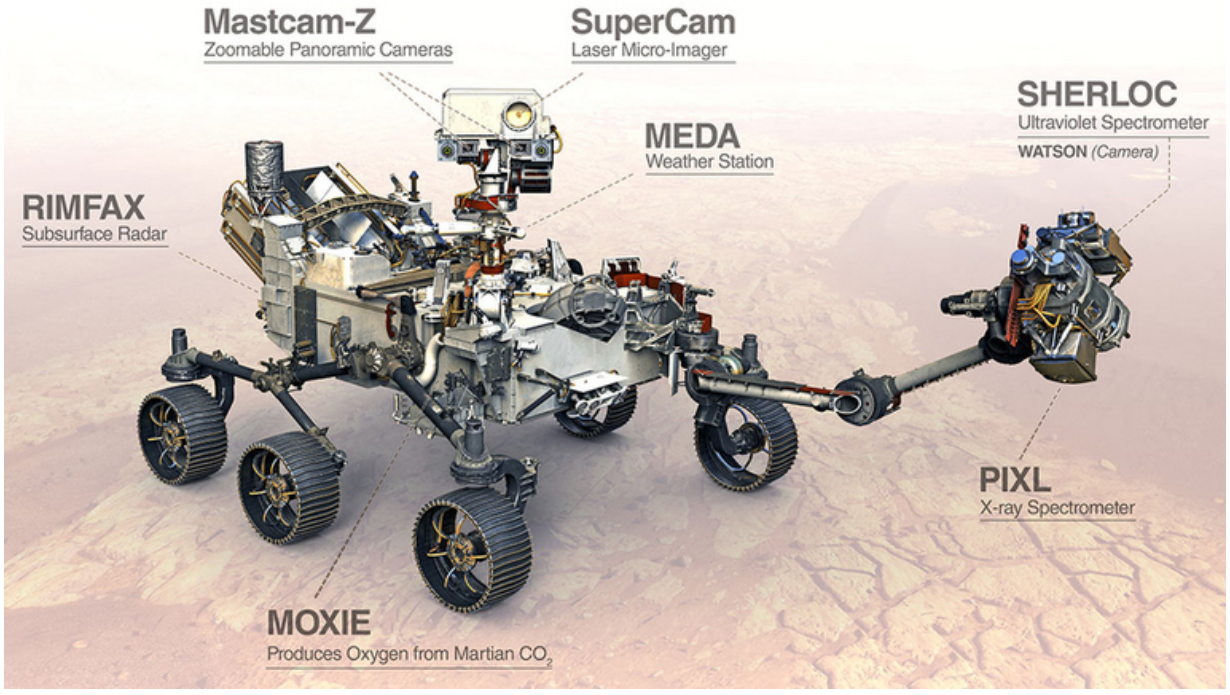

Figure 2.8: Image of the M2020 Perseverance rover with all its instruments indicated. In addition to the scientific payload, Perseverance also carries nine engineering cameras, and seven entry, descent and landing cameras. Credit: NASA/JPL-Caltech.

Perseverance's payload was selected for the purpose of fulfilling the science objectives outlined in Farley et al. (2020), which can be collected in four main goals:

1. Mars2020 should develop a global understanding of the geology of its landing site.
2. Mars2020 should identify ancient habitable environments, estimate the capability of rocks to preserve biosignatures, and identify potential biosignatures.
3. Mars2020 should collect and document several rock samples for possible Earth return.
4. Mars2020 should enable future Mars exploration especially by humans, and by demonstrating new technologies.

To achieve this, Perseverance is equipped with a primary payload suite of seven instruments; the multipurpose laser micro-imager SuperCam, the Norwegian built sub-surface radar RIMFAX, the weather station MEDA, the zoomable panoramic camera Mastcam-Z, the UV spectrometer SHERLOC, the X-ray spectrometer PIXL, and MOXIE for the production of O_2 from Martian atmospheric CO_2 (also summarized in Table 2.2. The respective locations of all instruments on the rover body are indicated in Figure 2.8). In total the rover weighs $1025\,\mathrm{kg}$, and is the size of small car at about $3\,\mathrm{m}$ long, $2.7\,\mathrm{m}$ wide and $2.2\,\mathrm{m}$ tall. Perseverance carries two microphones, and 23 cameras in total, more cameras than any other mission ever to reach Mars. Nine of which are intended for engineering purposes, seven for entry, descent and landing, and the remaining seven are for scientific use exclusively. Perseverance has already completed its primary mission duration (which was 2 years) and is currently in an extended phase of the mission.

Acronym	**Purpose**	**Technique**
SuperCam	Surface geology and atmosphere	Multipurpose laser micro-imager
RIMFAX	Subsurface structure	Sub-surface radar
MEDA	Environment and climate	Multi-sensor weather station
Mastcam-Z	Navigation	Zoomable panoramic camera
SHERLOC	Detection of organics and minerals and	UV raman spectrometer
PIXL	Geochemical assesment	X-ray spectrometer
MOXIE	Oxygen production	Technology demonstration

Table 2.2: Table showing the seven instruments carried by the Perseverance rover, listing their main scientific purpose.

The next big step in Mars exploration is the return of rock samples to Earth. Currently, ESA and NASA are working together towards this goal, and in this endeavor, Perseverance plays the crucial role of selecting, collecting and caching the samples on Mars. The next steps involve a Sample Retrieval Lander which will land near or in Jezero Crater, which also includes a small rocket. The primary mode of sample delivery to this rocket is by Perseverance itself, but a secondary capability to retrieve the samples will be provided by two Ingenuity-like helicopters which could travel to the sample depots already dropped by the rover. Once the sample cache is launched off Mars, another spacecraft in Mars orbit will capture it, and then return it to Earth by the mid 2030s.

2.3.1 SuperCam

SuperCam is a suite of remote sensing instruments that provide critical and complementary observations via four main techniques; laser-induced breakdown spectroscopy (LIBS), time-resolved Raman and Luminescence spectroscopy (TRR), and visible and near-infrared reflectance spectroscopy (VISIR). In addition, the instrument also offers high resolution color imaging and acoustic recordings.

The instrument is made up of three separate subsystems; the French Mast Unit (MU), the Body Unit (BU) provided by the United States, and the Spanish calibration target holder. The visible (VIS) and near-infrared (IRS) reflectance spectrometers, henceforth referred to collectively as VISIR, will be the main focus in this thesis, with emphasis on the IRS as shown in Figure 2.9.

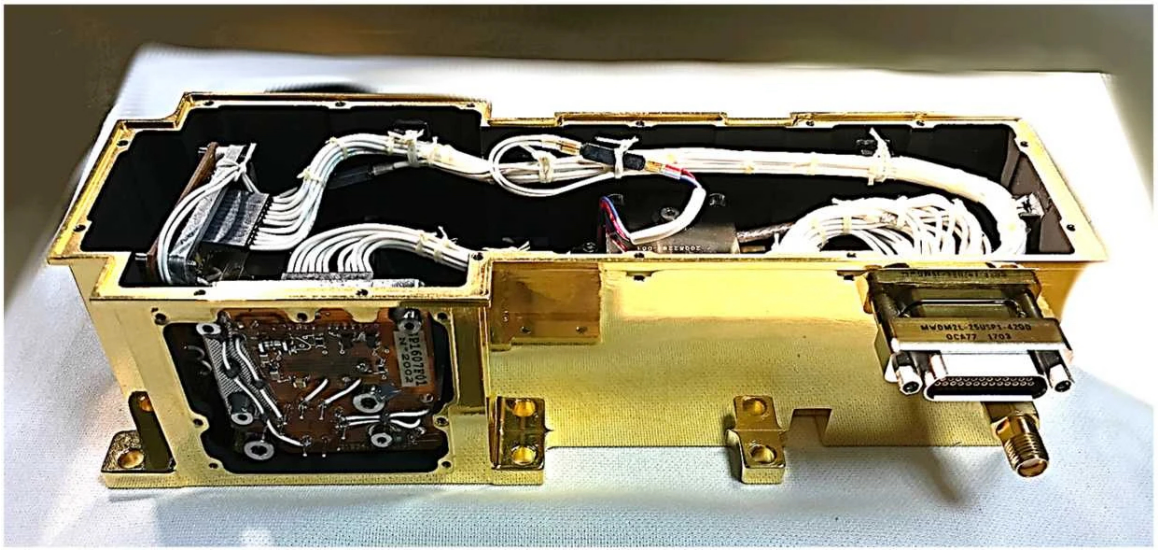

Figure 2.9: Image of the IR spectrometer with the cover off. The total length of the IRS is 170 mm and the mass is 402 grams. Credit: LESIA.

The science objectives for SuperCam as a whole are derived from the overall mission objectives, and includes eight specific goals as listed in Maurice et al. (2021):

1. Rock Identification
2. Sedimentary Stratigraphy and Facies/Hydrothermal Characterization
3. Organics and Biosignatures
4. Volatiles (Hydration and Halogens)
5. Context Morphology and Texture
6. Coatings and Varnishes
7. Regolith Characterization
8. Atmospheric Characterization

The IRS will be of particular importance to fulfill goals 1 and 7, and to a lesser extent 3 and 8. SuperCam and the IRS channel are mainly dedicated to geological purposes, amongst them studying the infrared spectral signatures of various rocks to further our understanding of their formation mechanisms and the geochemical conditions of their formation (Fouchet et al., 2022). The detection of carbonates, a type of altered minerals, is especially interesting as it is likely indicative of long periods during which Mars could have supported conditions that favored liquid water (e.g. (Ehlmann et al., 2008)). Carbonates have been found in Martian meteorites on Earth (Halevy et al., 2011), in orbital data from for example MRO (Ehlmann et al., 2008), and with the MER (Morris et al., 2010) and MSL rovers (Bristow et al., 2021). Assessing the abundance of carbonates is crucial to obtain a better inventory of the carbon budget on Mars, which itself is key to understanding the environmental evolution at the surface of the planet. The Mars 2020 mission and Perseverance now offer a unique opportunity

to exhaustively characterize Martian carbonates both in-situ and as samples being returned to Earth, to better assess past environmental conditions at the surface of Mars and search for traces of past life. Figure 2.10 from Clavé et al. (2023) shows an example of a carbonates detection, in fact the only target out of 16 (during the first 420 sols) with consistent carbonates signatures in all (LIBS, IRS, TRR) techniques. The target is named Garde, and is part of the Séítah formation, and was analyzed during sols 206–210. On the Garde abraded patch, a total of four IRS spectra were acquired as indicated by the zoomed in images in Figure 2.10 A1-3. In Figure 2.10 C, A1 corresponds to *"Garde_210, 7"*, A2 corresponds to *"Garde_207, 5"* and *"Garde_207, 8"* and lastly A3 corresponds to *"Garde_209a, 8"*.

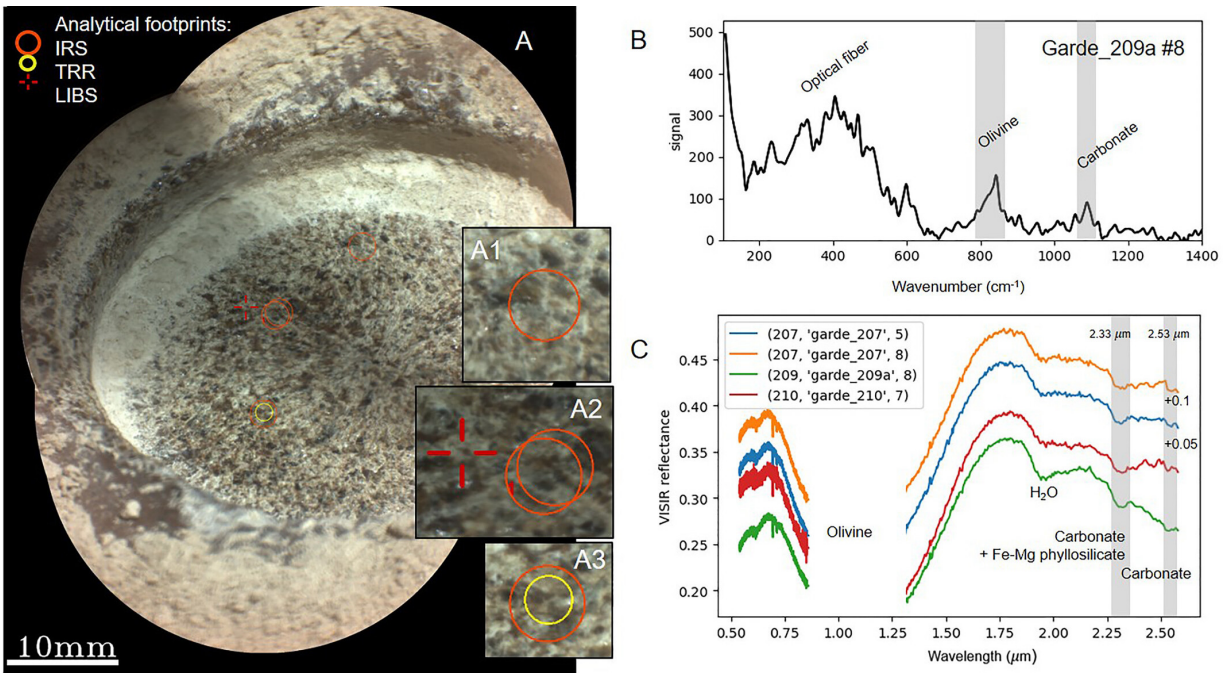

Figure 2.10: The Garde abraded patch with carbonates signatures. (a) Mosaic image of the Garde abraded patch with points corresponding to where carbonates were detected with LIBS (red cross), TRR (yellow circle), IRS (orange circles). (A1-3) Close-ups on the carbonates detected. (b) TRR spectrum with signatures of olivine and carbonate. (c) IR spectra (plotted with small offsets to reduce overlap, indicated to the right of the plot) with signatures of olivine, hydration, and carbonate and phyllosilicate. Credit: Clavé et al. (2023).

SuperCam VISIR

SuperCam's science objectives related to the atmosphere revolve around the column densities of certain neutral atmospheric species and aerosol parameters. For the purpose of this thesis, we focus on the near-surface atmosphere of Mars, and will aid in answering SuperCam science goal 8. The VIS spectrometer is used primarily for the retrieval of oxygen and dust parameters (McConnochie et al., 2022), but can also be used to measure water vapor by the line groups in the 719-730 nm and 810-835 nm (McConnochie et al., 2018). The VIS channel will in this thesis also be utilized for auroral detection attempts (more on this in Section 6.3). The main objective of the IRS channel is to measure water vapor and carbon monoxide, and in addition both the VIS and IRS channels are used to probe dust and ice opacities and aerosol sizes. Figure 2.11 summarizes the annual cycles of surface pressure, CO surface mixing ratio and H_2O column densities along with the total optical depth of dust at Jezero crater as extracted from the Mars Climate Database version 5.3 (MCD) for a typical non-GDS year. The database contains climatologies derived from general circulation model developed at the Laboratoire de Météorologie Dynamique (LMD GCM) (Forget et al., 1999; Millour et al., 2018).

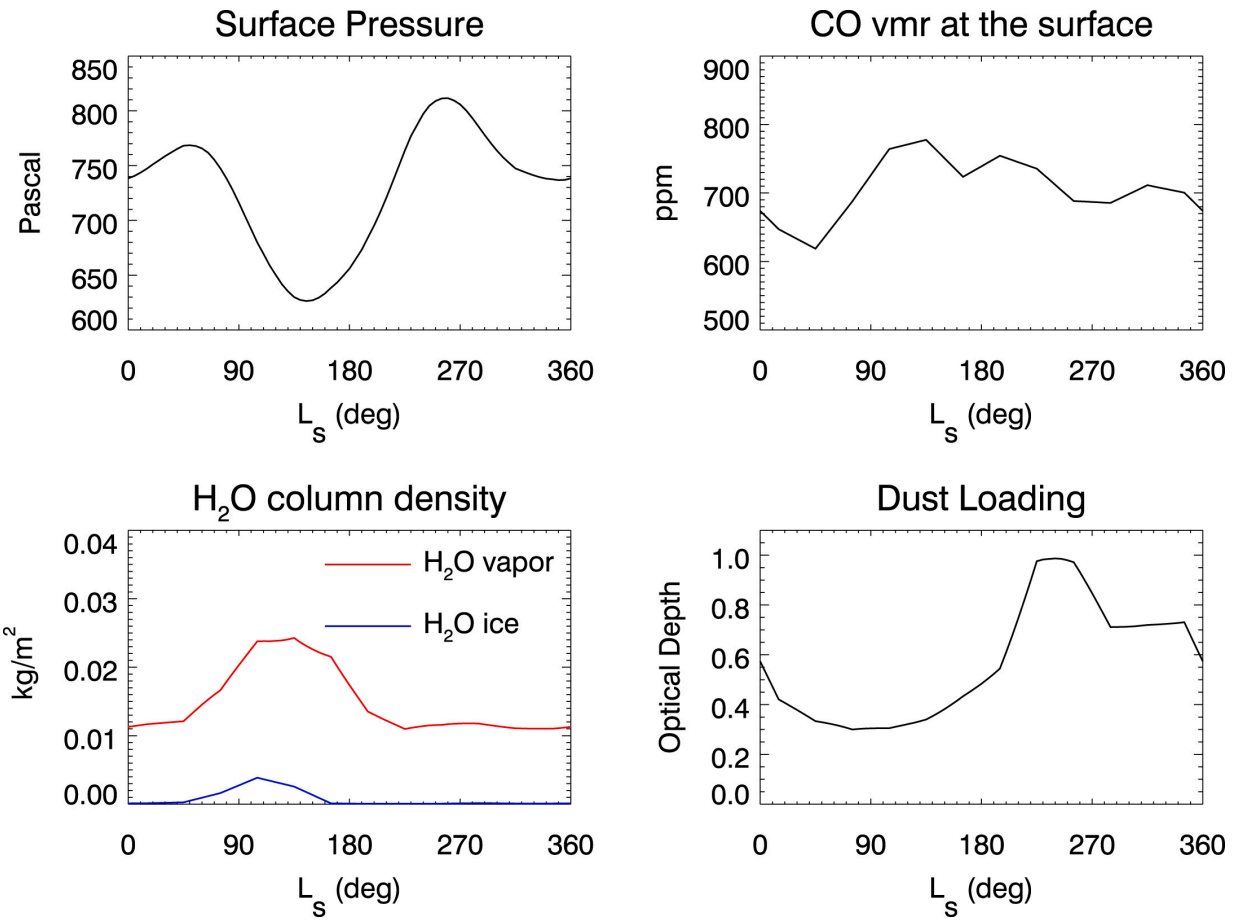

Figure 2.11: Annual cycles of surface pressure, CO surface mixing ratio, H_2O vapor and ice column densities along with the total optical depth of dust at Jezero crater as modelled by the LMD Mars Climate Database. Figure from Fouchet et al. (2022).

As described in Section 1.3.2, the surface pressure varies significantly with season as CO_2 is cycled in and out of a solid state at the winter pole. This is also evident at Jezero, where the lowest pressure is observed at ∼Ls=135°, and the maximum occurs at ∼Ls=250°. The water abundance follows an almost anti-correlated behaviour, with both vapor and ice maxima around Ls=120°, a time when the water ice at the NH winter pole has sublimed and been transported equatorward and into Jezero crater. Of particular interest is the near-surface water content. So far, ambiguities remain as to whether large-scale water-regolith interactions exists.

As a non-condensable gas, CO globally is clearly anti-correlated with surface pressure (Smith et al., 2009), yet at Jezero crater the relationship is not particularly prominent. The CO cycle exhibits strong seasonal and latitudinal variations, thus periodical measurements from the surface are complimentary to orbital data which tend to have lower measurement cadance over a specific location, and it will also be interesting to monitor any CO variability associated with the previously observed unexplainable changes in oxygen (McConnochie et al., 2022).

During periods with enhances dust loading, orbital instruments struggle to obtain reliable measurements of the column abundance of gaseous species, and assumptions need to be made regarding the distribution of each species below the altitude where the signal no longer reaches. Surface observations can thus provide an important perspective on water vapor abundance and distribution in particular, which is highly connected to aerosol loading.

To shed light on these topics, SuperCam IRS is unique as it opens a new wavelength interval from 1.3 µm to 2.6 µm for exploration from the surface of Mars. It is designed as a point spectrometer, where light is collected by a Cassegrain telescope located on the MU, with a focusing stage which collects light for the IRS (also located on the MU), and for the UV and visible spectrometers located

in the BU. As with SPICAM on MEX, the IRS also employs an AOTF which performs the wavelength selection (Maurice et al., 2021; Fouchet et al., 2022). The BU receive light from the telescope on the MU through an optical fiber, before the light is split in three bands: 245-340 nm and 385-465 nm for UV and violet, and 535-853 nm covering the visible part of the spectrum. The latter is a high-efficiency transmission spectrometer with an optical intensifier which can amplify a weak optical signal(Wiens et al., 2021). In this work, the IRS is used during daytime for the measurement of atmospheric absorption spectra due to CO_2, H_2O and CO, while the visible channel is used during the night for the observation of Martian auroral emission spectra. The optical design of the IRS is visualized in Figure 2.12.

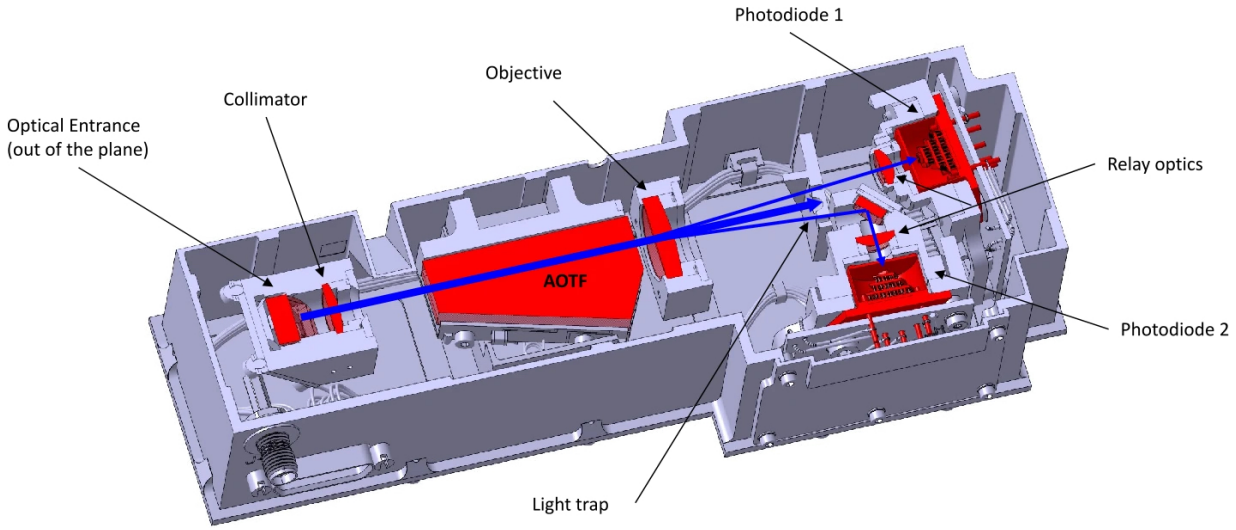

Figure 2.12: Cross section showing the optical design of the IRS. All optical elements are in red, and the light (in blue) follows the path through, most of it ending up at the light trap. Depending on the piezo frequency, one wavelength is diverted to photodiode 1, and the other order to photodiode 2 (backup). Figure from Maurice et al. (2021).

The technique of collecting atmospheric spectra of the Martian sky with SuperCam is named a *Passive Sky* observation, and was introduced with ChemCam on the MSL Curiosity rover for the retrieval of atmospheric properties (McConnochie et al., 2018). A passive sky measurement involves SuperCam pointing toward the sky at two different elevation angles, yielding spectra where the captured light has travelled in different optical paths through the atmosphere (more details on this in chapter 3.2. The sky is observed out of focus, resulting in an effective field of view of $\sim 3°$ diameter. By taking the ratio of the signals from the two pointing positions, one effectively eliminates the solar spectrum and any instrument responses in the spectra. Since the latter is $\sim$100 and $\sim$10 times larger than the signals of interest for the visible and infrared channels respectively, this technique isolates the signatures of gases quite successfully.

2.3.2 SuperCam IRS studying water vapor

The purpose of SuperCam with respect to this thesis is to provide another perspective on Martian water vapor. Again, the objective is to gain insight into the near-surface water vapor content, and particularly the near-surface vertical distribution. Instead of construing a complex processing technique from co-located orbital measurements, one can also complement orbital observations from ground. By observing spectral signatures of the atmosphere from the surface, where the lower atmosphere is directly observable, one can help constrain the vertical profiles retrieved from orbit.

ChemCam on the MSL Curiosity rover, and SuperCam on the M2020 Perseverance rover both have this capability in multiple wavelength regions when pointing the camera's upward to the sky.

SuperCam's sensitivity to the vertical distribution of water vapor has not yet been characterized, but we can use results from ChemCam as a first best estimate. McConnochie et al. (2018) showed that such surface-based water vapor measurements are mostly sensing the lower atmosphere, as demonstrated in Figure 2.13, where the cumulative volume-weighted averaging kernel is shown for different dust scenarios. Assuming for any given observation that the result is expressed as a column-averaged volume mixing ratio, Figure 2.13 shows the cumulative weights of the vertical averaging, and that the mixing ratio in, for example, the bottom $5\,\mathrm{km}$ has a 40–55% weight in the reported result. SuperCam will use water vapor diagnostic features at longer wavelengths (between 1.3 and 2.6 microns), but the vertical sensitivity is not expected to change significantly.

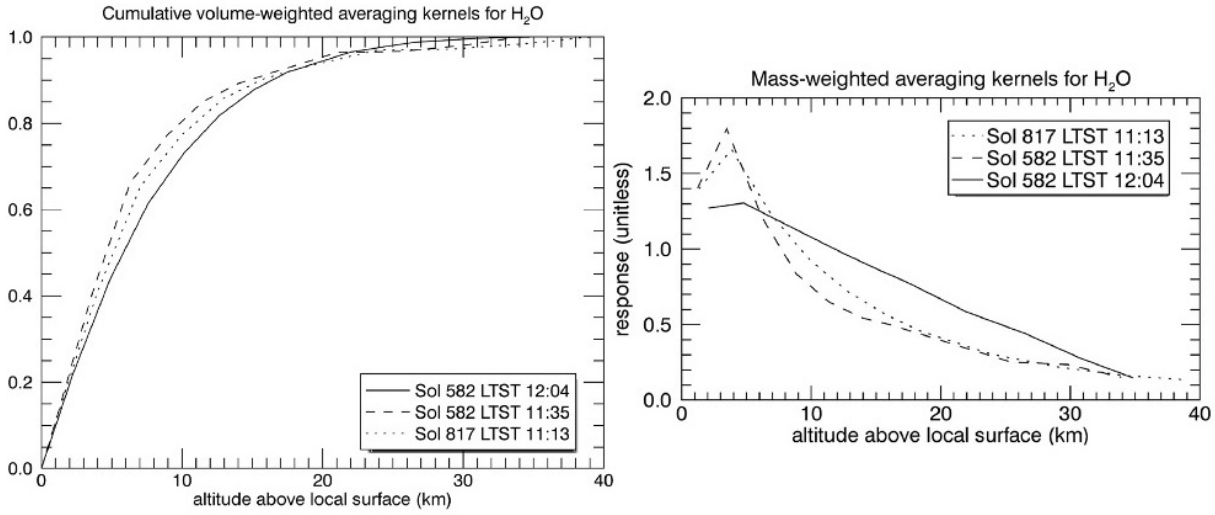

Figure 2.13: Cumulative volume-weighted vertical averaging kernels for water vapor for three different ChemCam passive sky observations. Observations during Sol 582 are in low opacity conditions, while the observation during Sol 817 was a typical high opacity case. Figure from McConnochie et al. (2018).

Chapter 3

Data processing

This chapter describes the data processing carried out for each instrument/technique used in the works that make up this thesis. First, an overview of the spectral synergy retrieval routine is given, including descriptions of the sensitivity of each instrument to the vertical distribution of water vapor, and how they compliment each other. Lastly the efforts to create a retrieval scheme for SuperCam is presented. The second section is somewhat different, in that it outlines the development phase of the pipeline for the IRS passive sky.

3.1 SPICAM and PFS in spectral synergy

The following section describes the data set and data processing done for the project that concluded with the articles Knutsen et al. (2022b) and Knutsen et al. (2022a). SPICAM and PFS on Mars Express was used, and the data set consists of observations taken over 1379 individual orbits distributed across seven Mars years from Ls $334°$ of MY 26 to Ls $297°$ of MY 34, with measurements from MY 30 and 31 being excluded due to instrumental problems with PFS. The geographical and seasonal coverage is highly variable from year to year, several being quite sparsely covered. Some sparsity is due to operational constraints, as not all instruments can be concurrently active, while most is due to the requirement of co-located measurements from both SPICAM and PFS.

After years of operation, an issue with PFS caused the interferogram peak to not always be centered. The instrument line-shape used here (a sine cardinal function with $1.3\,\mathrm{cm}^{-1}$ FWHM) is then not optimal, and could lead to biased water vapor retrievals, with a tendency of being too low. This issue started around orbit 6000 (MY 29), became particularly relevant after orbit 7500 (MY 30), but data obtained in MY 32 and after were less affected. To avoid this problem, we excluded all measurements during MY 30 and MY 31 from further analysis.

3.1.1 Synergistic retrieval

Montmessin and Ferron (2019) described two different approaches to the synergistic method; a parametric mode which establishes a two-parameter model of the water vapor vertical distribution, and one non-parametric Bayesian approach that uses MCD vertical profiles as a priori values. Only the non-parametric approach is described here, and used in the further analysis. The data set utilized follows almost the exact retrieval scheme described in Montmessin and Ferron (2019), so an overview will be given here where differences are highlighted. A general workflow is illustrated in Figure 3.1, indicating the main components and their role in the retrieval routine.

To perform a spectral synergy retrieval, spectra need to be acquired from roughly the same geographic location and the absorption/emission feature has to originate from different altitudes. For water vapor, this is the case for the $1.38\,\mu\mathrm{m}$ line covered by SPICAM, and the lines in the $\sim$20-30 $\mu\mathrm{m}$ interval. As is common when analysing atmospheric spectra, we average a number of consecutive

measurements to increase the signal-to-noise (SNR). The spectra for both instruments are calibrated in wavelength and radiance. The result of these steps are indicated in Figure 3.1 as "L1B PFS" and "L1B SPICAM".

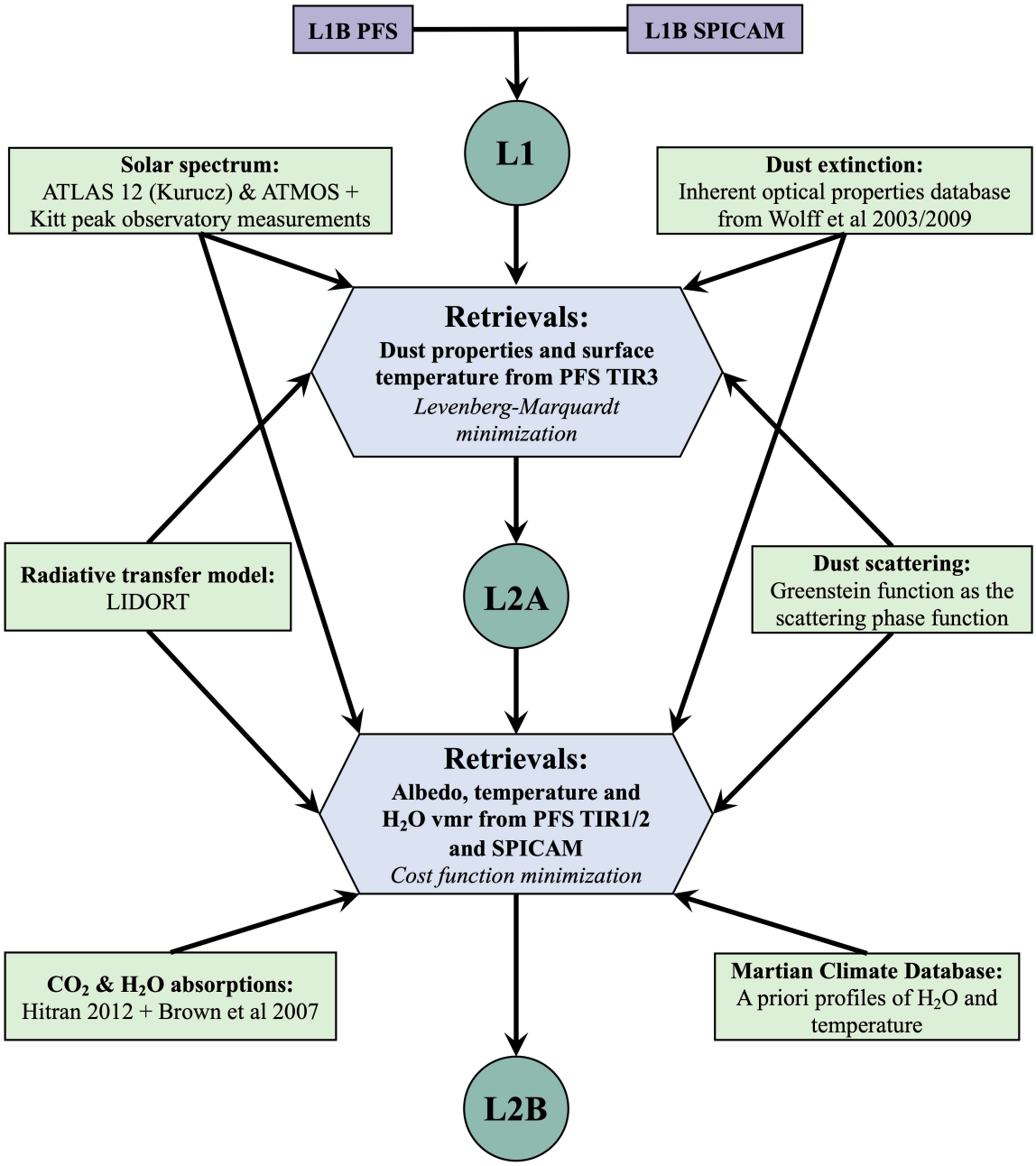

Figure 3.1: Schematic overview of the main components in the synergy retrieval routine. The flowchart details the routine from calibrated individual spectra to final data product with retrieved values for water vapor column abundances, vertical profiles, temperatures, aerosol parameters etc.

Nine PFS spectra are averaged, which corresponds to a cumulative surface footprint at the pericenter of $3900\,\mathrm{km}^2$, but as the orbit is elliptical, the footprint will vary depending on spacecraft altitude. Then, several spectra from SPICAM are averaged, the number was decided such that the cumulative SPICAM footprint is similar to that of PFS. The solution was 15 spectra, where the SPICAM observation closest in time to the central PFS spectrum is identified, then averaged with the seven

observations prior to it and the seven after it. Combined, the SPICAM and PFS average spectra constitute a co-located observation, which is denoted as the circular "L1" in Figure 3.1. Not all sets of co-located observations are fit for further analysis, thus a screening process is conducted, the details of which can be found in Montmessin and Ferron (2019). It is only on these selected sets that the actual inversion is performed.

Several ranges in the long wavelength channel of PFS were used for different purposes. The 8-10 μm and 19-25 μm windows were used to retrieve surface temperature and dust properties, while the 12-19 μm window was used to retrieve atmospheric temperature profiles as it contains the 15 μm CO_2 vibrational transition absorption feature which has been used for this purpose since at least the Mariner missions. The temperature and aerosol parameters retrieved with PFS are added to the level 1 files, and make up the "L2A" data level.

In the final spectral retrieval, the temperature and aerosol properties are injected into the synergistic routine. Then a simultaneous inversion of H_2O follows, according to the non-parametric approach outlined in Montmessin and Ferron (2019).

The spectral fitting procedure uses the HITRAN 2012 spectroscopic database (Rothman et al., 2013) as a baseline for the computation of absorption coefficients of H_2O and CO_2. It then relies on a Bayesian inference algorithm to find the best fitting values of water vapor and other parameters by maximizing the probability that a given retrieval satisfies both the observed averaged spectrum and falls within a range of plausible a priori values specified by estimates on absolute values and its dispersion. The weight of the a priori assumption in the retrieval is dictated by its a priori uncertainty, which is set equal to the a priori column abundance.

The MCD version 5.3 was used to provide a priori water vapor and temperature profiles. For each Martian year the corresponding scenario is selected, the exception being MY 34, which is not yet included (the version used was last updated on 11/01/2019). A composite scenario was created for MY 34, to most closely represent the observed conditions of that year, by combining the scenario of MY 33 with the standard MCD dust storm scenario 4 and the warm and dusty scenario 7 (for the intervals Ls=180°-200° and Ls=200°-220° respectively).

From the sets of combined PFS/TIR and SPICAM/NIR spectra, water vapor was inferred by a simultaneous inversion from both spectral domains. The routine adjusts the H_2O local abundance at each altitude point (2.5 km separation from ground to 10 km, and 5 km separation from 10-30 km. All nine points are correlated through a Gaussian kernel in such a way that the points become less strongly correlated with increasing distance, with a FWHM 5 km. The output "L2B" data product includes the retrieved vertical profile and the consequent column-integrated water abundance from said profile. Figure 3.2 shows an example of a co-located observation, with the averaged spectrum from SPICAM and PFS in the left and middle panel respectively. The right panel shows the retrieved water vertical profile in red, and the MCD a priori profile in black. In blue is an error ratio profile, where the retrieved error is divided by the a priori error at each altitude point. Low values signify a significant reduction in error. The error ratio is particularly small below 10 km, indicating that the synergy is indeed collecting new information within the boundary layer which has proved so challenging to capture with conventional observation and data processing techniques.

Also included in the L2B data product is the a posteriori co-variance matrix, the trace of which gives the total DOF value. This value normally lies somewhere around 1 when the retrieval is made from a single spectral region, implying that one independent parameter can be inferred from the measurement (water vapor column abundance in this case). With multiple spectral domains, a higher DOF is obtainable, which indicates that some information of the water vapor vertical distribution is available. The L2B data is filtered further and analyzed in chapter 4.

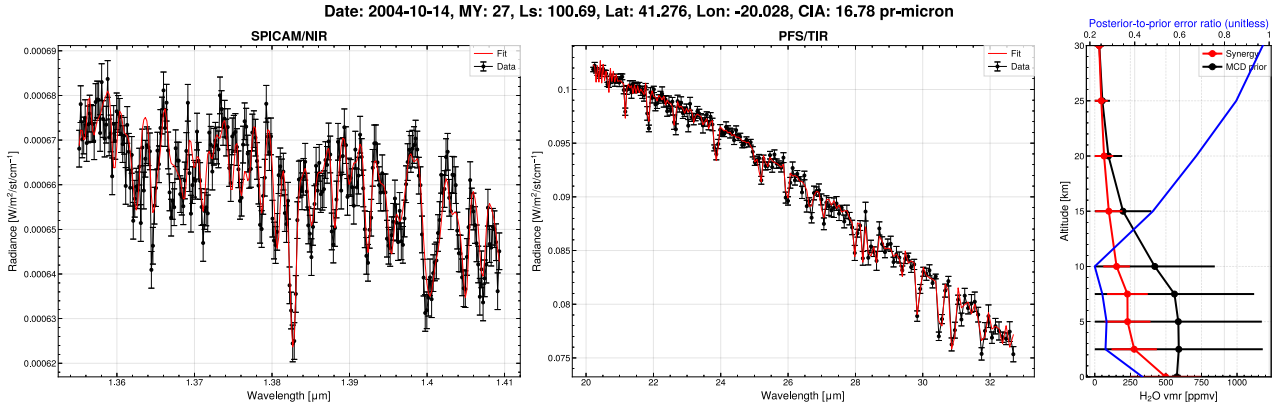

Figure 3.2: Example of average spectra for SPICAM and PFS, along with the resulting vertical profile of water vapor, and the ratio of posterior to prior (MCD) errors for each altitude level. Time, position and retrieved column integrated abundance of water for the co-located observation is given at top of the figure. Figure adapted from Knutsen et al. (2022b).

3.2 SuperCam IRS observations

This section describes the infrared channel passive sky routine. The observation strategy is laid out, the calibration and pre-processing is briefly outlined, and the details of the data post-processing is reported. The retrieval pipeline is not discussed here, but in Chapter 5.

The *passive sky* measurement technique was originally developed by McConnochie et al. (2018) for ChemCam on the MSL Curiosity rover. In short, it utilizes the fact that collected scattered skylight from two significantly separated elevation angles, has traced two different path lengths through the atmosphere, as illustrated in Figure 3.3. By dividing the low elevation signal by the high elevation signal, the goal is that the instrument response and solar spectral features are intrinsically removed.

A typical passive sky measurement consists of 16 individual spectra, where the camera slews between two predetermined elevation angles, normally 15-20° and ∼65°. The observation is conducted in the morning or around noon if possible (at least not in the afternoon) to avoid the instrument getting too hot which impairs sensitivity. The spectrum is acquired as the AOTF "scans" through the wavelength interval of 256 spectels with an integration time of 78 ms per spectel. A dark spectrum is also obtained for each sky spectrum. A full passive sky observation using the infrared channel takes roughly 21 minutes, although the activity is most commonly conducted in tandem with the visible channel, resulting in a typical total time of about 45 minutes.

A passive sky observation has to satisfy several instrument safety requirements while striving to maximize the atmospheric path length contrast. For sun-safety reasons, and to avoid overheating, the solar azimuth angle is recommended to be in the range 90°-300° (where a solar azimuth angle of 180° corresponds to the Sun being directly behind the camera, see Figure 3.3), with the instrument azimuth between 0° and 6°. Generally, angles are chosen such that the camera pointing is to the sky opposite to the noon position of the Sun. Observations are as mentioned most often performed in the morning, with solar elevation angles ranging from 15° to 80°.

The passive sky observation is a regularly occurring activity, being performed roughly every two weeks. The measurement frequency on any rover activity is always a trade-off between science return and rover resources. Scientifically, the passive sky cadence is based on the water vapor climatology in Jezero crater, shown in Figure 2.11 in Section 2.3.1. It is desirable to resolve the rapid change in water column during the onset time of the spring increase in water vapor around Ls=45°, but as there are not expected to be much detectable variations on time scales smaller than a few weeks, the frequency was set to one observation every two weeks.

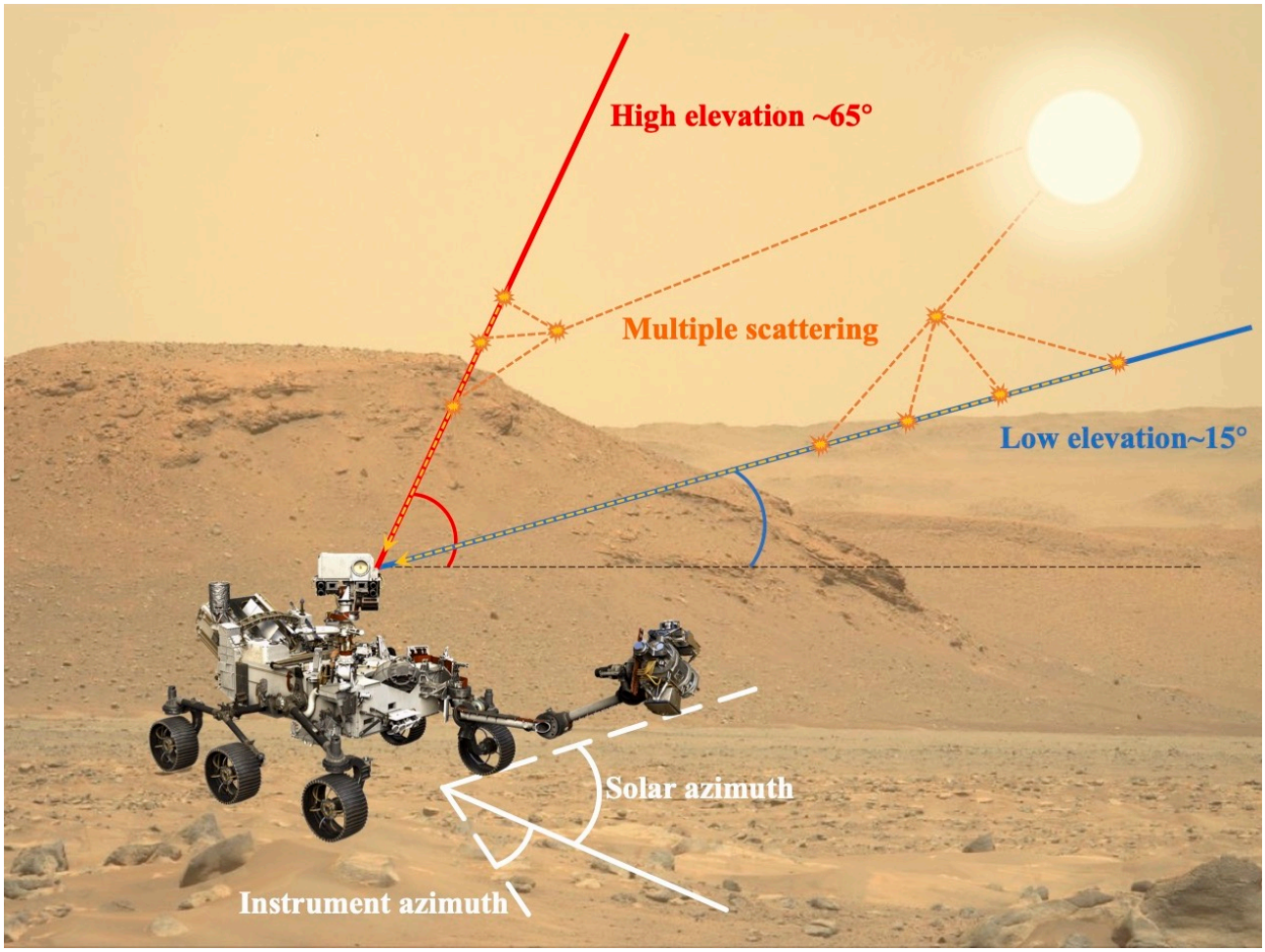

Figure 3.3: Graphic showing the physical geometry of a typical Passive Sky measurement as made by SuperCam on the Perseverance rove. It shows the elevation of the two camera angles used, and depicts how light is scattered multiple times due to aerosols into the field of view of the camera.

3.2.1 Passive sky pre-processing

Before SuperCam was integrated onto the rover body, the spectrometer underwent a calibration campaign where the radiometric and linearity responses of the instrument were characterized and the instrument transfer function was derived (Royer et al., 2020). The passive sky signal is received as digital numbers (DN), which is the unit for digitized raw detector output. This is then converted to radiance (in $\mathrm{W/m^2/sr/\mu m}$) by application of the transfer function, which gives the relationship between the measured DNs and the incident radiance on the SuperCam telescope aperture. The instrument is described in detail in Fouchet et al. (2022), where also the point spread function (PSF) used in this work was collected.

After landing, the first geological measurements showed new instrumental behaviors that required further characterization and calibration in order to derive unbiased data. The IRS radiometric response was calibrated using periodic observations of the Aluwhite SuperCam Calibration Target shown in Figure 3.4, and the instrumental dark and noise were characterized and modeled as described in Royer et al. (2023). The final reflectance calibrated data products are thus corrected for the main instrumental features, and deposited periodically on the NASA Planetary Data System.

For surface targets, geologists need to remove atmospheric signatures in the spectra, but for sky measurements this is what we want to analyze. As both the low and high elevation spectra taken during a passive sky measurement are calibrated using this white target, some portion of the atmospheric

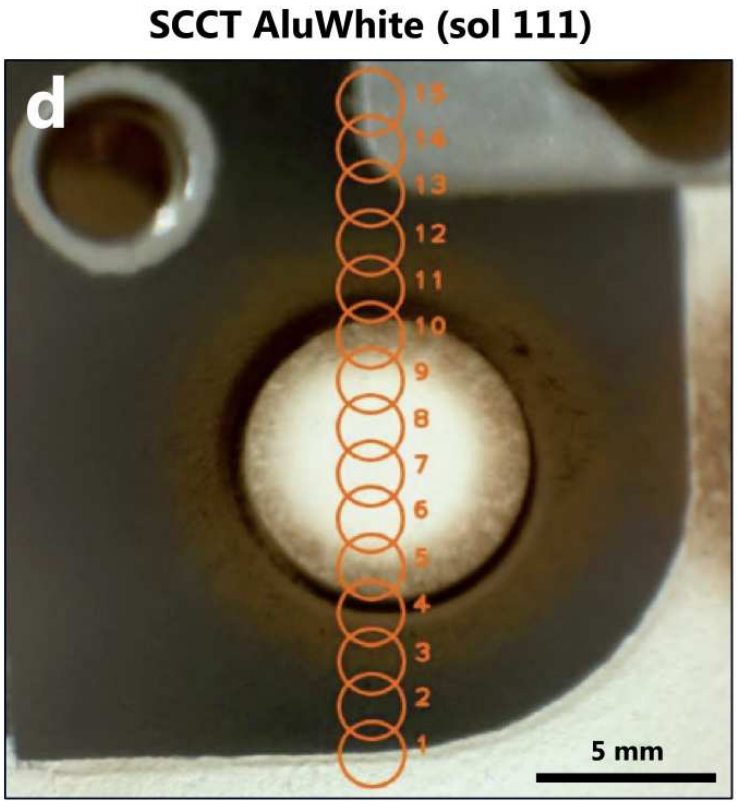

Figure 3.4: SuperCam RMI image and IRS pointing of a vertical observation showing dust accumulation around the AluWhite SuperCam Calibration Target. Red circles indicate the location of the field of view of the IRS. Figure from Mandon et al. (2023).

absorption is in effect removed from the received signal. This is particularly evident in the high elevation spectra which contain weaker atmospheric signatures. Some appear to contain an emission feature, while in others there seems to be no CO_2 absorption at all, as can be seen in Figure 3.5. The reflectance spectra in the third row of panels appear to be collected in two groups, this is due to the pattern of low and high pointing during a passive sky activity. Yet, by only considering the ratio of the low-to-high elevation spectra, effects related to calibration are intrinsically removed, and the spectrum is self calibrated, an example of which is shown in the bottom panel in Figure 3.5.

Early in the mission, it was found that the spectra were suffering from sporadic decreases in intensity which return to regular levels a 1-3 pixels later. In the observation in Figure 3.5, 6 of 16 individual spectra contained glitches (visible in the top row DN spectra). These glitches can be traced back in the housekeeping data as sporadic drops in the RF power applied to the AOTF crystal, and are at the time of writing corrected by linear interpolation. The glitches seem to be correlated to the temperature of the electronics and optical boxes. It has been found that the glitches appear when the optical box has a temperature within 20°-33°C. To obtain a spectrum with zero glitches, the electronics box needs a temperature warmer than -12°C, and an optical box of at least -20°C. A warmer optical box has the disadvantage of increasing the noise level, so a trade off is needed. To warm up the electronics box, and thus mitigate the glitches, 6-10 minutes of waiting time is added after the instrument is turned on. A routine to avoid the occurrence of glitches was designed from these temperature requirements, and was tested for the first time on Sol 841, and considered a success.

The glitches are one type of power failure, but in addition to them, another type of power failure also affects some spectra. On some occasions the RF power does not jump back to its original level shortly after dropping, but remains at a lower level, causing all subsequent spectels to be shifted down. These drops are sometimes there from the acquisition of the first spectel, leading to the whole spectrum being lowered and it is not apparent upon visual inspection of the spectrum that any failure

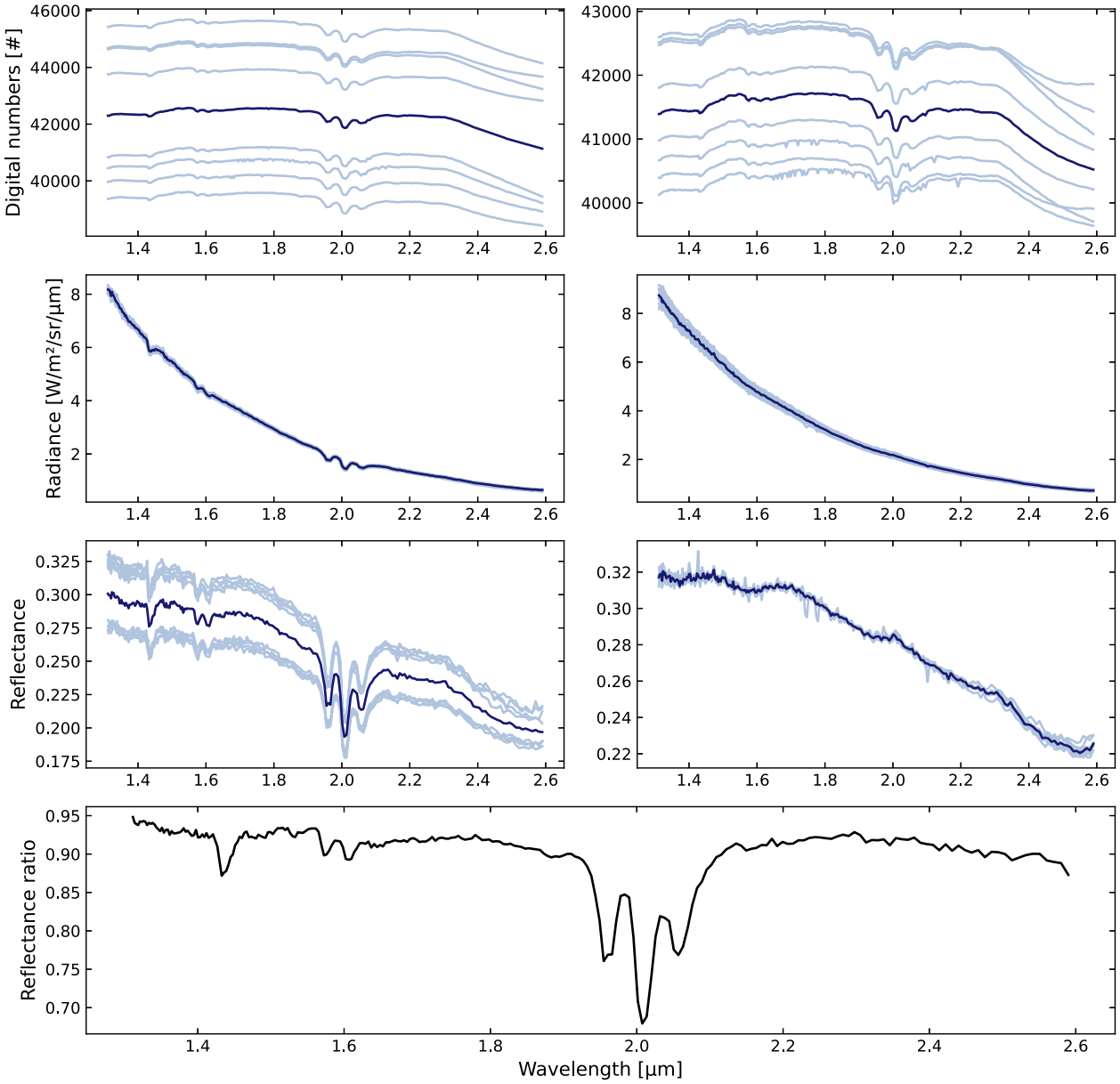

Figure 3.5: SuperCam IRS spectra for Sol 321 at various stages of processing, for low elevation (left column) and high elevation (right column) spectra separately. Light blue shades represent individual spectra, dark blue is the average spectrum. First row: raw spectra in DN. Second row: Dark-corrected radiance spectra. Third row: completely pre-processed reflectance spectra according to Royer et al. (2023). Bottom row: Ratio of low elevation average reflectance spectrum to high elevation average reflectance spectrum.

has occurred, as changing sky brightness conditions can also lower spectra (as seen in the middle right panel of Figure 3.6). Other times they happen in the middle of a spectrum, leading to a step-like form of the spectrum. This is visible in the bottom left panel of Figure 3.6, where the purple spectrum has experienced a power failure from the start, and the turquoise line fails at around 2.2 µm. The reason for the drops is still not well understood, and at the moment there is no correction implemented in the pre-processing to account for the drops. However, such drops are easily identified in the RF power spectrum and related IRS spectra can be discarded during post-processing.

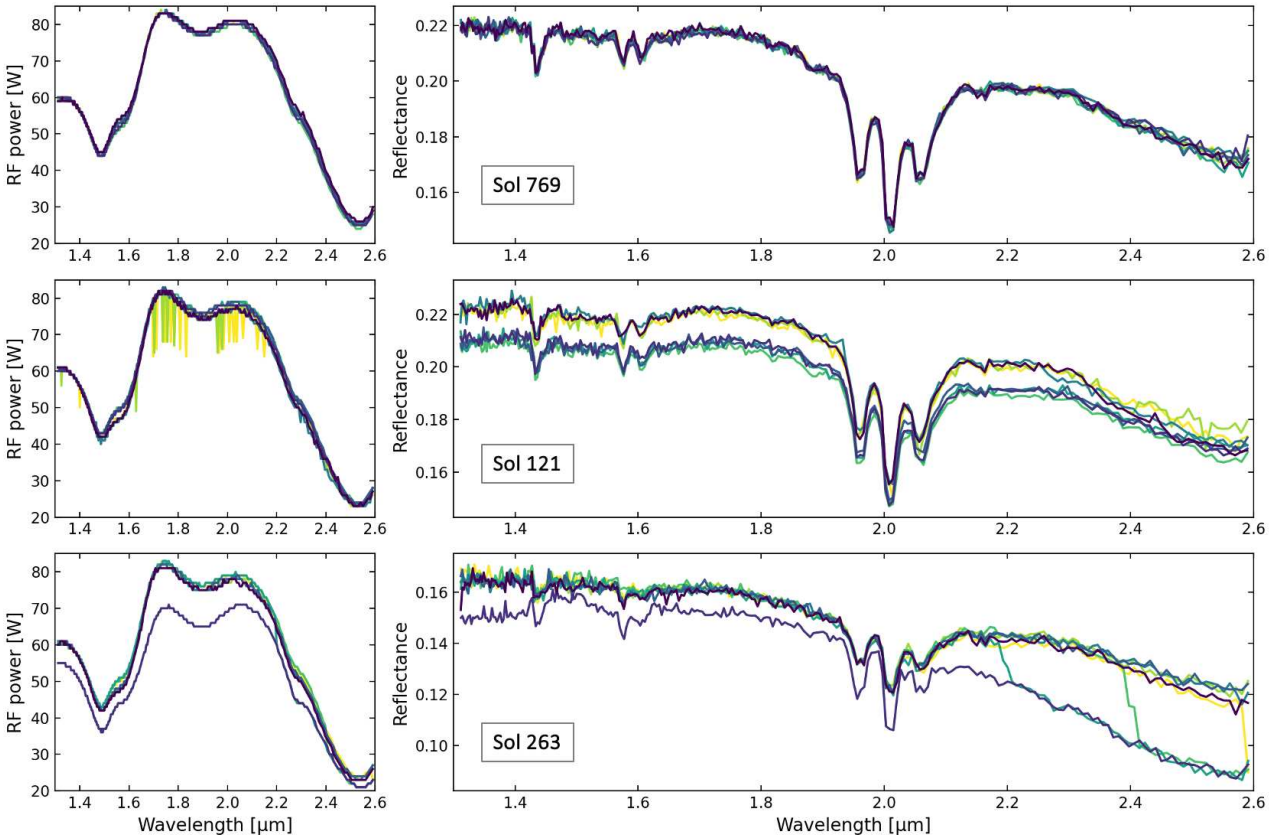

Figure 3.6: Illustration showing the effect of glitches and power failures on IRS spectra. Left column shows the RF power curves applied to the AOTF crystal, and the right column shows the resulting spectra. Sol 769, no glitches or power failures occurred. Sol 121, numerous glitches occurred during the acquisition of several spectra. Sol 263, three power failures occurred at different times during the observation. The line colors of the power curves correspond to the color of the IRS spectra. Only low elevation spectra are shown for visibility.

3.2.2 Passive sky post-processing

For the purposes of the work in this thesis, where we are still developing the forward model and retrieval scheme, we have selected only the most reliable spectra for further analysis. All spectra with a power failure, regardless of when it occurred during the acquisition, is disregarded along with those that contain more than five glitches, to ensure minimal loss of information. Other grounds for not including spectra were occasions where the low elevation line of sight intersected regolith, or for some reason the returned data contain only noise. Due to some RF stability issues longward of $2.4\,\mu$m spectra are not evaluated beyond this wavelength.

The final data download and selection was made on July 4th 2023, corresponding to Sol 842, at which point the rover had performed 64 passive sky observations. Note again that each passive sky before selection contains between 8 and 24 spectra, where 16 is the norm. After selection, about 120 individual spectra from 23 sols were selected for further analysis. Of the remaining spectra, all the low elevation and all the high elevation observations were averaged together for each separate sol, then the ratio was computed between the sets. Examples from Sols 111, 364 and 578 are shown in Figure 3.7. In the first three rows all the selected low and high elevation spectra are shown individually for each Sol, along with the average spectra. The bottom panel shows the final ratio spectrum for the three Sols. Here most of the background continuum features have been removed, and a relatively flat reflectance curve is obtained. It is on this ratio spectrum that the gaseous abundances and dust properties are retrieved, as described in Chapter 5.

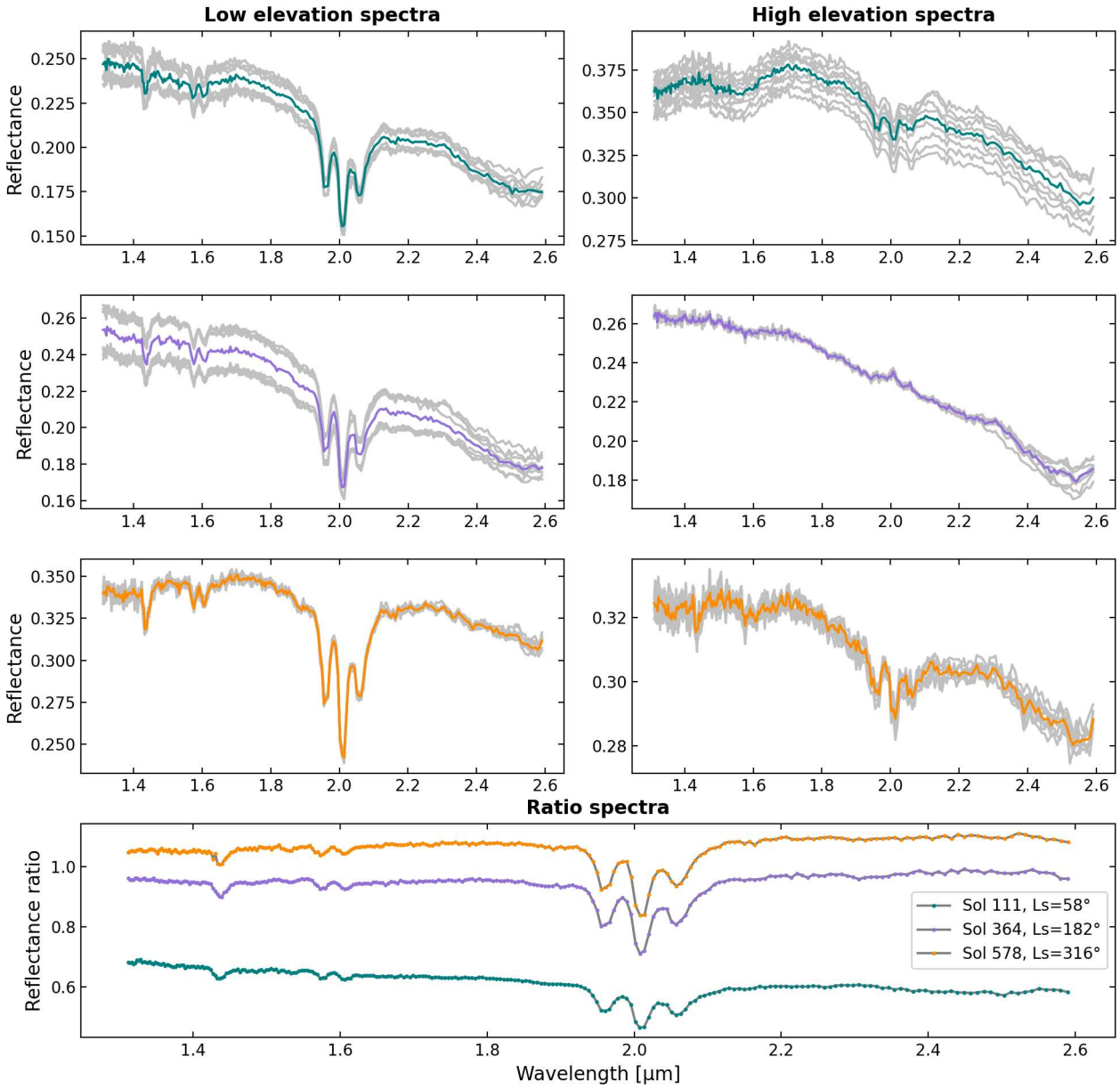

Figure 3.7: Example spectra from three Sols where no glitches or power failures occurred. The three top rows correspond to Sols 111, 364 and 578 respectively, for the low elevation spectra in the left column and the high elevation spectra in the right column. The bottom row displays the average ratio spectra for each of the three Sols. The season is indicated in the label, and the colors in the label correspond to the panels above.

Chapter 5 describes the development of the forward model in preparation for gaseous retrievals, and Sol 578 was chosen for testing and comparison purposes. That particular passive sky experienced no power failures or glitches, with a relatively high signal-to-noise compared to other spectra. For simplicity, ice is (for now) neglected in the forward model, so this particular passive sky was also selected as it was performed at Ls=316°, a season during which the contribution from ice clouds is expected to be minimal around Jezero crater (as shown in Figure 2.11).

Chapter 4

Water vapor from spectral synergy

As described in Chapter 1.6 and 2.2.3, one can probe the vertical profile of water vapor by doing a simultaneous inversion of spectra covering water vapor diagnostic features in different spectral ranges, provided those individual spectral ranges are sensitive to different altitude regions. This technique was utilized first at Mars in Montmessin and Ferron (2019), where the concept was tested on a small selection of co-located observations. In the following chapter, the results from the first project of my PhD are outlined. The results and figures presented are based on the peer-reviewed publication Knutsen et al. (2022b). After publication, we explored the topic a little further, focusing on the near-surface vertical distribution climatology. These newer results were later presented at the International Astronautical Congress, and section 4.5 highlights the main results from the conference proceedings article Knutsen et al. (2022a).

4.1 Data selection

In order to only select retrievals which are reliable enough to justify a deeper analysis, and with a high enough quality that information on the vertical water distribution can be extracted, four parameters were used to probe the robustness of each individual retrieval; the abundance-to-noise ratio (ANR ratio), the DOF, the *a posteriori-to-a priori* error ratio (error ratio) and the χ^2. The ANR, the retrieved water vapor column abundance divided by the *a posteriori* error, provides a measure of the amount of certainty one can have in the output value, strictly speaking it represents the sigma-level detection limit. The DOF represents how many individual pieces of information are available from the retrieval, a proxy value for the degree of vertical resolution, and gives a measure of the level of correlation between the points in the vertical profile (higher DOF means less correlation). The post-to-prior error ratio profiles provide a validation of the fact that the synergy is indeed adding information to the retrieval. Where the error ratio is less than one, the water abundance has been further constrained compared to the prior. As the goal of the synergy is to shed light on the vertical distribution of water in the lowest part of the atmosphere, an error ration of significantly less than one at lower altitudes is desired. The χ^2 is the convergence criterion for the retrieval itself, and its value represents the overall goodness of the final fit. As the NIR and TIR spectral domains are fitted simultaneously, the final χ^2 for the synergy is computed on the two spectra combined and normalized by the total number of datapoints. All four parameters were explored for each of the single-spectrum retrievals and compared to the synergy, as detailed in Knutsen et al. (2022b). It was clearly shown that the synergy outperforms the single-spectrum results for all parameters, particularly the DOF.

Criteria were established which the retained samples would have to comply with simultaneously: (a) an ANR ≥ 3 (3σ confidence interval), (b) a DOF for water vapor ≥ 1.25, (c) a post-to-prior error ratio at $2.5\,\mathrm{km}\leq 0.9$ for water volume mixing ratio at $2.5\,\mathrm{km}$ (Error ratio), and (d) a reduced χ^2 of the retrieval (Chi2) ≤ 4. Many criteria limits were explored to optimize the returned number of retrievals versus the quality of said retrievals. The limits of these criteria can also be tailored for a

specific purpose; the DOF limit was reduced to 1 for the assembly of a composite column abundance climatology, and increased to 2.25 for a limited study targeting the vertical distribution.

After application of these limits, Figure4.1 summarizes the statistical distribution of the relative numbers (per 10 000) and combinations of qualified retrievals for the single-spectrum as well as the synergy in MY27, as more than 30% of all co-located observations were from that year. Note that the synergy is also shown in full; the top row depicts the total number of synergistic retrievals while the other rows only depict retrievals from MY27. The third row show the relative numbers and distributions of retrievals with fulfilled criteria for the NIR-only, and the fourth row shows the TIR-only retrievals.

The benefits of using two spectral ranges are clearly visible, with more than 55% of all synergistic retrievals fulfilling all criteria compared to only 24% for SPICAM/NIR, and 16% for PFS/TIR, effectively demonstrating that the synergy yields more information than separately using the SPICAM or the PFS data set. For all cases the χ^2 is the most restrictive requirement (except for PFS/TIR where the DOF is the most restrictive), while the ANR is the least restrictive. The DOF increase provided by synergy compared to retrievals from single spectral domains is a direct evaluation of how much additional information synergy brings to constrain water vapor distribution. Only the measurements fulfilling all four requirements are considered in the following analysis.

4.2 Water vapor column abundance climatology

For the production of a multi-year composite column abundance climatology, two of the selection parameters described in 4.1 were slightly adjusted. As this is a column abundance climatology, no information on the vertical distribution is strictly necessary, so the DOF criteria was lowered from the standard 1.25 to 1, and the error ratio criteria was raised from 0.9 to 1. The resulting climatology consists of roughly 80 000 retrievals, averaged and illustrated as a function of season, latitude, and longitude in Figure 4.2. The data has been normalized to an equivalent surface pressure of 610 Pa using the MCD to constrain local pressure. Henceforth, the total column integrated abundance will be referred to as the CIA.

The co-located SPICAM and PFS measurements sample the atmosphere at overlapping yet not completely the same temporal intervals; SPICAM conduct nadir observations from early morning to late evening, while PFS measure only from 08:00 until 16:00 local time. It is therefore assumed that seasonal variations dominate over potential diurnal variability. The temporal and spatial coverage shown in Figure 4.2 is visibly incomplete (especially at latitudes south of -30°N, yet known trends of the water cycle appear unambiguously. The NH spring is overall a dry season (Figure 4.2 panel B), with abundances rarely higher than 10 pr-μm. The few instances with larger CIA occur late in northern spring at the edge of the NPC as water ice starts to sublime.

The time from Ls=90° to 135°, corresponding to the early northern summer season, is characterized by large latitudinal gradient between the polar region and the mid latitudes, with high water content in north which decreases monotonically southward, as can be discerned in Figure 4.2 panel C. At around Ls = 115°, a northern maximum of around 60 pr-μm is visible poleward of 70°N, while at the same time only $\sim$13 pr-μm is measured south of 30°N (in panel A). The northern hemisphere fall season shown in Figure 4.2 panel D displays a north polar region devoid of water vapor, most of which has been transported across to the southern hemisphere. The south polar maximum occurs shortly after the SH summer solstice (around Ls = 285°) and reaches an average total column abundance of 40 pr-μm, as seen in Figure 4.2 panel E. The dry sloping area seen around Ls = 300° in the southern hemisphere from equator to -60°N is constructed almost entirely from observations in MY 28, when a global dust storm occurred and is thought to aid transport of water vapor from the lower atmosphere to higher altitudes (Fedorova et al., 2018) where the synergy is no longer able to capture it.

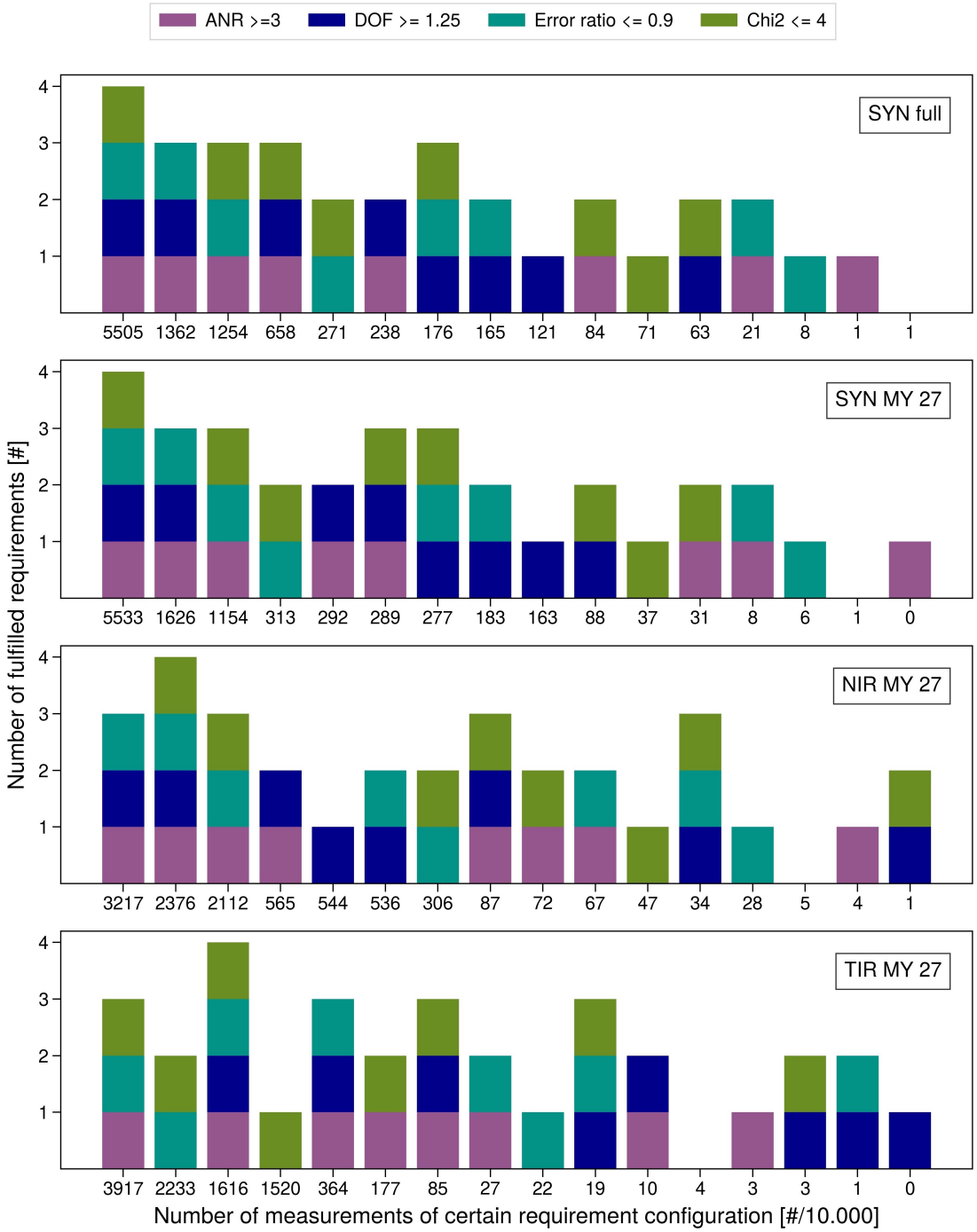

Figure 4.1: The statistical distributions of which parameter criteria are fulfilled. The full synergy data set is shown in the top panel, while the rest depict retrievals from MY 27 only. Second panel; synergy, third panel; SPICAM/NIR, bottom panel; PFS/TIR. The y-axis counts the number of fulfilled criteria, and the x-axis shows the number of retrievals per 10 000 which fulfill each criterion configuration, sorted with the most likely configuration to the left, and decreasingly likely configurations to the right. Figure from Knutsen et al. (2022b).

Panel A) shown in Figure 4.2, has become the standard way of displaying the Martian water cycle, yet other configurations can also highlight interesting aspects of the seasonal trends. Figure 4.3 shows the longitudinal and temporal averages of 15° seasonal intervals overlaid on top of each other, clearly contrasting the latitudinal variations for each seasonal interval. In Figure 4.3, the left and right columns show these seasonal curves for the southern and northern hemispheres respectively, while the top row show synergistically retrieved data and the middle row show the corresponding curves

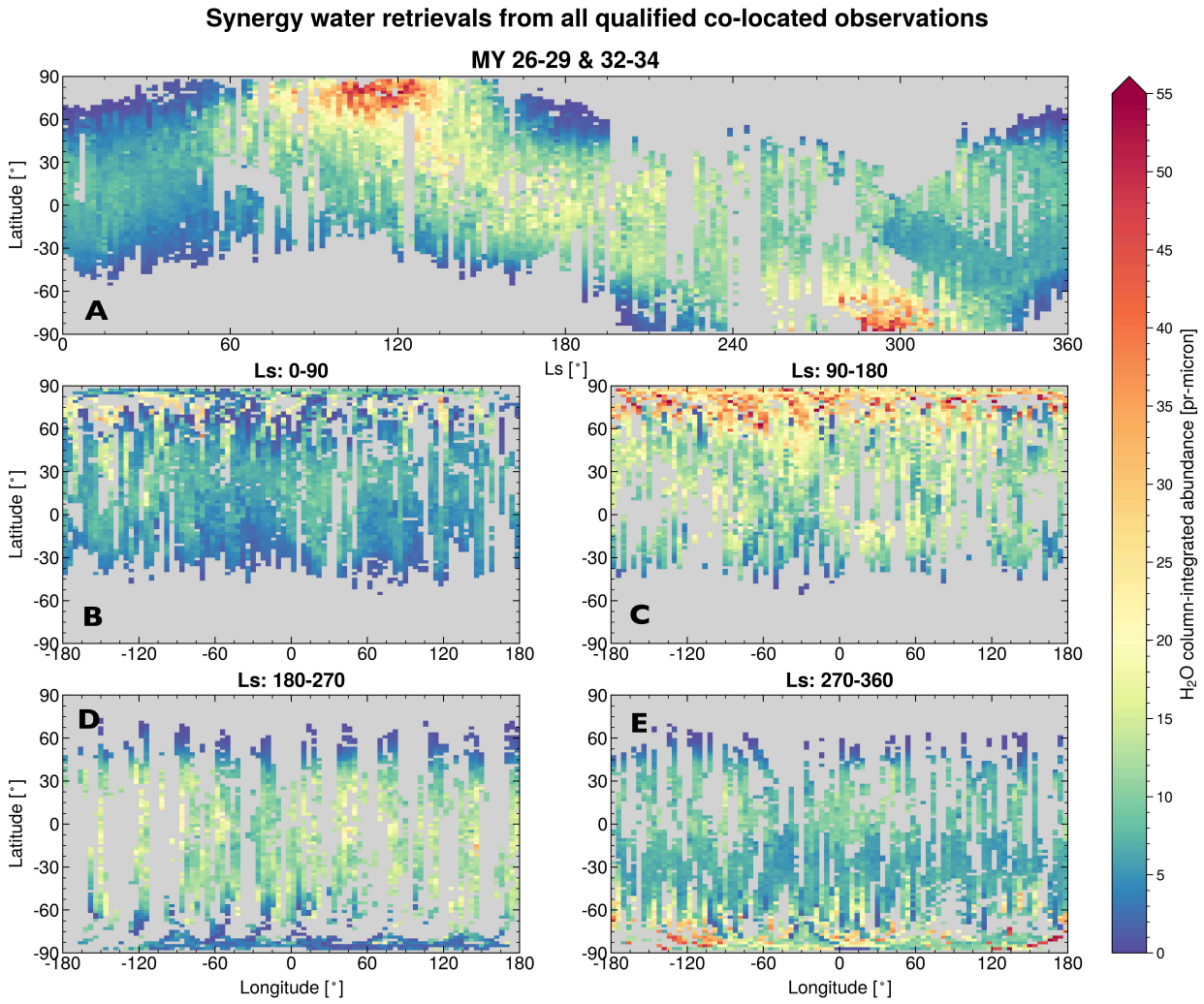

Figure 4.2: Normalized water vapor climatology showing seasonal and geographical variations. Panel A: Seasonal distribution of all qualified retrievals averaged in bins of 2°x2° Ls and latitude. Panels B–E: Geographical distribution of qualified retrievals for each seasonal interval, averaged in bins of 2°x4° latitude and longitude. Figure from Knutsen et al. (2022b).

provided by the MCD. The bottom row compares the averages for the MCD and synergy that covers the sublimation season for both hemispheres (Ls=255°–315° for the SH and Ls=75°–135° for the NH).

From Figure 4.3 one can easily compare corresponding seasons for each hemisphere; Both hemispheres remain fairly dry from the equator to mid latitudes during the spring-summer season, i.e. less than 20 pr-μm from equator until $\sim \pm 45°$N. However, the SH displays a smaller spread in seasonal variation and a smaller increase with latitude compared to the NH. From $\pm 45°$N, the water column starts to increase steadily for both hemispheres, although more steeply in the north. The gradual increase in the south stands in clear contrast to the northern sudden rise. The majority of the increase in SH water vapor appears to be caused by transport of water vapor from the northern to southern hemisphere (Montmessin et al., 2017), as opposed to be due to the sublimation of water ice in the north.

For both hemispheres the peak for each seasonal interval moves poleward as the seasons progress, but the northern maxima after Ls=135°–150° (Ls=315°–330° for the SH), contain almost double the water amount compared to the southern counterparts. The overall maximum is observed at 80°N in the Ls=105°–120° interval, same as in the SH, and reaches a peak value of 60 pr-μm, as opposed to

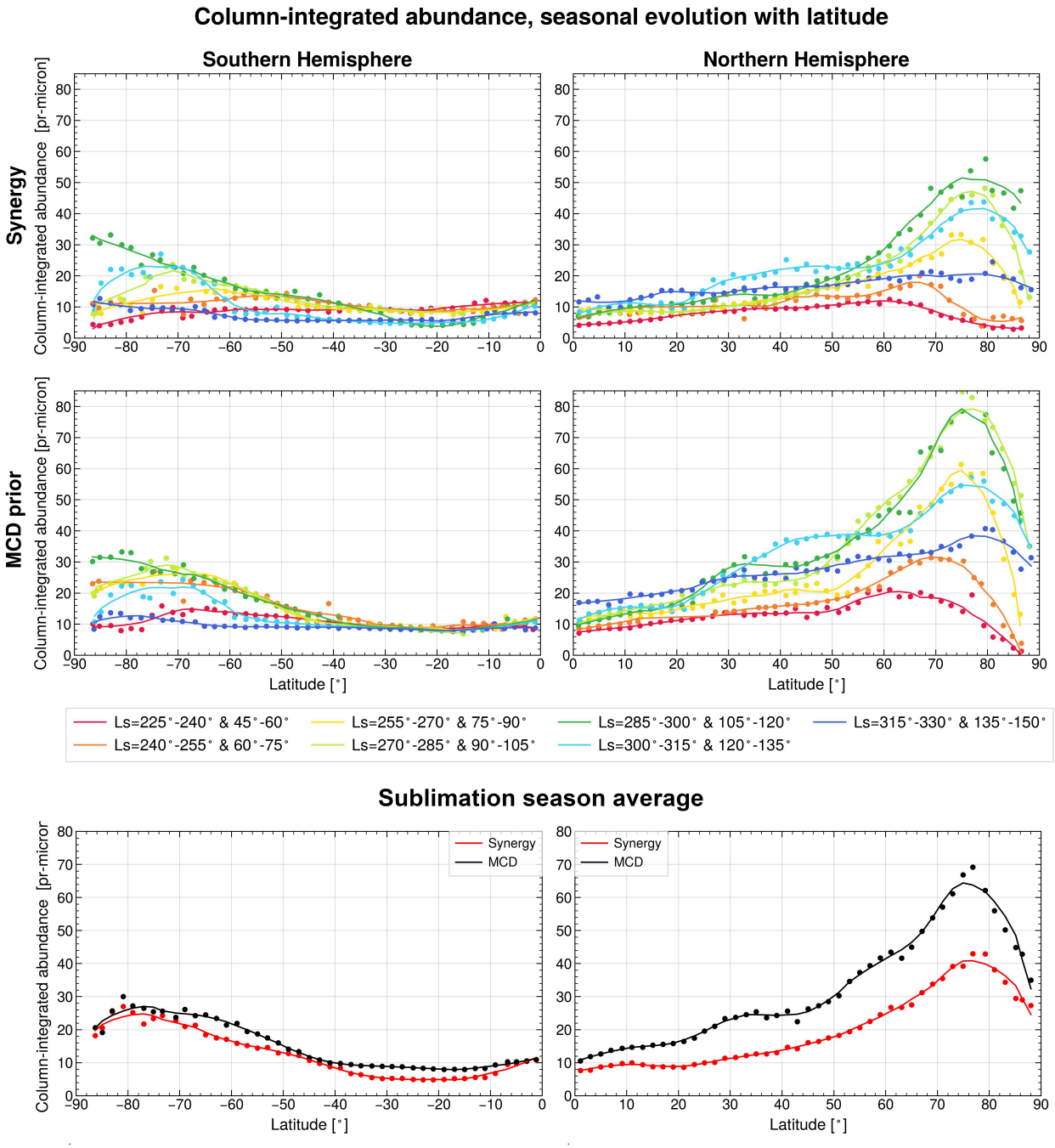

Figure 4.3: Zonal averages of H_2O column abundances from mid spring to mid summer for both hemispheres. Data from all years are averaged, the dots represents data points that have been averaged in bins of 2° latitude and 15° Ls, while the curves represent the smoothed bins. The top row illustrates the synergistic retrievals, while the middle row shows the corresponding MCD *a priori* column abundances for each hemisphere. Curves representing the same seasonal period for both hemispheres have identical colors, with the SH Ls interval listed first in the label. The two bottom panels compare the synergy and the MCD averages from Ls = 255°–315° for the SH and Ls=75°–135° for the NH, covering the sublimation season for both hemispheres. Figure from Knutsen et al. (2022b).

30 pr-μm in the south. The underlying reasons for the hemispherical asymmetry is a complex matter, in short it can be explained by a corresponding seasonal asymmetry of the height where tropical water ice clouds form. Along with the seasonal variation of the cross-equatorial Hadley circulation, a nonlinear pump is created which in sum favors the transport of water from the south to the north.

4.2.1 Column abundance comparison, Synergy vs MCD

Clear differences between retrieved values and model behaviour can also be found from Figure 4.3. For the southern hemisphere, the synergy and MCD agree quite well; All synergistically retrieved seasonal curves show a southern maximum which is migrating poleward with season, matched well by the MCD, and the obtained values also agree. The locations of the CIA peaks are found just south of the polar cap edge with a clear decreasing trend for all seasons in the extreme high latitudes poleward of the CIA maximum, as expected due to the effects of the polar cap breeze (Haberle and Jakosky, 1990). The most notable difference is the degree of seasonal spread. Distinguishable differences can be seen for all latitudes in the synergy, while only becoming clear after 40°S for the MCD. There is one exception, during the first seasonal average in mid-spring as shown in red (Ls=225°–240°), the curve is continuously decreasing, with the highest value at equator for the synergy, while the MCD finds a weak maximum of 15 pr-μm at 70°S for the same season.

Due to the polar cap breeze, it is expected that the CIA decreases poleward of the maximum for all seasons, and the effect should be stronger in the NH where the more massive ice cap generates a larger temperature gradient. This effect is well implemented in the MCD, yet in the synergy retrievals for the SH, the CIA does not always decrease poleward of the cap edge, it even continues to increase beyond 80°S for observations during Ls=285°–300°. This could be due to imperfect coverage of this region and season, or a variable polar cap breeze in mid-summer is not effectively transporting water vapor off the polar cap, or an effect of the averaging of data from multiple years (Pankine et al. (2010) reported high interannual variability of this behavior over the NPC).

In the north the MCD seems to be overestimating the sublimation peak by a significant amount. The overall maximum is observed at 80°N during Ls=105°–120° (which corresponds to the same seasonal interval as in the SH, dark green curves) and reaches a peak value of 60 pr-μm. The highest column abundance by the MCD occurs earlier (Ls=90°–105°) and is significantly stronger (83 pr-μm). Not only does the MCD maximum occur before the observed synergistic maximum, the sublimation onset is also found earlier in the MCD compared to the synergy. During Ls=60°–75° (orange curves), the synergy finds a gradually increasing latitudinal trend with a modest peak at 65°N just below 20 pr-μm, while the MCD already estimates a significant maximum of 30 pr-μm at 70°N, indicating that much more water has already sublimed at that point in the model.

This is further supported by the last row of panels in Figure 4.3, which shows seasonal averages of the intervals between Ls=255°–315° for the SH and Ls=75°–135° for the NH, thus covering the main sublimation period for both hemispheres. The CIA absolute values are interesting to compare, but even more so the meridional variation. In the south the trends and values are nearly identical, with the synergy only yielding slightly smaller average abundances in the 10°–30°S and 50°–70°S regions. In the north, the MCD deviates from the synergy most significantly in two places; at 20°N and at 50°N, where in both instances the MCD gradient distinctly increases with respect to the synergy. This results in a "triple-hump" shape of the MCD CIA that is not prominent in the synergy. The difference between the MCD and synergy is small toward the equator for both hemispheres, which might be indicative that the influence of the CIA sublimation peak diminishes at lower latitudes. The LMD GCM, which the MCD is based on, the summer sublimation peak is quite easily adjusted by tuning model parameters. On the other hand, latitudinal variations are subject to convection, transportation, and possible surface exchanges, and are not so straightforward to modify in order to obtain a specific desired output.

4.3 Near-surface water vapor content

To investigate the degree of vertical confinement of water vapor, a parameter was created which is defined as the integrated column abundance from the surface up to $5\,\mathrm{km}$, divided by the full column abundance. This results in a dimensionless parameter we call the partitioning index (PI), and indicates

what fraction of the total column is kept below $5\,\mathrm{km}$. As a reference to the reader, if water vapor is evenly mixed in the atmosphere with a scale height of $11\,\mathrm{km}$, the PI is equal to 0.63. Since we are now investigating the vertical confinement, some information about the vertical distribution is required. Therefore, in the further analysis we have applied the selection criteria first discussed in Section 4.1 and visualized in Figure 4.1.

Figure 4.4 shows the CIA and PI during Ls=90°–200° and for latitudes between 45°S and the North Pole, as this is where the observation density is highest. Again data from all available Martian years are averaged. The top row show the data on a Ls-latitude grid, while the bottom row displays the data on a latitude-longitude map. As the seasonal polar ice starts to sublime in early northern summer, the CIA increases drastically north of 60°N. There is no clear immediate reaction in the PI, which is already fairly high with values typically greater than 0.7 northward of 35°N and stays stable during Ls=95°–165°. The CIA reaches its maximum at polar latitudes between Ls=105° and 135°, and at the same time a local PI maximum is observed slightly southward of the CIA peak. The confinement in the polar region remains strong at least until Ls=170°, a period which undergo extreme variations in CIA at latitudes above 50°N, as seen in the top panels of Figure4.4. Extremely strong partitioning (PI=0.9) is seen at Ls=165° at latitudes around 60°N. At that time, almost no water remains in this region, indicating that after most of the water has sublimed and been transported south, what water vapor remains at high latitudes is kept close to the surface for the duration of the summer. PIs lower than 0.5 are rarely seen in the NH, suggesting that sublimed water vapor is transported southward at low altitudes.

Geographical variations stand out in the bottom panels, where the PI is enhanced over drier, elevated regions such as the Tharsis and Terra Sabaea regions (centered around $-120°$ and 30° longitude, respectively), while the confinement is small over low-elevation regions such as Hellas Planitia at longitudes between 60° and 90°. The PI index is a ratio of water columns, and should inherently be independent of topography, yet the correlation with elevation remains. Even though water vapor is vertically more homogeneously south of the equator with PIs around 0.5, it shows signs of topographical dependence in an anti-correlated fashion compared to the CIA, indicative of water being transported across the equator in "rivers" over regions of low elevations. Even after pressure normalization (which is supposed to even out the effects of topography), there are local variations in CIA related to changes in elevation, previously found to likely be linked to atmospheric dynamics (Fouchet et al., 2007).

Figure 4.5 has the same layout as Figure4.3 but shows PI datapoints as opposed to CIA values. Qualified datapoints from all Martian years are averaged across all longitudes in bins of 2° latitude and 15° Ls, showing meridional trends as found by both the synergy and the MCD for each hemisphere. Seasonal variations in the MCD PI appear small compared to the synergy, as can be seen by the level of spread of the different seasonal curves in the top four panels in Figure4.5. The shape of the MCD PI curves are quite linear being lowest at or near the equator for most seasons and increasing rather monotonically towards the polar regions. No such stable PI gradient is obtained by the synergy, instead finding a highly variable PI for all latitudes and seasons, but with no clear meridional tendency. For the sublimation season averages in the bottom row, a trend does emerge however.It exhibits a clear the wave-like behavior in both hemispheres, oscillating roughly around PI=0.5 in the south and around PI=0.65 in the north. As the synergy yields very stable column abundances at low to mid latitudes for all seasons, the partitioning varies greatly, particularly in the southern mid summer. The observed wave-like behavior is consistently higher than the estimated stable MCD PI. While the MCD indicates that around 40% of the water column is kept near the surface at all latitudes and seasons, the synergy finds that number to vary from 40% to 60%, with local maxima at equator, 50°S and at the pole. This trend is very similar to what is observed in the north, but here the wave amplitude is smaller. The MCD PI here is not as stable as in the south, and displays a fairly constantly increasing gradient from the mid latitudes (PI = 0.4) toward the North Pole (PI = 0.75). The synergy finds that the PI seasonal averages never go below 0.6, indicating that most of the column is always kept close to the surface.

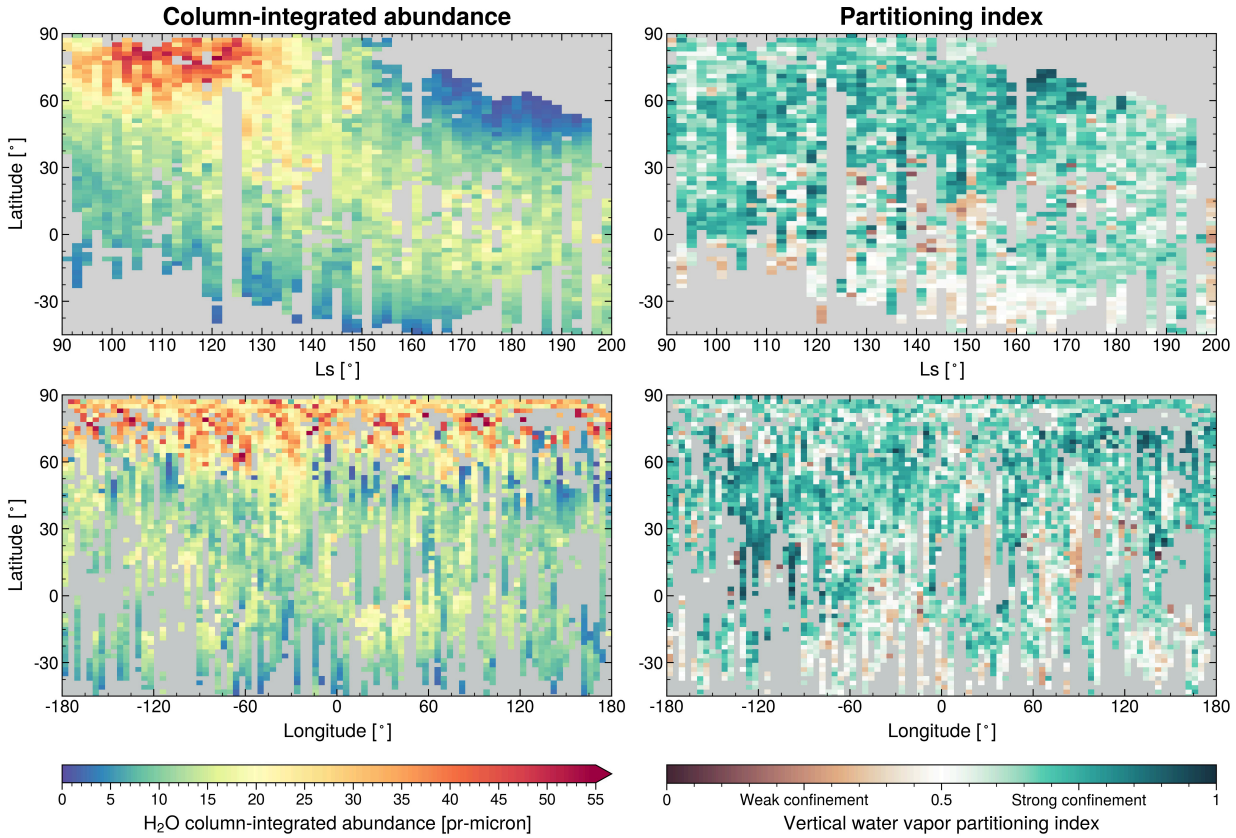

Figure 4.4: Normalized water vapor column-integrated abundance and partitioning indices for the NH sublimation season. For the partitioning index, values higher than 0.5 (green hues) indicate that more than 50% of the water vapor column is confined below 5 km, while lower values (brown hues) indicate that water vapor is more evenly dispersed with altitude. Data from all available years fulfilling all requirements have been averaged in bins of 2° latitude, 2° Ls, and 4° longitude. Figure from Knutsen et al. (2022b).

This leads to the synergy and MCD finding similar PI values only in the north polar region.

It should be noted that the number of data points in the SH are far fewer than in the NH, and the averages in this hemisphere should therefore be considered somewhat less precise. Yet the disagreement in latitudinal behaviour is clearly visible (to a lesser extent) also in the NH, indicating that the discord is likely not purely a result of poor sampling in the south, and strengthening our confidence that this wave-structure is a real feature. In the NH there is a clear tendency for the synergy PIs to rapidly increase poleward of 80°N while the total water content decreases (as can be seen in the top right panel of Figure 4.3). The MCD PI on the other hand is steadily increasing from the mid latitudes, and during late spring the PI decreases north of 80°N.

4.4 A closer look at the North Pole sublimation season

The northern polar region in spring and summer is of special interest as the sublimation of the seasonal NPC is the main source, and thus the main forcer, of the water cycle. Every summer, as the NPC is exposed to sunlight and its surface temperature increases, more than 10^9 tons of water vapor is released into the atmosphere (Smith, 2002), and transported around the globe as the seasons progress. Figure 4.6 shows the CIA and the vertical confinement in the form of polar plots to better visualize the spatial distribution of the observations, and their evolution. Data satisfying all four requirement

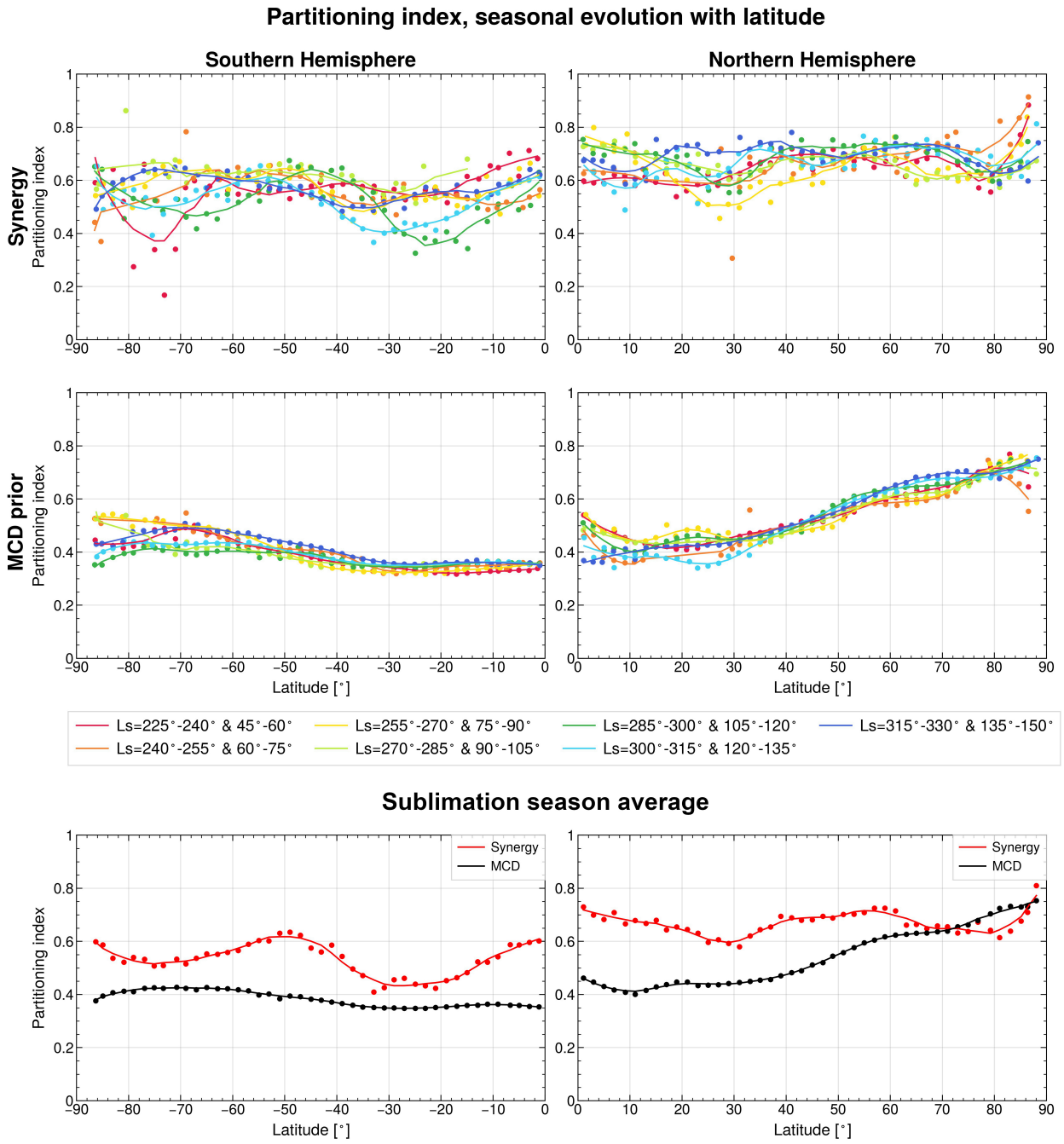

Figure 4.5: Zonal averages of the vertical partitioning index for each hemisphere from mid spring to mid summer. The top four panels show data for all years averaged in bins of 2° latitude and 15° Ls as dots, while the curves represent the smoothed bins. The top row illustrates the synergistically retrieved partitioning indices, while the middle row shows the corresponding MCD partitioning indices. Curves representing the same seasonal period for both hemispheres have identical colors, with the SH Ls interval listed first in the label. The two bottom panels compare the synergy and the MCD averages from Ls=255°–315° for the SH and Ls=75°–135° for the NH, covering the sublimation season for both hemispheres. Figure from Knutsen et al. (2022b).

from Figure 4.1 from all available years north of 45°N are averaged and displayed on a 1°x7° latitude-longitude grid. Each column represents a seasonal average of 30° of Ls, from late spring on the left to mid summer on the right. The two top rows of Figure 4.6 illustrate the CIA, the synergy on top and the MCD below, and the two bottom rows show the PI, again with the synergy first and the MCD last.

Overall, the MCD estimates a wetter polar region than the synergy (as was also shown in Figure 4.3), with high abundances extending further equatorward than what is observed. Another difference is that the sublimation season appears to be initiated earlier in the MCD than what is indicated by measurements, as can be seen by comparing the two first rows of the first column (Ls=60°–90°) of Figure4.6, and was also shown in Section 4.2.1. At 75°N, the MCD suggests column abundances higher than 40 pr-μm, when no observations for this time and place yield higher CIAs than 30 pr-μm. The situation is reversed for the vertical partitioning, where the synergy indicates a stronger near-surface confinement at all latitudes compared to the MCD. During Ls=90°–120°, the larger sublimation peak of the MCD is likely contributing to the overestimation of water vapor at mid latitudes. In the late northern summer during 120°–150° Ls, the MCD estimates a high PI restricted mainly to latitudes north of 60°, while the synergy finds a high PI reaching the mid latitudes. Overall, the MCD predicts the largest PI poleward of 75°N and gradually decreasing southwards, while the synergy indicate that the PI remains high for all latitudes, albeit more variable (this was explored in detail in Section 4.4). Yet, the largest differences in the vertical confinement are found in the mid latitudes and not in the polar regions, as illustrated in Figure 4.5.

4.5 Vertical distribution climatology

In this short in-depth study, the synergy was used to specifically investigate the vertical distribution of water vapor leading up to, during and following the NPC sublimation period. The data selection requirements described in Section 4.1 were applied with the modification that the DOF limit was now set to 2.25, ensuring low vertical correlation, and more available information on the vertical profile. Vertical profiles of high vertical resolution are still not accessible with this technique, and would require a DOF of $>$5. With the new DOF limit (and all other requirements kept the same), 6773 co-located measurements from 592 orbits were selected.

After selection, the water vapor profiles were re-sampled to a finer vertical grid, and smoothed using a second-order polynomial low-pass filter of width $5\,\mathrm{km}$ in order to dampen nonphysical sharp features. The profiles were then averaged in bins of 2°Ls and 1.5 km altitude. Figure 4.7 displays cross sections of the northern hemisphere, showing the water vapor vertical distribution evolution from early spring to late summer (Ls=30°-165°). The figure shows where water ice first sublimes and consequently where it is transported. Generally, water vapor is confined close to the surface, and until Ls=$\sim$100, contained mostly northward of 60°N.

In the top panel (Ls=30°-60°), the total water content is low for all latitudes, in line with established theory. During Ls=45°-75°, some H_2O has sublimed at the southernmost edge of the polar cap, while at the same time at 80°N a separate "bubble" of water appears. As data is averaged from multiple Mars years, such features could be the result of annual variations. In third and fourth panels (Ls=60°-90° and Ls=75°-105°) Mars transitions from northern spring to summer, and water is subliming at a rapid pace, creating a distinct near-surface layer spreading at low altitudes from 50°-80°N. In panels Ls=75°-105° and Ls=90°-120°, some vapor seems to be lifted up into a second layer and transported northward. Later, when water is subliming at higher latitudes, this lifted water brought north into the polar cap region combines with the recently sublimed water to create the familiar global maxima at 80°N at about 120°Ls.

Water that sublimed south of 75°N appears to remain near the surface as it's transported equatorward. The weak two-layer structure from early spring mid-latitudes has now diffused into a smoother vertical distribution. From Knutsen et al. (2022b) we know that the vertical distribution remains fairly stable throughout the year, but the largest variations are found at 20°-30°N. In this region, during Ls=75°-165°, the vertical partitioning index increases from 0.5 to 0.7.

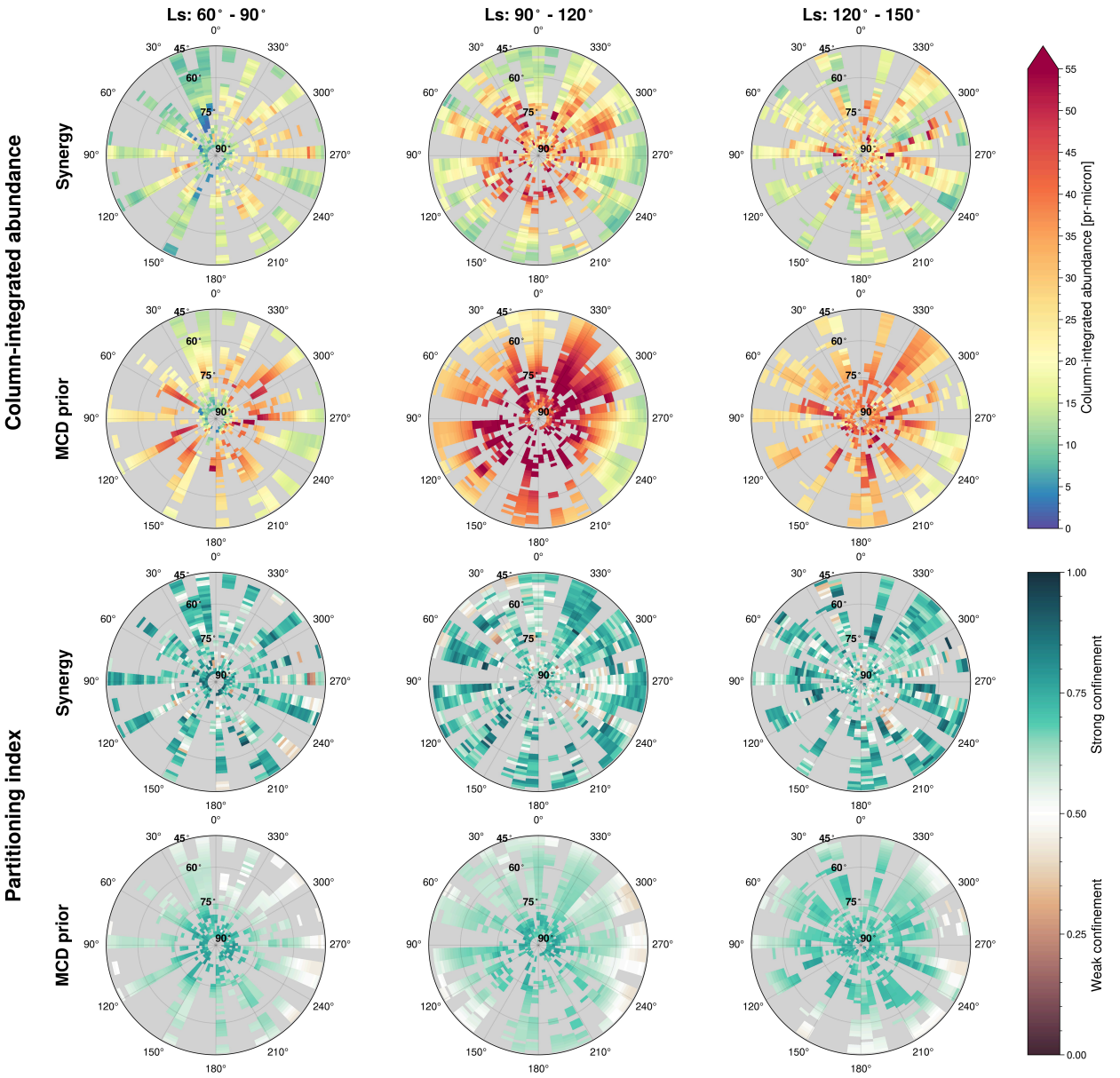

Figure 4.6: Polar view of the column-integrated water abundance and the partitioning index. Observations northward of 45° are averaged on a 1°x7° latitude-longitude grid, in intervals of 30° Ls. The top two rows show the full column abundance of the synergy retrieval (first row) and MCD a priori (second row). The bottom two rows show the retrieved partitioning index (third row) and the MCD partitioning index (bottom row). Figure from Knutsen et al. (2022b).

4.6 Summary

The spectral synergy has here been applied to PFS and SPICAM nadir measurements sampled over seven Martian years in order to study water vapor. The synergy produces a highly reliable water vapor climatology, and offers the unique capability of extracting information on the vertical distribution of water vapor from nadir observations. The synergy is unable to retrieve a high-resolution vertical profile, but it can set reliable constraints on the partitioning of the water column, differentiating between the near-surface content and the total column.

The climatology presented here is meant to serve as a reference climatology, with highly accurate column abundance values provided by the spectral synergy. It is a seven year data set compiled into a one-year composite average, where the spatial and temporal coverage is highly variable from

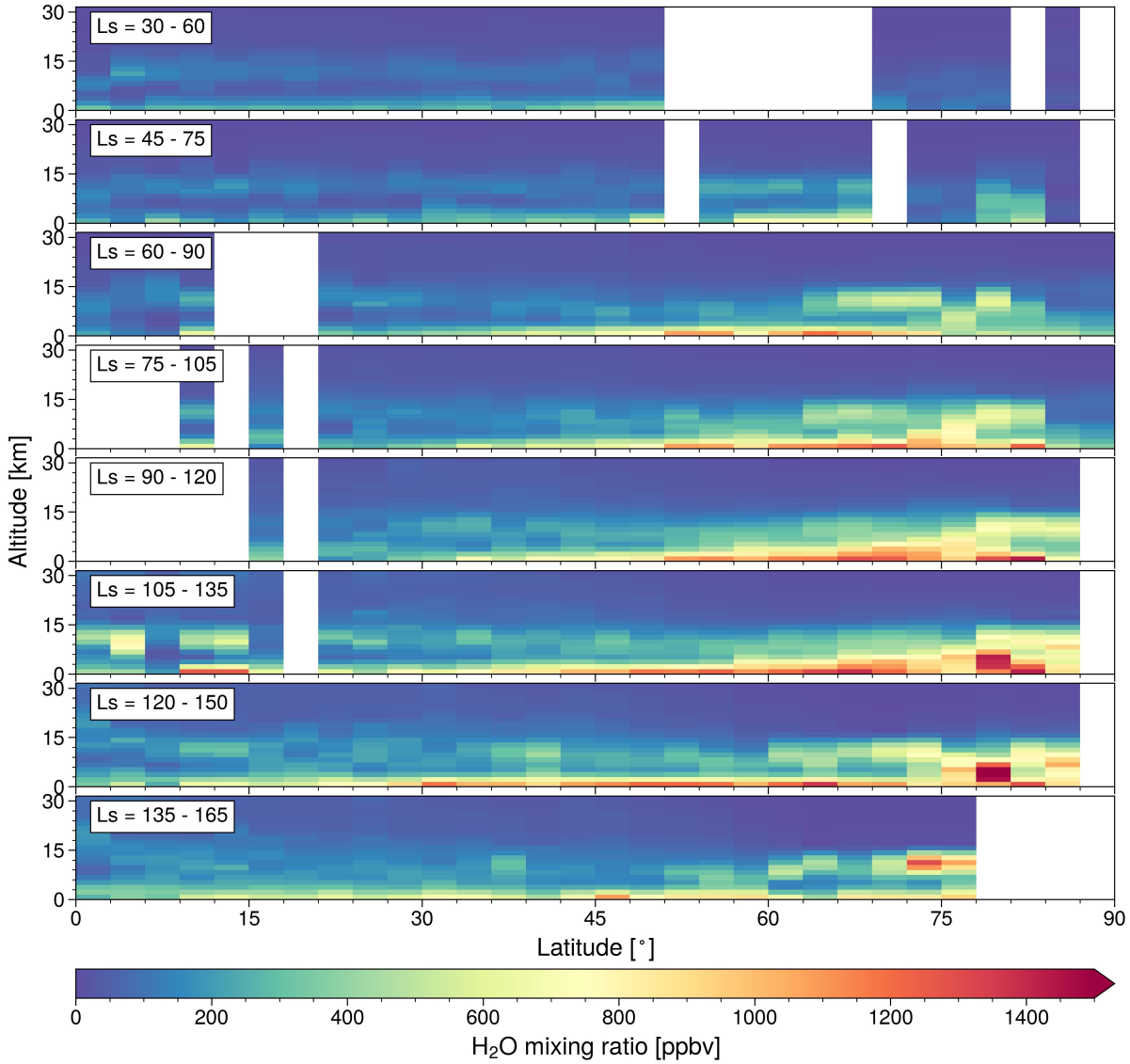

Figure 4.7: Variations of water vapor as a function of altitude and latitude. Data was averaged in bins of 3° latitude and 1.5 km altitude. Each panel represents a 30°Ls time interval, overlapping by 15°Ls in each step. The total period covered is Ls=30°-165°, including the polar cap sublimation period in early northern summer. White areas indicate periods with no available co-located observations. Figure from Knutsen et al. (2022a).

year to year. Because of this variable coverage, it was not meaningful to perform any inter-annual comparisons. Years with and without global dust storms are averaged together, but years with global dust storms are particularly sparsely populated due to the strict requirements we imposed on the SNR and DOF for the co-located observations, and should therefore not notably bias the total average.

The column abundance climatology is in good agreement with other similar data sets both in temporal patterns and abundance magnitude. The synergy finds very comparable column abundances to previous works using single spectral domain approaches with SPICAM and PFS (Fouchet et al., 2007; Trokhimovskiy et al., 2015), slightly higher values than CRISM (Smith et al., 2009), and a little lower than TES (Smith, 2002; Pankine et al., 2010). These differences could occur from various sources, the most likely candidates are differences in the environmental parameters used in the retrievals, different water vapor absorption models and different a priori vertical profiles, and to a smaller degree interannual variations.

Compared to the LMD MCD, some points regarding the column abundance trends are worth not-

ing; in general, the synergy tends to retrieve lower abundances, in absolute differences the deviation is largest for the NH summer sublimation peak, while in relative terms the most significant discrepancies are found at mid-latitudes. In the NH, the timing of the sublimation onset and the latitudinal extent of the sublimation season occurs earlier in the MCD, and extends much further equatorward, compared to the synergistic observations. In the SH the synergy and MCD correspond very well.

The purpose of using the spectral synergy is as outlined in Section 1.6 to learn about the near-surface water content. The work presented in this thesis has demonstrated that the spectral synergy can probe the lower atmosphere with greater sensitivity than with conventional single-instrument approaches. Most of our current understanding of the near-surface atmosphere has been obtained using 3D GCMs, so we have compared our retrievals to the MCD, and found three main differences:

1. overall, the vertical confinement was found to be significantly stronger than the MCD suggests,
2. the existence of a persistent double layer structure across the northern hemisphere in spring,
3. a sinusoidal behaviour of the latitudinal confinement in both hemispheres.

Points 1. and 2. are not too surprising; the commonly assumed uniform mixing below the boundary layer has been questioned for years, with a growing amount of evidence in support of a more complex and variable vertical structure. The latter point is however quite striking, as nothing similar exists in MCD. Further work will include investigating if this wave-like behaviour is correlated to topography, or if the minima/maxima correspond to latitudes of significance for any circulation patterns, such as the polar or Hadley cells.

It should also be noted that the synergy pipeline is still being improved upon. We have recently found that improvements in the χ^2 calculations slightly adjusts the retrieved column abundances, and imposes stricter constraints on how the vertical profile can deviate from the MCD profile. We are also preparing to update the PFS instrument line shape, which will add further robustness to our results, but this is not expected to significantly impact the retrieved quantities.

Chapter 5

SuperCam investigations

The SuperCam instrument consists of multiple modes and channels, as described in Section 2.3. This thesis includes studies that make use of the IRS and VIS channels, for daytime observations of the neutral atmosphere and nighttime observation of auroral emissions respectively (See chapter 6 and Section 6.3 for details on the auroral campaign with SuperCam). The measurement architecture and data processing concerning the daytime observations with the infrared channel are described in Section 3.2. The following chapter details the development of the retrieval scheme for the infrared channel, including the creation of a forward model and the minimization routine. This project has not yet been completed or published, and is a work in progress where various strategies are still being explored. The following sections describes the work done to date, and outlines the path forward.

5.1 The forward model

When commencing the work of analyzing SuperCam IR spectra and attempting to retrieve gaseous species, we hoped that a simple one-layer atmospheric model without taking scattering or radiative transfer into account would be sufficient. The plan was to take the ratio of the low and high elevation spectra, thus eliminating both the instrument background and the atmospheric continuum. Upon testing this approach we ran into two problems which are probably related. Taking the ratio did not sufficiently correct for the background, and the observed symmetry around the central lobe of the CO_2 triplet at 2 microns did not match the model. Another indicator of the inadequacy of the simple one layer assumption emerged after attempting to extract H_2O vmr for the first year of the mission, which turned out to deliver an unlikely stable vmr time series, whereas both model and orbiter observations show it varies by a factor of 2 or more over the same time frame. As for the first problem, it turned out that even though all the high and low elevation spectra are taken within 45 minutes, the background has often changed significantly during this time. This could be because of instrument temperature variations or other instrument causes, or actual sky brightness differences due to the passing of for example clouds or lifted dust, or of course a combination of these things. The problem related to reproducing the main CO_2 band is suspected to stem from using a one-layer atmosphere, and not considering multiple scattering. In any case, a more sophisticated atmospheric model seemed to be required to recreate the observed continuum, and it was decided to incorporate radiative transfer computations in our retrieval scheme.

5.1.1 Incorporating gases using the correlated-k method

Linelists for the gases CO_2, CO and H_2O were collected from the HITRAN 2016 database, and for the radiative transfer itself, the Discrete-Ordinate-Method Radiative Transfer (DISORT) (Laszlo et al., 2016) was used. DISORT is a plane-parallel radiative transfer program, which solves the radiative transfer equation for a vertically in-homogeneous atmosphere. It accounts for multiple scattering

and absorption between aerosol component and solar and thermal radiation. DISORT is a FORTRAN program, and we use it through a front-end python wrapper developed by Connour and Wolff (2021). The pyRT_Disort tool is a pre-processing front-end to help make DISORT simulations easier in Python, and helps set up all the input parameters required by DISORT, and streamlines much of the pre-processing needed to run efficient retrievals. The LMD MCD was used to create a reference set of temperature, pressure and gaseous altitude profiles, interpolated to correspond to the time of each passive sky and at the location of the Perseverance rover.

Absorption from rotational-vibrational transitions dominate absorption in (nearly) all cloudless planetary atmospheres in the near-to-far infrared. For any given species, there are millions of individual lines, making line-by-line radiative transfer calculations extremely computationally heavy. To make the inversions more efficient, a correlated-k method was employed (Lacis and Hansen, 1974). The technique has gained traction during the last two decades, and much work has been done to evaluate its accuracy and improve the technique (Goody et al., 1989; Lacis and Oinas, 1991).

In short, the correlated-k method utilizes the fact that integrating the frequency dependent absorption coefficient k_ν as a function of wavenumber is a highly repetitive process. Much can therefore be gained by doing the computation in k_ν probability space rather than wavenumber space. This is done by dividing the cross-section spectrum into bands *b*, and sorting the coefficients within each band.

First, we define a k-distribution function $h(k)$, which is the probability density function such that $h(k)dk$ is the fraction of a wavenumber interval within which the absorption cross section is between k and $k + dk$. $h(k)$ is normalized to 1 within (0, inf). In this way, the spectral-mean transmittance, $\mathcal{T}(u)$, does not depend on wavenumber, but on the k-distribution. In $\mathcal{T}(u)$, u is the path length through a homogeneous slab of atmosphere for a spectral interval between wavenumbers ν_1 and ν_2, and is given by equation 5.1.

$$\mathcal{T}(u) = \int_{\nu_1}^{\nu_2} \frac{e^{-k(\nu)\cdot u}}{\nu_2 - \nu_1} d\nu = \int_0^\infty e^{-k(\nu)\cdot u} h(k) dk \tag{5.1}$$

We can then define a probability function $g(k)$ where $g(0) = 0$, $g(k \to \infty) = 1$ and $dg(k) = h(k)dk$. It follows that $g(k)$ is a smooth, monotonically increasing function in k-space, and in Equation 5.2, we express the transmittance in terms of the cumulative probability g. $k(g)$ is the equivalent k-function, the inverse of $g(k)$, and since $g(k)$ is smooth in k-space, $k(g)$ must be smooth in g-space (probability space).

$$\begin{aligned} \mathcal{T}(u) &= \int_0^1 e^{-k(g)\cdot u} dg \\ &\approx \sum_{n=1}^{n_k^b} w_l^b \cdot e^{-k_l^b \cdot u} \end{aligned} \tag{5.2}$$

The last step of Equation 5.2 involves computing the integral under the now monotonically increasing curve for each spectral band. This is approximated by applying the Gauss-Legendre quadrature (GLQ) method; within each band the k_ν, specific roots (or integration points, *l*) and corresponding weights (w_l^b) are computed from the probability distribution of the cross-sections. The practical implementation in the code follows these steps:

1. select a band size (wavenumber interval) within which the cross-sections will be sorted,
2. divide the k_ν-coefficients into bands *b*, and sort them within each band to produce a cumulative distribution,
3. use the GLQ approximation to extract the weights for each root,

4. compute final transmittance for each band.

It is imperative that the band width is chosen with care; the spectral intervals have to be small compared to the FWHM of the instrument (30 cm^{-1} for SuperCam IRS), and also be so small that the atmospheric continuum, dominated by mostly aerosol scattering, does not change significantly within each interval. From this we chose a band width of 3 cm^{-1}. The radiative transfer equations are then solved for all GLQ-points within each band while keeping all other parameters fixed. The total transmittance as observed from the surface in each spectral interval is the weighted sum of the transmittance in each band, as described by equation 5.2.

We tested a variety of GLQ-points, and found that when using numbers around 10, the model was unable to reproduce the continuum level, even though the band depths were modeled well, as demonstrated in Figure 5.1. Eight GLQ-points were used in this specific example, with 3 cm^{-1} band widths. In the regions around $1.8\,\mu m$ and $2.3\,\mu m$, where there are no CO_2 absorption bands, the correlated-k model (dashed pink line) is constantly found below the line-by-line mode (solid blue), while inside strong absorption features they overlap.

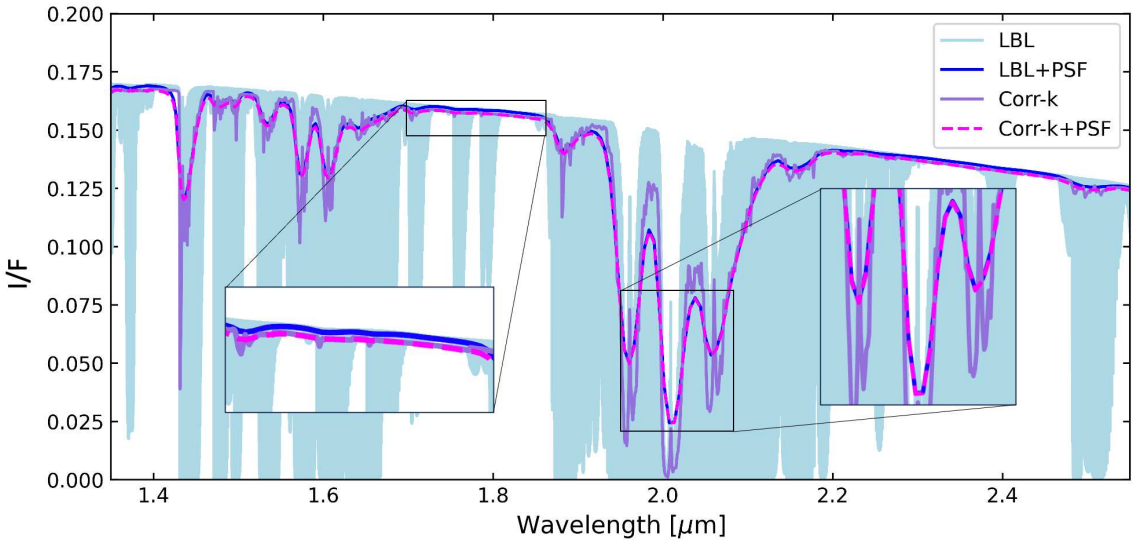

Figure 5.1: Demonstration of how a correlated-k method with too few GLQ-points (eight in this case) is unable to accurately reproduce the continuum level modeled using a line-by-line radiative transfer mode. CO_2 model spectra are shown, produced using line-by-line radiative transfer (blues) and with the correlated-k method (purple/pink), with and without the application of the PSF.

Larger numbers of GLQ-points were tested, and 20 points within each band of 3 cm^{-1} was found sufficient, as demonstrated in Figure 5.2. Here, each step of the correlated-k method is illustrated for a model atmosphere containing only CO_2. Panel a) shows one spectral band with a chosen width of $3\,cm^{-1}$ and the absorption coefficients of CO_2 as a function of wavenumber. In panel b) the coefficients have been sorted, and the GLQ-points have been selected provided a number of 20 quadrature points. Panel c) shows the comparison between the model computed line-by-line (light blue) with the result of the correlated-k method (purple), and then with the PSF applied to each shown as dark blue and dashed pink lines respectively. Panel c) contains zoomed in views of regions of interest, from roughly 1.7-1.9 μm where there are close to no gas absorption to compare the continuum calculations, and centered on the deepest CO_2 band around2 μm.

With a band width of band of 3 cm^{-1} and 20 GLQ-points, the correlated-k approach excellently reproduces the spectrum from the line-by-line solution, both in regions with no gas absorption, and within the CO_2 bands. With this configuration, the computation time was reduced by a factor of 300,

and the mean difference between the two models is roughly 1%, much less than any error which will be introduced by the instrument.

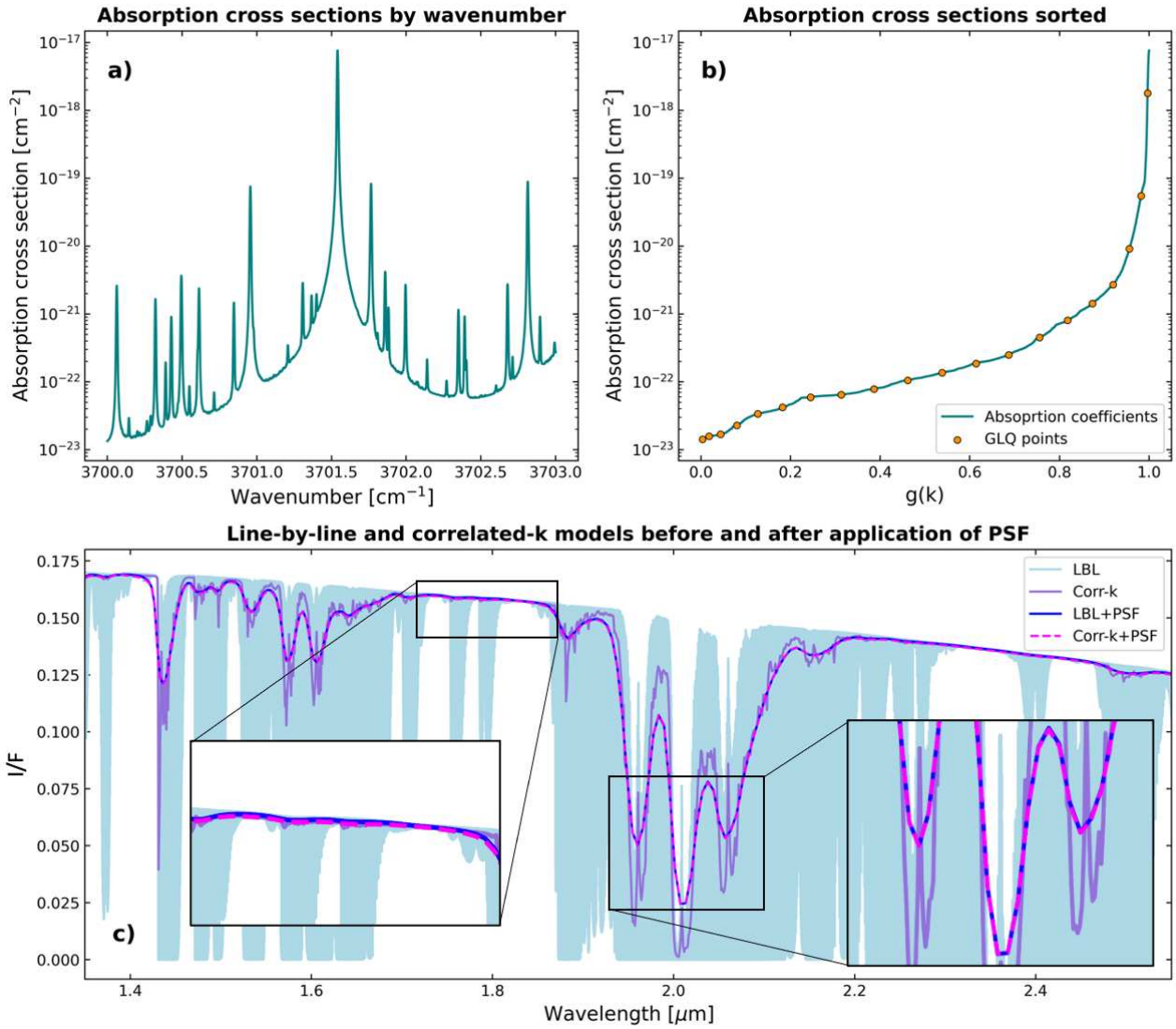

Figure 5.2: Demonstration of the correlated-k principle. CO_2 absorption coefficients are shown as a function of wavenumber in a), sorted by magnitude in b), and panel c) depicts the synthetic spectrum produced by the radiative transfer scheme with the line-by-line approach compared to the correlated-k method, before and after the application of the PSF.

Going forward, all model spectra have been computed using the correlated-k approach with these settings. The above work was done with only one absorbing gaseous species, CO_2, but CO and H_2O also have absorption lines within the wavelength interval of SuperCam IRS. In order to include these, we use Beer-Lambert's law with a correction factor of 1.7 for water line broadening in the 1.38 µm range where a strong water vapor band resides. Beer-Lambert's law states that the total optical depth of a slab of atmosphere is the sum of the individual optical depths of each gas, as shown in Equation 5.3;

$$\begin{aligned}\tau &= \sum_{i=1}^{N} \tau_i \\ &= \sum_{i=1}^{N} \sigma_i \cdot \int_0^L n_i(z)dz.\end{aligned} \tag{5.3}$$

Here, τ is the total optical depth, τ_i, σ_i and n_i is the optical depth, absorption cross section and number density, respectively, for species *i*, and *L* is the path length of the beam of light through the slab. Implementing this into the correlated-k scheme is done by doing the process outlined above for each species separately, and creating a total optical depth for each atmospheric layer as input into the radiative transfer code. In the following, H_2O and CO are also incorporated. The absorption coefficients for all the gases are sorted individually for all spectral intervals in all layers, and combined using equation 5.3 to find the total optical depth due to the gases of each layer.

5.1.2 Implementing dust

Aerosol scattering controls the shape of spectra in the infrared, and therefore contributes significantly to the overall form the IRS spectra (see Figure 3.7) in addition to instrumental effects. Creating the average ratio spectra, as seen in the bottom panel of Figure 3.7, removes much of the dust and instrumental effects that shape the continuum, but some artifacts of uncertain origin remain. It is therefore a crucial step to include aerosols into our model to simulate the observed IRS spectra as closely as possible, in order to accurately perform the gas retrievals. As a first step, water ice is ignored in our model, as we wish to properly quantify the effect of the different dust parameters on the continuum before adding more complexity.

The pyRT_Disort tool requires three dust parameters to initiate DISORT and the radiative transfer; a dust grain size, vertical distribution, and total opacity. As with temperature, pressure and gas profiles, the MCD was used to obtain a dust effective radius climatology for Jezero crater. The dust vertical profile is simulated using the Conrath approximation (Conrath, 1975). Opacity values are provided by ZCAM on Perseverance, which performs almost daily opacity measurements at multiple wavelengths (Lemmon et al., 2022). We select the opacity value closest in local time to when the passive sky was performed within ± 5 days. Figure 5.3 shows the selected opacity measurements from ZCAM and the MCD dust radii on the sol of each passive sky observation, as a function of sol and Ls. A seasonal trend in both parameters is evident, with both opacity and dust size maxima occurring during NH fall. There was a sudden and brief increase in the observed tau around Sol 578, where the total opacity doubled, before quickly dropping to normal levels.

Dust vertical distribution: The Conrath approximation

The Conrath approximation of the dust vertical distribution is an idealized vertical profile determined by the competing rates of sedimentation and vertical atmospheric diffusion. The ratio between these rates is the Conrath parameter, and if the dust mass mixing ratio is known at the surface, one can compute the dust altitude profile using Equation 1.1. The dust profiles shown in Figure 5.4 have all been normalized by the surface mixing ratio, and are shown for a selection of Conrath parameter values. A Conrath parameter equal to zero equates to a uniform mixing ratio, while larger values yield a progressively confined surface layer.

The Conrath profile was used as a first estimate as the pyRT_Disort tool has a built in option for this approximation. Conrath parameters can in theory also have negative values, but pyRT_Disort does not currently allow this. Negative values will create vertical profiles where the dust mixing ratio increases with altitude, a configuration which has been observed on Mars (Heavens et al., 2011). Due

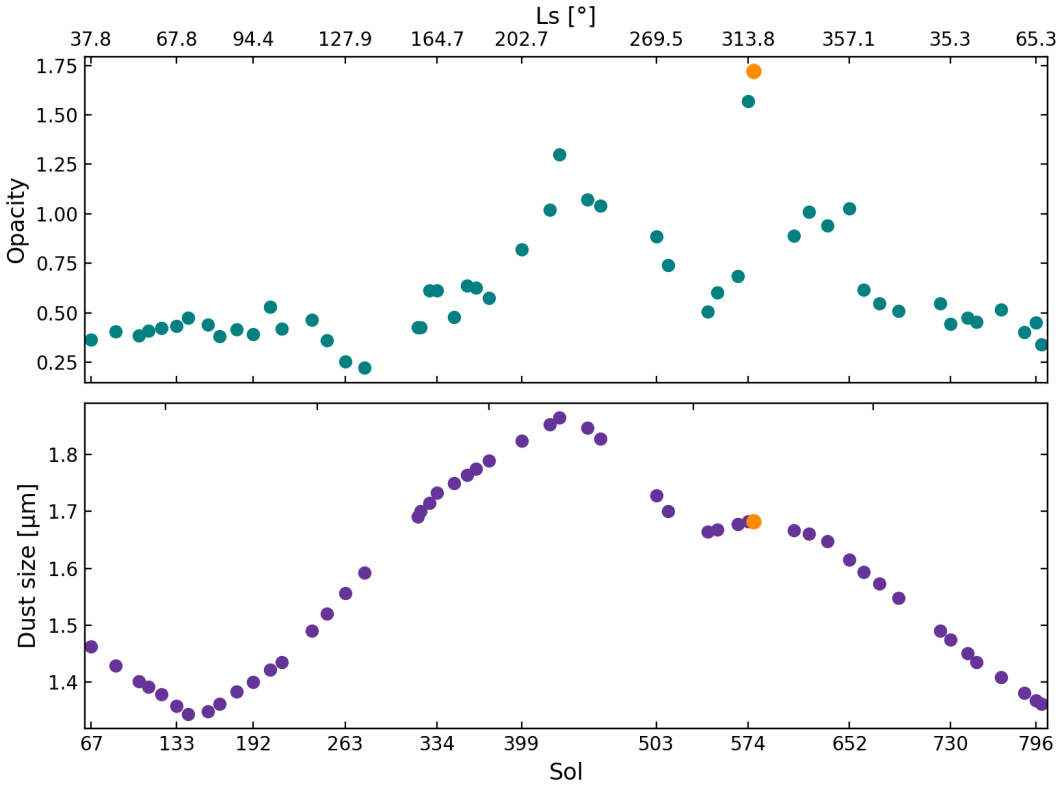

Figure 5.3: Dust conditions in Jezero crater. Figure shows the selected ZCAM opacity values (top) and the MCD effective dust radius values (bottom) for each passive sky observation. The bottom x-axis in both panels indicates the Sol number, while the top x-axis shows the season. Sol 578 is indicated in orange.

to this shortcoming in the pyRT_Disort tool, and other drawbacks of using the Conrath approximation (for example, it does not take into account dust removal from the condensation of volatiles), we are preparing to implement other means of modeling the dust vertical profile.

Effect of varying dust parameters

To investigate how dust size, vertical distribution and total opacity affect the observed spectrum, simulations are made with varying values for each of these three parameters. The resulting spectra (modelled for low elevation only) are displayed in Figure 5.5. The dust parameter values are indicated by the figure label, they correspond to half, equal to, and twice the values from the MCD (for dust size) and ZCAM (opacity). The Conrath parameters are selected based on the dust profiles shown in Figure 5.4, to cover a wide range of distributions.

Changing the total opacity and dust size significantly changes the continuum, in magnitude and shape, respectively, as can be seen from panel A). The continuum level drops with lower opacity, and the tilt of the continuum goes from a downwards slope towards longer wavelengths for small dust sizes, to a flatter spectrum for larger grains. Changing the Conrath parameter, on the other hand, has an insignificant impact on the continuum, but changes the gas band depths as visualized in panel C), with more shallow bands for higher values which corresponds to a more confined dust distribution.

5.1.3 H_2O and CO modeling

In addition to the dust parameters described above, the model also requires vertical profiles of temperature, pressure and the relevant gases. We use profiles from the MCD for all of these, at the location

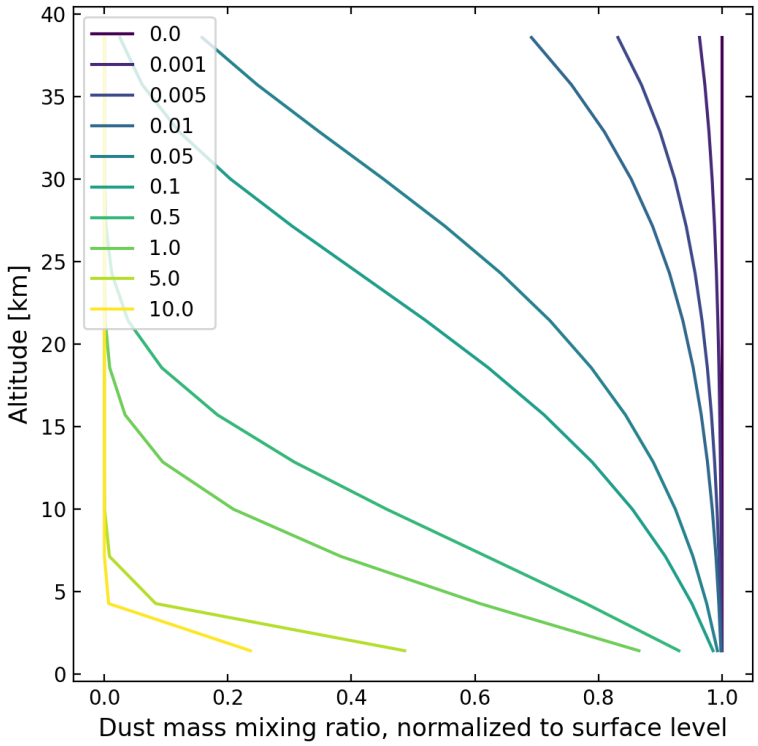

Figure 5.4: Vertical profiles of dust mass mixing ratios in ppmv. The profiles are shaped by the Conrath parameter, indicated in the figure legend. Larger Conrath parameters correspond to dust being more confined to low altitudes.

of Perseverance and at the time of year corresponding to the appropriate sol. In our current example, this is Sol 578 at Ls=316°, 10 am, as shown in Figure 5.6.

We then vary the water vapor and CO abundances to investigate how this would manifest in our simulated IRS spectra. The result is shown in Figure 5.7, where we have produced synthetic spectra with no water and CO (solid lines), with half the amount compared to the MCD (dashed), with equal the amount (black solid line), and twice the amount (dotted lines). When water is varied, the CO is kept as suggested by the MCD, and vice versa.

There are no deep features of water vapor or CO in the wavelength interval covered by IRS as shown in Figure 5.7. However, there are regions where water vapor (in blue) and carbon monoxide (in pink) displays broad and shallow absorption features. Three broad H_2O features are within the range of IRS. One at edge of the spectrum at $2.5\,\mu\mathrm{m}$ will most likely be unusable as IRS spectra tend to be noisy due to AOTF instability issues towards the end of the acquisition. The band at $1.8\,\mu\mathrm{m}$ lies in the wing of a CO_2 band, and is also most likely unattainable with our spectral resolution. That leaves the $1.38\,\mu\mathrm{m}$ band as our best option, the same band used by SPICAM and MAWD. It causes a significant depression in the spectrum with respect to the continuum, and is not contaminated by the CO_2 line at $1.43\,\mu\mathrm{m}$. The CO band at $2.35\,\mu\mathrm{m}$ lies in a region with no other gas absorption bands, so we are optimistic that for certain passive sky observations, even such a shallow absorption band should be above our noise limit, and CO abundances should be retrievable.

5.1.4 Final synthetic spectrum

To assess how well the forward model is able to reproduce what is observed by SuperCam, we compare the passive sky observation from Sol 578 with the synthetic spectra created using MCD and ZCAM values appropriate for that sol. The result is displayed in Figure 5.8, where the high and

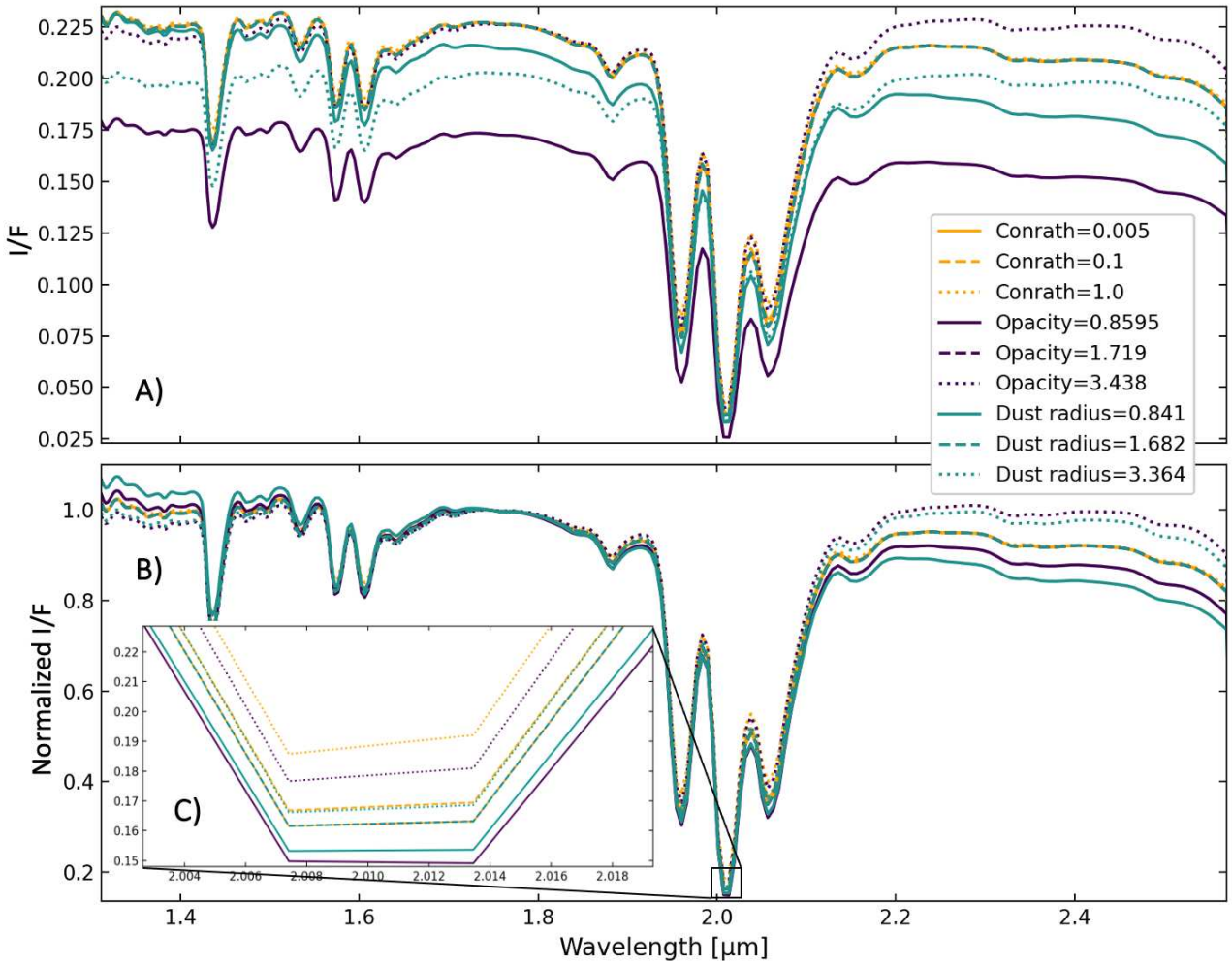

Figure 5.5: Synthetic spectra for a selection of dust parameter values. The colors represent spectra with varying total opacity (purple), dust size (teal), vertical distribution (yellow). The default setting for each parameter is 1.719, 1.682 and 0.005 respectively, and varied independently according to the legend. A) shows the synthetic spectra, in B) the spectra are normalized by the continuum value at 1.75 microns, and C) shows a zoomed in view of the central lobe of the CO_2 tripled band. Only low elevation simulations are shown.

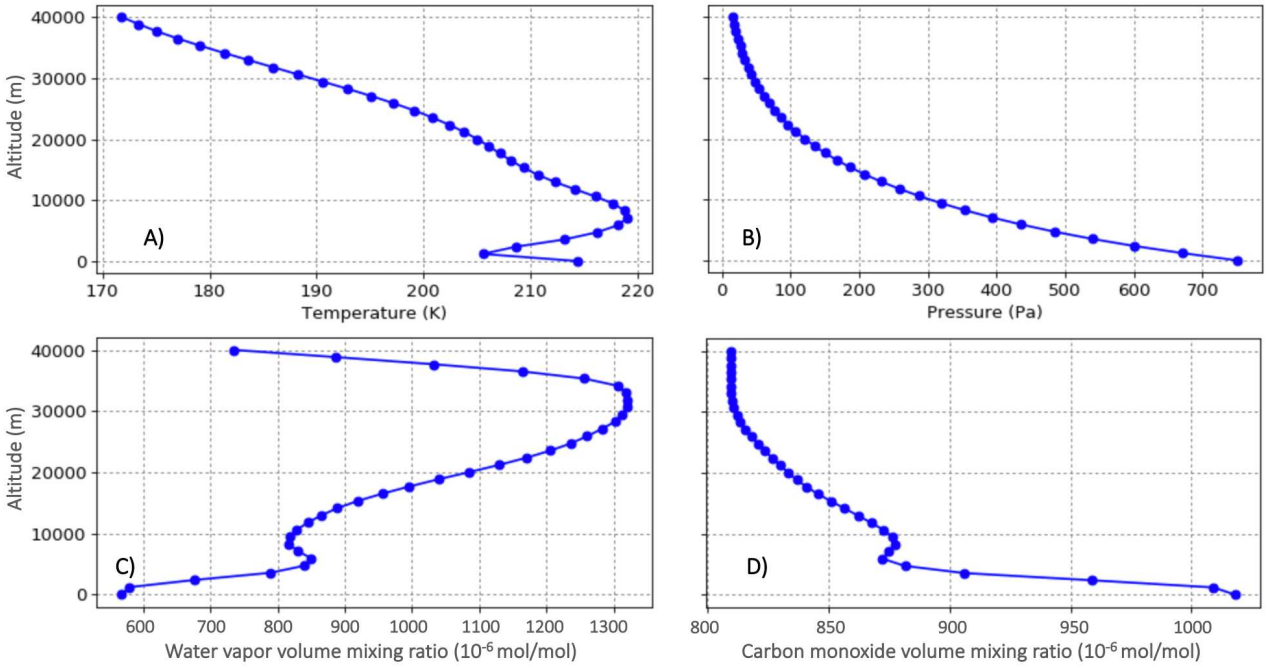

Figure 5.6: Atmospheric conditions in Jezero crater, simulated for Sol 578 at 10 a.m. Figure shows vertical profiles of A) temperature, B) pressure, C) water vapor, and D) carbon monoxide shown from 2 m altitude (rough height of SuperCam on the mast) to 40 km. Figure made using the MCD v6.1 web interface (https://www-mars.lmd.jussieu.fr/mcd_python/).

low elevation observations and simulations are shown individually in the top panel and then the ratio spectra are shown in the bottom panel.

The high and low elevation simulations should not be directly compared to the high and low elevation observations, as part of the pre-processing includes division by a calibration target spectrum, and some other adjustments. These are all multiplicative processes however, and are therefore removed when the ratio spectrum is created. From the passive sky, the low elevation average spectrum is brighter overall than the high elevation spectrum, the opposite situation from the modeled spectra. This can be explained by the choice of dust size and opacity, which, as was demonstrated in Figure 5.5, have significant impacts on the continuum.

The simulated and observed ratios of spectra are different in terms of continuum shape, band depths and shapes. Especially the CO_2 triplet band stands out, clearly appearing much deeper in the model, but also more asymmetric than whats is observed. This is reminiscent of the initial problem of fitting the CO_2 band, and even though progress has been made in replicating the observed spectrum, issues still remain.

CO_2 triplet asymmetry

This side-lobe asymmetry was investigated for all passive sky observations. The ratio between the band depths of the central lobe to each of the side lobes was compared to those of a simple model atmosphere containing only CO_2. The model does not include dust and does not involve radiative transfer. The modeled and observed lobe ratios are shown in Figure 5.9. The observed ratios are calculated on the average low elevation spectra separately, and on the elevation ratio spectra. The model lobe ratios are calculated for elevation ratio spectra only.

All model ratios (green lines) are significantly lower than all data ratios, indicating that the observed side-lobes are similar in depth to the central lobe, there is also no significant difference in lobe asymmetry between the ratios calculated on low elevation spectra only and elevation ratio spectra. The ratios for the right and left side-lobe are observed to be fairly similar, while in the model they are

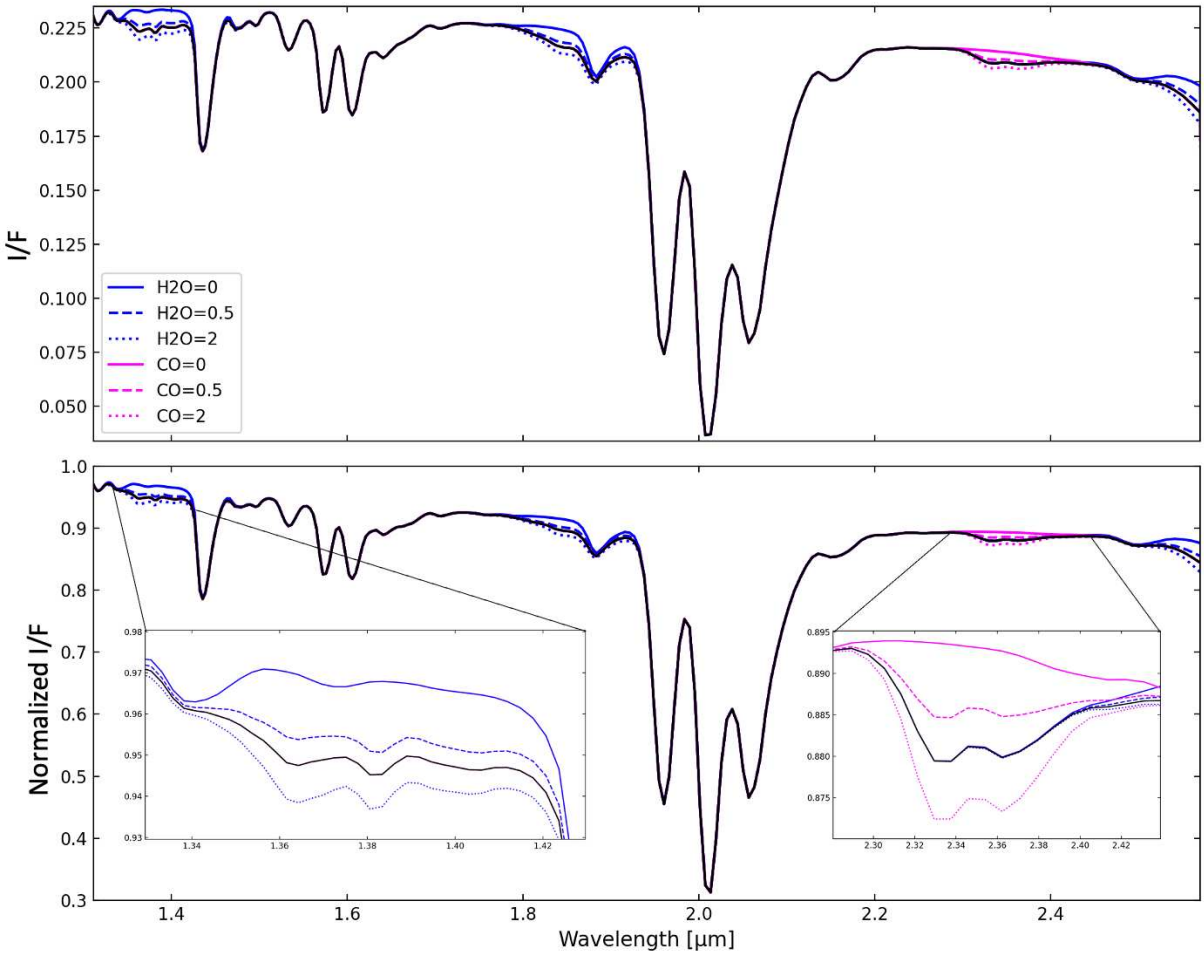

Figure 5.7: Synthetic spectra for a selection of trace gas abundances. The colors represent spectra with varying water vapor (blue) and carbon monoxide (magenta). The numbers in the legend refers to the factor multiplied to the MCD vertical profile for each gas, so that 0 indicates no gas present, 0.5 is half the amount suggested by the MCD, and 2 is twice the amount. Top panel shows simulated low elevation spectra, while the bottom panel shows low-to-high elevation ratios. The embedded figures are zoomed in views on the 1.38 μm water band and the 2.35 μm CO band.

separated by an an equal distance at all times with the right side-lobe having a greater band depth. The model ratios also seem to follow a seasonal trend which has no discernible equivalent in the observed side-lobe ratios. Clearly there is a systematic difference in the modeled and observed CO_2 triple band symmetry. By visual inspection of Figure 5.8, the side-lobes in the model produced with the full forward model appear relatively equal. We are in the process of reproducing the results in Figure 5.9 using the full forward model for all sols, to further investigate the asymmetry problem.

5.2 Minimization scheme

In order to accurately retrieve trace gas abundances from the SuperCam spectra, we need to first retrieve CO_2, as we will ultimately scale our trace gas abundances to the CO_2 abundance. As was shown in Figure 5.5, the CO_2 band shape and depth depends on the dust parameters, so as a first step we need to determine the three dust parameters. In the case of all of these retrievals, the number of parameters does not exceed the number of independent measurements. Therefore, the best-fit model is estimated through the usual χ^2 cost function. The solution for the best fit model is found

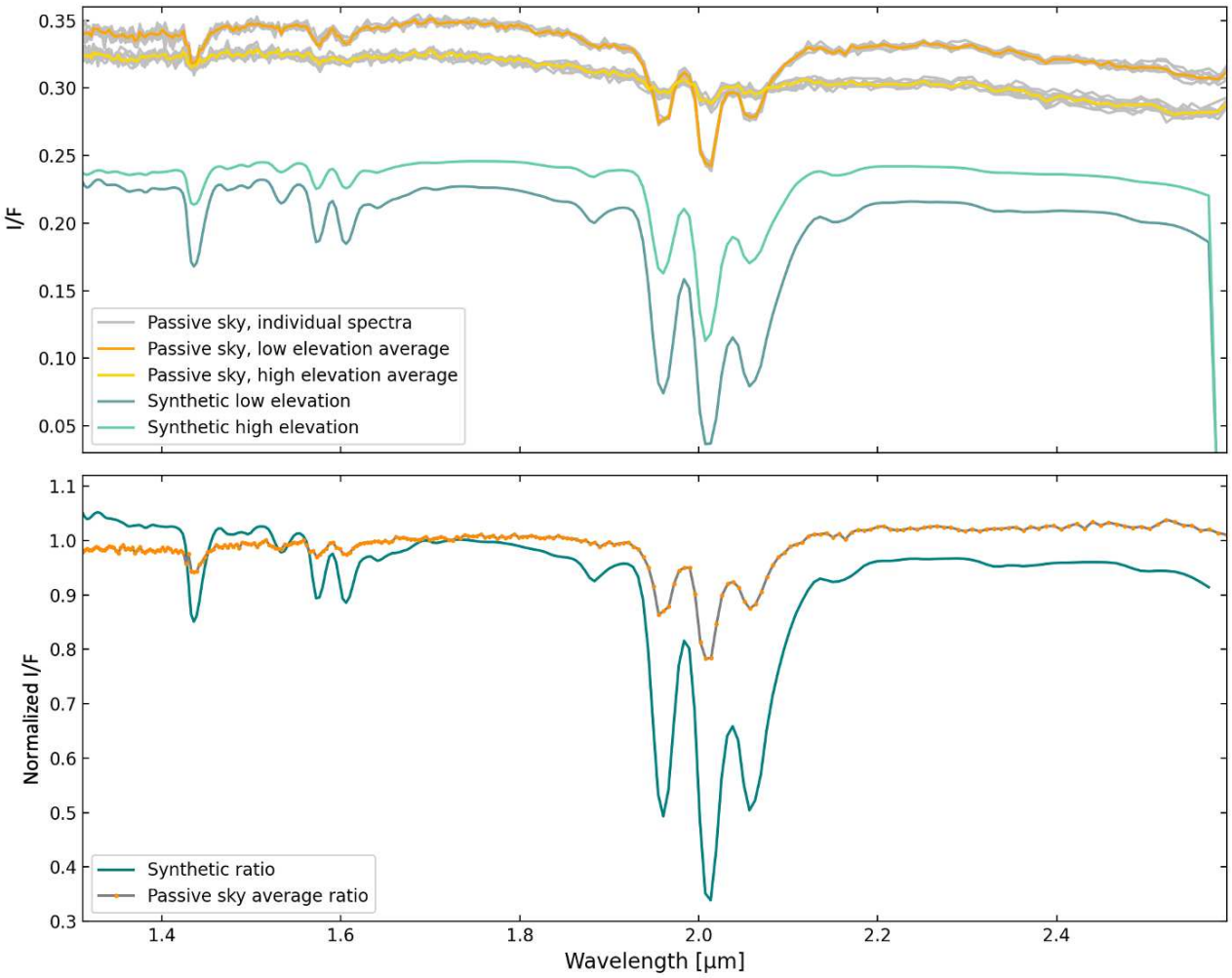

Figure 5.8: Observation and simulation of Sol 578, for low and high elevation spectra (top panel) as well as the ratio spectrum (bottom panel). The ratio spectra have both been normalized by their respective values at 1.75 µm. All observations are shown in hues of orange (and grey for the individual spectra), and the simulated spectra are shown in hues of teal.

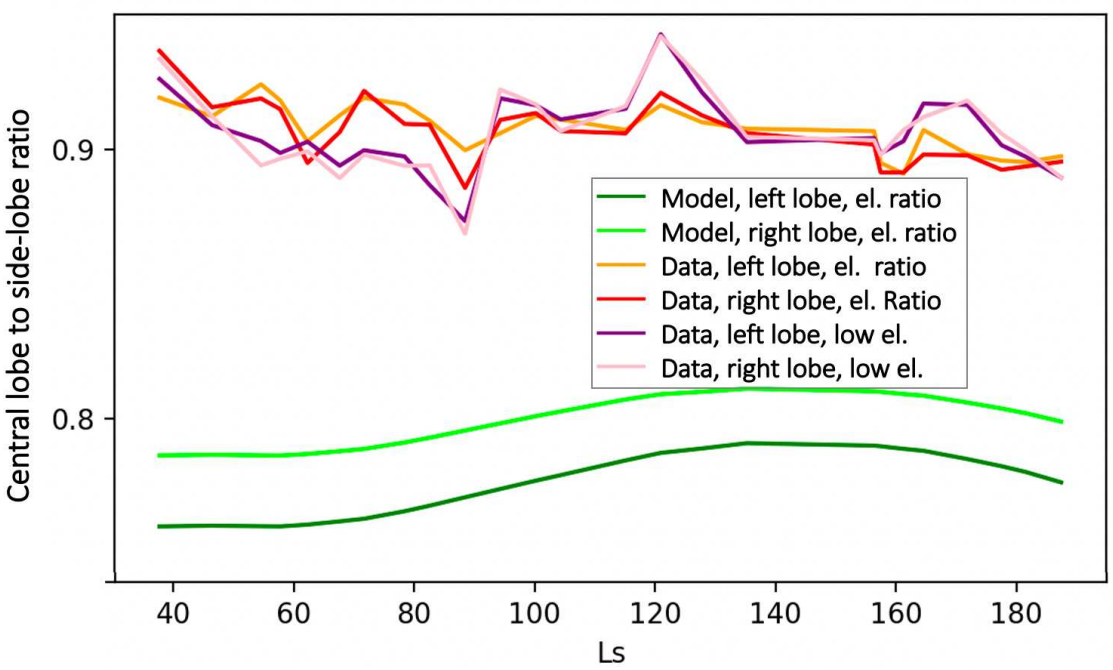

Figure 5.9: CO_2 triple band asymmetry investigation. Lines show the band depth ratios between the central lobe and each of the side lobes, computed from observed low elevation spectra (pink, purple), observed ratioed spectra (orange, red), and model spectra (green).

with the Powell conjugate direction method. Powell's method calculates the local minimum of a continuous function, and works well when the function does not have a mathematical definition as it is not necessary to calculate derivatives. This also makes Powell's method not very computationally expensive.

To create the synthetic spectrum on which to perform the retrieval, a ratioed spectra taken at two elevation angles is created just as for a passive sky observation. The model described in the previous section is run twice, one for each elevation, and the final model ratio for one example is as depicted in Figure 5.8, for a set of dust and gas parameters as suggested by the MCD and ZCAM. There is a significant difference in magnitude of the observed ratio compared to the synthetic spectrum (not evident from Figure 5.8 as there are normalized to the continuum in that case), which is clear already from the individual high and low elevation spectra. The mean value of the observed and simulated ratio spectra should be relatively similar, so we decided to introduce a shift, where we apply an additive constant to the ratio spectra in order to lower it towards the model ratio. We still need to investigate further if this shift is present for all observations, as so far only a small number have been studied in detail.

The minimization is performed in multiple steps, currently a total of three; 1) dust parameters + shift, 2) CO_2, 3) trace gases. In the first step, we will keep all gas abundances as suggested by the MCD, and retrieve the Conrath parameter, effective dust radius, opacity, and the shift values. We are still investigating whether doing the fitting across the entire 1.3-2.6 µm interval can be beneficial, as we are then fitting the dust parameters to the CO_2 band shape, or if it will suffice to select a CO_2 line near the water line at 1.38 microns, for example the 1.43 micron band. The rationale for only using these is that since the H_2O lines and this weak CO_2 line are optically thin, their column densities are to first order proportional to the line depths. Uncertainties due to the effects of surface and atmospheric properties, including dust opacity and the airmass factor are minimized, and we might not need to retrieve the dust parameters at all. By dividing the depth of a given water line by the depth of a nearby CO_2 line of comparable intensity, a reliable determination of the H_2O mixing ratio can be obtained.

5.3 Discussion and summary

5.3.1 Data handling

Due to glitches and power failures, many spectra are discarded when the strict selection scheme described in Section 3.2.2 is followed. In the future, we hope to salvage many of them by correcting for the effect of the failures when possible, and thereby increase the signal to noise as more spectra in each passive sky will be available to create the average spectrum for each elevation angle. The correction for the power failures seems easiest to correct, as it seems the spectrum is simply shifted by a constant factor after the failure occurred. If this factor is identified the spectrum can be restored to its original magnitude.

During the SuperCam passive sky activity, the camera changes elevation twice, acquiring spectra at the low elevation angle at the beginning and end of the observation (four spectra each time), and at high elevation angle in the middle (eight consecutive spectra). This means that about 10 minutes have passed between the first and last spectrum at each elevation, and the sky illumination may have changed. This has happened on several sols, for example on Sol 121, as visible in Figure 3.6 and on Sols 111 and 364 shown in Figure 3.7, where the low elevation spectra are bunched together in two distinct groups. At the moment all spectra at each elevation angle are averaged together, though in the future this will be changed so that the passive sky measurements are split in two segments, with four low and four high elevation spectra in each.

5.3.2 Retrieval routine

With respect to the synthetic spectrum, several ways of improvement are already in the process of being implemented;

- the Conrath parameter is deemed to not be very suitable to describe the dust vertical profile in Jezero crater, and a climatology of profiles from the MCD will be created, scaled to fit the tau observed by Perseverance/ZCAM,
- the linelist from HITRAN 2016 will soon be updated to HITRAN 2020,
- ice aerosols will be included in the forward model,
- and the MCD pressure profile will be constrained using Perseverance/MEDA pressure data.

To reduce the computational time even more than what has already been achieved with the correlated-k method, we could split the correlated-k bands in two, applying the Gauss-Legendre quadratures to the two parts separately. This will allow for a lower total number of roots, as the two different regions (the lower, more linear part of the sorted absorption coefficient, and the much more exponential part above e.g. 0.9) are more easily approximated separately.

We speculate that some of the difference in observed and simulated CO_2 band shapes might stem from either some non-multiplicative part of the pre-calibration, or some signal contribution from stray light. This problem must be solved if the CO_2 triplet band is to be used for retrievals, and so both options are under investigation. However, the problem can also be avoided by using another CO_2 line, for example the single line at 1.43 microns.

5.3.3 Summary

After roughly 2.5 years on Mars, a total of 64 passive sky observations are now available from SuperCam. A simple processing and data selection scheme has been designed, but further work will be done to maximize the number of spectra suitable for analysis. Most observations are subject to the

occurrence of some type of failure associated with the AOTF, but a modification to the activity has been made, and recently implemented, to avoid failures in the future. After a first test on Sol 841, the solution seems to be a success.

A first version of a retrieval routine has been developed, using the correlated-k method to include CO_2, H_2O and CO in the synthetic spectrum, along with dust. Ice is for the moment neglected. DISORT is used to handle the radiative transfer through a python-wrapper. Powell's method is currently used to find the best-fit model which is estimated through the common χ^2 cost function. So far, we have performed testing to understand the impact on the spectra of varying dust parameters such as the dust grain size, total opacity and the vertical distribution, along with investigating expected gas absorption signatures. This is very much a work in progress, where a continuous effort of testing and verification is still ongoing, so that at the point of writing, no reliable retrievals have been performed yet. Several points of improvements have already been identified and will be implemented in the near future.

Chapter 6

Space weather and Mars' magnetic environment

As mentioned in Chapter , my curiosity about planetary atmospheres and their interactions with the space environment has guided all my educational choices, the first of which was choosing my first research project, my master thesis, which focused on the dynamical and chemical effect of energetic particle precipitation in the Earth's atmosphere. Though not surprising to my supervisor Dr. Patrick Espy, I was astounded by the magnitude and duration of ozone depletion due to auroral particles. This, combined with an unforgettable six months spent in the Arctic and an awareness of the importance of knowledge of space weather for space exploration and eventual human exploration of Mars, laid the foundation for my interest in space weather, and Martian space weather specifically. I nurtured this interest through an ESA internship before starting this PhD, and continued collaborations on projects related to the long-term monitoring of space weather around Mars through my years in France. In the summer of 2022, Tim McConnochie and I started discussing the possibility of observing Martian aurora with SuperCam, and I was intrigued mostly by the science, but also by the opportunity to plan and propose our own observation campaign.

The following chapter includes three independent projects related to heliospheric and Martian space weather. Two I have conducted myself, and one was performed by an intern student of mine. The galactic cosmic ray study was initiated before the start of this PhD, but was completed during it. The other projects are either a continuation of that first study, or completely separate projects that I have initiated or participated in during my PhD. As they are not part of the main focus for my thesis, they are all collected here in a comprehensive summary of all the work I have conducted related to space weather.

6.1 Introduction to space weather

Heliospheric space weather refers to the dynamic plasma and particle conditions within our solar system that are created by the Sun's activity and the background galactic cosmic ray (GCR) radiation. The Sun is the primary source of energy within the solar system, and it continuously emits a stream of electromagnetic and particle radiation, known as the solar wind. The solar wind is a plasma consisting of protons, electrons and alpha particles originating in the solar corona. The concept of the solar wind was hypothesized by Dr. Eugene Parker in 1957 (Parker, 1958), to scathing comments from the scientific community. Yet after the launch of the Mariner II Venus mission, it unambiguously detected the solar wind and measured its properties Snyder et al., 1963. Since then much knowledge has been gained; we know that the solar wind properties vary, and depend on solar radial distance, longitude and latitude, the solar cycle and solar rotation (Richardson and Kasper, 2008; Schwenn, 2007). On average though, the particles have energies in the range of 0.05-$10\,\mathrm{keV}$, and travel with a speed of between 400-$800\,\mathrm{km/s}$ (Schwenn, 2007). As the Sun rotates with a 27-day period, its inherent

magnetic field twists into an Archimedean spiral called the Parker spiral (visualized in Figure 6.1), becoming the interplanetary magnetic field (IMF). The IMF is considered to be "frozen in" with the solar wind, meaning the solar electric and magnetic fields are carried by the plasma fluid motions (Alfvén, 1942).

This uninterrupted outflow of plasma frequently contains high-speed streams (HSS) of high density plasma originating from coronal holes. These holes appear as dark spots in X-ray or UV images, as they emit less at these wavelength. The plasma here is cooler and less dense compared to the surrounding corona, and field lines are openly connected to the IMF (Zirker, 1977). Coronal holes are cyclically concentrated in the polar regions during the solar minimum phase, and migrate to lower latitudes with rising solar activity, crossing the equator and congregate in the polar regions again (Maghradze et al., 2022). With a lifetime anywhere from a few weeks to several months, they are frequently present near the equatorial plane, causing HSS and high density plasma waves to sweep past the planets as the Sun rotates. The high-speed streams interact with the upstream slower streams and create regions of high particle number density and enhances the magnetic field strength. These regions are called co-rotating interaction regions (CIR) and when sweeping past the Earth, often induce geomagnetic storms (Gerontidou et al., 2018), and could also possibly be a source of aurora on Mars (Lee et al., 2018).

On top of the solar wind plasma and its frozen-in IMF, transient solar events add to the dynamic nature of space weather. Solar eruptions such as flares, coronal mass ejections (CMEs) and solar energetic particle events (SEPs) cause short-term disturbances in the plasma environment. More on these events in Section 6.1.2.

The last contribution to space weather is not of solar origin, but penetrate into our heliosphere from beyond our solar system. These particles travel at a considerable fraction of the speed of light, and mostly consist of protons. Galactic cosmic rays (GCRs) can be divided into a high and low energy component, where particles of lower energy are thought to be from sources within our galaxy (Blasi, 2013), while particles with extremely high energies are believed to be of extra-galactic origin (The Pierre Auger Collaboration et al., 2017). More details can be found below, in Section 6.1.1

6.1.1 Galactic background radiation

The heliosphere is actively shielding our solar system from much of the GCR radiation, yet not all incoming particles are deflected. Only higher-energy particles are able to penetrate into the heliosphere, causing a depressed GCR intensity within the heliosphere compared to beyond it (Wibberenz, 2002).

Three factors influence the modulation of GCR intensity within the ecliptic plane: time, heliocentric distance, and heliomagnetic longitude. Longitudinal effects are considered to be small compared to temporal and radial variations (De Simone et al., 2011). Particles with energies above than $30\,\mathrm{GeV}$ reach the inner solar system, but particles with lower energy are deflected by the solar wind (Blasi, 2013), causing an energy gradient as a function of solar distance. In this way, the GCR particle population that reaches a local planetary environment is filtered at multiple stages; the extra-galactic particles are filtered first upon entering the Milky Way, then both galactic and extra-galactic particles are filtered when entering our heliosphere, and lastly if penetrating a magnetosphere and traversing an atmosphere.

Temporal variations are due to the 11-year sunspot cycle and the 22-year magnetic polarity cycle of the Sun, which are superimposed on each other. As the Sun undergoes this cycle, the IMF, the sunspot number (SSN), and solar wind parameters change (Richardson et al., 2001). As a result, the inward diffusion of GCRs is modulated by the convection of the expanding solar wind and the particle drift on the IMF, giving rise to a GCR flux varying with an 11-year period (Gazis, 1996; Modzelewska et al., 2019).

The relationship between GCRs and the solar cycle has been observed at and around the Earth since the 1950s (Alania et al., 2014). A network of ground-based neutron monitors (NMs) is used

to study the temporal modulation of GCRs by measuring the flux of cascading particles produced by cosmic rays colliding with atmospheric atoms (Engel et al., 1992; Usoskin et al., 2017). In addition to exhibiting a temporal anti-correlation with solar activity, the GCR intensity also varies with heliocentric distance, increasing with 3–4% per AU (De Simone et al., 2011; Vos and Potgieter, 2016; Honig et al., 2019; Modzelewska et al., 2019).

The GCR environment at Mars has been much less studied, and no long term, systematic investigations have been conducted. In part this is because instruments with this capability have not continuously been operating at Mars. It was shown in Jiggens et al. (2019) that engineering housekeeping data has the potential of being a useful quantitative indicator of energetic particle incidents. A proof-of concept study was performed in Knutsen et al. (2021b), showing that such parameters could discern the solar cycle modulation and heliocentric distance variation of GCRs at Mars. The housekeeping parameter is further discussed in 6.2.1, while the results of the study are presented in Chapter 6.2.2.

6.1.2 Transient solar particle events

GCR radiation, although varying, make up a relatively stable level of background radiation in the heliosphere along with the quiescent solar wind. Major disturbances come in the form of transient solar particle events (SPEs) containing solar energetic particles (SEPs). SEPs are accelerated near the Sun, to energies ranging from the suprathermal (few keV) up to relativistic ($\sim$few GeV) velocities. In general there are two types of SPEs leading to SEPs; impulsive and gradual events, where the SEPs are accelerated by solar flares or coronal mass ejections (CMEs) respectively (Cane et al., 1986). The two types are illustrated in Figure 6.1, where it is illustrated that flare-accelerated events are much narrower and thus requires a direct magnetic connection between the relevant field lines and the planetary body if SEPs are to be transferred to it. CME-accelerated particles however cover a much broader area, and the chances of a planetry body intercepting these particles is greater. Often the two types occur simultaneously, and can be hard to disentangle. Yet, when isolated events happen, impulsive events tend to be short in duration (<1 day), while gradual events last for several days. How these energetic particles deposit their energy in planetary atmospheres has been extensively studied at Earth, and is becoming an increasing field of focus at Mars.

Solar flares have been observed for centuries, with the first known event being recorded in 1859, known as the Carrington Event, named after the Englishman Richard Carrington who is credited for cataloging it. Carrington was counting dark solar spots at the time (the nature of which was not understood at that point), when two intensely bright patches appeared. The bright spots remained for less than handful of minutes, and diminished rapidly (Carrington, 1859). Within 18 hours, Earth was engulfed in perhaps the most powerful geomagnetic storm ever. Compasses became useless and erratic, the skies lit up with intense aurora as far south as the Caribbean, and telegraph operators were unable to reach each other.

CMEs were discovered and established as separate, gradual particle acceleration events during the late seventies and early eighties (Kahler et al., 1978, 1986). It was found that CMEs can erupt without an accompanying solar flare, and even originate from inactive regions on the Sun. At the same time, flares may occur without any following CME. CMEs may produce SEP events, but not always. Some explanations as to why particle enhancements are not always observed are; the release region may not be magnetically connected to the observer region, inefficient acceleration at the shock front, or there were no particles released at the time of the eruption that could provide a seed population for shock acceleration (Lario et al., 2020).

Impulsive and gradual events can occur separately, but the stronger the event the more likely it is to encompass both types. This is called "big-flare syndrome" and is thought to occur because during strong events there is a massive reorganization of coronal fields leading to many different phenomena in great profusion. The stronger the CME, the more likely it is to have a higher proton-to-

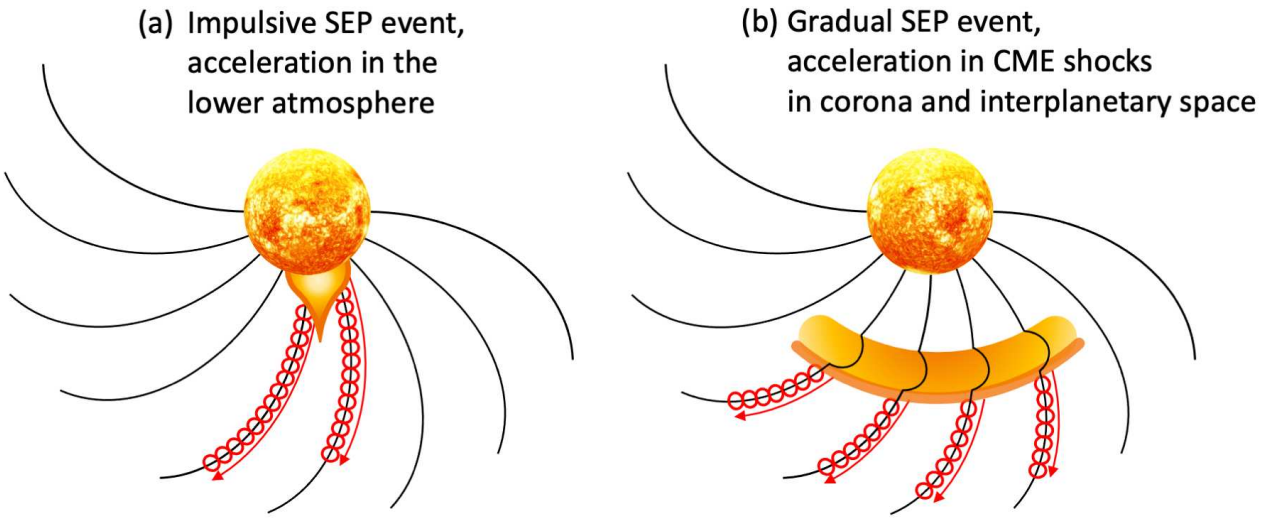

Figure 6.1: Illustration of the different particle acceleration mechanisms at the Sun. Black lines indicate the rotating IMF leading to the Parker spiral, and red helixes indicate charged particles being accelerated away from the event region. The orange/yellow structures represent a solar flare and subsequent impulsive SEP event (a), and a traversing CME and thus a gradual SEP event. The figure illustrates how a CME-driven shock wave accelerates charged particles and populates interplanetary magnetic field (IMF) lines over a large longitudinal area, while the solar flare populates only those IMF lines well-connected to the flare site.

electron density (Cliver and Ling, 2007). However, the mere fact that two phenomena occur together in many big events does not necessarily mean that they are causally related (Reames, 1999). In order to arrange and put single solar eruptions in context, the National Oceanic and Atmospheric Administration devised a category system for solar flares. The categories, from weakest to strongest, are named A, B, C, M and X, and is a logarithmic scale, meaning that a B flare is ten times stronger than an A flare. Within each category is a finer scale of 1 to 9, but the X class has no upper limit. C-class flares are in general too weak to cause much effect on a planetary system.

The distinctions between impulsive and gradual events has however recently become less clear. More recent observations indicate that composition, energy and temperature differences are more blurred than initially thought, suggesting that many gradual events for example accelerate remnant interplanetary material from recent impulsive events, or that gradual events often include direct contributions from flare-accelerated particles (Desai and Giacalone, 2016). Another idea has been put forth that rather than there being two distinct types of events, there is a continuum where smaller CMEs are associated with soft (A, B, C type) flares which are often undetected (Vršnak et al., 2005).

6.1.3 Influence of particle radiation on the Mars local environment

Mars is a unique planet in our solar system with respect to planetary magnetospheres as it is (as far as we know) the only planet with a hybrid magnetosphere, composed of an induced field and the crustal remnants of a past internal dynamo. Mars no longer has an internal dynamo capable of producing a global magnetic field, but remnants of it remains as local regions of magnetized crust (Acuña et al., 1999; Lillis et al., 2008). Figure 6.2 visualizes the Martian magnetic environment, showing the planetary bow shock where the solar wind drops from supersonic to subsonic velocities and the general shape of the induced magnetosphere and crustal fields. Any planetary body with an atmosphere in orbit around a star will create an ionosphere when solar extreme UV and X-ray radiation interacts with the top layer of the atmosphere, leading to photo-ionization of atoms and molecules. The vertical structure of the ionosphere has a strong diurnal dependence as can be seen

in the two panels of Figure 6.3, where the dayside main layer is produced by direct solar UV and X-ray radiation and is roughly an order of magnitude stronger than the nightside ionosphere which consists of separated varying layers created by the transport of injected electrons, SEPs, GCRs and interplanetary dust. The ionized upper atmosphere then becomes a conductive plasma, and interacts with the solar wind plasma, resulting in an induced magnetosphere.

In addition to the atmospherically induced magnetic field, Mars has localized regions of magnetized crust. Prior to the launch of MGS in 1996, the magnetic field of Mars was not well known and its origin was controversial. With MGS, the crustal fields were discovered (Acuña et al., 1999) and knowledge of the overall magnetosphere increased dramatically, by measuring over a thousand current sheet crossings (Halekas et al., 2006) and doing detailed mapping of the crustal fields (Mitchell et al., 2007). It was found that the configuration of Mars's induced magnetosphere is consistent with IMF field lines being draped around the planet and pulled back to the center of the tail by magnetic tension forces. MGS results also indicate that over crustal field regions, the current sheets are pushed above MGS altitudes. These results suggest that the tail region is highly condensed and much more chaotic than illustrated in Figure 6.2, and that magnetic reconnection processes are likely central for particle transport between the draped solar wind fields and crustal fields. With the arrival of MAVEN our understanding of Mars's magnetosphere, ionosphere and upper atmosphere (and their coupling) have increased further. We now have detailed three-dimensional models of the induced magnetic structure around Mars (Zhang et al., 2022a), and a third ionospheric layer created due to ablation of interplanetary dust was discovered (Crismani et al., 2017) (also see Figure 6.3, nightside panel) and the rate of atmospheric loss was measured (Jakosky et al., 2018).

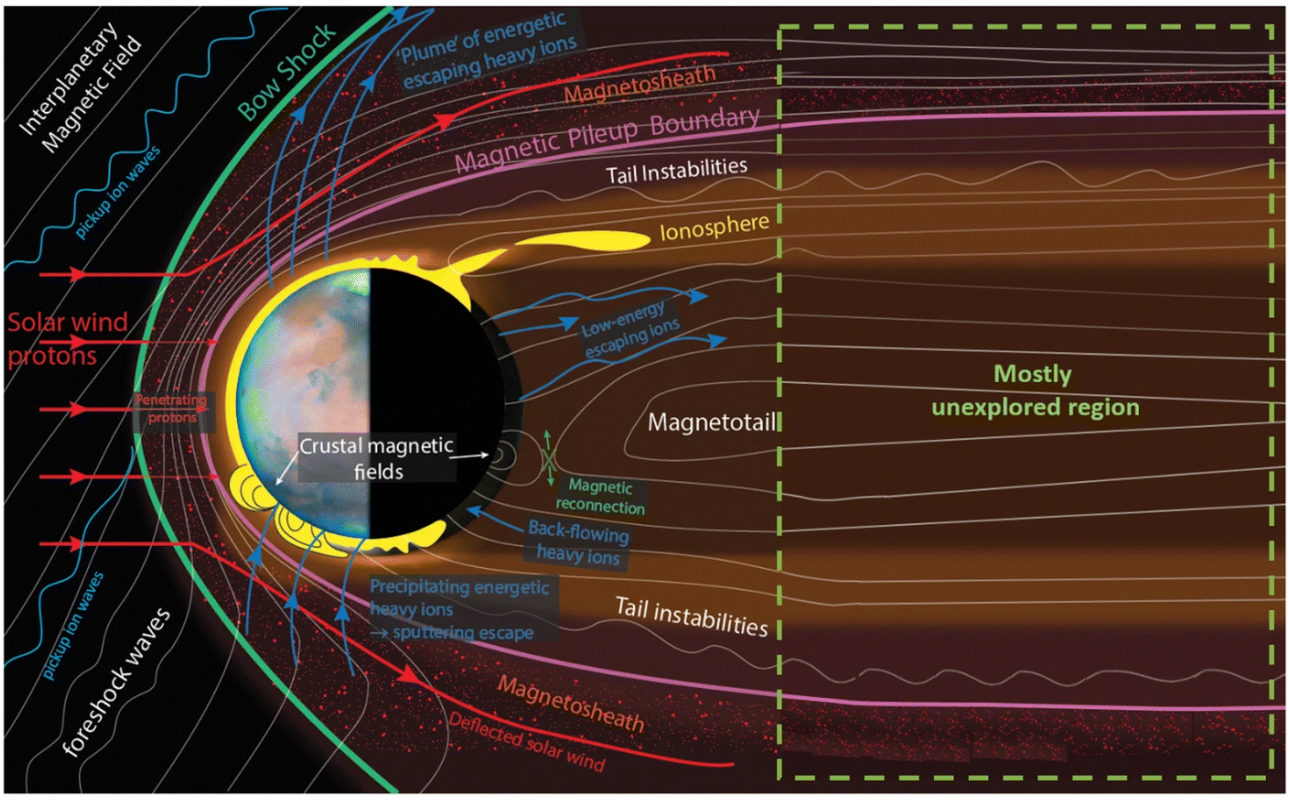

Figure 6.2: Schematic of Mars' plasma environment showing the main regions and physical processes known to occur in the Mars magnetic system. For context, the Sun is located out of frame to the left. Image adapted by Sánchez-Cano et al. (2022).

When transient solar particle events occur, electromagnetic radiation and charged particles are ejected from the Sun and accelerated, populating the local IMF and causing enhancement in the magnetic field magnitude, temperature and solar wind velocity. These enhancements move out through

the solar system and interacts with any obstacle they encounter. Flares, SEPs and CMEs all affect the Martian atmosphere. Flares greatly enhance the ionizing photon flux for short periods, solar energetic particle events can increase atmospheric ionization and temporarily alter the atmospheric chemistry, and coronal mass ejections and the subsequent interplanetary plasma and can cause field disturbances such as shocks, enhanced solar-wind dynamic pressures and magnetic-field magnitudes.

At Mars, the average angle between the Mars-Sun line and the IMF is 56^circ due to the nature of the Parker spiral, as shown in Figure 6.2. Mars's magnetosphere and atmosphere are effectively shielding the planetary surface from radiation, yet GCRs and sometimes SEPs, can penetrate and affect the lower atmosphere and even reach the surface (Zeitlin et al., 2010; Hassler et al., 2014), taking part in shaping Mars's varying ionospheric structure, as visualized in Figure 6.3. Superimposed on the Martian thermosphere and partially the mesosphere is the ionosphere, as shown in Figure 6.3. The ionosphere is the ionized outermost part of the Martian atmosphere. There, solar extreme UV radiation is breaking apart the neutral atmospheric components, creating a cold plasma of ions and free electrons. The electron densities vary with height, and there are two main peaks in the Martian ionosphere; the main layer M2 at $\sim$160 km, and the lower secondary layer M1 at around 110 km. There are also tertiary sporadic layers at lower altitudes which will be discussed further in Section 6.1.3.

High-energy electromagnetic radiation and particle precipitation contribute to an extraordinary production of ions and electrons in the ionosphere, and is on Earth closely related to airglow and auroral phenomena and is also believed to result in the highly irregular and variable atmospheric emissions at Mars. The nightside tail region of Mars's magnetosphere is largely unexplored, and stochastic tail instabilities could play a large role in particle transport and injection. High-energy electromagnetic radiation produces both nightglow and dayglow on Mars. It is most commonly observed in the UV (Barth et al., 1972), but has more recently also been observed at several wavelengths in the visible (Soret et al., 2022; Gérard et al., 2021).

While electromagnetic radiation causes airglow, charged energetic particles can cause aurora, and has also been correlated to the appearance of an additional nightside ionospheric layer causing radio blackouts (Sánchez-Cano et al., 2017). It is highly probable that these radio blackouts are closely associated with an auroral emission layer. To this date, four distinct types or auroras have been detected on Mars; dayside proton aurora (Deighan et al., 2018), nightside discrete aurora (Bertaux et al., 2006), diffuse aurora (Schneider et al., 2015) and sinuous aurora (Lillis et al., 2022). Proton and discrete aurora is thought to be linked to particle precipitation during quiescent solar wind conditions, though with different particle transport processes. Proton aurora is believed to be tied to energetic neutral atom production by solar wind protons directly interacting with the extended hydrogen corona surrounding Mars (Deighan et al., 2018), while discrete aurora is most likely produced by the precipitation of electrons onto crustal field lines where they are guided down into the neutral atmosphere where they undergo collisional processes with CO_2, CO and excited oxygen. As the discrete aurora is short-lived, spurious in its appearance and is mostly detected near magnetized crustal regions in the SH, the chances of observing it with SuperCam are low. For these reasons we focus on nightside diffuse aurora in the following section.

Diffuse aurora

Diffuse aurora was first observed in December 2014 by the IUVS instrument on MAVEN (Schneider et al., 2015). It was a bright, global and apparently smooth auroral phenomena that took scientists by surprise. Multiple spectral features were observed in the UV; multiple CO-Cameron peaks, the CO_2^+ ultraviolet doublet (CO_2 UVD) and a weak atomic oxygen signature at $297\,\mathrm{nm}$. The brightest of which was the CO_2 UVD emission reaching a maximum limb integrated intensity of 375 R at $70\,\mathrm{km}$ altitude. The oxygen signature reached an integrated limb intensity of roughly 112 R.

MAVEN made more or less concurrent electron and ion flux measurements, and the appearance

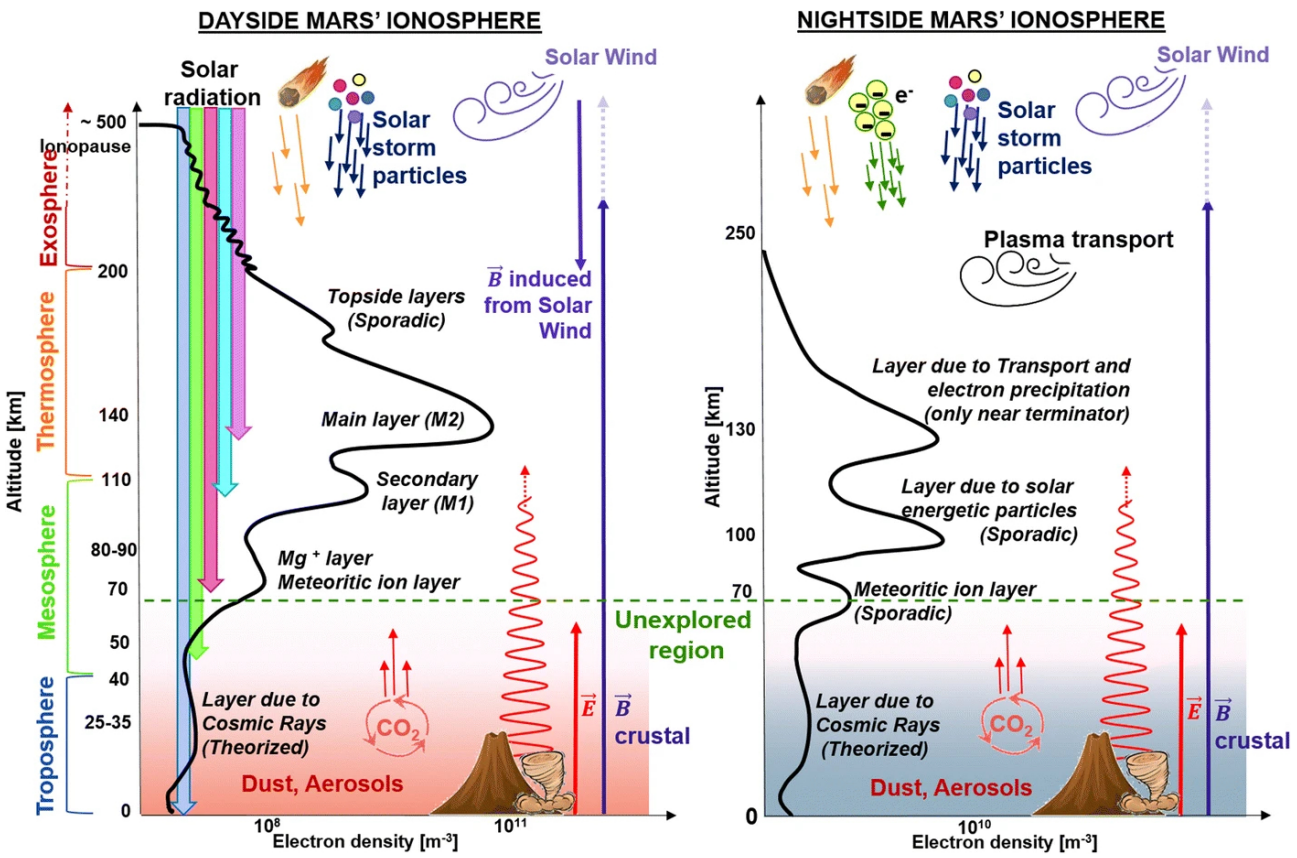

Figure 6.3: Typical profiles of electron densities in the Martian ionosphere for day and nightside. The atmospheric layers and main internal and external forcings are indicated; solar radiation, meteors, electron and solar storm particle precipitation, solar wind, magnetic fields, gravity waves, dust storms, and atmospheric cycles are also indicated. Figure from Sánchez-Cano et al. (2022).

of the aurora seemed to correspond well with the onset of an increase in both electron flux and energy. The diffuse aurora remained at detectable intensities for many days, along with the elevated electron flux. The vertical profile displayed a broad peak, and corresponded well with model profiles created using a sufficiently "hard" electron energy distribution, with substantial fluxes of electrons with energies up to at least 200 keV (Schneider et al., 2015). No obvious solar event was ever correlated to this detection of diffuse aurora.

Shortly after this incident, Jakosky et al. (2015a) reported a second detection of a diffuse auroral event in March of 2015. This time the aurora appeared to peak at two distinct time periods, indicating two separate events. Only the CO_2 UVD band was reported, but the limb intensity reached 750 R on both occasions. These auroral detections were clearly connected to a strong flare and multiple CMEs erupting in the direction of Mars. Again it seemed likely that electrons with energies above 100 keV were penetrating deep into the atmosphere and triggering the excitation and subsequent emissions, but ions were also recorded to coincide with the emissions during this event. Jakosky et al. (2015a) quantified the response of the Martian system to this disturbance, and found that the CME altered the morphology and dynamics of the bow shock and magnetosheath regions. In addition the production of pick-up ions was enhanced, and observations and models both show an increase in ion escape rates.

In September 2017 the Sun underwent a series of extremely energetic eruptive events which were detected and monitored from multiple vantage points throughout the solar system (Jiggens et al., 2019; Lee et al., 2018). The strongest diffuse aurora event detected to date was reported by Schneider et al. (2018) after a series of events impacted Mars. The CO_2 UVD emission peaked at 20 kR, and coincided with the peak in solar UV flux and the electron and ion fluxes, further solidifying the

correlation between SEP events and diffuse aurora. The $297\,\mathrm{nm}$ oxygen line was measured with a peak intensity of approximately 1.4 kR/nm. Figures 6.4 show UV images, spectra and vertical profiles for the detection aurora. In the top left image, the limb enhancement is barely visible at the storm onset, and the brightness of the disk is consistent with instrument noise and background. In the top right image taken during the peak of the event, auroral emission is enhanced across the entire disk, particularly visible at the limb where projection effects amplify the brightness. The bottom row shows the UV emission spectra where data is shown in black, with templates for known molecular emissions scaled to match. The plot uses square root scaling to show detail in fainter emissions. Vertical profiles were obtained with limb scans, where The ultraviolet doublet (UVD) shows a sharp peak at 60 km altitude, while the CO Cameron bands show a broader peak around 70 km. The UVD profile primarily reveals the profile of molecular excitation through particle precipitation. In contrast, the Cameron band profile is strongly affected at low altitudes by de-excitation through collisional quenching. Note that dayglow, driven by the absorption of solar extreme ultraviolet radiation, occurs much higher at altitudes around 130 km.

Recent modelling efforts suggest that both energetic protons and electrons contribute to the production of the observed aurora (Gérard et al., 2017; Nakamura et al., 2022), but electrons of higher energies are less efficient at producing any emissions, as the particles penetrate deeper into the atmosphere where collisional quenching becomes dominant. The "diffuseness" of diffuse aurora can possibly be explained if the emissions are mostly proton-driven, as high-energy protons have a gyroradii so large that if guided down into the atmosphere by draped field lines, the impacting area would be larger than the planet, and no pattern should appear.

At the time of writing, diffuse aurora is thought to be long-lasting (time-scale of days), global, and without discernible spatial or rapid temporal variations. However, these last two points stand without much observational evidence. Orbiters are poorly suited to resolve variability as aurora is most commonly observed at the limb with several seconds integration time, effectively smoothing out any variations. Any morphology is simply impossible to discern from limb scans. Spatial and/or temporal variations in the auroral emission will reveal the degree of rapid dynamics in the magnetotail. Orbiters schedule and coordinate their measurements weeks or months in advance, rendering them incapable of quick reaction and targeting CMEs inbound at Mars in a matter of days. In addition, no orbiter currently has the capability and/or dedicated time to detect aurora in the visible part of the spectrum. Yet, observation of multiple lines, and the subsequent calculation of intensity ratios, will constraint particle energy distributions and vertical depositions.

6.2 Space weather as sensed by EDAC counters

Space exploration is inherently a risky endeavour in a hazardous environment, in large part due to hard radiation in our Solar System. Understanding the chain of processes that control space weather at any planet or spacecraft on various time scales is important to accurately forecast and now-cast hazardous conditions and prevent damage to a spacecraft, and ultimately humans.

At the moment, most of the information about radiation hazards come from near-Earth satellites, where several national monitoring programs are in place for terrestrial space weather forecasting. However, as we are establishing our presence on Mars, and expanding our robotic solar system exploration in general, monitoring planetary space weather is an increasing necessity. However, few spacecraft are equipped with payloads optimized for plasma and radiation science, however all of them carry hundreds of housekeeping sensors.

Since the summer of 2020, I have taken part in multiple studies using spacecraft housekeeping data to qualitatively study the radiation environment around Mars and the heliosphere as a whole. Here is presented three science cases where housekeeping data have provided new and valuable insights; solar cycle modulation of GCRs at Mars, GCR variations with heliocentric distance, and the detection

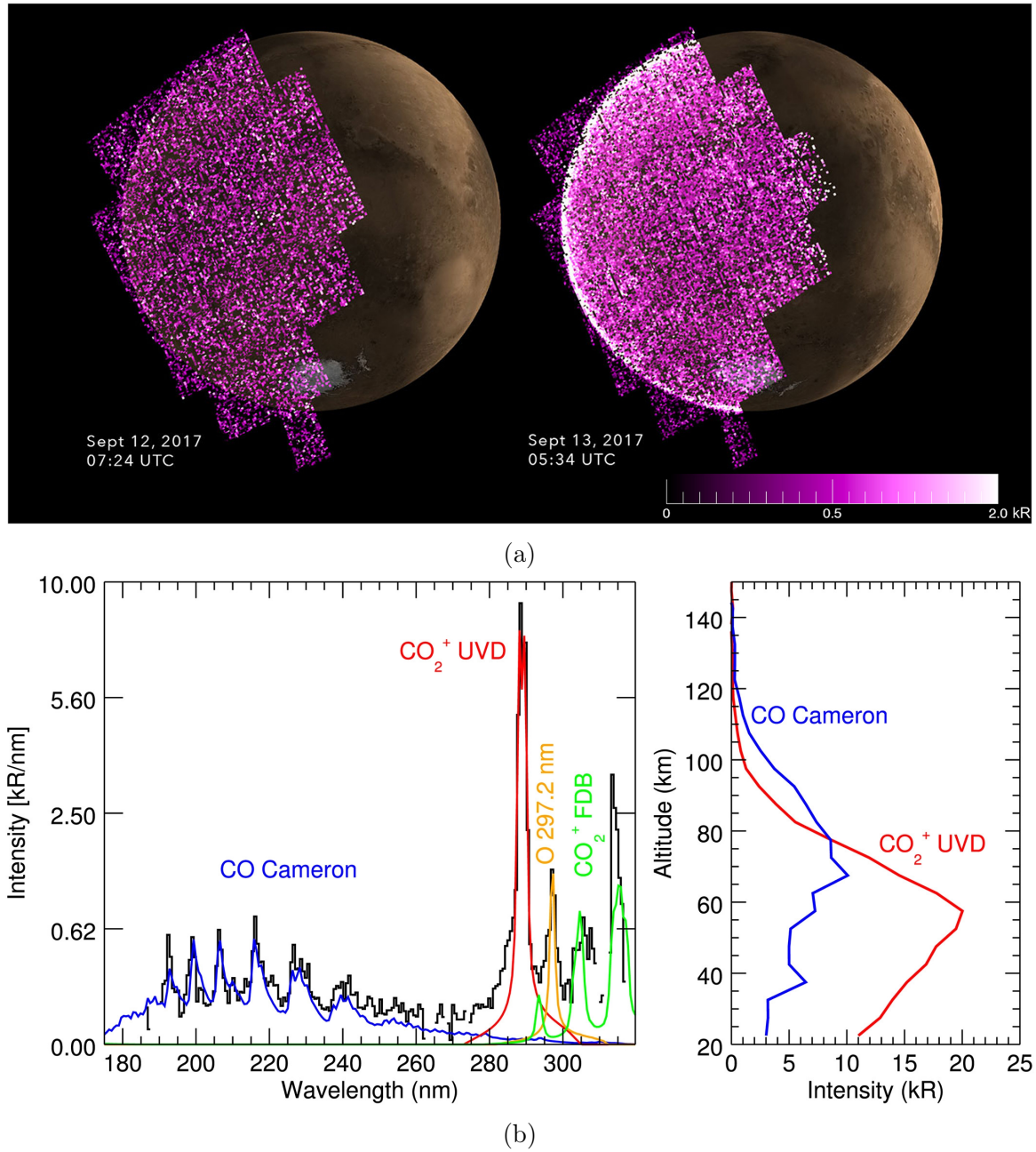

Figure 6.4: Observations by the UVIS instrument on board MAVEN of the September 2017 auroral event. a) Mid-ultraviolet images of Mars before (left) and during (right) the diffuse auroral event of September 2017. The purple-to-white brightness scale displays the brightness of emission matching the template for CO Cameron bands excited by particle precipitation, spanning the range 0–2.0 kR. b) UV spectrum (left) of the brightest auroral emission peaking at 60 km altitude and vertical profile (right) Limb scan spectrum Right: Vertical profiles of auroral emissions obtained from the same data, plotting the integrated intensity of the brightest two emissions versus altitude. Figures from Schneider et al. (2018).

of solar particle events at Mars. The results presented in the following sections are mainly based on the publications Knutsen et al. (2021b) and Viet et al. (2022).

6.2.1 EDAC data set and processing

All hardware in space are subject to radiation in forms of photons, electrons and ions. If this radiation is energetic enough, it has the capability to corrupt data stored in physical memory cells on board. Such events are called single-event upsets (SEUs), and represent a change of state caused by a single ionizing particle striking a node in a live memory cell, causing a bit-flip. SEUs are continuously monitored, corrected for as much as possible and each correction is counted. This is called the error detection and correction (EDAC) algorithm, and takes the form of a cumulative counter incrementing by one each time a bit-flip is corrected. If a SEU occurs, EDACs are able to identify the bit where the error occurred and correct it as shown in Figure 6.5. Memories have a control circuitry which is responsible for all memory operations including reading the correct address in the memory array (left panels in Figure 6.5). During normal operation, the control circuitry correctly reads the memory arrays which have no errors, while if an SEU occurs, the affected memory cell will change status. The control circuitry will read the correct address, but an error in one of the bits will be caught by the EDAC. The error is then corrected by writing the cell back to its previous status.

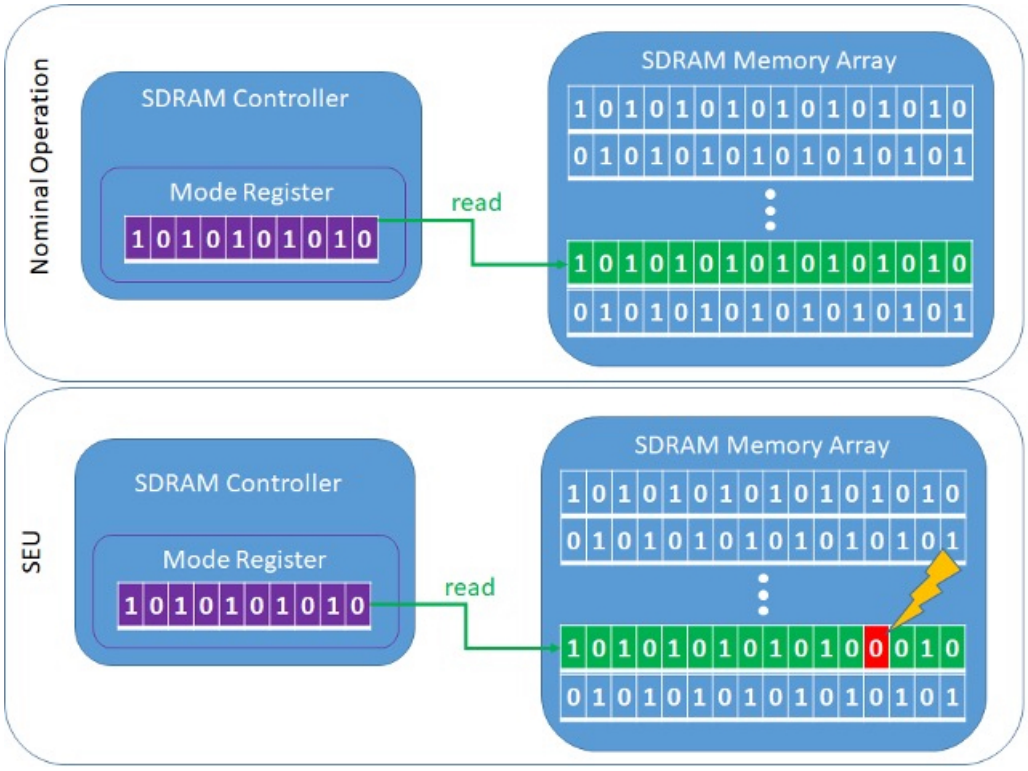

Figure 6.5: Diagram showing an on board memory cell, and how the EDAC counter registers single-event upsets. In the top panel nominal operations are showed, while the second panel displays a single-event upset. Green indicates good operations and red indicates detected errors. Figure from Sánchez-Cano et al. (2023).

Most spacecraft transmit dozens of these counters back to Earth as a collections of housekeeping parameters, constantly reporting on the health of the spacecraft, and are normally not used for any scientific purpose. However, as these errors are largely caused by highly energetic and charged particles, information about the radiation environment in our solar system are embedded in these parameters. The advantage of EDAC compared to regular payload instrumentation is that the EDAC counter is very often operating constantly, as opposed to going dormant for periods of time which is common

for instruments due to power limitations. There is also an immense untapped potential simply due to the vast number of spacecraft through history. If one could access EDAC counters from many satellites, old and new alike, one could achieve an unprecedented spatial and temporal coverage in our heliosphere.

It is a relatively safe assumption that the EDAC counter is only sensitive to protons, but the most obvious drawback of using EDACs is that there is little prospect of resolving particle energies. We know that highly energetic charged particles are required to make bit-flips, and that quiet solar wind conditions are not sufficiently energetic. One can make educated guesses if some knowledge on the memory cell location in the spacecraft exists, along with information about the shielding, but detailed 3D models of the spacecraft is strictly necessary if more than lower energy boundaries is desired.

In the work presented in this thesis, EDAC counters from MEX and Rosetta were used. MEX and Rosetta are very similar spacecraft, and the EDAC counter used on them are nearly identical in type and sensitivity, allowing for a direct comparison between the two. The MEX EDAC related to the data management system processor (parameter ID NDMW0D0G) operated continuously during the time interval for this work (2005-2020), reporting increments multiple times per day. The Rosetta EDAC related to the attitude and orbit control system counter (parameter ID NACW0D0A) was chosen due to its continuous temporal coverage (except during hibernation) and its high measurement frequency. The EDAC on Rosetta was only used for the GCR study in Section 6.2.2, while the MEX EDAC was used for the GCR work as well as for the solar particle event detections in Section 6.2.3.

The measuring frequency of EDACs can be quite irregular, varying from data points every 30 sec to fewer than one measurement per day. In order to compare EDACs and obtain a more manageable time series, the cumulative counter was re-sampled to a daily frequency, where any potential missing days were filled by linear interpolation.

On occasion, EDAC counters are set to zero, and their cumulative count is thus reset. In order to create one continuous smooth counter, the zero-resets are corrected by identifying each time such a reset is made, and adding the count value immediately before the reset to all consecutive data points. When this step is done, the EDACs look rather smooth, and exhibit an almost linear behaviour. This is attributed to the continuous presence and relatively steady flux of GCRs in the heliosphere. It is however not completely linear, a light curvilinear trend can barely be seen upon visual inspection of left panel of Figure 6.6.

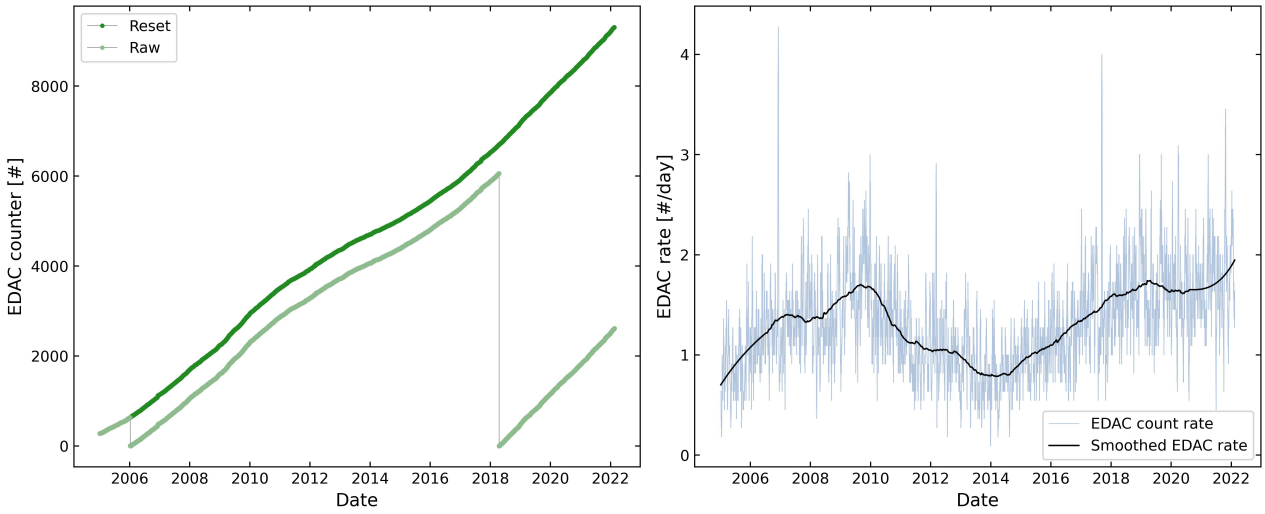

Figure 6.6: EDAC counter and daily EDAC count rates for almost the full duration of the MEX mission. The EDAC raw data is shown in the left panel along with the zero-reset and re-sampled daily counter, the right panel shows the daily EDAC count rate and the corresponding smoothed count rate. Figure adapted from Knutsen et al. (2021b).

In order to investigate the time variations more closely, a daily EDAC count rate is calculated. The approach for this calculation has evolved somewhat from the first project (Knutsen et al., 2021b), to the most recent one (Viet et al., 2022). In the first project a simple difference every 14 days was used, where all days within two weeks were given the value of this difference divided by 14. In Viet et al. (2022), a moving mean box with a length of 5 days and step size of 1 day was applied. Both studies note that large and previously well-studied solar particle events caused extreme jumps in the EDAC counter, causing an artificially large EDAC count rate for a certain amount of time. The need to isolate such extreme events was recognized, and corrected for by replacing the affected 14 days by the mean of the previous and consecutive rates in (Knutsen et al., 2021b), and by second order polynomial interpolation of the affected days in Viet et al. (2022). For either approach the result is a daily count rate, clearly exhibiting a wave-like behaviour with short-term variations. A smoothing routine is applied using a third-degree polynomial Savitzky-Golay low-pass filter with 1095-day (3-year) window, corresponding to approximately a quarter solar cycle, shown along with the raw daily count rate in the right panel of Figure 6.6. The implications of the variabilities in the resulting daily count rates (both smooth and raw) are explored in chapter 6.2.

6.2.2 Heliospheric Galactic Cosmic Ray behaviour

The study of GCR behaviour in the heliosphere using EDACs is twofold: firstly we investigated how the solar cycle modulates the GCR intensity at Mars, secondly we calculated the GCR intensity variations with heliocentric distance. For the part of this study that involves the solar cycle modulation of GCRs at Mars, the MEX EDAC housekeeping parameter was compared with sunspot numbers for the time period January 1, 2005 – September 17, 2020. The utilised sunspot data were downloaded from the World Data Center SILSO, Royal Observatory of Belgium, Brussels (Center 2020). For the study of GCR variations with heliocentric distance, the EDACs on MEX and Rosetta were utilised in the period from January 1 2005 until the end of the Rosetta mission on September 30 2016.

Solar cycle modulation of galactic cosmic rays at Mars

The flux of cosmic rays increases when moving away from the Sun as the solar dynamic pressure diminishes, but it is still modulated by solar activity and the solar cycle. We have monitored this modulation at Earth for many decades (Alania et al., 2014), and it has become a well-proven proxy indicator for GCR variability (Usoskin et al., 1998). At Mars no long-term corresponding study has ever been conducted. In this work we first verify that the EDAC can indeed provide similar information about the GCR environment as a neutron monitor by comparing with a neutron monitor at McMurdo station in Antarctica, collected from the Bartol Research Institute's website (http://neutronm.bartol.udel.edu). It must however be noted that NMs are Earth-based instruments and are influenced by our magnetosphere, which effectively deflects particles of lower energies to which the EDAC might still be susceptible.

Figure 6.7 shows the EDAC daily count rate (found by the method described in Knutsen et al. (2021b)) along with the daily NM count rate in panel A). In panel B) the linear relationship between the two count rates is qualitatively confirmed by plotting the smoothed EDAC count rate as a function of the smoothed NM count rate. In panel C) the strength of the correlation between the two counters is quantified using a cross-correlation analysis, finding that the maximum correlation at exactly 0 lag, indicating that if there is a delayed response of the GCR modulation at Earth compared to Mars, it is undetectable with this method. The solar cycle modulation on the GCR signal is clearly visible in both the NM and the EDAC time series, demonstrating the ability of the EDAC counter to probe the varying GCR intensity.

Now that the EDAC counter has been established as a reliable proxy for GCR intensity, we go on to investigate the GCR modulation at Mars. We use solar sunspot numbers (SSN) as an indicator for

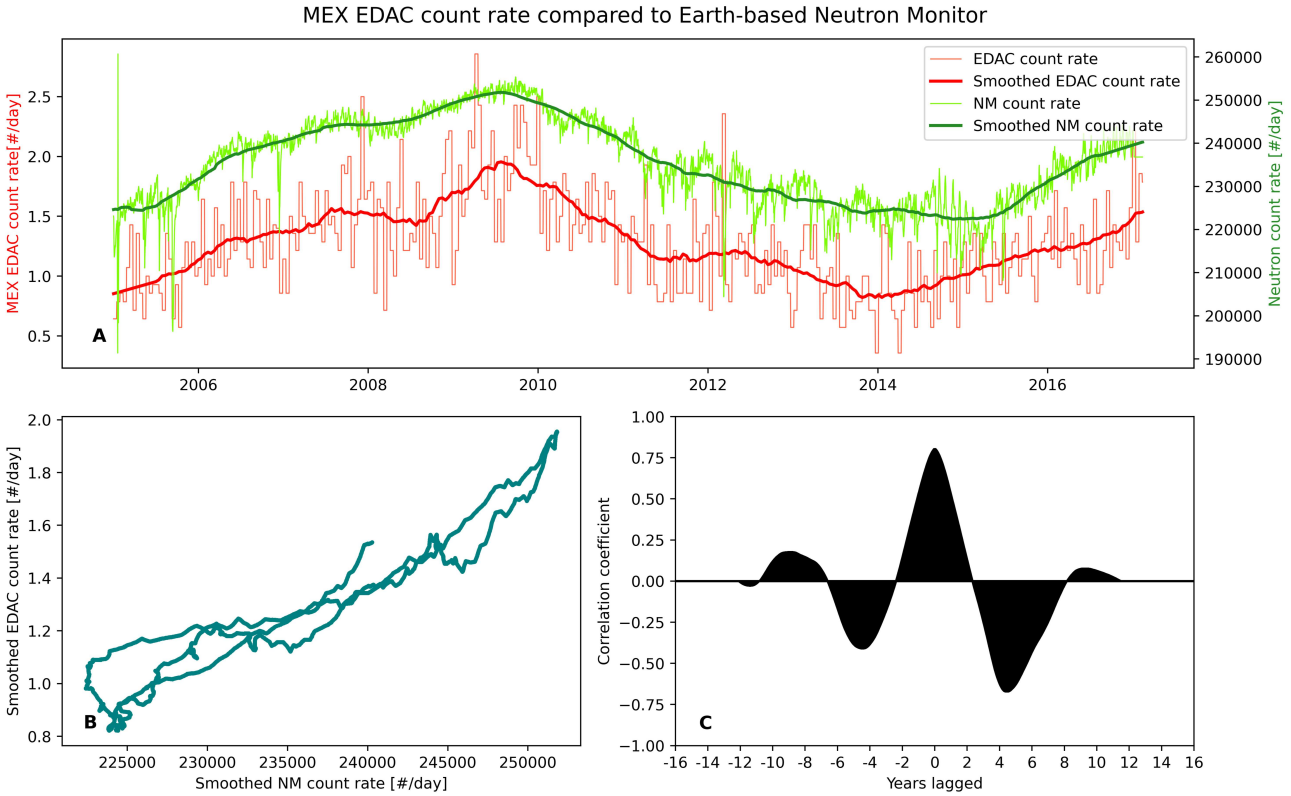

Figure 6.7: Demonstration of the similar properties of an EDAC counter in orbit and a ground-based Neutron Monitor. A) time series of the MEX EDAC count rate (red) and the McMurdo NM count rate (green). B) Smoothed EDAC rate as a function of the smoothed NM count rate. C) Cross-correlation between the two count rates. Figure from Knutsen et al. (2021b).

the solar cycle and compare those to the EDAC count rate. Figure 6.8 compares the MEX EDAC with solar activity over the course of 15 years. Panel A) highlights the cyclic behaviour of the two time series, and the relationship is shown as a scatter plot in panel B) with a recognizable linear relation. The daily EDAC count rate at Mars orbit during solar minimum is twice as high (1.9 counts per day) as the daily count rate during solar maximum (0.8 counts per day). Panel C) quantifies the lag, which is barely discernible by visual inspection in panel A), but by cross-correlation analysis a lag of 5.5 months is obtained. This lag time is in good agreement with results from previous studies of solar modulation at Earth (Bertucci et al., 2019; Ross and Chaplin, 2019). Interestingly, the origin of the delayed GCR response remains unknown.

Galactic cosmic rays as function of heliospheric distance

The flux of cosmic rays increases when moving away from the Sun, as the solar radiation pressure falls off with $1/R_S^2$, where R_S is the distance to the Sun. The flux also depends on the solar cycle as shown above, the measured energy interval, and heliocentric longitude and latitude. In this study the latter two are however considered to be negligible compared to the radial variation (De Simone et al., 2011; Vos and Potgieter, 2016). To obtain a GCR gradient independent of the solar cycle modulation, simultaneous EDAC measurements on multiple spacecraft at different locations are required, and in this particular study we used EDACs on MEX and on Rosetta. As the heliocentric distance of each spacecraft is known at all times, one can disentangle the radial effects from the solar cycle modulation effects observed.

To study the GCR intensity as a function of heliocentric distance, we found the difference in heliocentric distance between the two spacecraft for each day of Rosetta's lifetime. Then the relative change between the Rosetta and MEX EDAC rates is calculated and plotted as a function of the

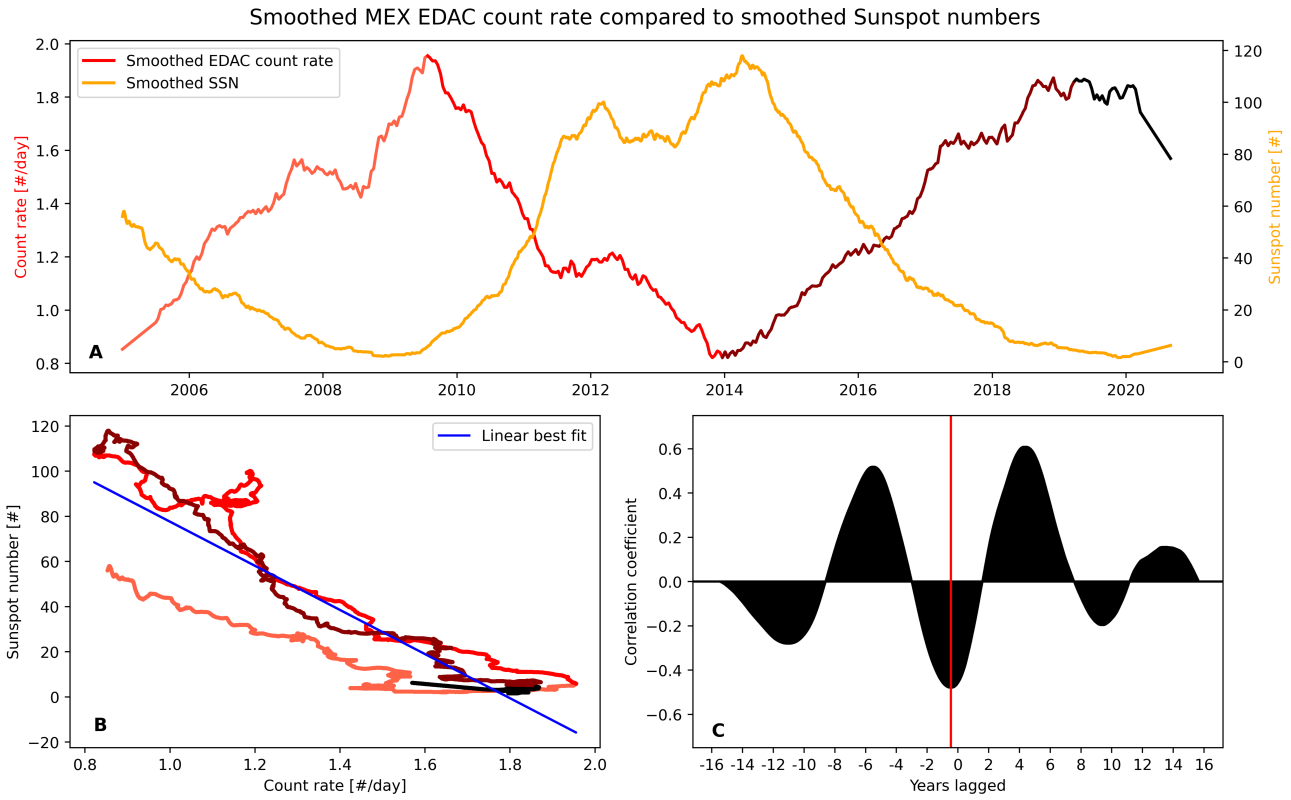

Figure 6.8: Long-term solar cycle modulation of GCRs at Mars. A) Smoothed sunspot numbers in orange along with smoothed MEX EDAC count rates in hues of red. The EDAC is color-coded according to the solar cycle phases to highlight the effect of solar modulation. The colors match those in panel B). B) Sunspot numbers as a function of EDAC. The blue line represents the linear best fit. C) Cross-correlation between smoothed sunspot numbers and EDAC, illustrating a cyclic anti-correlated relationship. Figure from Knutsen et al. (2021b).

difference between the solar distances of Rosetta and Mars in Figure 6.9. The x-axis is such that x=0 indicates that Rosetta is at mean Martian orbit, and x<0 translates to Rosetta being closer to the Sun than Mars.

A linear function was fitted to the data points where x$\geq$0, with an obtained slope of 5.3%, meaning the EDAC count rate, and subsequently the GCR flux, increased at an average rate of 5.3% per AU. If all measurements inside Mars orbit were included, the rate becomes 3.9% per AU . In previous studies (Honig et al., 2019; McDonald et al., 1997; Webber and Lockwood, 1991), it has been customary to take the natural logarithm of the count rate ratio when calculating a radial gradient of GCR fluxes. By doing this for the two cases, only measurements at and beyond Mars, and all measurements, slopes of 5.4% and 4.1% are obtained, respectively, in good agreement with those earlier works. The mean and median of these four ways of calculating the slopes both round up to 4.7, and thus our final estimate of the GCR radial gradient becomes 4.7$\pm$0.8%.

The black line segment in Figure 6.9 has a trend strikingly different to all other years. This can possibly be explained by how when Rosetta was at heliocentric distances equal to or smaller than mean Mars orbit, the spacecraft went through several maneuvers and multiple fly-bys. Planetary shielding effects and passing through Earth's Van Allen radiation belts on multiple occasions also adds complexity to our goal of isolating the radial GCR behaviour. This led us to differentiate between data points within and outside Martian orbit, yet not all of the negative trend is captured within this region. However, overall this result confirms what dedicated radiation instrumentation on other spacecraft have previously measured, showing a radial decreasing trend in GCR intensity of 4.7$\pm$0.8% per AU.

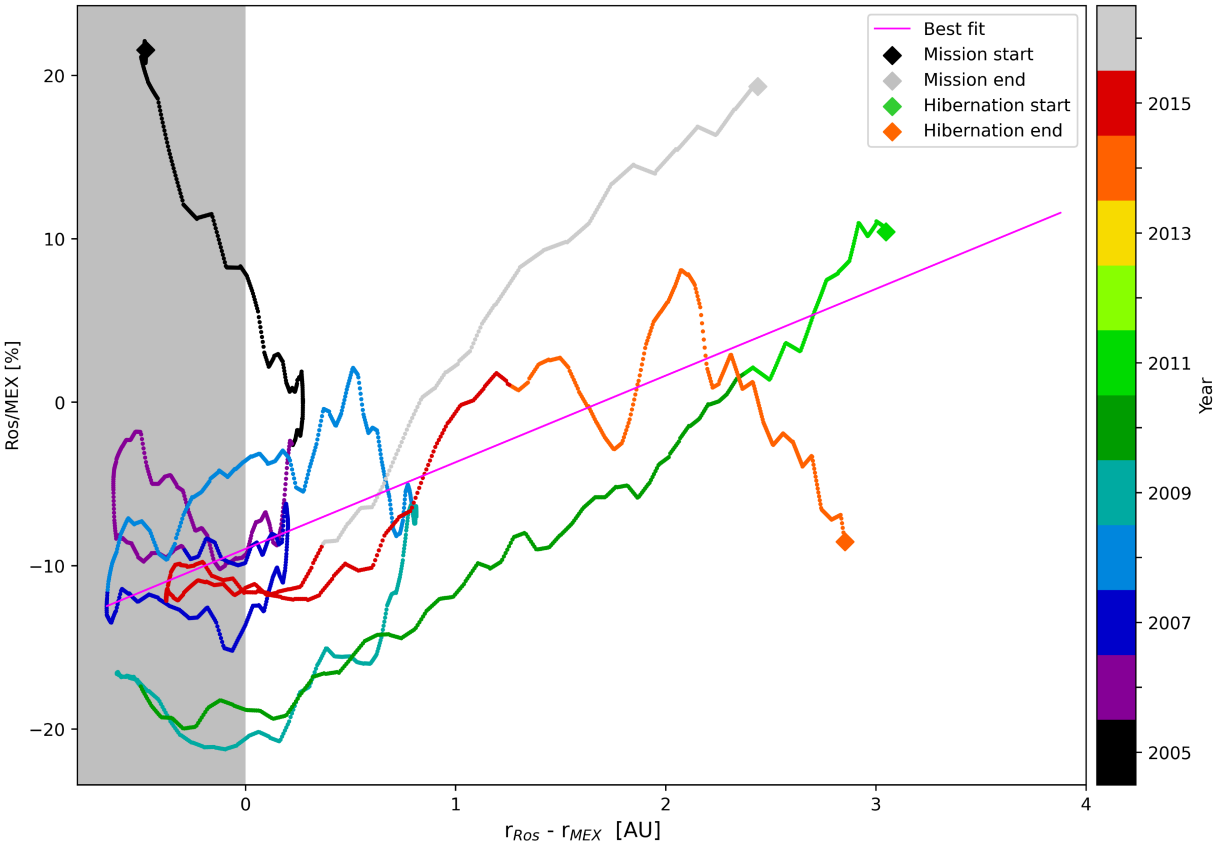

Figure 6.9: Relative change of Rosetta compared to MEX EDAC count rates as a function of the difference in their respective solar distances. Each colored line segment indicates a full terrestrial year, except for 2016 (grey), which was cut short on September 29th at the end of the Rosetta mission. The diamonds mark the start and end points of the Rosetta EDAC time series. The lightest shades of green and yellow are not present in the plot as they represent times when Rosetta was in hibernation. The shaded area for x<0 indicates when Rosetta was at or closer to the Sun than the mean Martian orbit. The magenta line shows the linear best fit of the data, but EDAC data points within the shaded region were not included in the best-fit procedure. Figure from Knutsen et al. (2021b).

6.2.3 Solar particle events at Mars

Knutsen et al. (2021b) found that in order to successfully isolate the solar cycle modulation of the GCR signal in the EDAC count rate, known strong SEP events needs to be identified and removed. In the following work, the opposite has been done; a refined method of calculating the GCR background counts in the EDAC was made, and used to remove said signal. The aim of this study was to develop an algorithm for the detection and investigation of space weather events around Mars by using the EDAC counters on the Mars Express satellite. When the solar cycle modulated GCR induced EDAC counts are corrected for, so that transient solar space weather events can be discerned from the background, visible as spikes in the count rate. A large number of events was detected in Mars orbit, and selected events are compared with other dedicated radiation instruments.

This work was carried out by Shayla Viet in the spring of 2022, a third year bachelor student at the time, and supervised by myself in collaboration with colleagues at ESA and the University of Leicester. She conducted a three month internship at LATMOS, which culminated in her presenting at the International Astronautical Congress in 2022 and a conference proceedings paper (Viet et al., 2022). Shayla will continue this work in 2024 for her master thesis, which I will also be supervising.

Charged particles can be accelerated from flares and CMEs (see Section 6.1.2), and become SEPs. Such particles, when impacting a spacecraft, will likely cause multiple bit-flips over an extended

period of time (hours to days) and be recorded as spikes in the EDAC count rate. Another consequence a CME might have on its local environment is called a Forbush decrease (FB), which entails a rapid decrease in the background GCR radiation due to the shielding effect of the passing plasma and embedded magnetic field. Forbush decreases have been detected at Earth, Mars, space stations and at other locations in the solar system (e.g. Freiherr von Forstner et al. (2021); Freiherr von Forstner et al. (2018); Guo et al. (2018)). Since we here remove the GCR background, a FB will manifest in the EDAC counter as a period with no (or fewer than normal) counts.

Solar particle event detection

To remove the GCR background signal from the EDAC signal, two daily count rates were computed. One with the purpose of maintaining the short-term variations which might be transient solar events, and another with the purpose of highlighting the solar cycle modulated GCR background. The first, henceforth referred to as the EDAC_{SEP}, was calculated using a 5-day moving mean. The second, named EDAC_{GCR}, was calculated using an 11-day moving window and applying a Savitzky-Golay low-pass filter with window length of 1095 days and of polynomial order of 3. A new dimensionless parameter we named the *SEP number* (Nb_{SEP}) is thus obtained as shown in equation 6.1, and visualized in Figure 6.10.

$$Nb_{SEP} = \frac{EDAC_{SEP} - EDAC_{GCR}}{EDAC_{GCR}} \tag{6.1}$$

The parameter Nb_{SEP} gives a number which is proportional to the number of SEP particles incident on the spacecraft relative to the nominal GCR background. The spacecraft will of course experience occasional random errors, and we should also assume that the GCR component was not perfectly removed, all of which creates a noise level. We make another assumption that a true SEP event can be distinguished from the remaining background by its production of multiple errors in a short time span. In order to isolate these true SEP events from the errors, lower and upper bounds for noise limits were investigated. In this way, Nb_{SEP} above the noise limit can be interpreted as errors induced by SEP particles causing errors, and Nb_{SEP} below the noise limit are interpreted as a period with fewer SEPs than normal EDAC_{GCR} background, likely caused by a Forbush decrease.

The Nb_{SEP} follow almost a Gaussian distribution with a mean of 0.11 and a standard deviation (σ) of 0.415. As is common practice, we implement a 2σ upper detection limit. For a spike in Figure 6.10 to be detected as a SEP event, it should exceed the background by at least 2σ. If an identical limit was applied for the lower bound, spikes below the noise interval would be excluded. After some testing the lower detection limit was set at 1.5σ. These limits correspond to the values -0.733 and 0.719. Any spikes above or below this threshold is defined as a *stormy day*.

In Figure 6.10 the Nb_{SEP} is shows as a time series, with the upper and lower noise limit shown as stippled lines. Many stormy days can be identified by inspection, three particularly large ones stand out in December 2006, March 2012, and September 2017. These were extremely energetic events, and are well known and much studied (Futaana et al., 2008; Jiggens et al., 2019; Soni et al., 2023).

It is likely that some spikes above or below the noise limit are still caused by natural or random variation and not true SEP events. In order to reduce the detection of false events, a two control were made for each detection; check that the Nb_{SEP} value is a certain amount above/below the upper/lower noise limit, and check that the number of consecutive stormy days is more than one. All stormy days not satisfying *one* of these requirements are discarded.

To choose the required Nb_{SEP} value a stormy day needs to be beyond the noise limit, all the distances between the spike heights and the noise limits were investigated (see Viet et al. (2022) for the full analysis). The criteria for a peak to still be included as a stormy day (when there were no other spikes in a $\pm$2day range) was determined to be 0.18 and 0.06 for the positive and negative spikes respectively, which corresponds to SEP numbers of Nb_{SEP}=0.899 and Nb_{SEP}=-0.833. If a day has a Nb_{SEP} in between these two limits, it was checked if the stormy day was within two days

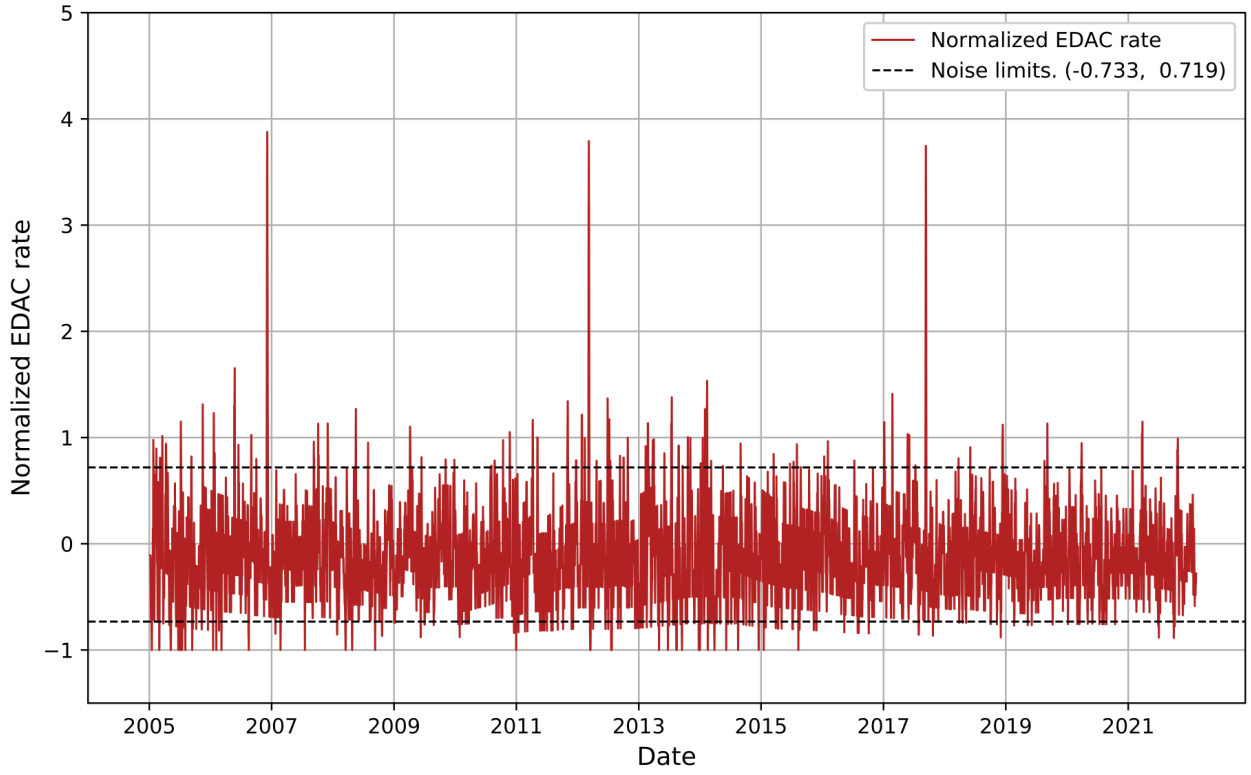

Figure 6.10: Time series of the relative change between highly varying count rate and the background count rate. The count rate is normalized by the GCR background count rate, we now obtain a non-solar cycle modulated signal proportional to the number of incident SEP particles. Figure from Viet et al. (2022).

of another stormy day. If not, the detection is discarded. 66 stormy days were discarded this way, leaving 414 individual days with elevated EDAC count rates over approximately 20 years.

The final step is to consider the duration of a SEP event, which might lead to an elevated radiation environment lasting several days. As such, considering individual stormy days is redundant, and thus the remaining stormy days were grouped into events. Consecutive stormy days of positive (negative) spikes were collected as SEP (FD) events, and if the time between two positive (negative) spikes were less than or equal to two days, they were considered to be a part of the same event. If the time between one positive and one negative spike was less than or equal to four days, then the stormy days were grouped into one SEP+FD event. In the end 157 events were identified.

The number of solar flares and CMEs are at a maximum at or slightly after solar maximum, so the identified stormy days should be concentrated in time around solar maxima. Figure 6.11 displays the smoothed sun spot numbers and the distribution of stormy days in time, clearly showing that the stormy days follow the sunspot trend well at all times; it even catches a local minima around year 2013 before reaching the global maximum in 2014, increasing our confidence that the method developed is mostly detecting true space weather events. The method was dubbed Space Weather Event EDAC Tracker (SWEET).

Solar particle event verification

In an effort to validate if the events identified by SWEET are indeed true events, we searched for the dates in literature. A list was compiled with dates from MAVEN (Lee et al., 2017), the neutron detector onboard Mars Odyssey (Livshits et al., 2017), RAD on the Curiosity rover (Guo et al., 2021), radar blackout events (Lester et al., 2022) and CMEs registered in the Space Weather Database Of Notifications, Knowledge, Information (DONKI). From this list, where all possible events to impact

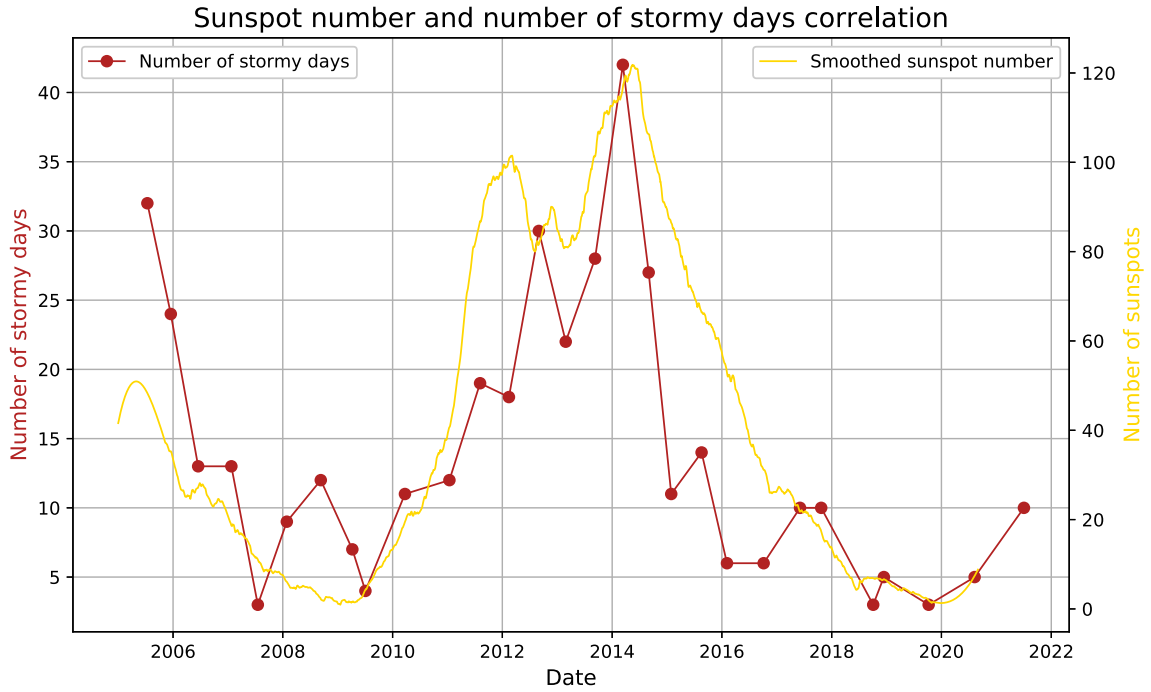

Figure 6.11: Time series demonstrating the correlation between the number of identified space weather events and the solar cycle. The red curve shows the number of stormy days found by the SWEET algorithm in time bins of 180 days from 2004 to 2021. The golden curve shows the smoothed sunspot number in the same time interval. Figure from Viet et al. (2022)

Mars were included (total of 346 dates), a second and stricter version was also assembled (144 dates), excluding any uncertain events.

When verifying the identified events, it was considered a match if the verification date was within one day before and three days after the starting date of a SWEET event for SEPs, and within the start date and seven days after the end date for the FDs, as they typically follows CMEs.

Out of the 157 SWEET events, 49 could be accounted for in the inclusive list, corresponding to 31.2%. When using the strict list as baseline, SWEET detected 44 out of the 144, which is a 30.6% detection rate. From the strict list, SWEET found three out of six events from RAD, 23 out of 70 dates from DONKI, 28 out of 82 dates from the radar blackouts detected from MEX, 15 out of 37 from radar blackouts from MRO, and four out of 21 dates from MAVEN. 30 of 117 dates from HEND, which were not included in the stricter validation list, were also detected.

The SWEET technique is still in development, and Shayla and I have several ideas for improvements both in terms of the actual method, and in the compilation of the validation list. Some of which include to use a Poisson distribution instead of Gaussian to define the detection noise limits, to implement stricter requirements when compiling the list of events impacting Mars by also check for solar ejection latitude. The continuation of this project will be part of Shayla's upcoming master thesis.

6.3 Martian aurora with SuperCam

The observation and modelling of Martian aurora sheds light on the dynamics of solar interactions with the upper atmosphere and thus supports studies of atmospheric evolution. Auroras are hallmarks of energetic particle deposition in the upper atmosphere, and they can be used as proxy to study the atmosphere itself, the enveloping radiation environment and the energetic particles themselves.

Dynamics, chemical composition, vertical structure, heating processes and atmospheric escape are some of the topics auroras can shed light on, as well as the energy and flux and vertical deposition of the particles entering the atmosphere (e.g. Nakamura et al. (2022); He et al. (2023); Soret et al. (2021)). Particularly the effect on the atmosphere has been widely studied here on Earth (Richmond and Roble, 1979; Sinnhuber et al., 2018), but is almost not explored at all on Mars, apart from the impact on atmospheric escape. Observations and models both show an enhancement in ion escape rates during magnetically disturbed times (Jakosky et al., 2015a). We can even use the study of turbulent periods to understand atmospheric evolution, as high solar activity periods resemble the activity level of a younger Sun. Observing ion loss during solar events can thereby give a window into early Mars history and the long-term evolution of the Mars atmosphere. The following section outlines the solar event targeting routine, instrument characterization for the VIS channel, and the subsequent results.

6.3.1 Auroral campaign preparations

SuperCam was never designed with nighttime atmospheric observations in mind, but its visible channel covers several known auroral emission lines. This subsection focuses on the preparations for our auroral observations, including the development of a solar event selection routine, observation strategies for instrumental characterization and aurora observation. As this project is still a work in progress, and only two observation have yet been performed, there is not much data processing described in this section. The processing and analysis of the data can be found in Chapter 6.3.2.

As outlined in Section 3.2, a regular passive sky observation includes both the visible and the infrared channels. Auroral emissions have been detected in planetary atmospheres in the UV (e.g. Bertaux et al. (2006); Schneider et al. (2015); Clarke et al. (2005)), visible (e.g. Dyudina et al. (2016); Frank et al. (1982)) and infrared (e.g. Lam et al. (1997); Stallard et al. (2008)) wavelengths. At Mars, aurora has only ever been observed in the UV, though emissions in the visible have been detected in Martian dayglow (Soret et al., 2022; Gérard et al., 2021). By observing aurora at multiple wavelengths, the energy distribution of the incoming particle population can be constrained, along with the vertical energy deposition in the atmosphere. However, the IR aurora is expected to be very faint at Mars, yet SuperCam has an intensifier in connection to the visible channel only. Therefore we are omitting the IR channel and only use the SuperCam VIS spectrometer (536-853) when targeting auroral emission lines. With the VIS channel we cover several possible emission lines; the common green oxygen line at 557.7, the red oxygen triplet at 630, 636.3 and 639.1 nm, and the oxygen ion far red doublet line at 732-733 nm. The green line is our prime target, while the presence (or not) of the red line will help constrain the particle energy distribution. We have no real expectancy of detecting the far red line.

Spectroscopic information is valuable for auroral observation in order to identify relevant emission lines and their intensities. Yet, most auroral research on Earth and other planetary bodies is done with imaging cameras. On Mars, images of aurora have only been taken in the UV (diffuse aurora (Schneider et al., 2018), sinuous aurora (Lillis et al., 2022)). The images in Lillis et al. (2022) show great variability, both temporal and spatial. We hypothesize that during solar storms at Mars, a diffuse auroral event could display internal variability as charged particles are accelerated along field lines by magnetotail reconnection in the current sheet (Harada et al., 2017), but this might not be discernible from orbital limb scans. For this reason, we have acquired access to Perseverance' ZCAM, a multispectral, stereoscopic imaging camera (for a detailed description of the instrument, see Bell et al. (2021)).

Solar event selection

The first obstacle when it comes to observe aurora on any planet or moon is the fact that auroras are transient phenomena. To most they also seem like random events, but they are to a certain extent predicable, and herein lies our first challenge. ESA and NASAs combined fleet of solar observatories all report the detection of solar flares and coronal mass ejections, which is collected by the Community Coordinated Modeling Center (CCMC) at the NASA Goddard Space Flight Center. The CCMC has developed the Space Weather Database Of Notifications, Knowledge, Information, called DONKI for short, and it includes reports of observations of space weather phenomena and their interpretation in real-time, forecasts, models, and notifications, provided since April 2010. By monitoring active regions on the Sun (maps and reports are published every day on multiple online sources) and DONKI, we evaluate space weather events on a daily basis, and we have found that flares and CMEs are ejected towards Mars quite often, on the order of around 5 times per month, though take note that this estimate is purely based on manual monitoring of DONKI for the past eight months.

Several space weather events reach Mars every month, but most of them are probably not aurora-inducing candidates, at least not at intensity levels detectable with SuperCam, or visible to the human eye. CMEs that are associated to flares are desired, as they are more likely to be stronger events, and CMEs associated with flares of M and X class are preferred. Having considered what the nominal solar wind conditions are at Mars orbit (Jakosky et al., 2015a; Ramstad et al., 2017), a list of parameters were selected with requirements which a solar event has to fulfill in order for us to request observation time with SuperCam, these are listed in Table 6.1. DONKI is of course not offering an accurate prediction and there are several caveats one should be aware of; the DONKI CME assessments may be based on incomplete or poor quality real-time data, the reports are compiled by observers with varying expertise in interpreting and fitting CME observations, and DONKI is inherently biased towards larger CMEs. There are also simply uncertainties in the estimation of the CME parameters. The most challenging part is deciding which day to perform the aurora activity. Assuming that a selected CME will indeed produce aurora, there is still a question of exactly at which day and time we should initiate our observation. Diffuse auroral events have only ever been observed on three occasions, but in all three instances the emission was detectable for several days. We therefore hope that even if we are not able to perform our measurement exactly during the peak of the event, we will still catch some part of it.

Particle parameters	**Quiet solar wind**	**CME requirements**
Velocity	370 km/h	800 km/h
Ion density	1-2 cm^3	6 cm^3
Magnetic field	2 nT	8 nT
Temperature	10 kK	100 kK
Latitude	-	$\pm 20°$

Table 6.1: Table listing the properties of the quiescent solar wind and the defined limits for a CME to be a qualified target.

In an effort to verify the onset time of an event, we use daily updates from the MEX EDAC (see sections 6.2 for more details on the EDAC). Diffuse aurora can most likely be induced by both energetic electrons and protons, but recent modeling work indicates that protons might be the major contributing factor (Nakamura et al., 2022). As the MEX EDAC is mostly sensitive to high energy protons, it could work as a proxy for incoming SEPs. Using EDACs to "nowcast" aurora on Mars is a logical extension of the work described in chapter 6.2. However, there was no clear correlation between the first diffuse auroral event and the EDAC, but there is also no CME recorded with a trajectory intercepting Mars in the relevant time period. There are however several significant flares, implying that the first two diffuse auroral events might have been triggered by solar flares with no

accompanying CMEs. These flare-accelerated SEPs are much narrower (see Figure 6.1) and pass Mars more quickly, and could also have been proton-poor, all these reasons could explain why the EDAC did not report any significant rise in errors during the period of aurora. The second event saw a modest rise in the EDAC counter, at roughly the same time as the occurrence of several flares and one glancing blow of a CMEs at Mars.

The third and by far strongest diffuse auroral event was caused by a series of M and X class flares, with an associated CME. A drastic increase in the EDAC counter is observed shortly after the flare ejection (September 10, early morning UT), as shown in Figure 6.12. The maximum count rate happened between September 10 and 11. A day later strong aurora is detected by MAVEN, peaking just when the count rate has returned to normal levels. When a space weather event includes a flare and CME, the flare-accelerated particles will reach Mars 1-3 days ahead of the CME, depending of the CME velocity. For our solar event targeting purposes, we are mostly interested in a flare-CME event, as we deem it more likely to induce long lasting aurora.

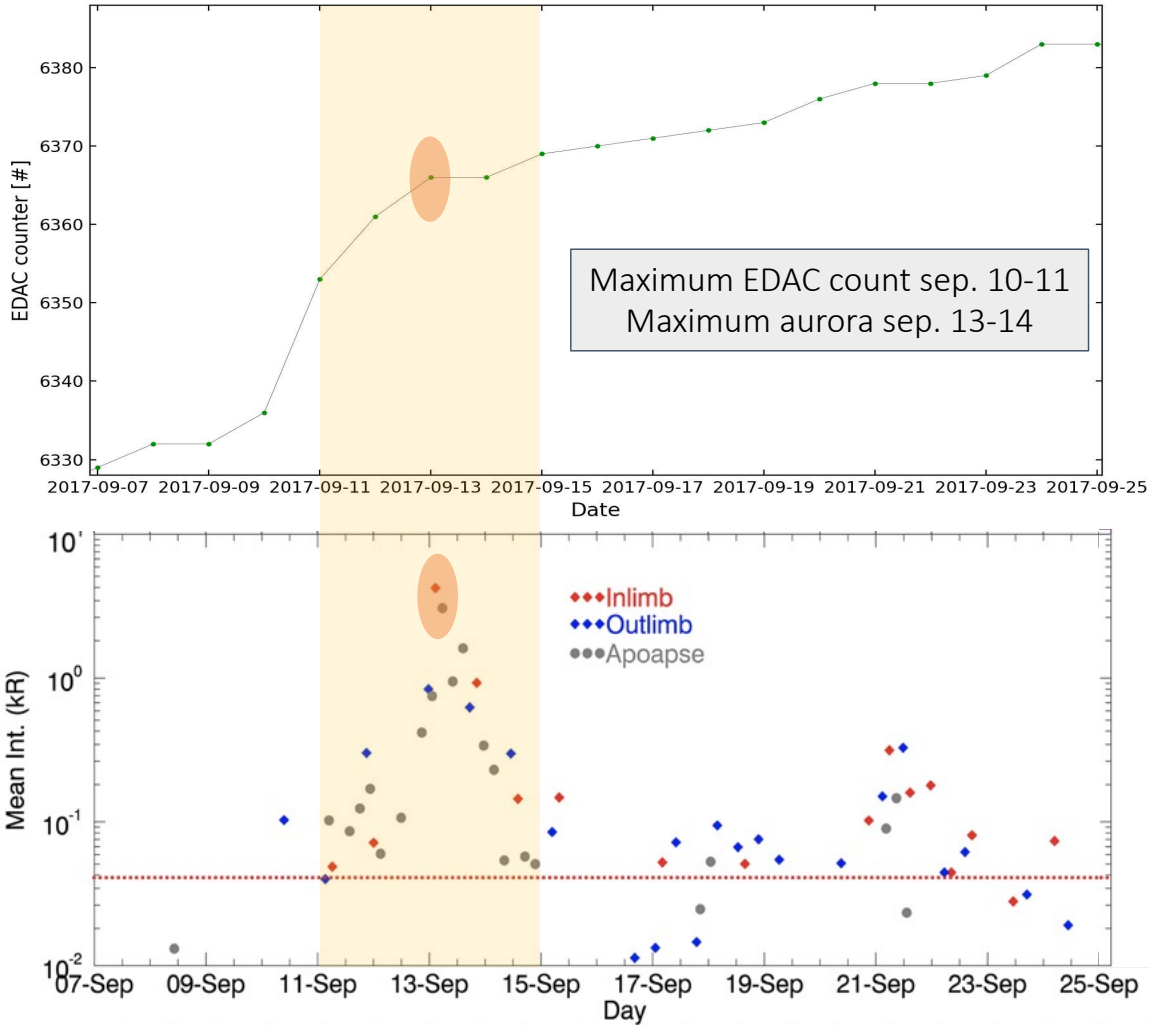

Figure 6.12: Illustration of the correlation between increased EDAC counts and the occurrence of diffuse aurora. Top panel: Daily MEX EDAC counter. Bottom panel: Mean integrated limb intensity of the aurora at peak altitude for the CO Cameron bands, adapted from Schneider et al. (2018). The red line shows the instrument noise floor which sets a minimum detectable brightness of about 50 R. The shaded orange areas highlight the period when the solar event engulfed Mars, with circles indicating the day with most intense aurora and corresponding EDAC count values.

The rate of CMEs being ejected from the Sun is solar cycle dependent, varying between 2-8 CMEs per day with the maximum rate happening a few months after peak solar cycle (Robbrecht et al., 2009), but there is no satisfying statistics about the occurrence rates of solar storms impacting Mars. My intern student during the spring of 2022, Shayla Viet, used an EDAC parameter on MEX and designed a solar event detection algorithm (as previously described in Section 6.2.3), and found that roughly seven days per month during solar maximum registered as days with higher error rates, strongly indicative of impacting solar events. Currently we are approaching solar maximum, with the peak expected in 2025 (Prasad et al., 2022). As the current solar cycle is similar to the previous one in intensity, we can expect a similar frequency of events in the next few years.

In addition, I have actively monitored DONKI and maps of active regions on the Sun since November 2022, in order to collect my own information and practice auroral forecasting on Earth to prepare for when permission is granted to use SuperCam. On March 16, a relatively slow but dense CME was ejected from the Sun towards Earth. I monitored the trajectory and CME parameters, and notified my family in Norway at what time they should go outside and look North. The image 6.13 was taken with my brother's mobile phone one hour after I predicted the auroral onset. From November 2022 to end of April 2023, several solar events were ejected towards Mars, three of which fulfilled our list of requirements (table 6.1). We therefore estimate to request an auroral passive sky observation roughly once every two months. When a candidate event is identified, the DONKI estimate for arrival time at Mars will be refined by daily EDAC updates from MEX, allowing us to make adjustments and postpone the observation if needed.

Figure 6.13: Aurora borealis over southern Norway right after midnight on March 16th 2023. Both the 557.7 nm and 630 nm green and red emissions are visible. Image credit: My brother, André Wright Knutsen.

Observation strategy

In the following section, the different observations strategies that were developed will be detailed. Every day of rover operations is an exercise in division of rover resources, thus the most crucial factors when planning our aurora activity are the required power and data volume. The aurora activity is performed at night with low temperatures resulting in a significant power consumption. In addition, since the science case is not part of the original science objectives for the overall mission, priority is low and likelihood of the activity being cancelled from the plan is high. In order to try to make our auroral observation as non-obtrusive on the mission as possible, we have developed several alternative observation strategies to be able to offer descope options. Since SuperCam has never been used at night, never been used with the intensifier turned to maximum gain, and never done such long integration times with the intensifier, a nighttime test observation was also planned, in addition to a ZCAM nighttime test to evaluate if the selected settings are appropriate. The details of the different aurora observation options and instrument test activities are listed below.

The basis for the auroral observation strategy is the visible channel passive sky at night, which resembles the regular passive sky both in physical geometry (which is exactly the same as an IRS passive sky, see Figure 3.3, and in execution, but as the auroral signal is expected to be very weak, the intensifier is set to maximum gain. Each observation returns three spectra; two lit averages consisting of 75 individual spectral exposures with 0.75 seconds integration time, and one dark average spectrum made from 75 individual acquisitions without the intensifier. This dark spectrum will help quantify the detector dark current contributing to its background noise. ZCAM will use both the R0 and L0 cameras and expose for two to three minutes, preceded and followed by the ZCAM equivalent of darks, using solar filters. The activity is performed around midnight if possible to ensure a completely dark sky, and is pointed in any direction apart from towards the east, where there are no remnant magnetic crustal fields within our field of view.

Full Aurora Observation Suite

The Full Aurora Suite is the optimal way for the Perseverance rover to attempt detecting aurora at Mars. It includes acquisition of visible spectra with SuperCam along with color images from ZCAM, and collection of dark spectra. The observation will start with the mast in stowed position, and SuperCam pointed at the ground. One average spectrum made from 75 individual spectral exposures with 0.75 seconds integration time and intensifier turned on with maximum gain. In this way the "glow" of the intensifier will be obtained as a "dark" for later signal correction.

Both instruments will observe at two elevation angles, typically $\sim$15-20° and $\sim$65° (just as a regular passive sky) but the exact angles will be adjusted according to local topography, and estimates of the line-of-sight elevation angle yielding maximum intensity, as it is highly dependant on dust loading. For the ZCAM low elevation we want the image to capture the black topographical horizon to obtain a striking visual contrast with the hopefully glowing green sky. For SCAM the low elevation angle should be centered on the angle of maximum emission. For the high elevation angle the two instruments will be pointing at the same angle. The purpose of the high elevation pointing is to compare the emission intensity at two angles to potentially constrain the vertical extent of the emitting layer, and to do photometry and disentangle any vertical variation with dust loading. SuperCam will collect a dark spectrum with the intensifier turned off in between each lit measurement at each elevation angle.

The returned data products consist of three dark spectra (one pointed at ground with intensifier on, two with intensifier off at each elevation angle), and four lit spectra (two at each observation angle), as well as two ZCAM images. The total power consumption is estimated to be $212\,\mathrm{W\,h}$, of which $137\,\mathrm{W\,h}$ is for heating. This corresponds to 8.3% of the total charge capacity of the rover battery. The data volume produced is 6 Mb for SCAM and 160 Mb for ZCAM, and the entire activity takes about 1 hour and 12 minutes.

Pre-pointed Aurora Observation Suite
The pre-pointed suite is identical to the full suite except that the stowed position dark spectrum is omitted, and only the low elevation angle is used, to capture the angle of maximum intensity with both cameras and also the horizon with ZCAM. Both cameras are here pre-pointed during the day at the chosen elevation angle, to avoid needing to heat the arm at night, thus saving a significant amount of power. The returned data products are thus one dark spectrum with the intensifier off at low elevation, two lit spectra at low elevation, and one ZCAM image. This descoping option will reduce all of the resources mentioned above; the new total power estimate is $116\,\mathrm{W\,h}$ ($85\,\mathrm{W\,h}$ for heating), which is 4.2% of the battery. SCAM will now produce 3 Mb of data, while ZCAM produces 64 Mb, all in a 43 minutes.

Pre-pointed SCAM-only Aurora Observation
A second descoping option is to exclude ZCAM completely, and use SCAM only at low elevation. This is the least expensive activity alternative we have designed and will return one dark spectrum with the intensifier off at low elevation and two lit spectra at low elevation. The whole activity will only last 28 minutes, require 3 Mb of data and and $27.3\,\mathrm{W\,h}$ (1.5% of the battery).

6.3.2 SuperCam VIS nighttime observations

To better understand what kind of solar events could trigger a detectable auroral emission with SuperCam, we use the September 2017 solar event as baseline for our calculations. That event induced a diffuse aurora event at Mars lasting for several days, reaching a peak limb integrated brightness of 1.4 kR/nm from the atomic oxygen line at $297.2\,\mathrm{nm}$. The UV $297.2\,\mathrm{nm}$ oxygen emission share the same excited upper state as that of the $557.7\,\mathrm{nm}$ visible emission, and the likelihood of each transition is determined by quantum mechanics. The visible-UV ratio has been obtained by observations of Martian dayglow, resulting in a value of 16.5 (Gérard et al., 2020), meaning that the visible emission should be more than 16 times brighter than the UV emission.

Taking into account the spectral resolution of SuperCam, the intensity ratio between the visible and UV emissions, and applying a multiple-scattering pseudo-spherical radiative transfer model (same model as was used in Clancy et al. (2017b)) to incorporate dust effects, we obtain a final observed intensity of 46.2 kR at the limb when tau is set to 0.5. Depending on the dust loading, a spatially uniform, diffuse aurora event will appear brightest when observing at a certain viewing angle. With tau=0.5, this angle is calculated to be 15°, at which angle the observed intensity is 3.1 kR, corresponding to 6.7% of the integrated limb intensity.

Aurora detection attempts

By early August, two separate detection attempts have been made. Both attempts used the "Pre-pointed Aurora Observation Suite" mode, and were made in early May, when there were several very active regions present on the Sun. Both events ended up as negative detections, for different reasons:

- The first event we selected was a bit optimistic. The CME barely qualified according to our selection criteria, and we received a SuperCam observation time slot almost 12 hours later than when the estimated maximum particle density would occur. So the non-detection could have been simply because the event was too weak (slow and/or not dense enough) to generate detectable emissions, or it did indeed produce aurora, but it was over by the time SuperCam was observing.

- The second solar storm we selected seemed much more promising. The event scored high on all our selection criteria, was headed directly for Mars, and the observation time we were granted was only a few hours after the estimated density peak. However, one day before estimated

impact, the forecast changed, adjusting the solar ejection longitude of the event, the effect being the CME was now barely impacting Mars with a glancing blow. We decided to keep our activity in the plan, even though the adjusted particle density and magnetic field disturbance estimates were drastically reduced. We assume that this particular non-detection was due to the event being too weak.

The storm forecast model is shown along with our detection attempts for both occasions in Figure 6.14. The models for both events show significant and rapid increases of all parameters, with the second event being significantly stronger in terms of ion density. As auroral detections on Mars are far from routine, there is no clear consensus on which parameters are most important for triggering diffuse aurora, but as auroral brightness is proportional to the number of incoming particles, we consider this parameter particularly when evaluating events.

Panels iii) for both subfigures show the obtained data with both SuperCam VIS and ZCAM. In the spectra, the black dots are the acquired data, while the white dots is a simulated auroral signal about 10 times weaker than the event observed in Schneider et al. (2018), demonstrating that we would be sensitive to such an event, and weaker ones. Both spectra have been dark-subtracted. During the first attempt, the observation was unintentionally scheduled while Phobos traversed the sky, and was captured by ZCAM, as can be seen in Figure 6.14a panel iii). The background noise level is slightly curved due to scattered light from Phobos. The noise level is also higher in the first attempt compared to the second, because an extra dark observation was added to the activity. The intensifier creates much less background noise than first anticipated, and consequently our detection limit improves. A signal significantly weaker than 10% of the Sep. 17 event would also clearly constitute a positive detection.

The ZCAM images are only partially processed, and contain only dark-subtraction, median-filtering, and a linear color stretch. The scene contains star trails (could potentially be used to measure atmospheric opacity) and sky background. in Figure 6.14b Phobos is in the sky but well outside the FOV. We generally wish to avoid observing when Phobos is in the sky, as we want any light in the ZCAM images to be dominated by the green diffuse glow of the aurora. Nevertheless, the presence of Phobos does not degrade the detection limit for SuperCam as the auroral feature is a sharp peak centered at $557.7\,\mathrm{nm}$, which will be added to the white light from Phobos.

6.4 Space weather summary

6.4.1 EDAC projects

In several studies we have demonstrated the scientific potential of EDAC housekeeping parameters. By combining EDACs on multiple spacecraft, one can study the radiation environment across the solar system at locations where no dedicated radiation payloads exist. One could for example track the trajectory of solar eruption events as they progress outward, aiding to improve our magnetohydrodynamical models of CME and SEP propagation and ultimately improve space weather forecasting. In order to properly take advantage of this, there is still the challenge of accessing detailed information of the spacecraft in question, as the spacecraft itself shields against the low-energy part of the GCR spectrum. Quantifying this effect is complicated and requires detailed knowledge of the spacecraft geometry and components.

By using an EDAC on MEX only, we measured the solar cycle modulation of GCRs at Martian orbit for more than one full solar cycle. This has never before been done for as long, or with as dense temporal coverage. As expected, the GCR variations at Mars follow a solar cycle modulation similar to that observed at Earth, with twice as high daily count rates during solar minimum compared to solar maximum, for those energies that the EDAC counter is sensitive to. The GCR-induced EDAC signal was found to lag behind the sunspot numbers by approximately 5.5 months. The same data

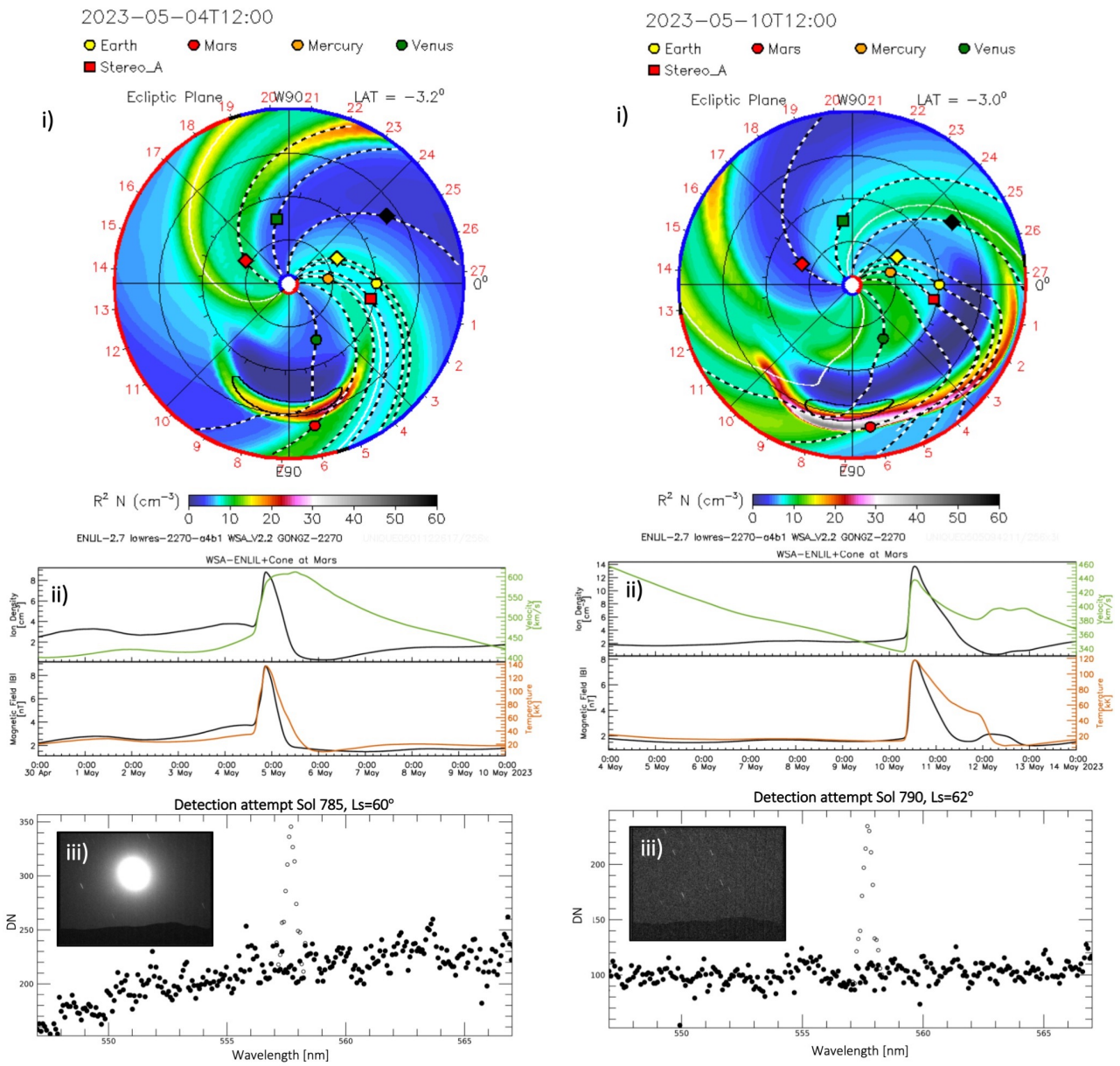

(a) Detection attempt 1, May 5th 2023, Sol 785. (b) Detection attempt 2, May 10th 2023, Sol 790.

Figure 6.14: Overview of the two detection attempts made so far (by August 2023). i) 2D Simulated solar storm forecast, showing the projected trajectory of the CMEs. The colors represent ion density normalized by distance to the Sun. ii) Forecast of plasma parameters at Mars, top panel: ion density (black) and solar wind velocity (green), bottom panel; magnetic field magnitude (black) and ion temperature (orange). Panels i) and ii) from https://ccmc.gsfc.nasa.gov. iii) SuperCam VIS auroral detection attempts, with inlaid ZCAM image of the horizon. Black dots represent the received signal, open circles show a simulated auroral signal. Credit to Tim McConnochie for the data processing and creation of Figures iii).

set was used to detect the impact of solar eruptive events at Mars, and a clear correlation was found between the frequency of impacts and the solar cycle; the number of days with potentially elevated radiation levels was eight times higher during solar maximum compared to during solar minimum.

6.4.2 Aurora with SuperCam

Several different kinds of auroral phenomena have been discovered at Mars, but so far they have only ever been observed in the UV and from orbit. These atomic transitions are also present in airglow, where their counterparts at visible wavelengths have been observed. From quantum theory and airglow observations we know that the auroral atomic oxygen emission should be about 16 times brighter in the visible compared to the UV emission. Here we have described an observation strategy for capturing diffuse aurora from the Martian surface, at visible wavelengths, for the first time.

Two solar storms were selected in early May as candidates that could potentially produce aurora, but both attempts resulted in non-detections. Auroral forecasting at Earth is challenging, and for Mars this endeavor is much more complex and much less constrained by observations and models. To be successful, we need to select a strong solar storm which impacts Mars with a favorable geometry, and to receive SuperCam observation time at the "right" time. There are many variables here, several of which are outside our control. Nevertheless, we will continue our efforts, as we are confident SuperCam has the ability to detect diffuse aurora given the right timing.

Conclusions and perspectives

The goal of this thesis was to learn more about the water vapor vertical distribution in the very lowest part of the Martian atmosphere, a part which is not easily accessible with conventional methods such as orbital single-wavelength domain nadir measurements or even solar occultations. We tackled this challenge by applying two different strategies; a spectral synergy where the utilization of two spectral bands sensitive to separate regions of the atmosphere places stricter constraints on the vertical profile retrieval, and by observing the water column from the surface of Mars where the lower atmosphere is directly available.

The main part of this work entailed the analysis of the complete set of co-located observations from SPICAM and PFS on Mars Express, spanning more than eight Mars years. The goal of probing the near-surface water profile was achieved with a spectral synergy retrieval method, which not only produced a highly robust column abundance climatology, but with a higher degree of freedom also provided information on the degree of vertical confinement. By careful evaluation of the complete data set, a strict selection scheme was designed in order to perform further analysis only on retrievals with accurate water column abundance values, and a high information content with regards to the vertical distribution. The resulting column abundance climatology is in good agreement with other published climatologies, with respect to both geographical and temporal patterns. Compared to the LMD MCD the overall trends are also similar, but they still differ in a few significant ways; the onset of the sublimation period is observed to start later, and the high-concentration sublimation plume is of much lesser latitudinal extent. The NH sublimation peak is also not as extreme. If considering absolute differences of column abundances between the synergy and the MCD, the deviation is biggest at the northern summer sublimation peak, while in relative terms the most significant discrepancies are found at mid-latitudes.

The largest impact of the synergy is when used to extract information on the water profile near the surface. In general we find that the vertical confinement is stronger than predicted by the MCD. The most surprising finding was the discovery of a sinusoidal behaviour of the latitudinal confinement, clearly present in both hemispheres with minima and maxima at corresponding latitudes. We speculate that this wave structure might correlate to latitudes of downwelling/upwelling in connection to the Hadley or polar cells. This will be investigated in detail in future work.

The synergy was exploited further in a project following the synergy climatology paper. By selecting only retrievals with a DOF higher than 2.25, we focus our attention to the NH spring and summer and create a composite near-surface vertical climatology. Even with such high DOFs, the synergy is still not able to produce water profiles of fine resolution, so individual profiles are not evaluated. However by studying hundreds of these profiles obtained at similar locations and times, statistical trends emerge than can be considered. From these retrievals, a two-layer structure is revealed. The double layer feature is consistently present from mid-spring until early summer across much of the northern hemisphere. One can also discern the transportation of water vapor from the subliming NPC edge, where part of the column of water is transported up and poleward in late spring, while some is transported equatorward at very low altitudes in early summer.

The second part of this thesis involved atmospheric measurements from the Martian surface with the infrared spectrometer channel of SuperCam on the Perseverance rover. The rover landed 2.5 months after the start of this PhD (February 2021), and conducted the first passive sky observations

roughly two months after that. Since then, atmospheric measurements have been performed about every two weeks, resulting in a set of 64 observations at the end of this PhD (August 2023) spanning one Martian year.

The quality of the data is significantly influenced by the temperature of different instrument components, and most of the 64 passive sky observations include spectra with glitches, missing spectels that are corrected for in post-processing. After much investigation by several people involved with SuperCam, we have created a procedure so that we avoid the occurrence of most glitches.

A first version of a full retrieval pipeline has been created, and is still being improved upon. The forward model assumes a plane-parallel geometry, and includes the gases CO_2, H_2O and CO, and takes dust aerosols and multiple scattering into account. The radiative transfer equations are solved with DISORT through a python wrapper. A line-by-line radiative transfer model was found to be extremely time-consuming, so a correlated-k method was implemented which reduced the computational time by more than a factor of 300.

The development of a minimization routine applies the traditional χ^2 cost function, and the solution for the best fit is found with the Powell algorithm. The retrieved values are currently the Conrath parameter, total opacity, the effective dust radius, along with an additive shift introduced because the synthetic spectrum is shifted compared to the observed spectrum. After this, the CO_2 abundance is retrieved separately, before the water vapor and CO column abundances are retrieved. We are still not quite able to produce synthetic spectra which systematically resemble the observed spectra, so no reliable retrievals have yet been performed. However, we have identified several points of improvement both regarding the data processing and the forward model, and now that we believe we have a solution for avoiding the occurrence of glitches, we are convinced that SuperCam IRS will provide atmospheric spectra rich in information.

Perspectives

The results and techniques explored and developed in this work will be of use for the further study of water vapor, but also other gaseous species. Specifically, the spectral synergy can be applied to any gas with spectral signatures originating from separate altitude regions, and the passive sky technique can, in time, shed light on H_2O and carbon monoxide in the lower atmosphere. With PFS nearing the end of its lifetime, and no other instrument on board MEX able to replace PFS' capability, the synergistic retrievals of water vapor at Mars are almost at an end, highlighting the uniqueness of the data set presented here. The synergy has already proven to be extremely useful, providing a wealth of new information on water vapor in the lower atmosphere. I am confident, that given more time, SuperCam will also contribute significantly to this effort.

We have in the past 20 years experienced a golden era of Mars exploration, with a record number of orbiters, landers and rovers. Our knowledge of the planet and its atmosphere has increased manyfold in these two decades. Regarding the atmosphere, remaining questions exist largely on topics of various trace species (oxygen, HCL, and methane etc.), details related to atmospheric escape, the origin of the global dust storms, the impact of energetic precipitating particles, and of course the near-surface vertical water vapor distribution. We have not unraveled all of Mars' mysteries, and there is still much to learn from studying Mars; about our own planet, about habitability, and planetary science as a whole. Mars science has greatly benefitted from a fairly pointed focus from the wider planetary community in recent years, and might not have the same luxury in the coming decade as Venus is the target of one of ESAs and two of NASAs future missions. Yet, with many agencies preparing for the human exploration of Mars, the future of Mars research does not seem to slow its pace.

"... humanity's drive out into the universe was maybe
one part hunger for adventure and exploration to
two parts just wanting to get the hell away from each other."

- James S.A. Corey, Persepolis Rising

List of publications

Lead author

Water vapor column abundances and vertical profiles obtained by the author, and the consequent analysis of near-surface water content, was published in the following works:

Knutsen, E.W., Montmessin, F., Verdier, L., Lacombe, G., Lefèvre, F., Ferron, S., Giuranna, M., Wolkenberg, P., Fedorova, A., Trokhimovskiy, A. and Korablev, O., 2022. Water vapor on Mars: A refined climatology and constraints on the near-surface concentration enabled by synergistic retrievals. Journal of Geophysical Research: Planets, 127(5), p.e2022JE007252.

The study of the Galactic Cosmic Ray behaviour in the heliosphere conducted by the author was published in the following work:

Knutsen, E.W., Witasse, O., Sanchez-Cano, B., Lester, M., Wimmer-Schweingruber, R.F., Denis, M., Godfrey, J. and Johnstone, A., 2021. Galactic cosmic ray modulation at Mars and beyond measured with EDACs on Mars Express and Rosetta. Astronomy & Astrophysics, 650, p.A165.

Search for organics in the Martian atmosphere conducted with the NOMAD instrument on ExoMars Trace Gas Orbiter conducted by the author published in the following works:

Knutsen, E.W., Villanueva, G.L., Liuzzi, G., Crismani, M.M., Mumma, M.J., Smith, M.D., Vandaele, A.C., Aoki, S., Thomas, I.R., Daerden, F. and Viscardy, S., 2021. Comprehensive investigation of Mars methane and organics with ExoMars/NOMAD. Icarus, 357, p.114266.

Contributed with topic expertise and discussion

Sánchez-Cano, B., Witasse, O., Knutsen, E.W., Meggi, D., Viet, S., Lester, M., Wimmer-Schweingruber, R.F., Pinto, M., et al. 2023. Solar energetic particle events detected in the housekeeping data of the European Space Agency's spacecraft flotilla in the Solar System. Space Weather,

Maurice, S., Chide, B., Murdoch, N., Lorenz, R.D., Mimoun, D., Wiens, R.C., Stott, A., Jacob, X., Bertrand, T., Montmessin, F. and Lanza, N.L., 2022. In situ recording of Mars soundscape. Nature, 605(7911), pp.653-658.

Villanueva, G.L., Liuzzi, G., Crismani, M.M., Aoki, S., Vandaele, A.C., Daerden, F., Smith, M.D., Mumma, M.J., Knutsen, E.W., Neary, L. and Viscardy, S., 2021. Water heavily fractionated as it ascends on Mars as revealed by ExoMars/NOMAD. Science Advances, 7(7), p.eabc8843.

Liuzzi, G., Villanueva, G.L., Viscardy, S., Mège, D., Crismani, M.M., Aoki, S., Gurgurewicz, J., Tesson, P.A., Mumma, M.J., Smith, M.D. and Faggi, S., 2021. Probing the atmospheric Cl isotopic ratio on mars: Implications for planetary evolution and atmospheric chemistry. Geophysical Research Letters, 48(9), p.e2021GL092650.

Crismani, M.M.J., Villanueva, G.L., Liuzzi, G., Smith, M.D., Knutsen, E.W., Daerden, F., Neary, L., Mumma, M.J., Aoki, S., Trompet, L. and Thomas, I.R., 2021. A global and seasonal perspective of Martian water vapor from ExoMars/NOMAD. Journal of Geophysical Research: Planets, 126(11), p.e2021JE006878.

Conference proceedings

Water vapor vertical distribution study, the abundance retrievals and data analysis was performed by the author:

Knutsen, E.W., Montmessin, F., Verdier, L., Lacombe, G., Lefèvre, F., Ferron, S., Giuranna, M., Wolkenberg, P., Fedorova, A., Trokhimovskiy, A. and Korablev, O., 2022. A spectral synergy method applied to PFS and SPICAM nadir observations to constrain near-surface water content in the Martian atmosphere. In 73th International Astronautical Congress. International Astronautical Federation, IAC-22.A3.3B.8

Supervised and closely collaborated in the development of the SWEET algorithm and the detection and study of space weather events around Mars, authored by Shayla Viet and published in the following work:

Viet, S., Knutsen, E.W., Montmessin, F., Witasse, O., Sanchez-Cano, B., Lester, M., Wimmer-Schweingruber, R.F., 2022. Detecting and investigating space weather events around Mars with EDAC counters. In 73th International Astronautical Congress. International Astronautical Federation, IAC-22/A3/IP/73284.

Mission concept for far-infrared observatory dedicated to the study of protoplanetary disks, the science case was developed by the author and published in the following works:

De Marco, G., Knutsen, E.W., Bolart, C., Breuhaus, M., Estanqueiro, L., Fröhlich, C., Guyot, M., Hegyesi, B., Lauksio, V., Owe, S.H. and Pinzón-Rodriguez, O., 2019. Frost, far-infrared observation spectroscopy telescopes. In 70th International Astronautical Congress. International Astronautical Federation.

List of public speaking events

Conferences

DPS-EPSC 2023, San Antonio, Texas, USA
"Atmospheric investigations with M2020 Perseverance/SuperCam"

ESLAB 2023, ESTEC, Noordwijk, Netherlands
"Vertical distribution of near-surface water vapor on Mars"

Trondheim Science Festival 2023, Trondheim, Norway
Invited speaker, "Mars exploration; What are we doing, why are we doing it and my part in all of it"

MAMO 2022, Paris, France
Knutsen, E.W., Montmessin, F., Verdier, L., Lacombe, G., Lefèvre, F., et al.. Water vapor on Mars: A refined climatology and near-surface concentration enabled by synergistic retrievals. Seventh international workshop on the Mars atmosphere: Modelling and observations, Jun 2022, Paris, France. ⟨insu-03747001⟩

IAC 2022, Paris, France
Knutsen, E.W., Montmessin, F., Verdier, L., Lacombe, G., Lefèvre, F., Ferron, S., Giuranna, M., Wolkenberg, P., Fedorova, A.A., Trokhimovskiy, A. and Korablev, O.I., 2022. A spectral synergy method applied to PFS and SPICAM nadir observations: Constraining near-surface water content on Mars

EPSC 2021, virtual meeting
Knutsen, E.W., Montmessin, F., Lefèvre, F., Giuranna, M. and Verdier, L., 2021. Constraints on water vapor content in the lower atmosphere of Mars (No. EPSC2021-528). Copernicus Meetings.

EGU 2021, virtual meeting
Knusten, E.W., Witasse, O., Sanchez-Cano, B., Lester, M., Wimmer-Schweingruber, R., Denis, M., Godfrey, J. and Johnstone, A., 2021. Galactic Cosmic Ray Modulation at Mars and beyond measured with EDACs on Mars Express and Rosetta (No. EGU21-11158). Copernicus Meetings.

International team meetings

M2020 Perseverance team meeting, June 2023, *Updates on the retrieval of water vapor with SuperCam*

Trace Gas Orbiter Atmospheric Chemistry Suite Science Working Team meeting, April 2021, *Search for methane and organics in the atmosphere of Mars*

Mars Express SPICAM/PFS Science Working Team meeting, May 2021, *Constraining near-surface*

water vapor on Mars: a spectral synergy climatological survey applied to PFS and SPICAM nadir observations

Mars Express & Trace Gas Orbiter Science Working Team meeting, September 2021, *Water vapor on Mars: A refined climatology and near-surface concentration enabled by synergistic retrievals*

Outreach and public engagement

Rotary meeting 2022, Larvik, Norway
Invited speaker, "Space news; First results from JWST, DART and the latest from Mars"

Montessori school visit 2022, Versailles, France
Invited speaker, "Journey through the solar system"

Recurring speaker with "Skype a scientist"
Giving talks to school classes internationally over skype, with students age between 10 and 17 about space exploration, the search for life on other planets, climate change and space weather.

Recurring speaker with "Scientist on screen"
Giving talks to school classes in Norway with students age between 16 and 18 about space exploration, the search for life on other planets, climate change and space weather.

Appendices

Appendix A

Article: Water Vapor on Mars: A Refined Climatology and Constraints on the Near-Surface Concentration Enabled by Synergistic Retrievals

Check for updates

21699100, 2022, 5, Downloaded from https://agupubs.onlinelibrary.wiley.com/doi/10.1029/2022JE007252 by Cochrane France, Wiley Online Library on [31/10/2022]. See the Terms and Conditions (https://onlinelibrary.wiley.com/terms-and-conditions) on Wiley Online Library for rules of use; OA articles are governed by the applicable Creative Commons License

JGR Planets

RESEARCH ARTICLE
10.1029/2022JE007252

Key Points:

- Using a spectral synergy retrieval method on nadir observations from SPICAM and PFS to obtain a highly accurate water vapor climatology
- The synergy method is sensitive to the vertical distribution of H_2O, and can distinguish near-surface water from the rest of the column
- Discrepancies in meridional and seasonal behavior of vertical confinement are revealed between the synergy and the Mars Climate Database

Correspondence to:
E. W. Knutsen,
elise-wright.knutsen@latmos.ipsl.fr

Citation:
Knutsen, E. W., Montmessin, F., Verdier, L., Lacombe, G., Lefèvre, F., Ferron, S., et al. (2022). Water vapor on Mars: A refined climatology and constraints on the near-surface concentration enabled by synergistic retrievals. *Journal of Geophysical Research: Planets*, *127*, e2022JE007252. https://doi.org/10.1029/2022JE007252

Received 18 FEB 2022
Accepted 6 MAY 2022
Corrected 31 MAY 2022

This article was corrected on 31 MAY 2022. See the end of the full text for details.

Author Contributions:
Conceptualization: Elise W. Knutsen, Franck Montmessin
Data curation: Elise W. Knutsen, Loïc Verdier, Gaétan Lacombe
Formal analysis: Elise W. Knutsen
Funding acquisition: Franck Montmessin
Investigation: Elise W. Knutsen
Methodology: Elise W. Knutsen, Franck Montmessin, Loïc Verdier, Stéphane Ferron

© 2022. The Authors.
This is an open access article under the terms of the Creative Commons Attribution-NonCommercial-NoDerivs License, which permits use and distribution in any medium, provided the original work is properly cited, the use is non-commercial and no modifications or adaptations are made.

Water Vapor on Mars: A Refined Climatology and Constraints on the Near-Surface Concentration Enabled by Synergistic Retrievals

Elise W. Knutsen[1], Franck Montmessin[1], Loïc Verdier[1], Gaétan Lacombe[1], Franck Lefèvre[1], Stéphane Ferron[2], Marco Giuranna[3], Paulina Wolkenberg[3], Anna Fedorova[4], Alexander Trokhimovskiy[4], and Oleg Korablev[4]

[1]LATMOS/IPSL, UVSQ Université Paris-Saclay, Sorbonne Université, CNRS, Guyancourt, France, [2]ACRI-ST, boulevard des Garennes, Guyancourt, France, [3]IAPS-INAF, Rome, Italy, [4]Space Research Institute (IKI), Moscow, Russia

Abstract With the utilization of a novel synergistic approach, we constrain the vertical distribution of water vapor on Mars with measurements from nadir-pointing instruments. Water vapor column abundances were retrieved simultaneously with PFS (sensing the thermal infrared range) and SPICAM (sensing the near-infrared range) on Mars Express, yielding distinct yet complementary sensitivity to different parts of the atmospheric column. We show that by exploiting a spectral synergy retrieval approach, we obtain more accurate water vapor column abundances compared to when only one instrument is used, providing a new and highly robust reference climatology from Mars Express. We present a composite global data set covering all seasons and latitudes, assembled from colocated observations sampled from seven Martian years. The synergy also offers a way to study the vertical partitioning of water, which has remained out of the scope of nadir observations made by single instruments covering a single spectral interval. Special attention is given to the north polar region, with extra focus on the sublimation of the seasonal polar cap during the late spring and summer seasons. Column abundances from the Mars Climate Database were found to be significantly higher than synergistically retrieved values, especially in the summer Northern Hemisphere. Deviations between synergy and model in both magnitude and meridional variation of the vertical confinement were also discovered, suggesting that certain aspects of the transport and dynamics of water vapor are not fully captured by current models.

Plain Language Summary Water vapor plays an important role in the weather and climate on Mars, even though little of it remains today. The behavior of water vapor has been studied for decades, yet how water vapor varies with altitude, especially close to the surface, remains an open question. In this study, we use measurements from two instruments on the Mars Express satellite to learn about the near-surface water vapor. By combining measurements from the SPICAM and PFS spectrometers, a composite full-year climatology is assembled. We measure the total amount of water vapor with great accuracy, and also obtain information about the vertical distribution. The north polar cap is studied in detail during early summer, when part of the polar ice cap sublimates into water vapor and is transported south. The results are compared to model data from the Mars Climate Database, and significant differences between the observations and the model are identified. The total water content is found to be smaller than model estimates, while observations indicate that more water than expected is confined near the surface. This suggests that some aspects of the atmospheric transport processes are not currently fully understood.

1. Introduction

Water vapor on Mars was first detected in 1963 with the use of a ground-based telescope which observed eleven near-infrared absorption lines (Spinrad et al., 1963). Since then, numerous observatories, ground-based, Earth-orbiting, Mars-orbiting, landers and rovers, have observed the highly volatile trace gas. Even as a minor atmospheric constituent, water vapor plays a major role in shaping the climate on Mars (along with the CO_2 and dust cycles). Water controls the stability of the atmosphere, as H_2O photolysis supplies hydroxyl radicals, the main oxidant of the Martian photochemical cycle (e.g., McElroy and Donahue (1972)), and impacts the radiative equilibrium through cloud formation (Madeleine et al., 2012).

The Mars Atmospheric Water Detector (MAWD) instruments on the Viking orbiters provided evidence that the Northern polar cap is the primary source of atmospheric water, and also indicated a strong north-south asymmetry

Journal of Geophysical Research: Planets 10.1029/2022JE007252

Project Administration: Franck Montmessin
Resources: Franck Montmessin
Software: Loïc Verdier, Gaétan Lacombe, Stéphane Ferron
Supervision: Franck Montmessin
Validation: Elise W. Knutsen, Franck Montmessin, Loïc Verdier, Stéphane Ferron
Visualization: Elise W. Knutsen
Writing – original draft: Elise W. Knutsen
Writing – review & editing: Elise W. Knutsen, Franck Montmessin, Loïc Verdier, Gaétan Lacombe, Franck Lefèvre, Marco Giuranna, Paulina Wolkenberg, Anna Fedorova, Alexander Trokhimovskiy, Oleg Korablev

in the atmospheric water abundance (Farmer et al., 1976; Jakosky & Farmer, 1982). The most complete climatology, upon which modern Martian water climatology is based, was obtained by the Mars Global Surveyor mission and its Thermal Emission Spectrometer (Smith, 2002, 2004). A revised retrieval scheme on TES observations provide an annual reference water vapor cycle with column abundance maximum at high latitudes during midsummer in both hemispheres, reaching a peak of ∼60 pr-μm on average in the north, and ∼25 pr-μm in the south (Pankine et al., 2010). Low water abundances are observed during fall and winter at middle and high latitudes of both hemispheres. General circulation models along with TES observations indicate that water from the southern summer maximum is transported to the Northern Hemisphere (NH) more efficiently than the reverse process (Montmessin et al., 2004; Steele et al., 2014).

One of the main objectives of the Mars Express (MEX) orbiter is to study the water cycle on Mars. Three spectrometers onboard MEX can measure the water vapor abundance in different spectral bands: the Planetary Fourier Spectrometer (PFS), the Observatoire pour la Minéralogie, l'Eau, les Glaces, et l'Activité (OMEGA), and SPectroscopy for the Investigation of the Characteristics of the Atmosphere of Mars (SPICAM). For the purpose of this study, PFS was selected for its coverage of water vapor diagnostic features in the thermal infrared (TIR) domain, while SPICAM was chosen over OMEGA to cover the near infrared (NIR) due to its higher spectral resolution, and the presence of CO_2 bands near the 2.6 μm water feature for OMEGA.

1.1. Water Vapor Vertical Distribution

Until recently, knowledge of the near-surface H_2O profile on Mars mostly relied on general circulation models. The vertical distribution of water vapor has been inferred from nadir measurements (Fouchet et al., 2007; Pankine & Tamppari, 2015) and measured directly by solar occultation viewing geometry with SPICAM on Mars-Express since 2004, and with the ExoMars Trace gas Orbiter (TGO) and its infrared spectrometers NOMAD and ACS since 2018. SPICAM occultation campaigns were not a primary focus of the spacecraft and are therefore not performed very often, whereas TGO, with its orbit adapted for occultation measurements with good vertical and temporal resolution, allows the study of dynamical behavior of water distribution including escape processes in great detail. With this technique, new knowledge has been obtained on the vertical distribution of water in the upper atmosphere as a result of supersaturation above the hygropause, and the occurrence of high altitude water during dust storms (e.g., (Aoki et al., 2019; Fedorova et al., 2020)). SPICAM solar occultations were also used to produce a climatology of vertical distribution covering the Martian years (MY) 27–34 that encompassed two global dust events (Fedorova et al., 2021). With solar occultation measurements one can obtain very fine vertical resolution, nevertheless, measurements below 10 km are relatively sparse as aerosol loading in the lower atmosphere leads to high opacities which reduces the transmittance significantly. The lower limit for observation is typically 5–10 km for dust-free conditions, and as high as 20–30 km during the dusty perihelion season (e.g., Aoki et al. (2019)). Only under very clear conditions will solar occultation observations be able to probe below 10 km, however, such conditions mostly occur at high latitudes. As a result, information about the low-atmosphere water vapor profile remains exceptional.

Below 10 km, surface-atmosphere interactions such as convection, frost sublimation, and deposition are expected to be the main forcers on the vertical distribution, along with adsorption and desorption. Above 10 km, water ice clouds are thought to be dominant (Montmessin et al., 2004; Richardson, 2002). Below the saturation level, controversy exists regarding whether water vapor is well-mixed with CO_2, or distributed in a more complex manner. Davies (1979) used Viking Orbiter 1 data to directly probe the location of water vapor with altitude for the first time. He found that H_2O vertical distribution was indistinguishable from the dust vertical distribution and was well-mixed up to about 10 km, which has been commonly assumed since. A recent analysis of data from the Surface Stereo Imager on the Phoenix lander by Tamppari and Lemmon (2020) shows that water is highly confined to a near-surface layer of 2.5 km, and that a well-mixed column is not supported by the data. Controversies remain, and it is also argued that water is either confined to, or reduced in the lower atmosphere, depending on the season and location. This has relevance to the amount of water vapor exchange occurring between the atmosphere and the regolith.

Adsorption of CO_2 by the Martian regolith was first suggested by Davis (1969), and the theory was later expanded upon to include water vapor by Fanale and Cannon (1971), whose adsorption isotherm expression has been widely used since (although found to require modification by Savijärvi and Harri (2021)). Using data from Viking 1 and 2, Jakosky et al. (1997) showed a nocturnal depletion of atmospheric water vapor, suggesting a diurnal

21699100, 2022, 5, Downloaded from https://agupubs.onlinelibrary.wiley.com/doi/10.1029/2022JE007252 by Cochrane France, Wiley Online Library on [31/10/2022]. See the Terms and Conditions (https://onlinelibrary.wiley.com/terms-and-conditions) on Wiley Online Library for rules of use; OA articles are governed by the applicable Creative Commons License

Journal of Geophysical Research: Planets 10.1029/2022JE007252

21699100, 2022, 5, Downloaded from https://agupubs.onlinelibrary.wiley.com/doi/10.1029/2022JE007252 by Cochrane France, Wiley Online Library on [31/10/2022]. See the Terms and Conditions (https://onlinelibrary.wiley.com/terms-and-conditions) on Wiley Online Library for rules of use; OA articles are governed by the applicable Creative Commons License

exchange cycle between the porous regolith and the atmosphere. Similar results were obtained with the thermal and electrical conductivity probe on the Phoenix lander by Zent et al. (2010) and Fischer et al. (2019). It was found that the layer that experiences a diurnal exchange of water with the surface was 0.5–1 km deep (Tamppari et al., 2010). This phenomenon was again confirmed by Harri et al. (2014) and Martínez et al. (2017), who used the REMS-H device on Curiosity rover to derive water vapor volume mixing ratios. Savijärvi and Harri (2021) found that regolith exchange is largely indifferent to surface properties, and that diurnal adsorption/desorption generates approximately 1% variation in the column abundance, which matches Earth analogue measurements very well. Results from Fouchet et al. (2007) indicate that the vertical distribution is controlled by an intermediate state where the water is controlled by atmospheric saturation on one hand, and confined to a surface layer on the other, pointing to significant regolith-atmosphere exchange processes. This result is inferred by investigating the correlation of water columns and pressure, and was not observed directly. Maltagliati, Montmessin, et al. (2011); Maltagliati, Titov, et al. (2011) and Trokhimovskiy et al. (2015) also attempted to discern a diurnal exchange process between atmosphere and regolith, but found no evidence of local time variation in H_2O abundances. Thus, the extent of exchange between regolith and atmosphere remains an open question.

1.2. Spectral Synergy

When observing an atmosphere in nadir viewing geometry, the outcome is normally a column abundance value of the target species. However, it is possible to obtain information about the vertical distribution of the species by combining multiple spectral domains in the retrieval process. This approach is commonly referred to as a spectral synergy, and was developed for Earth observation by Pan et al. (1995, 1998), who predicted higher sensitivity to near-surface layers of CO if near and thermal infrared spectral bands were combined. This was later confirmed by Edwards et al. (2009), who demonstrated that combining NIR and TIR measurements in a common retrieval allowed for a significantly higher sensitivity in the troposphere. The method has also been used to increase near-surface sensitivity to other gasses such as CO_2 (Christi & Stephens, 2004), O_3 (Landgraf & Hasekamp, 2007), and CH_4 (Razavi et al., 2009).

TIR measurements are mostly sensitive to the middle atmosphere (at the origin of the photon emission) where the temperature contrast of the atmosphere with respect to the surface is high. NIR measurements on the other hand are sensitive to any molecule present along the column as the technique relies on solar photons traversing the entire atmosphere back and forth. Although Trokhimovskiy et al. (2015) indicate the NIR technique is mostly sensitive to the atmosphere below 30 km, it is only true from a mixing ratio perspective, which favors the denser layers of the atmosphere. In other words, any given change in H_2O mixing ratio will be easier to sense in the bottom of the profile as pressure and number density are assumed to be continuously increasing toward the surface. If seen from a number of molecules perspective, the NIR inversion technique has no preference to a particular position of the column, unless this portion concentrates more water molecules at a specific location. One must note, however, that dust modulates this assertion. At high dust opacity, part of the incoming flux does not reach the surface and is sent back to space without sampling the entire column. Only in such cases will the NIR technique become altitude dependent.

This difference in sensitivity of NIR and TIR can be viewed as a difference in the shape and peak altitude of the weighting function of water vapor retrieval in a particular wavelength domain, and has been advocated to explain the dispersion of H_2O column abundance values retrieved by the various instruments of MEX (Tschimmel et al., 2008). On the other hand, the difference in sensitivity can also be considered a way to offer simultaneous access to different regions of the atmosphere, leading to the derivation of more than a single parameter representative of the whole column, as is usually the case with instruments that study water vapor using nadir observations. In fact, combining two spectral domains increases the degree of freedom (DOF) of the signal. The DOF gives an estimate of the number of independent bits of information in an atmospheric measurement (Rodgers, 2000), and a DOF higher than 1 indicates the presence of some amount of profile shape information.

If attempting to retrieve vertical information with only one instrument, one could argue that as the single instrument is primarily sensitive to a specific altitude region, the obtained vertical confinement is not a “real” partitioning. Instead, the obtained partitioning might be a product of a lack of sensitivity to other, and perhaps wetter, altitude regions, thus producing an artificial vertical partitioning. This problem is avoided with the use of a spectral synergy, as each wavelength interval is susceptible to emission/absorption signatures in separate regions, and therefore obtains information from different altitudes.

Journal of Geophysical Research: Planets 10.1029/2022JE007252

21699100, 2022, 5, Downloaded from https://agupubs.onlinelibrary.wiley.com/doi/10.1029/2022JE007252 by Cochrane France, Wiley Online Library on [31/10/2022]. See the Terms and Conditions (https://onlinelibrary.wiley.com/terms-and-conditions) on Wiley Online Library for rules of use; OA articles are governed by the applicable Creative Commons License

This consideration led Montmessin and Ferron (2019) to investigate the potential for a synergistic retrieval of water vapor in the Martian atmosphere using MEX, as the spacecraft constitutes the only asset at Mars observing water in both NIR (SPICAM, OMEGA, and PFS) and TIR (PFS) spectral intervals. Despite their differences in field-of-view, sampling and coverage, SPICAM (NIR) and PFS (TIR) were selected for this study as the two have the most extensive records of water vapor retrievals on Mars among the MEX instruments (Fedorova et al., 2006; Fouchet et al., 2007; Giuranna et al., 2019; Trokhimovskiy et al., 2015). As Montmessin and Ferron (2019) concluded on the promising potential for a synergistic retrieval of water vapor on Mars with MEX, this work is intended to follow-up on this earlier study and present the analysis of a multi-annual data set covering the period from MY 26 to 34.

The intention of this paper is to be largely descriptive, as this is the first time the spectral synergy has been applied to a larger data set. The numerous implications of the vertical partitioning results, and any differences to other observations or the MCD data base are beyond the scope of this paper, but will be the aim of future work using the synergy. The first part of the manuscript provides an overview of the instruments used in this study (Section 2), and continues in Section 3 with an outline of the synergistic retrieval method, including a description of the selection of measurements within the data set. The results are presented in Section 4, where in 4.1 a complete synergistic column abundance climatology is presented, followed by a comparison of the column abundance between the synergy, the model and the single spectral domain retrievals are made, before the vertical and spatial distribution is elaborated upon. A discussion of the results and how they compare to previous works follows in Section 5, and Section 6 concludes the findings of this study.

2. Instruments

The Mars Express mission was launched in June 2003, and began nominal science operations in mid-January 2004 (Chicarro et al., 2004), corresponding to the very end of MY 26. From a quasi-polar and highly elliptical orbit with a periapsis of ∼300 km and a period of 7.5 hr, MEX has a particularly detailed view of the polar caps at the sublimation onset. With three instruments able to measure the atmospheric water vapor content (OMEGA, PFS, and SPICAM), either in the solar reflected or in the thermal component, MEX has delivered a vast amount of valuable data with complete global and seasonal coverage. The PFS and SPICAM instruments cover the thermal and near-infrared domains, respectively, within which water vapor possesses diagnostic signatures.

The measurements used in the following analysis were retrieved from nadir observations, and were selected according to a number of criteria to ensure satisfactory quality of every individual measurement, sufficient geographical and seasonal coverages, and a minimum error of radiative transfer modeling due to surface inhomogeneity (Montmessin & Ferron, 2019). For a detailed description on the selection and averaging processes used for the creation of a data set compatible with a synergistic extraction of water vapor, the reader is referred to Montmessin and Ferron (2019).

2.1. Mars Express PFS

The Planetary Fourier Spectrometer is an infrared spectrometer with two wavelength channels optimized for atmospheric sensing. The short wavelength channel covers the range 1,700–8,200 cm^{-1} (∼1.22–5.88 μm) with a full width at half maximum (FWHM) of the instantaneous field of view (FOV) of 1.6°, while the long wavelength channel spans the 250–1,700 cm^{-1} (5.88–40 μm) with a FWHM FOV of 2.8°, which at the pericenter corresponds to a 440 km^2 surface footprint. Only the long wavelength channel was utilized for this work. Both channels have a spectral resolution of 1.3 cm^{-1}. For further details, see Formisano et al. (2005) and Giuranna et al. (2005).

For the synergistic approach, several windows in the long wavelength channel were selected. The windows from 8 to 10 μm and 19–25 μm were used to obtain surface temperature and dust model properties, the region at 12–19 μm is dominated by the absorption of the 15 μm CO_2 vibrational transition which was used to retrieve atmospheric temperature profiles, while the 20–35 μm thermal emission band was used to retrieve the water vapor abundance, henceforth referred to as TIR. Because PFS was used to retrieve several parameters, a high signal-to-noise ratio (SNR) is required, and one individual spectrum obtained with PFS is not satisfactory. Therefore, the retrievals were performed on the average of nine consecutive spectra. The total time passed between the acquisition of the first spectrum to the last of the nine to be averaged is 108 s, as it takes 4.5 s to acquire a single PFS interferogram and the repetition time is 8.5 s (Fouchet et al., 2007). This corresponds to a cumulative surface

Journal of Geophysical Research: Planets 10.1029/2022JE007252

21699100, 2022, 5, Downloaded from https://agupubs.onlinelibrary.wiley.com/doi/10.1029/2022JE007252 by Cochrane France, Wiley Online Library on [31/10/2022]. See the Terms and Conditions (https://onlinelibrary.wiley.com/terms-and-conditions) on Wiley Online Library for rules of use; OA articles are governed by the applicable Creative Commons License

footprint at the pericenter of 3,900 km^2, however, note that as the orbit is elliptical, this area will vary depending on spacecraft altitude.

After years of operation, an issue with PFS caused the interferogram peak to not always be centered. The instrument line-shape used here (a sine cardinal function with 1.3 cm^{-1} FWHM) is then not optimal, and could lead to biased water vapor retrievals, with a tendency of being too low. This issue started around orbit 6000 (MY 29), became particularly relevant after orbit 7500 (MY 30), but data obtained in MY 32 and after are less affected. In an effort to largely avoid this problem, we exclude all measurements during MY 30 and MY 31 from further analysis.

2.2. Mars Express SPICAM

The SPICAM UV-IR instrument (Spectroscopy for the Investigation of the Characteristics of the Atmosphere of Mars) is a dual-channel spectrometer designed to study the Martian atmosphere from top to bottom (Bertaux et al., 2006). In this study, only the IR channel was utilized working in the spectral range of 1–1.7 μm with a spectral resolution of 3.5–4.0 cm^{-1}, a complete description of which can be found in Korablev et al. (2006).

In nadir viewing geometry, the IR channel has an instantaneous FOV of 1°, corresponding to a footprint 230 km^2 on the surface when the spacecraft is at the pericenter of its orbit. The incoming flux is separated into two detectors, where detector 1 was used for this work as it provides significantly higher performance in nadir. The wavelength interval 1.34–1.43 μm is defined as the NIR range for the synergy, as it covers the strong water absorption band at 1.38 μm. Averages of ten SPICAM-IR spectra are demonstrated to have a SNR sufficient for reliable retrievals of water vapor column abundances (Fedorova et al., 2006; Trokhimovskiy et al., 2015). For the sake of the synergy, the SPICAM observation closest in time to the center PFS spectrum is selected, and averaged together with the seven previous and the seven following spectra. The 15 spectrum cumulative surface footprint area at pericenter corresponds roughly to 3,400 km^2, similar to that of the nine PFS spectrum average. Together, the SPICAM and PFS average spectra constitute a colocated observation.

3. Data Set and Retrieval

In the earlier demonstration of the synergy method applied to Martian water vapor, a subset of 449 colocated observations from 133 orbits distributed through MY 27 were presented (Montmessin & Ferron, 2019), showcasing that the synergy brings additional robustness to the retrieval of water vapor column abundance, and provides insight into the vertical distribution of water vapor. In this study, we expand on those findings, and conduct a comprehensive analysis of the complete synergistic data set available from MEX, which at the time of writing contains nearly 200,000 measurements.

The data set presented here consists of colocated observations taken over 1379 individual orbits distributed across seven Mars years from Ls 334° of MY 26 to Ls 297° of MY 34, with no measurements from MY 30 to 31 (Knutsen, 2022). The geographical and seasonal coverage is highly variable from year to year, several being quite sparsely covered. Some sparsity is due to operational constraints, as not all instruments can be concurrently active, while most is due to the requirement of colocated measurements from both SPICAM and PFS.

3.1. Synergistic Retrieval Routine

The synergistic approach requires a set of colocated PFS and SPICAM observations on which to apply the retrieval method. To obtain a satisfying PFS SNR for the fitting of multiple parameters, nine consecutive spectra are averaged together. The SPICAM observation closest in time to the central PFS spectrum is then selected and averaged with the seven observations prior to it and the seven after it, resulting in a combined FOV similar to that of the nine combined PFS observations. A screening process is conducted on this set of colocated observations, the details of which can be found in Montmessin and Ferron (2019). The simultaneous inversion of H_2O follows the approach outlined in Montmessin and Ferron (2019), and will only be briefly described here.

A priori water vapor and temperature profiles are extracted from the Mars Climate Database (MCD) based on the general circulation model developed at the Laboratoire de Météorologie Dynamique (LMD GCM) (Forget et al., 1999; Millour et al., 2018) with an uncertainty of the water equal to the abundance values. MCD version

Journal of Geophysical Research: Planets 10.1029/2022JE007252

21699100, 2022, 5, Downloaded from https://agupubs.onlinelibrary.wiley.com/doi/10.1029/2022JE007252 by Cochrane France, Wiley Online Library on [31/10/2022]. See the Terms and Conditions (https://onlinelibrary.wiley.com/terms-and-conditions) on Wiley Online Library for rules of use; OA articles are governed by the applicable Creative Commons License

5.3 is used. For each year the corresponding scenario is chosen, except for MY 34, which is not yet included (the version used was last updated on 11/01/2019). A composite scenario was therefore built for MY 34 by combining the scenario of MY 33 with the standard MCD dust storm scenario 4 and the warm and dusty scenario 7 (for the intervals Ls = 180°–200° and Ls = 200°–220°, respectively).

Temperature and aerosol parameters are retrieved individually from the PFS average spectra, which are then injected into the synergistic routine. The overall spectral fitting procedure uses the HITRAN 2012 spectroscopic database (Rothman et al., 2013) as a baseline for the computation of absorption coefficients of H_2O and CO_2, and then relies on a Bayesian approach that consists in maximizing the probability that a given retrieval satisfies both the observed averaged spectra and falls within a range of plausible a priori values specified by assumptions on the value and its dispersion. The weight of the a priori assumption in the retrieval is dictated by its a priori uncertainty, which is set equal to the integrated a priori water vapor profile.

Water vapor is inferred from the set of combined NIR and TIR spectra, by a simultaneous inversion from both spectral domains. In practice, the algorithm adjusts the water vapor abundance along the vertical profile at nine altitude points separated by 2.5 km from ground to 10 km, and by 5 km from 10 to 30 km. All points are correlated with a Gaussian kernel, such that the points are less strongly correlated when the distance between them is increasing. The results include a posteriori covariance matrix, from which the DOF can be calculated from the sum of the trace of the matrix. The DOF normally fluctuates around 1 when the retrieval includes a single spectral domain (NIR or TIR), which implies only one independent parameter can be inferred from a water vapor measurement (e.g., the column abundance), while with a higher DOF some information of the water vapor vertical distribution can be obtained.

Some example spectra are shown in the top row of Figure 1, where the selected NIR and TIR spectral intervals include strong diagnostic features of water vapor. The colocated observations shown here are from early summer of MY 27 at high latitudes. The corresponding vertical profile obtained from the synergistic retrieval performed on both spectra is shown in the bottom left, and is compared to the MCD a priori profile. In the bottom center and bottom right plots, the synergy is compared to the single spectral domain retrievals in terms of averaging kernels (bottom center) and the posterior-to-prior error ratio profiles (bottom right). MCD a priori profiles are used for all retrieval techniques (synergy, PFS-only, and SPICAM-only), such that the a posteriori-to-a priori (post-to-prior for short) error profiles are ratios at each altitude level of the retrieved posteriori error and the MCD a priori error. The post-to-prior profile indicates the amount of added information at each altitude, and shows that the synergy is more sensitive to the lower atmosphere than both PFS and SPICAM.

We quantify the amount of information added by the synergy at each altitude level by comparing the synergistically retrieved error profiles to the MCD a priori error profiles, shown in the bottom right panel of Figure 1. In this way, we demonstrate that the synergy does not simply reproduce the a priori when calculating vertical profiles, and that for the lower atmosphere, the synergy brings more information than the single spectral domain retrievals. The MCD a priori and the retrieved vertical mixing ratio profiles are close to identical above 15 km, but start to deviate below this, where the synergy provides a significant amount of added information.

3.2. Data Selection Scheme

The complete synergy data set is shown in Figure 2, where the seasonal coverage for all synergy column abundance retrievals is displayed as a function of latitude. Retrievals from MY 27 encompass more than 30% of all co-located observations. The total water columns here are not corrected for topography.

Several selection criteria were applied to the PFS and SPICAM measurements when assembling the synergy data set, yet not all selected retrievals yielded satisfying results. A few retrievals have extremely high values that are deemed unlikely to occur, while others yield poor fits and high values for the mean statistical variation of the residual spectra (reduced χ^2). The χ^2 thus corresponds to the misfit between measured and modeled spectra for the best-fit water vapor abundance.

The aforementioned benefit of an increased DOF by the use of a spectral synergy approach is demonstrated in Figure 3. While water vapor column abundances from all available colocated observations were shown in Figure 2, only data points with a reduced χ^2 of the retrieval equal to or smaller than 4 are shown in Figure 3, where the distribution of abundance-to-noise ratios (ANR) and the DOFs for the synergy is shown along with the

Journal of Geophysical Research: Planets 10.1029/2022JE007252

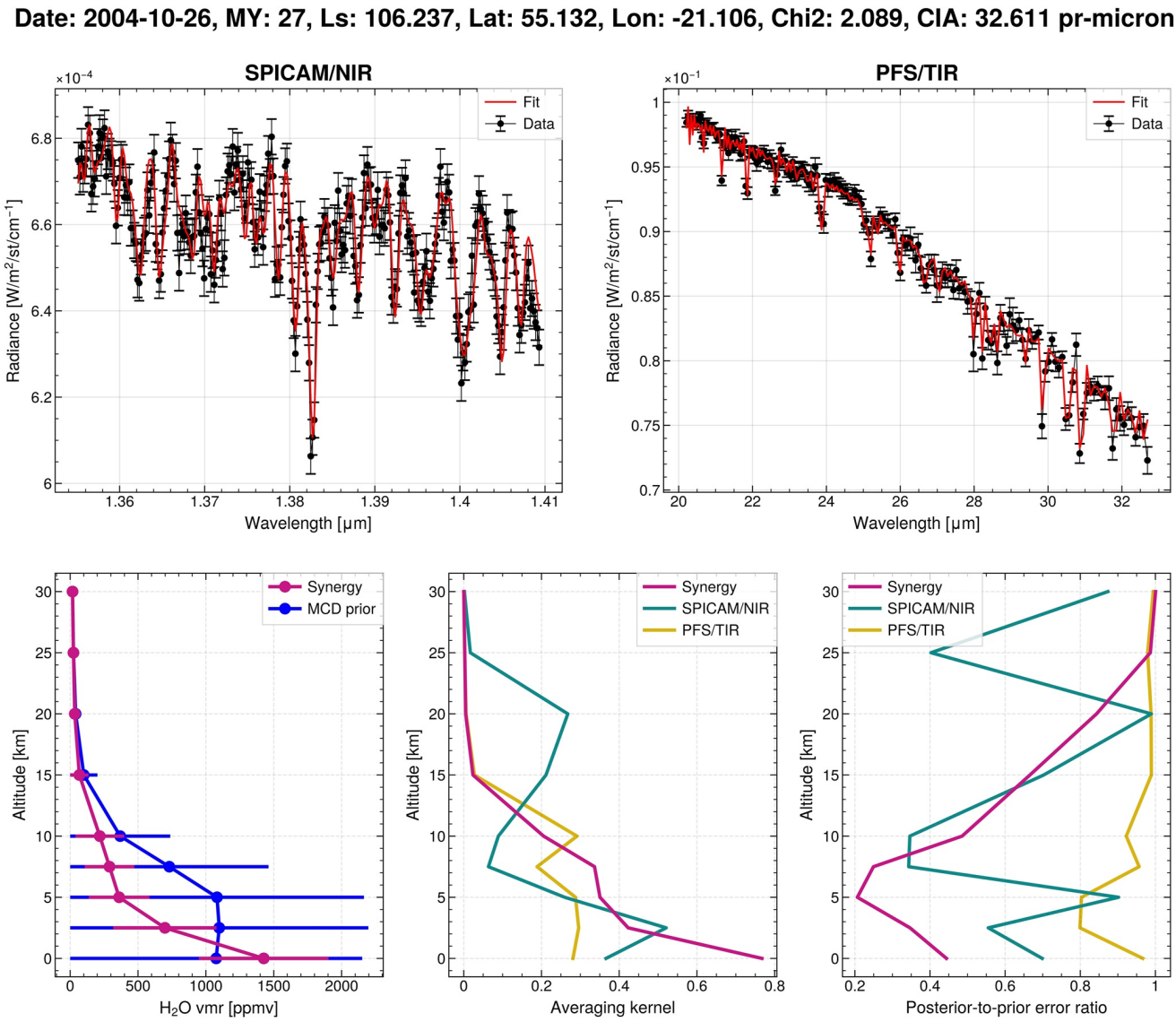

Figure 1. Typical example of averaged spectra from observations in the northern hemisphere high latitudes during early summer, with the corresponding vertical profile of water vapor mixing ratio and a demonstration of sensitivity along the vertical for the synergy. Top left) SPICAM-IR spectrum. Top right) Averaged PFS spectrum. Data in black and fit in red for both panels. Bottom left) Vertical profile of water vapor as obtained from simultaneous retrieval of both spectral domains, along with the MCD a priori vertical profile. Bottom center) Averaging kernel for retrieval made with the spectral synergy method, SPICAM/NIR, and PFS/TIR. Bottom right) post-to-prior error ratio by altitude for synergistic retrieval and single spectral domain retrievals.

parameters from SPICAM/NIR and PFS/TIR. The ANR, as the retrieved water vapor column abundance divided by the a posteriori error, provides a measure of the amount of certainty one can have in the output value. Note that for visibility reasons, the data points are layered according to method, such that PFS and SPICAM data points overprint those of the synergy.

The ANR values are shown as scattered dots for each individual retrieval, and the solid curves represent binned averages of 2° Ls. The selected data are limited to all retrievals with ANR ≥ 1 to ensure the presence of water vapor, as it corresponds to a 1-sigma detection limit. The synergy and SPICAM have very similar ANR distributions, both averaging at around ANR = 5, with the synergy only occasionally outperforming SPICAM mostly at midlatitudes, showing that the synergy provides highly robust column abundances. PFS/TIR displays the smallest spread in ANR, covering the range from ∼1.5 to 6 and with an average of around 4. SPICAM/NIR retrievals mostly range between 2 and 8 and remain above 4 for all latitudes north of −40°N.

21699100, 2022, 5, Downloaded from https://agupubs.onlinelibrary.wiley.com/doi/10.1029/2022JE007252 by Cochrane France, Wiley Online Library on [31/10/2022]. See the Terms and Conditions (https://onlinelibrary.wiley.com/terms-and-conditions) on Wiley Online Library for rules of use; OA articles are governed by the applicable Creative Commons License

Journal of Geophysical Research: Planets 10.1029/2022JE007252

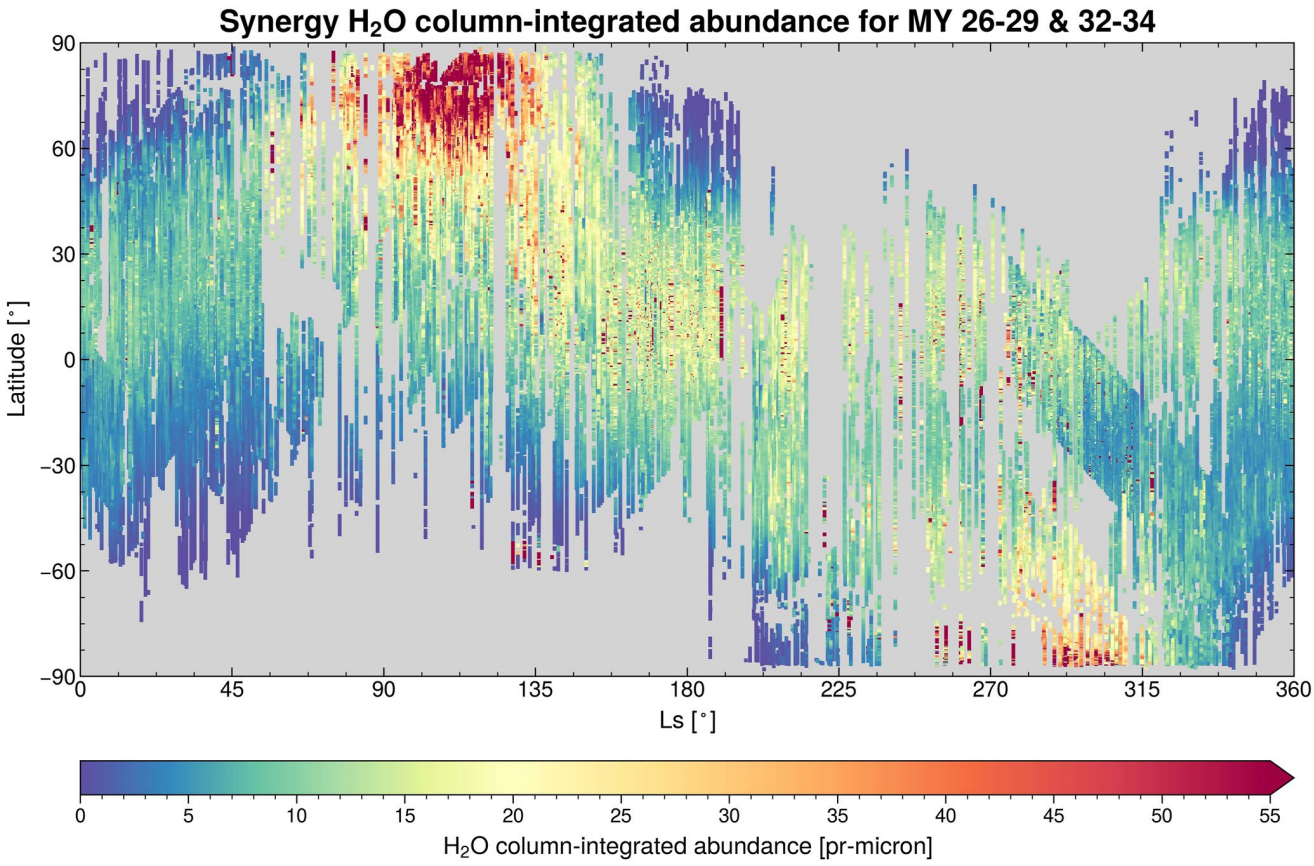

Figure 2. Total column-integrated abundance shown as a function of season and latitude. The figure includes all data points in the synergy data set. Note that no binning or selection has been done, and data points are partially overlapping with more recent observations on top.

The DOFs for each method is shown in the bottom panel of Figure 3, where the notable increase in DOF for the synergy verifies that the water content along the vertical can be roughly resolved. The DOF fluctuates around 1.0 for the NIR and TIR single spectral domain retrievals, while it typically exceeds 1.25 for the synergy, fluctuating around 1.5. Note that the spread in DOF values is small for NIR compared to TIR, and that NIR regularly achieves DOFs around 1.5, higher than what is ever obtained with TIR. In the southern hemisphere and near the north pole, the TIR DOFs nearly never exceed 1, while the synergy remains stable and high in the north polar region especially, but also performs reasonably well in the south. With a DOF consistently higher than one, the synergy is capable of providing information on the shape of the profile, and a vertical partitioning can be obtained.

The synergy returns a vertical profile and an integrated column abundance for each colocated observation. To ensure the synergy is not simply reproducing the a priori when retrieving a vertical profile and to demonstrate that the synergy is capable of distinguishing near-surface water vapor from the rest of the column, we quantified the amount of synergistically added information, compared to the MCD a priori profile, by altitude as a function of latitude and season. The ratio of the post-to-prior errors is visualized in Figure 4, where each panel represents an altitude indicated by the number on the left *y*-axis. Within each panel, data are binned by 2° in Ls and 2° in latitude. At higher altitudes, the error ratio is fairly close to one, meaning that the synergy brings little new information. However, deeper in the atmosphere, more information is progressively added by the synergy. The panels representing the atmosphere at 2.5–7.5 km are the altitude regions where most information is injected, and which benefits the most from the synergistic approach as was also evident from the single example in Figure 1. The retrieved profiles could be deviating from the MCD, which we will investigate further in Section 4.2, but the water mixing ratios are significantly more constrained, as also demonstrated in Figure 1.

In order to only select retrievals which are robust enough to justify a deeper analysis, and with a high enough quality that information on the vertical water distribution can be extracted, four criteria were established which

21699100, 2022, 5, Downloaded from https://agupubs.onlinelibrary.wiley.com/doi/10.1029/2022JE007252 by Cochrane France, Wiley Online Library on [31/10/2022]. See the Terms and Conditions (https://onlinelibrary.wiley.com/terms-and-conditions) on Wiley Online Library for rules of use; OA articles are governed by the applicable Creative Commons License

Journal of Geophysical Research: Planets 10.1029/2022JE007252

21699100, 2022, 5, Downloaded from https://agupubs.onlinelibrary.wiley.com/doi/10.1029/2022JE007252 by Cochrane France, Wiley Online Library on [31/10/2022]. See the Terms and Conditions (https://onlinelibrary.wiley.com/terms-and-conditions) on Wiley Online Library for rules of use; OA articles are governed by the applicable Creative Commons License

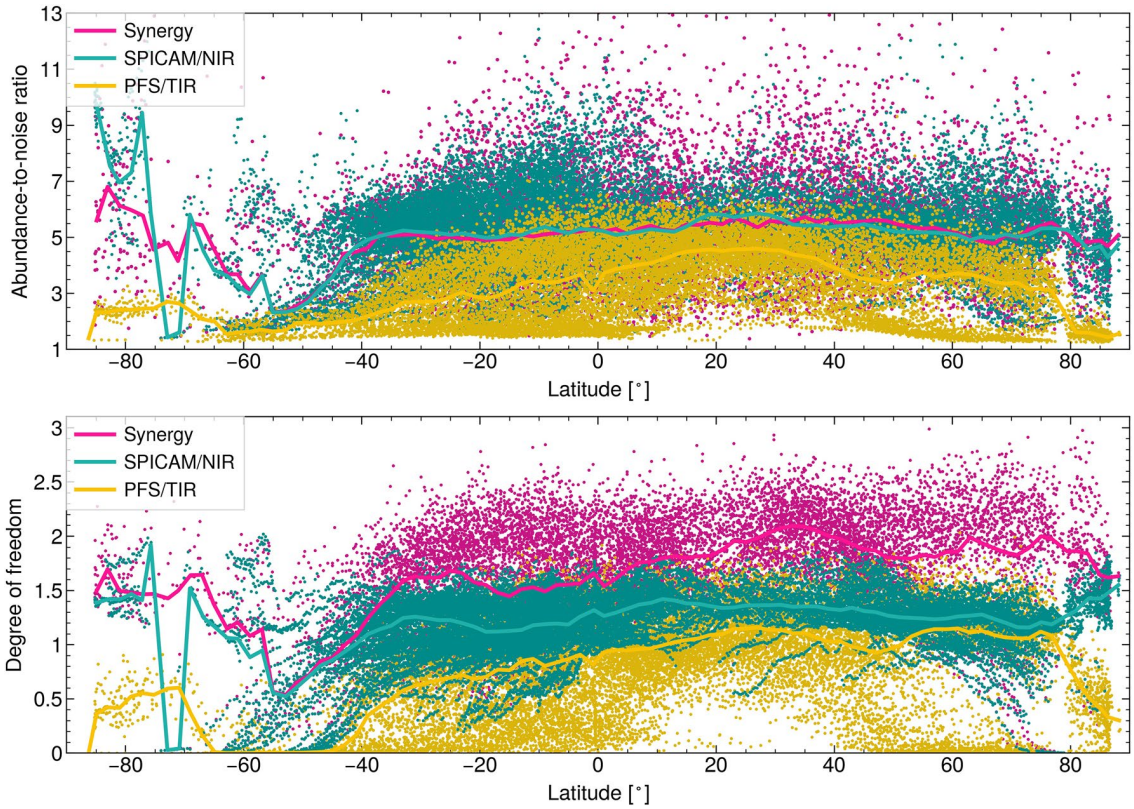

Figure 3. Abundance-to-noise ratio and degree of freedom from the synergy and the single spectral domain retrievals. Data set is limited to those retrievals which satisfy the criteria of a reduced χ^2 equal to or smaller than 4 and an abundance-to-noise ratios (ANR) equal to or larger than 1 in MY 27. Top panel: ANR for the synergy, Planetary Fourier Spectrometer (PFS) and SPICAM retrievals. Bottom panel: Degree of freedom for the synergy, PFS and SPICAM retrievals. Data points are layered, with the synergistic points at the bottom. Solid lines represent averages binned in intervals of 2° Ls.

the retained samples would have to comply with simultaneously: (a) an ANR ≥3 (3-sigma detection limit), (b) a DOF for water vapor ≥1.25, (c) a post-to-prior error ratio ≤0.9 for water volume mixing ratio at 2.5 km (Error ratio), and (d) a reduced χ^2 of the retrieval (Chi2) ≤4. Many criteria limits were explored to optimize the returned number of retrievals versus the quality of said retrievals. The limits of these criteria can also be tailored for a specific purpose; the DOF limit was reduced to 1 for the assembly of a composite column abundance climatology.

A visualization of the statistical distribution of the relative numbers (per 10,000) and combinations of fulfilled criteria is shown in Figure 5. The first panel of Figure 5 shows the distribution of fulfilled criteria when the synergistic retrieval method is used. The second and third panels visualize the relative numbers and distributions of fulfilled criteria when only the NIR and TIR spectral intervals are utilized.

The benefits of using two spectral ranges are clearly visible, with more than 55% of all synergy retrievals fulfilling all criteria compared to only 24% for SPICAM/NIR, and 16% for PFS/TIR, effectively demonstrating that the synergy yields more information than separately using the SPICAM or the PFS data set. For all cases the χ^2 is the most restrictive requirement (except for PFS/TIR where the DOF is the most restrictive), while the ANR is the least restrictive. The DOF increase provided by synergy compared to retrievals from single spectral domains is a direct evaluation of how much additional information synergy brings to constrain water vapor distribution. Only the measurements fulfilling all four requirements are considered in the following analysis.

4. Results

The results presented below were derived using data from two time intervals: Ls = 334° of MY 26 until the end of MY 29 and from the beginning of MY 32 to the end of MY 34. The spatial and temporal coverage within each year is highly variable. All four selection criteria described in Section 3.2 were applied, with limits as

Journal of Geophysical Research: Planets 10.1029/2022JE007252

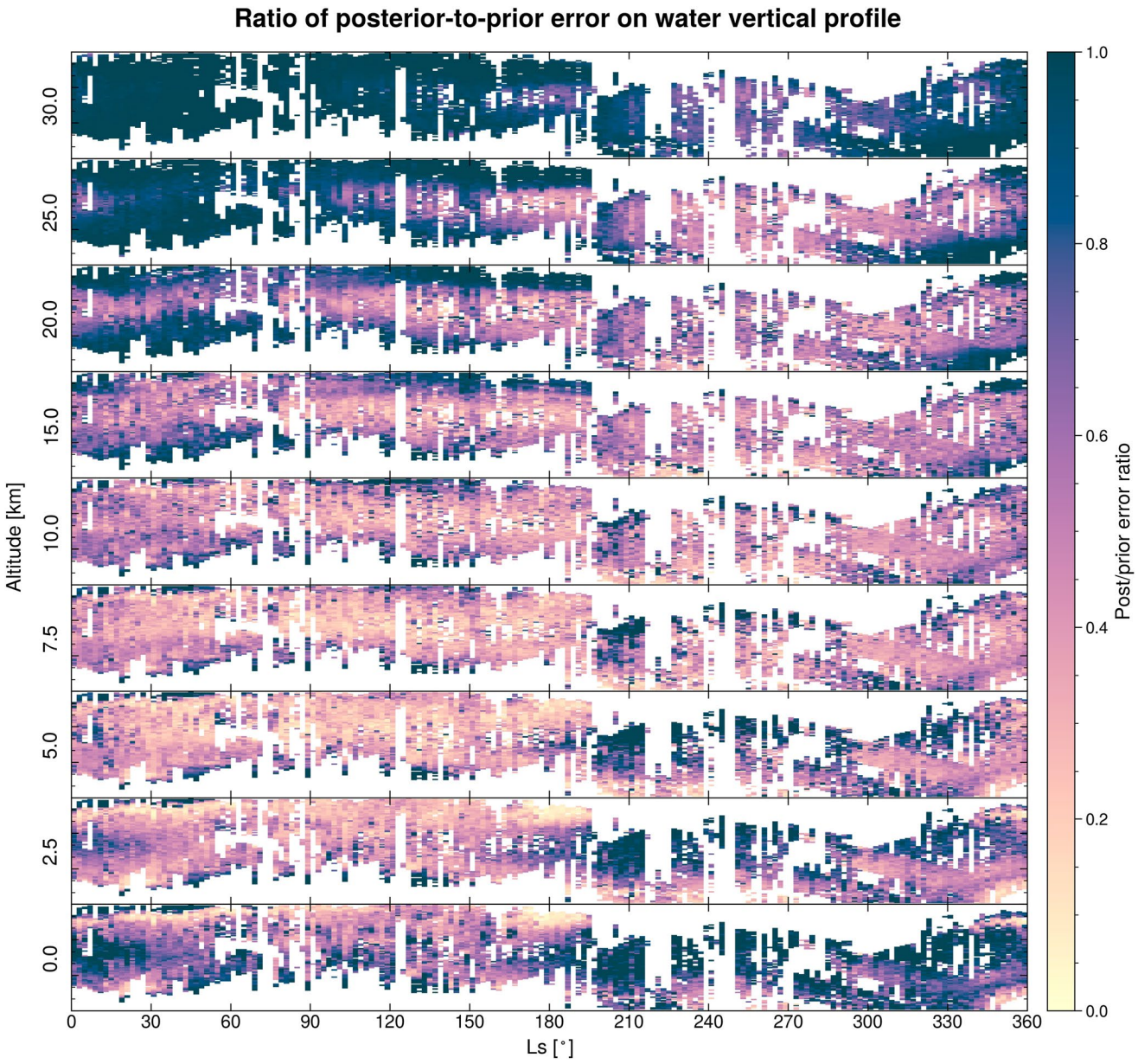

Figure 4. Illustration of the benefit of utilizing the synergistic retrieval by altitude, latitude, and season. Each panel represents an altitude level, with the given altitude in km given on the left. Within each panel, the *y*-axis represents latitude, with major ticks every 30°. Data were averaged in bins of 2° latitude and 2° Ls. The retrieved a posteriori errors are divided by the MCD a priori error profile, such that values below 1 represent retrievals where the uncertainty has been reduced, and thus the colocated observation has injected additional information into the retrieval process.

shown in Figure 5 (except for the assembly of the column abundance climatology in Section 4.1, which uses limits specifically adjusted for column abundances). The first part of this section focuses on the retrieval of total column abundances with the synergy compared to with single spectral domain approaches and to the MCD. Then, results concerning the vertical partitioning of water are shown, as seen in relation to the total column and model predictions, where special attention is given to the polar regions around the seasonal ice cap sublimation seasons.

4.1. Column Abundance Climatology

For the assembly of a complete and composite synergy climatology of water vapor, the criteria described in Section 3 are applied to the complete data set shown in Figure 2, with an adjustment to the DOF and error ratio

21699100, 2022, 5, Downloaded from https://agupubs.onlinelibrary.wiley.com/doi/10.1029/2022JE007252 by Cochrane France, Wiley Online Library on [31/10/2022]. See the Terms and Conditions (https://onlinelibrary.wiley.com/terms-and-conditions) on Wiley Online Library for rules of use; OA articles are governed by the applicable Creative Commons License

Journal of Geophysical Research: Planets 10.1029/2022JE007252

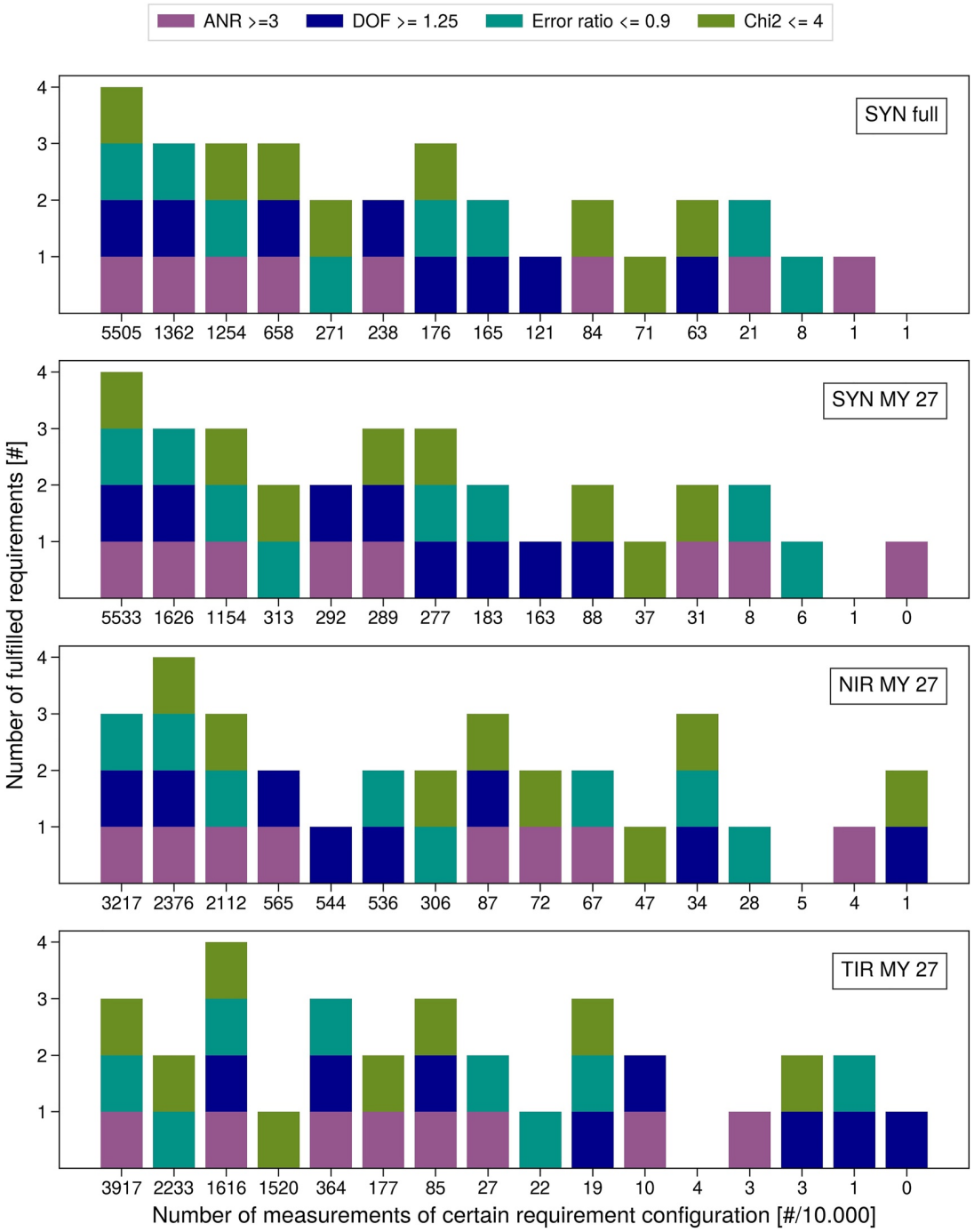

Figure 5. Overview of the relative statistical distributions of fulfilled criteria. The full synergy data set is shown in the top panel, the synergetic retrievals in MY 27 in the second, SPICAM/NIR is shown in the third panel, while PFS/TIR is illustrated in the bottom panel. Retrievals with the individual instruments were only conducted for MY 27. The *y*-axis counts the number of fulfilled criteria, and the *x*-axis shows the number of retrievals per 10,000 which fulfill each criterion configuration, sorted with the most likely configuration to the left, and decreasingly likely configurations toward the right.

limits. The DOF and error ratio requirements ensure retrievals with sufficient vertical information to justify further analysis of partitioning, and as there is no need for vertical information content for a column abundance climatology, the DOF and error ration limits are both set to 1, which is more than sufficient to infer a highly reliable column abundance.

21699100, 2022, 5, Downloaded from https://agupubs.onlinelibrary.wiley.com/doi/10.1029/2022JE007252 by Cochrane France, Wiley Online Library on [31/10/2022]. See the Terms and Conditions (https://onlinelibrary.wiley.com/terms-and-conditions) on Wiley Online Library for rules of use; OA articles are governed by the applicable Creative Commons License

Journal of Geophysical Research: Planets 10.1029/2022JE007252

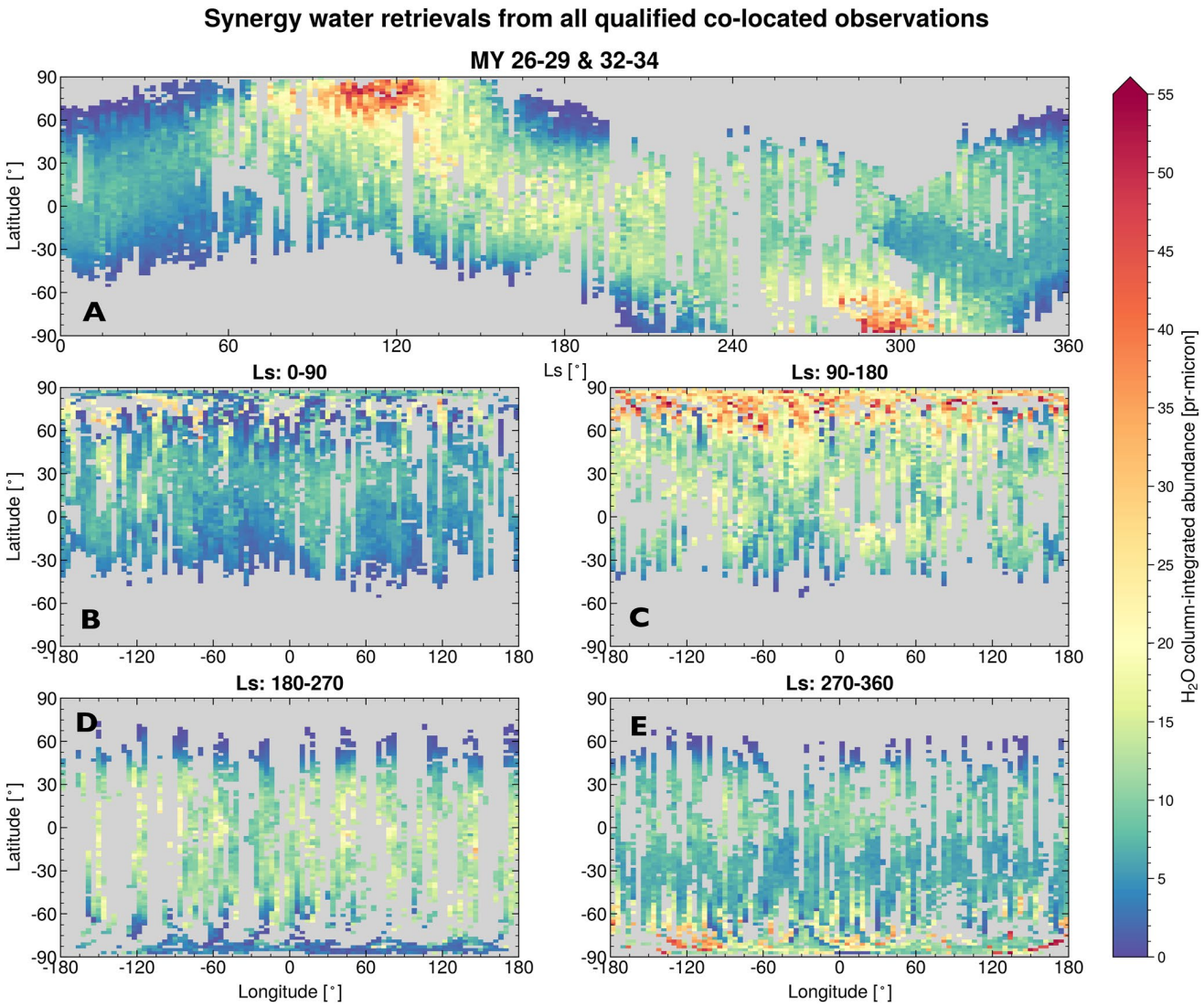

Figure 6. Seasonal and geographical variations in normalized total column abundances of water vapor. Panel (a) Seasonal distribution of all qualified retrievals averaged in bins of 2° × 2° Ls and latitude. Panels B–E: Geographical distribution of qualified retrievals for each seasonal interval, averaged in bins of 2° × 4° latitude and longitude.

After the adjusted selection criteria are applied, the remaining water vapor retrievals are illustrated as a function of season, latitude, and longitude in Figure 6. In order to account for topography, the total water columns are normalized to an equivalent surface pressure of 610 Pa using the MCD to constrain local pressure. However, this pressure normalization is made on the assumption that water vapor is well-mixed with the ambient gases, which might not always be the case. The total water columns are averaged in bins of 2° Ls, 2° latitude, and 4° longitude. Of all qualified retrievals, 31% are from MY 27, which for the most part contributes to the coverage of the northern summer. Henceforth, the total column integrated abundance will be referred to as the CIA. Later in this study, another parameter is used to measure the fraction of water vapor kept near the surface which is defined as the partitioning index (PI). The PI is equal to the integrated column of water from the surface to 5 km, divided by the CIA. If water vapor is evenly mixed in the atmosphere with a scale height of 11 km, the PI = 0.63.

Given the variation of the sampled local times (from early morning to late evening for SPICAM and from 08:00 to 16:00 for PFS), it is assumed that seasonal variations of water vapor column abundances dominate over any diurnal variability. Although the temporal and spatial coverage is incomplete, known trends of the water cycle appear unambiguously. The spring is overall a dry season (Figure 6 panel B), with abundances rarely higher than

21699100, 2022, 5, Downloaded from https://agupubs.onlinelibrary.wiley.com/doi/10.1029/2022JE007252 by Cochrane France, Wiley Online Library on [31/10/2022]. See the Terms and Conditions (https://onlinelibrary.wiley.com/terms-and-conditions) on Wiley Online Library for rules of use; OA articles are governed by the applicable Creative Commons License

Journal of Geophysical Research: Planets 10.1029/2022JE007252

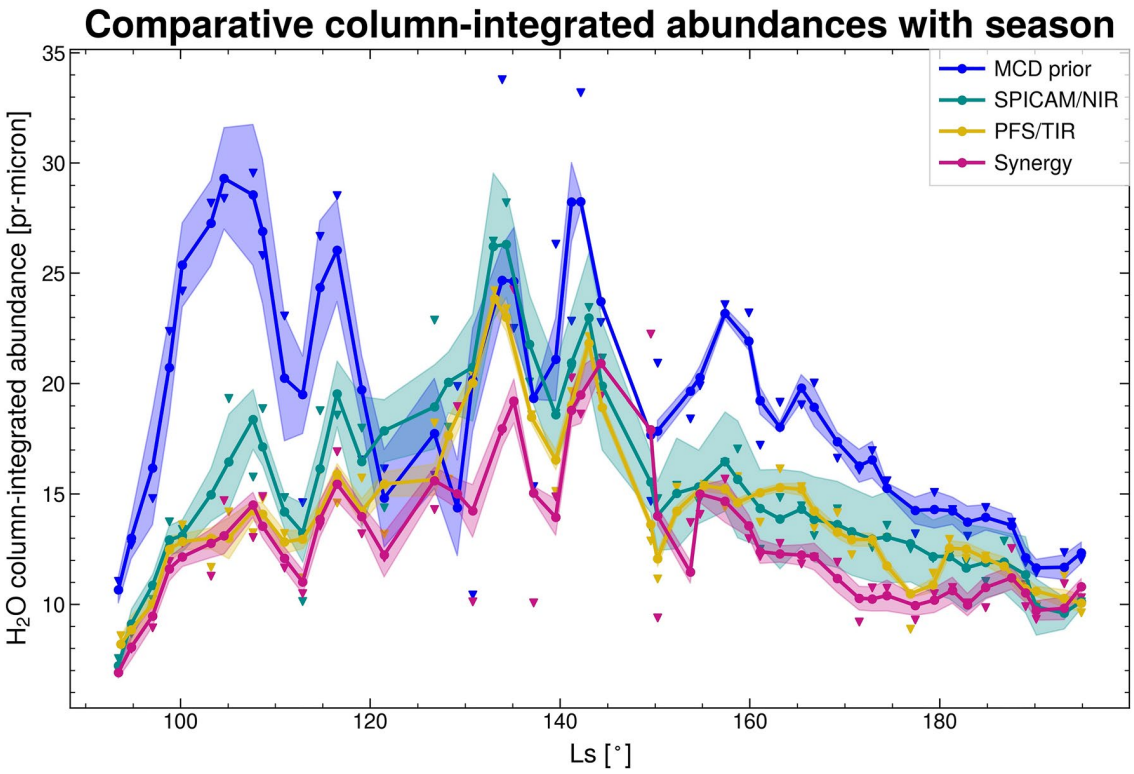

Figure 7. Seasonal evolution of column-integrated abundances of water vapor during summer of MY 27. Comparison between abundances predicted by the MCD used as a priori, the synergistic retrievals and the single spectral domain approaches for SPICAM and Planetary Fourier Spectrometer. Abundances are not normalized to an equivalent surface pressure. Data are averaged on the latitude interval 15°–45°, and in bins of 5° Ls. Triangles represent the average values for each bin, the solid curves are the smoothed abundance values, and the shaded areas represent the standard error for each bin average.

10 pr-μm. The few instances with larger CIA occur late in northern spring at the edge of the NPC. The early northern summer season (Ls = 90°−135°) is characterized by large latitudinal contrasts with high water content in the polar regions which decrease monotonically southward, this is particularly prominent in Panel C. At around Ls = 115°, a Northern maximum of ∼60 pr-μm is visible poleward of 70°N, while at the same time only around 13 pr-μm is measured south of 30°N (in panel A). The northern hemisphere fall season shown in panel D displays a north polar region now devoid of water vapor, most of which having been transported to the mid and low latitudes and across the equator. The south polar maximum occurs around Ls = 285° and reaches an average total column abundance of 40 pr-μm, as seen in Figure 6 panel E. A global dust storm occurred in MY 28, which degraded the quality of the measurements for some time, causing the number of qualified retrievals in MY 28 to be low even though many observations were conducted in this period. The drier patch around Ls = 300° in the southern hemisphere is constructed almost entirely from observations in MY 28, when the dust storm is thought to aid transport of water vapor from the lower atmosphere to higher altitudes (Fedorova et al., 2018).

4.2. Synergy Compared to Single Domain Retrievals and MCD

Numerous studies of the climatology of water vapor have been made using the PFS and SPICAM instruments individually. As this is the first time observations from both are used in synergy, a direct comparison has been made between them and the MCD. In Figure 7, synergy retrievals and MCD a priori values satisfying the adjusted criteria as described in Section 4.1 are plotted, along with single spectral domain retrievals for SPICAM and PFS. No criteria have been imposed on the single domain retrievals other than unphysically high abundances have been filtered out. CIAs are averaged across the 15°–45°N latitude band, the region which contains the longest continuous coverage, and in intervals of 5° Ls.

The selected time period covers the early northern summer, the polar cap sublimation season, and continues into late summer of MY 27. In general, the MCD predicts a much higher water vapor abundance than what is obtained

21699100, 2022, 5, Downloaded from https://agupubs.onlinelibrary.wiley.com/doi/10.1029/2022JE007252 by Cochrane France, Wiley Online Library on [31/10/2022]. See the Terms and Conditions (https://onlinelibrary.wiley.com/terms-and-conditions) on Wiley Online Library for rules of use; OA articles are governed by the applicable Creative Commons License

Journal of Geophysical Research: Planets 10.1029/2022JE007252

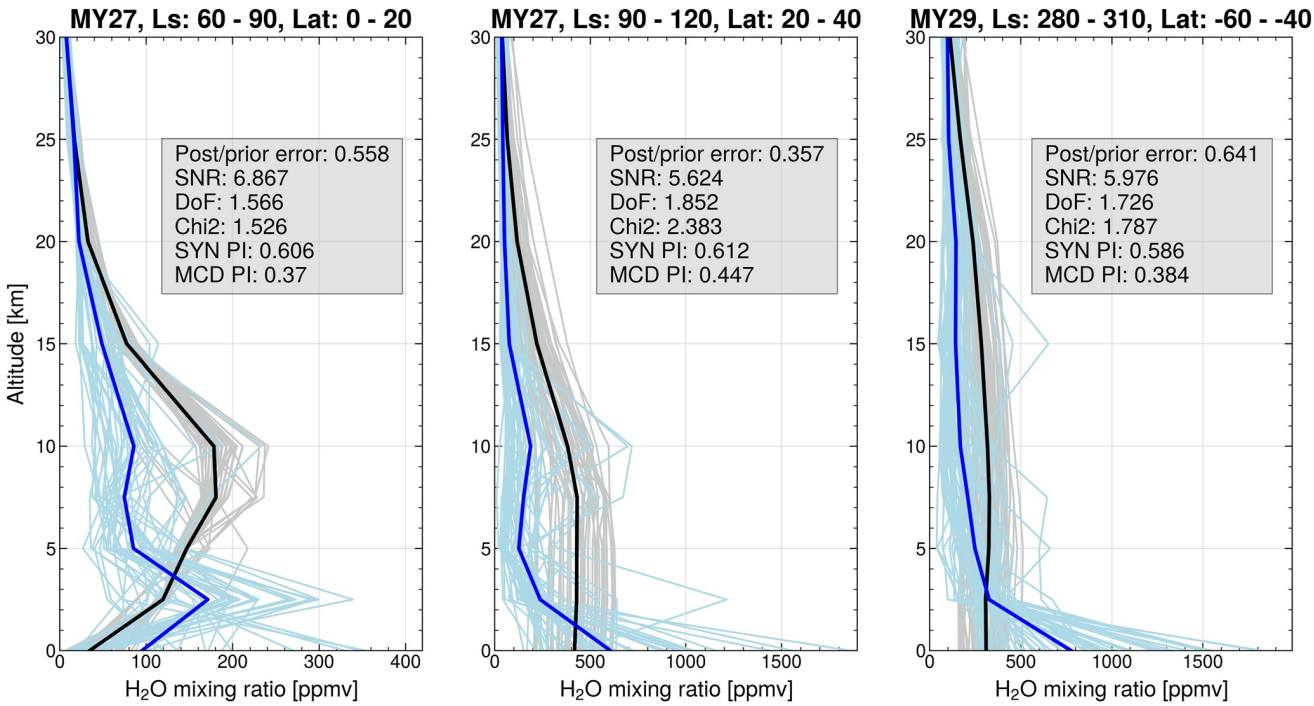

Figure 8. Selection of synergy and MCD a priori vertical profiles of water vapor. Light blues and greys are individual profiles, while dark blue and black are mean profiles. The three example periods are from left to right: NH low latitude late spring, NH midlatitude early summer, and SH midlatitude midsummer. The text boxes give the mean numerical values for the four selection criteria along with the a posteriori and a priori partitioning index values.

with either of the retrieval approaches (except during Ls = 120°–140°). The MCD agrees well with the observations only at the very beginning and end of the time period shown here, which corresponds to before the onset of the sublimation season, and after the water vapor has been transported beyond the area of focus. This might suggest that the transportation mechanisms dominant in the summer midlatitudes are currently not fully understood. Another factor which could impact this discrepancy is the large MCD sublimation peak, which might then propagate southward. The difference in the CIA, as well as the vertical partitioning, predicted by the MCD and the values retrieved by the synergy are further elaborated upon in Section 4.3.

The synergy and the single spectral domain retrievals with PFS/TIR are overall in good agreement, with the synergy yielding similar or slightly lower abundances. SPICAM/NIR also agrees well with the synergy and PFS, albeit with slightly larger abundances. The difference in abundances has been suggested to be related to effects in different spectral bands used and specific retrieval methods (Korablev et al., 2006; Maltagliati, Titov, et al., 2011). The general seasonal behavior displayed by the three retrieval approaches is similar; an increasing trend in the early summer, peaking at around Ls = 135°, when water vapor from the North Polar Cap (NPC) has sublimed and been transported to midlatitudes. The MCD predicts a much more rapid increase of the sublimed water, with CIA values a factor of 2.5 higher than the synergy at Ls = 100°. The decreasing CIA found after Ls = 140° by both the synergy and the single spectral domain retrievals as well as the MCD is expected, as the water is successively transported across the equator. The "double-hump" shape of the MCD abundances (also evident in Figure 10) are not clearly distinguishable from either of the retrieval techniques.

4.3. Vertical Partitioning of Water Vapor

The spectral synergy method produces vertical profiles of water vapor where the data points are highly correlated. Even though the synergy significantly increases the DOF of the water vapor retrieval, it is still too low to provide a true profile with individual mixing ratios. The points along the vertical profile are highly correlated, as the DOF is usually around 1.5. Figure 8 shows a selection of example profiles from specific regions and seasons of interest. Light hues are individual profiles, with the dark blue and black being the mean profiles from the synergy and MCD, respectively. The three example periods are from left to right: NH low latitude late spring, NH midlatitude

21699100, 2022, 5, Downloaded from https://agupubs.onlinelibrary.wiley.com/doi/10.1029/2022JE007252 by Cochrane France, Wiley Online Library on [31/10/2022]. See the Terms and Conditions (https://onlinelibrary.wiley.com/terms-and-conditions) on Wiley Online Library for rules of use; OA articles are governed by the applicable Creative Commons License

Journal of Geophysical Research: Planets 10.1029/2022JE007252

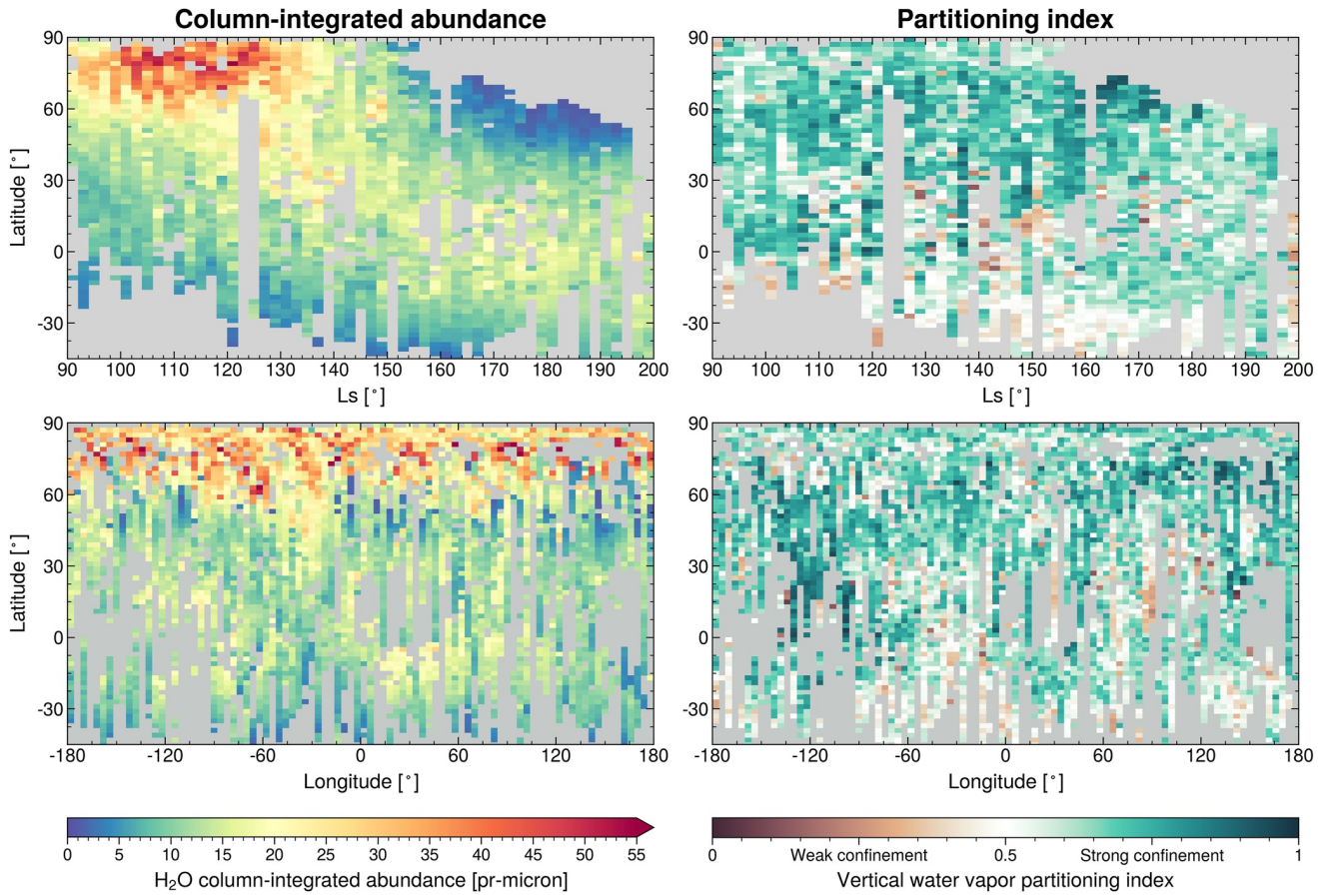

Figure 9. Composite maps of normalized water vapor column-integrated abundance and partitioning index. For the partitioning index, values higher than 0.5 (in green) indicate that more than 50% of the water vapor column is confined below 5 km, while lower values (in brown) indicate that water vapor is more evenly dispersed with altitude. Data from all available years fulfilling all requirements have been averaged in bins of 2° latitude, 2° Ls, and 4° longitude.

early summer, and SH midlatitude midsummer. For all three examples, the synergy obtained a higher PI, especially so for the NH early spring. The MCD profiles are most often fairly constant, with a very stable water mixing ratio with altitude. The exception is at low latitudes in NH early spring, when the MCD indicates the presence of a wet layer peaking at 10 km. The synergy also finds somewhat elevated vapor amounts here, but peaks instead near the surface at 2.5 km. In all cases the water vapor does not appear evenly mixed in the boundary layer, and shows a clear tendency for a strong near-surface water confinement. Note that if water vapor was evenly mixed in the atmosphere with a scale height of 11 km, the PI would be equal to 0.37, very similar to the MCD profiles shown in the right panel in Figure 8.

When water vapor is retrieved simultaneously from PFS/TIR and SPICAM/NIR, the degree of vertical confinement can be estimated by taking the ratio of the partial column from the surface up to 5 km, to the total column. The result is a dimensionless partitioning index (PI) representing the amount of water vapor confined within the first 5 km of the atmosphere compared to the rest. Average trends in the CIA and PI during the northern summer (Ls = 90–200) are shown in Figure 9, with focus on the latitudes between 45°S and the North Pole where the observation density is highest.

As the seasonal polar ice is subliming in early northern summer, the CIA increases drastically north of 60°N. There is no clear immediate reaction in the PI, which is fairly high (PI typically greater than 0.7) and stable from 30°N and northward during Ls = 90°–160°. At polar latitudes between Ls = 100° and 130°, when the CIA is at its highest, a local PI maximum is observed slightly southward of the CIA maximum. The confinement in the polar region remains strong at least until Ls = 170°, a period during which latitudes above 50°N undergo extreme variations in CIA, transitioning from the north polar summer maximum to a very dry late summer, as can be seen

21699100, 2022, 5, Downloaded from https://agupubs.onlinelibrary.wiley.com/doi/10.1029/2022JE007252 by Cochrane France, Wiley Online Library on [31/10/2022]. See the Terms and Conditions (https://onlinelibrary.wiley.com/terms-and-conditions) on Wiley Online Library for rules of use; OA articles are governed by the applicable Creative Commons License

Journal of Geophysical Research: Planets 10.1029/2022JE007252

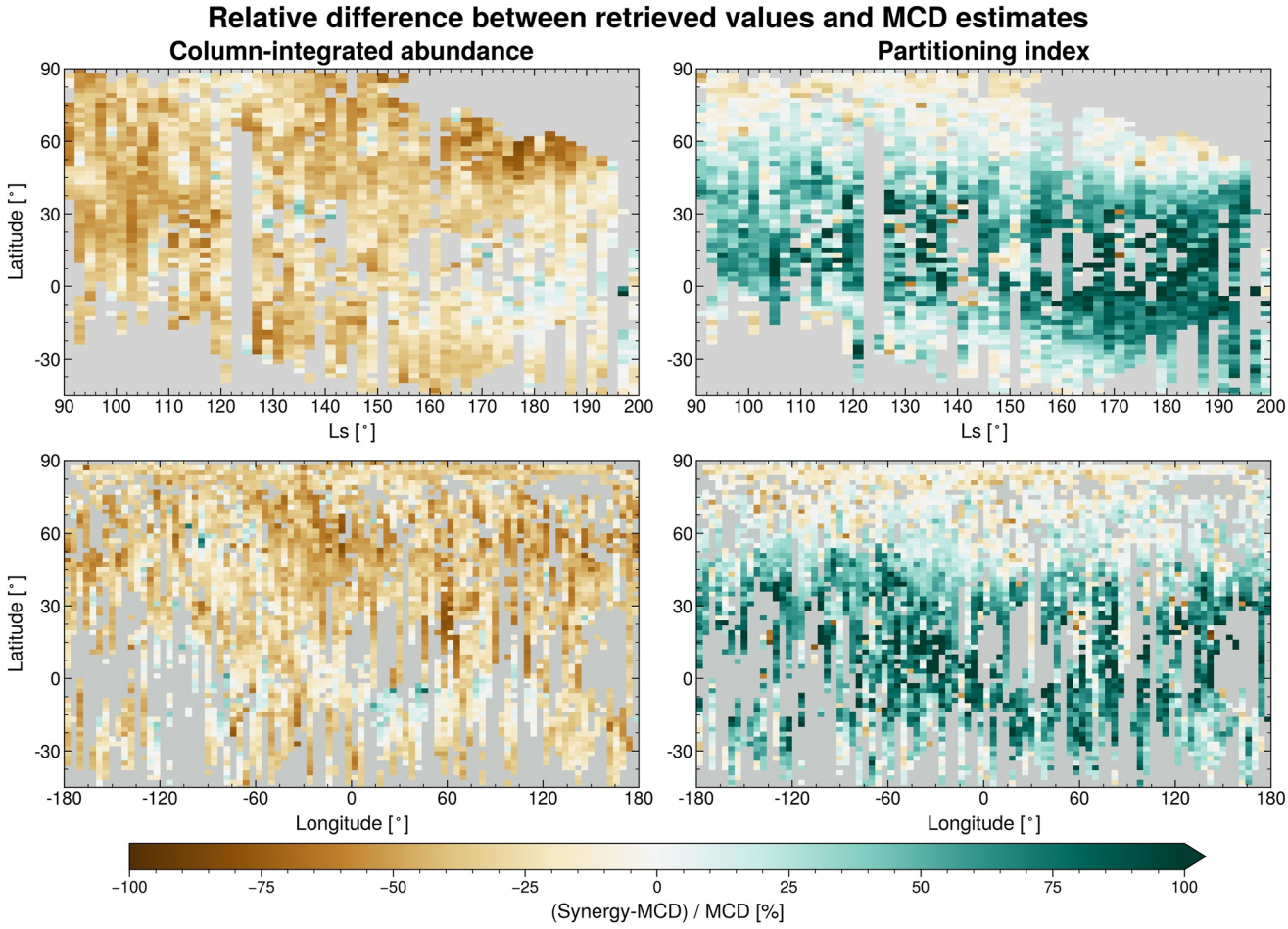

Figure 10. Illustration of the relationship between the retrieved values and the MCD a priori. The deviations of the synergy from the MCD estimates are calculated as a relative difference such that a value of 0 indicates where the synergy and the MCD are equal, and instances where the synergy yields larger values are positive. The left column shows the ratio of the a posteriori to the a priori full water vapor column, while the right column shows the ratio of the a posteriori to the a priori partitioning indices. The top row visualizes the data on a latitude by Ls grid, while the bottom row distributes the data on a latitude-longitude map. Data from all available years fulfilling all requirements have been averaged in bins of 2° latitude, 2° Ls, and 4° longitude.

from the top panels in Figure 9. Extremely strong partitioning (PI = 0.9) is seen at Ls = 165°, when almost no water remains in the far north. This indicates that after most of the water has sublimed and been transported south, what water vapor remains at high latitudes is kept close to the surface for the duration of the summer.

South of the equator the water vapor is more homogeneously distributed with altitude with a PI of around 0.5, with some regions at low latitudes showing signs of a drier boundary layer (PI ∼ 0.2). The PI is highly variable and related to topography in an anticorrelated fashion when compared to the CIA. Even after pressure normalization, there are local variations in CIA related to varying elevation, previously found to likely be linked to atmospheric dynamics (Fouchet et al., 2007). Geographical variations stand out in the bottom panels, where the PI is enhanced over drier, elevated regions such as the Tharsis and Terra Sabaea regions (centered around −120° and 30° longitude, respectively), while the confinement is small over low-elevation regions such as Hellas Planitia at longitudes between 60° and 90°. The PI index is a ratio of water columns, and should inherently be independent of topography, yet the correlation with elevation remains.

PIs smaller than 0.5 are rarely seen in the NH, suggesting that sublimed water vapor might be transported southward at low altitudes. At low latitudes, however, the water is transported across the equator over regions of low elevations.

21699100, 2022, 5, Downloaded from https://agupubs.onlinelibrary.wiley.com/doi/10.1029/2022JE007252 by Cochrane France, Wiley Online Library on [31/10/2022]. See the Terms and Conditions (https://onlinelibrary.wiley.com/terms-and-conditions) on Wiley Online Library for rules of use; OA articles are governed by the applicable Creative Commons License

Journal of Geophysical Research: Planets 10.1029/2022JE007252

21699100, 2022, 5, Downloaded from https://agupubs.onlinelibrary.wiley.com/doi/10.1029/2022JE007252 by Cochrane France, Wiley Online Library on [31/10/2022]. See the Terms and Conditions (https://onlinelibrary.wiley.com/terms-and-conditions) on Wiley Online Library for rules of use; OA articles are governed by the applicable Creative Commons License

4.4. Deviations From the MCD

The synergistically retrieved column abundances and vertical confinement shown in Figure 9 contain significant differences from the MCD a priori estimates. Figure 10 illustrates the deviations of these synergistic values from the MCD estimates as a relative difference with the MCD abundances as reference values ($rel.diff. = \frac{SYN - MCD}{MCD}$), such that a deviation of 0 means the synergy and the MCD are equal, and instances where the synergy gives the larger values are positive. The relationship between the retrieved and a priori CIA is shown in the left column, and of the retrieved and a priori PI in the right column.

Figure 10 shows that, on the whole, the synergy has a tendency to retrieve column abundances lower than the corresponding MCD a priori values. The sublimation peak in early summer (around Ls = 110°), which controls most of the total atmospheric water vapor throughout the year on the whole planet, is significantly smaller than the MCD estimate, yet agrees somewhat better with the MCD than the surrounding observations. The total water content in the tropical fall is a good indicator of meridional transport of vapor from northern polar regions (Navarro et al., 2014), and this is where the model and synergy are most similar.

The vertical confinement displays the opposite behavior, with the synergy often finding a PI comparable to the MCD at mid and high latitudes. Note that during the sublimation season the MCD quite accurately reproduces the observations, indicating that the sublimation processes of the NPC are quite well understood in terms of vertical distribution. The PI difference is highest at low and middle latitudes in late summer, when large amounts of water vapor are being transported from the NH and across the equator. At most, the synergy PI at low-latitudes in late summer is almost twice as strong as model predictions. This is in general a fairly dry area, with a CIA of 10–15 pr-μm, where the synergy indicates that roughly 60% of the column is confined below 5 km. The atmospheric behavior in this region is less dominated by temperature and more affected by wind. The details of local air flow patterns are typically known with less certainty than temperature variations, which could explain why the model deviates the most from the observations at low and midlatitudes.

4.5. Seasonal Evolution of Water Distribution With Latitude

The seasonal variations of the CIA and PI can be visualized by zonal averages plotted as a function of latitude. All data points in Figures 10 and 11 illustrate the CIA and PI averaged in bins of 2° latitude and 15° intervals of Ls, and the curves are smoothed using a Savitzky-Golay low-pass filter with a second order polynomial and a window corresponding to 20° latitude. Curves covering the same seasonal periods have identical colors for both hemispheres to aid cross-hemispherical comparison (e.g., the red curve corresponds to mid-spring for both hemispheres; Ls = 45°–60° in the NH and Ls = 225°–240° in the SH).

Both hemispheres are fairly dry from the equator to midlatitudes during the spring-summer season. The SH displays a smaller spread in seasonal variation and a smaller increase with latitude compared to the NH, remaining at around 10 pr-μm from the equator to 40°S. From there, the water column starts to increase steadily. Overall, the synergy and MCD agree very well in the SH, with the most noticeable difference being the degree of seasonal spread, distinguishable at all latitudes in the synergy, while only becoming distinguishable after 40°S for the MCD. All synergistically retrieved seasonal curves show a southern maximum which is migrating poleward with season, matched well by the MCD. The exception is the first seasonal average in mid-spring (Ls = 225°–240°) which displays a continuously decreasing curve, with the highest value at equator for the synergy, while the MCD finds a weak maximum of 15 pr-μm at 70°S for the same season. The SH sublimation season maximum occurs during Ls = 285°–300°, with a maximum value of 34 pr-μm near 87°S.

The MCD shows a decreasing trend for all seasons in the extreme high latitudes poleward of the CIA peak, as expected due to the polar cap circulation known as the polar cap breeze (Haberle & Jakosky, 1990), the Martian equivalent to the terrestrial sea breeze. The effect is expected to be stronger in the NH where the more massive ice cap generates a larger temperature gradient. In the retrieved synergy data, the CIA does not always decrease poleward of the cap edge in the SH, and most noticeably continues to increase even beyond 80°S for observations during Ls = 285°–300°. This could be due to averaging of data from multiple years (Pankine et al. (2010) reported high interannual variability of this behavior over the NPC), imperfect coverage of this region and season, or perhaps a variable polar cap breeze in midsummer is not effectively transporting water vapor off the polar cap.

Journal of Geophysical Research: Planets 10.1029/2022JE007252

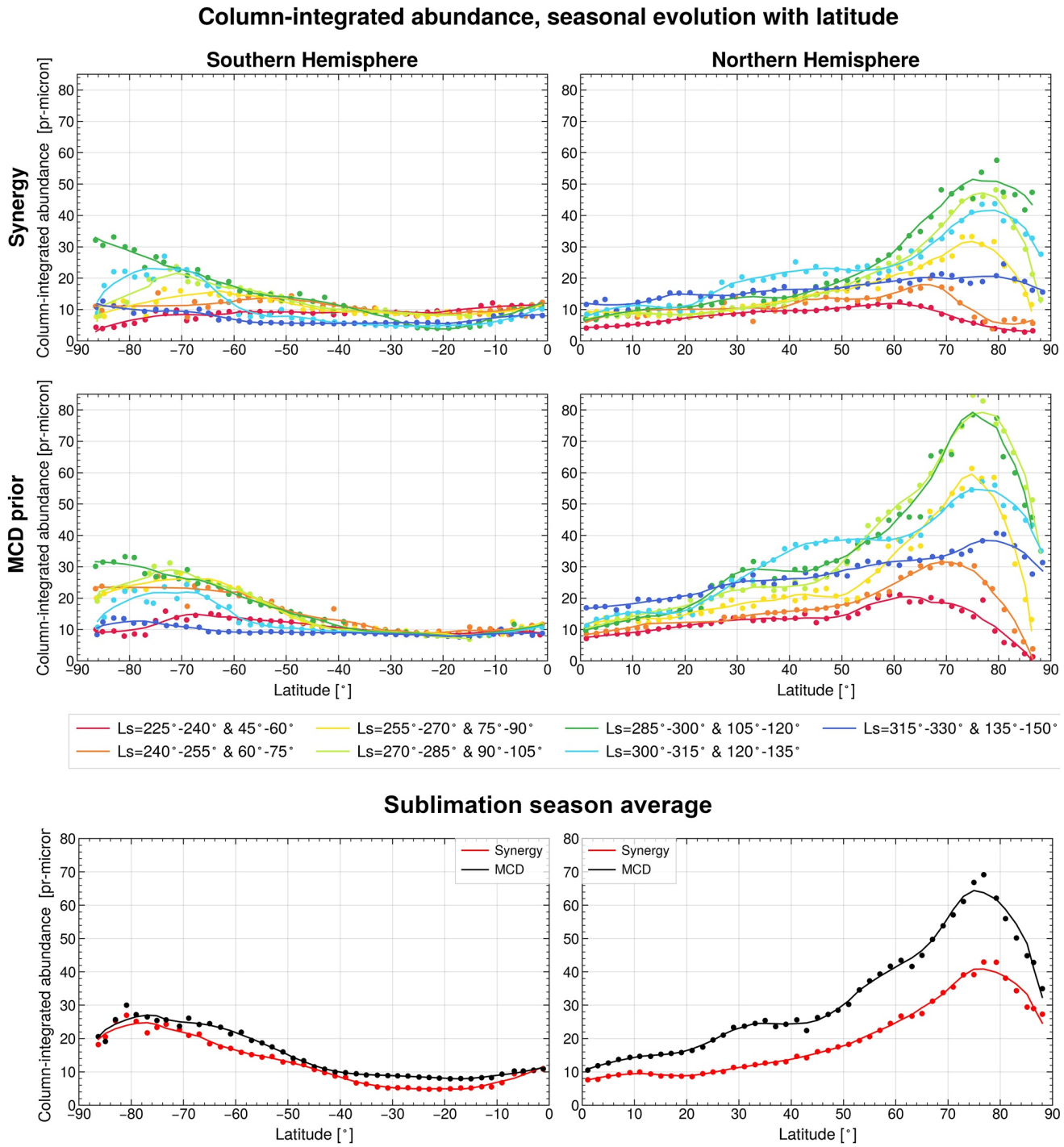

Figure 11. Zonal averages of water vapor column abundances from mid-spring to midsummer for both hemispheres. The top four panels show column abundances for all years, the dots are data points averaged in bins of 2° latitude and 15° Ls, while the curves represent the smoothed bins. The top row illustrates the synergistic retrievals, while the middle row shows the corresponding MCD a priori column abundances for each hemisphere. Curves representing the same seasonal period for both hemispheres have identical colors, with the SH Ls interval listed first. The two bottom panels compare the synergy and the MCD averages from Ls = 255°–315° for the SH and Ls = 75°–135° for the NH, covering the sublimation season for both hemispheres.

The NH is as expected far wetter than the SH. The CIA increases monotonically from the equator, and does not remain constant across large regions, as in the SH. Distinct maxima are visible with decreasing abundances northward of 80° latitude for all seasonal intervals, in agreement with the model. The overall maximum is observed

21699100, 2022, 5, Downloaded from https://agupubs.onlinelibrary.wiley.com/doi/10.1029/2022JE007252 by Cochrane France, Wiley Online Library on [31/10/2022]. See the Terms and Conditions (https://onlinelibrary.wiley.com/terms-and-conditions) on Wiley Online Library for rules of use; OA articles are governed by the applicable Creative Commons License

Journal of Geophysical Research: Planets 10.1029/2022JE007252

21699100, 2022, 5, Downloaded from https://agupubs.onlinelibrary.wiley.com/doi/10.1029/2022JE007252 by Cochrane France, Wiley Online Library on [31/10/2022]. See the Terms and Conditions (https://onlinelibrary.wiley.com/terms-and-conditions) on Wiley Online Library for rules of use; OA articles are governed by the applicable Creative Commons License

at 80°N in the Ls = 105°–120° interval, same as in the SH, and reaches a peak value of 60 pr-μm. The highest column abundance obtained by the MCD is in the interval Ls = 90°–105° and reaches 83 pr-μm. The locations of the CIA peaks are found just south of the polar cap edge with a clear decreasing trend for all seasons in the extreme high latitudes poleward of the CIA maximum, as expected due to the effects of the polar cap breeze. The sublimation onset is observed to occur later than what is predicted from the MCD, where during Ls = 60°–75°, the synergy finds a gradually increasing latitudinal trend with a modest peak at 65°N of just below 20 pr-μm, while the MCD already estimates a significant maximum of 30 pr-μm at 70°N.

In the bottom two panels of Figure 11, seasonal averages of the intervals Ls = 255°–315° for the SH and Ls = 75°–135° for the NH (covering the main sublimation period for both hemispheres) are shown to provide comparisons between the general trends in meridional CIA gradients from the synergy and MCD. The CIA absolute values are interesting to compare, but even more so the meridional variation. The summer sublimation maximum in the MCD is quite easily adjusted by tuning model parameters, while the change with latitude is subject to convection, transportation, and possible surface exchanges, and not so straightforward to modify to obtain the desired output. In the south the trends are nearly identical, with the synergy only yielding slightly smaller average abundances in the 10°–30°S and 50°–70°S regions. In the north, the MCD deviates from the synergy most significantly in two places; at 20°N and at 50°N, where in both instances the MCD gradient distinctly increases with respect to the synergy. The "double-hump" shape of the CIA is also much more prominent in the MCD. The difference between the MCD and synergy is small toward the equator for both hemispheres, which might be indicative that the influence of the CIA sublimation peak diminishes at lower latitudes.

Seasonal differences in the PI appear small in the MCD model compared to observations, as can be seen for all seasons in Figure 12, where all the curves are more or less stacked on top of each other. In our retrievals the partitioning exhibits a wave-like behavior in both hemispheres, oscillating roughly around PI = 0.5 in the south and around PI = 0.65 in the north. The shape of the MCD PI curves resembles those of the CIA seasonal averages, and do not have the same wave-like quality that the synergy finds. As the synergy yields very stable column abundances, for low/midlatitudes for all seasons, the partitioning varies greatly, particularly in the southern midsummer. However, the number of data points in the SH are far fewer than for the NH, and the averages from this region should therefore be considered somewhat less precise. This disagreement is also visible (to a lesser extent) in the NH, indicating that the discord is likely not purely a result of poor sampling in the south. In the NH there is a clear tendency for the partitioning to suddenly increase poleward of 80°N while the total water content decreases. The MCD PI on the other hand has been steadily increasing from the midlatitudes, and during late spring the PI even decreases north of 80°N. In the north, no stable PI gradient is observed as the MCD suggests. The synergy finds a highly variable PI for all latitudes and seasons, but with no clear meridional tendency.

These differences between the MCD and synergy are highlighted in the sublimation season averages for the PI in the two bottom panels of Figure 12, which clearly show the observed wave-like behavior being consistently higher than the estimated stable MCD PI. While the MCD indicates that around 40% of the water column is kept near the surface at all latitudes and seasons, the synergy finds that number to vary from 40% to 60%, with local maxima at equator, 50°S and at the pole. This trend is very similar to what is observed in the north, but here the wave amplitude is smaller. The MCD PI here is not as stable as in the south, and displays a fairly constantly increasing gradient from the midlatitudes (PI = 0.4) toward the North Pole (PI = 0.75). The synergy finds that the PI seasonal averages never go below 0.6, indicating that most of the column is always kept close to the surface. This leads to the synergy and MCD finding similar PI values only in the north polar region.

4.6. Closer Look at the North Pole

The northern polar region in spring and summer is of particular interest as the sublimation of the seasonal NPC is the main source, and thus the main forcing, of the water cycle. Every summer, as the NPC is exposed to sunlight and its surface temperature increases, more than one Gigaton of water vapor is released into the atmosphere (Smith, 2002), spreading around the entire globe as the seasons unfold. Figure 13 shows the CIA and the vertical confinement in the form of polar plots to better visualize the spatial distribution of the observations. Data from all available years north of 45°N are averaged in seasonal intervals of 30° of Ls, and on a 1° × 7° latitude-longitude grid. The two top rows of Figure 13 illustrate the CIA, and the two bottom rows show the PI. For each group the synergy values are followed by the MCD values.

Journal of Geophysical Research: Planets 10.1029/2022JE007252

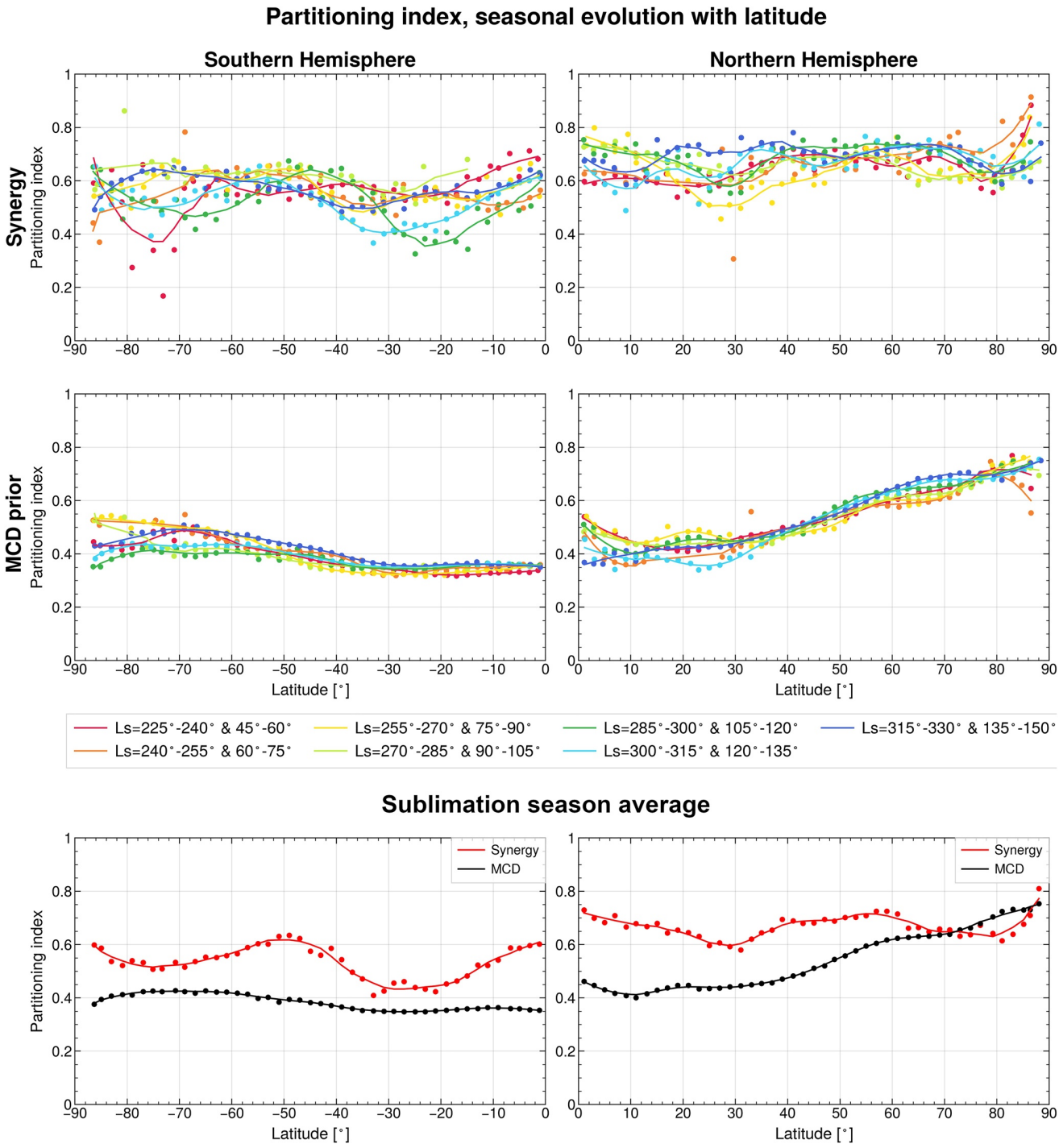

Figure 12. Zonal averages of the vertical partitioning index for each hemisphere from mid-spring to midsummer. The top four panels show data for all years averaged in bins of 2° latitude and 15° Ls as dots, while the curves represent the smoothed bins. The top row illustrates the synergistically retrieved partitioning indices, while the middle row shows the corresponding MCD a priori indices. Curves representing the same seasonal period for both hemispheres have identical colors, with the SH Ls interval listed first. The two bottom panels compare the synergy and the MCD averages from Ls = 255°–315° for the SH and Ls = 75°–135° for the NH, covering the sublimation season for both hemispheres.

Overall, the MCD predicts higher CIAs than the synergy (as also seen in Figure 10), with high abundances extending further equatorward, than what is observed. The sublimation season also appears to be initiated earlier in the MCD than what is observed, as can be seen by comparing the two first rows of the first column (Ls = 60°–90°)

21699100, 2022, 5, Downloaded from https://agupubs.onlinelibrary.wiley.com/doi/10.1029/2022JE007252 by Cochrane France, Wiley Online Library on [31/10/2022]. See the Terms and Conditions (https://onlinelibrary.wiley.com/terms-and-conditions) on Wiley Online Library for rules of use; OA articles are governed by the applicable Creative Commons License

Journal of Geophysical Research: Planets 10.1029/2022JE007252

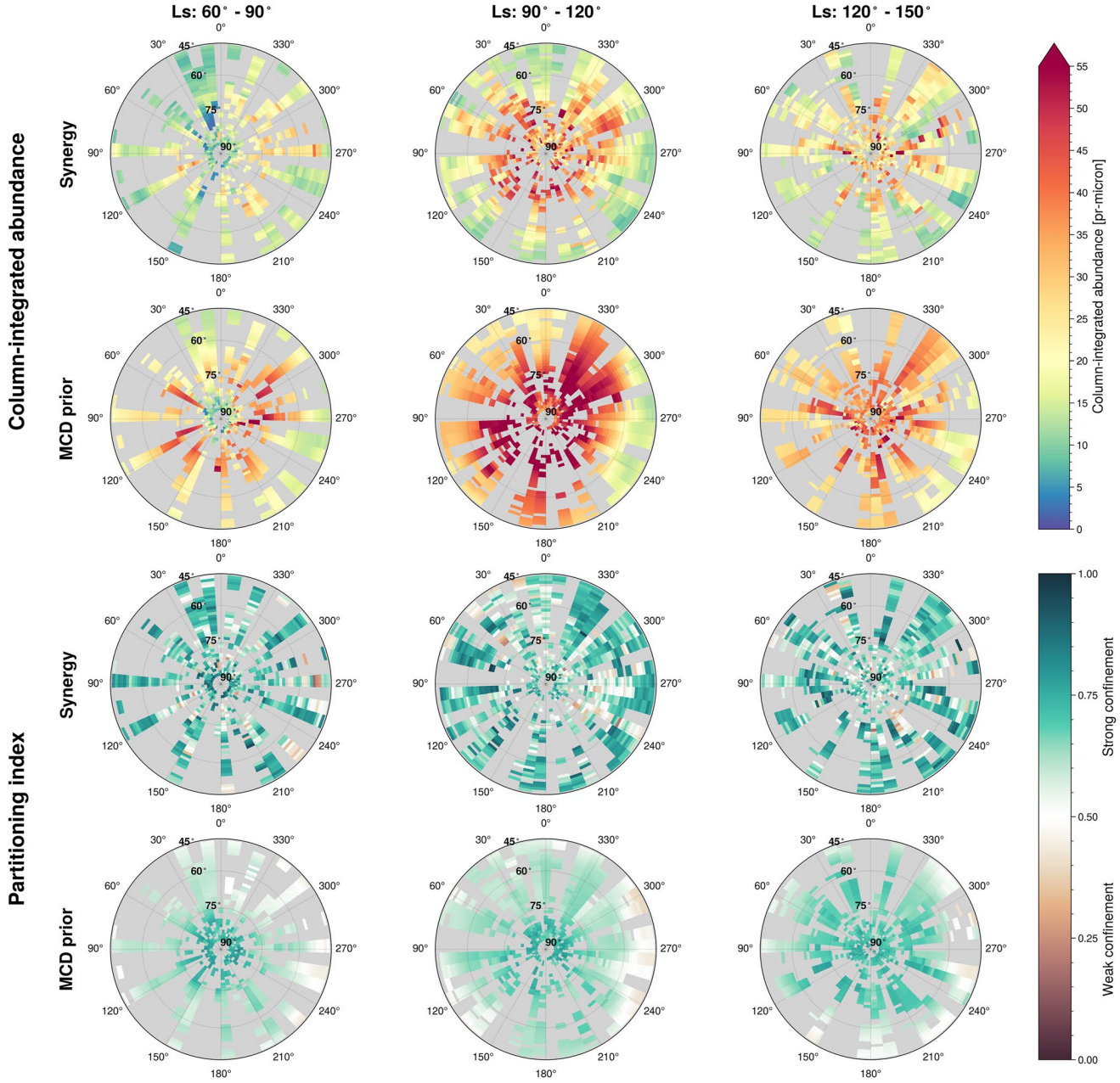

Figure 13. Polar view of the column-integrated water abundance and the partitioning index. Observations northward of 45° are averaged on a 1° × 7° latitude-longitude grid, in intervals of 30° Ls. The top two rows show the full column abundance of the synergy retrieval (first row) and MCD a priori (second row). The bottom two rows show the retrieved partitioning index (third row) and the MCD a priori partitioning index (bottom row). A higher partitioning index indicates that more water kept close to the surface.

of Figure 13, and was also shown in the previous section in Figure 11. At 75°N, the MCD finds column abundances higher than 40 pr-μm, when no observations for this time and place yield higher CIAs than 30 pr-μm. The situation is reversed for the vertical partitioning, where the synergy indicates a stronger near-surface confinement at all latitudes compared to the MCD. During Ls = 90°–120°, the larger sublimation peak of the MCD is likely contributing to the overestimation of water vapor at midlatitudes as seen in Figure 7. This was also shown in Figure 10, where the synergy is as much as 50% smaller than the MCD during Ls 90°–110°. For the late summer season 120°–150° Ls, the MCD predicts a high PI confined mainly to latitudes north of 60°, while the observations show a high PI reaching the midlatitudes. Overall, the MCD predicts the largest PI poleward of 75°N, while

21699100, 2022, 5, Downloaded from https://agupubs.onlinelibrary.wiley.com/doi/10.1029/2022JE007252 by Cochrane France, Wiley Online Library on [31/10/2022]. See the Terms and Conditions (https://onlinelibrary.wiley.com/terms-and-conditions) on Wiley Online Library for rules of use; OA articles are governed by the applicable Creative Commons License

Journal of Geophysical Research: Planets 10.1029/2022JE007252

21699100, 2022, 5, Downloaded from https://agupubs.onlinelibrary.wiley.com/doi/10.1029/2022JE007252 by Cochrane France, Wiley Online Library on [31/10/2022]. See the Terms and Conditions (https://onlinelibrary.wiley.com/terms-and-conditions) on Wiley Online Library for rules of use; OA articles are governed by the applicable Creative Commons License

the observations indicate that the PI remains high for all latitudes, albeit more variable (this was further explored in Section 4.5). Still, the largest differences in the vertical confinement are found in the midlatitudes and not in the polar regions, as illustrated in Figure 10.

5. Discussion

5.1. Column Abundance

In this work, the MCD was used to provide a priori values for the column abundance retrievals with the uncertainty set equal to the abundance. With a post-to-prior error ratio analysis, we demonstrated that the synergy injects a significant amount of information to the retrieval, and obtains highly robust column abundances. The climatology presented here displays a water vapor cycle consistent with established literature, both in terms of magnitude and seasonal and meridional variations. Water column abundances peak in early summer near the seasonal frost cap edge, where the vapor encircles and trails the retreating ice. It has been previously modeled (Houben et al., 1997), and more recently observed (Bibring et al., 2005; Kieffer & Titus, 2001), that water vapor subliming from the seasonal water frost annulus recondenses on the surface of the retreating CO_2 cap, which explains this behavior. The water decrease poleward of the annulus is observed consistently for all seasonal intervals, yet annual variations have been previously reported (Pankine et al., 2010), and are not discernible in in the composite averages presented here.

Although the overall behavior is well-known and the trend agrees well with the MCD model, significant differences do exist. The synergy column abundances deviate most prominently from the MCD in terms of absolute value with significantly lower abundances, particularly in the summer NH. The observed northern sublimation maximum is 30% lower than MCD estimates, and the sublimation season onset itself is observed to occur later in time. The discrepancies between measurements and the MCD have also previously been noted. The NH difference between synergy and MCD is very similar to the difference found by Savijärvi et al. (2019), where the MCD had to be scaled by a factor of 0.38 to agree with the local ChemCam data. When investigating the conditions at Jezero crater, Pla-García et al. (2020) also found that the CIA peak reached Jezero crater sooner and was higher in the MCD compared to TES measurements.

In the SH, the model and observations are in better agreement, and similar to what was reported by Clancy et al. (2017) using CRISM occultation data, who also found that retrieved water vapor abundances matched MCD model estimates better in the SH than in the NH. The synergy yields slightly higher values in the southern early summer, resulting in a somewhat asymmetrical relationship between the synergy and MCD, where the synergy finds a lower summer peak in the NH, but a larger peak in the SH.

When compared to previous works, the synergy northern maximum abundance was quite consistent with PFS, SPICAM and the revised TES abundances of 60–70 pr-μm (Fouchet et al., 2007; Pankine et al., 2010; Trokhimovskiy et al., 2015), while with CRISM a slightly lower sublimation peak was obtained in MY 28 and 29 of around 50 pr-μm (Smith et al., 2009). Although the synergy finds a smoothed average of around 50 pr-μm at 75°N and Ls = 105°–120°, some local and transient instances of abundances up to 100 pr-μm occur. Observations from the Limb and Nadir Observation channel of the NOMAD instrument on the ExoMars TGO satellite agree well with the synergy in terms of seasonal variations, however, the northern maximum obtained by the synergy is significantly higher than those found by NOMAD for the corresponding time and place (just above 30 pr-μm) (Crismani et al., 2020).

The southern maximum coincides in time with previous results, but the large asymmetry between the NH and SH maxima observed by SPICAM and CRISM is not as prominent in the synergy data set (see Figure 6, where a few very high column abundances are observed), as the northern maximum is normally a factor of 2 higher than the southern peak for the corresponding season (Figure 11). On average, the synergy finds a southern maximum of ∼33 pr-μm, significantly higher than SPICAM. It should be noted that the location where the largest SH abundances were observed were at latitudes not captured by previous TES and PFS studies. It should also be pointed out that observations in the south polar region are much sparser than elsewhere, and measurements from several years are binned together, whereas the observations of the north polar region are abundant and mostly from MY 27. Smith (2004) found that the year-to-year variations can be as high as 10 pr-μm, and might thus explain why we observe instances of high vapor abundances in the south.

Journal of Geophysical Research: Planets 10.1029/2022JE007252

21699100, 2022, 5, Downloaded from https://agupubs.onlinelibrary.wiley.com/doi/10.1029/2022JE007252 by Cochrane France, Wiley Online Library on [31/10/2022]. See the Terms and Conditions (https://onlinelibrary.wiley.com/terms-and-conditions) on Wiley Online Library for rules of use; OA articles are governed by the applicable Creative Commons License

Outside the summer maximums, the synergy again is most similar to SPICAM and PFS, and agrees very well also with NOMAD. During Ls = 0°–50°, the mean low latitude (0°-30°N) CIA was 7–8 pr-μm for the synergy, SPICAM, PFS, and NOMAD, and ∼5 pr-μm for CRISM. Later, during Ls = 150°–180° for the same latitudes, the mean abundances were 13–15 pr-μm for the synergy, SPICAM, NOMAD, and CRISM, ∼12 pr-μm for PFS.

The difference between the synergy and other data sets is most likely due to differences in calibration and data processing techniques, even though diurnal variations cannot be excluded. For example, NOMAD samples local times from 08:00 to 16:00, and PFS covers local times from morning into the late afternoon. TES sampled the equatorial region and midlatitudes around 14:00 and 02:00, with only data captured during the 10:00–14:00 range being used to assemble the revised data set presented by Pankine et al. (2010). No evidence supporting diurnal variations has yet been uncovered using OMEGA or SPICAM (Maltagliati, Montmessin, et al., 2011; Trokhimovskiy et al., 2015), and in the synergy, any diurnal variations are lost in the averaging process as PFS and SPICAM cover a broader time interval. Crismani et al. (2020) found no evidence for substantial diurnal variation in the total dayside water vapor column, thus the plausibility of diurnal variations causing such a large spread in column abundances is still considered unlikely.

5.2. Partitioning Index

The strongest motivation for the use of a spectral synergy retrieval approach is to access information on the vertical distribution of water vapor. We have shown that during the north polar sublimation period, the magnitude of the near-surface vertical confinement matches model predictions quite well, though discrepancies in the meridional partitioning gradient are significant. For both hemispheres the vertical partitioning remains high and fairly constant (±0.2) for all seasons and latitudes, while displaying a wave-like latitudinal behavior. As water vapor is located at very low altitudes, it is highly affected by complex circulation patterns and waves forced by topographic patterns. This could help in forcing the wave-structure of the meridional PI trend. Poleward of the polar cap edge, however, the hemispheres differ. In the south the partitioning index is observed to drop for all seasonal intervals except during mid spring. In the north the PI seems to be decreasing at first between 70° and 80°N, and then rapidly increases beyond the polar cap edge, especially so for mid and early spring. This polar cap behavior is well reproduced by the global climate model used to construct the MCD, except during spring for both hemispheres.

The largest relative difference in MCD and synergy vertical confinement in the northern hemisphere is found at midlatitudes after Ls = 150° (see Figure 10). The column abundance, which here never exceeds 20 pr-μm, agrees best with the MCD in this region (though still the synergy finds a lower value), while the obtained synergy partitioning was more than 50% higher than model estimates. This might be indicative of less water escaping through the hygropause than what is estimated in the MCD. For Ls = 135°–150°, Figure 12 shows that the MCD and synergy are quite consistent for high latitudes, both finding a PI of 0.7 at 70°N. In the drier low latitudes, where model and synergy agree quite well with regard to column abundances, the partitioning differs significantly. The model suggests the confinement decreases monotonically, reaching a PI = 0.4 at 20°N, while the synergy maintains a strong confinement, obtaining a PI of ∼0.7 at 20°N, having barely changed despite a drastic reduction in the total water column. This could suggest that the vertical circulation incorporated in the current model at low latitudes is too strong, causing the MCD partitioning to decrease more quickly toward the equator. The difference could also possibly be due to diurnal "breathing" of the regolith, actively exchanging water with the atmosphere and thus maintaining a near-surface layer. Near-surface meridional transport of sublimated water vapor from the poles could also cause these wave-like trends observed in both hemispheres.

Tamppari and Lemmon (2020) also investigated the near-surface water vapor confinement during early summer in the northern polar region (∼70°N) using a stereo camera on the Phoenix lander. The study indicates that at least 30% of the total column was kept below 2.5 km at all times, and that a well-mixed scenario in this low layer does not fit the data. Vertical profiles and the synergy partitioning index very well support these findings.

Overall, the synergy finds a more variable vertical partitioning than what the model suggests, which corresponds well with results from solar occultation observations with SPICAM (Maltagliati et al., 2013). This demonstrates that the synergy is particularly useful at mid to low latitudes where atmospheric dynamics influence the vertical partitioning, and over the polar regions where seasonal variations in the vertical partitioning are large and not well reproduced by the model. It would be of great interest to compare the synergistic partitioning with high resolution

Journal of Geophysical Research: Planets 10.1029/2022JE007252

vertical profiles from for example, the solar occultation instruments NOMAD and ACS on TGO. This will be included in future work, although as mentioned earlier, the ability of these instruments to probe the water vapor content in the very low atmosphere is not always present. As the southern hemisphere normally has a higher dust loading than the north, conditions for possibly probing the near-surface atmosphere with TGO are most favorable in the north high latitudes. At low latitudes where we observe large differences between synergy and model, continuously high dust loading will also make direct comparisons between synergy and TGO difficult.

6. Conclusions

Presented here are the results from a spectral synergistic retrieval method applied to water vapor nadir measurements from PFS and SPICAM sampled over seven Martian years. The synergy produces a highly reliable water vapor climatology with geographical and temporal patterns consistent with established literature. When compared to the LMD MCD, the synergy tends to retrieve lower total column abundances, in absolute differences the deviation is biggest for the northern summer sublimation peak, while in relative terms the most significant discrepancies are found at midlatitudes. In the southern hemisphere the synergy and MCD correspond very well. Other differences of note include timing and latitudinal extent of the sublimation onset, which occurs earlier in the MCD, and extends much further equatorward. The synergy finds very comparable column abundances to previous works using single spectral domain approaches with SPICAM and PFS (Fouchet et al., 2007; Trokhimovskiy et al., 2015), somewhat higher values than CRISM (Smith et al., 2009), and slightly lower than TES (Pankine et al., 2010; Smith, 2002).

The ability to extract information on the vertical distribution of water vapor from nadir observations is a unique capability of the spectral synergy approach. The synergy is unable to produce a vertical profile of fine resolution, but it can set reliable constraints on the partitioning of the water column, differentiating between the near-surface content below 5 km and the rest of the column. Overall, the synergy finds that water is strongly confined to a near-surface layer, and not evenly mixed in the boundary layer. Significant differences between the vertical partitioning over the north and south hemispheres are revealed, where the southern hemisphere exhibits a generally weaker confinement coupled with a stronger seasonal dependence and latitudinal variations than in the north. The near-surface confinement from the synergy overall differs from the MCD especially at low and middle latitudes where the synergy finds a stronger near-surface confinement than MCD estimates. The synergy also finds that the meridional spread of this strong confinement is larger than what the model suggests, maintaining large amounts of near-surface water vapor across most of the northern hemisphere. There appears to be no clear connection between a peak in total column abundance and the amount of vertical partitioning. In general, the synergy finds that the vertical confinement is subject to rapid and local variations, and can change significantly even while the total column abundance remains stable, or remain stable while the column abundance varies.

We have shown that by combining two separate spectral intervals, within which water vapor possesses diagnostic features, increased robustness is brought to the retrieval of column abundances as well as additional information about the vertical content, as compared to the commonly used single-interval retrieval approach. The combination of more accurate column abundances and constraints on the vertical distribution is essential for our understanding of the processes that control the distribution and transport of volatiles in the lower atmosphere.

Considering that current knowledge of the water distribution in the lowermost layer of the atmosphere is mainly based on GCMs, the comparison between the synergy partitioning results and the predictions of the MCD is of particular interest. The significant discrepancies between the two indicate that our understanding of the physics that shape the vertical distribution of atmospheric water on Mars is incomplete.

Data Availability Statement

The SPICAM and PFS data used in this study can be found at the ESA PSA server https://www.cosmos.esa.int/web/psa/mars-express. The complete processed data set used to produce the figures in this paper have been published at Knutsen, 2022 [Data set]. For model comparisons the Mars Climate Database was used, which can be accessed on this link: http://www-mars.lmd.jussieu.fr/mcd_python/.

21699100, 2022, 5, Downloaded from https://agupubs.onlinelibrary.wiley.com/doi/10.1029/2022JE007252 by Cochrane France, Wiley Online Library on [31/10/2022]. See the Terms and Conditions (https://onlinelibrary.wiley.com/terms-and-conditions) on Wiley Online Library for rules of use; OA articles are governed by the applicable Creative Commons License

Journal of Geophysical Research: Planets 10.1029/2022JE007252

Acknowledgments
This work was funded by CNES, the Agence Nationale de la Recherche (ANR, PRCI, CE31 AAPG2019, MCUBE project), and background for this project was funded by the European Union's Horizon 2020 Programme under grant agreement UPWARDS-633127. The SPICAM instrument was developed by the Laboratoire Atmospheres, Milieux, Observations Spatiales (LATMOS) in Guyancourt, and the Space Research Institute (IKI) in Moscow. The instrument development was funded by the National Centre for Space Studies of France (CNES) and Roscosmos. The PFS experiment has been built at the "Istituto di Astrofisica e Planetologia Spaziali" (IAPS) of the "Istituto Nazionale di Astrofisica" (INAF) and is currently funded by the Italian Space Agency (ASI) in the context of the Italian participation to the ESA's Mars Express Mission (grant ASI/INAF n. 2018-2-HH.0).

References

Aoki, S., Vandaele, A. C., Daerden, F., Villanueva, G. L., Liuzzi, G., Thomas, I. R., et al. (2019). Water vapor vertical profiles on Mars in dust storms observed by TGO/NOMAD. *Journal of Geophysical Research: Planets*, *124*(12), 3482–3497. https://doi.org/10.1029/2019JE006109

Bertaux, J.-L., Korablev, O., Perrier, S., Quémerais, E., Montmessin, F., Leblanc, F., et al. (2006). SPICAM on Mars Express: Observing modes and overview of UV spectrometer data and scientific results. *Journal of Geophysical Research*, *111*(E10), E10S90. https://doi.org/10.1029/2006JE002690

Bibring, J.-P., Langevin, Y., Gendrin, A., Gondet, B., Poulet, F., Berthé, M., et al. (2005). Mars surface diversity as revealed by the OMEGA/Mars express observations. *Science*, *307*(5715), 1576–1581. https://doi.org/10.1126/science.1108806

Chicarro, A., Martin, P., & Trautner, R. (2004). The Mars Express mission: An overview. *Mars Express: the scientific payload*, *1240*, 3–13.

Christi, M. J., & Stephens, G. L. (2004). Retrieving profiles of atmospheric CO_2 in clear sky and in the presence of thin cloud using spectroscopy from the near and thermal infrared: A preliminary case study: Retrieving profiles of CO_2. *Journal of Geophysical Research*, *109*(D4). https://doi.org/10.1029/2003JD004058

Clancy, R. T., Smith, M. D., Lefèvre, F., McConnochie, T. H., Sandor, B. J., Wolff, M. J., et al. (2017). Vertical profiles of Mars 1.27 μm O_2 dayglow from MRO CRISM limb spectra: Seasonal/global behaviors, comparisons to LMDGCM simulations, and a global definition for Mars water vapor profiles. *Icarus*, *293*, 132–156. https://doi.org/10.1016/j.icarus.2017.04.011

Crismani, M. M. J., Villanueva, G. L., Liuzzi, G., Smith, M. D., Knutsen, E. W., Daerden, F., et al. (2020). *A global and seasonal perspective of Martian water vapor from ExoMars/NOMAD*.

Davies, D. W. (1979). The vertical distribution of Mars water vapor. *Journal of Geophysical Research*, *84*(B6), 2875–2879. https://doi.org/10.1029/jb084ib06p02875

Davis, B. W. (1969). Some speculations on adsorption and desorption of CO_2 in Martian bright areas. *Icarus*, *11*(2), 155–158. https://doi.org/10.1016/0019-1035(69)90040-2

Edwards, D. P., Arellano, A. F., & Deeter, M. N. (2009). A satellite observation system simulation experiment for carbon monoxide in the lowermost troposphere. *Journal of Geophysical Research*, *114*(D14), D14304. https://doi.org/10.1029/2008JD011375

Fanale, F. P., & Cannon, W. A. (1971). Adsorption on the martian regolith. *Nature*, *230*(5295), 502–504. https://doi.org/10.1038/230502a0

Farmer, C. B., Davies, D. W., & Laporte, D. D. (1976). Mars: Northern summer ice cap–water vapor observations from viking 2. *Science*, *194*(4271), 1339–1341. https://doi.org/10.1126/science.194.4271.1339

Fedorova, A., Bertaux, J. L., Betsis, D., Montmessin, F., Korablev, O., Maltagliati, L., & Clarke, J. (2018). Water vapor in the middle atmosphere of Mars during the 2007 global dust storm. *Icarus*, *300*, 440–457. https://doi.org/10.1016/j.icarus.2017.09.025

Fedorova, A., Korablev, O., Bertaux, J.-L., Rodin, A., Kiselev, A., & Perrier, S. (2006). Mars water vapor abundance from SPICAM IR spectrometer: Seasonal and geographic distributions. *Journal of Geophysical Research*, *111*(E9), E09S08. https://doi.org/10.1029/2006JE002695

Fedorova, A., Montmessin, F., Korablev, O., Lefèvre, F., Trokhimovskiy, A., & Bertaux, J. (2021). Multi-annual monitoring of the water vapor vertical distribution on Mars by SPICAM on Mars express. *Journal of Geophysical Research: Planets*, *126*(1). https://doi.org/10.1029/2020JE006616

Fedorova, A., Montmessin, F., Korablev, O., Luginin, M., Trokhimovskiy, A., Belyaev, D. A., et al. (2020). Stormy water on Mars: The distribution and saturation of atmospheric water during the dusty season. *Science*, *367*(6475), 297–300. https://doi.org/10.1126/science.aay9522

Fischer, E., Martínez, G. M., Rennó, N. O., Tamppari, L. K., & Zent, A. P. (2019). Relative humidity on Mars: New results from the Phoenix TECP sensor. *Journal of Geophysical Research: Planets*, *124*(11), 2780–2792. https://doi.org/10.1029/2019JE006080

Forget, F., Hourdin, F., Fournier, R., Hourdin, C., Talagrand, O., Collins, M., et al. (1999). Improved general circulation models of the Martian atmosphere from the surface to above 80 km. *Journal of Geophysical Research*, *104*(E10), 24155–24175. https://doi.org/10.1029/1999JE001025

Formisano, V., Angrilli, F., Arnold, G., Atreya, S., Bianchini, G., Biondi, D., et al. (2005). The planetary Fourier spectrometer (PFS) onboard the European Mars express mission. *Planetary and Space Science*, *53*(10), 963–974. https://doi.org/10.1016/j.pss.2004.12.006

Fouchet, T., Lellouch, E., Ignatiev, N. I., Forget, F., Titov, D. V., Tschimmel, M., et al. (2007). Martian water vapor: Mars express PFS/LW observations. *Icarus*, *190*(1), 32–49. https://doi.org/10.1016/j.icarus.2007.03.003

Giuranna, M., Formisano, V., Biondi, D., Ekonomov, A., Fonti, S., Grassi, D., et al. (2005). Calibration of the Planetary Fourier Spectrometer long wavelength channel. *Planetary and Space Science*, *53*(10), 993–1007. https://doi.org/10.1016/j.pss.2005.02.007

Giuranna, M., Viscardy, S., Daerden, F., Neary, L., Etiope, G., Oehler, D., et al. (2019). Independent confirmation of a methane spike on Mars and a source region east of Gale Crater. *Nature Geoscience*, *12*(5), 326–332. https://doi.org/10.1038/s41561-019-0331-9

Haberle, R. M., & Jakosky, B. M. (1990). Sublimation and transport of water from the North residual polar cap on Mars. *Journal of Geophysical Research*, *95*(B2), 1423–1437. https://doi.org/10.1029/jb095ib02p01423

Harri, A.-M., Genzer, M., Kemppinen, O., Gomez-Elvira, J., Haberle, R., Polkko, J., et al. (2014). Mars Science Laboratory relative humidity observations: Initial results. *Journal of Geophysical Research: Planets*, *119*(9), 2132–2147. https://doi.org/10.1002/2013JE004514

Houben, H., Haberle, R. M., Young, R. E., & Zent, A. P. (1997). Modeling the Martian seasonal water cycle. *Journal of Geophysical Research*, *102*(E4), 9069–9083. https://doi.org/10.1029/97JE00046

Jakosky, B. M., & Farmer, C. B. (1982). The seasonal and global behavior of water vapor in the Mars atmosphere: Complete global results of the Viking Atmospheric Water Detector Experiment. *Journal of Geophysical Research*, *87*(B4), 2999. https://doi.org/10.1029/JB087iB04p02999

Jakosky, B. M., Zent, A. P., & Zurek, R. W. (1997). The Mars water cycle: Determining the role of exchange with the regolith. *Icarus*, *130*(1), 87–95. https://doi.org/10.1006/icar.1997.5799

Kieffer, H., & Titus, T. N. (2001). TES mapping of Mars' North seasonal cap. *Icarus*, *154*(1), 162–180. https://doi.org/10.1006/icar.2001.6670

Knutsen, E. W. (2022). Dataset of synergistically retrieved water vapor from SPICAM and PFS nadir observations [Data set]. Zenodo. https://doi.org/10.5281/ZENODO.6160793

Korablev, O., Bertaux, J.-L., Fedorova, A., Fonteyn, D., Stepanov, A., Kalinnikov, Y., et al. (2006). SPICAM IR acousto-optic spectrometer experiment on Mars Express. *Journal of Geophysical Research*, *111*(E9), E09S03. https://doi.org/10.1029/2006JE002696

Landgraf, J., & Hasekamp, O. P. (2007). Retrieval of tropospheric ozone: The synergistic use of thermal infrared emission and ultraviolet reflectivity measurements from space. *Journal of Geophysical Research*, *112*(D8), D08310. https://doi.org/10.1029/2006JD008097

Madeleine, J.-B., Forget, F., Millour, E., Navarro, T., & Spiga, A. (2012). The influence of radiatively active water ice clouds on the martian climate: Radiative effect of Martian clouds. *Geophysical Research Letters*, *39*(23). https://doi.org/10.1029/2012GL053564

Maltagliati, L., Montmessin, F., Fedorova, A., Korablev, O., Forget, F., & Bertaux, J.-L. (2011). Evidence of water vapor in excess of saturation in the atmosphere of Mars. *Science*, *333*(6051), 1868–1871. https://doi.org/10.1126/science.1207957

Maltagliati, L., Montmessin, F., Korablev, O., Fedorova, A., Forget, F., Määttänen, A., et al. (2013). Annual survey of water vapor vertical distribution and water–aerosol coupling in the martian atmosphere observed by SPICAM/MEx solar occultations. *Icarus*, *223*(2), 942–962. https://doi.org/10.1016/j.icarus.2012.12.012

21699100, 2022, 5, Downloaded from https://agupubs.onlinelibrary.wiley.com/doi/10.1029/2022JE007252 by Cochrane France, Wiley Online Library on [31/10/2022]. See the Terms and Conditions (https://onlinelibrary.wiley.com/terms-and-conditions) on Wiley Online Library for rules of use; OA articles are governed by the applicable Creative Commons License

Journal of Geophysical Research: Planets 10.1029/2022JE007252

Maltagliati, L., Titov, D. V., Encrenaz, T., Melchiorri, R., Forget, F., Keller, H. L., & Bibring, J.-P. (2011). Annual survey of water vapor behavior from the OMEGA mapping spectrometer onboard Mars Express. *Icarus*, *213*(2), 480–495. https://doi.org/10.1016/j.icarus.2011.03.030

Martínez, G. M., Newman, C. N., De Vicente-Retortillo, A., Fischer, E., Renno, N. O., Richardson, M. I., et al. (2017). The modern near-surface martian climate: A review of in-situ meteorological data from viking to curiosity. *Space Science Reviews*, *212*(1–2), 295–338. https://doi.org/10.1007/s11214-017-0360-x

McElroy, M. B., & Donahue, T. M. (1972). Stability of the martian atmosphere. *Science*, *177*(4053), 986–988. https://doi.org/10.1126/science.177.4053.986

Millour, E., Forget, F., Spiga, A., Vals, M., Zakharov, V., & Montabone, L. (2018). The Mars climate database. *Paper presented at the Mars science workshop "from Mars express to ExoMars"*. version 5.3. Held 27-28 February 2018 at ESAC, Spain, Id.68.

Montmessin, F., & Ferron, S. (2019). A spectral synergy method to retrieve martian water vapor column-abundance and vertical distribution applied to Mars Express SPICAM and PFS nadir measurements. *Icarus*, *317*, 549–569. https://doi.org/10.1016/j.icarus.2018.07.022

Montmessin, F., Forget, F., Rannou, P., Cabane, M., & Haberle, R. M. (2004). Origin and role of water ice clouds in the Martian water cycle as inferred from a general circulation model. *Journal of Geophysical Research*, *109*(E10), E10004. https://doi.org/10.1029/2004JE002284

Navarro, T., Madeleine, J. B., Forget, F., Spiga, A., Millour, E., Montmessin, F., & Määttänen, A. (2014). Global climate modeling of the Martian water cycle with improved microphysics and radiatively active water ice clouds. *Journal of Geophysical Research: Planets*, *119*(7), 1479–1495. https://doi.org/10.1002/2013JE004550

Pan, L., Edwards, D. P., Gille, J. C., Smith, M. W., & Drummond, J. R. (1995). Satellite remote sensing of tropospheric CO and CH_4: Forward model studies of the MOPITT instrument. *Applied Optics*, *34*(30), 6976. https://doi.org/10.1364/AO.34.006976

Pan, L., Gille, J. C., Edwards, D. P., Bailey, P. L., & Rodgers, C. D. (1998). Retrieval of tropospheric carbon monoxide for the MOPITT experiment. *Journal of Geophysical Research*, *103*(D24), 32277–32290. https://doi.org/10.1029/98JD01828

Pankine, A. A., & Tamppari, L. K. (2015). Constraints on water vapor vertical distribution at the Phoenix landing site during summer from MGS TES day and night observations. *Icarus*, *252*, 107–120. https://doi.org/10.1016/j.icarus.2015.01.008

Pankine, A. A., Tamppari, L. K., & Smith, M. D. (2010). MGS TES observations of the water vapor above the seasonal and perennial ice caps during northern spring and summer. *Icarus*, *210*(1), 58–71. https://doi.org/10.1016/j.icarus.2010.06.043

Pla-García, J., Rafkin, S. C. R., Martinez, G. M., Vicente-Retortillo, Á., Newman, C. E., Savijärvi, H., et al. (2020). Meteorological predictions for Mars 2020 perseverance rover landing site at Jezero crater. *Space Science Reviews*, *216*(8), 148. https://doi.org/10.1007/s11214-020-00763-x

Razavi, A., Clerbaux, C., Wespes, C., Clarisse, L., Hurtmans, D., Payan, S., et al. (2009). Characterization of methane retrievals from the IASI space-borne sounder. *Atmospheric Chemistry and Physics*, *9*(20), 7889–7899. https://doi.org/10.5194/acp-9-7889-2009

Richardson, M. I. (2002). Investigation of the nature and stability of the Martian seasonal water cycle with a general circulation model. *Journal of Geophysical Research*, *107*(E5), 5031. https://doi.org/10.1029/2001JE001536

Rodgers, C. D. (2000). *Inverse Methods for Atmospheric Sounding: Theory and Practice* (Vol. 2). WORLD SCIENTIFIC. https://doi.org/10.1142/3171

Rothman, L. S., Gordon, I. E., Babikov, Y., Barbe, A., Chris Benner, D., Bernath, P. F., et al. (2013). The HITRAN2012 molecular spectroscopic database. *Journal of Quantitative Spectroscopy and Radiative Transfer*, *130*, 4–50. https://doi.org/10.1016/j.jqsrt.2013.07.002

Savijärvi, H., & Harri, A.-M. (2021). Water vapor adsorption on Mars. *Icarus*, *357*, 114270. https://doi.org/10.1016/j.icarus.2020.114270

Savijärvi, H., McConnochie, T. H., Harri, A.-M., & Paton, M. (2019). Annual and diurnal water vapor cycles at Curiosity from observations and column modeling. *Icarus*, *319*, 485–490. https://doi.org/10.1016/j.icarus.2018.10.008

Smith, M. D. (2002). The annual cycle of water vapor on Mars as observed by the thermal emission spectrometer: Mars water vapor. *Journal of Geophysical Research*, *107*(E11), 25-1–25–19. https://doi.org/10.1029/2001JE001522

Smith, M. D. (2004). Interannual variability in TES atmospheric observations of Mars during 1999–2003. *Icarus*, *167*(1), 148–165. https://doi.org/10.1016/j.icarus.2003.09.010

Smith, M. D., Wolff, M. J., Clancy, R. T., & Murchie, S. L. (2009). Compact Reconnaissance Imaging Spectrometer observations of water vapor and carbon monoxide. *Journal of Geophysical Research*, *114*, E00D03. https://doi.org/10.1029/2008JE003288

Spinrad, H., Münch, G., & Kaplan, L. D. (1963). Letter to the editor: The detection of water vapor on Mars. *The Astrophysical Journal*, *137*, 1319. https://doi.org/10.1086/147613

Steele, L. J., Lewis, S. R., Patel, M. R., Montmessin, F., Forget, F., & Smith, M. D. (2014). The seasonal cycle of water vapour on Mars from assimilation of Thermal Emission Spectrometer data. *Icarus*, *237*, 97–115. https://doi.org/10.1016/j.icarus.2014.04.017

Tamppari, L. K., Bass, D., Cantor, B., Daubar, I., Dickinson, C., Fisher, D., et al. (2010). Phoenix and MRO coordinated atmospheric measurements. *Journal of Geophysical Research*, *115*, E00E17. https://doi.org/10.1029/2009JE003415

Tamppari, L. K., & Lemmon, M. T. (2020). Near-surface atmospheric water vapor enhancement at the Mars Phoenix lander site. *Icarus*, *343*, 113624. https://doi.org/10.1016/j.icarus.2020.113624

Trokhimovskiy, A., Fedorova, A., Korablev, O., Montmessin, F., Bertaux, J.-L., Rodin, A., & Smith, M. D. (2015). Mars' water vapor mapping by the SPICAM IR spectrometer: Five martian years of observations. *Icarus*, *251*, 50–64. https://doi.org/10.1016/j.icarus.2014.10.007

Tschimmel, M., Ignatiev, N. I., Titov, D. V., Lellouch, E., Fouchet, T., Giuranna, M., & Formisano, V. (2008). Investigation of water vapor on Mars with PFS/SW of Mars Express. *Icarus*, *195*(2), 557–575. https://doi.org/10.1016/j.icarus.2008.01.018

Zent, A. P., Hecht, M. H., Cobos, D. R., Wood, S. E., Hudson, T. L., Milkovich, S. M., et al. (2010). Initial results from the thermal and electrical conductivity probe (TECP) on Phoenix. *Journal of Geophysical Research*, *115*, E00E14. https://doi.org/10.1029/2009JE003420

Erratum

The funding information of this work has changed since publication. The grant RSF (Russian Science Foundation 20-42-0903) did not support this science and was included by mistake. It has been removed. The current funding information may be considered the version of record.

21699100, 2022, 5, Downloaded from https://agupubs.onlinelibrary.wiley.com/doi/10.1029/2022JE007252 by Cochrane France, Wiley Online Library on [31/10/2022]. See the Terms and Conditions (https://onlinelibrary.wiley.com/terms-and-conditions) on Wiley Online Library for rules of use; OA articles are governed by the applicable Creative Commons License

Appendix B

Conference proceedings: A spectral synergy method applied to PFS and SPICAM nadir observations to constrain near-surface water content in the Martian atmosphere

73rd International Astronautical Congress (IAC), Paris, France, 18-22 September 2022.
Copyright ©2022 by the International Astronautical Federation (IAF). All rights reserved.

IAC-22, A3,3B,8,x68604

A spectral synergy method applied to PFS and SPICAM nadir observations to constrain near-surface water content in the Martian atmosphere

Elise Wright Knutsen[a]*, Franck Montmessin[a], Loic Verdier[a], Gaetan Lacombe[a], Franck Lefevre[a], Stephane Ferron[b], Marco Giuranna[c], Paulina Wolkenberg[c], Anna Fedorova[d], Oleg Korablev[d], Alexander Trokhimovskiy[d]

[a] *LATMOS/IPSL, UVSQ Université Paris-Saclay, Sorbonne Université, CNRS, Guyancourt, France*, elise-wright.knutsen@latmos.ipsl.fr
[b] *ACRI-ST, Guyancourt, France*
[c] *IAPS-INAF, Rome, Italy*
[d] *Space Research Institute (IKI), Moscow, Russia*
* Corresponding author

Abstract

In this study we have applied a novel spectral synergy method in the retrieval of water vapor on Mars with measurements from nadir-pointing instruments. Water vapor column abundances were retrieved simultaneously with PFS (sensing the thermal infrared range) and SPICAM (sensing the near-infrared range) on Mars Express, yielding distinct yet complementary sensitivity to different parts of the atmospheric column. It has been shown that by exploiting a synergy retrieval approach, a more robust water vapor cclimatology can be obtained, compared to when only one instrument is used. The synergy also provides a rough resolution of the vertical distribution of water vapor, which remains out of the scope of classical nadir observations. Here, special attention is given to regions where atmospheric water might interact with the regolith, with extra focus on the sublimation of the north seasonal polar cap. The results are compared to the Mars Climate Database, and significant differences were discovered. Deviances between synergy and model in both magnitude and meridional variation suggesting that certain aspects of the transport and dynamics of water vapor are not fully captured by current models.

Keywords: Mars atmosphere, infrared spectroscopy, water vapor, transport, dynamics.

Acronyms/Abbreviations

- CIA – Column Integrated Abundance
- DOF – Degree of Freedom
- MEX – Mars Express
- NIR – Near-infrared spectral domain
- PI – Partitioning Index
- PFS – Planetary Fourier Spectrometer
- SPICAM – Spectroscopy for the Investigation of the Characteristics of the Atmosphere of Mars
- TIR – Therman infrared spectral domain

1. Introduction

Atmospheric water vapor is an important influencer of Martian weather and climate. Though little of Mars' original water content remains today, even as a trace species in the Martian atmosphere water vapor plays a major role in affecting the climate on Mars (along with the CO_2 and dust cycles). H_2O impacts the radiative equilibrium through cloud formation [1], and controls the stability of the atmosphere, as water vapor photolysis creates the main oxidant of the Martian photochemical cycle [2].

Knowledge of the low-altitude H_2O vertical distribution on Mars relied heavily on general circulation models until quite recently. Inferring vertical profiles of water vapor from nadir measurements ([3], [4]) were common, but also direct measurements by solar occultation viewing geometry have become available with SPICAM on Mars-Express since 2004, and with the ExoMars Trace gas Orbiter (TGO) and its infrared spectrometers NOMAD and ACS since 2018.

With this technique new knowledge has been obtained, especially in the upper atmosphere, as solar occultations suffer from low transmittances closer to the surface. The lower limit for observation is typically 5-10 km for dust-free conditions, and as high as 20-30 km during the dusty perihelion season [5].

The behavior of water vapor has been studied for decades, yet how water vapor varies with altitude, especially close to the surface, remains an open question. This work aims to shed light on the vertical distribution of water vapor, and its near-surface transportation from the north polar cap in spring towards lower latitudes.

2. Instruments

The European Mars Express (MEX) mission was launched in June 2003, and started science operations in

73rd International Astronautical Congress (IAC), Paris, France, 18-22 September 2022.
Copyright ©2022 by the International Astronautical Federation (IAF). All rights reserved.

January 2004 [6]. MEX is stationed in a quasi-polar and highly elliptical orbit with a 7.5-hour period and a periapsis of about 300 km. One of the main mission objectives is to study the Martian water cycle. Several instruments onboard provide this capability. The Planetary Fourier Spectrometer (PFS) and SPectroscopy for the Investigation of the Characteristics of the Atmosphere of Mars (SPICAM) are both able to monitor spectral diagnostic features of water vapor from a nadir viewing geometry. For the purpose of this study, PFS was selected for its coverage in the thermal infrared (TIR) domain, while SPICAM was chosen to cover the near-infrared (NIR). For detailed descriptions of each instrument, the reader is referred to [7], [8] and [9] for PFS and SPICAM respectively.

3. Method

3.1 The spectral synergy

The spectral synergy is an atmospheric retrieval approach, which combines co-located nadir observations of multiple spectral domains. Measurements in the thermal infrared (TIR) domain are mostly sensitive to the middle atmosphere (at the origin of the photon emission) where the temperature contrast of the atmosphere with respect to the surface is high. Measurements in the near-infrared (NIR) are on the other hand sensitive to any molecule present along the column as the technique relies on solar photons traversing the entire atmosphere back and forth. One should note however that dust modulates the NIR sensitivity in particular. When atmospheric dust loading is high, some of the incoming solar flux will not reach the surface, and is instead scattered back to space or absorbed, resulting in only part of the column being sampled. In such cases will the NIR technique become altitude dependent.

The utilisation of multiple spectral domains to increase vertical resolution is not a new concept. It was developed for atmospheric observations of terrestrial trace gases [10], [11]. Later the method was successfully tested for the study of Martian water vapor [12], and a large-scale climatology study was later performed using the same approach [13].

3.2 Retrieval routine

The retrieval of water vapor follows the routine outlined in [12], and pre-retrieval selection criteria are also described in the text therein. The synergistic method requires a set of co-located PFS and SPICAM measurements on which to apply the retrieval routine. To obtain a satisfying signal-to-noise ratio, nine consecutive spectra are averaged for PFS, and fifteen for SPICAM. The SPICAM observation closest in time to the central PFS spectrum is selected and averaged with the seven measurements prior to it and the seven after it, resulting in a combined field of view similar to that of the nine combined PFS measurements.

For water vapor and temperature *a priori* profiles, the Mars Climate Database (MCD) version 5.3 was used [14], [15]. Temperature and aerosol parameters were retrieved individually from the PFS average spectra, which were then injected into the synergistic routine. The HITRAN 2012 spectroscopic database [16] was used for the spectral fitting procedure, which then relies on a Bayesian curve-fitting approach.

To infer water vapor from the set of combined NIR/TIR spectra, a simultaneous inversion from both spectral domains is done by adjusting the H_2O abundance along the vertical profile. The altitude profile is sampled at nine points separated by 2.5 km from ground to 10 km, and by 5 km from 10 to 30 km. All points are correlated with a Gaussian kernel, such that the points are less strongly correlated when the distance between them is increasing. An example set of spectra for SPICAM and PFS and the consequent vertical profile is shown in Fig. 1

The results include a *a posteriori* covariance matrix, from which the degree of freedom (DOF) can be calculated from the sum of the trace of the matrix. For nadir observations the DOF normally fluctuates around 1 if the retrieval is made on a single spectral region which implies that one independent parameter can be inferred from the measurement (most commonly the column density), while with a higher DOF some information of the vapor vertical distribution can be obtained.

4. Data set and selection scheme

The data used in the following study is a subset of the complete data set previously used in [13]. The complete set covers 1379 individual orbits, with roughly 180 000 observations, distributed across seven Mars years from Ls 334° of MY 26 to Ls 297° of MY 34, with no measurements from MY 30-31.

After the inversion of water vapor, strict selection criteria are applied to the data set to ensure further analysis is only done on robust observations. The criteria applied to the data by [13] were as follows; i) an ANR ≥ 3 (3-sigma detection limit), ii) a DOF for water vapor ≥ 1.25, iii) a post-to-prior error ratio ≤ 0.9 for water volume mixing ratio at 2.5 km (Error ratio), iv) a reduced χ^2 of the retrieval ≤ 4 resulting in about 55% of the complete set being used for studying the vertical distribution of water vapor. In that work, a vertical partitioning index (PI) was defined as the integrated profile from ground to 5 km, divided by the full column abundance. With an average DOF of roughly 1.5, the vertical profile cannot actually be resolved, thus the PI was used to provide an estimate of how much of the total column of water is kept in the near-surface atmosphere. Note that if water vapor was evenly mixed in the atmosphere with a scale height of 11 km, the PI would be equal to 0.37, which is similar to what the MCD often estimates.

73rd International Astronautical Congress (IAC), Paris, France, 18-22 September 2022.
Copyright ©2022 by the International Astronautical Federation (IAF). All rights reserved.

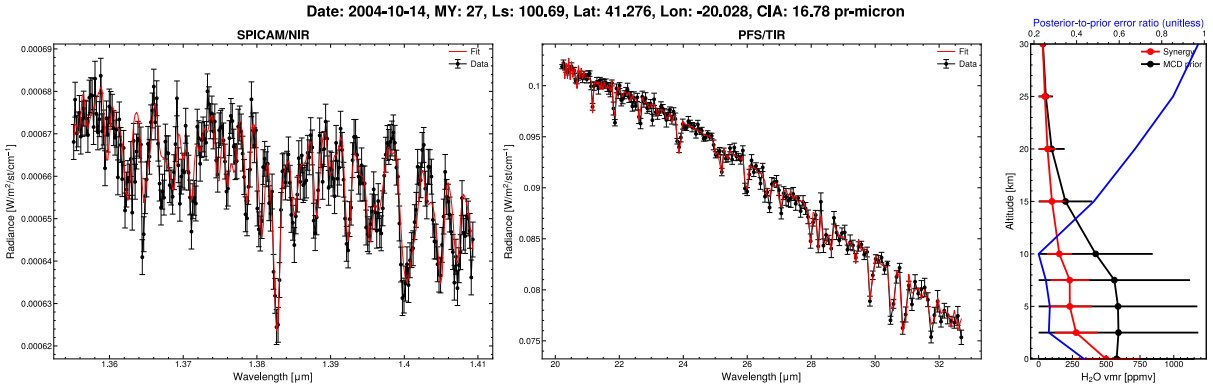

Figure 1: Example of average spectra for SPICAM and PFS, along with the resulting vertical profile of water vapor, and the ratio of posterior to prior (MCD) errors for each altitude level. Time, position and retrieved column abundance of water for the co-located observation is given at top of the figure.

For this work, the criteria limit for the DOF was made stricter, such that only measurements with a DOF ≥ 2.25 are used for further study. This is a trade-off between the need to maintain a large number of co-located observations to produce a climatology, and to ensure more highly resolved vertical profiles. The other criteria limits were kept as before. With the new DOF limit, 6773 co-located measurements from 592 orbits are left.

5. Results and Discussion

After selection, the water vapor profiles were resampled to a finer vertical grid, and smoothed using a Savitzky-Golay low-pass filter with a second order polynomial in order to dampen unphysically sharp features. The profiles were then averaged in bins of 2° Ls and 1.5 km altitude, or 2° latitude and 1.5 km, as can be seen in Figs. 2 and 3 respectively.

Fig. 2 displays hemispherical cross sections of the water vapor distribution that covers the entire northern hemisphere from early spring to late-summer (Ls=30°-165°). The figure shows the onset and peak of the polar cap sublimation season and the subsequent transport of water to equatorial latitudes. Overall, water vapor is confined close to the surface, and until Ls~100, contained mostly northward of 60°N.

In the Ls=30°-60° panel the atmospheric water vapor content is low for all latitudes, in line with established theory. By Ls=45°-75°, some H_2O seems to have sublimated from the southernmost edge of the polar cap, while at the same time at 80°N a separate "bubble" of water appears. As data is averaged from multiple Mars years, such features could also be the result of annual variations. In panels Ls=60°-90° and Ls=75°-105° (in the transition between spring and summer) water is sublimating rapidly at the surface, creating a distinct near-surface layer spreading at low altitudes from 50-80°N. in panels Ls=75°-105° and Ls=90°-120°, some vapor seems to be lifted up into a second layer and brought northward. Later, when water is sublimating at higher latitudes, this lifted water brought north into the polar cap region combines with the recently sublimated water to create the familiar global maxima at 80°N at about 120°Ls.

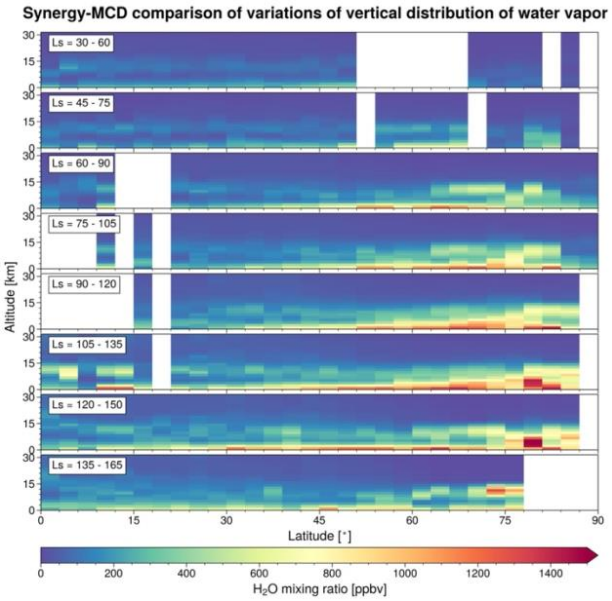

Figure 2: Variations of water vapor as a function of altitude and latitude. Data was averaged in bins of 3° latitude and 1.5 km altitude. Each panel represents a 30°Ls time interval, overlapping by 15°Ls in each step. The total time period is Ls=30°-165°, covering the polar cap sublimation period in early northern summer. White areas indicate periods with no available co-located observations.

Water that sublimated southward of 75°N appears to remain close to the surface while being transported equatorward. The weak two-layer structure from early spring mid-latitudes has now diffused into a smoother

73rd International Astronautical Congress (IAC), Paris, France, 18-22 September 2022.
Copyright ©2022 by the International Astronautical Federation (IAF). All rights reserved.

vertical distribution. From [13] we know that the vertical distribution remains fairly stable throughout the year, but the largest variations are found at 20°-30°N. in this region, from Ls=75°-105° to Ls=135°-165°, the vertical partitioning index increases from 0.5 to 0.7.

In Fig. 3 we focus on the mid-latitude region of 30°-45°N for a longer time period, starting from the beginning of spring and continuing into early autumn. It is in this region that the largest discrepancies between observations and model has been previously found [13]. The data was averaged zonally in order to smooth topographically induced variations.

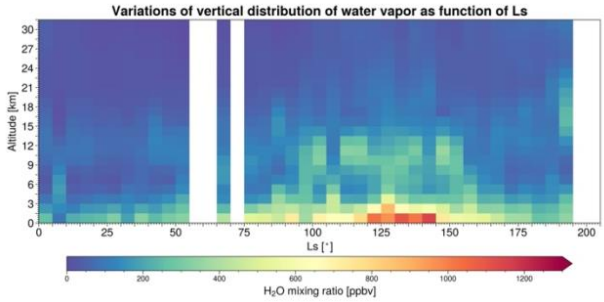

Figure 3: Variations of water vapor as a function of altitude and solar longitude, with spring beginning on the left and ending with early autumn on the right. Data is averaged in bins of 5° Ls and 1.5 km altitude, and over the latitude range lat=30°-45°. White areas indicate time periods with no available co-located observations.

While the overall northern polar cap sublimation maximum is spread out across Ls=100°-125° [13], the peak in near-surface water observed at mid-latitudes appears rather suddenly at 120°Ls. This suggests that the vapor is not becoming highly diffused under transport, but remains a dense and humid front. The sublimated water spends roughly 20°Ls being transported from 80°N, which corresponds to 37 sols.

To put these results in the context of current knowledge and understanding of Mars atmospheric transport and dynamics, a direct comparison between the synergistic observations and the MCD model was made in Fig. 4.

A ratio is calculated at each altitude step between the local mixing ratio of the synergy divided by the MCD predicted value. The ratios are then zero-centred to provide a symmetric solution. The colour-scale is such that grey colours indicate that observations and model values are equal, red tones indicate that observed water content is higher than the model and blue tones correspond to lower observed values than the MCD. Spatial and temporal binning remains as all other figures. The comparison is made for a selection of locations and time periods of special interest, namely the polar cap sublimation season (the top panel corresponds to the same measurements as the Ls=90°-120° panel in Fig. 2) and the mid-latitudes where it has previously been shown that data and model differ (the bottom panel shows the same measurements as in Fig. 3).

Both panels are largely blue in tone, indicating that for the most part, the synergy finds lower water contents than the MCD model. In both panels the colors flip at and near the surface where there is a rapid change and here we measure more water than model estimates. This means that overall, water is observed to be more strongly confined at low altitudes than model estimates.

In the top panel where we show a cross section of the northern hemisphere during early spring, observations and the MCD match fairly well above 18 km, especially northward of 55°N where they are close to equal. At polar latitudes at roughly 9-16 km, a distinct and isolated feature is visible. Above, below and south of this region, model and observations are not extremely different, but with the synergy measuring a dryer atmosphere. At 9-16 km north of 75°N however, the synergy yields an almost twice as wet local region. As can be seen from the Ls=90°-120° panel in Fig. 2, a second layer of humid air is found here, which is clearly not reproduced in the model.

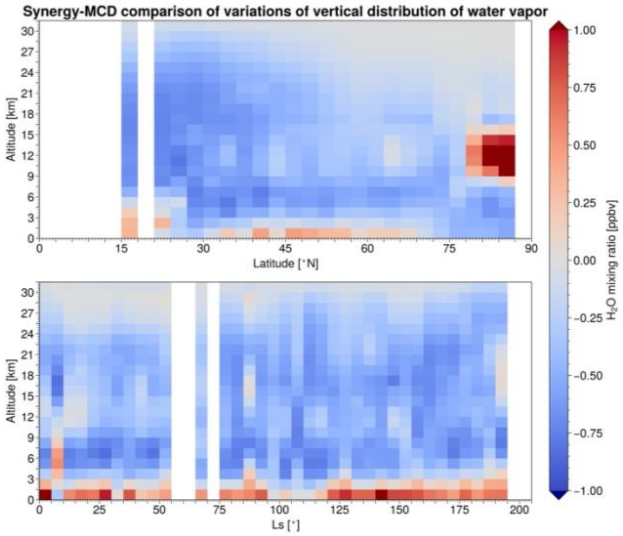

Figure 4: Ratio between synergistic observations and MCD model predictions, shown for the polar cap sublimation period (top) and mid-latitudes (bottom). The data has been zero-centred such that grey colours indicate that observations and model values are similar, red/blue tones indicate that the synergy finds a higher/lower water content compared to the MCD. Spatial and temporal binning remains as all other figures. The top panel corresponds to the same measurements as Ls=90°-120° panel in Fig. 2, and the bottom panel shows the same measurements as in Fig. 3. White areas indicate time periods with no available co-located observations.

7. Conclusion

Using a spectral synergy retrieval method, new information about the vertical distribution of water

73rd International Astronautical Congress (IAC), Paris, France, 18-22 September 2022.
Copyright ©2022 by the International Astronautical Federation (IAF). All rights reserved.

vapor has been achieved. With a data set covering almost eight Martian years, a composite climatology was created, and details of the hemispherical transport of water has been resolved in unprecedented detail.

Current model predictions estimate a much more uniform vertical profile than what is supported by observations. For higher altitudes, and particularly in polar regions, model and observations agree quite well, while between 5-20 km the synergy suggests the water vapor mixing ratio is lower than the MCD, except for a peculiar local feature at 9-16 km northward of 75°N, where the synergy finds a wet layer which seems to have been lifted from the polar cap edge and transported north. This isolated feature is not reproduced by the model, and could indicate a transport process currently not understood.

At very low altitudes, the spectral synergy suggests there is much more water present than the MCD estimates. The near-surface confinement is thus perhaps stronger, and vertical transport plays a less significant role, than currently thought.

Future work will include more detailed analysis on geographically localized areas, exploring possible differences in longitude related to topography or regolith-atmosphere interactions.

Acknowledgements

This work was funded by CNES, the Agence Nationale de la Recherche (ANR, PRCI, CE31 AAPG2019, MCUBE project), and background for this project was funded by the European Union's Horizon 2020 Programme under grant agreement UPWARDS-633127. The SPICAM instrument was developed by the Laboratoire Atmospheres, Milieux, Observations Spatiales (LATMOS) in Guyancourt, and the Space Research Institute (IKI) in Moscow. The instrument development was funded by the National Centre for Space Studies of France (CNES) and Roscosmos. The PFS experiment has been built at the "Istituto di Astrofisica e Planetologia Spaziali" (IAPS) of the "Istituto Nazionale di Astrofisica" (INAF) and is currently funded by the Italian Space Agency (ASI) in the context of the Italian participation to the ESA's Mars Express Mission (grant ASI/INAF n. 2018-2-HH.0).

References

[1] J.-B. Madeleine, F. Forget, E. Millour, T. Navarro, and A. Spiga, "The influence of radiatively active water ice clouds on the Martian climate: RADIATIVE EFFECT OF MARTIAN CLOUDS," *Geophys. Res. Lett.*, vol. 39, no. 23, p. n/a-n/a, Dec. 2012, doi: 10.1029/2012GL053564.

[2] M. B. McElroy and T. M. Donahue, "Stability of the Martian Atmosphere," *Science*, vol. 177, no. 4053, pp. 986–988, Sep. 1972, doi: 10.1126/science.177.4053.986.

[3] T. Fouchet *et al.*, "Martian water vapor: Mars Express PFS/LW observations," *Icarus*, vol. 190, no. 1, pp. 32–49, Sep. 2007, doi: 10.1016/j.icarus.2007.03.003.

[4] A. A. Pankine and L. K. Tamppari, "Constraints on water vapor vertical distribution at the Phoenix landing site during summer from MGS TES day and night observations," *Icarus*, vol. 252, pp. 107–120, May 2015, doi: 10.1016/j.icarus.2015.01.008.

[5] S. Aoki *et al.*, "Water Vapor Vertical Profiles on Mars in Dust Storms Observed by TGO/NOMAD," *J. Geophys. Res. Planets*, vol. 124, no. 12, pp. 3482–3497, Dec. 2019, doi: 10.1029/2019JE006109.

[6] A. Chicarro, P. Martin, and R. Trautner, "The Mars Express mission: an overview," 2004, vol. 1240, pp. 3–13.

[7] V. Formisano *et al.*, "The Planetary Fourier Spectrometer (PFS) onboard the European Mars Express mission," *Planetary and Space Science*, vol. 53, no. 10, pp. 963–974, Aug. 2005, doi: 10.1016/j.pss.2004.12.006.

[8] M. Giuranna *et al.*, "Calibration of the Planetary Fourier Spectrometer long wavelength channel," *Planetary and Space Science*, vol. 53, no. 10, pp. 993–1007, Aug. 2005, doi: 10.1016/j.pss.2005.02.007.

[9] O. Korablev *et al.*, "SPICAM IR acousto-optic spectrometer experiment on Mars Express," *J. Geophys. Res.*, vol. 111, no. E9, p. E09S03, 2006, doi: 10.1029/2006JE002696.

[10] L. Pan, D. P. Edwards, J. C. Gille, M. W. Smith, and J. R. Drummond, "Satellite remote sensing of tropospheric CO and CH_4: forward model studies of the MOPITT instrument," *Appl. Opt.*, vol. 34, no. 30, p. 6976, Oct. 1995, doi: 10.1364/AO.34.006976.

[11] L. Pan, J. C. Gille, D. P. Edwards, P. L. Bailey, and C. D. Rodgers, "Retrieval of tropospheric carbon monoxide for the MOPITT experiment," *J. Geophys. Res.*, vol. 103, no. D24, pp. 32277–32290, Dec. 1998, doi: 10.1029/98JD01828.

[12] F. Montmessin and S. Ferron, "A spectral synergy method to retrieve martian water vapor column-abundance and vertical distribution applied to Mars Express SPICAM and PFS nadir measurements," *Icarus*, vol. 317, pp. 549–569, Jan. 2019, doi: 10.1016/j.icarus.2018.07.022.

[13] E. W. Knutsen *et al.*, "Water Vapor on Mars: A Refined Climatology and Constraints on the Near-Surface Concentration Enabled by Synergistic Retrievals," *JGR Planets*, vol. 127, no. 5, May 2022, doi: 10.1029/2022JE007252.

[14] F. Forget *et al.*, "Improved general circulation models of the Martian atmosphere from the surface to above 80 km," *J. Geophys. Res.*, vol. 104, no. E10, pp. 24155–24175, Oct. 1999, doi: 10.1029/1999JE001025.

73rd International Astronautical Congress (IAC), Paris, France, 18-22 September 2022.
Copyright ©2022 by the International Astronautical Federation (IAF). All rights reserved.

[15] E. Millour, F. Forget, A. Spiga, M. Vals, V. Zakharov, and L. Montabone, "The Mars climate database (version 5.3)," *Paper pre- sented at the Mars Science Workshop "From Mars Express to ExoMars", held 27-28 February 2018 at ESAC, Spain, id.68.*, Feb. 2018.

[16] L. S. Rothman *et al.*, "The HITRAN2012 molecular spectroscopic database," *Journal of Quantitative Spectroscopy and Radiative Transfer*, vol. 130, pp. 4–50, Nov. 2013, doi: 10.1016/j.jqsrt.2013.07.002.

Appendix C

Article: Galactic cosmic ray modulation at Mars and beyond measured with EDACs on Mars Express and Rosetta

A&A 650, A165 (2021)
https://doi.org/10.1051/0004-6361/202140767
© E. W. Knutsen et al. 2021

Astronomy & Astrophysics

Galactic cosmic ray modulation at Mars and beyond measured with EDACs on Mars Express and Rosetta

E. W. Knutsen[1,2], O. Witasse[2], B. Sanchez-Cano[3], M. Lester[3], R. F. Wimmer-Schweingruber[4], M. Denis[5], J. Godfrey[5], and A. Johnstone[5]

[1] LATMOS/IPSL, UVSQ Université Paris-Saclay, Sorbonne Université, CNRS, Guyancourt, France
e-mail: elise-wright.knutsen@latmos.ipsl.fr
[2] European Space Agency, ESTEC, Noordwijk, The Netherlands
[3] School of Physics and Astronomy, University of Leicester, Leicester, UK
[4] Institute of Experimental and Applied Physics, Christian-Albrechts-University, Kiel, Germany
[5] European Space Agency, ESOC, Darmstadt, Germany

Received 9 March 2021 / Accepted 8 May 2021

ABSTRACT

Galactic cosmic rays (GCRs) are an intrinsic part of the heliospheric radiation environment and an inevitable challenge to long-term space exploration. Here we show solar-cycle-induced GCR modulation at Mars in the period 2005–2020, along with GCR radial gradients, by comparing Mars Express and Rosetta engineering parameters to sunspot number time series. The engineering parameters used are the error detection and correction (EDAC) counters, cumulative counters that are triggered by charged energetic particles that cause memory errors in onboard computers. EDAC data provide a new way of gaining insight into the field of particle transport in the heliosphere; these data also allow us to complement dedicated radiation instrumentation as EDAC software is present on all spacecraft. This dataset was used to capture variations in GCRs in both space and time, yielding the same qualitative information as ground-based neutron monitors. Our analysis of the Mars Express EDAC parameter reveals a strong solar cycle GCR modulation, with a time lag of ~5.5 months. By combining Mars Express with Rosetta data, we calculate a $4.7 \pm 0.8\%$ increase in EDAC count rates per astronomical unit, which we attribute to a radial gradient in GCR fluxes in accordance with established literature. The potential of engineering data for scientific purposes remains mostly unexplored. The results obtained from this work demonstrate, for the first time for heliophysics purposes, the usefulness of the EDAC engineering parameter, the usefulness of data mining, and the utility of keeping missions operational for many years, all of which provide complimentary data to nominal science instruments.

Key words. cosmic rays – Sun: heliosphere – interplanetary medium – methods: data analysis – space vehicles: instruments – radiation: dynamics

1. Introduction

The heliosphere is constantly permeated by charged particles originating from outside our Solar System. The cosmic rays are of Galactic origin and are isotropically incident on the heliopause. Galactic cosmic rays (GCRs), and the related radiation exposure, are seen as some of the main challenges for future long-duration exploration, especially beyond low Earth orbit. The steady flux of energetic particles exposes spacecraft hardware and humans to radiation, the magnitude of which is heavily influenced by several factors: the solar cycle, the presence of an atmosphere, magnetic fields, and relevant spacecraft shielding (Feynman & Gabriel 2000; Schwadron et al. 2014). Investigations of GCR variations over the course of a solar cycle and at multiple locations in the heliosphere provide valuable data for mission planning and for the improvement of our understanding of GCR variations, particle transport, and structures throughout the heliosphere.

Three factors influence the modulation of GCR intensity within the ecliptic plane: time, heliocentric distance, and heliomagnetic longitude. This last factor is outside the scope of this study as longitudinal effects are considered to be small compared to temporal and radial variations (De Simone et al. 2011). As the Sun undergoes its 11-year sunspot cycle and 22-year magnetic polarity cycle, the interplanetary magnetic field (IMF), the sunspot number (SSN), and solar wind parameters vary (Richardson et al. 2001), especially if considering time periods that are long relative to a solar rotation period. As a result, GCRs in the heliosphere are modulated in their inward diffusion by the convection of the expanding solar wind and the particle drift on the IMF, giving rise to a changing GCR flux (Gazis 1996; Modzelewska et al. 2019). Only higher-energy particles are able to penetrate into the heliosphere, causing a depressed GCR intensity within the heliosphere compared to beyond it (Wibberenz 2002). Particles with energies below a few 100 MeV nuc^{-1} are more strongly affected by solar modulation compared to particles with higher energies (Potgieter 2013). The relationship has been observed at and around the Earth since the 1950s (Alania et al. 2014). A network of ground-based neutron monitors (NMs) is used to study the temporal modulation of cosmic rays by measuring the flux of cascading particles produced by cosmic rays colliding with atmospheric atoms (Engel et al. 1992; Usoskin et al. 2017). In addition to exhibiting a temporal anti-correlation with solar activity, the GCR intensity also varies with heliocentric distance, increasing with 3–4% per AU (De Simone et al. 2011; Honig et al. 2019; Modzelewska et al. 2019; Vos & Potgieter 2016). This gradient is highly convolved with the solar and magnetic conditions at any given time and is

Open Access article, published by EDP Sciences, under the terms of the Creative Commons Attribution License (https://creativecommons.org/licenses/by/4.0), which permits unrestricted use, distribution, and reproduction in any medium, provided the original work is properly cited.

generally stronger for negative polarity periods ($A < 0$), when the magnetic field has a radial inward component in the northern hemisphere and the particle drifts are inwards along the current sheet (Burger et al. 2008), and weaker for times with positive polarity (Roussos et al. 2020).

Error detection and correction (EDAC) is a technique used on most spacecraft (Shirvani et al. 2000) to detect and correct errors in memory contents. On spacecraft, this corruption is principally due to bit flips caused by single event upsets (SEUs). An SEU can happen when an energetic particle hits a physical memory cell. If the particle deposits charge in it, a memory error can occur, which in turn can corrupt the data stored on the chips if not corrected. Such errors are caught and corrected by the EDAC algorithm. Once a correction is done, the relevant EDAC counter goes up by 1 (Shirvani et al. 2000).

The relatively steady cumulative EDAC increase is attributed to the continuous presence of cosmic rays as only highly energetic particles are expected to trigger an SEU and a subsequent count increment with the EDAC counter. Normal to elevated solar wind conditions are not expected to have any direct effects on the EDAC counter as such particle energies are much too low. However, solar energetic particle (SEP) events are known to cause irregularities such as jumps in the otherwise relatively monotone counter (see panel A in Fig. 1) and have resulted in various spacecraft failures or the forced initiation of safety modes (Limes et al. 2015). Some previous studies have explored using EDACs for the purpose of monitoring space weather, such as SEP events, with promising results (e.g., Jiggens et al. 2019). Otherwise, the EDAC parameter has been of little interest for scientific purposes thus far.

Understanding the radiation environment within our Solar System is not only key to many fundamental questions about particle transport processes within the heliosphere, it is also imperative when preparing for human and robotic space exploration, especially for human space flight beyond low Earth orbit. The extremely high energies of GCRs and the strict mass constraints in space flight represent a serious challenge (Durante & Cucinotta 2011). Tradeoffs between added weight and shielding can be further optimised if predictive models of GCR variations are improved. At present, dedicated instrumentation on specific spacecraft is used to this end in conjunction with sophisticated modelling efforts. Nevertheless, measurements are sparse, gaps in time coverage are frequent, and the spatial distribution of measurement points is very limited. By utilising EDAC counters in addition to scientific instruments, both spatial and temporal coverage can be greatly improved. EDACs are implemented on all spacecraft, past and present, and the datasets are increasingly becoming more easily available. By combining EDAC counters with tailored scientific payloads, the radiation monitoring within our Solar System can be greatly improved. This study endeavours to showcase the utility of the EDAC counter for long-term observations of GCR variations in our heliosphere, as well as to highlight some remaining challenges. Section 2 describes the datasets used and the data treatment process, Sect. 3 presents the results, and Sect. 4 reflects on the findings before a conclusion is given in Sect. 5.

2. Datasets

On June 2, 2003, Mars Express (MEX) was launched and reached Mars orbit in December of the same year (Chicarro et al. 2004). After an initial commissioning phase, nominal science operations began in mid-January 2004. As of December 2020, MEX was still operational and is expected to remain so until at least the end of 2022. The EDAC counter related to the data management system processor on MEX was utilised for this work (parameter ID NDMW0D0G), which reports increments multiple times per day. Rosetta was launched on March 2, 2004, and started its ten-year journey to reach Comet 67P/Churyumov-Gerasimenko (Glassmeier et al. 2007). The spacecraft was operational and in contact with the ground from launch until June 2011, at which point Rosetta entered a hibernation period that lasted until January 2014. Subsequently, Rosetta reached its target comet in August 2014 and remained operational until September 30, 2016. Out of the 18 available EDACs on Rosetta, the attitude and orbit control system counter (parameter ID NACW0D0A) was chosen for this study because of its continuous temporal coverage (except during hibernation) and its measurement frequency, which was higher and more even than the others.

For the part of this study that involves the solar cycle modulation of GCRs at Mars, the MEX EDAC housekeeping parameter was compared with SSNs for the time period January 1, 2005 – September 17, 2020. The utilised sunspot data were downloaded from the World Data Center SILSO, Royal Observatory of Belgium, Brussels (Center 2020). For the study of GCR variations with heliocentric distance, the EDACs on MEX and Rosetta from January 1, 2005, until the end of the Rosetta mission were utilised. These EDAC parameters are archived in mission databases at the European Space Operations Centre (ESOC) for all ESA spacecraft but are not necessarily publicly available as they are not scientific datasets. For some missions (such as Rosetta and Cluster), these datasets are also available in the online public archives of the European Space Astronomy Centre (ESAC).

To validate how well the EDAC parameter is suited for GCR monitoring, the counter was also compared to ground-based NM data. Neutron monitor data from several ground stations were collected from the Bartol Research Institute's website[1]. The NM provides proxy measurements of GCRs by measuring secondary particles created by their interaction with the atmosphere and inside the NMs (Simpson 2000).

Data processing

The EDAC parameter is a cumulative counter. However, on a few occasions over the course of the MEX and Rosetta missions, the counter was reset to zero. For the purposes of this study, these resets were corrected for by adding the count value immediately before the reset to all subsequent data points. The measuring frequency of the EDACs is quite irregular, varying from data points every 30 s to times with fewer than one measurement per day on average. In order to compare MEX and Rosetta EDACs, the cumulative counter was resampled with a daily frequency, and missing days were filled by linear interpolation. For each EDAC counter, a daily EDAC count rate was calculated by finding the difference in the counter every two weeks and dividing this number by 14 days. Different time bins were tested, and a 14-day average, approximately half a solar rotation period, was found to be the best compromise for removing daily variations and highlighting the solar cycle modulation. By calculating the 14-day daily average, much of the random background fluctuations even out; nevertheless, the rate is still susceptible to short-term variation and extreme space weather events.

Daily variations are caused by random fluctuations in the GCR background, which are largely removed by the previously

[1] http://neutronm.bartol.udel.edu

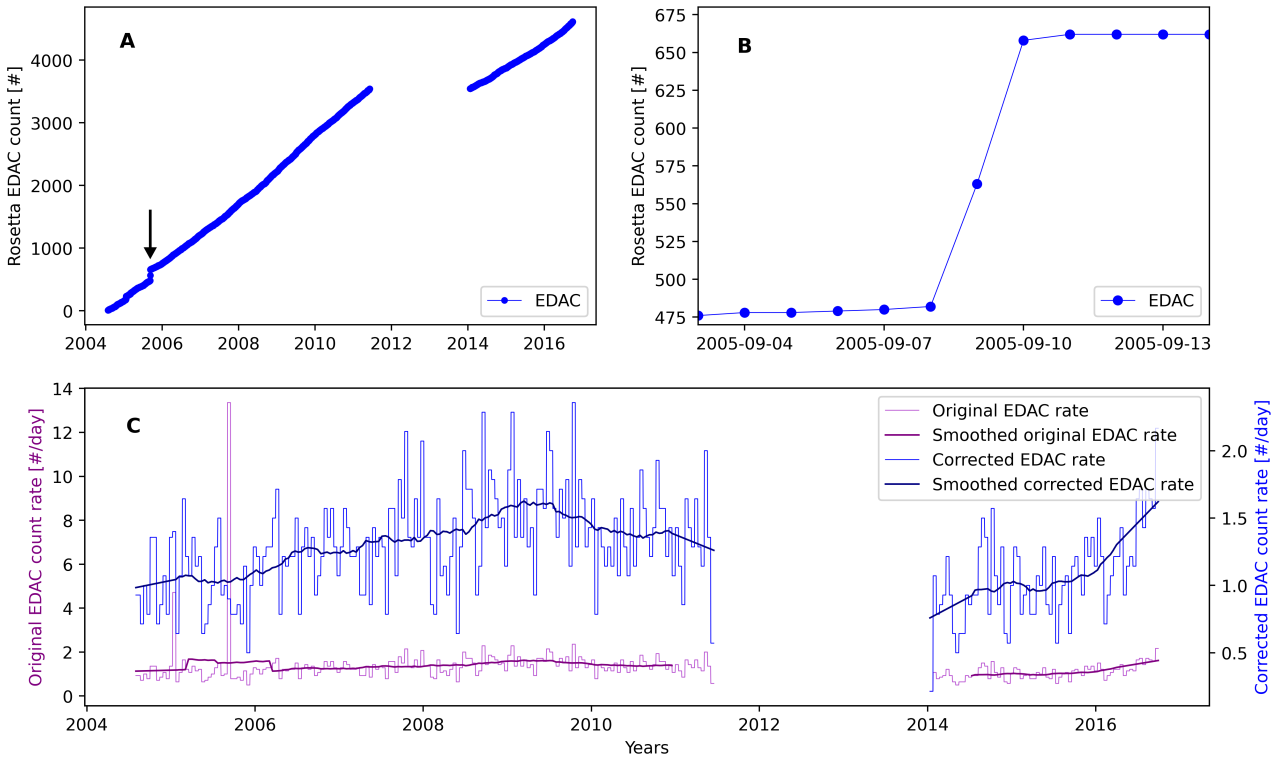

Fig. 1. Illustration of the removal process of SEP-induced disturbances (SPEs drastically influence the EDAC counters, artificially raising the calculated EDAC count rate for several months prior to and after the actual event). *Panel A*: Rosetta EDAC counter from January 2005 to end of mission; the blank space indicates the hibernation period and the black arrow points to an example SEP event. *Panel B*: close-up of the jump indicated in panel A. *Panel C*: smoothed and original EDAC count rates before (purple, left *y*-axis) and after (blue, right *y*-axis) removal of two distinct SEP events. We note that the original and modified count rates are plotted on different *y*-scales to highlight the extreme count rate values obtained if SEP events are not removed from the time series.

described steps, but also by the passing of energetic solar eruptions, such as coronal mass ejections or solar particle events (SPEs), that disturb the regular background of GCRs and cause irregularities in the EDAC counter. Many SPEs are detectable within these datasets; however, for both spacecraft two specific solar eruptions caused such extreme responses in the EDAC counter that it was deemed necessary to do a correction. Figure 1 illustrates this process using Rosetta as an example. In Fig. 1A the complete EDAC dataset from Rosetta is illustrated, including one clearly visible jump caused by an SPE and one smaller jump about 6 months earlier. The largest event is indicated by an arrow. This event is zoomed in on in Fig. 1B, where for two days the EDAC counter increases dramatically, with nearly 100 counts per day, compared to the 1.3 daily average. If no correction is made, the estimated 14-day moving average EDAC count rate around the point in time of the SPE leads to extreme values, as can be seen in the uncorrected EDAC count rates (purple) in Fig. 1C compared to the corrected count rates (blue). However, by replacing the EDAC rate in the 14-day interval around the SPEs with the mean of the rate before and after the event, a more realistic estimate of the GCR background can be obtained. The daily count rate average for the complete dataset before and after the extreme event correction remained very similar (reduced from 1.3 ± 0.88 to 1.25 ± 0.37 counts per day for Rosetta and from 1.39 ± 0.48 to 1.38 ± 0.32 for MEX) and is close to equal for both spacecraft.

To obtain daily count rates that reflect the long-term variations in GCR background radiation, a smoothing routine was applied after the removal of the two SEP anomalies (which occurred in January and September of 2005). A linear Savitzky-Golay low-pass filter with a 365-day window (Savitzky & Golay 1964) was applied to the EDAC count rate time series as well as to the SSN and NM data. In essence, this process smooths the data by removing high-frequency variations in the signal. If the SEP events had not been removed, the EDAC rates during these times would be an order of magnitude larger than the rest and the smoothed rate would be elevated to an artificially high level in the ±6 months surrounding the EDAC jumps, as illustrated in Fig. 1C. This would result in the solar cycle modulation of the cosmic rays appearing negligible. For studies on long timescales, this SEP-induced EDAC response removal is necessary to extract solar-induced modulation from the more intense but short term space weather phenomena. EDAC reactions to SEPs are, however, interesting in themselves. If one wanted to study these transient events, a smoothing routine with a much shorter time span would be applied. Such a study could be of use for the detection and diagnosing of space weather events, and Jiggens et al. (2019) demonstrated the feasibility of this method. Future work will investigate these responses.

3. Results

The datasets discussed here are EDAC counters with daily frequencies in the period from January 1, 2005, to September 17, 2020, for MEX and from January 1, 2005, to September 29, 2016, for Rosetta. Daily SSNs were compared to the MEX EDAC counter for the full duration of the MEX EDAC time period. To demonstrate the capabilities of the EDAC counter as a proxy for GCR variations, Sect. 3.1 compares the EDAC counter

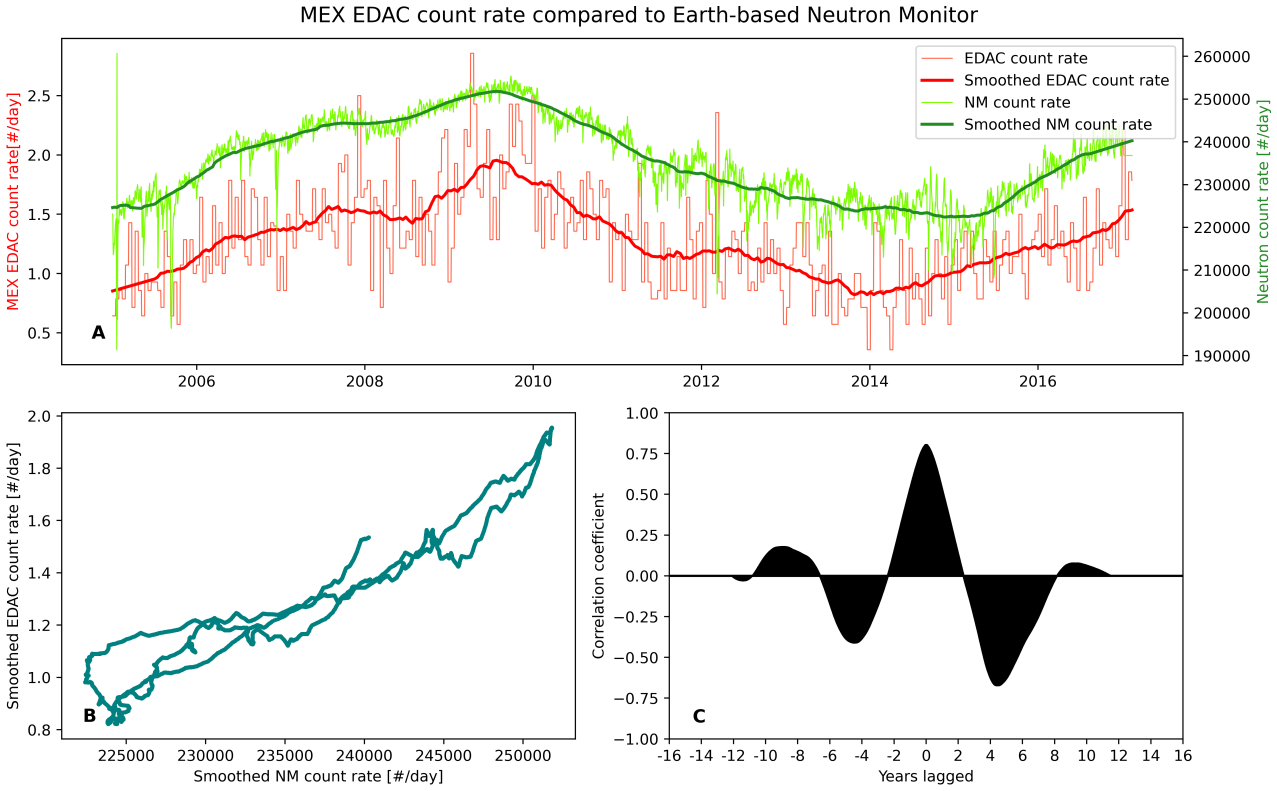

Fig. 2. Demonstration of the similar properties of the space-borne EDAC counter and the ground-based NM. *Panel A*: time series of the MEX EDAC count rate (red) and the McMurdo NM count rate (green). *Panel B*: smoothed EDAC rate as a function of the smoothed NM count rate. *Panel C*: cross-correlation between the two count rates; maximum correlation was found at exactly 0 lag, with a coefficient of 0.8.

with a ground-based NM, another well-established proxy indicator of GCR activity (Usoskin et al. 1998). Section 3.2 focuses on the solar cycle modulation on cosmic rays by comparing SSNs to the MEX EDAC. The Rosetta EDAC is not used for this purpose for two reasons. First, there is an interruption in the data series during the time Rosetta was in hibernation. Second, the orbit of Rosetta took the spacecraft to large heliocentric distances, which makes any direct comparison to Earth questionable. In Sect. 3.3, however, we derive a heliocentric GCR gradient by comparing the EDAC on Rosetta with the one on board MEX.

3.1. EDAC comparison with neutron monitor data

All NM data used in this work were collected from the Bartol research institute, which operates eight NMs; our primary source was measurements from the McMurdo station. Data from Thule and other NM stations were also compared with the EDAC rates (not shown) and yielded nearly identical results. Figure 2A directly compares the calculated MEX EDAC count rates to NM count rates, both raw and smoothed, and demonstrates that the EDAC count rate at Mars exhibits the same long-term temporal behaviour as the count rates registered at the McMurdo station on Earth. Figure 2B qualitatively confirms the linear relationship between the two count rates by plotting the smoothed EDAC count rates as a function of the smoothed NM count rates. To quantify the strength of the correlation between the two counters, a cross-correlation calculation was made, as seen in Fig. 2C. Maximum similarity between the two signals, with a coefficient of 0.8, is obtained at a lag of 0, indicating that if there is a delayed response of GCR modulation at Earth compared to Mars, it is undetectable with this method.

The solar cycle modulation is clearly visible in both the NM time series and the EDAC count rate, demonstrating the ability of the EDAC counter to measure the varying GCR intensity. The comparison between the two smoothed time series shows a strong correlation. Neutron monitor data is a well-established proxy for GCR measurements and makes for a good control set to validate the fitness of EDACs for the purpose of GCR variation studies. However, NMs are Earth-based instruments and are therefore influenced by magnetospheric effects – effectively being shielded from particles of lower energies to which the EDAC is still susceptible – which might cause the higher variability in the EDAC compared to the NM. This could be in part why the correlation coefficient is not even higher.

3.2. Solar cycle modulated GCRs at Mars

Measurements of the radiation environment around planetary bodies other than Earth are relatively sparse. The radiation field at Martian orbit was first measured in 2002 with instruments on Mars Odyssey (Zeitlin et al. 2010) and later with ExoMars Trace Gas Orbiter (Semkova et al. 2018), while measurements on the surface of Mars have been acquired since August 2012 (Hassler et al. 2012, 2014). Here we present cosmic ray variations due to solar cycle modulation in Martian orbit, for the first time recorded by engineering parameters. Figure 3 shows daily EDAC count rates and SSNs along with the smoothed time series of each dataset. All smoothing was done with a Savitzky-Golay low-pass filter, with a 365-day window and linear polynomial fit of the data. Figures 3A and B illustrate the changing rate of EDAC increments at Mars and Rosetta, respectively, as the GCR intensity varies with the solar cycle; the SSNs are shown

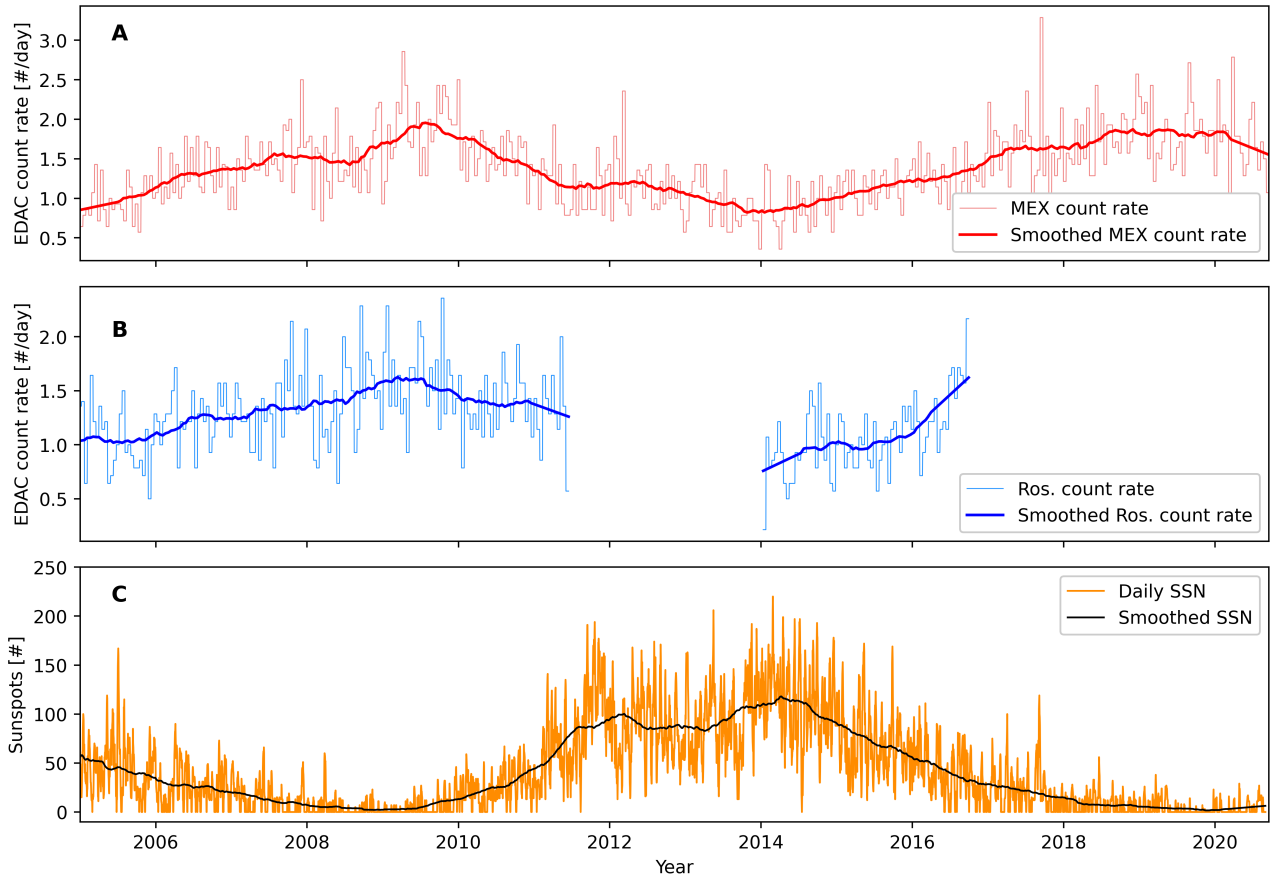

Fig. 3. Comparison between the two EDACs and the relevant solar cycle. *Panel A*: MEX EDAC daily count rates based on 14-day averages, with smoothed count rates. *Panel B*: Rosetta EDAC daily count rates based on 14-day averages, with smoothed count rates. *Panel C*: daily SSNs along with smoothed SSNs.

in Fig. 3C. From visual inspection, a pronounced anti-correlation can be discerned, which is further investigated in Fig. 4.

By inspection of Fig. 3, the GCR intensity minimum can be seen to occur during the time of highest solar activity at the very beginning of 2014, that is, during the polarity reversal phase of the solar magnetic dipole field (Janardhan et al. 2018). Due to the particularly strong warping of the heliospheric current sheet during solar maximum (Prölss 2004), cosmic ray access to the inner heliosphere is diminished during this time, causing the anti-correlation between GCR intensity and SSNs. The Rosetta and MEX EDACs exhibit very similar behaviours overall despite the difference in location. To investigate the EDAC-solar cycle relationship further, the MEX EDAC and SSN are compared in a correlation study in Fig. 4. The Rosetta EDAC is not used for this part of the analysis due to the long hibernation period interrupting the time series.

Figure 4 compares the MEX EDAC counter with solar activity over the course of 15 years. Panel A highlights the cyclic behaviour of the two time series, and the relationship is shown as a scatter plot in panel B with a clear linear relation. The daily EDAC count rate at Mars orbit during solar minimum is twice as high (1.9 counts day^{-1}) as the daily count rate during the months of maximum solar activity (0.8 counts day^{-1}). Panel C quantifies the lag, which is barely discernible by visual inspection in panel A, by cross-correlation analysis. A lag time of 5.5 months is obtained, which corresponds well with results from previous studies of solar modulation around the Earth; Bertucci et al. (2019) obtained a lag time of 6–8 months, and Ross & Chaplin (2019) found the lag to be 2–4 months. The difference between the two might be due to the difference in energies they measured. Interestingly, the origin of the delayed GCR response remains unknown.

3.3. GCR variations with radial distance

The flux of cosmic rays increases when moving away from the Sun, but it is also modulated by the solar activity and the solar cycle. It will also differ depending on the measured energy interval. In this study we utilise EDACs on MEX and on Rosetta as it journeyed outwards in the Solar System. To obtain a GCR gradient independent of the solar cycle modulation, simultaneous EDAC measurements on multiple spacecraft at different locations are required. As the heliocentric distance of each spacecraft is known at all times, one can disentangle the radial effects from the solar cycle modulation effects observed with Rosetta by comparing the EDAC counters on each spacecraft at the same time. Heliocentric longitudinal and latitudinal variations in the GCR flux are considered to be negligible compared to the radial variation in this study (De Simone et al. 2011; Vos & Potgieter 2016; Heber et al. 2009). To compare the MEX and Rosetta EDAC rates as a function of heliocentric distance, we calculated the difference in heliocentric distance between the spacecraft by subtracting the Mars-Sun distance from the Rosetta-Sun distance for each day of Rosetta's lifetime. The result is shown in Fig. 5, where the ratio between the Rosetta and MEX EDAC rates is plotted as a function of the difference between the solar distances

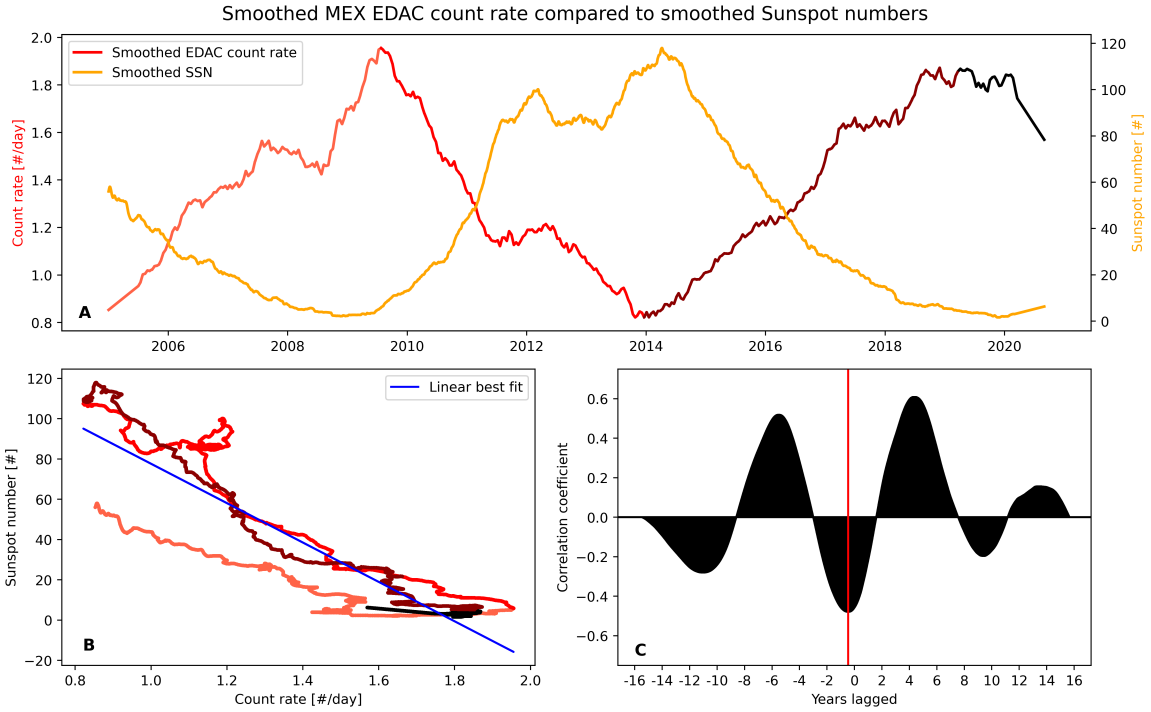

Fig. 4. Long-term solar cycle modulation of GCRs. *Panel A*: smoothed SSNs in orange along with smoothed MEX EDAC count rates in hues of red. The count rate is colour-coded according to the solar cycle phases to highlight the effect of solar modulation. The colours match the colours in panel B. *Panel B*: SSNs as a function of MEX count rates in hues of red as defined in panel A. The blue line is the linear best fit of the data points, indicating the relationship between the two parameters. *Panel C*: cross-correlation between smoothed SSN and MEX count rates, illustrating a cyclic anti-correlated relationship, where the EDAC rate lags 5.5 months behind the solar cycle as measured by the SSN.

of Rosetta and Mars. The x-axis in Fig. 5 is such that $x = 0$ indicates the heliocentric distance to the mean Martian orbit and any points at negative values translate to Rosetta being closer to the Sun than Mars.

A linear function was fitted to the data points where $x \geq 0$, with an obtained slope of 5.3%, meaning the EDAC count rate, and subsequently the GCR flux, increased at an average rate of 5.3% AU^{-1} for this dataset. If all measurements inside Mars orbit are also included, the rate becomes 3.9% AU^{-1}. In previous works (Honig et al. 2019; McDonald et al. 1997; Webber & Lockwood 1991), it has been customary to take the natural logarithm of the count rate ratio when calculating a radial gradient of GCR fluxes. By doing this for the two cases – all measurements and only measurements at and beyond Mars – slopes of 4.1% and 5.4% are obtained, respectively, which are similar to the values found in previous studies. The mean and median of these four slopes both round up to 4.7, and thus our final estimate of the GCR radial gradient becomes $4.7 \pm 0.8\%$.

As Rosetta's journey included a hibernation period, there are two additional end points in the time series, as indicated by the diamonds in Fig. 5. Immediately after the launch of Rosetta and after waking up at the end of hibernation, the relationship between the two EDAC rates differ from the remaining 14 years of data. This could be related to shortcomings of the smoothing algorithm at the edges or was possibly caused by cometary shielding for 2014, as discussed in Honig et al. (2019).

4. Discussion

In situ measurements of the radiation environment around Earth have been conducted for almost six decades, with Mariner 2 becoming the first satellite to travel from Earth to another planet (Neugebauer & Snyder 1962). Since then, specialised radiation instrumentation has flown on multiple spacecraft, providing detailed data of the solar modulation of GCR activity at and around the near-Earth environment. Zeitlin et al. (2010) recorded, for the first time, solar modulation of GCR activity in Martian orbit from 2004 to 2007. Here we have confirmed, and expanded upon, those results. Several SPEs were also detected by Zeitlin et al. (2010), and complimenting those measurements (and others) with EDAC data will be the focus of future work.

Recently, the radiation dose rate was measured in Martian orbit with the FREND (Fine Resolution Epithermal Neutron Detector) instrument during the insertion phase of the ExoMars Trace Gas Orbiter. With this instrument, Semkova et al. (2018) observed changes in the GCR-related dose rate in accordance with the declining phase of the solar cycle. The GCR radiation dose has also been measured at the Martian surface by the MSL-RAD instrument, where the solar cycle modulation was observed (Berger et al. 2020). The dose rate was found to be fairly similar to that on the Moon, although the presence of the Martian atmosphere shields the surface from lower-energy GCRs, resulting in a reduced modulation effect.

In this study we measure the solar cycle modulation of GCRs at Martian orbit and thus avoid the low-energy particle filtration effect of the Martian atmosphere. On the other hand, the spacecraft itself shields against the low-energy part of the GCR spectrum. Quantifying this effect is complicated and requires detailed knowledge of the spacecraft (geometry and components) and was not considered for this study.

As previously mentioned, longitudinal effects were assumed to be negligible (De Simone et al. 2011) for this work. In addition to longitudinal effects, Rosetta's trajectory does not at all times lie within the ecliptic plane (±8° latitude; Honig et al. 2019),

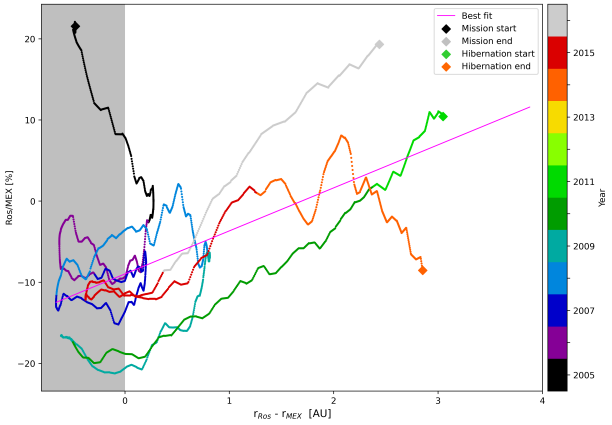

Fig. 5. Ratio of smoothed Rosetta and MEX EDAC count rates as a function of the difference in solar distance. The magenta line indicates the linear best fit of the data, with an obtained slope corresponding to a 5.3% AU^{-1} increase in GCR intensity. Each colour indicates a full terrestrial year, except for 2016 (grey), which ends on September 29. The diamonds mark the start and end points of the Rosetta EDAC time series. The lightest shades of green and yellow are not present in the plot as they represent times when Rosetta was in hibernation. The grey shaded area for $x < 0$ indicates when Rosetta was at or within mean Martian orbit. EDAC data points within this region were not included in the best-fit procedure illustrated in the figure.

and thus this adds to the already varying heliocentric latitude caused by the inclination of the Sun's rotational axis. MEX data was only used after orbit insertion around Mars, so radial and latitudinal effects are reduced to those caused by Mars' elliptical orbit and the inclination of the Sun's rotational axis. Latitudinal gradients, however, are known to be small (Heber et al. 2009). All heliocentric longitudes are covered. Thus, the effects these parameters might have on the EDAC counter are considered to be very small compared to solar cycle modulation and heliocentric distance effects.

Another aspect to consider is planetary shielding. Over the course of the MESSENGER mission, a neutron spectrometer was used for long-term study of GCR variations in the inner heliosphere (Lawrence et al. 2016). When the satellite was within a certain range of Mercury, the GCR intensity was observed to drop since the GCRs incident on the solid angle of the planet were intercepted and did not reach the spacecraft. Lawrence et al. (2016) therefore set a cautionary limit of 8000 km and abstained from using data when the spacecraft was within this range of the planet. MEX is in a highly elliptical quasi-polar orbit around Mars, with periapsis at 330 km, apoapsis at 10 500 km, and a period of 7 hours. More than 5 of those 7 hours are spent at altitudes higher than 5000 km, at which distance Mars subtends 4% of the total sky. Planetary shielding was therefore assumed to have a marginal effect on the MEX EDAC counter even when data from the full orbit were utilised and has therefore not been taken into account for either of the EDAC datasets considered here.

The solar cycle modulation of GCRs has been under intense study for decades (e.g., Forbush 1958; Usoskin et al. 1998; Bertucci et al. 2019), and though the existence of a time lag of GCR intensity relative to solar activity is well known, its origins remain elusive. In general, the lag is caused by the vast size of the heliosphere and the diffusive and drifting nature of the cosmic rays (Dorman & Dorman 1967), though the details of the process are unexplained. The lag is larger for odd numbered solar cycles than for even numbered ones (Usoskin et al. 1998), which is related to the polarity of the 22-year magnetic cycle of the Sun. This study spans almost 1.5 cycles, including solar cycle 24 in its entirety. The polarity reversal normally occurs near solar maximum for each cycle, with one hemisphere flipping about 1 year before the other (Pishkalo 2019). The lag obtained here of 5.5 months during an even numbered cycle is smaller than the lag found by Bertucci et al. (2019) for the period 2008–2012, which follows conventional predictions, but slightly larger than what Ross & Chaplin (2019) found for the same cycle (2–4 months).

The EDAC counter increase with heliocentric distance obtained by comparing the EDACs on MEX and Rosetta indicates an average GCR gradient of $4.7 \pm 0.8\%$ AU^{-1} between 2005 and 2020. The uncertainty stems from the calculation method used (simple count rate ratios or natural logarithm of said ratios) and whether or not data points Sunwards of the mean Mars orbit are included. This result confirms what dedicated radiation instrumentation on other spacecraft has previously measured. When Rosetta was at heliocentric distances equal to or smaller than mean Mars orbit, the spacecraft conducted several maneuvers and multiple fly-bys. Planetary shielding effects and the passing through Earth's Van Allen radiation belts on multiple occasions led us to differentiate between data points within and outside Martian orbit when Rosetta's trajectory was less convoluted. If all data points are included, the GCR gradient drops to 3.8% AU^{-1}.

By comparing three years of data from the Kiel Electron Telescope on the Ulysses spacecraft and the PAMELA (Payload for Antimatter Matter Exploration and Light-nuclei Astrophysics) instrument, De Simone et al. (2011) found a radial gradient of 2.7% per AU for particles in the range 1.6–1.8 GV during the solar cycle minimum between cycles 23 and 24. For the same time period and using the same instruments, Vos & Potgieter (2016) found a radial gradient of 4.25% AU^{-1}. Gradients are generally stronger during the negative polarity phase when $A < 0$ and the magnetic field has a radial inward component north of the current sheet, in this case during 2005–2014, and weaker for times with positive polarity. The recent work of Roussos et al. (2020) found similar values with Cassini data, with a peak gradient of 4% AU^{-1} and an average gradient of 3.5% AU^{-1} for $A < 0$ in the period 2006–2014. Our measurements span multiple polarity periods, and the gradient found here should therefore be considered a long-term average. Moreover, the rigidity of those particles responsible for EDAC counts is currently not well understood. A quantitative comparison with other methods is thus still elusive. Nevertheless, we expect our results to be robust if we compare between EDAC counters on other spacecraft as long as these counters provide comparable amounts of shielding for the spacecraft memories.

Honig et al. (2019) found a GCR gradient anomaly during the comet-approach phase of the Rosetta mission, when the GCR count rate dropped by 8% and thus exhibited a negative relationship with heliocentric distance. Our results also indicate that the GCR flux was different before and after hibernation. This effect was tentatively attributed to cometary shielding by Honig et al. (2019), although the phenomenon requires further investigation. In 2005, Rosetta was still for the most part within Martian orbit, and the closest approach fly-by of Earth was also during this period, which might have caused the elevated EDAC rate compared to MEX at the same time (see Fig. 3).

In this analysis, EDAC counters from two spacecraft were utilised to infer the solar cycle modulation of GCRs in the heliosphere and the increase in GCR intensity with heliocentric distance. By including EDAC counters from additional spacecraft, the spatial and temporal coverage would increase drastically. The

main caveat to using EDAC counters individually to infer GCR variations is the uncertain quantification of the energies or rigidities of the particles that are responsible for errors in the memory chips. The GCR spectrum covers a broad range of energies, and not all will be sufficient to penetrate the spacecraft and result in an EDAC increment. To understand this, knowledge of the 3D structure of the spacecraft is required. Since the solar effects on GCR variation is rigidity dependent, it is imperative to compare datasets with equal rigidities (De Simone et al. 2011). The particle energies that cause SEUs in one spacecraft might not be the same in another as it will depend on the location of the onboard computer and the shielding effect of the rest of the spacecraft. The spacecraft chosen for this study, Rosetta and MEX, are largely similar, designed with a large degree of commonality in several subsystems and with comparable solid-state mass memory units (Ferri et al. 2004), which gives us confidence in the results reported here. The potential scientific return from EDAC counters is irrefutable, and the benefits from supplementing the counters with science instruments are numerous.

5. Conclusion

Ground-based NMs on Earth have been utilised for decades to monitor the near-Earth GCR environment. Here we demonstrate that the EDAC engineering parameter can provide similar information from a multitude of locations in the Solar System. EDAC counters can be used to monitor the time evolution and 3D structure of the GCRs in the heliosphere.

We have shown that, as expected, the GCR variations at Mars follow a solar cycle modulation very similar to that observed at Earth, with twice as high daily count rates during solar minimum compared to solar maximum, for those energies that the EDAC counter is sensitive to. The GCR-induced EDAC signal was found to lag SSNs by approximately 5.5 months, comparable to previous results (Bertucci et al. 2019; Ross & Chaplin 2019).

By comparing the Rosetta and MEX EDAC counters, we found that EDAC count rates increased by $4.7 \pm 0.8\%$ per AU, which is in good agreement with previous studies of Rosetta radiation monitor data (Honig et al. 2019). This behaviour is expected as the flux of GCRs increases with increasing heliocentric distance (e.g., Ferreira & Potgieter 2004).

This work demonstrates the ability of EDAC counters and shows that they are well suited for GCR studies and can be used to identify long-term GCR variations in the heliosphere. Because all spacecraft are equipped with EDAC counters irrespective of their scientific objectives, EDAC data can provide information about the GCR flux at multiple locations in the heliosphere. In addition, shorter-term GCR variations in the form of Forbush decreases, as measured by EDACs, may inform on the propagation of large solar transient events (e.g., Sánchez-Cano et al. 2017; Witasse et al. 2017), particularly in those instances when there is no other instrumentation available to measure them. Future work will need to quantify the effect of different shielding geometries on the EDAC count rate, and methods for cross-calibration between different spacecraft will be needed to improve the quality of EDAC data for scientific studies. Nevertheless, the opportunity offered by such multi-point measurements to improve the understanding of particle transport processes in the heliosphere should be followed up on.

Acknowledgements. E.W.K. thanks the internship program at ESA-ESTEC for the opportunity and financial support to carry out this project. E.W.K. has changed institutions while finishing this work, and is now at LATMOS/CNRS. B.S.-C. and M.L. acknowledge support thought UK-STFC grant ST/N000749/1. B.S.-C. gratefully acknowledges ESA-ESTEC Faculty support. MEX EDAC data was provided by the ESOC Mars Express flight control team and is available upon request (Olivier.Witasse@esa.int). Rosetta data is available in the ESA planetary science archive. Neutron monitors of the Bartol Research Institute are supported by the National Science Foundation. We thank the Royal Observatory of Belgium and the World Data Center SILSO for providing freely accessible Sunspot number data.

References

Alania, M. V., Modzelewska, R., & Wawrzynczak, A. 2014, J. Geophys. Res.: Space Phys., 119, 4164
Berger, T., Matthiä, D., Burmeister, S., et al. 2020, J. Space Weather Space Clim., 10, 34
Bertucci, B., Fiandrini, E., Khiali, B., & Tomassetti, N. 2019, in Proceedings of Science, Madison, WI, USA, PoS(ICRC2019)1162
Burger, R. A., Kruger, T. P. J., Hitge, M., & Engelbrecht, N. E. 2008, ApJ, 674, 511
Center, S. W. D. 2020, International Sunspot Number Monthly Bulletin and online catalogue
Chicarro, A., Martin, P., & Trautner, R. 2004, The Mars Express Mission: an Overview, 3
De Simone, N., Di Felice, V., Gieseler, J., et al. 2011, Astrophys. Space Sci. Trans., 7, 425
Dorman, I. V., & Dorman, L. I. 1967, J. Geophys. Res., 72, 1513
Durante, M., & Cucinotta, F. A. 2011, Rev. Mod. Phys., 83, 1245
Engel, J., Gaisser, T. K., Lipari, P., & Stanev, T. 1992, Phys. Rev. D, 46, 5013
Ferreira, S. E. S., & Potgieter, M. S. 2004, ApJ, 603, 744
Ferri, P., Denis, M., Accomazzo, A., & Warhaut, M. 2004, Space OPS 2004 Conference (Montreal, Quebec, Canada: American Institute of Aeronautics and Astronautics)
Feynman, J., & Gabriel, S. B. 2000, J. Geophys. Res.: Space Phys., 105, 10543
Forbush, S. 1958, J. Geophys. Res., 63, 651
Gazis, P. R. 1996, Rev. Geophys., 34, 379
Glassmeier, K.-H., Boehnhardt, H., Koschny, D., Kührt, E., & Richter, I. 2007, Space Sci. Rev., 128, 1
Hassler, D. M., Zeitlin, C., Wimmer-Schweingruber, R. F., et al. 2012, Space Sci. Rev., 170, 503
Hassler, D. M., Zeitlin, C., Wimmer-Schweingruber, R. F., et al. 2014, Science, 343, 1244797
Heber, B., Kopp, A., Gieseler, J., et al. 2009, ApJ, 699, 1956
Honig, T., Witasse, O., Evans, H., et al. 2019, Ann. Geophys., 37, 903
Janardhan, P., Fujiki, K., Ingale, M., Bisoi, S. K., & Rout, D. 2018, A&A, 618, A148
Jiggens, P., Clavie, C., Evans, H., et al. 2019, Space Weather, 17, 99
Lawrence, D. J., Peplowski, P. N., Feldman, W. C., Schwadron, N. A., & Spence, H. E. 2016, J. Geophys. Res.: Space Phys., 121, 7398
Limes, G., Christa, S., & Pires, C. 2015, EDAC Events During the LADEE Mission (IEEE), 1
McDonald, F. B., Ferrando, P., Heber, B., et al. 1997, J. Geophys. Res.: Space Phys., 102, 4643
Modzelewska, R., Iskra, K., Wozniak, W., Siluszyk, M., & Alania, M. V. 2019, Sol. Phys., 294, 148
Neugebauer, M., & Snyder, C. W. 1962, Science, 138, 1095
Pishkalo, M. I. 2019, Sol. Phys., 294, 137
Potgieter, M. 2013, Liv. Rev. Sol. Phys., 10, 3
Prölss, G. W. 2004, Physics of the Earth's Space Environment (Berlin, Heidelberg: Springer, Berlin Heidelberg)
Richardson, J. D., Wang, C., & Paularena, K. I. 2001, Adv. Space Res., 27, 471
Ross, E., & Chaplin, W. J. 2019, Sol. Phys., 294, 8
Roussos, E., Dialynas, K., Krupp, N., et al. 2020, ApJ, 904, 165
Sánchez-Cano, B., Hall, B. E. S., Lester, M., et al. 2017, J. Geophys. Res.: Space Phys., 122, 6611
Savitzky, A., & Golay, M. 1964, J. Anal. Chem., 36, 1627
Schwadron, N. A., Blake, J. B., Case, A. W., et al. 2014, Space Weather, 12, 622
Semkova, J., Koleva, R., Benghin, V., et al. 2018, Icarus, 303, 53
Shirvani, P. P., Saxena, N. R., & McCluskey, E. J. 2000, IEEE Trans. Reliab., 49, 273
Simpson, J. A. 2000, Space Sci. Rev., 93, 11
Usoskin, I. G., Kananen, H., Mursula, K., Tanskanen, P., & Kovaltsov, G. A. 1998, J. Geophys. Res.: Space Phys., 103, 9567
Usoskin, I. G., Gil, A., Kovaltsov, G. A., Mishev, A. L., & Mikhailov, V. V. 2017, J. Geophys. Res.: Space Phys., 122, 3875
Vos, E. E., & Potgieter, M. S. 2016, Sol. Phys., 291, 2181
Webber, W., & Lockwood, J. 1991, J. Geophys. Res., 96, 15,899
Wibberenz, G. 2002, J. Geophys. Res., 107, 1353
Witasse, O., Sánchez-Cano, B., Mays, M. L., et al. 2017, J. Geophys. Res.: Space Phys., 122, 7865
Zeitlin, C., Boynton, W., Mitrofanov, I., et al. 2010, Space Weather, 8, S00E06

Bibliography

Acuña, M. H., Connerney, J. E. P., F., N., Ness, Lin, R. P., Mitchell, D., Carlson, C. W., McFadden, J., Anderson, K. A., Rème, H., Mazelle, C., Vignes, D., Wasilewski, P., and Cloutier, P. (1999). Global Distribution of Crustal Magnetization Discovered by the Mars Global Surveyor MAG/ER Experiment. *Science*, 284(5415):790–793.

Alania, M. V., Modzelewska, R., and Wawrzynczak, A. (2014). Peculiarities of cosmic ray modulation in the solar minimum 23/24: COSMIC RAY MODULATION IN MINIMUM 23/24. *Journal of Geophysical Research: Space Physics*, 119(6):4164–4174.

Albee, A. L., Palluconi, F. D., and Arvidson, R. E. (1998). Mars Global Surveyor Mission: Overview and Status. *Science*, 279(5357):1671–1672.

Alday, J., Trokhimovskiy, A., Irwin, P. G. J., Wilson, C. F., Montmessin, F., Lefévre, F., Fedorova, A. A., Belyaev, D. A., Olsen, K. S., Korablev, O., Vals, M., Rossi, L., Baggio, L., Bertaux, J.-L., Patrakeev, A., and Shakun, A. (2021). Isotopic fractionation of water and its photolytic products in the atmosphere of Mars. *Nature Astronomy*, 5(9):943–950.

Alfvén, H. (1942). Existence of electromagnetic-hydrodynamic waves. *Nature*, 150(3805):405–406.

Andrews-Hanna, J. C., Zuber, M. T., and Banerdt, W. B. (2008). The Borealis basin and the origin of the martian crustal dichotomy. *Nature*, 453(7199):1212–1215.

Aoki, S., Richter, M., DeWitt, C., Boogert, A., Encrenaz, T., Sagawa, H., Nakagawa, H., Vandaele, A. C., Giuranna, M., Greathouse, T. K., Fouchet, T., Geminale, A., Sindoni, G., McKelvey, M., Case, M., and Kasaba, Y. (2018). Stringent upper limit of CH4 on Mars based on SOFIA/EXES observations. *Astronomy & Astrophysics*, 610:A78.

Aoki, S., Vandaele, A. C., Daerden, F., Villanueva, G. L., Liuzzi, G., Clancy, R. T., Lopez-Valverde, M. A., Brines, A., Thomas, I. R., Trompet, L., Erwin, J. T., Neary, L., Robert, S., Piccialli, A., Holmes, J. A., Patel, M. R., Yoshida, N., Whiteway, J., Smith, M. D., Ristic, B., Bellucci, G., Lopez-Moreno, J. J., and Fedorova, A. A. (2022). Global Vertical Distribution of Water Vapor on Mars: Results From 3.5 Years of ExoMars-TGO/NOMAD Science Operations. *Journal of Geophysical Research: Planets*, 127(9).

Aoki, S., Vandaele, A. C., Daerden, F., Villanueva, G. L., Liuzzi, G., Thomas, I. R., Erwin, J. T., Trompet, L., Robert, S., Neary, L., Viscardy, S., Clancy, R. T., Smith, M. D., Lopez-Valverde, M. A., Hill, B., Ristic, B., Patel, M. R., Bellucci, G., Lopez-Moreno, J., and the NOMAD team (2019). Water Vapor Vertical Profiles on Mars in Dust Storms Observed by TGO/NOMAD. *Journal of Geophysical Research: Planets*, 124(12):3482–3497.

Appéré, T., Schmitt, B., Langevin, Y., Douté, S., Pommerol, A., Forget, F., Spiga, A., Gondet, B., and Bibring, J.-P. (2011). Winter and spring evolution of northern seasonal deposits on Mars from OMEGA on Mars Express. *Journal of Geophysical Research*, 116(E5):E05001.

Audouard, J., Poulet, F., Vincendon, M., Milliken, R. E., Jouglet, D., Bibring, J.-P., Gondet, B., and Langevin, Y. (2014). Water in the Martian regolith from OMEGA/Mars Express: Mars 3 μm absorption and water mobility. *Journal of Geophysical Research: Planets*, 119(8):1969–1989.

Barth, C., Stewart, A., Hord, C., and Lane, A. (1972). Mariner 9 ultraviolet spectrometer experiment: Mars airglow spectroscopy and variations in Lyman alpha. *Icarus*, 17(2):457–468.

Barth, C. A. (1974). The Atmosphere of Mars. *Annual Review of Earth and Planetary Sciences*, 2(1):333–367.

Barth, C. A., Hord, C. W., Pearce, J. B., Kelly, K. K., Anderson, G. P., and Stewart, A. I. (1971). Mariner 6 and 7 Ultraviolet Spectrometer Experiment: Upper atmosphere data. *Journal of Geophysical Research*, 76(10):2213–2227.

Bell, J. F., Maki, J. N., Mehall, G. L., Ravine, M. A., Caplinger, M. A., Bailey, Z. J., Brylow, S., Schaffner, J. A., Kinch, K. M., Madsen, M. B., Winhold, A., Hayes, A. G., Corlies, P., Tate, C., Barrington, M., Cisneros, E., Jensen, E., Paris, K., Crawford, K., Rojas, C., Mehall, L., Joseph, J., Proton, J. B., Cluff, N., Deen, R. G., Betts, B., Cloutis, E., Coates, A. J., Colaprete, A., Edgett, K. S., Ehlmann, B. L., Fagents, S., Grotzinger, J. P., Hardgrove, C., Herkenhoff, K. E., Horgan, B., Jaumann, R., Johnson, J. R., Lemmon, M., Paar, G., Caballo-Perucha, M., Gupta, S., Traxler, C., Preusker, F., Rice, M. S., Robinson, M. S., Schmitz, N., Sullivan, R., and Wolff, M. J. (2021). The Mars 2020 Perseverance Rover Mast Camera Zoom (Mastcam-Z) Multispectral, Stereoscopic Imaging Investigation. *Space Science Reviews*, 217(1):24.

Belyaev, D. A., Fedorova, A. A., Trokhimovskiy, A., Alday, J., Montmessin, F., Korablev, O. I., Lefèvre, F., Patrakeev, A. S., Olsen, K. S., and Shakun, A. V. (2021). Revealing a High Water Abundance in the Upper Mesosphere of Mars With ACS Onboard TGO. *Geophysical Research Letters*, 48(10):e2021GL093411.

Berger, J. A., Schmidt, M. E., Gellert, R., Campbell, J. L., King, P. L., Flemming, R. L., Ming, D. W., Clark, B. C., Pradler, I., VanBommel, S. J. V., Minitti, M. E., Fairén, A. G., Boyd, N. I., Thompson, L. M., Perrett, G. M., Elliott, B. E., and Desouza, E. (2016). A global Mars dust composition refined by the Alpha-Particle X-ray Spectrometer in Gale Crater. *Geophysical Research Letters*, 43(1):67–75.

Bertaux, J.-L., Korablev, O., Perrier, S., Quémerais, E., Montmessin, F., Leblanc, F., Lebonnois, S., Rannou, P., Lefèvre, F., Forget, F., Fedorova, A., Dimarellis, E., Reberac, A., Fonteyn, D., Chaufray, J. Y., and Guibert, S. (2006). SPICAM on Mars Express: Observing modes and overview of UV spectrometer data and scientific results. *Journal of Geophysical Research*, 111(E10):E10S90.

Bertaux, J.-L., Leblanc, F., Witasse, O., Quemerais, E., Lilensten, J., Stern, S. A., Sandel, B., and Korablev, O. (2005). Discovery of an aurora on Mars. *Nature*, 435(7043):790–794.

Bertucci, B., Fiandrini, E., Khiali, B., and Tomassetti, N. (2019). Time lag in cosmic-ray modulation and global properties of the Solar Cycle. In *Proceedings of Science*, Madison, WI, U.S.A. arXiv: 1908.01598.

Bhattacharyya, D., Clarke, J. T., Bertaux, J.-L., Chaufray, J.-Y., and Mayyasi, M. (2015). A strong seasonal dependence in the Martian hydrogen exosphere: SEASONAL DEPENDENCE OF MARTIAN H ESCAPE. *Geophysical Research Letters*, 42(20):8678–8685.

Bibring, J.-P., Langevin, Y., Mustard, J. F., Poulet, F., Arvidson, R., Gendrin, A., Gondet, B., Mangold, N., Pinet, P., Forget, F., Berthé, M., Bibring, J.-P., Gendrin, A., Gomez, C., Gondet, B., Jouglet, D., Poulet, F., Soufflot, A., Vincendon, M., Combes, M., Drossart, P., Encrenaz, T., Fouchet, T., Merchiorri, R., Belluci, G., Altieri, F., Formisano, V., Capaccioni, F., Cerroni, P., Coradini, A., Fonti, S., Korablev, O., Kottsov, V., Ignatiev, N., Moroz, V., Titov, D., Zasova, L., Loiseau, D., Mangold, N., Pinet, P., Douté, S., Schmitt, B., Sotin, C., Hauber, E., Hoffmann, H., Jaumann, R., Keller, U., Arvidson, R., Mustard, J. F., Duxbury, T., Forget, F., and Neukum, G. (2006). Global Mineralogical and Aqueous Mars History Derived from OMEGA/Mars Express Data. *Science*, 312(5772):400–404.

Bibring, J.-P., Langevin, Y., Poulet, F., Gendrin, A., Gondet, B., Berthé, M., Soufflot, A., Drossart, P., Combes, M., Bellucci, G., Moroz, V., Mangold, N., Schmitt, B., and Omega Team, T. (2004). Perennial water ice identified in the south polar cap of Mars. *Nature*, 428(6983):627–630.

Blamont, J. (2014). A roadmap to cave dwelling on the Moon and Mars. *Advances in Space Research*, 54(10):2140–2149.

Blasi, P. (2013). The origin of galactic cosmic rays. *The Astronomy and Astrophysics Review*, 21(1):70.

Bouche, J., Coheur, P., Giuranna, M., Wolkenberg, P., Nardi, L., Amoroso, M., Vandaele, A. C., Daerden, F., Neary, L., and Bauduin, S. (2021). Seasonal and Spatial Variability of Carbon Monoxide (CO) in the Martian Atmosphere From PFS/MEX Observations. *Journal of Geophysical Research: Planets*, 126(2).

Braude, A. S., Montmessin, F., Olsen, K. S., Trokhimovskiy, A., Korablev, O. I., Lefèvre, F., Fedorova, A. A., Alday, J., Baggio, L., Irbah, A., Lacombe, G., Forget, F., Millour, E., Wilson, C. F., Patrakeev, A., and Shakun, A. (2022). No detection of SO $_2$, H $_2$ S, or OCS in the atmosphere of Mars from the first two Martian years of observations from TGO/ACS. *Astronomy & Astrophysics*, 658:A86.

Bristow, T. F., Grotzinger, J. P., Rampe, E. B., Cuadros, J., Chipera, S. J., Downs, G. W., Fedo, C. M., Frydenvang, J., McAdam, A. C., Morris, R. V., Achilles, C. N., Blake, D. F., Castle, N., Craig, P., Des Marais, D. J., Downs, R. T., Hazen, R. M., Ming, D. W., Morrison, S. M., Thorpe, M. T., Treiman, A. H., Tu, V., Vaniman, D. T., Yen, A. S., Gellert, R., Mahaffy, P. R., Wiens, R. C., Bryk, A. B., Bennett, K. A., Fox, V. K., Millken, R. E., Fraeman, A. A., and Vasavada, A. R. (2021). Brine-driven destruction of clay minerals in Gale crater, Mars. *Science*, 373(6551):198–204.

Calvin, W., Cantor, B., and James, P. (2017). Interannual and seasonal changes in the south seasonal polar cap of Mars: Observations from MY 28-31 using MARCI. *Icarus*, 292:144–153.

Cane, H. V., McGuire, R. E., and von Rosenvinge, T. T. (1986). Two classes of solar energetic particle events associated with impulsive and long-duration soft X-ray flares. *The Astrophysical Journal*, 301:448.

Carr, M. H. and Head, J. W. (2010). Geologic history of Mars. *Earth and Planetary Science Letters*, 294(3-4):185–203.

Carrington, R. C. (1859). Description of a Singular Appearance seen in the Sun on September 1, 1859. *Monthly Notices of the Royal Astronomical Society*, 20:13–15. ADS Bibcode: 1859MNRAS..20...13C.

Chaffin, M., Deighan, J., Schneider, N., and Stewart, A. (2017). Elevated atmospheric escape of atomic hydrogen from Mars induced by high-altitude water. *Nature Geoscience*, 10(3):174–178.

Chaffin, M. S., Chaufray, J., Stewart, I., Montmessin, F., Schneider, N. M., and Bertaux, J. (2014). Unexpected variability of Martian hydrogen escape. *Geophysical Research Letters*, 41(2):314–320.

Chapman, C. R. (1974). Cratering on Mars. II. implications for future cratering studies from Mariner 4 reanalysis. *Icarus*, 22(3):292–300.

Chicarro, A., Martin, P., and Trautner, R. (2004). The Mars Express mission: an overview. *Mars Express: the scientific payload*, 1240:3–13.

Christensen, P. R., Bandfield, J. L., Clark, R. N., Edgett, K. S., Hamilton, V. E., Hoefen, T., Kieffer, H. H., Kuzmin, R. O., Lane, M. D., Malin, M. C., Morris, R. V., Pearl, J. C., Pearson, R., Roush, T. L., Ruff, S. W., and Smith, M. D. (2000). Detection of crystalline hematite mineralization on Mars by the Thermal Emission Spectrometer: Evidence for near-surface water. *Journal of Geophysical Research: Planets*, 105(E4):9623–9642.

Christensen, P. R., Bandfield, J. L., Hamilton, V. E., Ruff, S. W., Kieffer, H. H., Titus, T. N., Malin, M. C., Morris, R. V., Lane, M. D., Clark, R. L., Jakosky, B. M., Mellon, M. T., Pearl, J. C., Conrath, B. J., Smith, M. D., Clancy, R. T., Kuzmin, R. O., Roush, T., Mehall, G. L., Gorelick, N., Bender, K., Murray, K., Dason, S., Greene, E., Silverman, S., and Greenfield, M. (2001). Mars Global Surveyor Thermal Emission Spectrometer experiment: Investigation description and surface science results. *Journal of Geophysical Research: Planets*, 106(E10):23823–23871.

Christensen, P. R., McSween, H. Y., Bandfield, J. L., Ruff, S. W., Rogers, A. D., Hamilton, V. E., Gorelick, N., Wyatt, M. B., Jakosky, B. M., Kieffer, H. H., Malin, M. C., and Moersch, J. E. (2005). Evidence for magmatic evolution and diversity on Mars from infrared observations. *Nature*, 436(7050):504–509.

Christi, M. J. and Stephens, G. L. (2004). Retrieving profiles of atmospheric CO $_2$ in clear sky and in the presence of thin cloud using spectroscopy from the near and thermal infrared: A preliminary case study: RETRIEVING PROFILES OF CO $_2$. *Journal of Geophysical Research: Atmospheres*, 109(D4):n/a–n/a.

Clancy, R., Grossman, A., Wolff, M., James, P., Rudy, D., Billawala, Y., Sandor, B., Lee, S., and Muhleman, D. (1996). Water Vapor Saturation at Low Altitudes around Mars Aphelion: A Key to Mars Climate? *Icarus*, 122(1):36–62.

Clancy, R. T. (2003). Mars aerosol studies with the MGS TES emission phase function observations: Optical depths, particle sizes, and ice cloud types versus latitude and solar longitude. *Journal of Geophysical Research*, 108(E9):5098.

Clancy, R. T., Montmessin, F., Benson, J., Daerden, F., Colaprete, A., and Wolff, M. J. (2017a). Mars Clouds. In Haberle, R. M., Clancy, R. T., Forget, F., Smith, M. D., and Zurek, R. W., editors, *The Atmosphere and Climate of Mars*, pages 76–105. Cambridge University Press, 1 edition.

Clancy, R. T. and Nair, H. (1996). Annual (perihelion-aphelion) cycles in the photochemical behavior of the global Mars atmosphere. *Journal of Geophysical Research: Planets*, 101(E5):12785–12790.

Clancy, R. T., Sandor, B. J., Wolff, M. J., Christensen, P. R., Smith, M. D., Pearl, J. C., Conrath, B. J., and Wilson, R. J. (2000). An intercomparison of ground-based millimeter, MGS TES, and Viking atmospheric temperature measurements: Seasonal and interannual variability of temperatures and dust loading in the global Mars atmosphere. *Journal of Geophysical Research: Planets*, 105(E4):9553–9571.

Clancy, R. T., Sandor, B. J., Wolff, M. J., Smith, M. D., Lefèvre, F., Madeleine, J.-B., Forget, F., Murchie, S. L., Seelos, F. P., Seelos, K. D., Nair, H. A., Toigo, A. D., Humm, D., Kass, D. M., Kleinböhl, A., and Heavens, N. (2012). Extensive MRO CRISM observations of 1.27 μ m O $_2$ airglow in Mars polar night and their comparison to MRO MCS temperature profiles and LMD GCM simulations: MARS POLAR NIGHT O $_2$ SINGLET DELTA. *Journal of Geophysical Research: Planets*, 117(E11):n/a–n/a.

Clancy, R. T., Smith, M. D., Lefèvre, F., McConnochie, T. H., Sandor, B. J., Wolff, M. J., Lee, S. W., Murchie, S. L., Toigo, A. D., Nair, H., and Navarro, T. (2017b). Vertical profiles of Mars 1.27 μm O 2 dayglow from MRO CRISM limb spectra: Seasonal/global behaviors, comparisons to LMDGCM simulations, and a global definition for Mars water vapor profiles. *Icarus*, 293:132–156.

Clancy, T. R., Wolff, M. J., Lefèvre, F., Cantor, B. A., Malin, M. C., and Smith, M. D. (2016). Daily global mapping of Mars ozone column abundances with MARCI UV band imaging. *Icarus*, 266:112–133.

Clarke, J. T., Gérard, J.-C., Grodent, D., Wannawichian, S., Gustin, J., Connerney, J., Crary, F., Dougherty, M., Kurth, W., Cowley, S. W. H., Bunce, E. J., Hill, T., and Kim, J. (2005). Morphological differences between Saturn's ultraviolet aurorae and those of Earth and Jupiter. *Nature*, 433(7027):717–719.

Clavé, E., Benzerara, K., Meslin, P., Forni, O., Royer, C., Mandon, L., Beck, P., Quantin-Nataf, C., Beyssac, O., Cousin, A., Bousquet, B., Wiens, R. C., Maurice, S., Dehouck, E., Schröder, S., Gasnault, O., Mangold, N., Dromart, G., Bosak, T., Bernard, S., Udry, A., Anderson, R. B., Arana, G., Brown, A. J., Castro, K., Clegg, S. M., Cloutis, E., Fairén, A. G., Flannery, D. T., Gasda, P. J., Johnson, J. R., Lasue, J., Lopez-Reyes, G., Madariaga, J. M., Manrique, J. A., Le Mouélic, S., Núñez, J. I., Ollila, A. M., Pilleri, P., Pilorget, C., Pinet, P., Poulet, F., Veneranda, M., Wolf, Z. U., and the SuperCam team (2023). Carbonate Detection With SuperCam in Igneous Rocks on the Floor of Jezero Crater, Mars. *Journal of Geophysical Research: Planets*, 128(6):e2022JE007463.

Cliver, E. W. and Ling, A. G. (2007). Electrons and Protons in Solar Energetic Particle Events. *The Astrophysical Journal*, 658(2):1349–1356.

Connerney, J. E. P., Acuña, M. H., Wasilewski, P. J., Kletetschka, G., Ness, N. F., Rème, H., Lin, R. P., and Mitchell, D. L. (2001). The global magnetic field of Mars and implications for crustal evolution. *Geophysical Research Letters*, 28(21):4015–4018.

Connour, K. and Wolff, M. J. (2021). pyRT_disort: A pre-processing front-end to help make DISORT simulations easier in Python.

Conrad, P., Malespin, C., Franz, H., Pepin, R., Trainer, M., Schwenzer, S., Atreya, S., Freissinet, C., Jones, J., Manning, H., Owen, T., Pavlov, A., Wiens, R., Wong, M., and Mahaffy, P. (2016). In situ measurement of atmospheric krypton and xenon on Mars with Mars Science Laboratory. *Earth and Planetary Science Letters*, 454:1–9.

Conrath, B. J. (1975). Thermal structure of the Martian atmosphere during the dissipation of the dust storm of 1971. *Icarus*, 24(1):36–46.

Conrath, B. J., Pearl, J. C., Smith, M. D., Maguire, W. C., Christensen, P. R., Dason, S., and Kaelberer, M. S. (2000). Mars Global Surveyor Thermal Emission Spectrometer (TES) observations: Atmospheric temperatures during aerobraking and science phasing. *Journal of Geophysical Research: Planets*, 105(E4):9509–9519.

Creasey, J. E., Forbes, J. M., and Hinson, D. P. (2006). Global and seasonal distribution of gravity wave activity in Mars' lower atmosphere derived from MGS radio occultation data: GLOBAL GRAVITY WAVE ACTIVITY AT MARS. *Geophysical Research Letters*, 33(1):n/a–n/a.

Crismani, M. M. J., Schneider, N. M., Plane, J. M. C., Evans, J. S., Jain, S. K., Chaffin, M. S., Carrillo-Sanchez, J., Deighan, J. I., Yelle, R. V., Stewart, A. I. F., McClintock, W., Clarke, J., Holsclaw, G., Stiepen, A., Montmessin, F., and Jakosky, B. M. (2017). Detection of a persistent meteoric metal layer in the Martian atmosphere. *Nature Geoscience*, 10(6):401–404.

Curran, R. J., Conrath, B. J., Hanel, R. A., Kunde, V. G., and Pearl, J. C. (1973). Mars: Mariner 9 Spectroscopic Evidence for H_2O Ice Clouds. *Science*, 182(4110):381–383.

Daerden, F., Neary, L., Viscardy, S., García Muñoz, A., Clancy, R., Smith, M., Encrenaz, T., and Fedorova, A. (2019). Mars atmospheric chemistry simulations with the GEM-Mars general circulation model. *Icarus*, 326:197–224.

Davies, D. W. (1979). The Vertical Distribution of Mars Water Vapor. *Journal of Geophysical Research*, 84(B6):2875–2879.

Davis, B. W. (1969). Some speculations on adsorption and desorption of CO2 in Martian bright areas. *Icarus*, 11(2):155–158.

De Simone, N., Di Felice, V., Gieseler, J., Boezio, M., Casolino, M., Picozza, P., PAMELA Collaboration†, and Heber, B. (2011). Latitudinal and radial gradients of galactic cosmic ray protons in the inner heliosphere – PAMELA and Ulysses observations. *Astrophysics and Space Sciences Transactions*, 7(3):425–434.

Deighan, J., Jain, S. K., Chaffin, M. S., Fang, X., Halekas, J. S., Clarke, J. T., Schneider, N. M., Stewart, A. I. F., Chaufray, J.-Y., Evans, J. S., Stevens, M. H., Mayyasi, M., Stiepen, A., Crismani, M., McClintock, W. E., Holsclaw, G. M., Lo, D. Y., Montmessin, F., Lefèvre, F., and Jakosky, B. M. (2018). Discovery of a proton aurora at Mars. *Nature Astronomy*, 2(10):802–807.

Desai, M. and Giacalone, J. (2016). Large gradual solar energetic particle events. *Living Reviews in Solar Physics*, 13(1):3.

Dyudina, U. A., Ingersoll, A. P., Ewald, S. P., and Wellington, D. (2016). Saturn's aurora observed by the Cassini camera at visible wavelengths. *Icarus*, 263:32–43.

Edwards, D. P., Arellano, A. F., and Deeter, M. N. (2009). A satellite observation system simulation experiment for carbon monoxide in the lowermost troposphere. *Journal of Geophysical Research*, 114(D14):D14304.

Ehlmann, B. L., Mustard, J. F., Murchie, S. L., Poulet, F., Bishop, J. L., Brown, A. J., Calvin, W. M., Clark, R. N., Marais, D. J. D., Milliken, R. E., Roach, L. H., Roush, T. L., Swayze, G. A., and Wray, J. J. (2008). Orbital Identification of Carbonate-Bearing Rocks on Mars. *Science*, 322(5909):1828–1832.

Encrenaz, T., Bézard, B., Greathouse, T., Richter, M., Lacy, J., Atreya, S., Wong, A., Lebonnois, S., Lefèvre, F., and Forget, F. (2004). Hydrogen peroxide on Mars: evidence for spatial and seasonal variations. *Icarus*, 170(2):424–429.

Encrenaz, T., Fouchet, T., Melchiorri, R., Drossart, P., Gondet, B., Langevin, Y., Bibring, J.-P., Forget, F., and Bézard, B. (2006). Seasonal variations of the martian CO over Hellas as observed by OMEGA/Mars Express. *Astronomy & Astrophysics*, 459(1):265–270.

Engel, J., Gaisser, T. K., Lipari, P., and Stanev, T. (1992). Nucleus-nucleus collisions and interpretation of cosmic-ray cascades. *Physical Review D*, 46(11):5013–5025.

Fairén, A. G., Stokes, C. R., Davies, N. S., Schulze-Makuch, D., Rodríguez, J. A. P., Davila, A. F., Uceda, E. R., Dohm, J. M., Baker, V. R., Clifford, S. M., McKay, C. P., and Squyres, S. W. (2014). A cold hydrological system in Gale crater, Mars. *Planetary and Space Science*, 93-94:101–118.

Fanale, F. P. and Cannon, W. A. (1971). Adsorption on the Martian Regolith. *Nature*, 230(5295):502–504.

Farley, K. A., Stack, K. M., Shuster, D. L., Horgan, B. H. N., Hurowitz, J. A., Tarnas, J. D., Simon, J. I., Sun, V. Z., Scheller, E. L., Moore, K. R., McLennan, S. M., Vasconcelos, P. M., Wiens, R. C., Treiman, A. H., Mayhew, L. E., Beyssac, O., Kizovski, T. V., Tosca, N. J., Williford, K. H., Crumpler, L. S., Beegle, L. W., Bell, J. F., Ehlmann, B. L., Liu, Y., Maki, J. N., Schmidt, M. E., Allwood, A. C., Amundsen, H. E. F., Bhartia, R., Bosak, T., Brown, A. J., Clark, B. C., Cousin, A., Forni, O., Gabriel, T. S. J., Goreva, Y., Gupta, S., Hamran, S.-E., Herd, C. D. K., Hickman-Lewis, K., Johnson, J. R., Kah, L. C., Kelemen, P. B., Kinch, K. B., Mandon, L., Mangold, N., Quantin-Nataf, C., Rice, M. S., Russell, P. S., Sharma, S., Siljeström, S., Steele, A., Sullivan, R., Wadhwa, M., Weiss, B. P., Williams, A. J., Wogsland, B. V., Willis, P. A., Acosta-Maeda, T. A., Beck, P., Benzerara, K., Bernard, S., Burton, A. S., Cardarelli, E. L., Chide, B., Clavé, E., Cloutis, E. A., Cohen, B. A., Czaja, A. D., Debaille, V., Dehouck, E., Fairén, A. G., Flannery, D. T., Fleron, S. Z., Fouchet, T., Frydenvang, J., Garczynski, B. J., Gibbons, E. F., Hausrath, E. M., Hayes, A. G., Henneke, J., Jørgensen, J. L., Kelly, E. M., Lasue, J., Le Mouélic, S., Madariaga, J. M., Maurice, S., Merusi, M., Meslin, P.-Y., Milkovich, S. M., Million, C. C., Moeller, R. C., Núñez, J. I., Ollila, A. M., Paar, G., Paige, D. A., Pedersen, D. A. K., Pilleri, P., Pilorget, C., Pinet, P. C., Rice, J. W., Royer, C., Sautter, V., Schulte, M., Sephton, M. A., Sharma, S. K., Sholes, S. F., Spanovich, N., St. Clair, M., Tate, C. D., Uckert, K., VanBommel, S. J., Yanchilina, A. G., and Zorzano, M.-P. (2022). Aqueously altered igneous rocks sampled on the floor of Jezero crater, Mars. *Science*, 377(6614):eabo2196.

Farley, K. A., Williford, K. H., Stack, K. M., Bhartia, R., Chen, A., De La Torre, M., Hand, K., Goreva, Y., Herd, C. D. K., Hueso, R., Liu, Y., Maki, J. N., Martinez, G., Moeller, R. C., Nelessen, A., Newman, C. E., Nunes, D., Ponce, A., Spanovich, N., Willis, P. A., Beegle, L. W., Bell, J. F., Brown, A. J., Hamran, S.-E., Hurowitz, J. A., Maurice, S., Paige, D. A., Rodriguez-Manfredi, J. A., Schulte, M., and Wiens, R. C. (2020). Mars 2020 Mission Overview. *Space Science Reviews*, 216(8):142.

Farmer, C. B., Davies, D. W., and Laporte, D. D. (1976). Mars: Northern Summer Ice Cap–Water Vapor Observations from Viking 2. *Science*, 194(4271):1339–1341.

Fedorova, A., Bertaux, J.-L., Betsis, D., Montmessin, F., Korablev, O., Maltagliati, L., and Clarke, J. (2018). Water vapor in the middle atmosphere of Mars during the 2007 global dust storm. *Icarus*, 300:440–457.

Fedorova, A., Korablev, O., Bertaux, J.-L., Rodin, A., Kiselev, A., and Perrier, S. (2006). Mars water vapor abundance from SPICAM IR spectrometer: Seasonal and geographic distributions. *Journal of Geophysical Research*, 111(E9):E09S08.

Fedorova, A., Korablev, O., Bertaux, J.-L., Rodin, A., Montmessin, F., Belyaev, D., and Reberac, A. (2009). Solar infrared occultation observations by SPICAM experiment on Mars-Express: Simultaneous measurements of the vertical distributions of H2O, CO2 and aerosol. *Icarus*, 200(1):96–117.

Fedorova, A., Lefèvre, F., Guslyakova, S., Korablev, O., Bertaux, J.-L., Montmessin, F., Reberac, A., and Gondet, B. (2012). The O2 nightglow in the martian atmosphere by SPICAM onboard of Mars-Express. *Icarus*, 219(2):596–608.

Fedorova, A., Montmessin, F., Korablev, O., Lefèvre, F., Trokhimovskiy, A., and Bertaux, J. (2021). Multi-Annual Monitoring of the Water Vapor Vertical Distribution on Mars by SPICAM on Mars Express. *Journal of Geophysical Research: Planets*, 126(1).

Fedorova, A., Montmessin, F., Korablev, O., Luginin, M., Trokhimovskiy, A., Belyaev, D. A., Ignatiev, N. I., Lefèvre, F., Alday, J., Irwin, P. G. J., Olsen, K. S., Bertaux, J.-L., Millour, E., Määttänen, A., Shakun, A., Grigoriev, A. V., Patrakeev, A., Korsa, S., Kokonkov, N., Baggio, L., Forget, F., and Wilson, C. F. (2020). Stormy water on Mars: The distribution and saturation of atmospheric water during the dusty season. *Science*, 367(6475):297–300.

Fedorova, A., Montmessin, F., Rodin, A., Korablev, O., Määttänen, A., Maltagliati, L., and Bertaux, J.-L. (2014). Evidence for a bimodal size distribution for the suspended aerosol particles on Mars. *Icarus*, 231:239–260.

Fedorova, A., Montmessin, F., Trokhimovskiy, A., Luginin, M., Korablev, O., Alday, J., Belyaev, D., Holmes, J., Lefevre, F., Olsen, K., Patrakeev, A., and Shakun, A. (2023). A Two-Martian Years Survey of the Water Vapor Saturation State on Mars Based on ACS NIR/TGO Occultations. *Journal of Geophysical Research: Planets*, 128(1).

Fedorova, A., Trokhimovskiy, A., Lefèvre, F., Olsen, K. S., Korablev, O., Montmessin, F., Ignatiev, N., Lomakin, A., Forget, F., Belyaev, D., Alday, J., Luginin, M., Smith, M., Patrakeev, A., Shakun, A., and Grigoriev, A. (2022). Climatology of the CO Vertical Distribution on Mars Based on ACS TGO Measurements. *Journal of Geophysical Research: Planets*, 127(9).

Feldman, W. C., Pathare, A., Maurice, S., Prettyman, T. H., Lawrence, D. J., Milliken, R. E., and Travis, B. J. (2011). Mars Odyssey neutron data: 2. Search for buried excess water ice deposits at nonpolar latitudes on Mars. *Journal of Geophysical Research*, 116(E11):E11009.

Fischer, E., Martínez, G. M., Rennó, N. O., Tamppari, L. K., and Zent, A. P. (2019). Relative Humidity on Mars: New Results From the Phoenix TECP Sensor. *Journal of Geophysical Research: Planets*, 124(11):2780–2792.

Fishbaugh, K. (2001). Comparison of the North and South Polar Caps of Mars: New Observations from MOLA Data and Discussion of Some Outstanding Questions. *Icarus*, 154(1):145–161.

Forget, F., Hourdin, F., Fournier, R., Hourdin, C., Talagrand, O., Collins, M., Lewis, S. R., Read, P. L., and Huot, J.-P. (1999). Improved general circulation models of the Martian atmosphere from the surface to above 80 km. *Journal of Geophysical Research: Planets*, 104(E10):24155–24175.

Forget, F. and Montabone, L. (2017). Atmospheric dust on Mars: a review. In *International Conference on Environmental Systems*, South Carolina.

Formisano, V., Angrilli, F., Arnold, G., Atreya, S., Bianchini, G., Biondi, D., Blanco, A., Blecka, M., Coradini, A., Colangeli, L., Ekonomov, A., Esposito, F., Fonti, S., Giuranna, M., Grassi, D., Gnedykh, V., Grigoriev, A., Hansen, G., Hirsh, H., Khatuntsev, I., Kiselev, A., Ignatiev, N., Jurewicz, A., Lellouch, E., Lopez Moreno, J., Marten, A., Mattana, A., Maturilli, A., Mencarelli, E., Michalska, M., Moroz, V., Moshkin, B., Nespoli, F., Nikolsky, Y., Orfei, R., Orleanski, P., Orofino, V., Palomba, E., Patsaev, D., Piccioni, G., Rataj, M., Rodrigo, R., Rodriguez, J., Rossi, M., Saggin, B., Titov, D., and Zasova, L. (2005). The Planetary Fourier Spectrometer (PFS) onboard the European Mars Express mission. *Planetary and Space Science*, 53(10):963–974.

Formisano, V., Atreya, S., Encrenaz, T., Ignatiev, N., and Giuranna, M. (2004). Detection of Methane in the Atmosphere of Mars. *Science*, 306(5702):1758–1761.

Formisano, V., Grassi, D., Ignatiev, N., Zasova, L., and Maturilli, A. (2002). PFS for Mars Express: A new approach to study Martian atmosphere. *Advances in Space Research*, 29(2):131–142.

Fouchet, T., Lellouch, E., Ignatiev, N., Forget, F., Titov, D., Tschimmel, M., Montmessin, F., Formisano, V., Giuranna, M., Maturilli, A., and Encrenaz, T. (2007). Martian water vapor: Mars Express PFS/LW observations. *Icarus*, 190(1):32–49.

Fouchet, T., Reess, J.-M., Montmessin, F., Hassen-Khodja, R., Nguyen-Tuong, N., Humeau, O., Jacquinod, S., Lapauw, L., Parisot, J., Bonafous, M., Bernardi, P., Chapron, F., Jeanneau, A., Collin, C., Zeganadin, D., Nibert, P., Abbaki, S., Montaron, C., Blanchard, C., Arslanyan, V., Achelhi, O., Colon, C., Royer, C., Hamm, V., Beuzit, M., Poulet, F., Pilorget, C., Mandon, L., Forni, O., Cousin, A., Gasnault, O., Pilleri, P., Dubois, B., Quantin, C., Beck, P., Beyssac, O., Le Mouélic, S., Johnsson, J. R., McConnochie, T. H., Maurice, S., and Wiens, R. C. (2022). The SuperCam infrared spectrometer for the perseverance rover of the Mars2020 mission. *Icarus*, 373:114773.

Frank, L. A., Craven, J. D., Burch, J. L., and Winningham, J. D. (1982). Polar views of the Earth's aurora with Dynamics Explorer. *Geophysical Research Letters*, 9(9):1001–1004.

Freiherr von Forstner, J. L., Dumbović, M., Möstl, C., Guo, J., Papaioannou, A., Elftmann, R., Xu, Z., Christoph Terasa, J., Kollhoff, A., Wimmer-Schweingruber, R. F., Rodríguez-Pacheco, J., Weiss, A. J., Hinterreiter, J., Amerstorfer, T., Bauer, M., Belov, A. V., Abunina, M. A., Horbury, T., Davies, E. E., O'Brien, H., Allen, R. C., Bruce Andrews, G., Berger, L., Boden, S., Cernuda Cangas, I., Eldrum, S., Espinosa Lara, F., Gómez Herrero, R., Hayes, J. R., Ho, G. C., Kulkarni, S. R., Jeffrey Lees, W., Martín, C., Mason, G. M., Pacheco, D., Prieto Mateo, M., Ravanbakhsh, A., Rodríguez Polo, O., Sánchez Prieto, S., Schlemm, C. E., Seifert, H., Tyagi, K., and Yedla, M. (2021). Radial evolution of the April 2020 stealth coronal mass ejection between 0.8 and 1 AU: Comparison of Forbush decreases at Solar Orbiter and near the Earth. *Astronomy & Astrophysics*, 656:A1.

Freiherr von Forstner, J. L., Guo, J., Wimmer-Schweingruber, R. F., Hassler, D. M., Temmer, M., Dumbović, M., Jian, L. K., Appel, J. K., Čalogović, J., Ehresmann, B., Heber, B., Lohf, H., Posner, A., Steigies, C. T., Vršnak, B., and Zeitlin, C. J. (2018). Using Forbush Decreases to Derive the Transit Time of ICMEs Propagating from 1 AU to Mars. *Journal of Geophysical Research: Space Physics*, 123(1):39–56.

Futaana, Y., Barabash, S., Yamauchi, M., McKenna-Lawlor, S., Lundin, R., Luhmann, J., Brain, D., Carlsson, E., Sauvaud, J.-A., Winningham, J., Frahm, R., Wurz, P., Holmström, M., Gunell, H., Kallio, E., Baumjohann, W., Lammer, H., Sharber, J., Hsieh, K., Andersson, H., Grigoriev, A., Brinkfeldt, K., Nilsson, H., Asamura, K., Zhang, T., Coates, A., Linder, D., Kataria, D., Curtis, C., Sandel, B., Fedorov, A., Mazelle, C., Thocaven, J.-J., Grande, M., Koskinen, H. E., Sales, T., Schmidt, W., Riihela, P., Kozyra, J., Krupp, N., Woch, J., Fränz, M., Dubinin, E., Orsini, S., Cerulli-Irelli, R., Mura, A., Milillo, A., Maggi, M., Roelof, E., Brandt, P., Szego, K., Scherrer, J., and Bochsler, P. (2008). Mars Express and Venus Express multi-point observations of geoeffective solar flare events in December 2006. *Planetary and Space Science*, 56(6):873–880.

Garcia, R. F., Daubar, I. J., Beucler, E., Posiolova, L. V., Collins, G. S., Lognonné, P., Rolland, L., Xu, Z., Wójcicka, N., Spiga, A., Fernando, B., Speth, G., Martire, L., Rajšić, A., Miljković, K., Sansom, E. K., Charalambous, C., Ceylan, S., Menina, S., Margerin, L., Lapeyre, R., Neidhart, T., Teanby, N. A., Schmerr, N. C., Bonnin, M., Froment, M., Clinton, J. F., Karatekin, O., Stähler, S. C., Dahmen, N. L., Durán, C., Horleston, A., Kawamura, T., Plasman, M., Zenhäusern, G.,

Giardini, D., Panning, M., Malin, M., and Banerdt, W. B. (2022). Newly formed craters on Mars located using seismic and acoustic wave data from InSight. *Nature Geoscience*, 15(10):774–780.

Gazis, P. R. (1996). Solar cycle variation in the heliosphere. *Reviews of Geophysics*, 34(3):379–402.

Gerontidou, M., Mavromichalaki, H., and Daglis, T. (2018). High-Speed Solar Wind Streams and Geomagnetic Storms During Solar Cycle 24. *Solar Physics*, 293(9):131.

Gierasch, P. J. and Goody, R. M. (1972). The effect of dust on the temperature of the Martian atmosphere. *Journal of the Atmospheric Sciences*, 29:400–402. ADS Bibcode: 1972JAtS...29..400G.

Gillen, E., Rimmer, P. B., and Catling, D. C. (2020). Statistical analysis of Curiosity data shows no evidence for a strong seasonal cycle of martian methane. *Icarus*, 336:113407.

Giuranna, M., Formisano, V., Biondi, D., Ekonomov, A., Fonti, S., Grassi, D., Hirsch, H., Khatuntsev, I., Ignatiev, N., Malgoska, M., Mattana, A., Maturilli, A., Mencarelli, E., Nespoli, F., Orfei, R., Orleanski, P., Piccioni, G., Rataj, M., Saggin, B., and Zasova, L. (2005). Calibration of the Planetary Fourier Spectrometer long wavelength channel. *Planetary and Space Science*, 53(10):993–1007.

Giuranna, M., Viscardy, S., Daerden, F., Neary, L., Etiope, G., Oehler, D., Formisano, V., Aronica, A., Wolkenberg, P., Aoki, S., Cardesín-Moinelo, A., Marín-Yaseli de la Parra, J., Merritt, D., and Amoroso, M. (2019). Independent confirmation of a methane spike on Mars and a source region east of Gale Crater. *Nature Geoscience*, 12(5):326–332.

Golombek, M. P., Cook, R. A., Economou, T., Folkner, W. M., Haldemann, A. F. C., Kallemeyn, P. H., Knudsen, J. M., Manning, R. M., Moore, H. J., Parker, T. J., Rieder, R., Schofield, J. T., Smith, P. H., and Vaughan, R. M. (1997). Overview of the Mars Pathfinder Mission and Assessment of Landing Site Predictions. *Science*, 278(5344):1743–1748.

Gooding, J. L. (1986). Martian dust particles as condensation nuclei: A preliminary assessment of mineralogical factors. *Icarus*, 66(1):56–74.

Goody, R., West, R., Chen, L., and Crisp, D. (1989). The correlated-k method for radiation calculations in nonhomogeneous atmospheres. *Journal of Quantitative Spectroscopy and Radiative Transfer*, 42(6):539–550.

Grassi, D., Fiorenza, C., Zasova, L., Ignatiev, N., Maturilli, A., Formisano, V., and Giuranna, M. (2005). The Martian atmosphere above great volcanoes: Early planetary Fourier spectrometer observations. *Planetary and Space Science*, 53(10):1053–1064.

Greeley, R., Kraft, M., Sullivan, R., Wilson, G., Bridges, N., Herkenhoff, K., Kuzmin, R. O., Malin, M., and Ward, W. (1999). Aeolian features and processes at the Mars Pathfinder landing site. *Journal of Geophysical Research: Planets*, 104(E4):8573–8584.

Grotzinger, J. P., Sumner, D. Y., Kah, L. C., Stack, K., Gupta, S., Edgar, L., Rubin, D., Lewis, K., Schieber, J., Mangold, N., Milliken, R., Conrad, P. G., DesMarais, D., Farmer, J., Siebach, K., Calef, F., Hurowitz, J., McLennan, S. M., Ming, D., Vaniman, D., Crisp, J., Vasavada, A., Edgett, K. S., Malin, M., Blake, D., Gellert, R., Mahaffy, P., Wiens, R. C., Maurice, S., Grant, J. A., Wilson, S., Anderson, R. C., Beegle, L., Arvidson, R., Hallet, B., Sletten, R. S., Rice, M., Bell, J., Griffes, J., Ehlmann, B., Anderson, R. B., Bristow, T. F., Dietrich, W. E., Dromart, G., Eigenbrode, J., Fraeman, A., Hardgrove, C., Herkenhoff, K., Jandura, L., Kocurek, G., Lee, S., Leshin, L. A., Leveille, R., Limonadi, D., Maki, J., McCloskey, S., Meyer, M., Minitti, M., Newsom, H., Oehler, D., Okon, A., Palucis, M., Parker, T., Rowland, S., Schmidt, M., Squyres, S., Steele, A., Stolper, E., Summons, R., Treiman, A., Williams, R., Yingst, A., Team, M. S.,

Kemppinen, O., Bridges, N., Johnson, J. R., Cremers, D., Godber, A., Wadhwa, M., Wellington, D., McEwan, I., Newman, C., Richardson, M., Charpentier, A., Peret, L., King, P., Blank, J., Weigle, G., Li, S., Robertson, K., Sun, V., Baker, M., Edwards, C., Farley, K., Miller, H., Newcombe, M., Pilorget, C., Brunet, C., Hipkin, V., Leveille, R., Marchand, G., Sanchez, P. S., Favot, L., Cody, G., Fluckiger, L., Lees, D., Nefian, A., Martin, M., Gailhanou, M., Westall, F., Israel, G., Agard, C., Baroukh, J., Donny, C., Gaboriaud, A., Guillemot, P., Lafaille, V., Lorigny, E., Paillet, A., Perez, R., Saccoccio, M., Yana, C., Armiens-Aparicio, C., Rodriguez, J. C., Blazquez, I. C., Gomez, F. G., Gomez-Elvira, J., Hettrich, S., Malvitte, A. L., Jimenez, M. M., Martinez-Frias, J., Martin-Soler, J., Martin-Torres, F. J., Jurado, A. M., Mora-Sotomayor, L., Caro, G. M., Lopez, S. N., Peinado-Gonzalez, V., Pla-Garcia, J., Manfredi, J. A. R., Romeral-Planello, J. J., Fuentes, S. A. S., Martinez, E. S., Redondo, J. T., Urqui-O'Callaghan, R., Mier, M.-P. Z., Chipera, S., Lacour, J.-L., Mauchien, P., Sirven, J.-B., Manning, H., Fairen, A., Hayes, A., Joseph, J., Sullivan, R., Thomas, P., Dupont, A., Lundberg, A., Melikechi, N., Mezzacappa, A., DeMarines, J., Grinspoon, D., Reitz, G., Prats, B., Atlaskin, E., Genzer, M., Harri, A.-M., Haukka, H., Kahanpaa, H., Kauhanen, J., Paton, M., Polkko, J., Schmidt, W., Siili, T., Fabre, C., Wray, J., Wilhelm, M. B., Poitrasson, F., Patel, K., Gorevan, S., Indyk, S., Paulsen, G., Bish, D., Gondet, B., Langevin, Y., Geffroy, C., Baratoux, D., Berger, G., Cros, A., d'Uston, C., Forni, O., Gasnault, O., Lasue, J., Lee, Q.-M., Meslin, P.-Y., Pallier, E., Parot, Y., Pinet, P., Schroder, S., Toplis, M., Lewin, E., Brunner, W., Heydari, E., Achilles, C., Sutter, B., Cabane, M., Coscia, D., Szopa, C., Robert, F., Sautter, V., Le Mouelic, S., Nachon, M., Buch, A., Stalport, F., Coll, P., Francois, P., Raulin, F., Teinturier, S., Cameron, J., Clegg, S., Cousin, A., DeLapp, D., Dingler, R., Jackson, R. S., Johnstone, S., Lanza, N., Little, C., Nelson, T., Williams, R. B., Jones, A., Kirkland, L., Baker, B., Cantor, B., Caplinger, M., Davis, S., Duston, B., Fay, D., Harker, D., Herrera, P., Jensen, E., Kennedy, M. R., Krezoski, G., Krysak, D., Lipkaman, L., McCartney, E., McNair, S., Nixon, B., Posiolova, L., Ravine, M., Salamon, A., Saper, L., Stoiber, K., Supulver, K., Van Beek, J., Van Beek, T., Zimdar, R., French, K. L., Iagnemma, K., Miller, K., Goesmann, F., Goetz, W., Hviid, S., Johnson, M., Lefavor, M., Lyness, E., Breves, E., Dyar, M. D., Fassett, C., Edwards, L., Haberle, R., Hoehler, T., Hollingsworth, J., Kahre, M., Keely, L., McKay, C., Bleacher, L., Brinckerhoff, W., Choi, D., Dworkin, J. P., Floyd, M., Freissinet, C., Garvin, J., Glavin, D., Harpold, D., Martin, D. K., McAdam, A., Pavlov, A., Raaen, E., Smith, M. D., Stern, J., Tan, F., Trainer, M., Posner, A., Voytek, M., Aubrey, A., Behar, A., Blaney, D., Brinza, D., Christensen, L., DeFlores, L., Feldman, J., Feldman, S., Flesch, G., Jun, I., Keymeulen, D., Mischna, M., Morookian, J. M., Pavri, B., Schoppers, M., Sengstacken, A., Simmonds, J. J., Spanovich, N., Juarez, M. d. l. T., Webster, C. R., Yen, A., Archer, P. D., Cucinotta, F., Jones, J. H., Morris, R. V., Niles, P., Rampe, E., Nolan, T., Fisk, M., Radziemski, L., Barraclough, B., Bender, S., Berman, D., Dobrea, E. N., Tokar, R., Cleghorn, T., Huntress, W., Manhes, G., Hudgins, J., Olson, T., Stewart, N., Sarrazin, P., Vicenzi, E., Bullock, M., Ehresmann, B., Hamilton, V., Hassler, D., Peterson, J., Rafkin, S., Zeitlin, C., Fedosov, F., Golovin, D., Karpushkina, N., Kozyrev, A., Litvak, M., Malakhov, A., Mitrofanov, I., Mokrousov, M., Nikiforov, S., Prokhorov, V., Sanin, A., Tretyakov, V., Varenikov, A., Vostrukhin, A., Kuzmin, R., Clark, B., Wolff, M., Botta, O., Drake, D., Bean, K., Lemmon, M., Schwenzer, S. P., Lee, E. M., Sucharski, R., Hernandez, M. A. d. P., Avalos, J. J. B., Ramos, M., Kim, M.-H., Malespin, C., Plante, I., Muller, J.-P., Navarro-Gonzalez, R., Ewing, R., Boynton, W., Downs, R., Fitzgibbon, M., Harshman, K., Morrison, S., Kortmann, O., Williams, A., Lugmair, G., Wilson, M. A., Jakosky, B., Balic-Zunic, T., Frydenvang, J., Jensen, J. K., Kinch, K., Koefoed, A., Madsen, M. B., Stipp, S. L. S., Boyd, N., Campbell, J. L., Perrett, G., Pradler, I., VanBommel, S., Jacob, S., Owen, T., Savijärvi, H., Boehm, E., Bottcher, S., Burmeister, S., Guo, J., Kohler, J., Garcia, C. M., Mueller-Mellin, R., Wimmer-Schweingruber, R., Bridges, J. C., McConnochie, T., Benna, M., Franz, H., Bower, H., Brunner, A., Blau, H., Boucher, T., Carmosino, M., Atreya, S., Elliott, H., Halleaux, D., Renno, N., Wong, M., Pepin, R., Elliott, B., Spray, J., Thompson, L., Gordon, S., Ollila, A., Williams, J., Vasconcelos, P., Bentz, J., Nealson, K., Popa, R., Moersch, J., Tate, C.,

Day, M., Francis, R., McCullough, E., Cloutis, E., ten Kate, I. L., Scholes, D., Slavney, S., Stein, T., Ward, J., Berger, J., and Moores, J. E. (2014). A Habitable Fluvio-Lacustrine Environment at Yellowknife Bay, Gale Crater, Mars. *Science*, 343(6169):1242777–1242777.

Guendelman, I. and Kaspi, Y. (2018). An Axisymmetric Limit for the Width of the Hadley Cell on Planets With Large Obliquity and Long Seasonality. *Geophysical Research Letters*, 45(24).

Guo, J., Lillis, R., Wimmer-Schweingruber, R. F., Zeitlin, C., Simonson, P., Rahmati, A., Posner, A., Papaioannou, A., Lundt, N., Lee, C. O., Larson, D., Halekas, J., Hassler, D. M., Ehresmann, B., Dunn, P., and Böttcher, S. (2018). Measurements of Forbush decreases at Mars: both by MSL on ground and by MAVEN in orbit. *Astronomy & Astrophysics*, 611:A79.

Guo, J., Zeitlin, C., Wimmer-Schweingruber, R. F., Hassler, D. M., Ehresmann, B., Rafkin, S., Freiherr von Forstner, J. L., Khaksarighiri, S., Liu, W., and Wang, Y. (2021). Radiation environment for future human exploration on the surface of Mars: the current understanding based on MSL/RAD dose measurements. *The Astronomy and Astrophysics Review*, 29(1):8.

Guzewich, S. D., Smith, M. D., and Wolff, M. J. (2014). The vertical distribution of Martian aerosol particle size: Vertical Profile of Mars Aerosol Size. *Journal of Geophysical Research: Planets*, 119(12):2694–2708.

Guzewich, S. D., Talaat, E. R., Toigo, A. D., Waugh, D. W., and McConnochie, T. H. (2013). High-altitude dust layers on Mars: Observations with the Thermal Emission Spectrometer: TES OBSERVATIONS OF MARS DUST LAYERS. *Journal of Geophysical Research: Planets*, 118(6):1177–1194.

Gérard, J., Aoki, S., Gkouvelis, L., Soret, L., Willame, Y., Thomas, I. R., Depiesse, C., Ristic, B., Vandaele, A. C., Hubert, B., Daerden, F., Patel, M. R., López-Moreno, J., Bellucci, G., Mason, J. P., and López-Valverde, M. A. (2021). First Observation of the Oxygen 630 nm Emission in the Martian Dayglow. *Geophysical Research Letters*, 48(8).

Gérard, J.-C., Aoki, S., Willame, Y., Gkouvelis, L., Depiesse, C., Thomas, I. R., Ristic, B., Vandaele, A. C., Daerden, F., Hubert, B., Mason, J., Patel, M. R., López-Moreno, J.-J., Bellucci, G., López-Valverde, M. A., and Beeckman, B. (2020). Detection of green line emission in the dayside atmosphere of Mars from NOMAD-TGO observations. *Nature Astronomy*, 4(11):1049–1052.

Gérard, J.-C., Soret, L., Shematovich, V., Bisikalo, D., and Bougher, S. (2017). The Mars diffuse aurora: A model of ultraviolet and visible emissions. *Icarus*, 288:284–294.

Haberle, R. M., Clancy, R. T., Forget, F., Smith, M. D., Zurek, R. W., and editors (2017). *The Atmosphere and Climate of Mars*. Cambridge University Press.

Haberle, R. M. and Jakosky, B. M. (1990). Sublimation and Transport of Water From the North Residual Polar Cap on Mars. *JOURNAL OF GEOPHYSICAL RESEARCH*, 95(B2):1423–1437.

Haberle, R. M., Leovy, C. B., and Pollack, J. B. (1982). Some effects of global dust storms on the atmospheric circulation of Mars. *Icarus*, 50(2-3):322–367.

Halekas, J. S., Brain, D. A., Lillis, R. J., Fillingim, M. O., Mitchell, D. L., and Lin, R. P. (2006). Current sheets at low altitudes in the Martian magnetotail. *Geophysical Research Letters*, 33(13):L13101.

Halevy, I., Fischer, W. W., and Eiler, J. M. (2011). Carbonates in the Martian meteorite Allan Hills 84001 formed at 18 ± 4 °C in a near-surface aqueous environment. *Proceedings of the National Academy of Sciences*, 108(41):16895–16899.

Hanel, R., Conrath, B., Hovis, W., Kunde, V., Lowman, P., Maguire, W., Pearl, J., Pirraglia, J., Prabhakara, C., Schlachman, B., Levin, G., Straat, P., and Burke, T. (1972). Investigation of the Martian environment by infrared spectroscopy on Mariner 9. *Icarus*, 17(2):423–442.

Harada, Y., Halekas, J. S., McFadden, J. P., Espley, J., DiBraccio, G. A., Mitchell, D. L., Mazelle, C., Brain, D. A., Andersson, L., Ma, Y. J., Larson, D. E., Xu, S., Hara, T., Ruhunusiri, S., Livi, R., and Jakosky, B. M. (2017). Survey of magnetic reconnection signatures in the Martian magnetotail with MAVEN: TAIL RECONNECTION AT MARS. *Journal of Geophysical Research: Space Physics*, 122(5):5114–5131.

Harri, A., Genzer, M., Kemppinen, O., Gomez-Elvira, J., Haberle, R., Polkko, J., Savijärvi, H., Rennó, N., Rodriguez-Manfredi, J. A., Schmidt, W., Richardson, M., Siili, T., Paton, M., Torre-Juarez, M. D., Mäkinen, T., Newman, C., Rafkin, S., Mischna, M., Merikallio, S., Haukka, H., Martin-Torres, J., Komu, M., Zorzano, M., Peinado, V., Vazquez, L., and Urqui, R. (2014). Mars Science Laboratory relative humidity observations: Initial results. *Journal of Geophysical Research: Planets*, 119(9):2132–2147.

Hartmann, W. K. and Neukum, G. (2001). Cratering Chronology and the Evolution of Mars. In *Chronology and Evolution of Mars*, volume 12, pages 165–194. Springer Netherlands, Dordrecht. Series Title: Space Sciences Series of ISSI.

Hassler, D. M., Zeitlin, C., Wimmer-Schweingruber, R. F., Ehresmann, B., Rafkin, S., Eigenbrode, J. L., Brinza, D. E., Weigle, G., Bottcher, S., Bohm, E., Burmeister, S., Guo, J., Kohler, J., Martin, C., Reitz, G., Cucinotta, F. A., Kim, M.-H., Grinspoon, D., Bullock, M. A., Posner, A., Gomez-Elvira, J., Vasavada, A., Grotzinger, J. P., Team, M. S., Kemppinen, O., Cremers, D., Bell, J. F., Edgar, L., Farmer, J., Godber, A., Wadhwa, M., Wellington, D., McEwan, I., Newman, C., Richardson, M., Charpentier, A., Peret, L., King, P., Blank, J., Schmidt, M., Li, S., Milliken, R., Robertson, K., Sun, V., Baker, M., Edwards, C., Ehlmann, B., Farley, K., Griffes, J., Miller, H., Newcombe, M., Pilorget, C., Rice, M., Siebach, K., Stack, K., Stolper, E., Brunet, C., Hipkin, V., Leveille, R., Marchand, G., Sanchez, P. S., Favot, L., Cody, G., Steele, A., Fluckiger, L., Lees, D., Nefian, A., Martin, M., Gailhanou, M., Westall, F., Israel, G., Agard, C., Baroukh, J., Donny, C., Gaboriaud, A., Guillemot, P., Lafaille, V., Lorigny, E., Paillet, A., Perez, R., Saccoccio, M., Yana, C., Armiens-Aparicio, C., Rodriguez, J. C., Blazquez, I. C., Gomez, F. G., Hettrich, S., Malvitte, A. L., Jimenez, M. M., Martinez-Frias, J., Martin-Soler, J., Martin-Torres, F. J., Jurado, A. M., Mora-Sotomayor, L., Caro, G. M., Lopez, S. N., Peinado-Gonzalez, V., Pla-Garcia, J., Manfredi, J. A. R., Romeral-Planello, J. J., Fuentes, S. A. S., Martinez, E. S., Redondo, J. T., Urqui-O'Callaghan, R., Mier, M.-P. Z., Chipera, S., Lacour, J.-L., Mauchien, P., Sirven, J.-B., Manning, H., Fairen, A., Hayes, A., Joseph, J., Squyres, S., Sullivan, R., Thomas, P., Dupont, A., Lundberg, A., Melikechi, N., Mezzacappa, A., Berger, T., Matthia, D., Prats, B., Atlaskin, E., Genzer, M., Harri, A.-M., Haukka, H., Kahanpaa, H., Kauhanen, J., Kemppinen, O., Paton, M., Polkko, J., Schmidt, W., Siili, T., Fabre, C., Wray, J., Wilhelm, M. B., Poitrasson, F., Patel, K., Gorevan, S., Indyk, S., Paulsen, G., Gupta, S., Bish, D., Schieber, J., Gondet, B., Langevin, Y., Geffroy, C., Baratoux, D., Berger, G., Cros, A., d'Uston, C., Forni, O., Gasnault, O., Lasue, J., Lee, Q.-M., Maurice, S., Meslin, P.-Y., Pallier, E., Parot, Y., Pinet, P., Schroder, S., Toplis, M., Lewin, E., Brunner, W., Heydari, E., Achilles, C., Oehler, D., Sutter, B., Cabane, M., Coscia, D., Israel, G., Szopa, C., Dromart, G., Robert, F., Sautter, V., Le Mouelic, S., Mangold, N., Nachon, M., Buch, A., Stalport, F., Coll, P., Francois, P., Raulin, F., Teinturier, S., Cameron, J., Clegg, S., Cousin, A., DeLapp, D., Dingler, R., Jackson, R. S., Johnstone, S., Lanza, N., Little, C., Nelson, T., Wiens, R. C., Williams, R. B., Jones, A., Kirkland, L., Treiman, A., Baker, B., Cantor, B., Caplinger, M., Davis, S., Duston, B., Edgett, K., Fay, D., Hardgrove, C., Harker, D., Herrera, P., Jensen, E., Kennedy, M. R., Krezoski, G., Krysak, D., Lipkaman, L., Malin, M., McCartney, E., McNair, S., Nixon, B., Posiolova, L., Ravine, M., Salamon, A., Saper, L., Stoiber, K., Supulver, K., Van Beek, J., Van Beek, T., Zimdar,

R., French, K. L., Iagnemma, K., Miller, K., Summons, R., Goesmann, F., Goetz, W., Hviid, S., Johnson, M., Lefavor, M., Lyness, E., Breves, E., Dyar, M. D., Fassett, C., Blake, D. F., Bristow, T., DesMarais, D., Edwards, L., Haberle, R., Hoehler, T., Hollingsworth, J., Kahre, M., Keely, L., McKay, C., Wilhelm, M. B., Bleacher, L., Brinckerhoff, W., Choi, D., Conrad, P., Dworkin, J. P., Floyd, M., Freissinet, C., Garvin, J., Glavin, D., Harpold, D., Jones, A., Mahaffy, P., Martin, D. K., McAdam, A., Pavlov, A., Raaen, E., Smith, M. D., Stern, J., Tan, F., Trainer, M., Meyer, M., Voytek, M., Anderson, R. C., Aubrey, A., Beegle, L. W., Behar, A., Blaney, D., Calef, F., Christensen, L., Crisp, J. A., DeFlores, L., Ehlmann, B., Feldman, J., Feldman, S., Flesch, G., Hurowitz, J., Jun, I., Keymeulen, D., Maki, J., Mischna, M., Morookian, J. M., Parker, T., Pavri, B., Schoppers, M., Sengstacken, A., Simmonds, J. J., Spanovich, N., Juarez, M. d. l. T., Webster, C. R., Yen, A., Archer, P. D., Jones, J. H., Ming, D., Morris, R. V., Niles, P., Rampe, E., Nolan, T., Fisk, M., Radziemski, L., Barraclough, B., Bender, S., Berman, D., Dobrea, E. N., Tokar, R., Vaniman, D., Williams, R. M. E., Yingst, A., Lewis, K., Leshin, L., Cleghorn, T., Huntress, W., Manhes, G., Hudgins, J., Olson, T., Stewart, N., Sarrazin, P., Grant, J., Vicenzi, E., Wilson, S. A., Hamilton, V., Peterson, J., Fedosov, F., Golovin, D., Karpushkina, N., Kozyrev, A., Litvak, M., Malakhov, A., Mitrofanov, I., Mokrousov, M., Nikiforov, S., Prokhorov, V., Sanin, A., Tretyakov, V., Varenikov, A., Vostrukhin, A., Kuzmin, R., Clark, B., Wolff, M., McLennan, S., Botta, O., Drake, D., Bean, K., Lemmon, M., Schwenzer, S. P., Anderson, R. B., Herkenhoff, K., Lee, E. M., Sucharski, R., Hernandez, M. A. d. P., Avalos, J. J. B., Ramos, M., Malespin, C., Plante, I., Muller, J.-P., Navarro-Gonzalez, R., Ewing, R., Boynton, W., Downs, R., Fitzgibbon, M., Harshman, K., Morrison, S., Dietrich, W., Kortmann, O., Palucis, M., Sumner, D. Y., Williams, A., Lugmair, G., Wilson, M. A., Rubin, D., Jakosky, B., Balic-Zunic, T., Frydenvang, J., Jensen, J. K., Kinch, K., Koefoed, A., Madsen, M. B., Stipp, S. L. S., Boyd, N., Campbell, J. L., Gellert, R., Perrett, G., Pradler, I., VanBommel, S., Jacob, S., Owen, T., Rowland, S., Atlaskin, E., Savijärvi, H., Garcia, C. M., Mueller-Mellin, R., Bridges, J. C., McConnochie, T., Benna, M., Franz, H., Bower, H., Brunner, A., Blau, H., Boucher, T., Carmosino, M., Atreya, S., Elliott, H., Halleaux, D., Renno, N., Wong, M., Pepin, R., Elliott, B., Spray, J., Thompson, L., Gordon, S., Newsom, H., Ollila, A., Williams, J., Vasconcelos, P., Bentz, J., Nealson, K., Popa, R., Kah, L. C., Moersch, J., Tate, C., Day, M., Kocurek, G., Hallet, B., Sletten, R., Francis, R., McCullough, E., Cloutis, E., ten Kate, I. L., Kuzmin, R., Arvidson, R., Fraeman, A., Scholes, D., Slavney, S., Stein, T., Ward, J., Berger, J., and Moores, J. E. (2014). Mars' Surface Radiation Environment Measured with the Mars Science Laboratory's Curiosity Rover. *Science*, 343(6169):1244797–1244797.

He, F., Fan, K., Hughes, A., Wei, Y., Cui, J., Schneider, N., Fraenz, M., Yao, Z., Rong, Z., Chai, L., Yan, L., Wu, S., and Zhang, X. (2023). Martian Proton Aurora Brightening Reveals Atmospheric Ion Loss Intensifying. *Geophysical Research Letters*, 50(5):e2023GL102723.

Heavens, N. G., Kleinböhl, A., Chaffin, M. S., Halekas, J. S., Kass, D. M., Hayne, P. O., McCleese, D. J., Piqueux, S., Shirley, J. H., and Schofield, J. T. (2018). Hydrogen escape from Mars enhanced by deep convection in dust storms. *Nature Astronomy*, 2(2):126–132.

Heavens, N. G., Richardson, M. I., Kleinböhl, A., Kass, D. M., McCleese, D. J., Abdou, W., Benson, J. L., Schofield, J. T., Shirley, J. H., and Wolkenberg, P. M. (2011). Vertical distribution of dust in the Martian atmosphere during northern spring and summer: High-altitude tropical dust maximum at northern summer solstice. *Journal of Geophysical Research*, 116(E1):E01007.

Hinson, D., Pätzold, M., Tellmann, S., Häusler, B., and Tyler, G. (2008). The depth of the convective boundary layer on Mars. *Icarus*, 198(1):57–66.

Hinson, D. P. (2004). Temperature inversions, thermal tides, and water ice clouds in the Martian tropics. *Journal of Geophysical Research*, 109(E1):E01002.

Hitchcock, D. R. and Lovelock, J. E. (1967). Life detection by atmospheric analysis. *Icarus*, 7(1-3):149–159.

Holmes, J., Lewis, S., Patel, M., Chaffin, M., Cangi, E., Deighan, J., Schneider, N., Aoki, S., Fedorova, A., Kass, D., and Vandaele, A. (2021). Enhanced water loss from the martian atmosphere during a regional-scale dust storm and implications for long-term water loss. *Earth and Planetary Science Letters*, 571:117109.

Honig, T., Witasse, O., Evans, H., Nieminen, P., Kuulkers, E., Taylor, M., Heber, B., Guo, J., and Sánchez-Cano, B. (2019). Multi-point galactic cosmic ray measurements between 1 and 4.5 AU over a full solar cycle. *Annales Geophysicae*, 37(5):903–918.

Houben, H., Haberle, R. M., Young, R. E., and Zent, A. P. (1997). Modeling the Martian seasonal water cycle. *Journal of Geophysical Research: Planets*, 102(E4):9069–9083.

Hurowitz, J. A., McLennan, S. M., Tosca, N. J., Arvidson, R. E., Michalski, J. R., Ming, D. W., Schröder, C., and Squyres, S. W. (2006). In situ and experimental evidence for acidic weathering of rocks and soils on Mars: EVIDENCE FOR ACIDIC WEATHERING ON MARS. *Journal of Geophysical Research: Planets*, 111(E2):n/a–n/a.

Ivanov, B. A. (2001). [No title found]. *Space Science Reviews*, 96(1/4):87–104.

Jakosky, B., Brain, D., Chaffin, M., Curry, S., Deighan, J., Grebowsky, J., Halekas, J., Leblanc, F., Lillis, R., Luhmann, J., Andersson, L., Andre, N., Andrews, D., Baird, D., Baker, D., Bell, J., Benna, M., Bhattacharyya, D., Bougher, S., Bowers, C., Chamberlin, P., Chaufray, J.-Y., Clarke, J., Collinson, G., Combi, M., Connerney, J., Connour, K., Correira, J., Crabb, K., Crary, F., Cravens, T., Crismani, M., Delory, G., Dewey, R., DiBraccio, G., Dong, C., Dong, Y., Dunn, P., Egan, H., Elrod, M., England, S., Eparvier, F., Ergun, R., Eriksson, A., Esman, T., Espley, J., Evans, S., Fallows, K., Fang, X., Fillingim, M., Flynn, C., Fogle, A., Fowler, C., Fox, J., Fujimoto, M., Garnier, P., Girazian, Z., Groeller, H., Gruesbeck, J., Hamil, O., Hanley, K., Hara, T., Harada, Y., Hermann, J., Holmberg, M., Holsclaw, G., Houston, S., Inui, S., Jain, S., Jolitz, R., Kotova, A., Kuroda, T., Larson, D., Lee, Y., Lee, C., Lefevre, F., Lentz, C., Lo, D., Lugo, R., Ma, Y.-J., Mahaffy, P., Marquette, M., Matsumoto, Y., Mayyasi, M., Mazelle, C., McClintock, W., McFadden, J., Medvedev, A., Mendillo, M., Meziane, K., Milby, Z., Mitchell, D., Modolo, R., Montmessin, F., Nagy, A., Nakagawa, H., Narvaez, C., Olsen, K., Pawlowski, D., Peterson, W., Rahmati, A., Roeten, K., Romanelli, N., Ruhunusiri, S., Russell, C., Sakai, S., Schneider, N., Seki, K., Sharrar, R., Shaver, S., Siskind, D., Slipski, M., Soobiah, Y., Steckiewicz, M., Stevens, M., Stewart, I., Stiepen, A., Stone, S., Tenishev, V., Terada, N., Terada, K., Thiemann, E., Tolson, R., Toth, G., Trovato, J., Vogt, M., Weber, T., Withers, P., Xu, S., Yelle, R., Yiğit, E., and Zurek, R. (2018). Loss of the Martian atmosphere to space: Present-day loss rates determined from MAVEN observations and integrated loss through time. *Icarus*, 315:146–157.

Jakosky, B. M. and Farmer, C. B. (1982). The seasonal and global behavior of water vapor in the Mars atmosphere: Complete global results of the Viking Atmospheric Water Detector Experiment. *Journal of Geophysical Research*, 87(B4):2999.

Jakosky, B. M., Grebowsky, J. M., Luhmann, J. G., Connerney, J., Eparvier, F., Ergun, R., Halekas, J., Larson, D., Mahaffy, P., McFadden, J., Mitchell, D. L., Schneider, N., Zurek, R., Bougher, S., Brain, D., Ma, Y. J., Mazelle, C., Andersson, L., Andrews, D., Baird, D., Baker, D., Bell, J. M., Benna, M., Chaffin, M., Chamberlin, P., Chaufray, Y.-Y., Clarke, J., Collinson, G., Combi, M., Crary, F., Cravens, T., Crismani, M., Curry, S., Curtis, D., Deighan, J., Delory, G., Dewey, R., DiBraccio, G., Dong, C., Dong, Y., Dunn, P., Elrod, M., England, S., Eriksson, A., Espley, J., Evans, S., Fang, X., Fillingim, M., Fortier, K., Fowler, C. M., Fox, J., Gröller, H., Guzewich,

S., Hara, T., Harada, Y., Holsclaw, G., Jain, S. K., Jolitz, R., Leblanc, F., Lee, C. O., Lee, Y., Lefevre, F., Lillis, R., Livi, R., Lo, D., Mayyasi, M., McClintock, W., McEnulty, T., Modolo, R., Montmessin, F., Morooka, M., Nagy, A., Olsen, K., Peterson, W., Rahmati, A., Ruhunusiri, S., Russell, C. T., Sakai, S., Sauvaud, J.-A., Seki, K., Steckiewicz, M., Stevens, M., Stewart, A. I. F., Stiepen, A., Stone, S., Tenishev, V., Thiemann, E., Tolson, R., Toublanc, D., Vogt, M., Weber, T., Withers, P., Woods, T., and Yelle, R. (2015a). MAVEN observations of the response of Mars to an interplanetary coronal mass ejection. *Science*, 350(6261):aad0210.

Jakosky, B. M., Lin, R. P., Grebowsky, J. M., Luhmann, J. G., Mitchell, D. F., Beutelschies, G., Priser, T., Acuna, M., Andersson, L., Baird, D., Baker, D., Bartlett, R., Benna, M., Bougher, S., Brain, D., Carson, D., Cauffman, S., Chamberlin, P., Chaufray, J.-Y., Cheatom, O., Clarke, J., Connerney, J., Cravens, T., Curtis, D., Delory, G., Demcak, S., DeWolfe, A., Eparvier, F., Ergun, R., Eriksson, A., Espley, J., Fang, X., Folta, D., Fox, J., Gomez-Rosa, C., Habenicht, S., Halekas, J., Holsclaw, G., Houghton, M., Howard, R., Jarosz, M., Jedrich, N., Johnson, M., Kasprzak, W., Kelley, M., King, T., Lankton, M., Larson, D., Leblanc, F., Lefevre, F., Lillis, R., Mahaffy, P., Mazelle, C., McClintock, W., McFadden, J., Mitchell, D. L., Montmessin, F., Morrissey, J., Peterson, W., Possel, W., Sauvaud, J.-A., Schneider, N., Sidney, W., Sparacino, S., Stewart, A. I. F., Tolson, R., Toublanc, D., Waters, C., Woods, T., Yelle, R., and Zurek, R. (2015b). The Mars Atmosphere and Volatile Evolution (MAVEN) Mission. *Space Science Reviews*, 195(1-4):3–48.

Jakosky, B. M. and Phillips, R. J. (2001). Mars' volatile and climate history. *Nature*, 412(6843):237–244.

Jakosky, B. M., Zent, A. P., and Zurek, R. W. (1997). The Mars Water Cycle: Determining the Role of Exchange with the Regolith. *Icarus*, 130(1):87–95.

James, P. B. and North, G. R. (1982). The seasonal CO_2 cycle on Mars: An application of an energy balance climate model. *Journal of Geophysical Research*, 87(B12):10271.

Jiggens, P., Clavie, C., Evans, H., O'Brien, T. P., Witasse, O., Mishev, A. L., Nieminen, P., Daly, E., Kalegaev, V., Vlasova, N., Borisov, S., Benck, S., Poivey, C., Cyamukungu, M., Mazur, J., Heynderickx, D., Sandberg, I., Berger, T., Usoskin, I. G., Paassilta, M., Vainio, R., Straube, U., Müller, D., Sánchez-Cano, B., Hassler, D., Praks, J., Niemelä, P., Leppinen, H., Punkkinen, A., Aminalragia-Giamini, S., and Nagatsuma, T. (2019). In Situ Data and Effect Correlation During September 2017 Solar Particle Event. *Space Weather*, 17(1):99–117.

Kahler, S. W., Cliver, E. W., Cane, H. V., McGuire, R. E., Stone, R. G., and Sheeley, Jr., N. R. (1986). Solar Filament Eruptions and Energetic Particle Events. *The Astrophysical Journal*, 302:504. ADS Bibcode: 1986ApJ...302..504K.

Kahler, S. W., Hildner, E., and Van Hollebeke, M. A. I. (1978). Prompt solar proton events and coronal mass ejections. *Solar Physics*, 57(2):429–443.

Kahre, M., Haberle, R., Hollingsworth, J., and Wolff, M. (2020). MARCI-observed clouds in the Hellas Basin during northern hemisphere summer on Mars: Interpretation with the NASA/Ames Legacy Mars Global Climate Model. *Icarus*, 338:113512.

Kaplan, L. D., Connes, J., and Connes, P. (1969). Carbon Monoxide in the Martian Atmosphere. *The Astrophysical Journal*, 157:L187. ADS Bibcode: 1969ApJ...157L.187K.

Khayat, A., Villanueva, G., Mumma, M., and Tokunaga, A. (2015). A search for SO2, H2S and SO above Tharsis and Syrtis volcanic districts on Mars using ground-based high-resolution submillimeter spectroscopy. *Icarus*, 253:130–141.

Kieffer, H. H. (1979). Mars south polar spring and summer temperatures: A residual CO $_2$ frost. *Journal of Geophysical Research*, 84(B14):8263.

Kieffer, H. H., Chase, S. C., Martin, T. Z., Miner, E. D., and Palluconi, F. D. (1976). Martian North Pole Summer Temperatures: Dirty Water Ice. *Science*, 194(4271):1341–1344.

Kirk, R. L., Howington-Kraus, E., Rosiek, M. R., Anderson, J. A., Archinal, B. A., Becker, K. J., Cook, D. A., Galuszka, D. M., Geissler, P. E., Hare, T. M., Holmberg, I. M., Keszthelyi, L. P., Redding, B. L., Delamere, W. A., Gallagher, D., Chapel, J. D., Eliason, E. M., King, R., and McEwen, A. S. (2008). Ultrahigh resolution topographic mapping of Mars with MRO HiRISE stereo images: Meter-scale slopes of candidate Phoenix landing sites. *Journal of Geophysical Research*, 113:E00A24.

Klein, H. P. (1979). The Viking mission and the search for life on Mars. *Reviews of Geophysics*, 17(7):1655.

Kleinböhl, A., Schofield, J. T., Kass, D. M., Abdou, W. A., Backus, C. R., Sen, B., Shirley, J. H., Lawson, W. G., Richardson, M. I., Taylor, F. W., Teanby, N. A., and McCleese, D. J. (2009). Mars Climate Sounder limb profile retrieval of atmospheric temperature, pressure, and dust and water ice opacity: MCS RETRIEVALS. *Journal of Geophysical Research: Planets*, 114(E10):n/a–n/a.

Kliore, A., Cain, D. L., Levy, G. S., Eshleman, V. R., Fjeldbo, G., and Drake, F. D. (1965). Occultation Experiment: Results of the First Direct Measurement of Mars's Atmosphere and Ionosphere. *Science*, 149(3689):1243–1248.

Knutsen, E. W., Montmessin, F., Verdier, L., Lacombe, G., Lefevre, F., Ferron, S., Giuranna, M., Wolkenberg, P., Fedorova, A., Korablev, O., and Trokhimovskiy, A. (2022a). A spectral synergy method applied to PFS and SPICAM nadir observations to constrain near- surface water content in the Martian atmosphere. In *Proceedings of the International Astronautical Congress, IAC*. International Astronautical Federation.

Knutsen, E. W., Montmessin, F., Verdier, L., Lacombe, G., Lefèvre, F., Ferron, S., Giuranna, M., Wolkenberg, P., Fedorova, A., Trokhimovskiy, A., and Korablev, O. (2022b). Water Vapor on Mars: A Refined Climatology and Constraints on the Near-Surface Concentration Enabled by Synergistic Retrievals. *Journal of Geophysical Research: Planets*, 127(5).

Knutsen, E. W., Villanueva, G. L., Liuzzi, G., Crismani, M. M. J., Mumma, M. J., Smith, M. D., Vandaele, A. C., Aoki, S., Thomas, I. R., Daerden, F., Viscardy, S., Erwin, J. T., Trompet, L., Neary, L., Ristic, B., Lopez-Valverde, M. A., Lopez-Moreno, J. J., Patel, M. R., Karatekin, O., and Bellucci, G. (2021a). Comprehensive investigation of Mars methane and organics with ExoMars/NOMAD. *Icarus*, 357:114266.

Knutsen, E. W., Witasse, O., Sanchez-Cano, B., Lester, M., Wimmer-Schweingruber, R. F., Denis, M., Godfrey, J., and Johnstone, A. (2021b). Galactic cosmic ray modulation at Mars and beyond measured with EDACs on Mars Express and Rosetta. *Astronomy & Astrophysics*.

Korablev, O., Bertaux, J.-L., Fedorova, A., Fonteyn, D., Stepanov, A., Kalinnikov, Y., Kiselev, A., Grigoriev, A., Jegoulev, V., Perrier, S., Dimarellis, E., Dubois, J. P., Reberac, A., Van Ransbeeck, E., Gondet, B., Montmessin, F., and Rodin, A. (2006). SPICAM IR acousto-optic spectrometer experiment on Mars Express. *Journal of Geophysical Research*, 111(E9):E09S03.

Korablev, O., Montmessin, F., Fedorova, A. A., Trokhimovskiy, A., Forget, F., Lefèvre, F., Daerden, F., Thomas, I. R., Trompet, L., Erwin, J. T., Aoki, S., Robert, S., Neary, L., Viscardy, S., Grigoriev, A. V., Ignatiev, N. I., Shakun, A., Patrakeev, A., Belyaev, D. A., Bertaux, J.-L., Olsen, K. S.,

Baggio, L., Alday, J., Ivanov, Y. S., Ristic, B., Mason, J., Willame, Y., Depiesse, C., Hetey, L., Berkenbosch, S., Clairquin, R., Queirolo, C., Beeckman, B., Neefs, E., Patel, M. R., Bellucci, G., López-Moreno, J.-J., Wilson, C. F., Etiope, G., Zelenyi, L., Svedhem, H., Vago, J. L., and Teams, T. A. a. N. S. (2019). No detection of methane on Mars from early ExoMars Trace Gas Orbiter observations. *Nature*, 568(7753):517–520.

Korablev, O., Montmessin, F., Trokhimovskiy, A., Fedorova, A. A., Shakun, A. V., Grigoriev, A. V., Moshkin, B. E., Ignatiev, N. I., Forget, F., Lefèvre, F., Anufreychik, K., Dzuban, I., Ivanov, Y. S., Kalinnikov, Y. K., Kozlova, T. O., Kungurov, A., Makarov, V., Martynovich, F., Maslov, I., Merzlyakov, D., Moiseev, P. P., Nikolskiy, Y., Patrakeev, A., Patsaev, D., Santos-Skripko, A., Sazonov, O., Semena, N., Semenov, A., Shashkin, V., Sidorov, A., Stepanov, A. V., Stupin, I., Timonin, D., Titov, A. Y., Viktorov, A., Zharkov, A., Altieri, F., Arnold, G., Belyaev, D. A., Bertaux, J. L., Betsis, D. S., Duxbury, N., Encrenaz, T., Fouchet, T., Gérard, J.-C., Grassi, D., Guerlet, S., Hartogh, P., Kasaba, Y., Khatuntsev, I., Krasnopolsky, V. A., Kuzmin, R. O., Lellouch, E., Lopez-Valverde, M. A., Luginin, M., Määttänen, A., Marcq, E., Martin Torres, J., Medvedev, A. S., Millour, E., Olsen, K. S., Patel, M. R., Quantin-Nataf, C., Rodin, A. V., Shematovich, V. I., Thomas, I., Thomas, N., Vazquez, L., Vincendon, M., Wilquet, V., Wilson, C. F., Zasova, L. V., Zelenyi, L. M., and Zorzano, M. P. (2018). The Atmospheric Chemistry Suite (ACS) of Three Spectrometers for the ExoMars 2016 Trace Gas Orbiter. *Space Science Reviews*, 214(1):7.

Korablev, O., Olsen, K. S., Trokhimovskiy, A., Lefèvre, F., Montmessin, F., Fedorova, A. A., Toplis, M. J., Alday, J., Belyaev, D. A., Patrakeev, A., Ignatiev, N. I., Shakun, A. V., Grigoriev, A. V., Baggio, L., Abdenour, I., Lacombe, G., Ivanov, Y. S., Aoki, S., Thomas, I. R., Daerden, F., Ristic, B., Erwin, J. T., Patel, M., Bellucci, G., Lopez-Moreno, J.-J., and Vandaele, A. C. (2021). Transient HCl in the atmosphere of Mars. *Science Advances*, 7(7):eabe4386.

Krasnopolsky, V. A. (2003). Spectroscopic mapping of Mars CO mixing ratio: Detection of north-south asymmetry: MAPPING OF CO ON MARS. *Journal of Geophysical Research: Planets*, 108(E2):n/a–n/a.

Krasnopolsky, V. A. (2006). A sensitive search for nitric oxide in the lower atmospheres of Venus and Mars: Detection on Venus and upper limit for Mars. *Icarus*, 182(1):80–91.

Krasnopolsky, V. A. (2007). Long-term spectroscopic observations of Mars using IRTF/CSHELL: Mapping of O2 dayglow, CO, and search for CH4. *Icarus*, 190(1):93–102.

Krasnopolsky, V. A., Bjoraker, G. L., Mumma, M. J., and Jennings, D. E. (1997). High-resolution spectroscopy of Mars at 3.7 and 8 μm: A sensitive search for H_2O_2, H_2CO, HCl, and CH_4, and detection of HDO. *Journal of Geophysical Research: Planets*, 102(E3):6525–6534.

Krasnopolsky, V. A., Maillard, J. P., and Owen, T. C. (2004). Detection of methane in the martian atmosphere: evidence for life? *Icarus*, 172(2):537–547.

Kuiper, G. (1950). Planetary and satellite atmospheres. *Reports on Progress in Physics*, 13(1):247–275.

Kuiper, G. P. (1952). *The atmospheres of the earth and planets.* Publication Title: Chicago ADS Bibcode: 1952aoep.book.....K.

Lacis, A. A. and Hansen, J. (1974). A Parameterization for the Absorption of Solar Radiation in the Earth's Atmosphere. *Journal of the Atmospheric Sciences*, 31(1):118–133.

Lacis, A. A. and Oinas, V. (1991). A description of the correlated *k* distribution method for modeling nongray gaseous absorption, thermal emission, and multiple scattering in vertically inhomogeneous atmospheres. *Journal of Geophysical Research*, 96(D5):9027.

Lam, H. A., Achilleos, N., Miller, S., Tennyson, J., Trafton, L. M., Geballe, T. R., and Ballester, G. E. (1997). A Baseline Spectroscopic Study of the Infrared Auroras of Jupiter. *Icarus*, 127(2):379–393.

Landgraf, J. and Hasekamp, O. P. (2007). Retrieval of tropospheric ozone: The synergistic use of thermal infrared emission and ultraviolet reflectivity measurements from space. *Journal of Geophysical Research*, 112(D8):D08310.

Langevin, Y., Bibring, J.-P., Montmessin, F., Forget, F., Vincendon, M., Douté, S., Poulet, F., and Gondet, B. (2007). Observations of the south seasonal cap of Mars during recession in 2004-2006 by the OMEGA visible/near-infrared imaging spectrometer on board Mars Express: OMEGA-SOUTH SEASONAL CAP OF MARS. *Journal of Geophysical Research: Planets*, 112(E8).

Lario, D., Kwon, R. Y., Balmaceda, L., Richardson, I. G., Krupar, V., Thompson, B. J., Cyr, O. C. S., Zhao, L., and Zhang, M. (2020). Fast and Wide CMEs without Observed >20 MeV Protons. *The Astrophysical Journal*, 889(2):92.

Laskar, J., Correia, A., Gastineau, M., Joutel, F., Levrard, B., and Robutel, P. (2004). Long term evolution and chaotic diffusion of the insolation quantities of Mars. *Icarus*, 170(2):343–364.

Laszlo, I., Stamnes, K., Wiscombe, W. J., and Tsay, S.-C. (2016). The Discrete Ordinate Algorithm, DISORT for Radiative Transfer. In Kokhanovsky, A., editor, *Light Scattering Reviews, Volume 11*, pages 3–65. Springer Berlin Heidelberg, Berlin, Heidelberg.

Lee, C. O., Hara, T., Halekas, J. S., Thiemann, E., Chamberlin, P., Eparvier, F., Lillis, R. J., Larson, D. E., Dunn, P. A., Espley, J. R., Gruesbeck, J., Curry, S. M., Luhmann, J. G., and Jakosky, B. M. (2017). MAVEN observations of the solar cycle 24 space weather conditions at Mars. *Journal of Geophysical Research: Space Physics*, 122(3):2768–2794.

Lee, C. O., Jakosky, B. M., Luhmann, J. G., Brain, D. A., Mays, M. L., Hassler, D. M., Holmström, M., Larson, D. E., Mitchell, D. L., Mazelle, C., and Halekas, J. S. (2018). Observations and Impacts of the 10 September 2017 Solar Events at Mars: An Overview and Synthesis of the Initial Results. *Geophysical Research Letters*, 45(17):8871–8885.

Lefèvre, F. and Krasnopolsky, V. (2017). Atmospheric Photochemistry. In Haberle, R. M., Clancy, R. T., Forget, F., Smith, M. D., and Zurek, R. W., editors, *The Atmosphere and Climate of Mars*, pages 405–432. Cambridge University Press, 1 edition.

Leighton, R. B. and Murray, B. C. (1966). Behavior of Carbon Dioxide and Other Volatiles on Mars: A thermal model of the Martian surface suggests that Mars's polar caps are solid carbon dioxide. *Science*, 153(3732):136–144.

Lellouch, E., Encrenaz, T., de Graauw, T., Erard, S., Morris, P., Crovisier, J., Feuchtgruber, H., Girard, T., and Burgdorf, M. (2000). The 2.4– spectrum of Mars observed with the infrared space observatory. *Planetary and Space Science*, 48(12-14):1393–1405.

Lemmon, M. T., Smith, M. D., Viudez-Moreiras, D., De La Torre-Juarez, M., Vicente-Retortillo, A., Munguira, A., Sanchez-Lavega, A., Hueso, R., Martinez, G., Chide, B., Sullivan, R., Toledo, D., Tamppari, L., Bertrand, T., Bell, J. F., Newman, C., Baker, M., Banfield, D., Rodriguez-Manfredi, J. A., Maki, J. N., and Apestigue, V. (2022). Dust, Sand, and Winds Within an Active Martian Storm in Jezero Crater. *Geophysical Research Letters*, 49(17).

Lemmon, M. T., Wolff, M. J., Smith, M. D., Clancy, R. T., Banfield, D., Landis, G. A., Ghosh, A., Smith, P. H., Spanovich, N., Whitney, B., Whelley, P., Greeley, R., Thompson, S., Bell, J. F., and Squyres, S. W. (2004). Atmospheric Imaging Results from the Mars Exploration Rovers: Spirit and Opportunity. *Science*, 306(5702):1753–1756.

Leovy, C. B. and Zurek, R. W. (1979). Thermal tides and Martian dust storms: Direct evidence for coupling. *Journal of Geophysical Research*, 84(B6):2956.

Leovy, C. E., Zurek, R. W., and Pollack, J. B. (1973). Mechanisms for Mars Dust Storms. *Journal of the Atmospheric Sciences*, 30(5):749–762.

Lester, M., Sanchez-Cano, B., Potts, D., Lillis, R., Cartacci, M., Bernardini, F., Orosei, R., Perry, M., Putzig, N., Campbell, B., Blelly, P., Milan, S., Opgenoorth, H., Witasse, O., Redrojo, E. M. M., and Russell, A. (2022). The Impact of Energetic Particles on the Martian Ionosphere During a Full Solar Cycle of Radar Observations: Radar Blackouts. *Journal of Geophysical Research: Space Physics*, 127(2).

Lillis, R. J., Brain, D. A., Bougher, S. W., Leblanc, F., Luhmann, J. G., Jakosky, B. M., Modolo, R., Fox, J., Deighan, J., Fang, X., Wang, Y. C., Lee, Y., Dong, C., Ma, Y., Cravens, T., Andersson, L., Curry, S. M., Schneider, N., Combi, M., Stewart, I., Clarke, J., Grebowsky, J., Mitchell, D. L., Yelle, R., Nagy, A. F., Baker, D., and Lin, R. P. (2015). Characterizing Atmospheric Escape from Mars Today and Through Time, with MAVEN. *Space Science Reviews*, 195(1-4):357–422.

Lillis, R. J., Deighan, J., Brain, D., Fillingim, M., Jain, S., Chaffin, M., England, S., Holsclaw, G., Chirakkil, K., Al Matroushi, H., Lootah, F., Al Mazmi, H., Thiemann, E., Eparvier, F., Schneider, N., and Curry, S. (2022). First Synoptic Images of FUV Discrete Aurora and Discovery of Sinuous Aurora at Mars by EMM EMUS. *Geophysical Research Letters*, 49(16).

Lillis, R. J., Frey, H. V., Manga, M., Mitchell, D. L., Lin, R. P., Acuña, M. H., and Bougher, S. W. (2008). An improved crustal magnetic field map of Mars from electron reflectometry: Highland volcano magmatic history and the end of the martian dynamo. *Icarus*, 194(2):575–596.

Livshits, M. A., Zimovets, I. V., Golovin, D. V., Nizamov, B. A., Vybornov, V. I., Mitrofanov, I. G., Kozyrev, A. S., Litvak, M. L., Sanin, A. B., and Tretyakov, V. I. (2017). Catalog of hard X-ray solar flares detected with Mars Odyssey/HEND from the Mars orbit in 2001–2016. *Astronomy Reports*, 61(9):791–804.

Madeleine, J.-B., Forget, F., Millour, E., Montabone, L., and Wolff, M. J. (2011). Revisiting the radiative impact of dust on Mars using the LMD Global Climate Model. *Journal of Geophysical Research*, 116(E11):E11010.

Madeleine, J.-B., Forget, F., Millour, E., Navarro, T., and Spiga, A. (2012). The influence of radiatively active water ice clouds on the Martian climate: RADIATIVE EFFECT OF MARTIAN CLOUDS. *Geophysical Research Letters*, 39(23):n/a–n/a.

Maghradze, D. A., Chargeishvili, B. B., Japaridze, D. R., Oghrapishvili, N. B., and Chargeishvili, K. B. (2022). Long-term variation of coronal holes latitudinal distribution. *Monthly Notices of the Royal Astronomical Society*, 511(4):5217–5224.

Maguire, W. C. (1977). Martian isotopic ratios and upper limits for possible minor constituents as derived from Mariner 9 infrared spectrometer data. *Icarus*, 32(1):85–97.

Maltagliati, L., Montmessin, F., Fedorova, A., Korablev, O., Forget, F., and Bertaux, J.-L. (2011a). Evidence of Water Vapor in Excess of Saturation in the Atmosphere of Mars. *Science*, 333(6051):1868–1871.

Maltagliati, L., Montmessin, F., Korablev, O., Fedorova, A., Forget, F., Määttänen, A., Lefèvre, F., and Bertaux, J.-L. (2013). Annual survey of water vapor vertical distribution and water–aerosol coupling in the martian atmosphere observed by SPICAM/MEx solar occultations. *Icarus*, 223(2):942–962.

Maltagliati, L., Titov, D. V., Encrenaz, T., Melchiorri, R., Forget, F., Keller, H. L., and Bibring, J.-P. (2011b). Annual survey of water vapor behavior from the OMEGA mapping spectrometer onboard Mars Express. *Icarus*, 213(2):480–495.

Mandon, L., Quantin-Nataf, C., Royer, C., Beck, P., Fouchet, T., Johnson, J. R., Dehouck, E., Le Mouélic, S., Poulet, F., Montmessin, F., Pilorget, C., Gasnault, O., Forni, O., Mayhew, L. E., Beyssac, O., Bertrand, T., Clavé, E., Pinet, P., Brown, A. J., Legett, C., Tarnas, J., Cloutis, E. A., Poggiali, G., Fornaro, T., Maurice, S., Wiens, R. C., and The SuperCam Team (2023). Reflectance of Jezero Crater Floor: 2. Mineralogical Interpretation. *Journal of Geophysical Research: Planets*, 128(7):e2022JE007450.

Marinova, M. M., Aharonson, O., and Asphaug, E. (2008). Mega-impact formation of the Mars hemispheric dichotomy. *Nature*, 453(7199):1216–1219.

Marov, M. and Petrov, G. (1973). Investigations of Mars from the Soviet automatic stations Mars 2 and 3. *Icarus*, 19(2):163–179.

Martínez, G. M., Newman, C. N., De Vicente-Retortillo, A., Fischer, E., Renno, N. O., Richardson, M. I., Fairén, A. G., Genzer, M., Guzewich, S. D., Haberle, R. M., Harri, A.-M., Kemppinen, O., Lemmon, M. T., Smith, M. D., de la Torre-Juárez, M., and Vasavada, A. R. (2017). The Modern Near-Surface Martian Climate: A Review of In-situ Meteorological Data from Viking to Curiosity. *Space Science Reviews*, 212(1-2):295–338.

Masursky, H. (1973). An overview of geological results from Mariner 9. *Journal of Geophysical Research*, 78(20):4009–4030.

Maurice, S., Wiens, R. C., Bernardi, P., Caïs, P., Robinson, S., Nelson, T., Gasnault, O., Reess, J.-M., Deleuze, M., Rull, F., Manrique, J.-A., Abbaki, S., Anderson, R. B., André, Y., Angel, S. M., Arana, G., Battault, T., Beck, P., Benzerara, K., Bernard, S., Berthias, J.-P., Beyssac, O., Bonafous, M., Bousquet, B., Boutillier, M., Cadu, A., Castro, K., Chapron, F., Chide, B., Clark, K., Clavé, E., Clegg, S., Cloutis, E., Collin, C., Cordoba, E. C., Cousin, A., Dameury, J.-C., D'Anna, W., Daydou, Y., Debus, A., Deflores, L., Dehouck, E., Delapp, D., De Los Santos, G., Donny, C., Doressoundiram, A., Dromart, G., Dubois, B., Dufour, A., Dupieux, M., Egan, M., Ervin, J., Fabre, C., Fau, A., Fischer, W., Forni, O., Fouchet, T., Frydenvang, J., Gauffre, S., Gauthier, M., Gharakanian, V., Gilard, O., Gontijo, I., Gonzalez, R., Granena, D., Grotzinger, J., Hassen-Khodja, R., Heim, M., Hello, Y., Hervet, G., Humeau, O., Jacob, X., Jacquinod, S., Johnson, J. R., Kouach, D., Lacombe, G., Lanza, N., Lapauw, L., Laserna, J., Lasue, J., Le Deit, L., Le Mouélic, S., Le Comte, E., Lee, Q.-M., Legett, C., Leveille, R., Lewin, E., Leyrat, C., Lopez-Reyes, G., Lorenz, R., Lucero, B., Madariaga, J. M., Madsen, S., Madsen, M., Mangold, N., Manni, F., Mariscal, J.-F., Martinez-Frias, J., Mathieu, K., Mathon, R., McCabe, K. P., McConnochie, T., McLennan, S. M., Mekki, J., Melikechi, N., Meslin, P.-Y., Micheau, Y., Michel, Y., Michel, J. M., Mimoun, D., Misra, A., Montagnac, G., Montaron, C., Montmessin, F., Moros, J., Mousset, V., Morizet, Y., Murdoch, N., Newell, R. T., Newsom, H., Nguyen Tuong, N., Ollila, A. M., Orttner, G., Oudda, L., Pares, L., Parisot, J., Parot, Y., Pérez, R., Pheav, D., Picot, L., Pilleri, P., Pilorget, C., Pinet, P., Pont, G., Poulet, F., Quantin-Nataf, C., Quertier, B., Rambaud, D., Rapin, W., Romano, P., Roucayrol, L., Royer, C., Ruellan, M., Sandoval, B. F., Sautter, V., Schoppers, M. J., Schröder, S., Seran, H.-C., Sharma, S. K., Sobron, P., Sodki, M., Sournac, A., Sridhar, V., Standarovsky, D., Storms, S., Striebig, N., Tatat, M., Toplis, M., Torre-Fdez, I., Toulemont, N., Velasco, C., Veneranda, M., Venhaus, D., Virmontois, C., Viso, M., Willis, P., and Wong, K. W. (2021). The SuperCam Instrument Suite on the Mars 2020 Rover: Science Objectives and Mast-Unit Description. *Space Science Reviews*, 217(3):47.

McCleese, D. J., Heavens, N. G., Schofield, J. T., Abdou, W. A., Bandfield, J. L., Calcutt, S. B., Irwin, P. G. J., Kass, D. M., Kleinböhl, A., Lewis, S. R., Paige, D. A., Read, P. L., Richardson, M. I., Shirley, J. H., Taylor, F. W., Teanby, N., and Zurek, R. W. (2010). Structure and dynamics of the Martian lower and middle atmosphere as observed by the Mars Climate Sounder: Seasonal variations in zonal mean temperature, dust, and water ice aerosols. *Journal of Geophysical Research*, 115(E12):E12016.

McConnochie, T. H., Smith, M. D., Wolff, M. J., Bender, S., Lemmon, M., Wiens, R. C., Maurice, S., Gasnault, O., Lasue, J., Meslin, P.-Y., Harri, A.-M., Genzer, M., Kemppinen, O., Martínez, G. M., DeFlores, L., Blaney, D., Johnson, J. R., and Bell, J. F. (2018). Retrieval of water vapor column abundance and aerosol properties from ChemCam passive sky spectroscopy. *Icarus*, 307:294–326.

McConnochie, T. H., Trainer, M. G., Smith, M. D., Guzewich, S. D., Franz, H. B., Newman, C. E., Lo, D. Y., Atreya, S., Moores, J. E., Sapers, H. M., Lemmon, M. T., Wolff, M. J., Montmessin, F., Knutsen, E. W., Fouchet, T., Bertrand, T., Gasnault, O., Lasue, J., Forni, O., Pilleri, P., Maurice, S., Legett, Iv, C., Newell, R. T., Venhaus, D., Lanza, N., Wiens, R. C., Hecht, M., Zorzano, M. P., Khayat, A., Lefèvre, F., Daerden, F., Fedorova, A., and Trokhimovskiy, A. (2022). Unexplained Oxygen Variability: New Results on Molecular Oxygen in the Lower Martian Atmosphere from Chemcam and Supercam Passive Sky Observations. Conference Name: Seventh International Workshop on the Mars Atmosphere: Modelling and Observations Pages: 3403 ADS Bibcode: 2022mamo.conf.3403M.

McDonald, F. B., Ferrando, P., Heber, B., Kunow, H., McGuire, R., Müller-Mellin, R., Paizis, C., Raviart, A., and Wibberenz, G. (1997). A comparative study of cosmic ray radial and latitudinal gradients in the inner and outer heliosphere. *Journal of Geophysical Research: Space Physics*, 102(A3):4643–4651.

McElroy, M. B. and Donahue, T. M. (1972). Stability of the Martian Atmosphere. *Science*, 177(4053):986–988.

Melchiorri, R., Encrenaz, T., Drossart, P., Fouchet, T., Forget, F., Titov, D., Maltagliati, L., Altieri, F., Vincendon, M., Langevin, Y., and Bibring, J. (2009). OMEGA/Mars Express: South Pole Region, water vapor daily variability. *Icarus*, 201(1):102–112.

Melosh, H. J. and Vickery, A. M. (1989). Impact erosion of the primordial atmosphere of Mars. *Nature*, 338(6215):487–489.

Menzel, D. H. (1926). The Atmosphere of Mars. *The Astrophysical Journal*, 63:48.

Michelangeli, D. V., Toon, O. B., Haberle, R. M., and Pollack, J. B. (1993). Numerical Simulations of the Formation and Evolution of Water Ice Clouds in the Martian Atmosphere. *Icarus*, 102(2):261–285.

Millour, E., Forget, F., Spiga, A., Vals, M., Zakharov, V., and Montabone, L. (2018). The Mars climate database (version 5.3). *Paper pre- sented at the Mars Science Workshop "From Mars Express to ExoMars", held 27-28 February 2018 at ESAC, Spain, id.68.*

Mischna, M. A., Baker, V., Milliken, R., Richardson, M., and Lee, C. (2013). Effects of obliquity and water vapor/trace gas greenhouses in the early martian climate: OBLIQUITY/TRACE GAS GREENHOUSES ON MARS. *Journal of Geophysical Research: Planets*, 118(3):560–576.

Mitchell, D. L., Lillis, R. J., Lin, R. P., Connerney, J. E. P., and Acuña, M. H. (2007). A global map of Mars' crustal magnetic field based on electron reflectometry. *Journal of Geophysical Research*, 112(E1):E01002.

Mitchell, D. M., Montabone, L., Thomson, S., and Read, P. L. (2015). Polar vortices on Earth and Mars: A comparative study of the climatology and variability from reanalyses. *Quarterly Journal of the Royal Meteorological Society*, 141(687):550–562.

Modzelewska, R., Iskra, K., Wozniak, W., Siluszyk, M., and Alania, M. V. (2019). Features of the Galactic Cosmic Ray Anisotropy in Solar Cycle 24 and Solar Minima 23/24 and 24/25. *Solar Physics*, 294(10):148.

Montabone, L., Forget, F., Millour, E., Wilson, R., Lewis, S., Cantor, B., Kass, D., Kleinböhl, A., Lemmon, M., Smith, M., and Wolff, M. (2015). Eight-year climatology of dust optical depth on Mars. *Icarus*, 251:65–95.

Montmessin, F., Belyaev, D. A., Lefèvre, F., Alday, J., Vals, M., Fedorova, A. A., Korablev, O. I., Trokhimovskiy, A. V., Chaffin, M. S., and Schneider, N. M. (2022). Reappraising the Production and Transfer of Hydrogen Atoms From the Middle to the Upper Atmosphere of Mars at Times of Elevated Water Vapor. *Journal of Geophysical Research: Planets*, 127(5):e2022JE007217.

Montmessin, F. and Ferron, S. (2019). A spectral synergy method to retrieve martian water vapor column-abundance and vertical distribution applied to Mars Express SPICAM and PFS nadir measurements. *Icarus*, 317:549–569.

Montmessin, F., Forget, F., Rannou, P., Cabane, M., and Haberle, R. M. (2004). Origin and role of water ice clouds in the Martian water cycle as inferred from a general circulation model. *Journal of Geophysical Research*, 109(E10):E10004.

Montmessin, F., Gondet, B., Bibring, J.-P., Langevin, Y., Drossart, P., Forget, F., and Fouchet, T. (2007). Hyperspectral imaging of convective CO $_2$ ice clouds in the equatorial mesosphere of Mars. *Journal of Geophysical Research*, 112(E11):E11S90.

Montmessin, F., Korablev, O. I., Trokhimovskiy, A., Lefèvre, F., Fedorova, A. A., Baggio, L., Irbah, A., Lacombe, G., Olsen, K. S., Braude, A. S., Belyaev, D. A., Alday, J., Forget, F., Daerden, F., Pla-Garcia, J., Rafkin, S., Wilson, C. F., Patrakeev, A., Shakun, A., and Bertaux, J. L. (2021). A stringent upper limit of 20 pptv for methane on Mars and constraints on its dispersion outside Gale crater. *Astronomy & Astrophysics*, 650:A140.

Montmessin, F. and Määttänen, A. (2018). Temperature, Clouds, and Aerosols in the Terrestrial Bodies of the Solar System. In Deeg, H. J. and Belmonte, J. A., editors, *Handbook of Exoplanets*, pages 1–29. Springer International Publishing, Cham.

Montmessin, F., Quémerais, E., Bertaux, J. L., Korablev, O., Rannou, P., and Lebonnois, S. (2006). Stellar occultations at UV wavelengths by the SPICAM instrument: Retrieval and analysis of Martian haze profiles. *Journal of Geophysical Research*, 111(E9):E09S09.

Montmessin, F., Smith, M. D., Langevin, Y., Mellon, M. T., and Fedorova, A. (2017). The Water Cycle. In *The Atmosphere and Climate of Mars*, pages 338–373. Cambridge University Press, Cambridge.

Morris, R. V., Ruff, S. W., Gellert, R., Ming, D. W., Arvidson, R. E., Clark, B. C., Golden, D. C., Siebach, K., Klingelhöfer, G., Schröder, C., Fleischer, I., Yen, A. S., and Squyres, S. W. (2010). Identification of Carbonate-Rich Outcrops on Mars by the Spirit Rover. *Science*, 329(5990):421–424.

Muirhead, B. K., Nicholas, A., and Umland, J. (2020). Mars Sample Return Mission Concept Status. In *2020 IEEE Aerospace Conference*, pages 1–8, Big Sky, MT, USA. IEEE.

Mumma, M. J., Novak, R. E., Bonev, B. P., and DiSanti, M. (2003). A sensitive search for methane on Mars. In *Bulletin of the American Astronomical Society*, volume 35. Bulletin of the American Astronomical Society.

Mumma, M. J., Villanueva, G. L., Novak, R. E., Hewagama, T., Bonev, B. P., DiSanti, M. A., Mandell, A. M., and Smith, M. D. (2009). Strong Release of Methane on Mars in Northern Summer 2003. *Science*, 323(5917):1041–1045.

Murchie, S. L., Mustard, J. F., Ehlmann, B. L., Milliken, R. E., Bishop, J. L., McKeown, N. K., Noe Dobrea, E. Z., Seelos, F. P., Buczkowski, D. L., Wiseman, S. M., Arvidson, R. E., Wray, J. J., Swayze, G., Clark, R. N., Des Marais, D. J., McEwen, A. S., and Bibring, J.-P. (2009). A synthesis of Martian aqueous mineralogy after 1 Mars year of observations from the Mars Reconnaissance Orbiter. *Journal of Geophysical Research*, 114:E00D06.

Määttänen, A., Lefèvre, F., Verdier, L., Montmessin, F., Listowski, C., Guilbon, S., Fedorova, A., and Korablev, O. (2022). Ozone vertical distribution in Mars Years 27–30 from SPICAM/MEX UV occultations. *Icarus*, 387:115162.

Määttänen, A., Montmessin, F., Gondet, B., Scholten, F., Hoffmann, H., González-Galindo, F., Spiga, A., Forget, F., Hauber, E., Neukum, G., Bibring, J.-P., and Bertaux, J.-L. (2010). Mapping the mesospheric CO2 clouds on Mars: MEx/OMEGA and MEx/HRSC observations and challenges for atmospheric models. *Icarus*, 209(2):452–469.

Nair, H., Allen, M., Anbar, A. D., Yung, Y. L., and Clancy, R. (1994). A Photochemical Model of the Martian Atmosphere. *Icarus*, 111(1):124–150.

Nakamura, Y., Terada, N., Leblanc, F., Rahmati, A., Nakagawa, H., Sakai, S., Hiruba, S., Kataoka, R., and Murase, K. (2022). Modeling of Diffuse Auroral Emission at Mars: Contribution of MeV Protons. *Journal of Geophysical Research: Space Physics*, 127(1).

Navarro, T., Madeleine, J.-B., Forget, F., Spiga, A., Millour, E., Montmessin, F., and Määttänen, A. (2014). Global climate modeling of the Martian water cycle with improved microphysics and radiatively active water ice clouds. *Journal of Geophysical Research: Planets*, 119(7):1479–1495.

Neary, L., Daerden, F., Aoki, S., Whiteway, J., Clancy, R. T., Smith, M., Viscardy, S., Erwin, J., Thomas, I. R., Villanueva, G., Liuzzi, G., Crismani, M., Wolff, M., Lewis, S. R., Holmes, J. A., Patel, M. R., Giuranna, M., Depiesse, C., Piccialli, A., Robert, S., Trompet, L., Willame, Y., Ristic, B., and Vandaele, A. C. (2020). Explanation for the Increase in High-Altitude Water on Mars Observed by NOMAD During the 2018 Global Dust Storm. *Geophysical Research Letters*, 47(7).

Neugebauer, G., Miinch, G., Kieffer, H., Chase, Jr., S. C., and Miner, E. (1971). Mariner 1969 Infrared Radiometer Results: Temperatures and Thermal Properties of the Martian Surface. *The Astronomical Journal*, 76:719.

Neukum, G., Jaumann, R., Hoffmann, H., Hauber, E., Head, J. W., Basilevsky, A. T., Ivanov, B. A., Werner, S. C., van Gasselt, S., Murray, J. B., McCord, T., and Team, T. H. C.-I. (2004). Recent and episodic volcanic and glacial activity on Mars revealed by the High Resolution Stereo Camera. *Nature*, 432(7020):971–979.

Newman, C. E., Lewis, S. R., Read, P. L., and Forget, F. (2002). Modeling the Martian dust cycle, 1. Representations of dust transport processes: MODELING THE MARTIAN DUST CYCLE, 1. *Journal of Geophysical Research: Planets*, 107(E12):6–1–6–18.

Oehler, D. Z. and Etiope, G. (2017). Methane Seepage on Mars: Where to Look and Why. *Astrobiology*, 17(12):1233–1264.

Ojha, L., Wilhelm, M. B., Murchie, S. L., McEwen, A. S., Wray, J. J., Hanley, J., Massé, M., and Chojnacki, M. (2015). Spectral evidence for hydrated salts in recurring slope lineae on Mars. *Nature Geoscience*, 8(11):829–832.

Olsen, K. S., Trokhimovskiy, A., Montabone, L., Fedorova, A. A., Luginin, M., Lefèvre, F., Korablev, O. I., Montmessin, F., Forget, F., Millour, E., Bierjon, A., Baggio, L., Alday, J., Wilson, C. F., Irwin, P. G. J., Belyaev, D. A., Patrakeev, A., and Shakun, A. (2021). Seasonal reappearance of HCl in the atmosphere of Mars during the Mars year 35 dusty season. *Astronomy & Astrophysics*, 647:A161.

Orosei, R., Lauro, S. E., Pettinelli, E., Cicchetti, A., Coradini, M., Cosciotti, B., Di Paolo, F., Flamini, E., Mattei, E., Pajola, M., Soldovieri, F., Cartacci, M., Cassenti, F., Frigeri, A., Giuppi, S., Martufi, R., Masdea, A., Mitri, G., Nenna, C., Noschese, R., Restano, M., and Seu, R. (2018). Radar evidence of subglacial liquid water on Mars. *Science*, 361(6401):490–493.

Owen, T., Biemann, K., Rushneck, D. R., Biller, J. E., Howarth, D. W., and Lafleur, A. L. (1977). The composition of the atmosphere at the surface of Mars. *Journal of Geophysical Research*, 82(28):4635–4639.

Owen, T., Maillard, J. P., De Bergh, C., and Lutz, B. L. (1988). Deuterium on Mars: The Abundance of HDO and the Value of D/H. *Science*, 240(4860):1767–1767.

Oyama, V. I., Berdahl, B. J., Carle, G. C., Lehwalt, M. E., and Ginoza, H. S. (1976). The search for life on Mars: Viking 1976 gas changes as indicators of biological activity. *Origins of Life*, 7(3):313–333.

Pan, L., Edwards, D. P., Gille, J. C., Smith, M. W., and Drummond, J. R. (1995). Satellite remote sensing of tropospheric CO and CH_4: forward model studies of the MOPITT instrument. *Applied Optics*, 34(30):6976.

Pan, L., Gille, J. C., Edwards, D. P., Bailey, P. L., and Rodgers, C. D. (1998). Retrieval of tropospheric carbon monoxide for the MOPITT experiment. *Journal of Geophysical Research: Atmospheres*, 103(D24):32277–32290.

Pankine, A. A., Tamppari, L. K., and Smith, M. D. (2010). MGS TES observations of the water vapor above the seasonal and perennial ice caps during northern spring and summer. *Icarus*, 210(1):58–71.

Parish, H. F., Schubert, G., Hickey, M. P., and Walterscheid, R. L. (2009). Propagation of tropospheric gravity waves into the upper atmosphere of Mars. *Icarus*, 203(1):28–37.

Parker, E. (1958). Suprathermal Particle Generation in the Solar Corona. *The Astrophysical Journal*, 128:677.

Parkinson, T. D. and Hunten, D. M. (1972). Spectroscopy and Acronomy of O $_2$ on Mars. *Journal of the Atmospheric Sciences*, 29(7):1380–1390.

Pearl, J. C., Smith, M. D., Conrath, B. J., Bandfield, J. L., and Christensen, P. R. (2001). Observations of Martian ice clouds by the Mars Global Surveyor Thermal Emission Spectrometer: The first Martian year. *Journal of Geophysical Research: Planets*, 106(E6):12325–12338.

Pepin, R. O. (1994). Evolution of the Martian Atmosphere. *Icarus*, 111(2):289–304.

Piqueux, S., Byrne, S., Kieffer, H. H., Titus, T. N., and Hansen, C. J. (2015a). Enumeration of Mars years and seasons since the beginning of telescopic exploration. *Icarus*, 251:332–338.

Piqueux, S., Kleinböhl, A., Hayne, P. O., Kass, D. M., Schofield, J. T., and McCleese, D. J. (2015b). Variability of the martian seasonal CO2 cap extent over eight Mars Years. *Icarus*, 251:164–180.

Pollack, J. B., Colburn, D. S., Flasar, F. M., Kahn, R., Carlston, C. E., and Pidek, D. (1979). Properties and effects of dust particles suspended in the Martian atmosphere. *Journal of Geophysical Research*, 84(B6):2929.

Prasad, A., Roy, S., Sarkar, A., Chandra Panja, S., and Narayan Patra, S. (2022). Prediction of solar cycle 25 using deep learning based long short-term memory forecasting technique. *Advances in Space Research*, 69(1):798–813.

Rabkin, Y. M. (1987). Technological Innovation in Science: The Adoption of Infrared Spectroscopy by Chemists. *Isis*, 78(1):31–54.

Ramstad, R., Barabash, S., Futaana, Y., Yamauchi, M., Nilsson, H., and Holmström, M. (2017). Mars Under Primordial Solar Wind Conditions: Mars Express Observations of the Strongest CME Detected at Mars Under Solar Cycle #24 and its Impact on Atmospheric Ion Escape. *Geophysical Research Letters*, 44(21).

Razavi, A., Clerbaux, C., Wespes, C., Clarisse, L., Hurtmans, D., Payan, S., Camy-Peyret, C., and Coheur, P. F. (2009). Characterization of methane retrievals from the IASI space-borne sounder. *Atmospheric Chemistry and Physics*, 9(20):7889–7899.

Reames, D. V. (1999). Particle acceleration at the Sun and in the heliosphere. *Space Science Reviews*, 90(3/4):413–491.

Richardson, J. and Kasper, J. (2008). Solar cycle variations of solar wind dynamics and structures. *Journal of Atmospheric and Solar-Terrestrial Physics*, 70(2-4):219–225.

Richardson, J. D., Wang, C., and Paularena, K. I. (2001). The solar wind: from solar minimum to solar maximum. *Advances in Space Research*, 27(3):471–479.

Richardson, M. I. (2002). Investigation of the nature and stability of the Martian seasonal water cycle with a general circulation model. *Journal of Geophysical Research*, 107(E5):5031.

Richmond, A. and Roble, R. (1979). Dynamic effects of aurora-generated gravity waves on the mid-latitude ionosphere. *Journal of Atmospheric and Terrestrial Physics*, 41(7-8):841–852.

Robbrecht, E., Berghmans, D., and Van der Linden, R. A. M. (2009). AUTOMATED LASCO CME CATALOG FOR SOLAR CYCLE 23: ARE CMEs SCALE INVARIANT? *The Astrophysical Journal*, 691(2):1222–1234.

Rodgers, C. D. (2000). *Inverse Methods for Atmospheric Sounding: Theory and Practice*, volume 2 of *Series on Atmospheric, Oceanic and Planetary Physics*. WORLD SCIENTIFIC.

Rodin, A., Korablev, O., and Moroz, V. (1997). Vertical Distribution of Water in the Near-Equatorial Troposphere of Mars: Water Vapor and Clouds. *Icarus*, 125(1):212–229.

Ross, E. and Chaplin, W. J. (2019). The Behaviour of Galactic Cosmic-Ray Intensity During Solar Activity Cycle 24. *Solar Physics*, 294(1):8.

Rossi, L., Vals, M., Alday, J., Montmessin, F., Fedorova, A., Trokhimovskiy, A., Korablev, O., Lefèvre, F., Gonzalez-Galindo, F., Luginin, M., Bierjon, A., Forget, F., and Millour, E. (2022). The HDO Cycle on Mars: Comparison of ACS Observations With GCM Simulations. *Journal of Geophysical Research: Planets*, 127(8).

Rothman, L., Gordon, I., Babikov, Y., Barbe, A., Chris Benner, D., Bernath, P., Birk, M., Bizzocchi, L., Boudon, V., Brown, L., Campargue, A., Chance, K., Cohen, E., Coudert, L., Devi, V., Drouin, B., Fayt, A., Flaud, J.-M., Gamache, R., Harrison, J., Hartmann, J.-M., Hill, C., Hodges, J., Jacquemart, D., Jolly, A., Lamouroux, J., Le Roy, R., Li, G., Long, D., Lyulin, O., Mackie, C., Massie, S., Mikhailenko, S., Müller, H., Naumenko, O., Nikitin, A., Orphal, J., Perevalov, V., Perrin, A., Polovtseva, E., Richard, C., Smith, M., Starikova, E., Sung, K., Tashkun, S., Tennyson, J., Toon, G., Tyuterev, V., and Wagner, G. (2013). The HITRAN2012 molecular spectroscopic database. *Journal of Quantitative Spectroscopy and Radiative Transfer*, 130:4–50.

Royer, C., Fouchet, T., Mandon, L., Montmessin, F., Poulet, F., Forni, O., Johnson, J. R., Legett, C., Le Mouélic, S., Gasnault, O., Quantin-Nataf, C., Beck, P., Dehouck, E., Clavé, E., Ollila, A. M., Pilorget, C., Bernardi, P., Reess, J., Pilleri, P., Brown, A., Newell, R. T., Cloutis, E., Maurice, S., Wiens, R. C., and The SuperCam Team (2023). Reflectance of Jezero Crater Floor: 1. Data Processing and Calibration of the Infrared Spectrometer (IRS) on SuperCam. *Journal of Geophysical Research: Planets*, 128(1).

Royer, C., Poulet, F., Reess, J.-M., Pilorget, C., Hamm, V., Fouchet, T., Maurice, S., Forni, O., Bernardi, P., Montmessin, F., Lapauw, L., Parisot, J., Bonafous, M., Gasnault, O., and Wiens, R. C. (2020). Pre-launch radiometric calibration of the infrared spectrometer onboard SuperCam for the Mars2020 rover. *Review of Scientific Instruments*, 91(6):063105.

Ryan, J. A., Henry, R. M., Hess, S. L., Leovy, C. B., Tillman, J. E., and Walcek, C. (1978). Mars meteorology: Three seasons at the surface. *Geophysical Research Letters*, 5(8):715–718.

Ryan, J. A., Sharman, R. D., and Lucich, R. D. (1982). Mars water vapor, near-surface. *Journal of Geophysical Research*, 87(C9):7279.

Sachs, A. (1974). Babylonian observational astronomy. *Philosophical Transactions of the Royal Society of London. Series A, Mathematical and Physical Sciences*, 276(1257):43–50.

Salese, F., Di Achille, G., Neesemann, A., Ori, G. G., and Hauber, E. (2016). Hydrological and sedimentary analyses of well-preserved paleofluvial-paleolacustrine systems at Moa Valles, Mars: FLUVIAL SYSTEMS AT MOA VALLES, MARS. *Journal of Geophysical Research: Planets*, 121(2):194–232.

Saunders, R., Arvidson, R., Badhwar, G., Boynton, W., Christensen, P., Cucinotta, F., Feldman, W., Gibbs, R., Kloss Jr., C., Landano, M., Mase, R., McSmith, G., Meyer, M., Mitrofanov, I., Pace, G., Plaut, J., Sidney, W., Spencer, D., Thompson, T., and Zeitlin, C. (2004). 2001 Mars Odyssey Mission Summary. *Space Science Reviews*, 110(1/2):1–36.

Savijärvi, H. and Harri, A.-M. (2021). Water vapor adsorption on Mars. *Icarus*, 357:114270.

Schneider, N. M., Deighan, J. I., Jain, S. K., Stiepen, A., Stewart, A. I. F., Larson, D., Mitchell, D. L., Mazelle, C., Lee, C. O., Lillis, R. J., Evans, J. S., Brain, D., Stevens, M. H., McClintock, W. E., Chaffin, M. S., Crismani, M., Holsclaw, G. M., Lefevre, F., Lo, D. Y., Clarke, J. T., Montmessin, F., and Jakosky, B. M. (2015). Discovery of diffuse aurora on Mars. *Science*, 350(6261):aad0313.

Schneider, N. M., Jain, S. K., Deighan, J., Nasr, C. R., Brain, D. A., Larson, D., Lillis, R., Rahmati, A., Halekas, J. S., Lee, C. O., Chaffin, M. S., Stiepen, A., Crismani, M., Evans, J. S., Stevens, M. H., Lo, D. Y., McClintock, W. E., Stewart, A. I. F., Yelle, R. V., Clarke, J. T., Holsclaw, G. M., Lefevre, F., Montmessin, F., and Jakosky, B. M. (2018). Global Aurora on Mars During the September 2017 Space Weather Event. *Geophysical Research Letters*, 45(15):7391–7398.

Schulze-Makuch, D., Irwin, L. N., Lipps, J. H., LeMone, D., Dohm, J. M., and Fairén, A. G. (2005). Scenarios for the evolution of life on Mars. *Journal of Geophysical Research*, 110(E12):E12S23.

Schwenn, R. (2007). Solar Wind Sources and Their Variations over the Solar Cycle. In Baker, D. N., Klecker, B., Schwartz, S. J., Schwenn, R., and Von Steiger, R., editors, *Solar Dynamics and Its Effects on the Heliosphere and Earth*, volume 22, pages 51–76. Springer New York, New York, NY. Series Title: Space Sciences Series of ISSI.

Shaposhnikov, D. S., Medvedev, A. S., Rodin, A. V., and Hartogh, P. (2019). Seasonal Water "Pump" in the Atmosphere of Mars: Vertical Transport to the Thermosphere. *Geophysical Research Letters*, 46(8):4161–4169.

Sharaf, O., Amiri, S., AlDhafri, S., Withnell, P., and Brain, D. (2020). Sending hope to Mars. *Nature Astronomy*, 4(7):722–722.

Simon, J. I., Hickman-Lewis, K., Cohen, B. A., Mayhew, L. E., Shuster, D. L., Debaille, V., Hausrath, E. M., Weiss, B. P., Bosak, T., Zorzano, M., Amundsen, H. E. F., Beegle, L. W., Bell, J. F., Benison, K. C., Berger, E. L., Beyssac, O., Brown, A. J., Calef, F., Casademont, T. M., Clark, B., Clavé, E., Crumpler, L., Czaja, A. D., Fairén, A. G., Farley, K. A., Flannery, D. T., Fornaro, T., Forni, O., Gómez, F., Goreva, Y., Gorin, A., Hand, K. P., Hamran, S., Henneke, J., Herd, C. D. K., Horgan, B. H. N., Johnson, J. R., Joseph, J., Kronyak, R. E., Madariaga, J. M., Maki, J. N., Mandon, L., McCubbin, F. M., McLennan, S. M., Moeller, R. C., Newman, C. E., Núñez, J. I., Pascuzzo, A. C., Pedersen, D. A., Poggiali, G., Pinet, P., Quantin-Nataf, C., Rice, M., Rice, J. W., Royer, C., Schmidt, M., Sephton, M., Sharma, S., Siljeström, S., Stack, K. M., Steele, A., Sun, V. Z., Udry, A., VanBommel, S., Wadhwa, M., Wiens, R. C., Williams, A. J., and Williford, K. H. (2023). Samples Collected From the Floor of Jezero Crater With the Mars 2020 Perseverance Rover. *Journal of Geophysical Research: Planets*, 128(6):e2022JE007474.

Sindoni, G., Formisano, V., and Geminale, A. (2011). Observations of water vapour and carbon monoxide in the Martian atmosphere with the SWC of PFS/MEX. *Planetary and Space Science*, 59(2-3):149–162.

Singer, R. B., McCord, T. B., Clark, R. N., Adams, J. B., and Huguenin, R. L. (1979). Mars surface composition from reflectance spectroscopy: A summary. *Journal of Geophysical Research*, 84(B14):8415.

Sinnhuber, M., Berger, U., Funke, B., Nieder, H., Reddmann, T., Stiller, G., Versick, S., Von Clarmann, T., and Wissing, J. M. (2018). NOy production, ozone loss and changes in net radiative heating due to energetic particle precipitation in 2002–2010. *Atmospheric Chemistry and Physics*, 18(2):1115–1147.

Smith, D. E., Zuber, M. T., Solomon, S. C., Phillips, R. J., Head, J. W., Garvin, J. B., Banerdt, W. B., Muhleman, D. O., Pettengill, G. H., Neumann, G. A., Lemoine, F. G., Abshire, J. B., Aharonson, O., David, C., Brown, Hauck, S. A., Ivanov, A. B., McGovern, P. J., Zwally, H. J., and Duxbury, T. C. (1999). The Global Topography of Mars and Implications for Surface Evolution. *Science*, 284(5419):1495–1503.

Smith, M. D. (2002). The annual cycle of water vapor on Mars as observed by the Thermal Emission Spectrometer: MARS WATER VAPOR. *Journal of Geophysical Research: Planets*, 107(E11):25–1–25–19.

Smith, M. D. (2004). Interannual variability in TES atmospheric observations of Mars during 1999–2003. *Icarus*, 167(1):148–165.

Smith, M. D. (2008). Spacecraft Observations of the Martian Atmosphere. *Annual Review of Earth and Planetary Sciences*, 36(1):191–219.

Smith, M. D. (2009). THEMIS observations of Mars aerosol optical depth from 2002–2008. *Icarus*, 202(2):444–452.

Smith, M. D., Daerden, F., Neary, L., and Khayat, A. (2018). The climatology of carbon monoxide and water vapor on Mars as observed by CRISM and modeled by the GEM-Mars general circulation model. *Icarus*, 301:117–131.

Smith, M. D., Pearl, J. C., Conrath, B. J., and Christensen, P. R. (2001). Thermal Emission Spectrometer results: Mars atmospheric thermal structure and aerosol distribution. *Journal of Geophysical Research: Planets*, 106(E10):23929–23945.

Smith, M. D., Wolff, M. J., Clancy, R. T., and Murchie, S. L. (2009). Compact Reconnaissance Imaging Spectrometer observations of water vapor and carbon monoxide. *Journal of Geophysical Research*, 114:E00D03.

Smith, S. and Smith, B. (1972). Diurnal and seasonal behavior of discrete white clouds on Mars. *Icarus*, 16(3):509–521.

Snyder, C. W., Neugebauer, M., and Rao, U. R. (1963). The solar wind velocity and its correlation with cosmic-ray variations and with solar and geomagnetic activity. *Journal of Geophysical Research*, 68(24):6361–6370.

Soni, S. L., Selvakumaran, R., and Thampi, R. S. (2023). Assessment of the arrival signatures of the March 2012 CME–CME interaction event with respect to Mercury, Venus, Earth, STEREO-B, and Mars locations. *Frontiers in Astronomy and Space Sciences*, 9:1049906.

Soret, L., Gérard, J., Aoki, S., Gkouvelis, L., Thomas, I. R., Ristic, B., Hubert, B., Willame, Y., Depiesse, C., Vandaele, A. C., Patel, M. R., Mason, J. P., Daerden, F., López-Moreno, J., and Bellucci, G. (2022). The Mars Oxygen Visible Dayglow: A Martian Year of NOMAD/UVIS Observations. *Journal of Geophysical Research: Planets*, 127(6).

Soret, L., Gérard, J., Schneider, N., Jain, S., Milby, Z., Ritter, B., Hubert, B., and Weber, T. (2021). Discrete Aurora on Mars: Spectral Properties, Vertical Profiles, and Electron Energies. *Journal of Geophysical Research: Space Physics*, 126(10).

Spinrad, H., Münch, G., and Kaplan, L. D. (1963). Letter to the Editor: the Detection of Water Vapor on Mars. *The Astrophysical Journal*, 137:1319. ADS Bibcode: 1963ApJ...137.1319S.

Sprague, A. L., Boynton, W. V., Kerry, K. E., Janes, D. M., Kelly, N. J., Crombie, M. K., Nelli, S. M., Murphy, J. R., Reedy, R. C., and Metzger, A. E. (2007). Mars' atmospheric argon: Tracer for understanding Martian atmospheric circulation and dynamics. *Journal of Geophysical Research*, 112(E3):E03S02.

Stallard, T., Miller, S., Lystrup, M., Achilleos, N., Bunce, E. J., Arridge, C. S., Dougherty, M. K., Cowley, S. W. H., Badman, S. V., Talboys, D. L., Brown, R. H., Baines, K. H., Buratti, B. J., Clark, R. N., Sotin, C., Nicholson, P. D., and Drossart, P. (2008). Complex structure within Saturn's infrared aurora. *Nature*, 456(7219):214–217.

Steele, L. J., Lewis, S. R., Patel, M. R., Montmessin, F., Forget, F., and Smith, M. D. (2014). The seasonal cycle of water vapour on Mars from assimilation of Thermal Emission Spectrometer data. *Icarus*, 237:97–115.

Stone, S. W., Yelle, R. V., Benna, M., Lo, D. Y., Elrod, M. K., and Mahaffy, P. R. (2020). Hydrogen escape from Mars is driven by seasonal and dust storm transport of water. *Science*, 370(6518):824–831.

Sundararajan, V. (2013). Mangalyaan - Overview and Technical Architecture of India's First Interplanetary Mission to Mars. In *AIAA SPACE 2013 Conference and Exposition*, San Diego, CA. American Institute of Aeronautics and Astronautics.

Sánchez-Cano, B., Lester, M., Andrews, D. J., Opgenoorth, H., Lillis, R., Leblanc, F., Fowler, C. M., Fang, X., Vaisberg, O., Mayyasi, M., Holmberg, M., Guo, J., Hamrin, M., Mazelle, C., Peter, K., Pätzold, M., Stergiopoulou, K., Goetz, C., Ermakov, V. N., Shuvalov, S., Wild, J. A., Blelly, P.-L., Mendillo, M., Bertucci, C., Cartacci, M., Orosei, R., Chu, F., Kopf, A. J., Girazian, Z., and Roman, M. T. (2022). Mars' plasma system. Scientific potential of coordinated multipoint missions: "The next generation". *Experimental Astronomy*, 54(2-3):641–676.

Sánchez-Cano, B., Hall, B. E. S., Lester, M., Mays, M. L., Witasse, O., Ambrosi, R., Andrews, D., Cartacci, M., Cicchetti, A., Holmström, M., Imber, S., Kajdič, P., Milan, S. E., Noschese, R., Odstrcil, D., Opgenoorth, H., Plaut, J., Ramstad, R., and Reyes-Ayala, K. I. (2017). Mars plasma system response to solar wind disturbances during solar minimum. *Journal of Geophysical Research: Space Physics*, 122(6):6611–6634.

Sánchez-Cano, B., Witasse, O., Knutsen, E. W., Meggi, D., Viet, S., Lester, M., Wimmer-Schweingruber, R. F., Pinto, M., Moissl, R., Benkhoff, J., Opgenoorth, H., Auster, U., De Brujine, J., Collins, P., De Marchi, G., Fischer, D., Futaana, Y., Godfrey, J., Heyner, D., Holmstrom, M., Johnstone, A., Joyce, S., Lakey, D., Martinez, S., Milligan, D., Montagnon, E., Müller, D., Livi, S. A., Prusti, T., Raines, J., Richter, I., Schmid, D., Schmitz, P., Svedhem, H., Taylor, M. G. G. T., Tremolizzo, E., Titov, D., Wilson, C., Wood, S., and Zender, J. (2023). Solar Energetic Particle Events Detected in the Housekeeping Data of the European Space Agency's Spacecraft Flotilla in the Solar System. *Space Weather*, 21(8):e2023SW003540.

Tamppari, L. K., Bass, D., Cantor, B., Daubar, I., Dickinson, C., Fisher, D., Fujii, K., Gunnlaugsson, H. P., Hudson, T. L., Kass, D., Kleinböhl, A., Komguem, L., Lemmon, M. T., Mellon, M., Moores, J., Pankine, A., Pathak, J., Searls, M., Seelos, F., Smith, M. D., Smrekar, S., Taylor, P., Holstein-Rathlou, C., Weng, W., Whiteway, J., and Wolff, M. (2010). Phoenix and MRO coordinated atmospheric measurements. *Journal of Geophysical Research*, 115:E00E17.

Tamppari, L. K. and Lemmon, M. T. (2020). Near-surface atmospheric water vapor enhancement at the Mars Phoenix lander site. *Icarus*, 343:113624.

Tanaka, K. L. (1986). The stratigraphy of Mars. *Journal of Geophysical Research*, 91(B13):E139.

The Pierre Auger Collaboration, Aab, A., Abreu, P., Aglietta, M., Al Samarai, I., Albuquerque, I. F. M., Allekotte, I., Almela, A., Alvarez Castillo, J., Alvarez-Muñiz, J., Anastasi, G. A., Anchordoqui, L., Andrada, B., Andringa, S., Aramo, C., Arqueros, F., Arsene, N., Asorey, H., Assis, P., Aublin, J., Avila, G., Badescu, A. M., Balaceanu, A., Barbato, F., Barreira Luz, R. J., Beatty, J. J., Becker, K. H., Bellido, J. A., Berat, C., Bertaina, M. E., Bertou, X., Biermann, P. L., Billoir, P., Biteau, J., Blaess, S. G., Blanco, A., Blazek, J., Bleve, C., Boháčová, M., Boncioli, D., Bonifazi, C., Borodai, N., Botti, A. M., Brack, J., Brancus, I., Bretz, T., Bridgeman, A., Briechle, F. L., Buchholz, P., Bueno, A., Buitink, S., Buscemi, M., Caballero-Mora, K. S., Caccianiga, L., Cancio, A., Canfora, F., Caramete, L., Caruso, R., Castellina, A., Cataldi, G., Cazon, L., Chavez, A. G., Chinellato, J. A., Chudoba, J., Clay, R. W., Cobos, A., Colalillo, R., Coleman, A., Collica, L., Coluccia, M. R., Conceição, R., Consolati, G., Contreras, F., Cooper, M. J., Coutu, S., Covault, C. E., Cronin, J., D'Amico, S., Daniel, B., Dasso, S., Daumiller, K., Dawson, B. R., de Almeida, R. M., de Jong,

S. J., De Mauro, G., de Mello Neto, J. R. T., De Mitri, I., de Oliveira, J., de Souza, V., Debatin, J., Deligny, O., Di Giulio, C., Di Matteo, A., Díaz Castro, M. L., Diogo, F., Dobrigkeit, C., D'Olivo, J. C., Dorosti, Q., dos Anjos, R. C., Dova, M. T., Dundovic, A., Ebr, J., Engel, R., Erdmann, M., Erfani, M., Escobar, C. O., Espadanal, J., Etchegoyen, A., Falcke, H., Farrar, G., Fauth, A. C., Fazzini, N., Fenu, F., Fick, B., Figueira, J. M., Filipčič, A., Fratu, O., Freire, M. M., Fujii, T., Fuster, A., Gaior, R., García, B., Garcia-Pinto, D., Gaté, F., Gemmeke, H., Gherghel-Lascu, A., Ghia, P. L., Giaccari, U., Giammarchi, M., Giller, M., Głas, D., Glaser, C., Golup, G., Gómez Berisso, M., Gómez Vitale, P. F., González, N., Gorgi, A., Gorham, P., Grillo, A. F., Grubb, T. D., Guarino, F., Guedes, G. P., Hampel, M. R., Hansen, P., Harari, D., Harrison, T. A., Harton, J. L., Haungs, A., Hebbeker, T., Heck, D., Heimann, P., Herve, A. E., Hill, G. C., Hojvat, C., Holt, E., Homola, P., Hörandel, J. R., Horvath, P., Hrabovský, M., Huege, T., Hulsman, J., Insolia, A., Isar, P. G., Jandt, I., Jansen, S., Johnsen, J. A., Josebachuili, M., Jurysek, J., Kääpä, A., Kambeitz, O., Kampert, K. H., Katkov, I., Keilhauer, B., Kemmerich, N., Kemp, E., Kemp, J., Kieckhafer, R. M., Klages, H. O., Kleifges, M., Kleinfeller, J., Krause, R., Krohm, N., Kuempel, D., Kukec Mezek, G., Kunka, N., Kuotb Awad, A., LaHurd, D., Lauscher, M., Legumina, R., de Oliveira, M. A. L., Letessier-Selvon, A., Lhenry-Yvon, I., Link, K., Lo Presti, D., Lopes, L., López, R., López Casado, A., Luce, Q., Lucero, A., Malacari, M., Mallamaci, M., Mandat, D., Mantsch, P., Mariazzi, A. G., Mariş, I. C., Marsella, G., Martello, D., Martinez, H., Martínez Bravo, O., Masías Meza, J. J., Mathes, H. J., Mathys, S., Matthews, J., Matthews, J. A. J., Matthiae, G., Mayotte, E., Mazur, P. O., Medina, C., Medina-Tanco, G., Melo, D., Menshikov, A., Merenda, K.-D., Michal, S., Micheletti, M. I., Middendorf, L., Miramonti, L., Mitrica, B., Mockler, D., Mollerach, S., Montanet, F., Morello, C., Mostafá, M., Müller, A. L., Müller, G., Muller, M. A., Müller, S., Mussa, R., Naranjo, I., Nellen, L., Nguyen, P. H., Niculescu-Oglinzanu, M., Niechciol, M., Niemietz, L., Niggemann, T., Nitz, D., Nosek, D., Novotny, V., Nožka, L., Núñez, L. A., Ochilo, L., Oikonomou, F., Olinto, A., Palatka, M., Pallotta, J., Papenbreer, P., Parente, G., Parra, A., Paul, T., Pech, M., Pedreira, F., Pkala, J., Pelayo, R., Peña-Rodriguez, J., Pereira, L. A. S., Perlín, M., Perrone, L., Peters, C., Petrera, S., Phuntsok, J., Piegaia, R., Pierog, T., Pieroni, P., Pimenta, M., Pirronello, V., Platino, M., Plum, M., Porowski, C., Prado, R. R., Privitera, P., Prouza, M., Quel, E. J., Querchfeld, S., Quinn, S., Ramos-Pollan, R., Rautenberg, J., Ravignani, D., Revenu, B., Ridky, J., Riehn, F., Risse, M., Ristori, P., Rizi, V., de Carvalho, W. R., Rodriguez Fernandez, G., Rodriguez Rojo, J., Rogozin, D., Roncoroni, M. J., Roth, M., Roulet, E., Rovero, A. C., Ruehl, P., Saffi, S. J., Saftoiu, A., Salamida, F., Salazar, H., Saleh, A., Salesa Greus, F., Salina, G., Sánchez, F., Sanchez-Lucas, P., Santos, E. M., Santos, E., Sarazin, F., Sarmento, R., Sarmiento, C. A., Sato, R., Schauer, M., Scherini, V., Schieler, H., Schimp, M., Schmidt, D., Scholten, O., Schovánek, P., Schröder, F. G., Schulz, A., Schumacher, J., Sciutto, S. J., Segreto, A., Settimo, M., Shadkam, A., Shellard, R. C., Sigl, G., Silli, G., Sima, O., Śmiałkowski, A., Šmída, R., Snow, G. R., Sommers, P., Sonntag, S., Sorokin, J., Squartini, R., Stanca, D., Stanič, S., Stasielak, J., Stassi, P., Strafella, F., Suarez, F., Suarez Durán, M., Sudholz, T., Suomijärvi, T., Supanitsky, A. D., Šupík, J., Swain, J., Szadkowski, Z., Taboada, A., Taborda, O. A., Tapia, A., Theodoro, V. M., Timmermans, C., Todero Peixoto, C. J., Tomankova, L., Tomé, B., Torralba Elipe, G., Travnicek, P., Trini, M., Ulrich, R., Unger, M., Urban, M., Valdés Galicia, J. F., Valiño, I., Valore, L., van Aar, G., van Bodegom, P., van den Berg, A. M., van Vliet, A., Varela, E., Vargas Cárdenas, B., Varner, G., Vázquez, R. A., Veberič, D., Ventura, C., Vergara Quispe, I. D., Verzi, V., Vicha, J., Villaseñor, L., Vorobiov, S., Wahlberg, H., Wainberg, O., Walz, D., Watson, A. A., Weber, M., Weindl, A., Wiencke, L., Wilczyński, H., Wirtz, M., Wittkowski, D., Wundheiler, B., Yang, L., Yushkov, A., Zas, E., Zavrtanik, D., Zavrtanik, M., Zepeda, A., Zimmermann, B., Ziolkowski, M., Zong, Z., and Zuccarello, F. (2017). Observation of a large-scale anisotropy in the arrival directions of cosmic rays above 8×10^{18} eV. *Science*, 357(6357):1266–1270.

Thomas, N. (1991). The early history of spectroscopy. *Journal of chemical education*, 68(8):631.

Théodore, B., Lellouch, E., Chassefière, E., and Hauchecorne, A. (1993). Solstitial Temperature Inversions in the Martian Middle Atmosphere: Observational Clues and 2-D Modeling. *Icarus*, 105(2):512–528.

Trainer, M. G., Wong, M. H., McConnochie, T. H., Franz, H. B., Atreya, S. K., Conrad, P. G., Lefèvre, F., Mahaffy, P. R., Malespin, C. A., Manning, H. L., Martín-Torres, J., Martínez, G. M., McKay, C. P., Navarro-González, R., Vicente-Retortillo, A., Webster, C. R., and Zorzano, M. (2019). Seasonal Variations in Atmospheric Composition as Measured in Gale Crater, Mars. *Journal of Geophysical Research: Planets*, 124(11):3000–3024.

Trokhimovskiy, A., Fedorova, A., Korablev, O., Montmessin, F., Bertaux, J.-L., Rodin, A., and Smith, M. D. (2015). Mars' water vapor mapping by the SPICAM IR spectrometer: Five martian years of observations. *Icarus*, 251:50–64.

Tschimmel, M., Ignatiev, N. I., Titov, D., Lellouch, E., Fouchet, T., Giuranna, M., and Formisano, V. (2008). Investigation of water vapor on Mars with PFS/SW of Mars Express. *Icarus*, 195(2):557–575.

Usoskin, I. G., Gil, A., Kovaltsov, G. A., Mishev, A. L., and Mikhailov, V. V. (2017). Heliospheric modulation of cosmic rays during the neutron monitor era: Calibration using PAMELA data for 2006-2010: MODULATION POTENTIAL FOR NM ERA. *Journal of Geophysical Research: Space Physics*, 122(4):3875–3887.

Usoskin, I. G., Kananen, H., Mursula, K., Tanskanen, P., and Kovaltsov, G. A. (1998). Correlative study of solar activity and cosmic ray intensity. *Journal of Geophysical Research: Space Physics*, 103(A5):9567–9574.

Vago, J., Witasse, O., Svedhem, H., Baglioni, P., Haldemann, A., Gianfiglio, G., Blancquaert, T., McCoy, D., and De Groot, R. (2015). ESA ExoMars program: The next step in exploring Mars. *Solar System Research*, 49(7):518–528.

Vals, M., Rossi, L., Montmessin, F., Lefèvre, F., Gonzalez-Galindo, F., Fedorova, A., Luginin, M., Forget, F., Millour, E., Korablev, O., Trokhimovskiy, A., Shakun, A., Bierjon, A., and Montabone, L. (2022). Improved Modeling of Mars' HDO Cycle Using a Mars' Global Climate Model. *Journal of Geophysical Research: Planets*, 127(8).

Vandaele, A. C., Lopez-Moreno, J.-J., Patel, M. R., Bellucci, G., Daerden, F., Ristic, B., Robert, S., Thomas, I. R., Wilquet, V., Allen, M., Alonso-Rodrigo, G., Altieri, F., Aoki, S., Bolsée, D., Clancy, T., Cloutis, E., Depiesse, C., Drummond, R., Fedorova, A., Formisano, V., Funke, B., González-Galindo, F., Geminale, A., Gérard, J.-C., Giuranna, M., Hetey, L., Ignatiev, N., Kaminski, J., Karatekin, O., Kasaba, Y., Leese, M., Lefèvre, F., Lewis, S. R., López-Puertas, M., López-Valverde, M., Mahieux, A., Mason, J., McConnell, J., Mumma, M., Neary, L., Neefs, E., Renotte, E., Rodriguez-Gomez, J., Sindoni, G., Smith, M., Stiepen, A., Trokhimovsky, A., Vander Auwera, J., Villanueva, G., Viscardy, S., Whiteway, J., Willame, Y., Wolff, M., and Team, T. N. (2018). NOMAD, an Integrated Suite of Three Spectrometers for the ExoMars Trace Gas Mission: Technical Description, Science Objectives and Expected Performance. *Space Science Reviews*, 214(5):80.

Viet, S., Knutsen, E. W., Montmessin, F., Witasse, O., Sanchez-Cano, B., Lester, M., and Wimmer-Schweingruber, R. (2022). Detecting and investigating space weather events around Mars with EDAC counters. In *73rd International Astronautical Congress Proceedings*, Paris. International Astronautical Federation.

Villanueva, G., Mumma, M., Novak, R., Radeva, Y., Käufl, H., Smette, A., Tokunaga, A., Khayat, A., Encrenaz, T., and Hartogh, P. (2013). A sensitive search for organics (CH4, CH3OH, H2CO, C2H6, C2H2, C2H4), hydroperoxyl (HO2), nitrogen compounds (N2O, NH3, HCN) and chlorine species (HCl, CH3Cl) on Mars using ground-based high-resolution infrared spectroscopy. *Icarus*, 223(1):11–27.

Villanueva, G. L., Liuzzi, G., Aoki, S., Stone, S. W., Brines, A., Thomas, I. R., Lopez-Valverde, M. A., Trompet, L., Erwin, J., Daerden, F., Ristic, B., Smith, M. D., Mumma, M. J., Faggi, S., Kofman, V., Robert, S., Neary, L., Patel, M., Bellucci, G., Lopez-Moreno, J. J., and Vandaele, A. C. (2022). The Deuterium Isotopic Ratio of Water Released From the Martian Caps as Measured With TGO/NOMAD. *Geophysical Research Letters*, 49(12).

Villanueva, G. L., Liuzzi, G., Crismani, M. M. J., Aoki, S., Vandaele, A. C., Daerden, F., Smith, M. D., Mumma, M. J., Knutsen, E. W., Neary, L., Viscardy, S., Thomas, I. R., Lopez-Valverde, M. A., Ristic, B., Patel, M. R., Holmes, J. A., Bellucci, G., Lopez-Moreno, J. J., and NOMAD team (2021). Water heavily fractionated as it ascends on Mars as revealed by ExoMars/NOMAD. *Science Advances*, 7(7):eabc8843.

Villanueva, G. L., Mumma, M. J., Novak, R. E., Käufl, H. U., Hartogh, P., Encrenaz, T., Tokunaga, A., Khayat, A., and Smith, M. D. (2015). Strong water isotopic anomalies in the martian atmosphere: Probing current and ancient reservoirs. *Science*, 348(6231):218–221.

Viúdez-Moreiras, D., Gómez-Elvira, J., Newman, C., Navarro, S., Marin, M., Torres, J., and de la Torre-Juárez, M. (2019). Gale surface wind characterization based on the Mars Science Laboratory REMS dataset. Part I: Wind retrieval and Gale's wind speeds and directions. *Icarus*, 319:909–925.

Vos, E. E. and Potgieter, M. S. (2016). Global Gradients for Cosmic-Ray Protons in the Heliosphere During the Solar Minimum of Cycle 23/24. *Solar Physics*, 291(7):2181–2195.

Vršnak, B., Sudar, D., and Ruždjak, D. (2005). The CME-flare relationship: Are there really two types of CMEs? *Astronomy & Astrophysics*, 435(3):1149–1157.

Wang, H. (2002). Martian clouds observed by Mars Global Surveyor Mars Orbiter Camera. *Journal of Geophysical Research*, 107(E10):5078.

Webber, W. and Lockwood, J. (1991). AN OBSERVATION OF A HELIOSPHERIC MAGNETIC CYCLE DEPENDENCE FOR THE INTEGRAL RADIAL GRADIENT OF E > 60 MEV COSMIC RAYS. *JOURNAL OF GEOPHYSICAL RESEARCH*, 96(A9):15,899–15,905.

Webster, C. R., Mahaffy, P. R., Atreya, S. K., Flesch, G. J., Mischna, M. A., Meslin, P.-Y., Farley, K. A., Conrad, P. G., Christensen, L. E., Pavlov, A. A., Martin-Torres, J., Zorzano, M.-P., McConnochie, T. H., Owen, T., Eigenbrode, J. L., Glavin, D. P., Steele, A., Malespin, C. A., Archer, P. D., Sutter, B., Coll, P., Freissinet, C., McKay, C. P., Moores, J. E., Schwenzer, S. P., Bridges, J. C., Navarro-Gonzalez, R., Gellert, R., Lemmon, M. T., and the MSL Science Team (2015). Mars methane detection and variability at Gale crater. *Science*, 347(6220):415–417.

Webster, C. R., Mahaffy, P. R., Atreya, S. K., Moores, J. E., Flesch, G. J., Malespin, C., McKay, C. P., Martinez, G., Smith, C. L., Martin-Torres, J., Gomez-Elvira, J., Zorzano, M.-P., Wong, M. H., Trainer, M. G., Steele, A., Archer, D., Sutter, B., Coll, P. J., Freissinet, C., Meslin, P.-Y., Gough, R. V., House, C. H., Pavlov, A., Eigenbrode, J. L., Glavin, D. P., Pearson, J. C., Keymeulen, D., Christensen, L. E., Schwenzer, S. P., Navarro-Gonzalez, R., Pla-García, J., Rafkin, S. C. R., Vicente-Retortillo, A., Kahanpää, H., Viudez-Moreiras, D., Smith, M. D., Harri, A.-M., Genzer, M., Hassler, D. M., Lemmon, M., Crisp, J., Sander, S. P., Zurek, R. W., and Vasavada, A. R. (2018).

Background levels of methane in Mars' atmosphere show strong seasonal variations. *Science*, 360(6393):1093–1096.

Webster, C. R., Mahaffy, P. R., Moores, J. E., Atreya, S. K., Flesch, G. J., Malespin, C. A., Teinturier, S. M., Kalucha, H., Smith, C. L., Viudez-Moreiras, D., Pla-Garcia, J., Rafkin, S. C. R., and Vasavada, A. R. (2021). Day-night differences in Mars methane suggest nighttime containment at Gale crater. *Astronomy & Astrophysics*.

Wibberenz, G. (2002). A simple concept for modeling cosmic ray modulation in the inner heliosphere during solar cycles 20–23. *Journal of Geophysical Research*, 107(A11):1353.

Wiens, R. C., Maurice, S., Robinson, S. H., Nelson, A. E., Cais, P., Bernardi, P., Newell, R. T., Clegg, S., Sharma, S. K., Storms, S., Deming, J., Beckman, D., Ollila, A. M., Gasnault, O., Anderson, R. B., André, Y., Michael Angel, S., Arana, G., Auden, E., Beck, P., Becker, J., Benzerara, K., Bernard, S., Beyssac, O., Borges, L., Bousquet, B., Boyd, K., Caffrey, M., Carlson, J., Castro, K., Celis, J., Chide, B., Clark, K., Cloutis, E., Cordoba, E. C., Cousin, A., Dale, M., Deflores, L., Delapp, D., Deleuze, M., Dirmyer, M., Donny, C., Dromart, G., George Duran, M., Egan, M., Ervin, J., Fabre, C., Fau, A., Fischer, W., Forni, O., Fouchet, T., Fresquez, R., Frydenvang, J., Gasway, D., Gontijo, I., Grotzinger, J., Jacob, X., Jacquinod, S., Johnson, J. R., Klisiewicz, R. A., Lake, J., Lanza, N., Laserna, J., Lasue, J., Le Mouélic, S., Legett, C., Leveille, R., Lewin, E., Lopez-Reyes, G., Lorenz, R., Lorigny, E., Love, S. P., Lucero, B., Madariaga, J. M., Madsen, M., Madsen, S., Mangold, N., Manrique, J. A., Martinez, J. P., Martinez-Frias, J., McCabe, K. P., McConnochie, T. H., McGlown, J. M., McLennan, S. M., Melikechi, N., Meslin, P.-Y., Michel, J. M., Mimoun, D., Misra, A., Montagnac, G., Montmessin, F., Mousset, V., Murdoch, N., Newsom, H., Ott, L. A., Ousnamer, Z. R., Pares, L., Parot, Y., Pawluczyk, R., Glen Peterson, C., Pilleri, P., Pinet, P., Pont, G., Poulet, F., Provost, C., Quertier, B., Quinn, H., Rapin, W., Reess, J.-M., Regan, A. H., Reyes-Newell, A. L., Romano, P. J., Royer, C., Rull, F., Sandoval, B., Sarrao, J. H., Sautter, V., Schoppers, M. J., Schröder, S., Seitz, D., Shepherd, T., Sobron, P., Dubois, B., Sridhar, V., Toplis, M. J., Torre-Fdez, I., Trettel, I. A., Underwood, M., Valdez, A., Valdez, J., Venhaus, D., and Willis, P. (2021). The SuperCam Instrument Suite on the NASA Mars 2020 Rover: Body Unit and Combined System Tests. *Space Science Reviews*, 217(1):4.

Williams, R. M. E., Grotzinger, J. P., Dietrich, W. E., Gupta, S., Sumner, D. Y., Wiens, R. C., Mangold, N., Malin, M. C., Edgett, K. S., Maurice, S., Forni, O., Gasnault, O., Ollila, A., Newsom, H. E., Dromart, G., Palucis, M. C., Yingst, R. A., Anderson, R. B., Herkenhoff, K. E., Le Mouélic, S., Goetz, W., Madsen, M. B., Koefoed, A., Jensen, J. K., Bridges, J. C., Schwenzer, S. P., Lewis, K. W., Stack, K. M., Rubin, D., Kah, L. C., Bell, J. F., Farmer, J. D., Sullivan, R., Van Beek, T., Blaney, D. L., Pariser, O., Deen, R. G., MSL Science Team, Kemppinen, O., Bridges, N., Johnson, J. R., Minitti, M., Cremers, D., Edgar, L., Godber, A., Wadhwa, M., Wellington, D., McEwan, I., Newman, C., Richardson, M., Charpentier, A., Peret, L., King, P., Blank, J., Weigle, G., Schmidt, M., Li, S., Milliken, R., Robertson, K., Sun, V., Baker, M., Edwards, C., Ehlmann, B., Farley, K., Griffes, J., Miller, H., Newcombe, M., Pilorget, C., Rice, M., Siebach, K., Stolper, E., Brunet, C., Hipkin, V., Léveillé, R., Marchand, G., Sobrón Sánchez, P., Favot, L., Cody, G., Steele, A., Flückiger, L., Lees, D., Nefian, A., Martin, M., Gailhanou, M., Westall, F., Israël, G., Agard, C., Baroukh, J., Donny, C., Gaboriaud, A., Guillemot, P., Lafaille, V., Lorigny, E., Paillet, A., Pérez, R., Saccoccio, M., Yana, C., Aparicio, C. A., Caride Rodríguez, J., Carrasco Blázquez, I., Gómez Gómez, F., Elvira, J. G., Hettrich, S., Lepinette Malvitte, A., Marín Jiménez, M., Frías, J. M., Soler, J. M., Torres, F. J. M., Molina Jurado, A., Sotomayor, L. M., Muñoz Caro, G., Navarro López, S., González, V. P., García, J. P., Rodriguez Manfredi, J. A., Planelló, J. J. R., Alejandra Sans Fuentes, S., Sebastian Martinez, E., Torres Redondo, J., O'Callaghan, R. U., Zorzano Mier, M.-P., Chipera, S., Lacour, J.-L., Mauchien, P., Sirven, J.-B., Manning, H., Fairén, A., Hayes, A., Joseph, J., Squyres,

S., Thomas, P., Dupont, A., Lundberg, A., Melikechi, N., Mezzacappa, A., DeMarines, J., Grinspoon, D., Reitz, G., Prats, B., Atlaskin, E., Genzer, M., Harri, A.-M., Haukka, H., Kahanpää, H., Kauhanen, J., Paton, M., Polkko, J., Schmidt, W., Siili, T., Fabre, C., Wray, J., Wilhelm, M. B., Poitrasson, F., Patel, K., Gorevan, S., Indyk, S., Paulsen, G., Bish, D., Schieber, J., Gondet, B., Langevin, Y., Geffroy, C., Baratoux, D., Berger, G., Cros, A., Uston, C. D., Lasue, J., Lee, Q.-M., Meslin, P.-Y., Pallier, E., Parot, Y., Pinet, P., Schröder, S., Toplis, M., Lewin, , Brunner, W., Heydari, E., Achilles, C., Oehler, D., Sutter, B., Cabane, M., Coscia, D., Szopa, C., Robert, F., Sautter, V., Nachon, M., Buch, A., Stalport, F., Coll, P., François, P., Raulin, F., Teinturier, S., Cameron, J., Clegg, S., Cousin, A., DeLapp, D., Dingler, R., Jackson, R. S., Johnstone, S., Lanza, N., Little, C., Nelson, T., Williams, R. B., Jones, A., Kirkland, L., Treiman, A., Baker, B., Cantor, B., Caplinger, M., Davis, S., Duston, B., Fay, D., Hardgrove, C., Harker, D., Herrera, P., Jensen, E., Kennedy, M. R., Krezoski, G., Krysak, D., Lipkaman, L., McCartney, E., McNair, S., Nixon, B., Posiolova, L., Ravine, M., Salamon, A., Saper, L., Stoiber, K., Supulver, K., Van Beek, J., Zimdar, R., French, K. L., Iagnemma, K., Miller, K., Summons, R., Goesmann, F., Hviid, S., Johnson, M., Lefavor, M., Lyness, E., Breves, E., Dyar, M. D., Fassett, C., Blake, D. F., Bristow, T., DesMarais, D., Edwards, L., Haberle, R., Hoehler, T., Hollingsworth, J., Kahre, M., Keely, L., McKay, C., Bleacher, L., Brinckerhoff, W., Choi, D., Conrad, P., Dworkin, J. P., Eigenbrode, J., Floyd, M., Freissinet, C., Garvin, J., Glavin, D., Harpold, D., Mahaffy, P., Martin, D. K., McAdam, A., Pavlov, A., Raaen, E., Smith, M. D., Stern, J., Tan, F., Trainer, M., Meyer, M., Posner, A., Voytek, M., Anderson, R. C., Aubrey, A., Beegle, L. W., Behar, A., Brinza, D., Calef, F., Christensen, L., Crisp, J. A., DeFlores, L., Feldman, J., Feldman, S., Flesch, G., Hurowitz, J., Jun, I., Keymeulen, D., Maki, J., Mischna, M., Morookian, J. M., Parker, T., Pavri, B., Schoppers, M., Sengstacken, A., Simmonds, J. J., Spanovich, N., De La Torre Juarez, M., Vasavada, A. R., Webster, C. R., Yen, A., Archer, P. D., Cucinotta, F., Jones, J. H., Ming, D., Morris, R. V., Niles, P., Rampe, E., Nolan, T., Fisk, M., Radziemski, L., Barraclough, B., Bender, S., Berman, D., Dobrea, E. N., Tokar, R., Vaniman, D., Leshin, L., Cleghorn, T., Huntress, W., Manhès, G., Hudgins, J., Olson, T., Stewart, N., Sarrazin, P., Grant, J., Vicenzi, E., Wilson, S. A., Bullock, M., Ehresmann, B., Hamilton, V., Hassler, D., Peterson, J., Rafkin, S., Zeitlin, C., Fedosov, F., Golovin, D., Karpushkina, N., Kozyrev, A., Litvak, M., Malakhov, A., Mitrofanov, I., Mokrousov, M., Nikiforov, S., Prokhorov, V., Sanin, A., Tretyakov, V., Varenikov, A., Vostrukhin, A., Kuzmin, R., Clark, B., Wolff, M., McLennan, S., Botta, O., Drake, D., Bean, K., Lemmon, M., Lee, E. M., Sucharski, R., Hernández, M. D. P., Blanco Ávalos, J. J., Ramos, M., Kim, M.-H., Malespin, C., Plante, I., Muller, J.-P., González, R. N., Ewing, R., Boynton, W., Downs, R., Fitzgibbon, M., Harshman, K., Morrison, S., Kortmann, O., Williams, A., Lugmair, G., Wilson, M. A., Jakosky, B., Zunic, T. B., Frydenvang, J., Kinch, K., Stipp, S. L. S., Boyd, N., Campbell, J. L., Gellert, R., Perrett, G., Pradler, I., VanBommel, S., Jacob, S., Owen, T., Rowland, S., Savijärvi, H., Boehm, E., Böttcher, S., Burmeister, S., Guo, J., Köhler, J., García, C. M., Mellin, R. M., Schweingruber, R. W., McConnochie, T., Benna, M., Franz, H., Bower, H., Brunner, A., Blau, H., Boucher, T., Carmosino, M., Atreya, S., Elliott, H., Halleaux, D., Rennó, N., Wong, M., Pepin, R., Elliott, B., Spray, J., Thompson, L., Gordon, S., Williams, J., Vasconcelos, P., Bentz, J., Nealson, K., Popa, R., Moersch, J., Tate, C., Day, M., Kocurek, G., Hallet, B., Sletten, R., Francis, R., McCullough, E., Cloutis, E., Ten Kate, I. L., Arvidson, R., Fraeman, A., Scholes, D., Slavney, S., Stein, T., Ward, J., Berger, J., and Moores, J. E. (2013). Martian Fluvial Conglomerates at Gale Crater. *Science*, 340(6136):1068–1072.

Wilson, R. J. (1997). A general circulation model simulation of the Martian polar warming. *Geophysical Research Letters*, 24(2):123–126.

Witasse, O., Duxbury, T., Chicarro, A., Altobelli, N., Andert, T., Aronica, A., Barabash, S., Bertaux, J.-L., Bibring, J.-P., Cardesin-Moinelo, A., Cichetti, A., Companys, V., Dehant, V., Denis, M., Formisano, V., Futaana, Y., Giuranna, M., Gondet, B., Heather, D., Hoffmann, H., Holmström, M., Manaud, N., Martin, P., Matz, K.-D., Montmessin, F., Morley, T., Mueller, M., Neukum, G.,

Oberst, J., Orosei, R., Pätzold, M., Picardi, G., Pischel, R., Plaut, J., Reberac, A., Pardo Voss, P., Roatsch, T., Rosenblatt, P., Remus, S., Schmedemann, N., Willner, K., and Zegers, T. (2014). Mars Express investigations of Phobos and Deimos. *Planetary and Space Science*, 102:18–34.

Wolkenberg, P., Giuranna, M., Smith, M., Grassi, D., and Amoroso, M. (2020). Similarities and Differences of Global Dust Storms in MY 25, 28, and 34. *Journal of Geophysical Research: Planets*, 125(3).

Wray, J. J., Hansen, S. T., Dufek, J., Swayze, G. A., Murchie, S. L., Seelos, F. P., Skok, J. R., Irwin, R. P., and Ghiorso, M. S. (2013). Prolonged magmatic activity on Mars inferred from the detection of felsic rocks. *Nature Geoscience*, 6(12):1013–1017.

Wright, W. H. (1925). Photographs of Mars made with light of different colors. *Lick Observatory Bulletins*, 12:48–61.

Yin, A. (2012). Structural analysis of the Valles Marineris fault zone: Possible evidence for large-scale strike-slip faulting on Mars. *Lithosphere*, 4(4):286–330.

Zeitlin, C., Boynton, W., Mitrofanov, I., Hassler, D., Atwell, W., Cleghorn, T. F., Cucinotta, F. A., Dayeh, M., Desai, M., Guetersloh, S. B., Kozarev, K., Lee, K. T., Pinsky, L., Saganti, P., Schwadron, N. A., and Turner, R. (2010). Mars Odyssey measurements of galactic cosmic rays and solar particles in Mars orbit, 2002-2008: MARS ODYSSEY MEASUREMENTS. *Space Weather*, 8(11):n/a–n/a.

Zent, A. P., Hecht, M. H., Cobos, D. R., Wood, S. E., Hudson, T. L., Milkovich, S. M., DeFlores, L. P., and Mellon, M. T. (2010). Initial results from the thermal and electrical conductivity probe (TECP) on Phoenix. *Journal of Geophysical Research*, 115:E00E14.

Zhang, C., Rong, Z., Klinger, L., Nilsson, H., Shi, Z., He, F., Gao, J., Li, X., Futaana, Y., Ramstad, R., Wang, X., Holmström, M., Barabash, S., Fan, K., and Wei, Y. (2022a). Three-Dimensional Configuration of Induced Magnetic Fields Around Mars. *Journal of Geophysical Research: Planets*, 127(8).

Zhang, X., Berkinsky, D., Markus, C. R., Chitturi, S. R., Grieman, F. J., Okumura, M., Luo, Y., Yung, Y. L., and Sander, S. P. (2022b). Reaction of methane and UV-activated perchlorate: Relevance to heterogeneous loss of methane in the atmosphere of Mars. *Icarus*, 376:114832.

Zirker, J. B. (1977). Coronal holes and high-speed wind streams. *Reviews of Geophysics*, 15(3):257.

Zou, Y., Zhu, Y., Bai, Y., Wang, L., Jia, Y., Shen, W., Fan, Y., Liu, Y., Wang, C., Zhang, A., Yu, G., Dong, J., Shu, R., He, Z., Zhang, T., Du, A., Fan, M., Yang, J., Zhou, B., Wang, Y., and Peng, Y. (2021). Scientific objectives and payloads of Tianwen-1, China's first Mars exploration mission. *Advances in Space Research*, 67(2):812–823.

Zuber, M. T., Solomon, S. C., Phillips, R. J., Smith, D. E., Tyler, G. L., Aharonson, O., Balmino, G., Banerdt, W. B., Head, J. W., Johnson, C. L., Lemoine, F. G., McGovern, P. J., Neumann, G. A., Rowlands, D. D., and Zhong, S. (2000). Internal Structure and Early Thermal Evolution of Mars from Mars Global Surveyor Topography and Gravity. *Science*, 287(5459):1788–1793.